

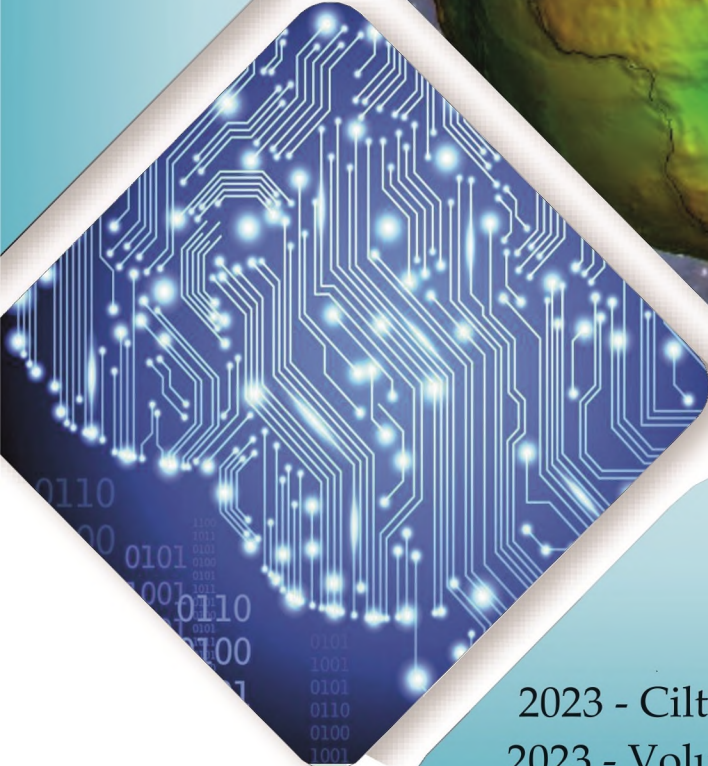


# Konya Mühendislik Bilimleri Dergisi

## Konya Journal of Engineering Sciences



**(KONJES)**  
E-ISSN: 2667-8055



2023 - Cilt : 11 - Sayı : 4  
2023 - Volume - Issue : 4

**KONYA JOURNAL OF ENGINEERING SCIENCES (KONJES)  
KONYA MÜHENDİSLİK BİLİMLERİ DERGİSİ**

**HAKEMLİ DERGİDİR**

OWNER/SAHİBİ

Owner on Behalf of Engineering and Natural Sciences Faculty of Konya Technical University **Prof. Dr. Ali KÖKEN**  
Konya Teknik Üniversitesi Mühendislik ve Doğa Bilimleri Fakültesi Adına Dekan **Prof. Dr. Ali KÖKEN**

Editor-in-Chief/Şef Editör

**Prof. Dr. Mustafa TABAKCI**

Editors/Editörler

**Prof. Dr. Halife KODAZ**

**Assoc. Prof. Dr. Ömer Kaan BAYKAN**

Section Editors/Alan Editörleri

Prof. Dr. Niyazi B L M

Assoc. Prof. Dr. Farabi TEMEL

Assoc. Prof. Dr. smail NCE

Assoc. Prof. Dr. O uzhan ÖZTÜRK

**Assoc. Prof. Dr. Ömer Kaan BAYKAN**

**Assoc. Prof. Dr. Selim DO AN**

**Assoc. Prof. Dr. Sercan BÜLBÜL**

**Assoc. Prof. Dr. Volkan KALEM**

**Assist. Prof. Dr. Alper DÖYEN**

Assist. Prof. Dr. Kemal ERDO AN

Assist. Prof. Dr. Muhammed Arif EN

Assist. Prof. Dr. Muharrem Hilmi AKSOY

Advisory Board/Danışma Kurulu

**Prof.Dr. Ferruh YILDIZ, Konya Technical University**

**Prof.Dr. Reşat ULUSAY, Hacettepe University**

**Prof.Dr. Ibaraki SOICHI, Kyoto University**

**Prof.Dr. Matchavariani LIA, Tbilisi State University**

**Prof.Dr. Seref SAGIROGLU, Gazi University**

**Prof.Dr. Vijay P. SINGH, Texas A and M University**

**Prof.Dr.-Ing. Rudolf STAIGER, Bochum University of Applied Sciences**

**Prof.Dr. Chryssy POTSIOU, National Technical University of Athens**

**Prof.Dr. Lena HALOUNOVA, Czech Technical University**

**Prof.Dr. Petros PATIAS, The Aristotle University**

**Prof.Dr. Sitki KULUR, Istanbul Technical University**

Language Editing/Yabancı Dil Editörü

**Prof. Dr. Ali BERKTAY**

Secretary/Sekreter

Assist. Prof. Dr. Emel Zeray ÖZTÜRK

Composition and Printing/Baskı ve Dizgi

Assist. Prof. Dr. smail KOÇ

**Res. Assist. Emir Ali D NSEL**

**Res. Assist. Aybüke BABADA**

Correspondance Address/ Yazışma Adresi

Konya Teknik Üniversitesi Mühendislik ve Doğa Bilimleri Fakültesi Dekanlığı

42075-Kampüs, Selçuklu, Konya-TURKEY

Tel : 0 332 223 88 18

Fax : 0 332 241 06 35

E-mail : konjes@ktun.edu.tr

Web : <http://dergipark.org.tr/konjes>

## **Editorial Board/Yayın Kurulu**

Ahmet Afsin Kulaksiz, Konya Technical University, TURKEY

Alla Anohina-Naumeca, Riga Technical University, LATVIA

Ashok K. Mishra, Clemson University, USA

Baris Binici, Middle East Technical University, TURKEY

Coskun Bayrak, University of Arkansas, USA

Demetrio Fuentes Ferrera, University of Castilla-La Mancha, SPAIN

Fahrettin Ozturk, The Petroleum Institute, UAE

Haci Murat Yilmaz, Aksaray University, TURKEY

Heinz Ruther University of Cape Town, SOUTH AFRICA

Homayoun Moghimi, Payame Noor University, IRAN

Ihsan Ozkan, Konya Technical University, TURKEY

John Trinder, The University of New South Wales, AUSTRALIA

Kerim Kocak, Konya Technical University, TURKEY

Loredana Judele, Technical University of Iasi, ROMANIA

Mohamed Bouabaz, Université 20 août 1955-Skikda, ALGERIA

Mohd Arif Wani, California State University, USA

Mortaza Yari, University of Tabriz, IRAN

Ömer Aydan, University of the Ryukyus, JAPAN

Sanchoy K. Das, New Jersey Institute of Technology, USA

Selim Dogan, Konya Technical University, TURKEY

Spase Shumka, Agricultural University of Tirana, ALBANIA

Tahira Geroeva, Baku State University, AZERBAIJAN

Vladimir Androkhonov, Novosibirsk Soil Research Institute, RUSSIA

Ali Kocak, Yildiz Technical University, TURKEY

Alpaslan Yarar, Konya Technical University, TURKEY

Ataur Rahman, University of Western Sydney, AUSTRALIA

Cihan Varol Sam Houston State University, USA

Dan Stumbea, Alexandru Ioan Cuza University of Iasi, ROMANIA

Eva Burgetova, Czech Technical University, CZECH REPUBLIC

Georgieva Lilia, Heriot-Watt University, UNITED KINGDOM

Halil Kursad Ersoy, Konya Technical University, TURKEY

Hi-Ryong Byun, Pukyong National University, SOUTH KOREA

Huseyin Deveci, Konya Technical University, TURKEY

Iraida Samofalova, Perm University, RUSSIA

Juan Maria Menendez Aguado, University of de Oviedo, SPAIN

Laramie Vance Potts, New Jersey Institute of Technology, USA

Mila Koeva, University of Twente, NETHERLANDS

Mohamed Metwaly Abu Anbar, Tanta University, EGYPT

Moonis Ali Khan, King Saud University, KSA

Murat Karakus, University of Adelaide, AUSTRALIA

Saadettin Erhan Kesen, Konya Technical University, TURKEY

Selcuk Kursat Isleyen, Gazi University, TURKEY

Shukri Maxhuni, Prizen University, KOSOVA REPUBLIC

Syed Tufail Hussain Sherazi, University of Sindh, PAKISTAN

Thomas Niedoba, AGH University of Science and Technology, POLAND

Zoran Sapuric, University American College Skopje, MACEDONIA

**KONYA MÜHENDİSLİK BİLİMLERİ DERGİSİ**  
**Konya Journal of Engineering Sciences**  
**(KONJES)**

ISSN 2667 – 8055 (Elektronik/Electronic)

---

Cilt	11	Aralık	2023	Sayı	4
Volume	11	December	2023	Issue	4

---

**İÇİNDEKİLER (CONTENTS)**

**Araştırma Makalesi (Research Article)**

**DEVELOPMENT of Cu MATRIX COMPOSITE CONTACTORS REINFORCED by NICKEL COATED SiC**

Cemalettin ARVAS, İbrahim ALTINSOY, Tuba YENER, Gözde Fatma ÇELEBİ EFE ..... 894-904

**FABRICATION OF TERNARY SILICA-CALCIUM-MAGNESIUM AEROGELS: EFFECT OF FEEDING RATE AND MOLAR RATIO ON PROPERTIES**

Burcu KARAKUZU İKİZLER, Pınar TERZİOĞLU, Tülay Merve TEMEL SOYLU, Sevil YÜCEL .....905-915

**DÖNER DARBELİ DELİK DELME PERFORMANS ANALİZİ ve UYGUN UÇ SEÇİMİ: KAYSERİ HİMMETDEDE OCAĞI ÖRNEĞİ**

Evaluation of Percussive Drilling and Selection of Suitable Bit: The Case of Kayseri Himmetdede Quarry

Mehmet OSMANOĞLU ..... 916-927

**STATISTICAL METHOD FOR ESTIMATING SELECTED GEOTECHNICAL PROPERTIES OF QUATERNARY SEDIMENT**

Abbas Jawad AL-TAIE ..... 928-941

**DEMOGRAFİK ÖZELLİKLERİN ÇEVİRİMİÇİ MARKET ALIŞVERİŞİ KULLANIMINA ETKİSİNİN MAKİNE ÖĞRENMESİ YÖNTEMLERİ İLE TAHMİNİ**

Prediction of The Effect of Demographic Features on Online Market Shopping Using Machine Learning Methods

Burak BAHÇIVAN, Atınc YILMAZ ..... 942-957

**SHIELDING EFFECTIVENESS OF CFRP COMPOSITES**

Ferhat YILDIRIM ..... 958-972

**IMPROVEMENT OF HIGH PLASTICITY CLAY BY USING FILTER SLUDGE**

İlyas ÖZKAN, Yavuz YENGİNAR ..... 973-985

**MINIMIZING ERRORS IN PCB MILLING PROCESSES THROUGH A 3-AXIS PCB ROUTER**

Emrehan YAVSAN, Burak SELVI, Tarik UNLER, İlhan İLHAN ..... 986-1005

<b>A COMPARATIVE STUDY OF RELEASE KINETICS BEHAVIOR MODELS AND SHELF LIFE ASSESSMENT OF BACITRACIN ZINC-LOADED PLA COMPOSITES</b> Ali Can ÖZARSLAN, Fatih CİFTÇİ .....	1006-1015
<b>DETERMINING THE OPTIMUM PARKING ANGLES FOR VARIOUS RECTANGULAR-SHAPED PARKING AREAS: A PARTICLE SWARM OPTIMIZATION-BASED MODEL</b> Ziya ÇAKICI, Abdullah Tahir ŞENSOY .....	1016-1034
<b>ANALYSIS OF SPATIAL AND TEMPORAL VARIABILITY OF AEROSOL OPTICAL DEPTH OVER KARABUK USING MODIS</b> Duygu ARIKAN, Ferruh YILDIZ .....	1035-1046
<b>A TWO STAGE MODEL FOR DAY-AHEAD ELECTRICITY PRICE FORECASTING: INTEGRATING EMPIRICAL MODE DECOMPOSITION AND CATBOOST ALGORITHM</b> Ceyhun YILDIZ .....	1047-1060
<b>OLIVE LEAF EXTRACT INCORPORATED CHITOSAN FILMS FOR ACTIVE FOOD PACKAGING</b> Aslıhan KAZAN, Fatma DEMİRÇİ .....	1061-1072
<b>THE IMPACT OF EUROPEAN UNION LEGISLATION ON CADASTRAL SURVEYORS: A COMPARATIVE ANALYSIS AND RESULTS IN THE EUROPEA AND TÜRKİYE</b> Orhan ERCAN .....	1073-1095
<b>THE EFFECT OF THE AEGEAN SEA EARTHQUAKE, OCCURRED ON OCTOBER 30, 2020, ON TUSAGA STATIONS</b> Tunahan GUNDOĞAN, Sercan BÜLBÜL, Cevat İNAL .....	1096-1105
<b>SPACE COOLING WITH GROUNDWATER PUMPED BY A SOLAR DRIVEN PUMP</b> Hakan DUMRUL, Selçuk SELİMLİ, Sezayi YILMAZ, Baris KORKMAZ .....	1106-1117
<b>GENDER IDENTIFICATION FROM LEFT HAND-WRIST X-RAY IMAGES WITH A HYBRID DEEP LEARNING METHOD</b> Cüneyt ÖZDEMİR, Mehmet Ali GEDİK, Hüdaverdi KÜÇÜKER, Yılmaz KAYA .....	1118-1133
<b>THEORETICAL ANALYSIS OF SOLAR THERMOELECTRIC GENERATORS INTEGRATED WITH RADIATIVE COOLER</b> Aminu YUSUF .....	1134-1145



## DEVELOPMENT of Cu MATRIX COMPOSITE CONTACTORS REINFORCED by NICKEL COATED SiC

<sup>1</sup> Cemalettin ARVAS , <sup>2</sup> İbrahim ALTINSOY , <sup>2\*</sup> Tuba YENER , <sup>1</sup> Gözde Fatma ÇELEBİ EFE 

<sup>1</sup> Sakarya University of Applied Sciences, Faculty of Technology, Department of Metallurgical and Materials Engineering, Sakarya, TÜRKİYE

<sup>2</sup> Sakarya University, Faculty of Engineering, Department of Metallurgical and Materials Engineering, Sakarya, TÜRKİYE

<sup>1</sup>y195012057@subu.edu.tr, <sup>2</sup>ialtinsoy@sakarya.edu.tr, <sup>2</sup>tcerezci@sakarya.edu.tr, <sup>1</sup>gcelebi@subu.edu.tr

### Highlights

- 1 In this study, Cu-Ni SiC (Copper-Nickel coated SiC) composite samples were produced by electric current assisted sintering (ECAS) method
- 2 The matrix component Copper powder was successfully produced by cementation method.
- 3 SiC powders were coated with Ni by electroless plating method.



## DEVELOPMENT of Cu MATRIX COMPOSITE CONTACTORS REINFORCED by NICKEL COATED SiC

<sup>1</sup> Cemalettin ARVAS , <sup>2</sup> İbrahim ALTINSOY , <sup>2\*</sup> Tuba YENER , <sup>1</sup> Gözde Fatma ÇELEBİ EFE 

<sup>1</sup> Sakarya University of Applied Sciences, Faculty of Technology, Department of Metallurgical and Materials Engineering, Sakarya, TÜRKİYE

<sup>2</sup> Sakarya University, Faculty of Engineering, Department of Metallurgical and Materials Engineering, Sakarya, TÜRKİYE

<sup>1</sup>y195012057@subu.edu.tr, <sup>2</sup>ialtinsoy@sakarya.edu.tr, <sup>2\*</sup>tcerezci@sakarya.edu.tr, <sup>1</sup>gcelebi@subu.edu.tr

(Received: 23.02.2023; Accepted in Revised Form: 30.07.2023)

**ABSTRACT:** In this study, Cu-Ni coated SiC composite samples were produced by electric current assisted sintering (ECAS) method by adding electroless nickel coated SiC powders to copper powders produced by cementation method at the ratios of 0.5, 1 and 1.5 wt%. The relative densities of the produced samples were measured by Archimedes' principle, their microstructures were examined by SEM-EDS, dominant phases were determined by XRD technique; microhardness and electrical conductivity measurements were made. The relative density of undoped copper was determined as 99.42% and the relative density value of Cu-Ni SiC composite samples decreased to 98.35% at most with increasing SiC ratio. The hardness values of Cu-Ni SiC composite samples increased from 120HV to 145HV with the addition of SiC; electrical conductivity values decreased from 90.41 IACS (International annealed copper standard) to 58.56 IACS.

**Keywords:** Cu-Ni SiC, Copper Matrix Composite, Cementation, Relative Density, IACS

### 1. INTRODUCTION

Copper is the 26th most abundant element on earth. The electrical conductivity of copper ranks 2nd after silver among all metals. It has an important place in the industry and has a wide range of uses because it makes alloys such as brass and bronze [1]–[3]. There are different copper production methods depending on the properties of the ore used as raw material. These methods are grouped as hydrometallurgy, pyrometallurgy and electrometallurgy.

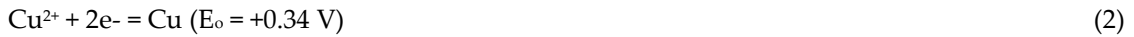
In this study, the matrix material was produced by precipitating copper powder from copper sulphate solution by cementation method. Reduction and precipitation of copper from dilute sulfuric acid leach solutions with the help of iron is the oldest hydrometallurgical method. The process of reducing and precipitating a metal in its aqueous solution with the help of another metal without the aid of any electric current is called cementation. In the cementation method, the more noble metal ion in the solution is precipitated by adding a more basic metal to the solution in a neutral state. In this method, the metal reduced from the solution is called "cement" and the more basic metal added to the solution is called "cementator". The general reaction equation for this precipitation process is as follows :



In this equation, "N" indicates the more noble metal and "M" indicates the reducing metal. In copper cementation, Cu<sup>2+</sup> ions are reduced by more basic metals such as iron, zinc, aluminum as a result of the electrochemical process. The reactions that take place in the cementation of copper with iron are as follows;

Semicellular reactions;

\*Corresponding Author: Tuba YENER, [tcerezci@sakarya.edu.tr](mailto:tcerezci@sakarya.edu.tr)



Full reaction;



The reaction for copper sulphate solution is as follows;



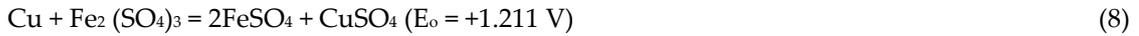
In addition to these, there are also side reactions that can occur in the solution, which can be shown as the main factors that reduce the efficiency of the cementation process. Solutions used on an industrial scale may contain  $\text{Fe}^{2+}$  and  $\text{Fe}^{3+}$  ions. Another side reaction that will occur in this case;



The other reaction that may occur is as follows;



The reverse reaction that can occur with reduced copper is as follows;



Since waste copper solutions usually contain sulfuric acid, another reaction that can occur during the cementation of copper with iron is as follows;



Copper and its alloys are very important engineering materials to date due to their high corrosion resistance, excellent electrical and thermal conductivity, attractive appearance, high ductility and ease of forming. They have the best electrical conductivity after silver and very high thermal conductivity between silver and gold [4]. However, due to their high cost, silver and gold are rarely used in conductive applications. In terms of bulk applications, the most commonly used conductive materials are aluminium and copper. Copper is preferred mainly because of its higher conductivity and higher strength compared to aluminium [5], [6]. A significant disadvantage of copper is its strength of 390 MPa. This is because pure copper, even if hardened by cold forming, recrystallizes at temperatures close to 100°C and therefore loses its strength quickly. Adequate electrical conductivity and high strength and hardness compared to pure copper can be obtained by alloying pure copper. However, since it is not desirable to reduce the electrical conductivity too much, the alloying elements to be added to pure copper

are only 2%, and in many applications in smaller amounts. The disadvantage of low-alloyed copper used in conductivity applications is the rapid loss of properties due to the coarsening of precipitate particles at high temperature. In order to solve this problem, copper matrix metal matrix composites reinforced with ceramics such as oxide, boride and carbide have been developed due to the stability of ceramic particles at high temperatures [3]. In this study, in order to increase the strength of the copper matrix, it is aimed to reinforce it with SiC due to its high elastic modulus and high thermal conductivity. In order to avoid wetting problems at the Cu and SiC interface, SiC particles were coated with Nickel by electroless plating method.

Electroless nickel plating is a pretreatment technique especially for materials with high surface resistance [7]. Electroless nickel plating is the more popular variation of electroless plating with some different properties [8]. Electroless nickel plating technique is based on the conversion of nickel ions into nickel metal by reducing the effect of nickel ions on the catalytic material surface. It was first developed by Brenner and Riddel in 1946. A reductant, sodium hypophosphite, added by the researchers to remove unwanted oxidation products from electrolytic nickel plating baths, led to nickel deposition and thus a very important industrial metal plating method was permanently discovered. The major advantage of electrolytic nickel plating is that it provides a uniform coating thickness so that it can be easily coated on uneven surfaces and in any contact with the solution [9]. It is used in almost every field. It has a wide range of applications from simple knitting needles to aerospace applications. The most important feature of electroless nickel coatings is wear resistance and corrosion resistance [8], [9].

Cu-SiC composites combine both the superior ductility and toughness of copper and the high strength and high modulus of SiC reinforcements. They can be used as electrical contact materials in relays, contactors, switches, circuit breakers and other switchgear components [10].

In this study, Cu-Ni SiC composite samples were obtained by ECAS method by using the powder mixtures of cemented copper and Ni coated SiC. The microstructure and morphologies of these samples were examined by SEM, phase structures were dedected by SEM-EDS and XRD analysis and their relative densities, hardnesses and electrical conductivities were measured and compared with each other.

## 2. MATERIAL AND METHODS

### 2.1. 1. Copper Powder Production

Anhydrous  $\text{CuSO}_4$  (99% purity, Merck),  $\text{H}_2\text{SO}_4$  (Sulfuric Acid) (99% purity), Pure Fe Powder (99% purity, 10  $\mu\text{m}$  Merck) and Distilled Water were used to produce Cu powders by cementation. Copper powder was obtained by precipitation from 0.1 M  $\text{CuSO}_4$  solution by cementation method. The equation for the cementation method is as in Equation 10.



The production flow chart of copper powder is given in Figure 1.

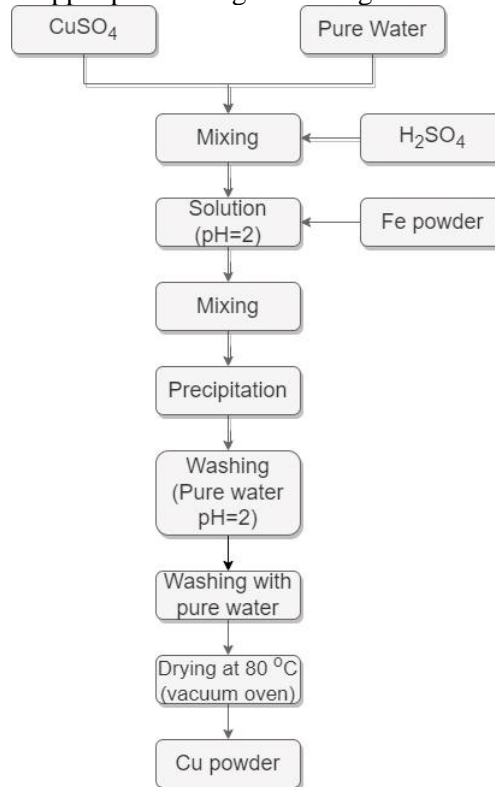


**Figure 1.** Schematic representation of the production of cemented copper powder

### 2.2. Nickel Plating of SiC

For electroless Ni plating of SiC powders; SiC powder (Struers 80-99.9% purity),  $\text{SnCl}_2$  solution (Sigma-Aldrich, 99.9% purity), purified water, HCl Acid, Ammonia ( $\text{NH}_3$ ) (Sigma-Aldrich, 99% purity), Sodium stearate (Sigma-Aldrich, 99% purity), and nickel powder (Sigma-Aldrich 1 $\mu\text{m}$ ) were used. The main purpose of electroless Ni coating on SiC is to increase the wetting between SiC and Cu. In order to perform this process, the solution prepared from the mixture of SiC,  $\text{SnCl}_2$ ,  $\text{H}_2\text{O}$ , and HCl weighed in cytometric ratios was stirred with a magnetic stirrer at 1500 rpm for 1 hour. After filtration, activation, coating, washing and drying, Ni coating on SiC powders were obtained. The main objective of electroless nickel plating technique is to keep the coating thickness at minimum level and to maximize the wettability with the matrix material. The electroless Ni coating process is shown schematically in Figure 2.

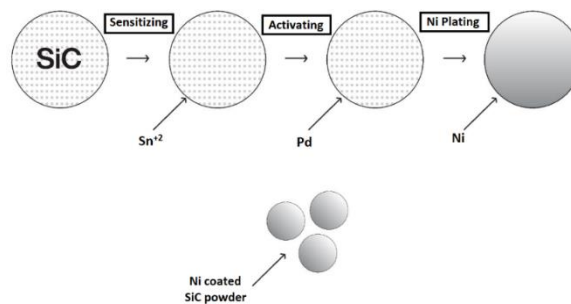


**Figure 2.** Schematic representation of Electroless Ni coating on SiC.

After sintering, the compacts were hot pressed at 400°C under 200 MPa pressure with a uniaxial hydraulic press. After pressing samples were grinded and metallographically prepared. The schematic representation of sintering by ECAS method is given in Fig. 3. The produced composite samples were grinded to 1200 grit sandpaper level and polished with 0.3  $\mu\text{m}$  alumina in accordance with metallographic sample preparation methods. The polished samples were characterized by SEM-EDS, hardness and electrical conductivity methods.

### 2.3. Fabrication of Copper-Ni coated SiC Composites

Cemented copper powders and Ni coated SiC powders were homogeneously mixed as Cu-0,5-1,5wt.% Ni-SiC and pressed under 150 MPa pressure in a uniaxial hydraulic press to obtain compact samples. The compacts were embedded in graphite powder and placed in the mould in an ECAS process

Using ECAS for sample consolidation results in shorter process and faster heating times, as well as lower sintering temperatures. To consolidate or synthesis the sample for required configuration and density, this technology applies an electric current while also applying mechanical pressure [11]–[14]. The compacts were sintered with an electric current in the range of 2200-2500 amperes for 2 minutes.

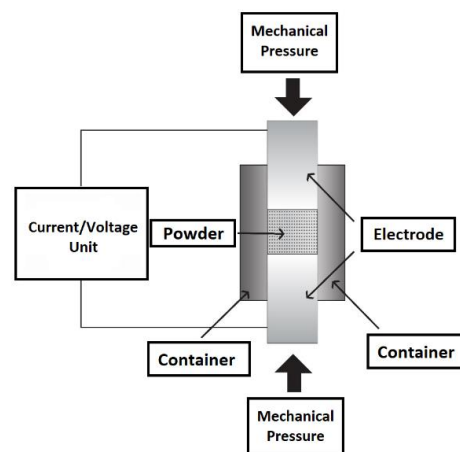


**Figure 3.** Schematic representation of sintering by ECAS Method [11], [15].

### 2.4. Characterization

Microstructural characterization and elemental examination of the phases of as-prepared composites were carried out by using SEM-EDS (JEOL LV6060, in HV with 20 kV)

Phase characterization and verification of EDS were realized by XRD analysis using Cu-K $\alpha$  radiation

with wavelength of 1.54 nm in a range of 20-90°.

Hardness measurements of the samples are important in terms of providing information about the properties of the material such as strength and elastic modulus. Hardness values were determined by taking the arithmetic mean of 6 different measurements under 100 g load from metallographically prepared samples with an Emcotest DuroScan 70G5 model microhardness indenter.

Electrical conductivities of composites as well as cemented copper sample were measured by using Sigmatest D 2.068 model instrument.

Relative densities of composite samples were measured according to Archimedes method by taking of both dry and wet weights of each samples.

### 3. RESULTS AND DISCUSSION

SEM images of copper powders produced by cementation method at different magnifications are given in Figure 4.

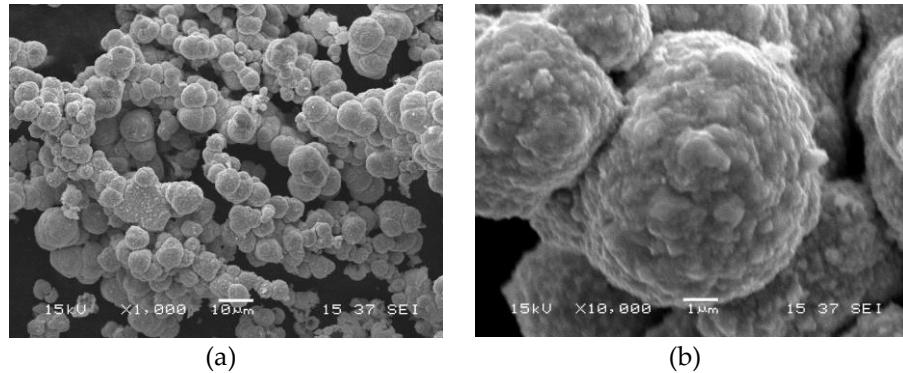
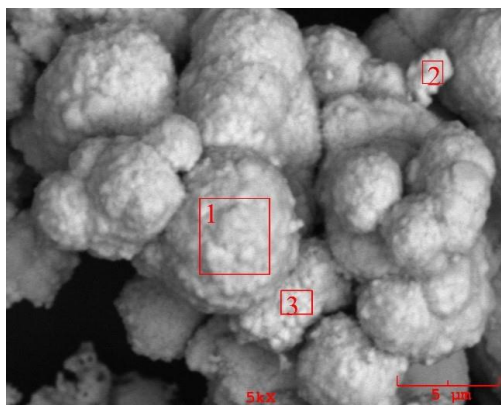


**Figure 4.** SEM image of copper powder produced by cementation at different magnifications

SEM images show that the powders are about 5-10 μm in size (Fig. 4a), but at higher magnification it is seen that real size of Cu powders are in submicron size and they agglomerated (Fig. 4b). It is thought that the first nucleated powders were submicron sized and then coalesced and agglomerated. The formed powders have a spherical morphology. G. Granata et al. reported that both temperature and surfactants have an important role on particle size [16]. R. Jhajharia et al. stated that the powders obtained in cemented copper production have polygonal morphology [17].

Figure 5 shows the SEM-EDS analyses of cemented copper powders. It is seen from the SEM image in the analysis that the powders are submicron in size. In addition, it was determined from the SEM-EDS analysis result that the powder grains are completely copper and contain trace amounts of oxygen.



Wt. %	1	2	3
O	0.142	1.561	0.416
Cu	99.858	98.439	99.584

**Figure 5.** SEM-EDS analysis of copper powders produced by cementation

XRD analysis of copper powders produced by cementation method is shown in Fig. 6. Characteristic peaks of copper and a very small peak of  $\text{Cu}_2\text{O}$  were obtained. It is thought that the trace amount of  $\text{Cu}_2\text{O}$  formation occurs during the drying stage of the cemented copper powder after production.

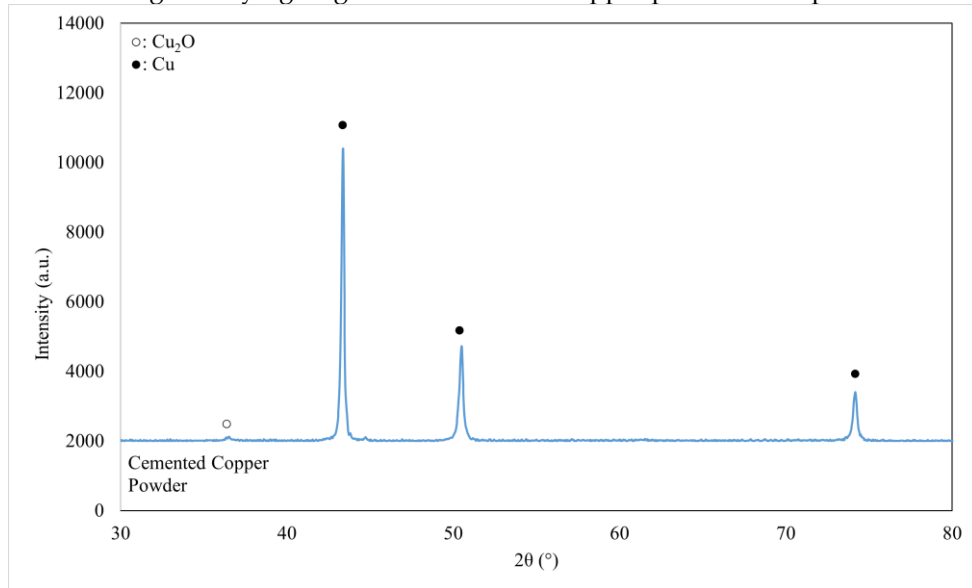


Figure 6. XRD graph of cemented copper powders.

SEM micrographs of electroless nickel coated SiC powders at different magnifications are shown in Figure 7. SiC grains are dark grey and light grey/white flashes indicate nickel coating. It is seen that SiC grains are homogeneously coated with Ni. Ni coated SiC powder helps to reduce the Kirkendall voids between SiC-Cu when it is added to copper matrix. Nickel/Copper (Ni/Cu) interfaces are applied in various fields such as the fabrication of thermoelectric modules and soldering applications [17]. At Cu-Ni interfaces, it has been shown that nickel can inhibit dislocation slip and reduce effective dislocation velocities [18], [19].

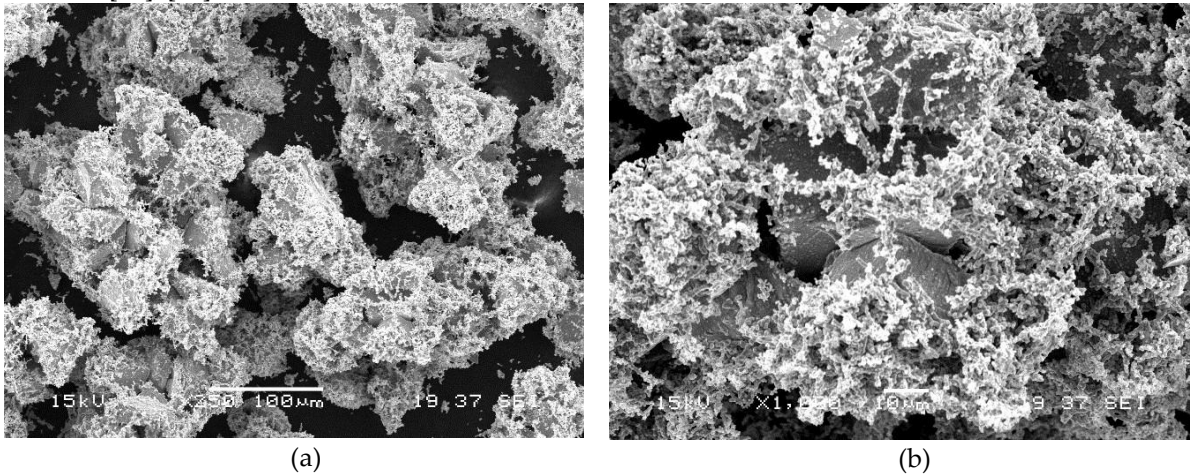
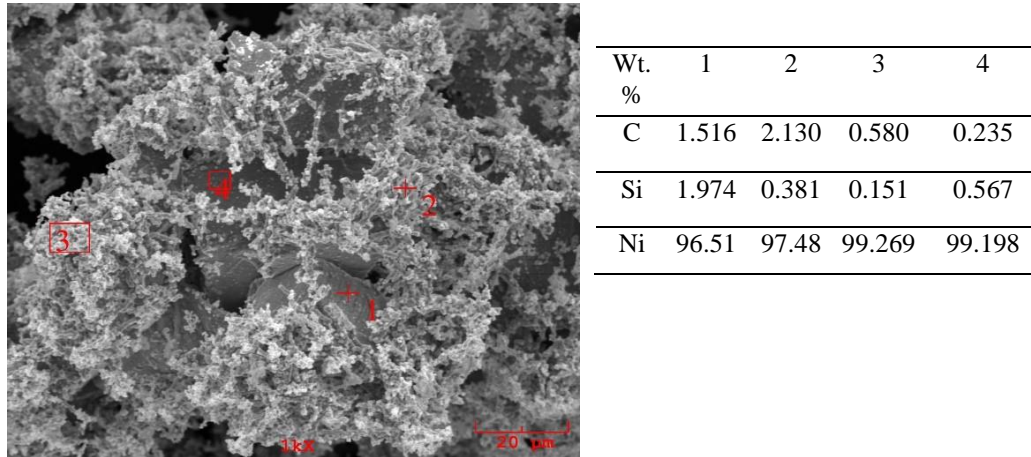


Figure 7. SEM images of electroless Ni coated SiC powders at different magnifications.

The SEM-EDS analysis result of Ni coated SiC powders is given in Figure 8. From the SEM image, it can be seen that Ni coating occurs by nucleating and stacking on top of each other. All the dots in the EDS analysis results taken from different points indicate Ni and prove that the electroless Ni coating process was successful.



**Figure 8.** EDS analysis of electroless Ni coated SiC powders.

After this section, the abbreviation Cu-Ni SiC is used when referring to Cu matrix composite specimens reinforced with Ni coated SiC sintered by ECAS method. The relative densities of the test specimens measured by the Archimedes method are given in Table 1 together with pure copper. Considering the results obtained, a relative density of more than 99% was obtained in pure copper. This value is higher than the values in the literature produced by cementation method. In addition, with the addition of Ni SiC, the relative density values of Cu-Ni SiC composite samples decreased slightly. This is thought to be due to the pre-coating of SiC particles with Ni. As a matter of fact, Cu-Ni surfaces came together instead of Cu-SiC. Since Cu and Ni atoms are fully soluble in each other, a good bonding was formed at the interface.

**Table 1.** Relative density values of cemented Cu and Cu- 0.5-1-1.5wt. % NiSiC composites

Wt. %SiC	Relative Density, %Number
0	99.42
0.5	98.60
1	98.45
1.5	98.35

SEM micrographs of Cu-Ni SiC composite samples sintered by ECAS method at 700 °C for 2 minutes are given in Figure 9. In Figure 9, the Cu matrix is in grey color, and the reinforcement component is darker. As can be seen from the figures, Ni coated SiC particles, which are the reinforcement component, are relatively dispersed homogeneously in the matrix.

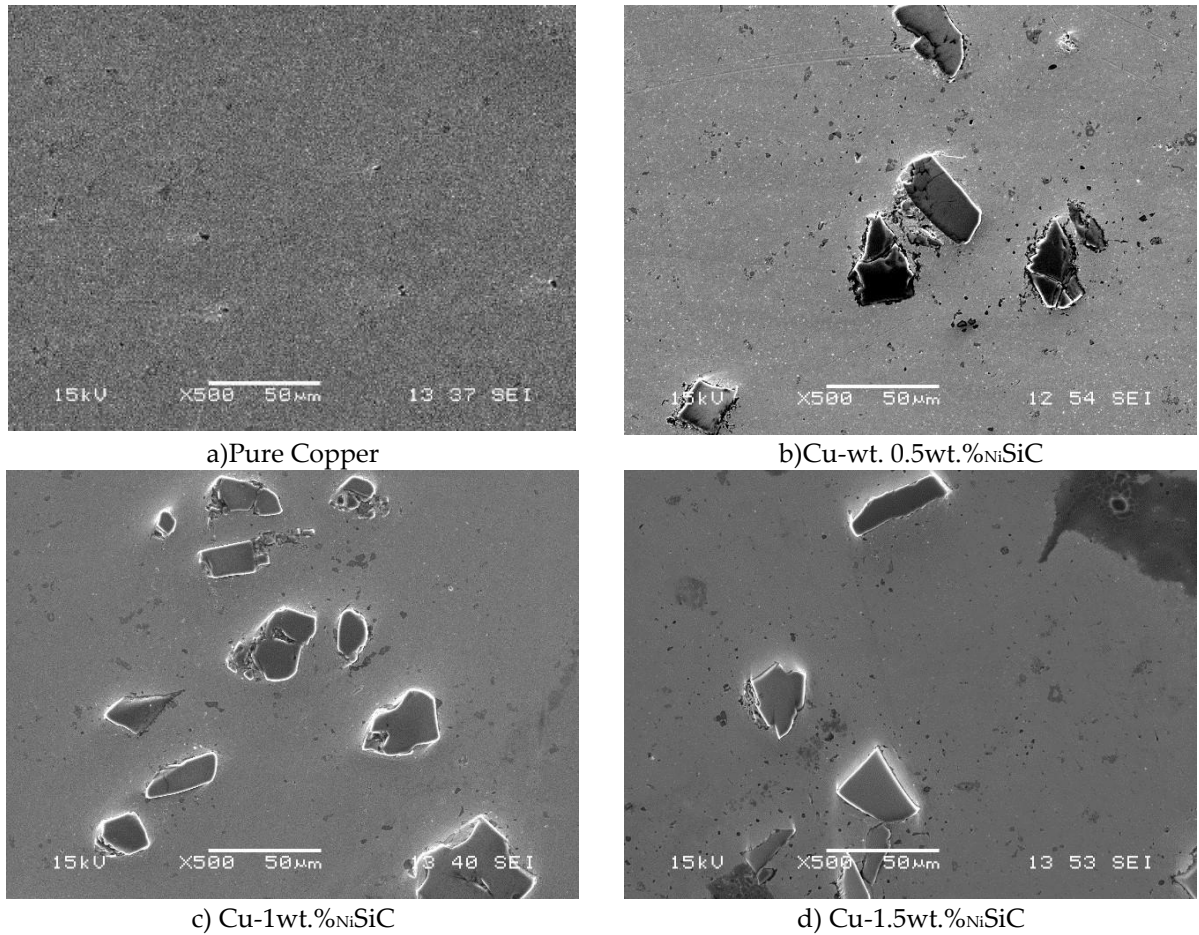


**Figure 9.** SEM images of cemented Cu and Cu-0.5-1-1.5 wt.% Ni SiC composites

SEM-EDS analysis of Cu-0.5wt.Ni SiC composite sintered at 700°C is given in Figure 10. The presence of Ni was detected in dot analyses obtained from Cu-SiC interfaces which shows that the Ni coating is successful.

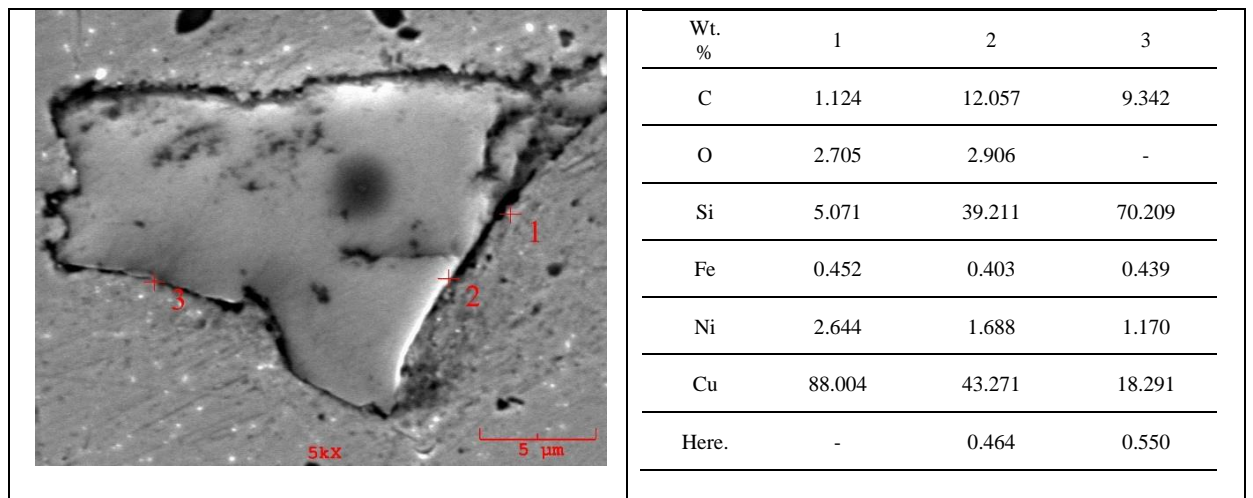


**Figure 10.** SEM-EDS analysis of cemented Cu-0.5wt.%Ni SiC composite

XRD patterns of Cu-Ni SiC composites are given in Figure 11. All characteristic peaks of Cu and SiC were detected and the intensity of SiC peaks increased with the increasing amount of the SiC.

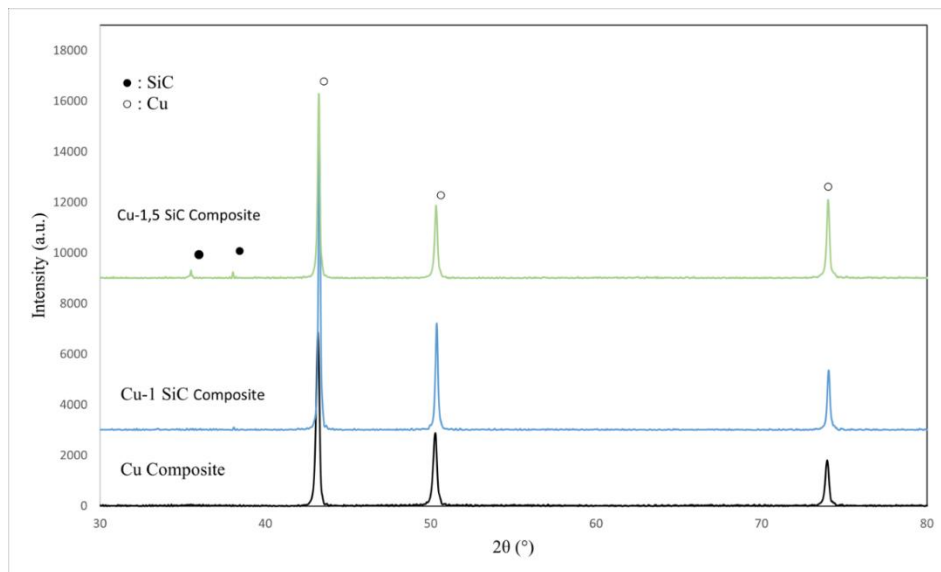


**Figure 11.** XRD patterns of cemented Cu and Cu 1-1.5 wt.%  $\text{NiSiC}$  composites

The microhardness values of the test specimens with pure copper measured by the Vickers hardness method are given in Table 2. In the microhardness measurements, care was taken to ensure relatively homogeneous coverage of Cu and SiC by the indenter. As can be seen from Table 2, the hardness of the composite samples increased with increasing reinforcement amount. In their study, M. Barmouz et al. reached a maximum hardness of 115 HV 0.1 in composite samples with SiC added to copper [2].

**Table 2.** Relative density values of cemented Cu and Cu-% $\text{NiSiC}$  composites

wt.% $\text{NiSiC}$	Sintering Temperature 700° C	
	Microhardness (HV)	
0	132	
0.5	140	
1	145	
1.5	148	

The electrical conductivity variation versus SiC amount is given in Figure 12 showing that the increase in the amount of reinforcement component shows that the electrical conductivity of the samples decreases compared to pure copper. The addition of SiC, which is an insulator in pure copper, prevents electron movement in the structure and decreases the conductivity since the electron movements are homogeneous and short distance distributed in the structure [3].

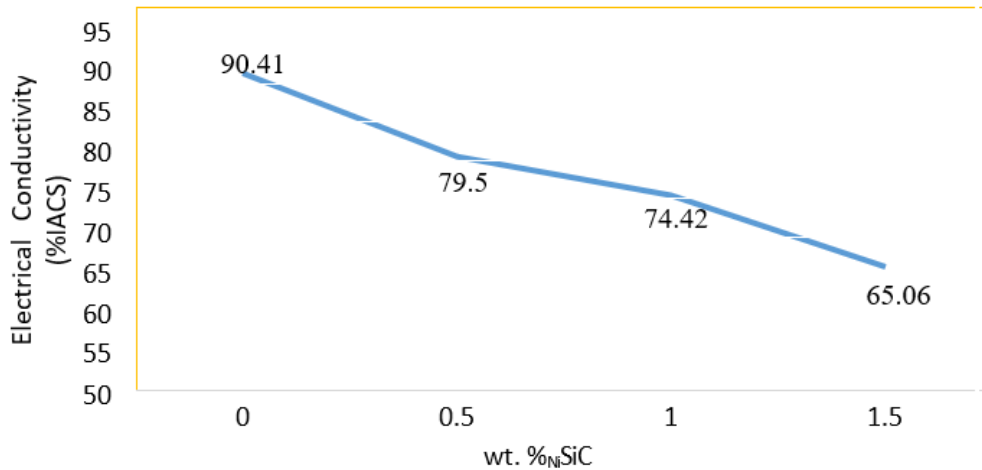


**Figure 12.** Electrical conductivity (%IACS) variation of cemented Cu and Cu-Ni SiC composites

#### 4. CONCLUSIONS

In this study the matrix component Copper powder was successfully produced by cementation method. SiC powders were coated with Ni by electroless plating method. The production technique was ECAS while producing Cu-Ni SiC composites Sintering procedure was conducted at 2200-2500 amperes for 2 minutes. From the SEM examinations of the composite samples it was observed that Ni -SiC particles were homogeneously dispersed in the copper matrix. Hardness of the Cu-Ni SiC composites increased and the relative densities decreased slightly with the increase in the SiC ratio added to copper. Relative density results showed that the density of the Cu- 1.5wt.% NiSiC composite decreased by only 0.5% compared to 100% Cu without NiSiC. Cu and SiC were identified as the dominant components in XRD patterns. The electrical conductivity values of the composites decreased by 27% at most with an increase in the amount of reinforcing component and they are in agreement with the density and hardness results. All results show that Cu-Ni SiC composites can be used in on-off contacts up to 1 wt%<sub>NiSiC</sub> reinforcement.

#### Declaration of Competing Interest

There is no conflict of interest in this study.

#### Funding / Acknowledgements

There is no funding for this study.

#### REFERENCES

- [1] G. Celebi Efe, S. Zeytin, and C. Bindal, "The effect of SiC particle size on the properties of Cu-SiC composites," *Materials and Design*, vol. 36, pp. 633–639, Apr. 2012.
- [2] M. Barmouz, P. Asadi, M. K. Besharati Givi, and M. Taherishargh, "Investigation of mechanical properties of Cu/SiC composite fabricated by FSP: Effect of SiC particles' size and volume fraction," *Materials Science and Engineering A*, vol. 528, no. 3, pp. 1740–1749, Jan. 2011.
- [3] G. Celebi Efe, T. Yener, I. Altinsoy, M. Ipek, S. Zeytin, and C. Bindal, "The effect of sintering temperature on some properties of Cu-SiC composite," *Journal of Alloys and Compounds*, vol. 509, no. 20, pp. 6036–6042, May 2011.
- [4] D. T. Tran, J. W. Choi, and Y. S. Yun, "Feasibility of direct conversion of copper present in waste printed circuit boards to oxidation-resistant materials employing eco-benign iron(III) sulfate and ascorbic acid," *Sustainable Materials and Technologies*, vol. 33, Sep. 2022.

- [5] J. Huang, C. Gui, H. Ma, P. Li, W. Wu, and Z. Chen, "Surface metallization of PET sheet: Fabrication of Pd nanoparticle/polymer brush to catalyze electroless nickel plating," *Composites Science and Technology*, vol. 202, Jan. 2021.
- [6] P. V. Racheva, N. P. Milcheva, F. Genc, and K. B. Gavazov, "A centrifuge-less cloud point extraction-spectrophotometric determination of copper(II) using 6-hexyl-4-(2-thiazolylazo)resorcinol," *Spectrochimica Acta - Part A: Molecular and Biomolecular Spectroscopy*, vol. 262, Dec. 2021.
- [7] P. Sahoo and S. K. Das, "Tribology of electroless nickel coatings - A review," *Materials and Design*, vol. 32, no. 4, pp. 1760–1775, Apr. 2011.
- [8] T. M. Reis, C. D. Boeira, F. L. Serafini, M. C. M. Farias, C. A. Figueroa, and A. F. Michels, "Micro-abrasive wear resistance of heat-treated electroless nickel-phosphorus coatings deposited on copper-beryllium alloy C17200," *Surface & Coatings Technology*, vol. 438, p. 128374, 2022.
- [9] V. Genova, G. Pedrizzetti, L. Paglia, F. Marra, C. Bartuli, and G. Pulci, "Diffusion aluminide coating modified via electroless nickel plating for Ni-based superalloy protection," *Surface & Coatings Technology*, vol. 439, p. 128452, 2022.
- [10] G. Celebi Efe, S. Zeytin, and C. Bindal, "The effect of SiC particle size on the properties of Cu–SiC composites," *Materials & Design (1980-2015)*, vol. 36, pp. 633–639, Apr. 2012.
- [11] S. C. Yener, T. Yener, and R. Mutlu, "A Process Control Method for the Electric Current Activated/Assisted Sintering System Based on the Container Consumed Power and Temperature Estimation," *Journal of Thermal Analysis and Calorimetry*, vol. 134, no. 2, pp. 1243–1252, 2018.
- [12] T. Yener, S. C. Yener, and S. Zeytin, "Nb addition effect on microstructural properties of Ti–TiAl<sub>3</sub> in situ composites produced by resistive sintering," *Journal of Thermal Analysis and Calorimetry*, vol. 134, no. 2, pp. 1359–1365, 2018.
- [13] T. Yener, S. C. Yener, and R. Mutlu, "Finite Difference Analysis of a Resistive Sintering System Container," *Journal of Nanoelectronics and Optoelectronics*, vol. 14, pp. 1–5, 2019.
- [14] A. Erdogan, T. Yener, and S. Zeytin, "Fast production of high entropy alloys (CoCrFeNiAl<sub>x</sub>Ti<sub>y</sub>) by electric current activated sintering system," *Vacuum*, vol. 155, no. May, pp. 64–72, 2018.
- [15] R. Orrù, R. Licheri, A. M. Locci, A. Cincotti, and G. Cao, "Consolidation/synthesis of materials by electric current activated/assisted sintering," *Materials Science and Engineering: R: Reports*, vol. 63, no. 4–6, pp. 127–287, 2009.
- [16] G. Granata, U. Tsendorj, W. Liu, and C. Tokoro, "Direct recovery of copper nanoparticles from leach pad drainage by surfactant-assisted cementation with iron powder," *Colloids and Surfaces A: Physicochemical and Engineering Aspects*, vol. 580, Nov. 2019.
- [17] R. Jhajharia, D. Jain, A. Sengar, A. Goyal, and P. R. Soni, "Synthesis of copper powder by mechanically activated cementation," *Powder Technology*, vol. 301, pp. 10–15, Nov. 2016.
- [18] A. Selimov, K. Chu, and D. L. McDowell, "Effects of interdiffusion on shear response of semi-coherent {111} interfaces in Ni/Cu," *International Journal of Plasticity*, vol. 157, Oct. 2022.
- [19] S. D. Park, D. Kim, and S. Y. Kim, "Effect of oxidation on mechanical properties of Ni/Cu interface: A density functional theory study," *Materials Today Communications*, vol. 33, Dec. 2022.

## FABRICATION OF TERNARY SILICA-CALCIUM-MAGNESIUM AEROGELS: EFFECT OF FEEDING RATE AND MOLAR RATIO ON PROPERTIES

<sup>1</sup>Burcu KARAKUZU İKİZLER , <sup>2,\*</sup>Pınar TERZİOĞLU ,  
<sup>3</sup>Tülay Merve TEMEL SOYLU , <sup>4</sup>Sevil YÜCEL 

<sup>1,3,4</sup>Yıldız Technical University, Chemical and Metallurgical Engineering Faculty, Bioengineering Department, Istanbul, TÜRKİYE

<sup>2</sup>Bursa Technical University, Engineering and Natural Sciences Faculty, Polymer Materials Engineering Department, Bursa, TÜRKİYE

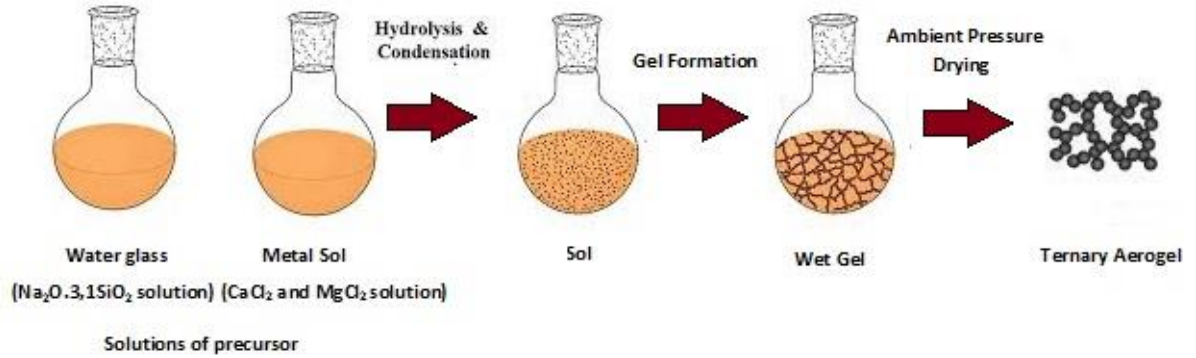
<sup>1</sup>[burcukarakuzu@hotmail.com](mailto:burcukarakuzu@hotmail.com), <sup>2</sup>[pinar.terzioglu@btu.edu.tr](mailto:pinar.terzioglu@btu.edu.tr),

<sup>3</sup>[tlymrvtml@gmail.com](mailto:tlymrvtml@gmail.com), <sup>4</sup>[syucel@yildiz.edu.tr](mailto:syucel@yildiz.edu.tr)

### Highlights

- Si/(Ca:Mg) ternary aerogels were synthesized via the solvent exchange method
- The molar ratio of Si/(Ca:Mg) have remarkable effect on final properties
- Ambient-dried ternary aerogels with unique properties should be used in several applications

### Graphical Abstract



Flowchart of the Silica-Calcium-Magnesium ternary aerogel production



## FABRICATION OF TERNARY SILICA-CALCIUM-MAGNESIUM AEROGELS: EFFECT OF FEEDING RATE AND MOLAR RATIO ON PROPERTIES

<sup>1</sup>Burcu KARAKUZU İKİZLER , <sup>2,\*</sup>Pınar TERZİOĞLU ,  
<sup>3</sup>Tülay Merve TEMEL SOYLU , <sup>4</sup>Sevil YÜCEL 

<sup>1,3,4</sup>Yıldız Technical University, Chemical and Metallurgical Engineering Faculty, Bioengineering Department, Istanbul, TÜRKİYE

<sup>2</sup>Bursa Technical University, Engineering and Natural Sciences Faculty, Polymer Materials Engineering Department, Bursa, TÜRKİYE

<sup>1</sup>[burcukarakuzu@hotmail.com](mailto:burcukarakuzu@hotmail.com), <sup>2</sup>[pinar.terzioglu@btu.edu.tr](mailto:pinar.terzioglu@btu.edu.tr),

<sup>3</sup>[tlymrvtml@gmail.com](mailto:tlymrvtml@gmail.com), <sup>4</sup>[syucel@yildiz.edu.tr](mailto:syucel@yildiz.edu.tr)

(Received: 06.03.2023; Accepted in Revised Form: 01.08.2023)

**ABSTRACT:** The silica-calcium-magnesium ternary aerogels were prepared by a solvent exchange method and a subsequent ambient pressure drying process. The effect of process parameters such as feeding rate (9-70 mL.min<sup>-1</sup>) and molar ratio (Si/(Ca:Mg) = 1:1 - 3:1) on the material characteristics including density, elemental content, surface area, pore size, pore volume, and morphology of powders were investigated. Aerogels were characterized by Fourier transform infrared spectroscopy (FTIR), inductively coupled plasma optical emission spectroscopy (ICP-OES), scanning electron microscopy (SEM), Brunauer–Emmett–Teller (BET), Barrett–Joiner–Halenda (BJH) and tapping density analysis. It was found that the molar ratio of Si/(Ca:Mg) could remarkably affect the surface area and density of aerogels, while the feeding rate had slight effect. The resultant aerogels exhibited high specific surface areas. The results showed that the aerogel has a Si/(Ca:3Mg) molar composition obtained with 9 mL.min<sup>-1</sup> had the highest surface area (524 m<sup>2</sup>.g<sup>-1</sup>). The increase of Ca to Mg molar ratio caused a decrease in the surface area and density of samples. The resultant aerogels are promising candidates as adsorbents to remove various contaminants.

**Keywords:** Ambient pressure drying, Co-doped silica, Pore structure, Structural evolution, Ternary aerogel

### 1. INTRODUCTION

Silica aerogels are three-dimensional porous nanostructures which have exceptional and unique features such as high porosity (80-99 %), high surface area (up to 1200 m<sup>2</sup>.g<sup>-1</sup>), low density (down to 0.003 g.cm<sup>-3</sup>) and low thermal conductivity (0.005-0.021 W (m.K)<sup>-1</sup>) [1,2]. Accordingly, silica aerogels have attracted great attention in various applications ranging from thermal insulation to the aerospace sector during the past decades [3].

Since silica aerogels are potential candidates for a wide variety of applications, scientists are actively studying on the production of aerogels with suitable properties to be used in different branches of industry. The range of aerogels can be efficiently increased by incorporating a minor component to the silica aerogel [4]. Many researchers have focused on the preparation of different types of silica aerogels such as silica [5], alumina-silica [6, 7,8], copper-silica [4], titania-silica [9,10], zirconia-silica [11,12], vanadium-silica [13], calcium-silica [14], and alumina-silica-titania [15, 16] aerogels. The charming point of multi-component aerogel production is the possibility of processing their structural, textural, and catalytic properties according to specific requirements [16]. However, the production of multi-component aerogels is generally complicated and expensive depending on the different hydrolysis rates of the starting sols and supercritical drying method. The surface areas of multi-component aerogels are generally low compared to the traditional silica aerogels. The commercialization of hybrid aerogels can be enhanced via the optimization of process parameters and also by employing simple ambient pressure

\*Corresponding Author: Pınar TERZİOĞLU, [pinar.terzioglu@btu.edu.tr](mailto:pinar.terzioglu@btu.edu.tr)

drying processes instead of supercritical drying [17, 18].

The present study aimed to synthesize silica-calcium-magnesium ternary aerogels using water glass as silica precursor via ambient pressure drying method. To the best of our knowledge, this is the first study investigating the effect of different synthesis parameters such as feeding rate (9-70 mL.min<sup>-1</sup>) and Si/(Ca:Mg) molar ratio on the structure and properties of silica-calcium-magnesium ternary aerogels. The properties of the aerogels were carried out using FT-IR, ICP-OES, SEM, and N<sub>2</sub> adsorption-desorption techniques to describe their structural evolution.

## 2. MATERIAL AND METHODS

### 2.1. Materials

Calcium chloride dihydrate (CaCl<sub>2</sub>.2H<sub>2</sub>O), Magnesium chloride hexahydrate (MgCl<sub>2</sub>.6H<sub>2</sub>O), n-Heptane (for analysis) and Ethanol (absolute, ≥99.0%) purchased from Merck KGaA (Darmstadt, Germany). Sodium Silicate (Na<sub>2</sub>O.3,1SiO<sub>2</sub>, Module-2 - Bome 36-50) Chem Pure purchased from Ege Kimya (Istanbul, Türkiye).

### 2.2. Preparation of silica-calcium-magnesium ternary aerogels

The silica sol was prepared by diluting water glass (Na<sub>2</sub>O.3,1SiO<sub>2</sub>) with distilled water (1:4 v/v). The metal sol was prepared by dissolving the appropriate amount of CaCl<sub>2</sub>.2H<sub>2</sub>O and MgCl<sub>2</sub>.6H<sub>2</sub>O in distilled water (150 mL). Then the metal sol was fed into the silica sol via a peristaltic pump (Heidolph Pumpdrive 5201, Germany) at a feeding rate of 9, 35 or 70 mL/min while the silica sol was constantly stirred. The precipitate was further vigorously stirred for 15 minutes. The reaction flask was capped with a watch glass and then the precipitate was aged for 24 hours at 50 °C in an oven dryer (Elektro-mag, Turkey). After the aging step, the gel was washed with distilled water (300 mL) to remove the excessive sodium salts. Subsequently, the gel was soaked in ethanol (150 mL) and stirred vigorously using a mechanic stirrer (Heidolph RZR 1, Germany) for 1 minute to remove water from the pores. The mixture was filtered and the same solvent exchange step was repeated for a second time. However in the second cycle instead of filtering the ethanol, the gel was aged in ethanol for 24 hours at 50 °C. Then ethanol was replaced with n-heptane using the same procedure. The surface modification of gels was achieved by aging in n-heptane for 24 hours at 50 °C. Finally, the mixture was filtered and the gels were dried in gradually at 70 °C for 20 hours, 90 °C for 2 hours and 110°C for 2 hours in an air dryer.

**Table 1.** The molar composition of produced silica-calcium-magnesium aerogels

Composition	Si/(Ca:Mg) ratio
Si/(Ca:3Mg)	1/1
Si/(Ca:Mg)	1/1
Si/(3Ca:Mg)	1/1
2Si/(Ca:3Mg)	2/1
2Si/(Ca:Mg)	2/1
2Si/(3Ca:Mg)	2/1
3Si/(Ca:3Mg)	3/1
3Si/(Ca:Mg)	3/1
3Si/(3Ca:Mg)	3/1

After the determination of a suitable feeding rate, the aerogels were produced with different molar ratios of Si/(Ca:Mg) (shown in Table 1). The molar ratio of silica to total of calcium and magnesium was taken as 1:1, 2:1 and 3:1 and also, the ratio of calcium and magnesium between each other was selected as 1:1, 1:3, and 3:1.

### 2.3. Characterization of silica-calcium-magnesium ternary aerogels

Surface area, pore size and pore volume of aerogels were determined using a Micromeritics TriStar II 3020 surface area and pore distribution analyzer at 77 K. The BET method was used to estimate the specific surface area of aerogels (SBET), while the BJH method was used for pore size and pore volume calculation. The SEM was conducted using a modal of ZEISS EVO® LS 10. FTIR spectra were recorded with a Shimadzu IR Prestige 21 spectrometer. The ICP-OES were performed by Shimadzu ICPE-9000 to determine the elemental composition of aerogels. The tapping density was evaluated as described by Temel et al. [3].

## 3. RESULTS AND DISCUSSION

### 3.1. Effect of the feeding rate on the properties of silica-calcium-magnesium ternary aerogels

Feeding rate may have an important role in the textural properties and morphology of materials [19]. The variation of surface area, pore size, pore volume and density of aerogels due to the feeding rate of the sol was demonstrated in Table 2. It is obvious from the results that the surface area of aerogels increased slightly with the decreased feeding rate. The maximum BET-specific surface area ( $469 \text{ m}^2 \text{ g}^{-1}$ ) occurred in the aerogel with  $9 \text{ mL} \cdot \text{min}^{-1}$  feeding rate. Increasing the feeding rate from 9 to  $70 \text{ mL} \cdot \text{min}^{-1}$ , led to the decrease of surface area to  $433 \text{ m}^2 \cdot \text{g}^{-1}$  and also the pore size. The aerogels had mesopore sizes ranging from 3.15–4.44 nm which shows that the particles were small [3]. Additionally, the mesopore volumes of aerogels were in the range of 0.26 to  $0.37 \text{ cm}^3 \cdot \text{g}^{-1}$ . When the tapping density of aerogels was investigated, the aerogel obtained with  $9 \text{ mL} \cdot \text{min}^{-1}$  feeding rate tendered the lowest density value ( $0.287 \text{ g} \cdot \text{cm}^{-3}$ ). Keeping these in view, further experiments were conducted using  $9 \text{ mL} \cdot \text{min}^{-1}$  feeding rate.

**Table 2.** Effect of the feeding rate on the textural properties and density of silica-calcium-magnesium ternary aerogels

Feeding rate ( $\text{mL} \cdot \text{min}^{-1}$ )	$S_{\text{BET}}$ ( $\text{m}^2 \cdot \text{g}^{-1}$ )	BJH Pore size* (nm)	Pore volume ( $\text{cm}^3 \cdot \text{g}^{-1}$ )	Density ( $\text{g} \cdot \text{cm}^{-3}$ )
9	469	4.44	0.37	0.287
35	468	3.25	0.27	0.487
70	433	3.15	0.26	0.393

\* The pore size values were obtained from the desorption part of the N<sub>2</sub> adsorption-desorption isotherm

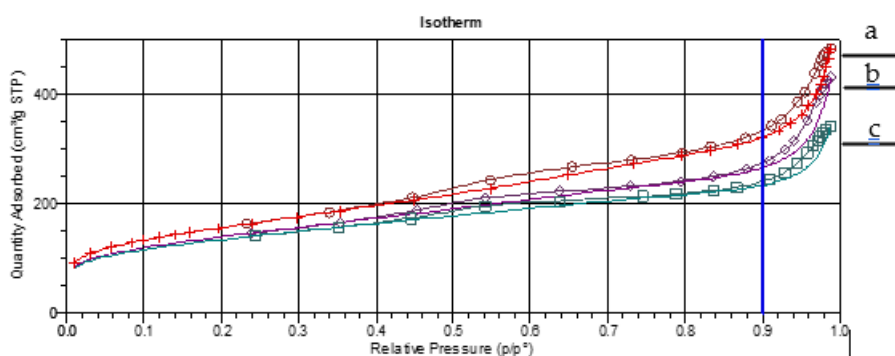


**Figure 1.** N<sub>2</sub> adsorption-desorption isotherms of the aerogels prepared with a) 9 b) 35 c)  $70 \text{ mL} \cdot \text{min}^{-1}$  feeding rate

Figure 1 shows the N<sub>2</sub> adsorption-desorption isotherms of silica-calcium-magnesium ternary aerogels. A type IV isotherm with a combination of H1-type hysteresis loops was encountered for the aerogels. These indicate the presence of interconnected mesopores with cylindrical geometries and open at both ends. It is clear from the N<sub>2</sub> sorption isotherms that the volume adsorbed increases slowly at low relative pressure. This result can be attributed to the fact that the samples contain little amount of

micropores [15].

**Table 3.** Effect of the feeding rate on the elemental content of silica-calcium-magnesium ternary aerogels

Feeding rate (mL.min <sup>-1</sup> )	Elemental content (%)			
	Si	Ca	Mg	Na
9	94.08	1.37	4.19	0.36
35	88.65	2.14	9.21	<0.123
70	93.68	1.89	4.43	<0.123

The effect of the feeding rate on the elemental content of silica-calcium-magnesium ternary aerogels is given in Table 3. The feeding rate of metal sol slightly effected the elemental content of ternary aerogels. It was determined that the incorporation of Ca and Mg was higher when the feeding rate was 35 mL.min<sup>-1</sup>. The incorporation trend was similar for 9 mL.min<sup>-1</sup> and 70 mL.min<sup>-1</sup> feeding rates.

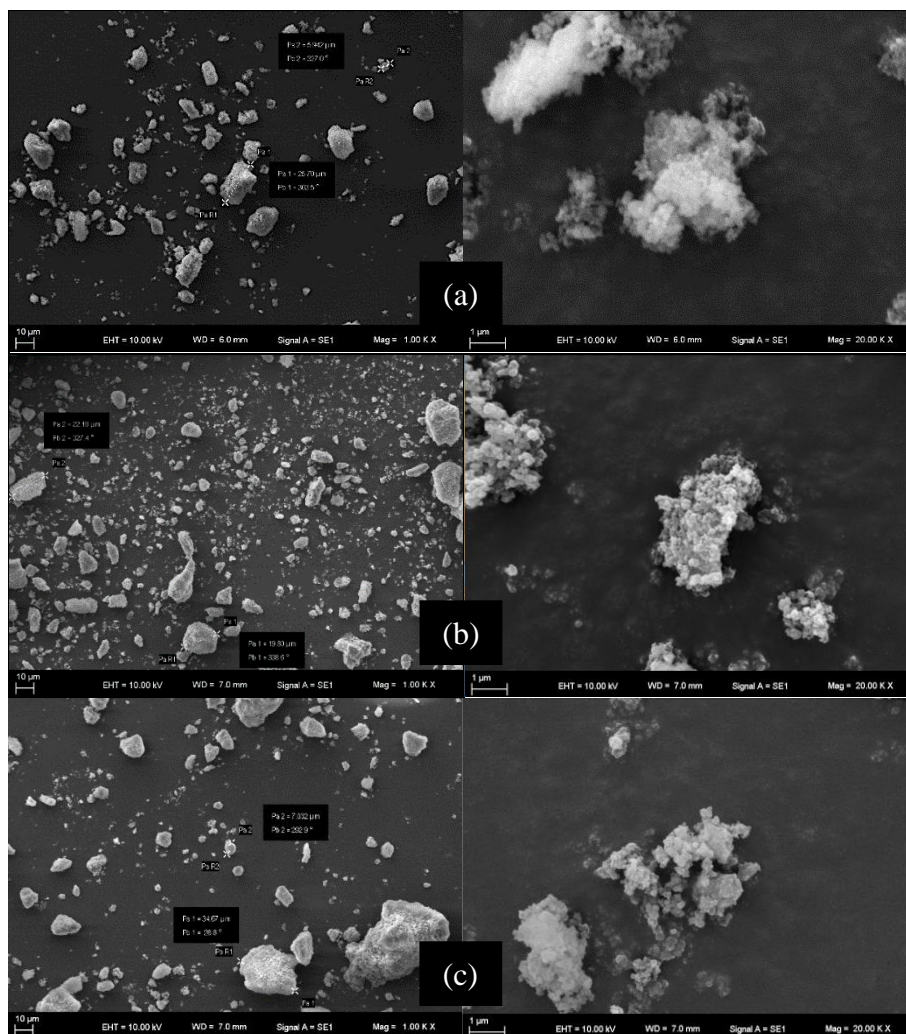


**Figure 2.** SEM micrographs of aerogels prepared with a) 9 mL.min<sup>-1</sup>, b) 35 mL.min<sup>-1</sup>, c) 70 mL.min<sup>-1</sup> feeding rate

Figure 2 displays SEM micrographs of the ternary aerogels prepared with different feeding rates. The micrographs reveal that the aerogel prepared with 35 and 70 mL.min<sup>-1</sup> feeding rate was made of small agglomerates of spherical particles. Interestingly, the aerogel prepared with 9 mL.min<sup>-1</sup> are observed to be composed of cloud-like nanoclusters. This further verifies the previous N<sub>2</sub> adsorption/desorption results.

### 3.2. Effect of the molar ratio on the properties of silica-calcium-magnesium ternary aerogels

Initial sol parameters including the precursors for the silica and other components, the molar composition of precursors, water content, and catalyst considerably affects the pore characteristics and other properties (e.g. morphology, transparency etc.) of the final aerogels [20]. The effect of the molar ratio on surface area, pore size, pore volume and density of aerogels is given in Table 4. It was clear that the variation in molar ratio had a considerable effect on the textural properties of aerogels. All the ternary aerogels exhibited high surface area except 3Si/(3Ca:Mg) aerogel ( $161 \text{ m}^2\cdot\text{g}^{-1}$ ), small pore volume ( $\leq 0.37 \text{ cm}^3\cdot\text{g}^{-1}$ ), and small pore size ( $\leq 5.46 \text{ nm}$ ). The increase of Si to (Ca:Mg) molar ratio led to a decrease in surface area while the increase in density. When the Si to (Ca:Mg) molar ratio increased from 1 to 3 the surface area of aerogel decreased from 524 to  $393 \text{ m}^2\cdot\text{g}^{-1}$ . The surface area and density of samples decreased with the increase of Ca to Mg molar ratio in the ternary system whereas, a reverse trend was found for the pore sizes. Conversely, the surface area and density of aerogels increased with the increment of the Mg to Ca molar ratio. When all these results are evaluated together it could be seen that the Si/(Ca:3Mg) sample had the highest surface area ( $524 \text{ m}^2\cdot\text{g}^{-1}$ ).

During the silica-calcium-magnesium ternary aerogel preparation process, various bonds (e.g. Si-O-Si, Si-OH) were produced by hydrolysis reaction. Hereby, bonds interconnect to form a three-dimensional network structure [21]. Therefore, the variation of textural properties could be attributed to the different hydrolysis and condensation reaction rates of the chemicals (e.g. the cation exchange reaction of CaO with SiO- groups to form  $\text{Ca}(\text{OSi})_2$  and the (Mg, Ca) O replaced with the Na<sub>2</sub>O in the  $\text{Na}_2\text{O}n\text{SiO}_2$ ) [22]. We propose that too much Ca might diminish the cross-linking degree of the bonds which results in the deterioration of the pore structure of aerogel. In this situation, compact particles form and thus a reduction in the specific surface area occurs due to the lack of nitrogen access into some of the pores. However, the incorporation of magnesium led to the occurrence of porous agglomerates in the network accordingly raises the surface area.

The pore volume of ternary aerogels ranged from 0.23 to  $0.37 \text{ cm}^3\cdot\text{g}^{-1}$ . In general, the porosity of aerogels was related not only to the pore size but also to the number of pores [23]. In this study, the porosity of the aerogels depends substantially on the pore size. This indicates that probably the number of pores was almost equal for all the samples and their sizes primarily effect the pore volume.

**Table 4.** Effect of the molar ratio on the textural properties and density of silica-calcium-magnesium ternary aerogels

Molar Composition of Aerogels	$S_{\text{BET}}$ ( $\text{m}^2\cdot\text{g}^{-1}$ )	BJH Pore size (nm)	Pore volume ( $\text{cm}^3\cdot\text{g}^{-1}$ )	Density ( $\text{g}\cdot\text{cm}^{-3}$ )
Si/(Ca:3Mg)	524	4.37	0.33	0.366
Si/(Ca:Mg)	469	4.44	0.37	0.287
Si/(3Ca:Mg)	420	4.93	0.37	0.266
2Si/(Ca:3Mg)	514	3.22	0.29	0.473
2Si/(Ca:Mg)	434	3.50	0.29	0.385
2Si/(3Ca:Mg)	242	5.16	0.30	0.245
3Si/(Ca:3Mg)	393	3.21	0.23	0.569
3Si/(Ca:Mg)	301	4.20	0.29	0.397
3Si/(3Ca:Mg)	161	5.46	0.28	0.313

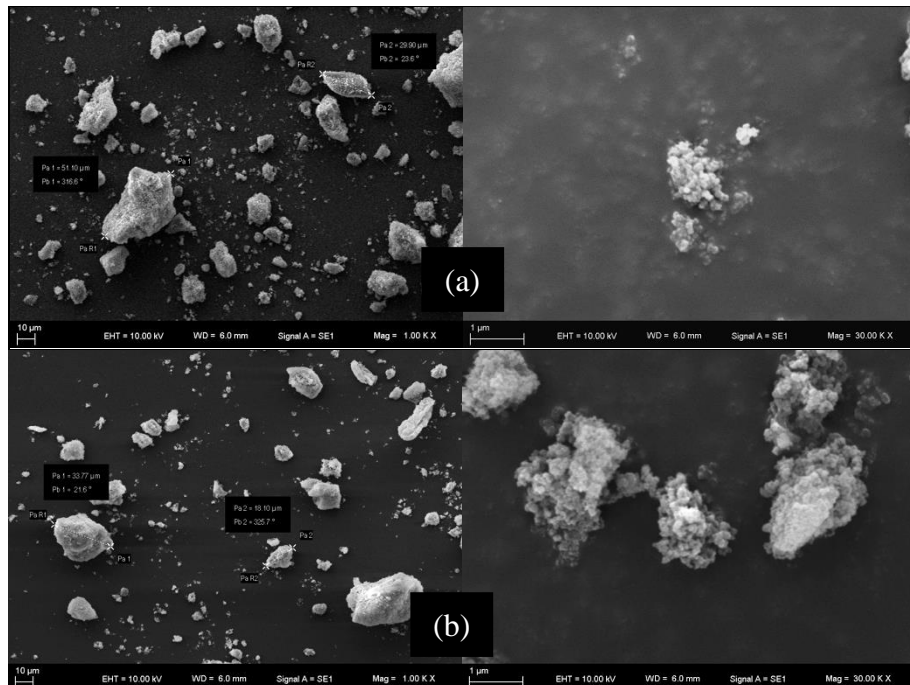
The reported textural properties of binary and ternary silica aerogels are summarized in Table 5. The surface area of different aerogels varied from  $158 \text{ m}^2\cdot\text{g}^{-1}$  to  $524 \text{ m}^2\cdot\text{g}^{-1}$ . Thus, the surface area as well as pore size and pore volume of aerogels can differ by many factors including molar composition and process parameters.

**Table 5.** Comparison of textural properties of silica-calcium-magnesium ternary aerogels with hybrid aerogels

Aerogel Type	S <sub>BET</sub> (m <sup>2</sup> .g <sup>-1</sup> )	Pore size (nm)	Pore volume (cm <sup>3</sup> .g <sup>-1</sup> )	Reference
Alumina/Silica	231	31.7	1.86	[24]
Ceria/Silica	404	-	-	[25]
Iron/Silica	158	-	0.27	[26]
Zirconia/Silica	395	10.9	1.09	[11]
Alumina/Titania/Silica	235	22.6	1.29	[15]
Calcium/ Silica	198	4.37	0.203	[14]
Calcium/Magnesium/Silica	524	4.37	0.33	In this study

The variation of molar ratio had no effect on the type of N<sub>2</sub> adsorption–desorption isotherms (not given). The type isotherms of the aerogel were determined to be of type IV which is characteristic of mesoporous materials [27].

The SEM micrographs of aerogels prepared with various Si-, Ca- and Mg molar ratios are given in Fig 3-5. As can be seen from SEM images, aerogels are composed of small particles and pores. The diameters of the particles were in the range 2-80 μm. Aerogels consisted of irregular agglomerates that were formed by spherical nanoparticles. Agglomerates had a grape-like appearance. We supposed that the grape-like structure was made up of spherical particles and also a porous spongy structure was formed spontaneously. The samples with higher Mg molar ratio had bigger agglomerates compared with the samples with higher Ca molar ratio (Fig.4 a-c). This verifies that the particle growth of the aerogels was limited by the incorporation of calcium.

**Figure 3.** SEM micrographs of aerogels with (a) Si/(Ca:3Mg), (b)Si/(3Ca:Mg) molar composition

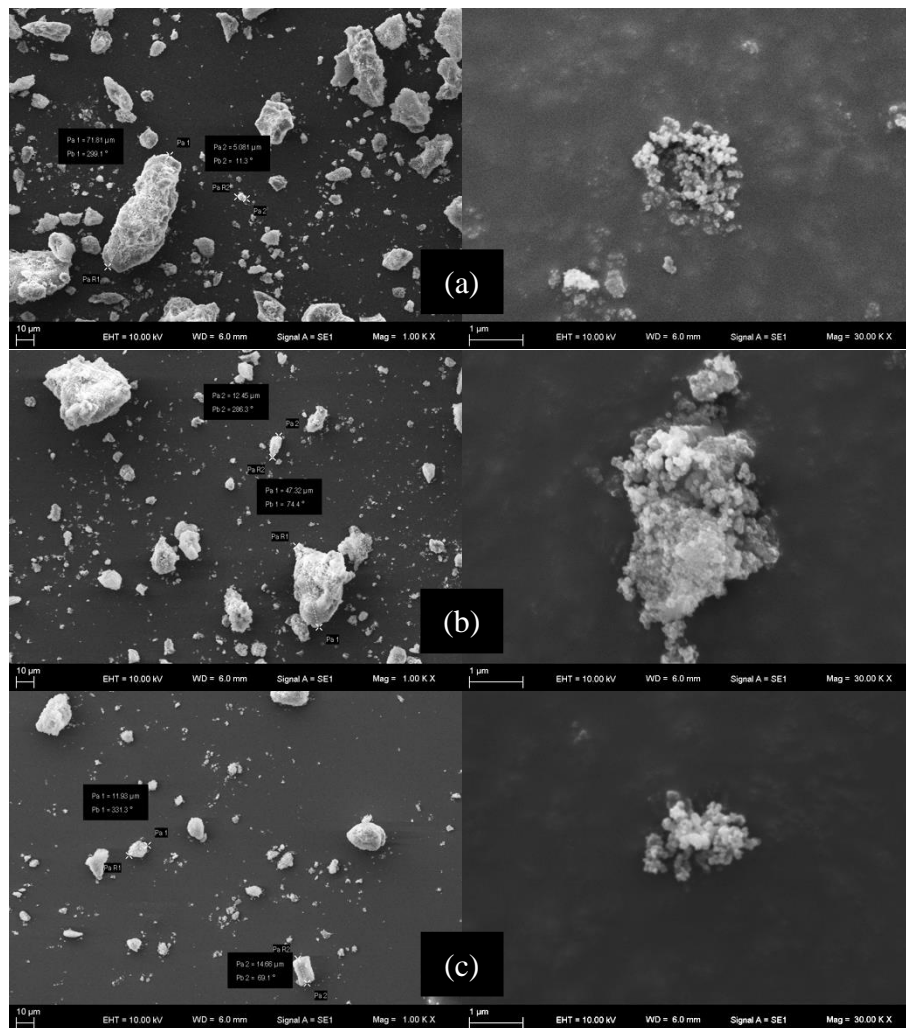


**Figure 4.** SEM micrographs of aerogels with (a)  $2\text{Si}/(\text{Ca}:3\text{Mg})$ , (b)  $2\text{Si}/(\text{Ca}:\text{Mg})$ , (c)  $2\text{Si}/(3\text{Ca}:\text{Mg})$  molar composition

Figure 6 presents the FTIR analysis of the silica-calcium-magnesium ternary aerogels. Pure silica aerogel is known to exhibit the asymmetric and symmetric vibration of the three-dimensional Si–O–Si work at nearly  $1062$  and  $794\text{ cm}^{-1}$ , respectively as previously reported by Temel et. al. [3]. For the ternary aerogels, FT-IR showed that the  $1062\text{ cm}^{-1}$  band shifted towards a lower wave number ( $1010\text{ cm}^{-1}$ ). The shift confirms the incorporation of Ca and Mg to the network. Similar result was reported by Wu [27] for metal incorporated silica aerogels. The other main difference was the formation of a peak at about  $1450\text{ cm}^{-1}$  with the increased Ca amount (Fig. 6 c). This behavior may result from the formation of calcium carbonate due to the reaction of surface adsorbed carbon dioxide with calcium [15]. In addition, the broad band between  $3750$  and  $3200\text{ cm}^{-1}$  and centered at about  $1630\text{ cm}^{-1}$  ascribed to the surface adsorbed OH groups (water).

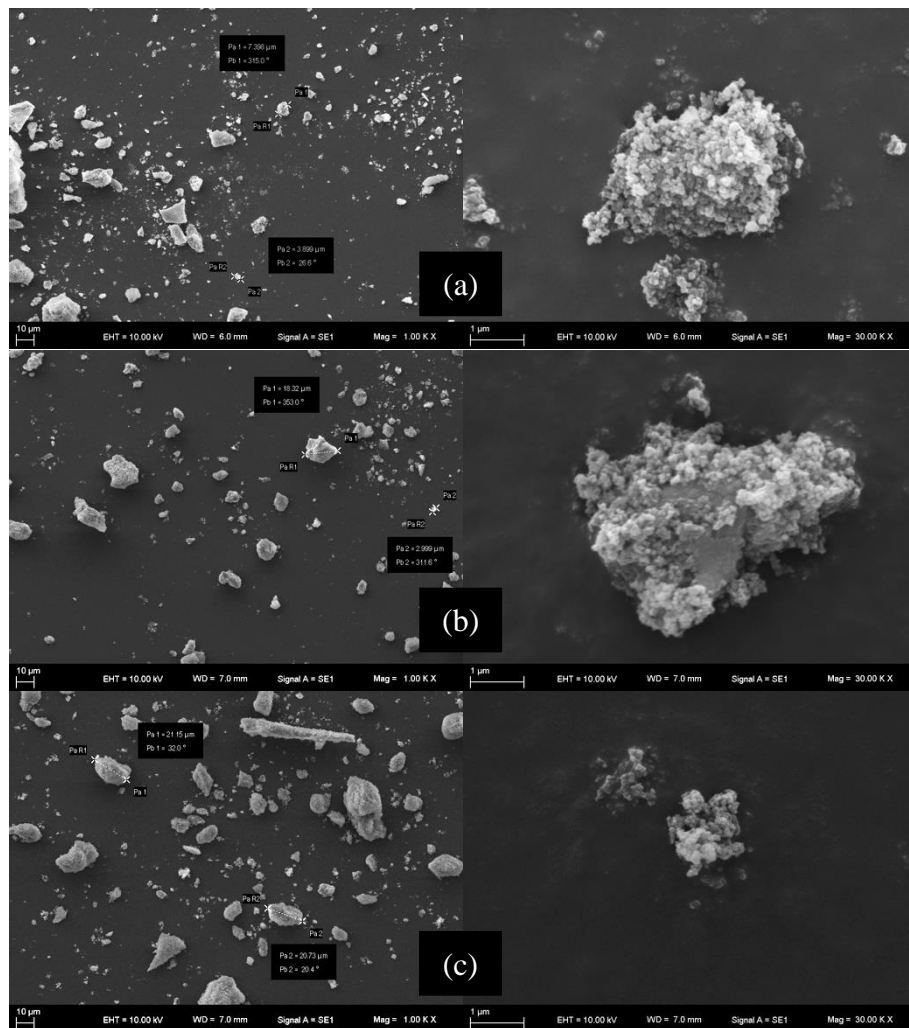


Figure 5. SEM micrographs of aerogels with (a)3Si/(Ca:3Mg), (b)3Si/(Ca:Mg), (c)3Si/(3Ca:Mg) molar composition

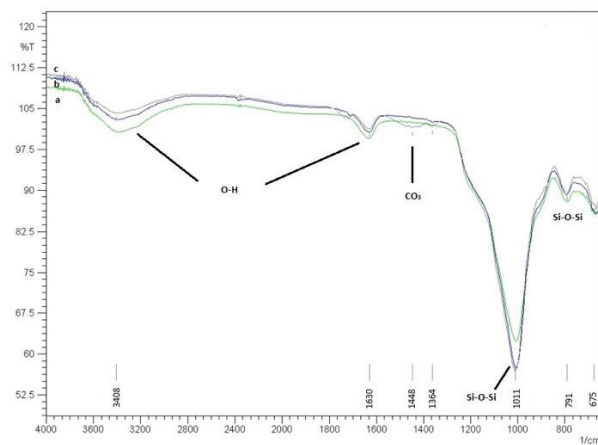


Figure 6. FT-IR spectra of silica-calcium-magnesium ternary aerogels with a)Si/(Ca:3Mg), b)Si/(Ca:Mg) c) Si/(3Ca:Mg) molar composition

**Table 6.** Effect of the molar ratio on the elemental content of silica-calcium-magnesium ternary aerogels

Sample	Elemental content (%)			
	Si	Ca	Mg	Na
Si/(Ca:3Mg)	94.06	0.75	4.73	0.46
Si/(Ca:Mg)	94.08	1.37	4.19	0.36
Si/(3Ca:Mg)	91.20	2.87	5.69	0.24
2Si/(Ca:3Mg)	90.50	0.89	8.25	0.36
2Si/(Ca:Mg)	92.11	2.67	4.60	0.62
2Si/(3Ca:Mg)	91.29	5.47	2.72	0.52
3Si/(Ca:3Mg)	90.51	1.96	6.33	1.20
3Si/(Ca:Mg)	89.88	4.45	4.81	0.87
3Si/(3Ca:Mg)	88.39	7.90	2.88	0.83

The effect of the molar ratio on the elemental content of silica-calcium-magnesium ternary aerogels is presented in Table 6. The results showed that there was small amount of sodium salts in the aerogel structure. The total incorporation of Ca and Mg increased with the increased silica content as expected.

#### 4. CONCLUSIONS

It is important to control the process parameters during the aerogel production. A series of mesoporous silica-calcium-magnesium ternary aerogels with various feeding rates and Si/(Ca:Mg) molar ratio were prepared by a solvent exchange method followed by an ambient pressure drying method. The aerogel prepared with 9 mL.min<sup>-1</sup> feeding rate exhibited a higher surface area (469 m<sup>2</sup>.g<sup>-1</sup>) than the samples prepared with higher feeding rates. All the aerogels were mesoporous confirmed with a type IV N<sub>2</sub> sorption isotherm. The surface area and density of aerogels were greatly affected by the Si/(Ca:Mg) molar ratio. The surface area and density of produced aerogels varied from 161 m<sup>2</sup>.g<sup>-1</sup> to 524 m<sup>2</sup>.g<sup>-1</sup> and 0.245 g.cm<sup>-3</sup> to 0.569 g.cm<sup>-3</sup>, respectively. The surface area and density of aerogels increased with increasing Mg/Ca molar ratio from 1 to 3. The results showed that aerogels having different properties could be obtained by varying the process parameters.

#### Declaration of Ethical Standards

The authors declare that the study complies with all applicable laws and regulations and meets ethical standards.

#### Declaration of Competing Interest

The authors declare that they have no known competing financial interests or personal relationships that could have appeared to influence the work reported in this paper.

#### Funding / Acknowledgements

This work was supported by the TUBITAK (The Scientific and Technological Research Council of Turkey) with a 1005 project (Project No: 115M469).

#### Data Availability

Data will be made available on request.

## REFERENCES

- [1] T. Zhou, X. Cheng, Y. Pan, C. Li, L. Gong, and H. Zhang, "Mechanical performance and thermal stability of glass fiber reinforced silica aerogel composites based on co-precursor method by freeze drying," *Applied Surface Science*, vol. 437, pp. 321–328, 2018.
- [2] F. Pan, B. Zhang, Y. Ding, L. Wang, F. Xie, W. Cai, S. Liu, and J. Zhou, "New composite aerogel-like adsorbents for thiophene based on  $\pi$ -complexation," *Separation and Purification Technology*, 192, pp. 46–54, 2018.
- [3] T. M. Temel, B. K. İkizler, P. Terzioğlu, S. Yücel, and Y. B. Elalmış, "The effect of process variables on the properties of nanoporous silica aerogels: an approach to prepare silica aerogels from biosilica," *Journal of Sol-Gel Science and Technology*, vol. 84, no. 1, pp. 51–59, Jul. 2017.
- [4] J. L. Mohanan and S. L. Brock, "Influence of Synthetic and Processing Parameters on the Surface Area, Speciation, and Particle Formation in Copper Oxide/Silica Aerogel Composites," *Chemistry of Materials*, vol. 15, no. 13, pp. 2567–2576, May 2003.
- [5] C. Zhao, Y. Li, W. Ye, X. Shen, X. Yuan, C. Ma, and Y. Cao, "Performance regulation of silica aerogel powder synthesized by a two-step Sol-gel process with a fast ambient pressure drying route," *Journal of Non-Crystalline Solids*, vol. 567, pp.120923, Sep 2021.
- [6] X. Wu, G. Shao, S. Cui, L. Wang, and X. Shen, "Synthesis of a novel Al<sub>2</sub>O<sub>3</sub>-SiO<sub>2</sub> composite aerogel with high specific surface area at elevated temperatures using inexpensive inorganic salt of aluminum," *Ceramics International*, vol. 42, no. 1, Part A, pp. 874–882, Jan. 2016.
- [7] X. Hou, R. Zhang, and D. Fang, "Novel whisker-reinforced Al<sub>2</sub>O<sub>3</sub>-SiO<sub>2</sub> aerogel composites with ultra-low thermal conductivity," *Ceramics International*, vol. 43, no. 12, pp. 9547–9551, Aug. 2017.
- [8] J. Yao, X. Gao, Y. Wu, X. Zhao, and X. Li, "High-temperature resistant ambient pressure-dried aluminum doped silica aerogel from inorganic silicon and aluminum sources." *Ceramics International*, vol. 48, pp.15006-15016, Jun. 2022.
- [9] S. Zhang, Z. Zhang, J. Pei, R. Li, J. Zhang, J. Cai, and J. Cui, "A novel TiO<sub>2</sub>-SiO<sub>2</sub> aerogel nanocomposite absorbent: preparation, characterization and photocatalytic degradation effects on automobile exhaust," *Materials Research Express*, vol. 5, no. 2, p. 025036, Feb. 2018.
- [10] W. Zou, H. Bian, J. Guo, J. Xu and B. Guo, "Preparation of Titania-Silica Composite Aerogel at Atmospheric Pressure and Its Catalytic Performance in the Synthesis of Poly (Butylene Succinate)" *Materials*, vol 16, pp. 3296, Apr. 2023.
- [11] G. Zu, J. Shen, L. Zou, W. Zou, D. Guan, Y. Wu, and Y. Zhang, "Highly thermally stable zirconia/silica composite aerogels prepared by supercritical deposition," *Microporous and Mesoporous Materials*, vol. 238, pp. 90–96, Jan. 2017.
- [12] Y. Han, Y. Wu, H. Zhang, S. Huang, S. Wu, and Z. Liang, "A three-dimensional network modifier (dimethyldiethoxysilane) makes ZrO<sub>2</sub>-SiO<sub>2</sub> aerogel with excellent thermal insulation performance and high-temperature stability." *Colloids and Surfaces A: Physicochemical and Engineering Aspects*, vol. 671, pp. 131716, Aug. 2023.
- [13] L. M. Hair, P. R. Coronado, and J. G. Reynolds, "Mixed-metal oxide aerogels for oxidation of volatile organic compounds," *Journal of Non-Crystalline Solids*, vol. 270, no. 1–3, pp. 115–122, May 2000.
- [14] B. Karakuzu İkizler, E. Yapıcı, S. Yucel, and E. Ermis, "Production and Characterization of Calcium Silica Aerogel Powder as a Food Additive," *ACS omega*, vol. 8, no.12, pp.11479-11491, March 2023.
- [15] X. Wu, W. Li, G. Shao, X. Shen, S. Cui, J. Zhou, Y. Wei, and X. Chen, "Investigation on textural and structural evolution of the novel crack-free equimolar Al<sub>2</sub>O<sub>3</sub>-SiO<sub>2</sub>-TiO<sub>2</sub> ternary aerogel during thermal treatment," *Ceramics International*, vol. 43, no. 5, pp. 4188–4196, Apr. 2017.
- [16] X. Li, G. Qin, Y. Wang, and W. Wei, "Preparation and characterization of equimolar SiO<sub>2</sub>-Al<sub>2</sub>O<sub>3</sub>-TiO<sub>2</sub> ternary aerogel beads," *Journal of Porous Materials*, vol. 21, no. 5, pp. 611–621, Apr. 2014.

- [17] V. G. Parale, W. Han, H.N.R. Jung, K.Y. Lee, and H.H. Park, "Ambient pressure dried tetrapropoxysilane-based silica aerogels with high specific surface area," *Solid State Sciences*, vol. 75, pp. 63–70, Jan. 2018.
- [18] B. Karakuzu, T. M. Temel, S. Yücel, P. Terzioğlu, and Y. Elalmiş, "Effect of Acid Type and Gelation pH on The Structural Properties of Silica Aerogels Prepared by Use of Rice Hull," *Sigma Journal of Engineering and Natural Sciences*, vol. 34, no. 2, pp. 175–182, Jun. 2016.
- [19] P. Terzioğlu, and S. Yucel, "Synthesis of Magnesium Silicate from Wheat Husk Ash," *Bioresources* vol. 7, pp. 5435-5447, 2012.
- [20] J.H. Lee, S.Y. Choi, C.E. Kim, and G.D. Kim, "The effects of initial sol parameters on the microstructure and optical transparency of TiO<sub>2</sub>-SiO<sub>2</sub> binary aerogels," *Journal of Materials Science*, vol. 32, no. 13, pp. 3577–3585, 1997.
- [21] J. Chen, B. Zhang, G. Miao, and J. Men, "New SiO<sub>2</sub>-NiO Aerogel Sorbents for Desulfurization by  $\pi$ -Complexation: Influence of Molar Ratio of Si/Ni," *Industrial & Engineering Chemistry Research*, vol. 55, no. 17, pp. 5036–5042, Apr. 2016.
- [22] G. S. Pappas, P. Liatsi, I. A. Kartsonakis, I. Danilidis, and G. Kordas, "Synthesis and characterization of new SiO<sub>2</sub>-CaO hollow nanospheres by sol-gel method: Bioactivity of the new system," *Journal of Non-Crystalline Solids*, vol. 354, no. 2, pp. 755–760, Jan. 2008.
- [23] R. Akkari, A. Ghorbel, N. Essayem, and F. Figueras, "Synthesis and characterization of mesoporous silica-supported nano-crystalline sulfated zirconia catalysts prepared by a sol-gel process: Effect of the S/Zr molar ratio," *Applied Catalysis A: General*, vol. 328, no. 1, pp. 43–51, Aug. 2007.
- [24] F. He, L. Zhou, X. Zhang, W. Li, L. Yang, H. Zhao, and X. He, "Synthesis and anisotropic properties of alumina-silica aerogels constructed by silica sols infiltrated into unidirectional frozen alumina templates," *Ceramics International*, vol. 45, no. 9, pp. 11963–11970, Jun. 2019.
- [25] L. F. Posada, M. K. Carroll, A. M. Anderson, and B. A. Bruno, "Inclusion of Ceria in Alumina- and Silica-Based Aerogels for Catalytic Applications," *The Journal of Supercritical Fluids*, vol. 152, p. 104536, Oct. 2019.
- [26] H. Hu, N. Chen, W. Wei, H. Li, Z. Jiang, Y. Xu, and J. Xie, "The effect of solvent parameters on properties of iron-based silica binary aerogels as adsorbents," *Journal of Colloid and Interface Science*, vol. 549, pp. 189–200, Aug. 2019.
- [27] Z.G. Wu, Y.X. Zhao, and D.S. Liu, "The synthesis and characterization of mesoporous silica-zirconia aerogels," *Microporous and Mesoporous Materials*, vol. 68, no. 1–3, pp. 127–132, Mar. 2004.



## DÖNER DARBELİ DELİK DELME PERFORMANS ANALİZİ ve UYGUN UÇ SEÇİMİ: KAYSERİ HİMMETDEDE OCAĞI ÖRNEĞİ

Mehmet OSMANOĞLU 

Askom Mühendislik, Ankara, TÜRKİYE  
[osmanoglu.mehmet@outlook.com](mailto:osmanoglu.mehmet@outlook.com)

### Önemli Katkılar (Highlights)

- Delgi veriminde pasa irilikleri (PİK) performansları kıyaslanarak değerlendirme yapılmıştır.
- Delgi hızı (PR) istatistikleri ile delici uç performansları analiz edilmiştir.
- Delici uç tipinin ve dizaynının delgi hızı(PR) ile pasa irilik kat sayısı (PİK) arasındaki ilişki incelenmiştir.
- Button tip delici uçların araştırma için kullanılan sahada daha az pasa kırıntısı ürettiği ve daha hızlı ilerlediği gözlemlenmiştir.



## DÖNER DARBELİ DELİK DELME PERFORMANS ANALİZİ ve UYGUN UÇ SEÇİMİ: KAYSERİ HİMMETDEDE OCAĞI ÖRNEĞİ

\* Mehmet OSMANOĞLU

Askom Mühendislik, Ankara, TÜRKİYE  
[osmanoglu.mehmet@outlook.com](mailto:osmanoglu.mehmet@outlook.com)

(Geliş/Received: 07.10.2022; Kabul/Accepted in Revised Form: 06.08.2023)

**ÖZ:** Bu çalışmada Himmetdede ocaklarında kullanılan delici makineler ile delgi işlemi yapılmıştır. Delici uçlarının özelliklerine göre 3 farklı bit tipi kullanılmıştır. Button ve yarı balistik olarak adlandırılan bu delici uç tiplerinin işletme sahasında verimliliği kıyaslanması yapılmıştır. Delik delme verimlerinde gerçekleşen değişimlerin incelenmesi amacıyla arazide delik delme süreleri ölçülmüş ve buna bağlı olarak her bir delici ucun delme hızları (PR) hesaplanmış ve delik delme işlemi sonucunda açığa çıkan kırıntılardan temsili örnekler alınarak laboratuvarda elek serisi ile sınıflandırılarak her bir delik için pasa irilik katsayıları (PİK) hesaplanmıştır. Elde edilen bütün veriler birlikte değerlendirilerek farklı delici uç tipleri için delme verimlerinde gerçekleşen değişimlerin incelenmesi ile söz konusu granitoid ocaklarında gerçekleştirilen delme işlemi için uygun uç tipi belirlenmeye çalışılmıştır.

**Anahtar Kelimeler:** Delgi Biti, İlerleme hızı, Pasa irilik kat sayısı (PIK)

### Evaluation of Percussive Drilling and Selection of Suitable Bit: The Case of Kayseri Himmetdede Quarry

**ABSTRACT:** In this study, drilling was done with the drilling machines used in Himmetdede quarries. According to the characteristics of the drill bits, 3 different bit types were used. Efficiency comparisons of these drill bit types, called button and semi-ballistic, were made in the field of operation. To determine the changes inefficiency of drilling operations, penetration rates were observed on the field and drilling rates (PR) of each drill bit accordingly calculated. Then the coarseness index was calculated. As a result of the drilling operations the coarseness index was calculated for each hole by taking representative samples from exposed crumbs and classified by sieve series in the laboratory. Suitable bit type was tried to identify for the granitoid quarries by examining the all data together which includes the changes in efficiency of drilling operations.

**Keywords:** Drill bit, Penetration rate, Coarseness index (CI)

#### 1. GİRİŞ (INTRODUCTION)

Delme patlatma yöntemi ile üretim yapılan bir işletmede delik delme makinesinin seçiminden sonra uygun delici ucun seçimi de çok önemlidir. Delme işleminin maksimum verim de olabilmesi için delici uç seçimi yapılırken uç özellikleri ile delme işleminin yapılacağı formasyonun özelliklerinin ilintili olması gerekir. Bu nedenle delme işleminin yapılacağı formasyonun özelliklerine göre delik delme işleminde kullanılacak uç tipinin iyi belirlenmiş olması gerekir. Aksi halde delme verimliliği oldukça düşecek ve dolayısıyla da maliyet yükselecektir.

Açık ocak maden işletmeciliği çalışmalarında patlatmaya yönelik delme işleminin amacı, kayaya mekanik enerji uygulayarak içine patlayıcı maddelerin yerleştirilebileceği deliklerin oluşturulmasıdır. Kayaçlarda delme işlemi, delici uç tipleri, delme hızı, delinecek formasyonun fiziksel, mekanik ve jeoteknik özelliklerine bağlıdır. Bu özellikler göz önüne alınarak delme işleminde istenen verimde

\*Corresponding Author: Mehmet OSMANOĞLU, [osmanoglu.mehmet@outlook.com](mailto:osmanoglu.mehmet@outlook.com)

çalışılması durumunda hem işletme hem de üretim maliyeti önemli ölçüde etkilenmektedir. Delme işleminde uygun çalışma parametrelerinin belirlenmemesi sonucu uçlarda aşırı aşınma ve yüksek miktarda uç tüketimi kaçınılmaz olmaktadır. Bu nedenle, uygun makine parametreleri ve uç tipinin seçimi önemli olmaktadır. Uygulamalarda çeşitli formasyonlar için çok farklı uç tipleri kullanılmaktadır. Yumuşak ve sert kaya oluşumlarının delinmesi, delgi uçlarının ömrünü önemli ölçüde azaltabilir. Bu, delme sırasında üretilen sıcaklığın ve dikkate alınan çalışma parametrelerinin birleşik etkisinden kaynaklanmaktadır [4]. Matkap ucunun aşınma hızı, kaya örneğinin aşınmasına bağlı olarak belirlenmiştir. Bu, kaya örneğinin silika (SiO<sub>2</sub>) içeriğinden kaynaklanmaktadır. Bu nedenle, kaya özelliklerinin incelenmesi, optimum delme parametrelerinin ve matkap ucu tipinin seçiminde yardımcı olacaktır [1].

[2], yaptıkları çalışmada delik delme işleminde uç tipinin ve pasa irilik kat sayısının delik delme hızına etkisini incelemişlerdir. 3 farklı uç tipi için delik delme hızı ve pasa irilik katsayıları belirlemişlerdir. Pasa irilik katsayısı arttıkça delme hızının da arttığı belirlenmiştir [3], farklı uç tiplerinde yeraltında farklı formasyonlarda delme amacına göre delme hızları ve verimleri arasında kıyaslama bilgileri mevcuttur. [5] ve [7] yapılan çalışmalarda kaya formasyonlarındaki değişkenliklerin delinebilirliğe etkilerinin analizlerinden bahsedilmiştir.

Kazı mekaniği deneyleri gerçek boyutlu keskinlerin kullanıldığı tam boyutlu doğrusal kazı seti kullanılarak yapılan kesilebilirlik deneylerinden oluşmaktadır. Bu deneylerde kayacı kesmek için gerekli olan kesme kuvvetleri (Kesme kuvveti, FC; Normal kuvvet, FN) ve sarf edilen spesifik enerji (SE) belirlenir. Kazı deneyleri sonrasında ortaya çıkan pasaların bir elek seti ile 5 elenerek parça boyut dağılımı tespit edilerek buradan pasa irilik katsayısı (PİK) hesaplanmaktadır [9].

Çalışılan formasyonun değişkenliği göz önünde bulundurularak delici uç seçiminde sarf ve süre olarak en iyi performans gösteren özellikteki uç türlerinin tercih edilmesi gerekmektedir.

Bu çalışma kapsamında Kayseri Himmetdede bölgesinde bulunan maden sahalarında kullanılan delici makinelerin, bölge formasyonuna göre belirlenmiş delici uçlar ile patlatma/numune delik delme işlemleri gerçekleştirilmiştir. Çalışma sırasında buton, balistik ve yarı balistik delgi ucu özellikleri olan ekipmanlar kullanılmıştır.. Çalışmalar sırasında makinenin çalışma parametreleri sabit tutularak farklı uç çeşitlerine bağlı olarak performans analizleri yapılmıştır. Bunun için arazide delme işlemi süresince zaman etüdü(kronometraj) çalışması gerçekleştirilmiştir. Bu veriler birlikte değerlendirilerek hangi uç tipinin kullanımının uygun olacağı belirlenmeye çalışılmıştır.

Delgi hızları seçilen delici uçlara göre aşınma dereceleri ile doğru orantılı olarak azalmıştır. Delgi işlemi esnasında çıkan pasalardan alınan numuneler ile pasa irilik katsayıları mukayese edilmiştir. Pasalardaki iriliklerinin artması veya azalması işletmeye ek bir işlem tanımlamadığı için PİK değerinin yüksek olması delgi hızının daha fazla olmasının etkenlerindedir.

## 2. MATERYALVEMETOT (MATERIALANDMETHOD)

### 2.1. Delici Makine ve Kullanılan Delici Uçlar (Drilling Machine and Drilling Bit)

Hammadde maliyetine etki eden masraf kalemlerinden birisi de delik delme maliyetidir. Delik delme maliyetlerine etki eden parametreler ise delici uç tipi, makinenin çalışma parametreleri ve kayacın özellikleridir. Uygun çalışma parametrelerinin belirlenmemesi sonucu uçlar da aşırı aşınma ve yüksek uç tüketimi kaçınılmaz olmaktadır. Bu nedenle, uygun makine parametreleri ve uç tipinin seçimi önemli olmaktadır. Uygulamada çeşitli formasyonlar için çok farklı uç tipleri kullanılmaktadır.

Bu çalışma kapsamında, Himmetdede Granitoid ocağında delik delme işlemlerinde kullanılan Delici makineye (Şekil 1) farklı delici uçlar temin edilmiştir. Granitoid ocağında 3 farklı delici uç tipi kullanılmıştır.



Şekil1.Delici makinenin genel görünüş  
Figure1.General view of the drilling machine

Delici ucun görevi, kullanılacağı formasyonda en iyi penetrasyon(ilerleme) oranı ile delik delmektir. Delici uç seçimi yapılırken aşağıdaki parametreler mutlaka değerlendirilmelidir;

- Kayaç Özellikleri
- Delici Tabanca Özellikleri
- Penetrasyon Oranı
- Servis Ömrü
- Bileme Aralıkları
- Delik Kalitesi

Çalışılacak olan zemine göre, farklı tipte tasarlanmış delici uçlar mevcuttur. Sert formasyonlarda küresel(spherical), yumuşak zeminlerde ise sivri (ballistic) butonlu bitler tercih edilmelidir [6].

.Maksimum penetrasyon oranı ile iyi delikler delebilmek için, formasyonun özelliklerine göre uç seçimi, en önemli parametrelerden biridir. Çatlaklı ve delik çökmesinin yaşanabileceği zeminler de retrac (bıçaklı) tip uç tercih edilmesi uygundur. Bitin arkasında bulunan bıçak şeklindeki yapı, delik ilerlemesi esnasında, delinen malzemenin uç arkasında toplanmasını, olası çökmelerde sıkışmayı engellemek amacı ile tasarlanmıştır [6].

Uçlar delik delerken doğal olarak aşınacaklar ve bir müddet sonra ömürlerini tamamlayacaklardır. Busüreyimaksimumdüzeydetutmakişletmemaliyetiaçısındanoldukçaönemlidir.Aşınandeliciuçları bilemek, uç ömrünü uzatmak için tercih edilebilir [6].

Himmetdede 'de bulunan madende ve serbest piyasa taleplerine hammadde sağlamak için Granitoid ocağında yapılan delme işlemlerinde, mevcut delici makinede uygun farklı uçlar kullanılması planlanmaktadır. Kullanılan uçların başlangıç aşamasındaki durumları Şekil 2'de ve uçların ömrünü tamamlamış olduğu durumları Şekil 3'de verilmiştir. Denenmesi planlanan farklı uçların, makine üzerindedğiştirilerekaynıformasyondadeliksayısvedelmemiktarişitolacakşekildekullanılmasına dikkat edilmiştir. Delici makinenin Granitoidteki delme işlemlerinde, çalışma parametreleri (baskı kuvveti, dönme hızı, akışkan hava basıncı, darbe basıncı) kullanılan uçların verimliliği gözlemlenmesi için tüm delme işlemlerinde sabit tutulmuştur.

Delici makinelerin sahadaki çalışmalarını kıyaslamalarının daha uygun yapılabilmesi için makine çalışma parametrelerinin sabitlenmesi gerekmektedir. Bu proje çalışmasında kullanılan delici makinenin çalışma parametreleri Çizelge 1'de verilmiştir.



Şekil2.Çalışma kapsamında kullanılan delici uçların başlangıç durumları (a):tipi(Buton), (b):B tipi (Yarı Balistik), (c) : A tipi (Yarı Balistik)

Figure2. Initial states of the drill bit used in the work(a):(A)Type A(Button) (b):Type B(Semi-Ballistic) (c):Type A(Semi-Ballistic)



Şekil3.Çalışma kapsamında kullanılan delici uçların delgi işlemleri sonrası durumu (A):A tipi (Buton), (B) : B tipi (Yarı Balistik), (C) : A tipi (Yarı Balistik)

Figure3.Initial states of the drill bit used in the work (a):(A)Type A(Button)(b):Type B(Semi-Ballistic)(c):Type A(Semi-Ballistic)

### Çizelge1.Delici makinenin çalışma parametreleri

Table 1.Working parameters of the drilling machine

Hava Basıncı	6 bar
Dönme Hızı	30–50 bar
Baskı Basıncı	BirinciDarbe50 bar İkinciDarbe85bar
Darbe Basıncı	Birincidarbe70bar İkinciDarbe95bar

## 2.2. Arazi Çalışmaları ve Uygulamalar (Field Works And Applications)

Arazi çalışmaları Himmetdede Granitoid ocağında gerçekleştirilmiştir. Ocakta delik delme öncesinde örtü kazı işlemleri yapılmaktadır (Şekil 4). Çalışmalarda ocakta uygulanan delik paterni planlama aşamasında uygulanmaktadır. Delici uçların kıyaslanması için Pasa İrilik Katsayısının (PIK) değerlendirilmesi önemlidir.

Arazi çalışmaları, delikler delinirken delme süreleri ve delik boylarının kaydedilmesi ve deliklerden açığa çıkan pasalardan örnek alınmasını (Şekil 5) kapsamaktadır. Bu çalışmaların sağlıklı bir şekilde yapılabilmesi için arazi çalışmaları sırasında deliklerden alınan kırıntılardan konikleme dörtleme şeklinde temsili numune alınmıştır.



**Şekil 4.** Açık ocak örtü kazı işinden bir görünüm  
*Figure 4.* A view from the open pit cover excavation



**Şekil 5.** Delik delme işleminde çıkan kırıntılardan örnek alım işlemi  
*Figure 5.* Sampling process from the part removed in the hole drilling process

Delik delme sırasında deliğe başlandığı andan delik bitimine kadar olan süreler kronometre ile ölçülmüştür. Delikler delinirken üç farklı süre tutulmaktadır. Bunlardan birincisi delme işleminin başlangıç zamanı ile bitiş zamanı arasındaki fark, ikincisi o delikte tabancanın iş yaptığı toplam süre, diğeri ise bir tij boyu delinmesinde geçen süre olmaktadır. Toplam delik süresi içinde hem delme işi hem de deliğin temizleme işi yapıldığından dolayı üç ayrı süre hesabı yapılmaktadır. Bu nedenle, delik delme süresi içinde deliğin temizleme zamanı, manevra hareketleri, tij değişim süreleri, pozisyon alma süreleri çıkarılarak net delik delme süresi ( $PR_{net}$ ) her bir delik için ayrı ayrı hesaplanmıştır. Delik boylarının değişken olması sebebiyle, her bir delikte bir tij boyu olan 3 metrelik mesafeler için net delgi süreleri de kayıt altına alınmıştır.

Daha sonra ölçülen delme sürelerinden her delik için brüt delme hızı ( $PR$ ) ve net delme hızları ( $PR_{net}$ ) Eşitlik 1 ve 2 yardımıyla hesaplanmıştır. Bu delme hızlarına ilişkin bazı veriler örnek olarak Çizelge 2' de verilmiştir.

$$PR = \frac{H}{T} \quad (1)$$

$$PR_{net} = \frac{H}{T_{net}} \quad (2)$$

Burada; PR: Brüt delme hızı (cm/dak), PR<sub>net</sub>: Net delme hızı (cm/dak), T:Toplam delik delme süresi (dakika), T<sub>net</sub>: Net delik delme süresi (dakika), H : Delik boyu (cm)

**Çizelge 2.** A-Yarı balistik uç ile beş adet delik için hesaplanmış net delme hızları

*Table 2. A-Net drilling rates calculated for five holes with semi-ballistic bit*

Delik No	Delik Delme Süresi	Delik Boyu	Ne Delik Delme Süresi	1TijDelme Süresi(3m)	Brüt Delme Hızı	Net Delme Hızı	Delik Verimi
	s	m	s	s	cm/dk	cm/dk	%
1	503	4,40	307	209	52,51	86,12	60,98
2	527	4,80	322	201	54,61	89,55	62,00
3	528	5,00	322	193	56,87	93,26	60,00
4	536	5,00	327	196	56,00	91,84	61,00
5	476	5,00	290	174	63,08	103,45	62,00

Delik verimleri ise brüt delme hızının net delme hızına oranı Eşitlik 3 yöntemi ile hesaplanmaktadır.

$$Delik Verimi = \frac{PR}{PR_{net}} * 100 \quad (3)$$

### 3. BULGULAR VE TARTIŞMA (FINDINGS AND DISCUSSION)

#### 3.1. Sahanın Jeolojisi (Geology of the Site)

Himmetdede genel olarak yaşlıdan gence doğru metamorfikler (şist-kireçtaşı), Granitoidik-granodiyoritik sokulum, piroklastikler ve gölsel tortullar yer almaktadır.

Bölgesel ölçekte bilinen, Kayseri'den Nevşehir'e doğru uzanan kıvrımlı bindirme zonunun bir parçası arazi çalışmalarında tespit edilmiştir. Bindirme zonu içerisinde yer alan, şistlerle beraber bulunan yaşlı kireçtaşları, metamorfik seri içerisinde yer almaktadır. Cevherleşme büyük olasılıkla bindirme zonu içerisinde taşınan metamorfize olmuş, boşlukça zengin kireçtaşlarının hidrotermal çıkışlara sebep olan tektonik aktive sırasında yeryüzüne çıkan sıcak suların taşıdığı metal içeriğini depolamasıyla cevherleşme için uygun ana kaya içerisinde oluşmuştur. Fakat burada tektonik aktivite tek başına cevherleşmeye kaynak olabilecek yeterlilikte değildir. Besleyici bir sokulum kütlesi de olmalıdır.

Çalışılan sahaların yakın çevresinde bulunan kaplıcalar, bölgede günümüzde de devam eden bir hareketlilik olduğunu göstermektedir. Zaten sahada da rastlanan hidrotermal breşler ve traverten oluşukları da bunun en iyi işaretidir. Değerli metalik maden yataklarının sıcak suların etkisiyle oluşup ve/veya zenginleştiği düşünüldüğünde bölgenin önemi daha da artmaktadır.

Yapılan hendek çalışmalarında silisleşmiş, arjilleşmiş, stokvork kuvars-karbonat damarcıklı porfiritik dokulu intruzif ve silisleşmiş killeşmiş metasedimentler gözlenmiştir. Özellikle altere porfiri sokulum içerisinde çok yoğun mangan ve demiroksitler gözlenmektedir.

Granitoid işletmesi içerisinde yapılan patlatma çalışmalarında formasyon içerisinde kılcal olarak damarlı yapıda sokulumlar gözlemlenmiştir. Açık ocak faaliyet alanında delme işlemi yapılan bölgeler genel itibariyle 2 bölümde toplanmaktadır. Üst kazı tabakası ve basamak patlatmalarından oluşan iki aşama üretim bölgeleri içinde killi formasyonda delici uçların net delme işlemi hızlarındaki farklılıkları

gözlemlenmektedir. Açık ocak faaliyeti genel tesis beslemesi, Himmetdede işletmesi talebi ile doğru orantılı gitmesinden ötürü uçların karşılaştırma imkânları net olarak aynı formasyonda delinebilmiştir.

### 3.2. Delici Uçların Performansı (Performance Of Drilling Bits)

Granitoid ocağında toplam olarak 1060 adet delik delme işleminde yaklaşık toplam 5016 m delik delinmiştir. Kullanılan delici makinelerin teknik özellikleri ve üretim metodu sebebiyle ortalama delik boyu 4-6 m'dir. Çalışma kapsamında üç farklı uç tipi kullanılarak her bir uç için eşit uzunlukta delikler delinmeye çalışılmıştır (Çizelge3). Her delikte kronometraj çalışması yapılmış ve her delikte oluşan kırıntılardan temsili kırıntı örnekleri alınmıştır. Arazi çalışmaları sırasında kaydedilen kronometraj verileri değerlendirilerek her bir uç tipi için delme performansları incelenmiştir. Yapılan çalışmalar süresinde elde edilen veriler delici uç tiplerine ve imalatçı firmalara göre değişkenlikler gözlemlenmiştir.

**Çizelge 3.** Ocakta delinen toplam delik mesafesi

*Table 3. Total distance of holes drilled in the open pit*

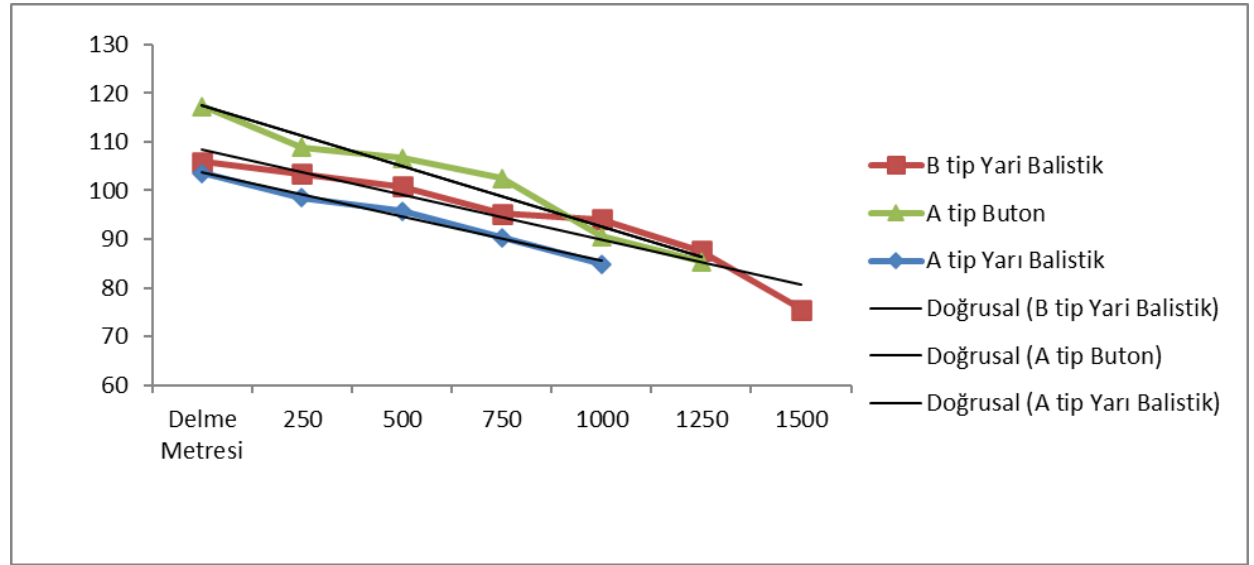
Uç Tipi	Yarı Balistik (Btip)	Yarı Balistik (Atip)	Buton (Atip)	Toplam
Toplam Delik Uzunluğu(m)	1844,9	1407,9	1763,2	5016

Delikler delinirken delik delme süreleri her bir delik için başlangıç ve son manevra süreleri arasındaki zamanlar tutulmuştur. Delme işleminin başlangıç zamanı ile bitiş zamanı arasındaki fark brüt delik delme süresi olarak alınmıştır. Bu süre içerisinde tij değiştirme, delik içi manevra ve delik temizleme süreleri dâhildir. Çalışma sırasında ikinci bir kronometre ile sadece tabancanın çalışma süresi yani sadece delme işleminde geçen süre tutulmuştur. Bu süre net delik delme süresi olarak alınmıştır. Bu süreler delik boyuna bölünerek ilerleme hızları (sırasıyla PR ve PRnet) belirlenmiştir. Kullanılan farklı tip uçların her biri için 250, 500, 750, 1000, 1250, 1500, 1750 metrelerindeki net delgi hızları Çizelge 4 'de verilmiştir. Toplam delik metrajlarında artış bitlerde aşınmayı getirmiş ve dakikada delik uzunluğu ters orantılı olarak azalmıştır. İlk delgi işlemi başlaması itibariyle net bir şekilde A tipi buton özellikte olan delici uçun diğerlerine göre daha uzun delgi yaptığı görülmektedir. Değerlendirildiğinde delici uçların kullanım ömürleri artıka hızlarında ortalama %10 civarı bir yavaşlama görülmektedir. Delik mesafelerinin artması ile buton tip delici uçların elmaslarındaki aşınma ve kayıpların artması delme hızlarında daha belirgin düşüşlerin olmasına sebep olmuştur. Delici uçların her biri için 250 metrelik mesafelerde ara değerler alınarak delgi hızlarının değerlendirmeleri mukayese edilmesi sonucu (Şekil 6) belirlenen formasyon ve ekipmanlar için A tip buton ucun uygun olduğu görülmektedir[8].

Her bir uç için ortalama brüt ilerleme hızları, ortalama net ilerleme hızları ve bu deliklerden elde edilen PİK değerlerinin ortalamaları Çizelge 5'de verilmiştir. Üretim yöntemi ve sonrasındaki çalışmalarda delikten çıkan kırıntıların (pasaların) bir önemi olmadığı için tane boyutu delme hızına etkisi efektif değerlendirilebilmektedir. Pasa irilik katsayısı artması delme işleminin hızıyla doğru orantılıdır. Daha küçük kırıntı üretilmediği için delgi ekipmanında aşınma ve ilerleme fazladır. Osmanoglu (2016).

**Çizelge 4.** Ocakta kullanılan farklı uçların metrelerce göre net delgi hızları*Table 4. Net drilling speeds according to meters of different bits used in the open pit*

Delme Metresi	Net Delme Hızı (cm/dk)		
	B Tip Yarı Balistik	A Tip Yarı Balistik	A Tip Buton
250	105,87	103,54	117,24
500	103,49	98,45	108,85
750	100,87	95,83	106,63
1000	95,24	90,37	102,54
1250	94,03	84,91	90,63
1500	87,57	-	85,35
1750	75,61	-	79,67

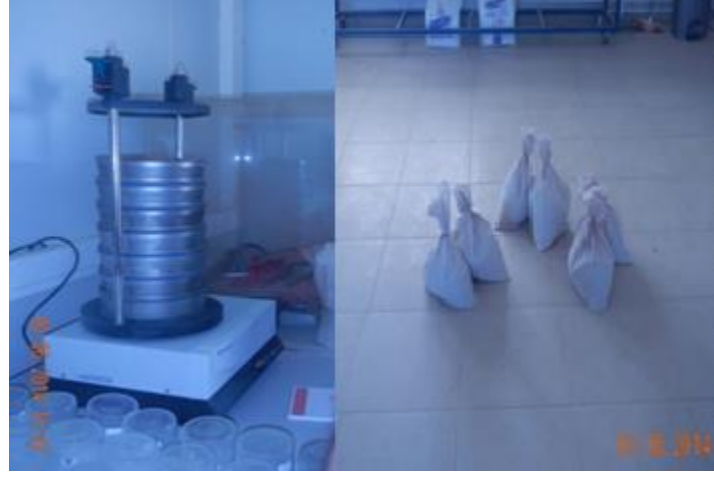
**Şekil 6.** Uçların Net Delme Hızı–Kümülatif delme mesafesi ilişkisi*Figure 6. Net Drilling speed of bits–Cumulative drilling distance relationship***Çizelge 5.** Ocakta kullanılan farklı uçların performansları*Table 5. Performances of different tips used in the open pit*

Uç Tipi	Ort.PR(cm/dk)	Ort.PRnet(cm/dk)	Ort.PİK
(BTip) Yarı Balistik	58,98	98,48	379,02
	55,08	90,33	425,32
	68,44	103,44	506,41
(ATip) Yarı Balistik	55,08	90,33	425,32
	68,44	103,44	506,41
	58,98	98,48	379,02
(A Tip) Buton	68,44	103,44	506,41
	58,98	98,48	379,02
	55,08	90,33	425,32

### 3.3. Pasa İrilik Katsayısının Belirlenmesi (Coarseness index (CI))

Delik delme işleminin performansını analiz etmek için her delikten temsili olarak yaklaşık 12 kg pasa (kırıntı malzeme) alınmış ve laboratuarda 2 kez konileme-dörtleme yapılarak numune miktarı azaltılmıştır. Delme işlemleri sırasında oluşan pasalar,  $3\sqrt[3]$  yöntemine göre oluşturulmuş bir elek serisi

(4.75, 2.36, 1.18, 0.600, 0.300, 0.150 mm) ile otomatik titreşimli elek ile 5 dakika elenmiş (Şekil 7) ve elek analiz tabloları oluşturulmuştur. 6 adet elek kullanılarak yapılan elek analizleri sonucunda 7 ürün elde edilmiş ve oluşturulan bu elek analiz tablolarından bu ürünlerin kümülatif yüzde toplamları alınarak PİK değerleri hesaplanmıştır. Osmanoglu (2016).



**Şekil 7.** Arazi çalışmasında alınan numuneler ve eleme işlemi  
*Figure 7. Samples taken during field work and sieving process*

Btip-Yarı Balistik tip uç için 394, A tip-Yarı Balistik tip uç için 295 ve Atip-Buton Tip uç için 371 adet delik olmak üzere gerekli verilerin değerlendirilmesi Çizelge 7’de verilmiştir. Her uç tipi için eş değer alanlardan alınan 20 delik numunesi sonucunda üç farklı uç tipi için PİK değerleri hesaplanmış ve Çizelge 6–7 de verilmiştir [8]. 3 numaralı delikten örnek olarak yapılan bu çalışmada delgi sürecinde kullanılan bitlerin aşınmalarının az olduğu öngörüsü ile delikten çıkan pasaların tane boyunun dağılımının biraz daha küçük olduğu gözlemlenmektedir.

Arazi çalışması kapsamında yapılan delgilere eşlik edilerek her bir delgi biti için alın 20 numunenin tane boyutu dağılımının en yoğun olduğu tür buton tip olduğu görülmüştür. Literatürde belirtilen genel durumlar ve yine saha gözlemleri ile desteklenmesi ile oluşan urum buton tip bitin PİK değerinin fazla olması delme hızını ve bit ömrünün fazla olduğunu göstermektedir.

**Çizelge 6.** Ocakta delinen 3 numaralı delik için pasa irilik katsayısının (PİK) hesaplanması

*Table 6. Calculation of the rust coarseness coefficient (PIK) for the hole number 3 drilled in the quarry*

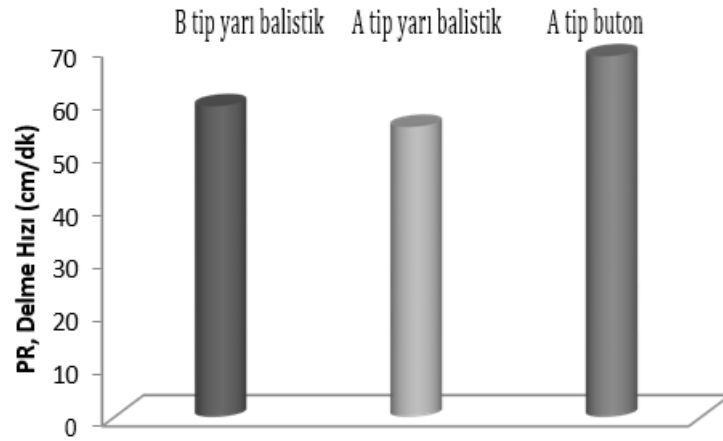
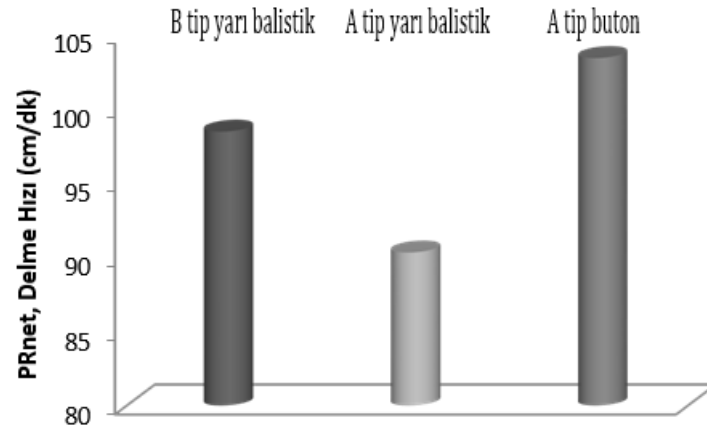
Numune	Ağırlık (g)	Yüzde (%)	%EÜ Toplamı
+ 4,75mm	265,26	8,90	8,90
+ 2,36mm	517,95	17,38	26,28
+ 1,18mm	507,80	17,04	43,32
+ 600mikron	389,79	13,08	56,40
+ 300mikron	378,72	12,71	69,11
+ 150mikron	347,39	11,66	80,77
- 150mikron	573,06	19,23	100,00
<u>Toplam</u>	2979,97	<b>PİK</b>	<b>384,79</b>

**Çizelge 7.** Kaya kütlesi için PİK değerler*Table 7. PIK values for rock mass*

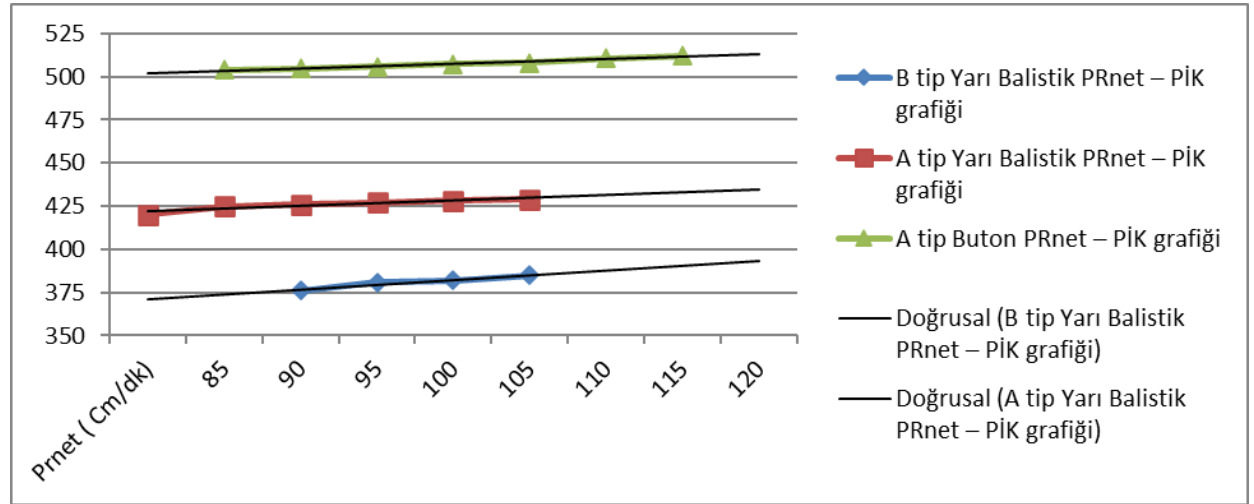
Uç Tipi	PİK Değeri (ORT±S.S.)	Numune Alınan Delik Sayısı	Toplam Delinen Delik Sayısı
Yarı Balistik (Btip)	383,04± 3.82	20	394
Yarı Balistik (Atip)	427,52± 1.06	20	295
Buton (Atip)	508,83± 3.72	20	371

Granitoid işletmesi çalışmalarının yürütüldüğü 3 farklı uç tipi için bütün deliklerin ortalaması alınarak elde edilen brüt delme hızı Şekil 8 de analiz edilmiştir. Brüt delme sürelerin içerisinde delici ekipmanın konumlanması, tijin sürülmesi, yeni tij eklenmesi vb. süreçlerin olması sebebiyle süre başına yapılan metraj değerleri düşük olduğu görülmektedir. Delgi bitinin delici makine tarafından harekete başlatılması ile yapılan tüm delme işlemi aşamasına net delme hızı denir. Bu veri ise Şekil 9'de bitler için mukayese edilmiştir.

Delgi süreleri çalışma işinde önemli verileri bizler ile paylaşmaktadır. Üretim öncesi hazırlıklardan olan ve önemli bir zaman tutan bu çalışmadır. Bu hazırlık faaliyetinin azalması ile günlük delik sayısında artma, iş gücünü doğru yönetme ve maliyetlerin doğru analizi sebebiyle efektif hale getirilmesi şirketlere kar/fayda sağlayacaktır.

**Şekil 8.** Ortalama brüt delik delme hızları*Figure 8. Average gross drilling speeds***Şekil 9.** Ortalama net delik delme hızları*Figure 9. Average net hole drilling speeds*

Çalışma sahasında, laboratuarda ve sonrasında yapılan hesaplamalarda elde edilen verilerin son kıyaslaması için PRnet- PİK grafiği hazırlanmıştır (Şekil 10). Hem tane boyutu olarak en yoğun olan veriyi üretmiş hem de delme hızlarına göre mukayese edildiğinde en kısa sürede en fazla delik uzunluğuna ulaşan A tip buton delici uç olmuştur.



Şekil 10. Delici Uçların PRnet-PİK grafiği

Figure 10. Drilling bits PRnet-PİK graphic

#### 4. SONUÇ ve TARTIŞMALAR (RESULTS and DISCUSSIONS)

Sabit iş makineleri ve operatörler ile yapılan delme işlemlerinde, ilerleme hızları verimliliği dikkate alındığında en uygun uç tipinin buton olduğu görülmektedir. Yapılan saha çalışmalarında da kullanılan A tip buton ucun verimli olduğu gözlemlenmiştir. Çizelgeler incelendiğinde ocakta delme hızı(verimi) en yüksek uç tipi Buton(A tip) olduğu görülmüştür

Operatörlerin rutin çalışmalarında ekipman değişimlerinde genel olarak gözle yapılan kontroller sonrasında delici uçların değişimi yapılmaktadır. Yarı balistik delici uçlar arasında B tip delici uç A yarı balistik uca göre daha fazla mesafe kat etmiştir. Farklı firmaların delici uç dizaynlarının (bitlerin üzerindeki elmasların konumları, elmas adetleri, soğutucu kanalların dizaynları vb.) farklı olması benzer bit tiplerinde de olsa değişik veriler ürettiği gözlemlenmiştir.

Pasa irilik katsayılarına göre en verimli uç tipinin Buton tip delici uç kullanılmasıyla elde edilmiştir. Bu da ucun delik yüzeyinden daha iri malzeme ayırdığını böylece delik içinde öğütmenin en az olduğunu göstermektedir. Delik içi öğütmenin az olması istendiği için (bazı operasyonlarda özel olarak istenebiliyor) buton tip bit verimliliği görülmüştür.

Daha hızlı delgi, daha az delik için tane boyutu oluşturması ekipmanın daha uzun kullanımı sağlamaktadır. Ürünlerin birim maliyetlerinin çok yakın olduğu varsayımı üzerinden değerlendirme yapılmıştır. Bu sonuçlar göz önüne alındığında ocak için delik delme işleminde kullanılacak en uygun delici ucun Buton olduğunu göstermektedir.

#### Etik Standartlar Bildirimi (Declaration of Ethical Standards)

Çalışma etik standartlara uygun olarak gerçekleştirilmiştir.

#### Yazar Katkı Beyannamesi (Credit Authorship Contribution Statement)

Bu çalışmanın tüm aşamaları Mehmet Osmanoglu tarafından yürütülmüştür.

**Çıkar Çatışması Beyannamesi (Declaration of Competing Interest)**

Yazarlar herhangi bir çıkar çatışması olmadığını beyan etmektedir.

**Destek / Teşekkür (Funding / Acknowledgements)**

Bu çalışmanın yürütülmesi esnasında herhangi bir kurum veya kuruluştan maddi bir destek alınmamıştır.

**Veri Kullanılabilirliği (Data Availability)**

Bu çalışmadan elde edilen veriler diğer araştırmacılar tarafından kullanılabilir.

**KAYNAKLAR (REFERENCES)**

- [1] RK. Abbas, 'Yağlı matkap uçlarının aşınmasına ilişkin bir inceleme (aşınma azaltma ve niceleme için geleneksel ve son teknoloji yaklaşımlar)' Eng Başarısızlığı Anal 90, 554-584, 2018.
- [2] R. Altındağ, N. Şengün, E. Totiç, F. Ürün, 'Kireçtaşı Ocağındaki Darbeli Delme İşleminde Kayaç Özelliklerinin Delici Uç Aşınmasına Etkisi ve Uygun Delici Uç Seçimi.' TÜBİTAK Proje No: 109M02, 2011.
- [3] D. Akbay, R. Altındağ, 'Antalya-Kemer-Tekirova Güzergahında Açılan Altan Ayağ Tüneli (T3 Tüneli) Kaya Saplaması Uygulaması Delik Delme Performans Analizi', 3. Uluslararası Ulaşımında Yeraltı Kazıları Sempozyumu Kitabı, 5-11, 2013.
- [4] F.C. Appl, C.C. Wilson, I. Lakshman 'Kaya kesmede PDC kesicilerin kuvvetlerinin, sıcaklıklarının ve aşınmasının ölçülmesi', Aşınma 169(1), 9-24, 1993.
- [5] D.F.Howarth, J.C. Rowlands, 'Quantitative Assessment of Rock Tex tureand Correlation with Drill ability and Strength Properties', Rock Mech Rock Eng 20, 57-85.1987
- [6] İMMB (İş Makineleri Mühendisleri Birliği), 'Uygun Uç Seçimi', İş Makineleri Mühendisleri Birliği Dergisi 51,10, 2015.
- [7] S. Kahraman, N. Bilgin, C. Feridunoğlu, 'Dominant Rock Properties Affecting The Penetration Rate of Percussive Drills', International Journal of Rock Mechanics&Mining Sciences 40722711-723, 2003.
- [8] M. Osmanoğlu, 'Himmetdede Ocağında Döner – Darbeli Delik Delme Performans Analizi ve Uygun Uç Seçimi' Yüksek Lisans Tezi, Süleyman Demirel Üniversitesi Mühendislik Fakültesi Maden Mühendisliği Bölümü, Isparta, TÜRKİYE 2016.
- [9] H. Tunçdemir, 'Kollu Galeri Açma Makinelerinin veya Benzer Makinelerin Cevher Kazısında Kullanımının Araştırılması' Doktora Tezi, İstanbul Teknik Üniversitesi Maden Fakültesi Maden Mühendisliği Bölümü, İstanbul, TÜRKİYE, 2002.



## STATISTICAL METHOD FOR ESTIMATING SELECTED GEOTECHNICAL PROPERTIES OF QUATERNARY SEDIMENT

\*Abbas Jawad AL-TAIE 

*Al-Nahrain University, Civil Engineering Department, Baghdad, IRAQ*  
[al.taiegeo@gmail.com](mailto:al.taiegeo@gmail.com), [abbas.j.al-taie@nahrainuniv.edu.iq](mailto:abbas.j.al-taie@nahrainuniv.edu.iq)

### *Highlights*

- Some geotechnical properties of Quaternary sediments have been presented.
- Data base for geotechnical properties of Quaternary sediments has been presented both statistically and graphically.
- Statistical correlations have been carried out with the assistance of regression analysis method by using a specialized and advanced software package in the statistical analysis.
- The geotechnical parameters of quaternary clay may be easily and rapidly estimated based on simple engineering test data, using one of the equations proposed in this paper.



## STATISTICAL METHOD FOR ESTIMATING SELECTED GEOTECHNICAL PROPERTIES OF QUATERNARY SEDIMENT

\*Abbas Jawad AL-TAIE 

*Al-Nahrain University, Civil Engineering Department, Baghdad, IRAQ*  
[al.taiegeo@gmail.com](mailto:al.taiegeo@gmail.com), [abbas.j.al-taie@nahrainuniv.edu.iq](mailto:abbas.j.al-taie@nahrainuniv.edu.iq)

(Geliş/Received: 05.03.2021; Kabul/Accepted in Revised Form: 06.08.2023)

**ABSTRACT:** Quaternary sediments have characteristics that distinguish them from older soils. In engineering practice, these sediments are of particular interest to engineering geologists and geotechnical engineers because many engineering constructions have to be founded on, or in, them. This paper describes a method for rapidly estimating selected geotechnical properties of some Quaternary soil from the Mesopotamian Plain using statistical correlation equations. The paper explored an expedient statistical method to estimate some geotechnical properties (including total and dry unit weights, void ratio, porosity, Atterberg limits, and compression index) rapidly without running time-consuming and expensive laboratory tests. It was found that the selected properties showed a relatively moderate to high correlation with independent properties. Both the unit weight and void ratio depicted a high correlation with initial water content. while a moderate correlation existed between compression index and initial water content. Also, the plasticity index has a strong correlation with liquid limit values. The results of this study accord an additional usage as facultative engineering tools for geotechnical engineers to utilize for any preliminary engineering design.

**Keywords:** *Statistical method, Quaternary soil, Geotechnical properties*

### 1. INTRODUCTION

It is almost certain that the commonest materials (soil or rock), from the geological point of view, occurring closes to, or at, the earth's surface is of quaternary age. The characteristics of quaternary origin soils distinguish these soils from older soils [1], [2]. Geotechnical engineers, particularly, are interested in soils of the quaternary age. This particular interest is due to the that the quaternary soils are the foundation at which most of the engineering structures are founded. Also, some of these structures are founded in quaternary soils. Quaternary soils are of great significance for various activities, they form the founding materials for the major important parts of engineering construction. Almost a third of Iraq are quaternary deposits [3], [4], [5].

In the Mesopotamian Plain, the thickness of these sediments is more than 250m, Figure 1. In general, these sediments consist of levee silts and clays, flood plain clays and stacked river channel sand bodies with occasional marsh deposits [6], [7], [8]. Quaternary sediments are characterized by their physical and engineering properties; they are unconsolidated and usually finer grain than underlying formations [9], [10], [11], [12], [13]. Any development in Iraq may be affected by the existence of quaternary sediments, therefore, these important soils should be attained special interest and further detail is required to complete characterization for their geotechnical properties

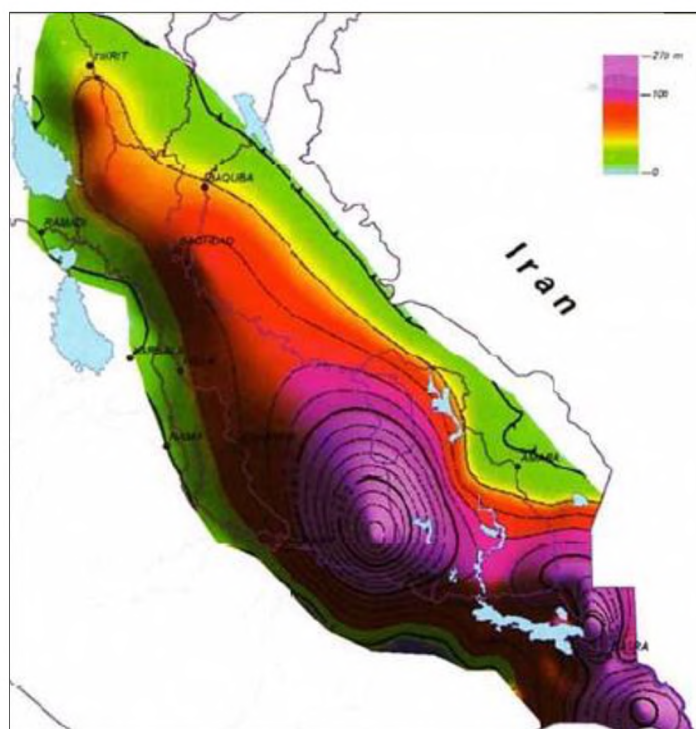


**Figure 1.** The thickness of Mesopotamian Plain's quaternary sediments [3].

During the last three decades, many constructions and engineering projects have been conducted in different areas of Iraq. A significant experience of geotechnical engineering data has been accumulated during this period, [14], [15], [16], [17], [18], [19], [20], [21], many empirical equations and relationships correlating quaternary soils' engineering properties can, therefore, be established in an accurate way. The development of such equations and correlations can accord an additional usage and as facultative engineering tools for geotechnical engineers to utilize for any preliminary engineering design. Furthermore, such equations and correlations allow fast and economical alternatives to design and construction in, or on, quaternary soils.

In the last decades, few researches were conducted to correlate the geotechnical properties of the Quaternary soil from the Mesopotamian Plain, essentially to evaluate the quaternary sediments. This paper investigates an expedient way to estimate (statistically) some index and engineering soil properties and parameters (including Atterberg limits, soil unit weights, moisture content, void ratio, porosity, and compression index) using basic soil properties (as water content, total unit weight, and specific gravity) without conducting (expensive and time-consuming) laboratory tests. Such statistical correlations have been carried out with the assistance of regression analysis method by using a specialized and advanced software package in the statistical analysis (Number-Cruncher-Statistical System (NCSS)).

## 2. THE DATA COMPILING AND DESCRIPTION

Numerous test results have been collected as the first stage of this study. These results included standard consolidation test and different physical tests. It should be mentioned that all these tests have been conducted in accordance with ASTM standards. Originally, a part of the result was compiled by [13] and the rest compiles (for the purpose of this study) from various geotechnical investigations located in Iraq. The results of sixty-three different locations were compiled, checked, tabulated. They are for quaternary soil samples obtained during site investigation for different engineering projects from the south part of Iraq. Such investigations were carried out by private companies and public agencies. The compiled data included initial void ratio ( $e_0$ ), total and dry unit weight ( $\gamma_t$  and  $\gamma_d$ ), water content ( $w$ ), liquid and plastic limits (LL and PL), plasticity index (PI), specific gravity ( $G_s$ ), and compression index

(Cc). The investigated soils can be described as a cohesive fine-grained soil. They have low to high liquid limit values; they are mainly lean clay (CL) according to ASTM specifications (ASTM D2487) [22]. Also, the degree of compressibility of these soils can be described as a low to intermediate. Actually, they are a part of Mesopotamian Plain, Figure 2, which were resulted from interaction of Euphrates river and Tigris river, they are quaternary deposits [13].

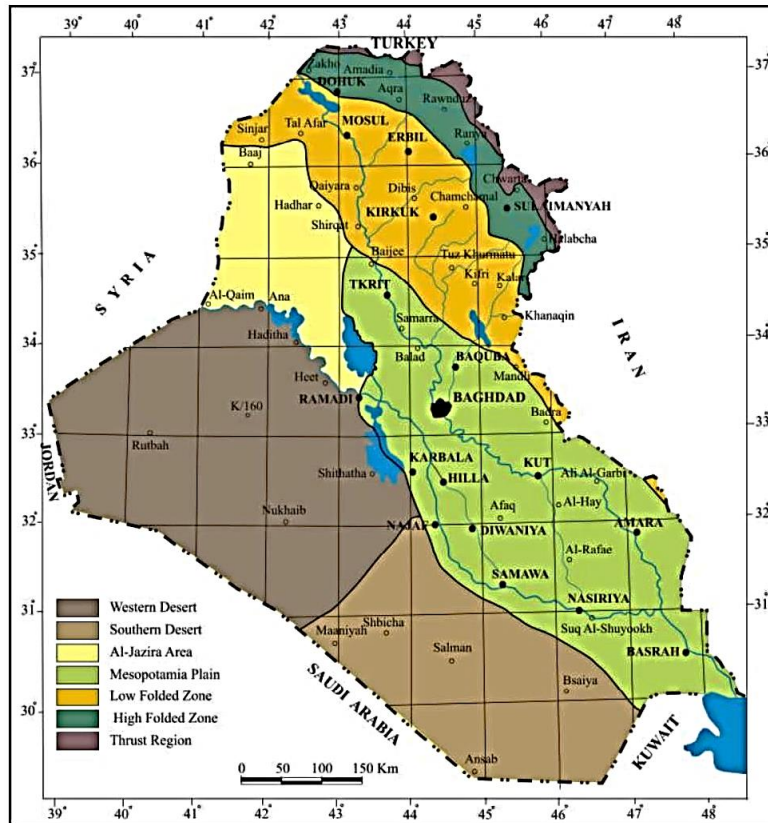


Figure 2. Location map of the Mesopotamia Plain [23]

### 3. DESCRIPTIVE STATISTICS FOR DATA USED

The results of the procedure used to describe the geotechnical parameters (of this paper) are shown in Figure 3 and Table 1. The variables were presented both statistically and graphically. For each single parameter, numerical descriptors (statistics) and statistical information about spread (variability), location (center), and distribution of data were provided. In this study, the location of variables (the center) on the number line was described by mean, median, and mode. As can be seen from Table 1, the values of mean and median of the geotechnical parameters are very close, thus, it is most unlikely there is an outlier in the soil parameters data, also, one can expect a slight skew in the distribution of data. The variability or dispersion of soil parameters, i.e. the pattern of these parameters' values around the location of variables (the center), was also studied by measuring the range and standard deviation. It should be mentioned that, to some degree, both of these dispersion measures are affected by outlier [24]. Due to a skewed distribution, the median has been adopted as a measure of central tendency in this study. Figure 3 presents histogram plots of the geotechnical parameters. It can be seen that the geotechnical data are generally bell shaped with nearly symmetric pattern of distribution. Approximately, these data appeared to have a single center. As it is appeared, the condition of normal distribution is generally satisfied for geotechnical paraments of this study.

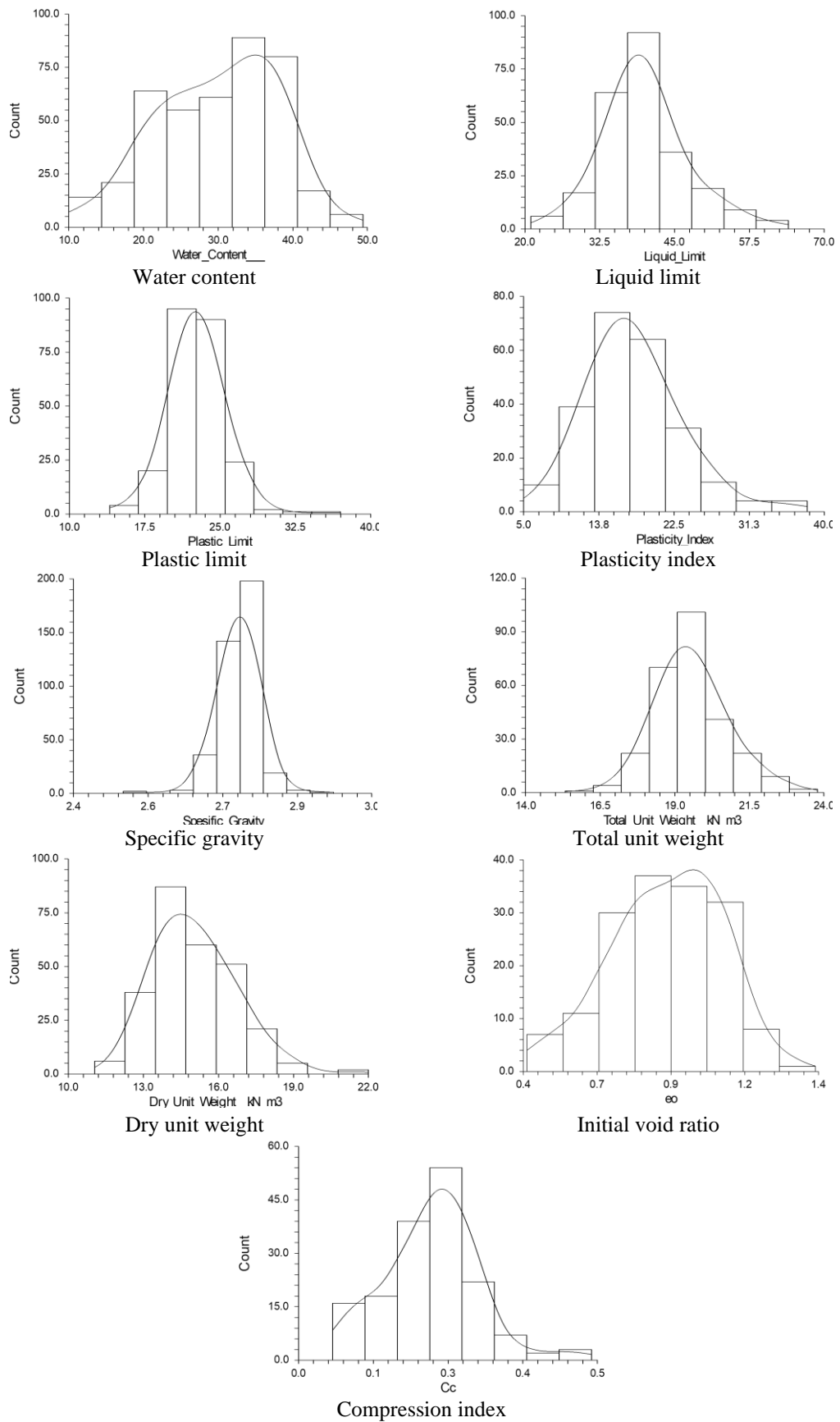


Figure 3. Histogram plots of the geotechnical parameters

**Table 1.** Descriptive statistics for data used

Parameters	Mean	Median	Mode	Standard Deviation	Standard Error	Minimum	Maximum	Range
w, %	29.92	30.55	22.00	8.01	0.40	10.00	49.40	39.40
LL, %	39.96	39.00	38.00	7.08	0.45	21.00	64.00	43.00
PL, %	22.68	22.00	22.00	2.78	0.18	14.00	37.00	23.00
PI, %	17.73	17.00	14.00	5.60	0.36	5.00	38.00	33.00
Gs	2.73	2.74	2.75	0.04	0.00	2.50	2.92	0.42
$\gamma_t$ (kN/m <sup>3</sup> )	19.56	19.54	0.00	1.21	0.07	15.33	23.78	8.45
$\gamma_d$ (kN/m <sup>3</sup> )	15.06	14.76	16.00	1.64	0.10	11.05	22.00	10.95
eo	0.886	0.885	0.720	0.190	0.015	0.412	1.390	0.978
Cc	0.223	0.230	0.270	0.080	0.006	0.057	0.490	0.433

## 4. RESULT AND DISCUSSION

### 4.1. Predicting unknown quaternary sediment geotechnical properties

Correlations were obtained from regression analysis of geotechnical data from Quaternary Sediment of Mesopotamian Plain. Such correlations may be useful for predicting some unknown soil properties including water content Atterberg limits, void ratio, porosity, unit weight, and compression index without carrying out expensive laboratory engineering tests. Also, these correlations, with other published correlations, enable the assessment of soil engineering properties without waiting for the prerequisite laboratory testing. To examine whenever the engineering properties of Quaternary sediment can be predicted from the knowledge of other soil properties, regression analysis performed using the database compiled in this paper. The analysis was carried out using an advanced statistical analysis software package named "Number Cruncher Statistical System" (NCSS). The improvement in developed correlations was examined with assistance of the correlation coefficient, (R). A correlation coefficient (R) with a value ( $R \geq |\pm 0.5|$ ) was adopted in the current regression models. In fact, a quantitative measure of strength of variables relationships can be examine with assistance of this coefficient. According to Montgomery and Runger [25], correlation coefficient less than  $|0.5|$  are, generally, considered weak, while R with values above  $|0.8|$  are, generally, considered strong. Also, another indicator has been used in the assessment of correlation, that the mean absolute error or (MAE). It should be mentioned that both R and MAE were calculated using the following expressions:

$$R = \frac{\sum_{i=1}^n (X_j - \bar{X})(Y_j - \bar{Y})}{\sqrt{\sum_{i=1}^n (X_j - \bar{X})^2 \sum_{i=1}^n (Y_j - \bar{Y})^2}} \quad (1)$$

$$MAE = \frac{1}{n} \sum_{i=1}^n |X_j - Y_j| \quad (2)$$

Where,  $Y_j$  is the predicted soil property;  $X_j$  is the measured soil property; and n is the number of datapoints used in the evaluation [21].

### 4.2. Prediction of water content

For a given quaternary clay, unknown water content (w, %) can be determined by measuring the wet unit weight ( $\gamma_t$ ) using a standard method and apply the following equation (also shown in Figure 4):

$$w^2 = 4968 - 200 \gamma_t \quad (3)$$

Where  $\gamma_t$  = total unit weight, kN/m<sup>3</sup>. Eq. 3 is based on a non-linear regression of 258 data points with  $R = 0.535$  and  $MAE = 6.1$ .

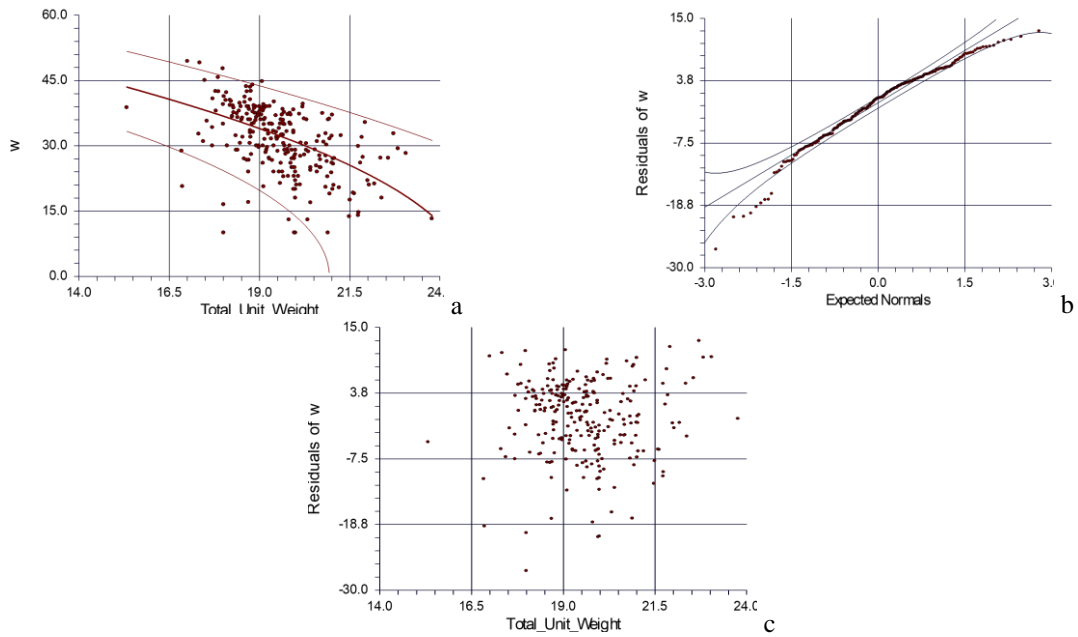


**Figure 4.** a, Correlation water content and total unit weight; b Probability plot of water content; c, Residual vs total unit weight

### 4.3. Predicting Atterberg limits

An expedient prediction method of Liquid limit (LL, %) is to conduct a plastic limit test and apply the following equations (Figure 5):

$$LL = 6.35 + 1.5 PL \tag{4}$$

Where PL = plastic limit. Eq. 4 was experimentally obtained using non-linear regression of 237 data points from quaternary clay, R = 0.609, and MAE = 5.1.

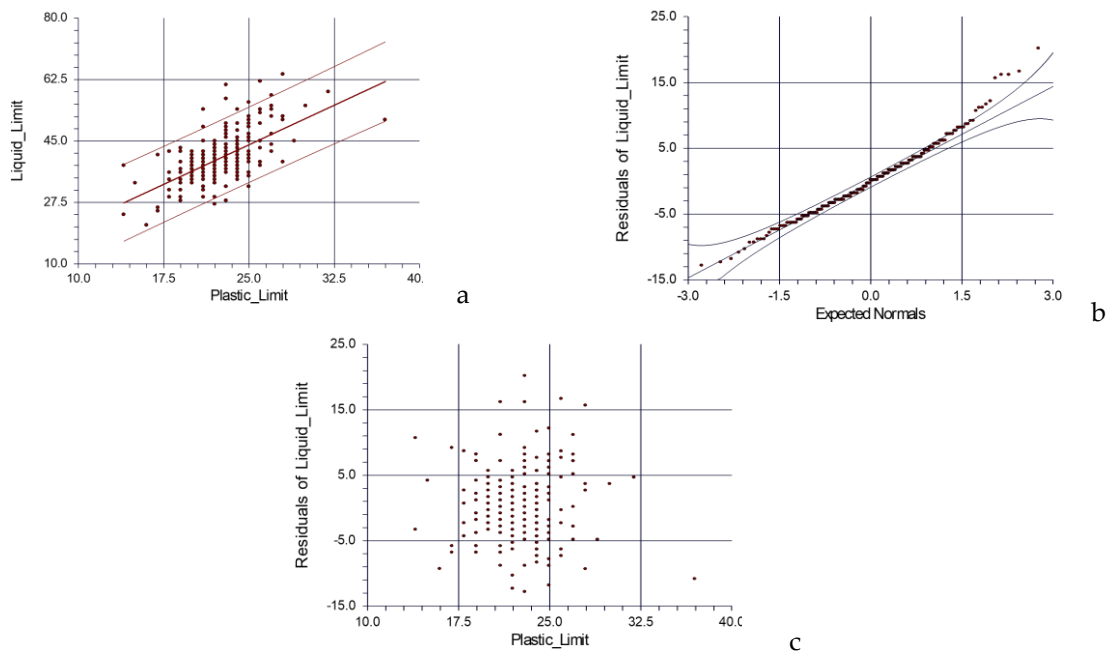


**Figure 5.** a, Correlation LL and PL; b Probability plot of LL; c, Residual vs PL

On the other hand, the plasticity index (PI, %) of the quaternary clay can be predicted from liquid limit value by using the following equation:

$$PI = 0.752 LL - 12.67 \quad (5)$$

Eq. 3 is characterized by the correlation coefficient of (0.919) which reflects a high functional relation, and MAE = 4.3. As a result, the plasticity index of investigated soil can be directly obtained with sufficient accuracy from Eq. 5 or from graphical construction shown in Figure 6.

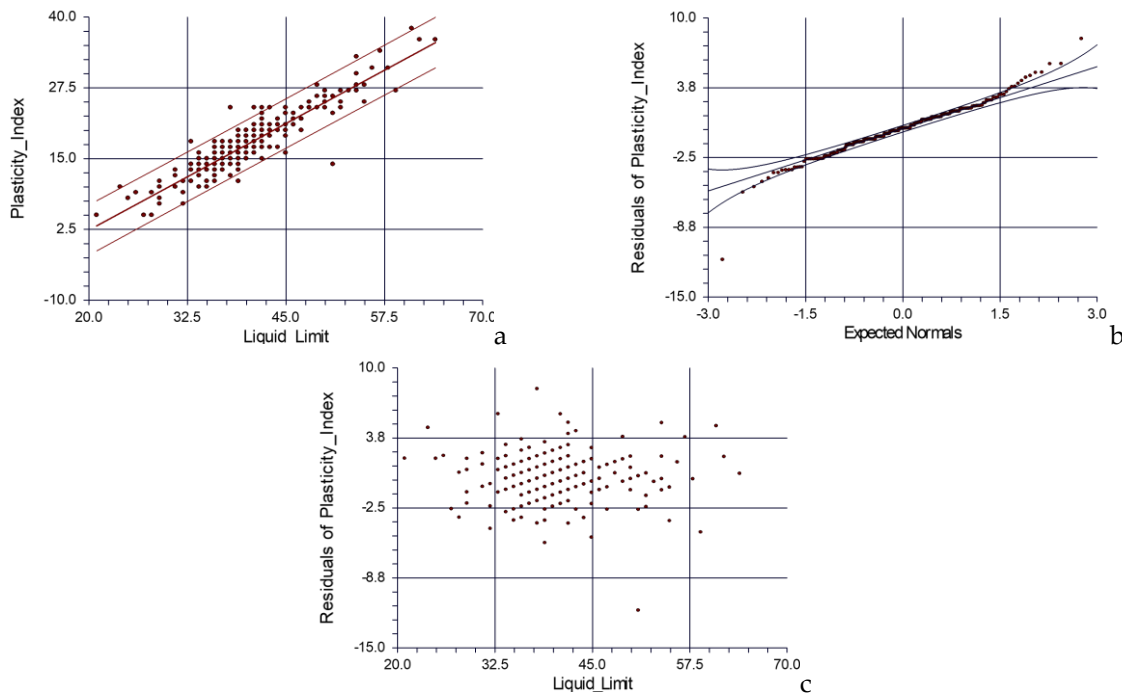


**Figure 6.** a, Correlation plasticity index and liquid limit; b Probability plot of plasticity index; c, Residual vs liquid limit

#### 4.4. Predicting unit weights, void ratio, and porosity

It is well known in soil mechanics that void ratio, porosity, total unit weight and dry unit weight of soil are calculated from parameters such as water content, degree of saturation, and specific gravity. To predict the total unit weight of quaternary clay when only the water content is known, the following equation may be used or from graphical construction shown in Figure 7.

$$\gamma_t = 21.06 - 0.0014 w^2 \quad (6)$$

Where

$\gamma_t$  = total unit weight, kN/m<sup>3</sup>

w = water content percent

Totally of 258 data points were used to obtain Eq. 6 by using non-linear regression analysis. The correlation coefficient of Eq. 4 is (R=0.536) while MAE is 1.0.

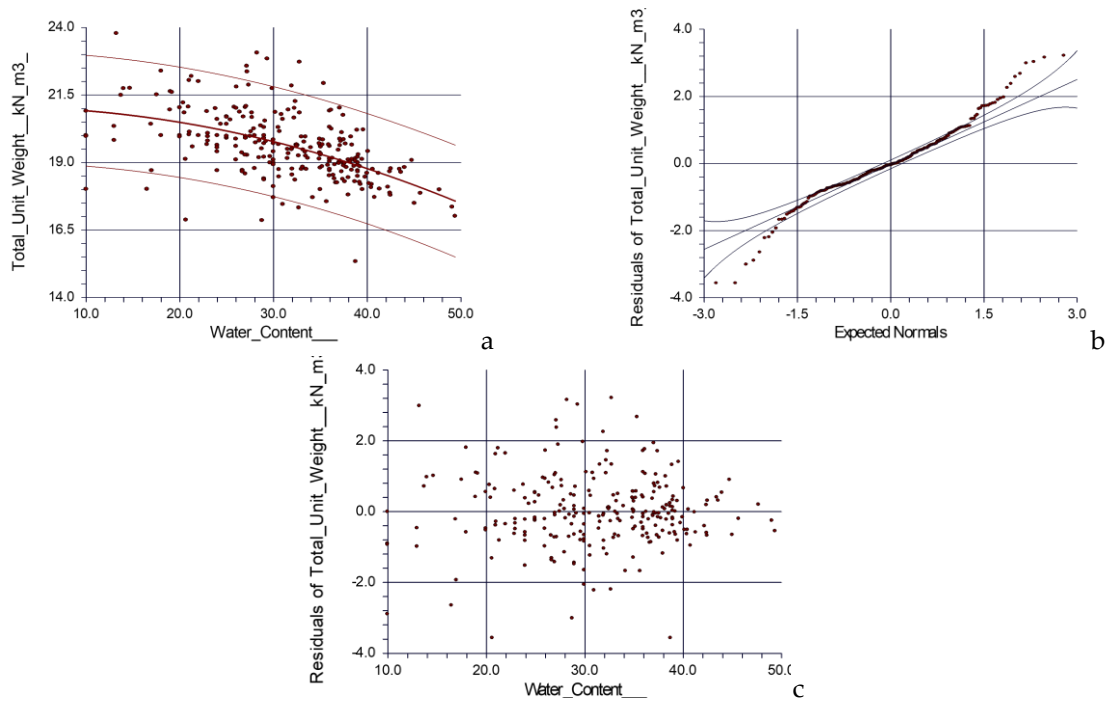


**Figure 7.** a, Correlation total unit weight and w; b Probability plot of total unit weight; c, Residual vs w

To predict the dry unit weight when the water content is known, but total unit weight is not, the following equation may be used:

$$1/\gamma_d^2 = 0.0028 - 0.00001 w + 0.000002 w^2 \tag{7}$$

where

$\gamma_d$  = dry unit weight, kN/m<sup>3</sup>

w = water content percent

According to regression analysis of 258 data points, Eq. 7 is obtained. This equation is characterized by the correlation coefficient of (0.860) which reflects a good functional relation and MAE is 1.3. As a result, the dry unit weight of investigated soil can be directly obtained with sufficient accuracy from Eq. 5 or from graphical construction shown in Figure 8.

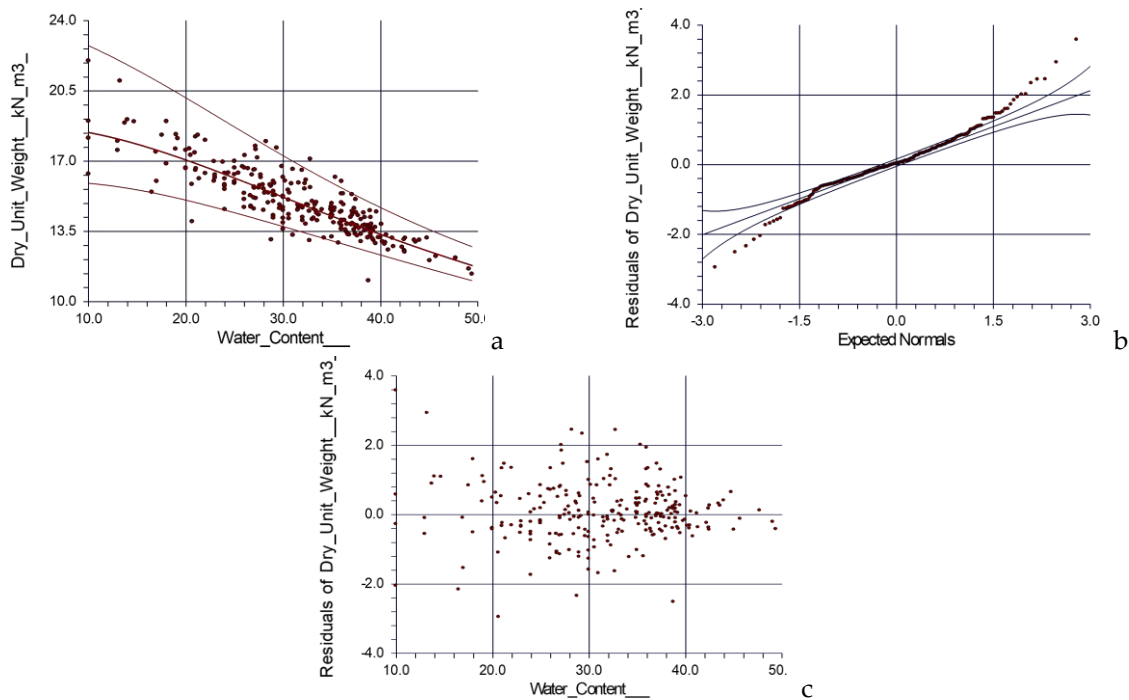


Figure 8 a, Correlation dry unit weight and w; b Probability plot of dry unit weight; c, Residual vs w

The ratio of the volume of voids ( $V_v$ ) to the volume of soils ( $V_s$ ) in a given volume is void ratio. It is usually expressed as a decimal. A useful relation for the void ratio in terms of degree of saturation ( $S$ ), water content ( $w$ ) and specific gravity ( $G_s$ ) is shown below [26]:

$$e = G_s w/S \tag{8}$$

To predict the initial void ratio ( $e_o$ ) of the quaternary clay when the water content is known, but specific gravity and degree of saturation are not, the following equation, obtained from multiple regression analysis, can be used (Figure 9):

$$e_o^2 = 0.096 + 0.0007 w^2 \tag{9}$$

where

$e_o$  = initial void ratio

$w$  = natural water content percent

Eq. 9 is based on 160 data points with correlation coefficient ( $R = 0.907$ ), which is a good functional relation correlation, while MAE is 0.158.

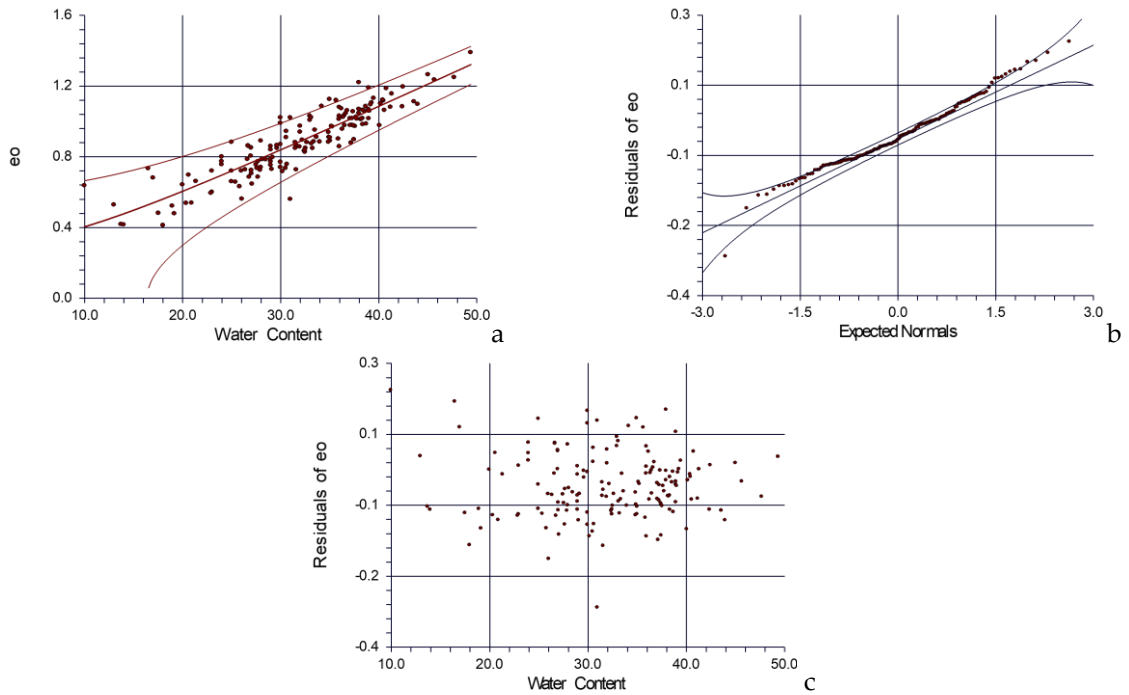


**Figure 9.** a, Correlation void ratio and water content; b Probability plot of void ratio; c, Residual vs water content

If water content and specific gravity are both known, but degree of saturation is not, the following equation can be used to predict the void ratio:

$$e_o^2 = 0.0735 + 0.00009 (w G_s)^2 \tag{10}$$

where

w = water content percent

G<sub>s</sub> = specific gravity of solids

A Good functional correlation coefficient (R=0.933) and MAE (0.161) obtained from nonlinear regression analysis based on 121 data points. The resulting functional relation (Eq. 10) is graphically illustrated on Figure 10 for more rapid determination of initial void ratio of the quaternary clay. It can be notes that the initial void ratio can be successfully estimated from the water content and specific gravity using Eq. 10.

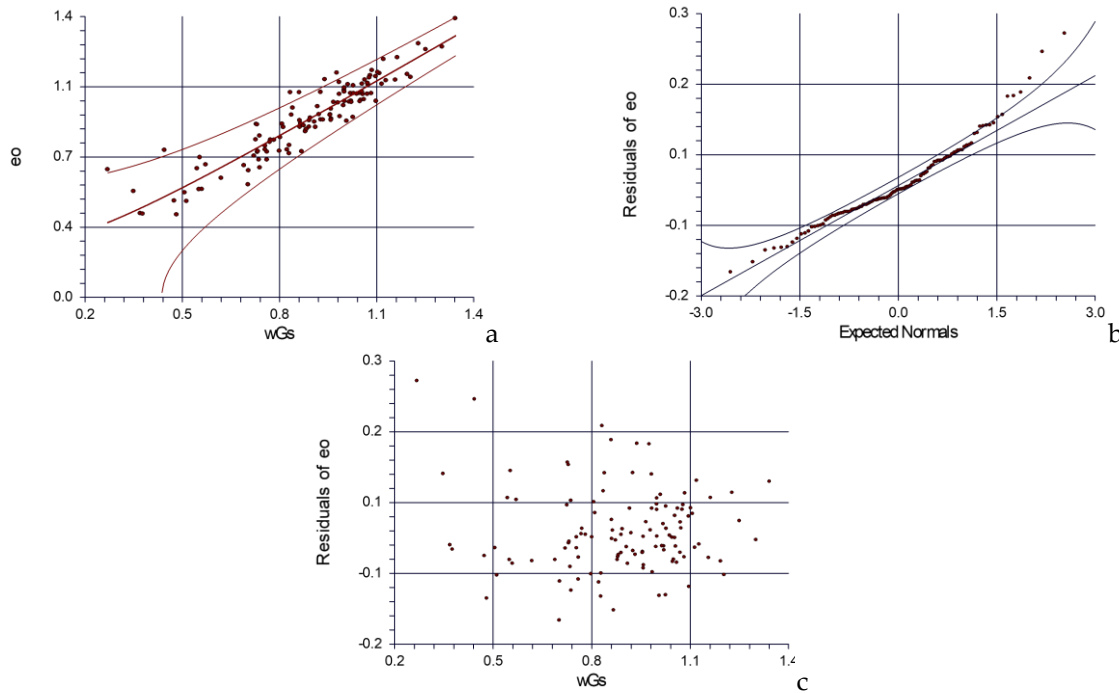


**Figure 10.** a, Correlation void ratio and water content and specific gravity; b Probability plot of void ratio; c, Residual vs water content and specific gravity

The Porosity ( $n$ ) which is the ratio of the volume of voids to the total volume, [26], can be obtained from relationship with void ratio ( $e$ ) as shown in the textbook Eq. 11:

$$n = e / (1 + e) \tag{11}$$

Combining Equations 9 and 11 allows estimation of the porosity from the natural water content as shown in Eq. 12:

$$n = (0.096 + 0.0007 w^2)^{1/2} / 1 + (0.096 + 0.0007 w^2)^{1/2} \tag{12}$$

#### 4.5. Rapid estimation of consolidation properties

It is very important in geotechnical engineering to know the compressibility properties of the soils. These properties are used for the calculation of settlement of soil (consolidation). They are, conventionally, determined by time consuming laboratory oedometer test. For this reason, it is necessary to estimate such properties with reasonable accuracy for preliminary calculations and to control the validity of consolidation tests.

For determining compression index knowing only the water content of the quaternary soil, an approximate equation (Eq. 13) is obtained from the statistical analysis of 160 data points with correlation coefficient ( $R=0.784$ ) and MAE (0.064).

$$\ln(Cc) = 1.277 \ln(w) - 5.941 \tag{13}$$

where:

$Cc$  = compression index

$w$  = water content percent

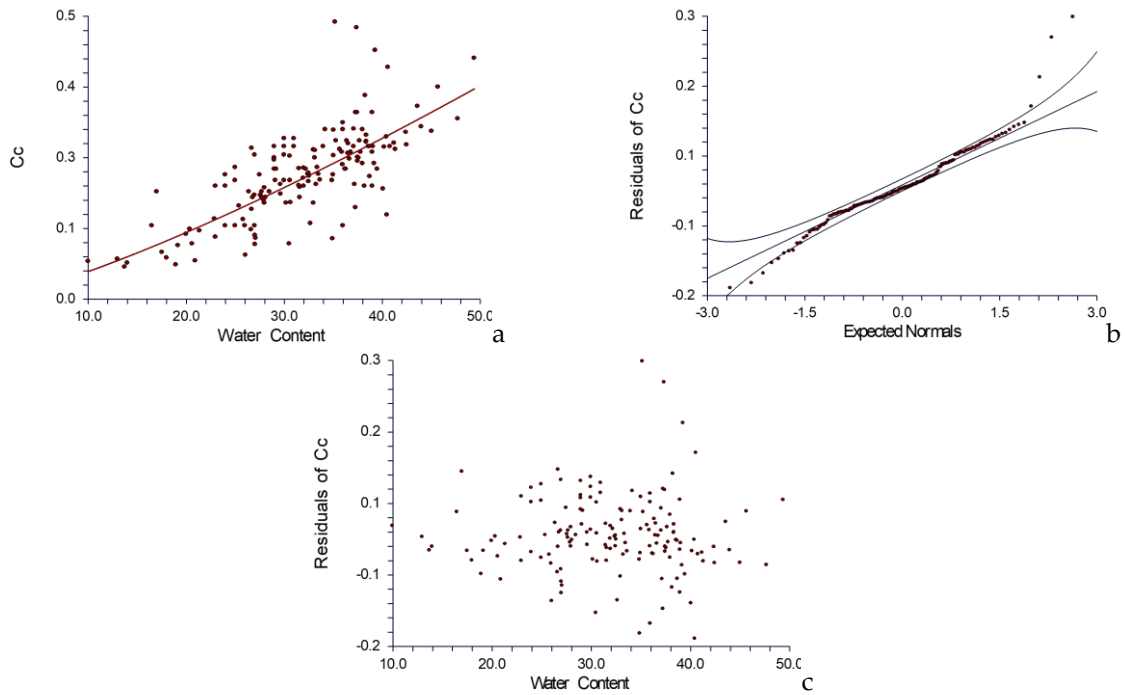


**Figure 11.** a, Correlation compression index and water content; b Probability plot of compression index; c, Residual vs water content

**5. CONCLUSION**

This paper investigates an expedient way to estimate (statistically) some index and engineering soil properties and parameters (including Atterberg limits, soil unit weights, moisture content, void ratio, porosity, and compression index) using basic soil properties (as water content and specific gravity) without conducting (expensive and time-consuming) laboratory tests. Such statistical correlations have been carried out with the assistance of regression analysis method by using a specialized and advanced software package in the statistical analysis (Number-Cruncher-Statistical System (NCSS)). According to the finding of this study, the above geotechnical parameters of quaternary clay may be easily and rapidly estimated based on simple engineering test data, using one of the following nine equations:

Estimating parameter	Equation
Water content (%) from total unit weight kN/m <sup>3</sup>	$w^2 = 4968 - 200 \gamma_t$
Liquid limit (%) from plastic limit (%)	$LL = 6.35 + 1.5 PL$
Plasticity index (%) from liquid limit (%)	$PI = 0.752 LL - 12.67$
Total unit weight kN/m <sup>3</sup> from water content (%)	$\gamma_t = 21.06 - 0.0014 w^2$
Dry unit weight kN/m <sup>3</sup> from water content (%)	$1/\gamma_d^2 = 0.0028 - 0.0001 w + 0.000002 w^2$
Initial void ratio from water content (%)	$e_o^2 = 0.096 + 0.0007 w^2$
Initial void ratio from water content (%) and G <sub>s</sub>	$e_o^2 = 0.0735 + 0.00009 (w G_s)^2$
Initial porosity from water content (%)	$n = (0.096 + 0.0007 w^2)^{1/2} / 1 + (0.096 + 0.0007 w^2)^{1/2}$
Compression index from water content (%)	$\ln(Cc) = 1.277 \ln(w) - 5.941$

It should be mentioned that the above equations do not substitute the standard laboratory tests. All these equations are aimed to be utilized as guidance for estimating purposes only.

### Declaration of Ethical Standards

As the author of this study, I declare that all ethical standards have been complied with.

### Credit Authorship Contribution Statement

In this study, the author contribution rate was determined as 100%.

### Declaration of Competing Interest

As the author of this study, I declare that there are no declarations of conflict.

### Funding / Acknowledgements

This study was not funded by any institution.

### Data Availability

The data that support the findings of this study are available from the corresponding author.

### REFERENCES

- [1] M.G. Culshaw, J. C. Cripps, F. G. Bell and C. F. Moon, "Engineering geology of quaternary soils: I. Processes and properties," *Geological Society, London, Engineering Geology Special Publications*, vol. 7, p. 3-38, 1991.
- [2] A. J. Al-Taie, D. Al-Jeznawi and N. S. Faraj, "Engineering characterization of quaternary sandy soil in the Mesopotamia Plain," *International Review of Civil Engineering (IRECE)*, vol. 12, p. 40-48, 2021, <https://doi.org/10.15866/irece.v12i1.18770>.
- [3] S. Z. Jassim, and J. C. Goff, *Geology of Iraq*, Dolin, Prague and Moravian Museum, Brno, 2006.
- [4] A. J. Al-Taie and B. S. Albusoda, "Earthquake hazard on Iraqi soil: Halabjah earthquake as a case study," *Geodesy and Geodynamics*, vol. 10, p.196-204, 2019, <https://doi.org/10.1016/j.geog.2019.03.004>
- [5] A. J. Al-Taie, "Effect of determination method on the liquid limit of quaternary soils," *Civil Engineering Beyond Limits*, vol. 3, p. 24-30, 2020, <https://doi.org/10.36937/cebel.2020.003.005>
- [6] G. Philip, "Note on the petrography of the Khabour," *Quartzite. Bul. Coll. Sci.*, Baghdadi, Iraq, 1967.
- [7] Z. Kukal and A. Saadallah, "Aeolian admixtures in the sediments of the northern Persian Gulf," In: B. H. Purser (ed). *The Persian Gulf*, Springer. Verlag, Berlin, 115-121, 1973.
- [8] A. J. Al-Taie, "Practical aid to identify and evaluate plasticity, swelling and collapsibility of the soil encountered in Badrah, Shatra and Nassirya Cities," *Journal of Engineering And Sustainable Development*, vol. 20, p. 38-47, 2016.
- [9] R.C. Bellen, H.V. Dunnington, R. Wetzell and D. Morton, "Lexique stratigraphique internal Asie. Iraq," *Intern. Geol. Conger. Comm. Stratigr*, vol. 3, p. 333, 1959.
- [10] K. M. Naqib, "Geology of Arabian Peninsula, southeastern Iraq," *USGS Professional*, vol. 560 G., p. 54, 1967.
- [11] A.A.M. Al-Siddiqi, "Subsurface geology of southeastern Iraq," *10<sup>th</sup> Arab. Pet. Cong.*, Paper no. 141 (B-3), 47, 1978, Tripoli- Libya.
- [12] A. J. Al-Taie and B. S. Al-Busoda, "An Attempt to relate consolidation properties: A case study in Baghdad cohesive soil," *International Journal of Advances in Applied Sciences*, vol. 2, p. 77-84, 2013.
- [13] A. J. Al-Taie, "Profiles and geotechnical properties for some Basra soils," *Al-Khawarizmi Engineering Journal*, vol. 11, p. 74-85, 2015.

- [14] A. Albadran and B. Albadran, B., "Geotechnical properties of Khor Al-Zubair and Khor Abdallah sediments, NW of the Arabian Gulf," *Iraqi J. of Science*, vol. 35, p. 729-746, 1994.
- [15] A. Al-Marsoumi, M. Kadhum and S. Kadhum, "Some mechanical properties of sandy gypseferous soils in Rumaila Khor Al-Zubair Area, Southern Iraq," *Marina Mesopotamica*, vol. 23, p. 333-347, 2008.
- [16] B. S. Al-Busoda and B.S., A. J. Al-Taie, "Statistical estimation of the compressibility of Baghdad cohesive soil," *Journal of Engineering*, vol. 16, p. 5863-5876, 2010.
- [17] W. Muttashar, F. Al-Amari and M. Abd Al-Hussein, "Geotechnical analysis for types of surficial fine-grained soils at eastern side of Basra region, Southern Iraq," *Journal of Thi-Qar University*, vol. 7, p. 101-112, 2012.
- [18] A. J. Al-Taie, A. Al-Bayati, Z. Taki, "Compression index and compression ratio prediction by artificial neural networks," *Journal of Engineering*, vol. 23, p. 96-106, 2017.
- [19] A. J. Al-Taie, A. Al-Bayati, "Application of artificial neural networks to predict soil recompression index and recompression ratio," *Kufa Journal of Engineering*, vol. 9, p. 246-257, 2018.
- [20] I. Alkroosh, S. Alzabeebee and A. J. Al-Taie, "Evaluation of the accuracy of commonly used empirical correlations in predicting the compression index of Iraqi fine-grained soils," *Innovative Infrastructure Solutions*, vol. 5, p. 1-10, 2020, <https://doi.org/10.1007/s41062-020-00321-y>
- [21] S. Alzabeebee, Y. Alshkane, A. J. Al-Taie and K. A. Rashed, "Soft computing of the recompression index of fine-grained soils," *Soft Computing*, vol. 25, p. 15297-15312, 2021, <https://doi.org/10.1007/s00500-021-06123-3>
- [22] ASTM, *American Society for Testing Materials. ASTM Standards. Volume 04.08*, 2003.
- [23] M. M. Mustafa, "Mineral resources and industrial deposits in the Mesopotamia Plain," *Iraqi Bull. Geol. Min.*, vol. 4, p. 105- 118, 2011.
- [24] J. L. Hintze, *NCSS Help System*. Kaysville, Utah 84037.
- [25] D. C. Montgomery and G. C. Runger, *Applied statistics and probability for engineers*. 6<sup>th</sup> edition, John Wiley & Sons, 2014.
- [26] M. Carter and S. P. Bentley, *Soil properties and their correlations*. 2<sup>nd</sup> edition, John Wiley & Sons, Ltd, 2016.



## DEMOGRAFİK ÖZELLİKLERİN ÇEVİRİMİÇİ MARKET ALIŞVERİŞİ KULLANIMINA ETKİSİNİN MAKİNE ÖĞRENMESİ YÖNTEMLERİ İLE TAHMİNİ

<sup>1</sup>Burak BAHÇIVAN<sup>ID</sup>, <sup>2,\*</sup>Atınc YILMAZ<sup>ID</sup>

<sup>1</sup>*İstanbul Beykent Üniversitesi, Lisansüstü Eğitim Enstitüsü, Bilgisayar Mühendisliği Bölümü, İstanbul,  
TÜRKİYE*

<sup>2</sup>*İstanbul Beykent Üniversitesi, Mühendislik-Mimarlık Fakültesi, Bilgisayar Mühendisliği Bölümü, İstanbul,  
TÜRKİYE*

<sup>1</sup>[burakbahcivan@gmail.com](mailto:burakbahcivan@gmail.com), <sup>2</sup>[atincyilmaz@beykent.edu.tr](mailto:atincyilmaz@beykent.edu.tr)

### Önemli Katkılar (Highlights)

- Genellikle performans ölçümü ve bankacılık sektöründe tercih edilen skorlama Lojistik Regresyon algoritması gauss dağılımı ile birlikte kullanılmıştır.
- Sık kullanılan makine öğrenmesi yöntemleri kullanılarak bir kullanıcının bir kategoriden alışveriş yapma olasılığını öngörülmesi ve bu tercihi etkileyen demografik özellikler üzerine odaklanılmıştır
- Çalışmada Lojistik Regresyon, Karar Ağacı, K-En Yakın Komşu, Gradyan Arttırılmış Ağaçlar ve Rastgele Orman yöntemleri uygulanmıştır.
- Çevrimiçi market uygulaması ya da web hizmeti sunan tüm firmaların fayda sağlayabilmesi adına herhangi bir kategoriden alışveriş yapabilecek kullanıcının sahip olması gereken özellikler ortaya çıkartılabilmekte; bu sayede kişiselleştirilmiş tahmin sistemi tasarlanabilmektedir.



## DEMOGRAFİK ÖZELLİKLERİN ÇEVİRİMİÇİ MARKET ALIŞVERİŞİ KULLANIMINA ETKİSİNİN MAKİNE ÖĞRENMESİ YÖNTEMLERİ İLE TAHMİNİ

<sup>1</sup>Burak BAHÇIVAN , <sup>2,\*</sup>Atınç YILMAZ 

<sup>1</sup>*İstanbul Beykent Üniversitesi, Lisansüstü Eğitim Enstitüsü, Bilgisayar Mühendisliği Bölümü, İstanbul, TÜRKİYE*

<sup>2</sup>*İstanbul Beykent Üniversitesi, Mühendislik-Mimarlık Fakültesi, Bilgisayar Mühendisliği Bölümü, İstanbul, TÜRKİYE*

<sup>1</sup>[burakbahcivan@gmail.com](mailto:burakbahcivan@gmail.com), <sup>2</sup>[atincyilmaz@beykent.edu.tr](mailto:atincyilmaz@beykent.edu.tr)

(Geliş/Received: 10.07.2022; Kabul/Accepted in Revised Form: 07.08.2023)

**ÖZ:** Çevrimiçi market alışverişi hizmeti sağlayan firmaların ürün satışlarını arttırmak ve yeni müşteriler elde etmek amacıyla hayata geçirdikleri birçok kampanyanın başarıya ulaşamadığı görülmektedir. Çevrimiçi alışverişte ürün satışlarının artmasını ve kampanyaların başarılı olmasını amaçlayarak, çevrimiçi market üzerinden alışveriş yapan 394 kullanıcıya ait çeşitli veriler anket aracılığı ile toplanmıştır. Çalışmada, sık kullanılan makine öğrenmesi algoritmaları ile modelleme yapılarak çevrimiçi market kullanıcılarının kişisel bakım kategorisinden alışveriş yapma eğilimlerinin öngörülmesini sağlayan bir model ortaya konulmuştur. Karar Ağaçları, K-En Yakın Komşu, Gradyan Arttırılmış Ağaçlar, Rastgele Orman ve Lojistik Regresyon yöntemleri modelleme için kullanılmıştır. Son olarak da ortaya çıkan eğri altında kalan alan (EAKA-AUC), geri çağırma (recall), f<sub>1</sub>-skor (f<sub>1</sub>-score) değerleri üzerinden yöntemlerin performans karşılaştırılması yapılmıştır. Çalışma sonucunda en yüksek performans 0.928 doğruluk oranı ve 0.92 AUC değerleri ile rastgele orman yöntemi ile elde edilirken; Gradyan Arttırılmış Ağaçlar yöntemi uygulanan model ise 0.704 doğruluk oranı ve 0.70 AUC değeri ile en düşük performansa ulaşmıştır. Çalışmada elde edilen bulgulara göre, özellikleri "43-47 yaş altı, günlük internet kullanımı fazla, kapıda kredi kartı ile ödeme tercihi yapmayan" kullanıcıların kişisel bakım kategorisinden alışveriş yapmayı tercih ettikleri analiz edilmiştir. Elde edilen sonuçlar incelendiğinde, şirketlerin çalışmada ortaya konan model ile hedef müşteri kitlelerini daha iyi belirlemelerine olanak sağlanacağı ve bu sayede yapılan gereksiz yatırımların önüne geçilebileceği öngörülmektedir.

**Anahtar Kelimeler:** Makine Öğrenmesi, Sınıflandırma, Skorlama, Çevrimiçi Alışveriş Tahmini

### Prediction of The Effect of Demographic Features on Online Market Shopping Using Machine Learning Methods

**ABSTRACT:** It is seen that many of the campaigns implemented by companies providing online shopping services to increase their product sales and acquire new customers have not been successful. In order to increase product sales in online shopping and to make campaigns successful, various data of 394 users who shopped on the online market were collected through a survey. In the study, a model that provides prediction of the shopping tendencies of online market users from the personal care category has been presented by applying frequently used machine learning algorithms. Decision Trees, K-Nearest Neighbor, Gradient Boosted Trees, Random Forest and Logistic Regression methods were used for modeling. In addition, analysis has been done with AUC (Area under the Curve), recall, f<sub>1</sub>-score values to compare the performance of the applied models. As a result of the study, the highest performance was obtained with the random forest method with an accuracy rate of 0.928 and AUC of 0.92. The model which applied with Gradient Boosted Trees method was achieved the lowest performance values with an accuracy rate of 0.704 and an AUC value of 0.70. According to the findings in the study, it has been analyzed that users whose properties are "under the age of 43-47, high daily internet user, do not choice to pay by credit card at the door" prefer shopping from the personal care category. When the results

obtained are examined, it is predicted that the model set forth in the study will enable companies to determine their target customer groups better, and thus, unnecessary investments can be prevented.

**Keywords:** *Machine Learning, Classification, Scoring, Online Shopping Prediction*

## 1. GİRİŞ (INTRODUCTION)

Teknolojinin hızla gelişmesi beraberinde tüketimin teknoloji ile olan etkileşimini arttırmaktadır. Günümüzde birçok firma çevrimiçi satış hizmetini müşterilerine sağlamak adına çeşitli yatırımlar yapmaktadır. Bu yatırımlar, ürün satışlarını arttırmak, yeni müşteri elde etmek, stok miktarını azaltma ve kârlılığı arttırma gibi amaçlar doğrultusunda yapılmaktadır. Ancak bu kampanyaların bir kısmının hedefine ulaşmadığı, kullanıcılar tarafından kullanılmadığı görülmektedir. Bu da şirketlerin kampanyalar için yaptığı yatırımların istenilen faydayı sağlamadığını ortaya çıkartmaktadır. Bu çalışma ile var olan bu sorun ele alınarak, müşterilerden elde edilecek olan demografik bilgiler ile kişisel bakım kategorisinden alışverişin tercih durumuna ilişkin bir öngörü oluşturmak amaçlanmaktadır. Bu sayede etkin bir kampanya stratejisi için şirketlerin faydalanabileceği bir model oluşturmak ve alanda devam eden çalışmalara katkı sağlanması düşünülmektedir.

Genellikle performans ölçümleri ve bankacılık sektöründeki kredi risk skorlaması gibi alanlarda tercih edilen skorlama için lojistik regresyon algoritması ile gauss dağılımı çalışmada birlikte kullanılmıştır. Uygulamada kullanılan veri seti, rastgele seçilen 394 çevrimiçi market kullanıcısının demografik ve çevrimiçi market alışveriş tecrübesine ait bilgilerin anket aracılığı ile elde edilmesi ile oluşturulmuştur. Toplamam bu veriler ile model oluşturulmuş ve kullanıcıların "Kişisel Bakım" kategorisinden alışveriş yapmayı tercih etme durumu öngörülmeye çalışılmıştır. Ayrıca, çalışma sırasında kullanıcıların hangi demografik özelliklerinin etken olduğu tespit edilmesi amaçlanmıştır. Çalışmanın şirketlerin yapacağı gereksiz yatırımların önüne geçmesi, hangi kullanıcılara bu kategoriden kampanya sunması gerektiğine dair bir fikir sağlaması hedeflenmiştir [1].

Wang ve ark., 2022 yılında çevrimiçi alışveriş davranışlarını baz alarak kronik hastalıklarının tahmini için öğrenme tabanlı modelleme kullanmışlardır [2]. Çalışmada kronik hastalık olarak diyabet ve depresyon öngörüsü hedeflenmiş ve önerdikleri öğrenme tabanlı model ile yüksek doğruluk elde etmişlerdir. Moon ve ark., 2021 yılında müşterilerin çevrimiçi platformlarda alışveriş davranışlarını makine öğrenmesi algoritmaları ile analiz ederek müşteri memnuniyetini arttırmayı amaçlamışlardır [3]. Çalışmada Naif Bayes, Apriori, Karar Ağacı ve Rastgele Orman yöntemleri uygulanmış; en yüksek doğruluğa Apriori algoritması modeli ile %88 ve Naif Bayes modeli ile %87 olarak elde edilmiştir. Koehn ve ark., 2020 yılında derin öğrenme yöntemi ile kullanıcıların tıklama verilerini kullanarak alışveriş davranışlarını tahmin etmişlerdir [4]. Çalışmada kapalı tekrarlayan birime sahip derin sinir ağları, uzun kısa süreli bellek modelleri ve tekrarlayan sinir ağları modelleri kullanılmıştır. Wang ve ark., 2022 yılında makine öğrenmesi algoritmalarını kullanarak çevrimiçi konut reklamlarının analizi ile kentsel sosyoekonomik durum analizi üzerinde çalışmışlardır [5]. Çalışmada yedi farklı makine öğrenmesi algoritması modelleme için kullanılmış; ağaç tabanlı algoritmaların uzamsal tahmin için daha güçlü sonuçlar elde ettiği gözlenmiştir. Volkmar ve ark., 2022 yılında yaptıkları çalışmada pazarlama yönetimi alanında yapay zeka algoritmaları ile geleceğe yönelik engellerin ve gelişmelerin öngörülmesini amaçlamışlardır [6]. Çalışma neticesinde yapılan anket çalışması sonucunda karar verme, müşteri yönetimi ve strateji oluşturma ve uygulama konusunda organizasyonların yaşadığı zorluklar olarak gruplandırıldığı belirtilmiştir. Salminen ve ark., 2019 yılında içerik yönetimi konusunda pazarlama verimliliğini arttırmak için makine öğrenimi algoritmalarını kullanmışlardır [7]. Çalışmada çevrimiçi içerik otomatik olarak etiketlenmesi sağlanmış; yapay sinir ağı yöntemi ile en yüksek doğruluğa %70 değeri ile ulaşılmıştır. Can 2021 yılında yaptığı çalışmada üniversite sınavına katılan katılımcıların katılımından oluşan anket sonucunda elde ettiği veri seti ile üniversiteye yerleştirilmeye hak kazanılmasının farklı makine öğrenmesi algoritmaları kullanarak sonuçları karşılaştırmıştır [8]. Çalışmada Lojistik Regresyon, Karar Ağaçları, Rastgele Orman, Destek Vektör Makineleri, K-En Yakın Komşu ve Gaussian Naif Bayes algoritmalarını kullanmıştır. Bu karşılaştırma sonucunda algoritmalar

arasında en yüksek tahmin yapan algoritma %73.77 doğruluk değeri ile Gaussian Naif Bayes algoritması olmuştur. Kaynar ve ark. 2017 yılındaki bir çalışmada, müşteri davranışlarının incelenerek ayrıştırılması mümkün olan müşterileri kategori halinde ayırarak algoritmalar arasında karşılaştırma yapılmıştır. Bu çalışmada Destek Vektör Makineleri, Yapay Sinir Ağları ve Naif Bayes algoritmaları kullanılmış; çalışma sonucunda %91.35 doğruluk değeri elde edilerek en iyi skor yapay sinir ağları yöntemi ile sağlanmıştır [9]. Işık ve ark.'nın 2021 yılında yapmış olduğu çalışma, teknoloji kabul modeli kullanarak çevrimiçi süpermarket alışveriş yapan tüketicilerin, tüketim tercihlerini etkileyen faktörleri açıklamaya çalışmaktadır. Çalışma kapsamında verilerin analizinde basit doğrusal regresyonu ve korelasyon katsayısı metotları uygulanmıştır [10]. Danışmaz'ın 2020 yılında yaptığı çalışmada, Türkiye'de yaşayan 200 kişiye yöneltilmiş anket ile Covid-19 pandemisi sonrası tüketicilerin çevrimiçi alışveriş tercihine etkisini incelemektedir. Covid-19 salgını öncesi kullanıcılar tarafından en çok tercih ettiği ürün grubu olan giyimin yerini gıdaya bıraktığını tespit etmiştir. Buna ek olarak bireylerin tüm toplumu etkileyen salgın esnasında gıda ürün grubu konusunda tedarik sorunları yaşayacağı korkusu etkili olmuş ve bu korku ile stok yapma amacıyla bu kategoriye yöneldiğini belirtmiştir [11]. Nizam ve ark. 2014 yılında makine öğrenmesi yöntemleri kullanılarak sosyal medya kullanan kullanıcılara ait duygu analizi çalışması yapmışlardır. Bu çalışmada, Naif Bayes, Rastgele Orman, Sıralı Minimal Optimizasyon, Karar Ağacı ve K-En Yakın Komşu sınıflandırma algoritmaları modellenmiş ve karşılaştırma yapılmıştır. Sıralı Minimal Optimizasyon yöntemi, %72.33 doğruluk oranıyla en iyi performans gösteren algoritma olmuştur [12]. Saydan 2008 yılında yaptığı çalışmada, çevrimiçi alışveriş deneyimine sahip tüketiciler ile bu deneyime sahip olmayan tüketicilerin demografik özelliklerini ayırtmak, tüketicilerin geleneksel alışveriş ve çevrimiçi alışverişlerde algılanan risk ve faydaları saptamak ve daha önce çevrimiçi alışveriş deneyimi bulunmayan tüketicilerin çevrimiçi alışveriş tercih etme olasılığını arttıracak durumları tespit etmeyi amaçlamaktadır [13]. Hendri ve ark. 2020 yılında internet tabanlı bir uygulama üzerinden hasta şikayetlerinden türetilen doktor seçiminin K-En Yakın Komşu ve Karar Ağacı C4.5 algoritmaları kullanılarak yapılmasına ilişkin bir çalışma gerçekleştirmiştir. En başarılı sonucu %100 doğruluk oranı ile K-En Yakın Komşu algoritmasının elde ettiği gözlemlenmiştir. Çalışmada kullanılan diğer algoritma olan Karar Ağacı C4.5 algoritması ise %80 oranında doğruluk elde etmiştir [14]. Saygılı 2014 yılında yaptığı çalışmada, kullanıcıları motive eden faydacı ve hazcı etmenlerin çevrimiçi satın alma niyeti üzerine etkisini incelemiştir. Çalışma kapsamında 481 katılımcıya anket uygulanmış ve anket sonucunda oluşturulan veri seti SPSS programı aracılığı ile Yapısal Eşitlik Modellemesi yöntemi ile incelenmiştir. Araştırma sonucunda kullanıcıları motive eden faydacı ve hazcı etmenlerin çevrimiçi satın alma niyeti üzerinde etkili olduğu tespit edilmiştir. Faydacı alışveriş etmenlerinin hazcı alışveriş etmenlere oranla etkisinin daha fazla olduğunu saptamıştır [15].

Benzer çalışmalardan farklı olarak bu çalışmada en sık kullanılan makine öğrenimi yöntemlerinin uygulanmasının yanında Lojistik Regresyon algoritması gauss dağılımı ile kullanılarak skorlama yapılmıştır. Genellikle performans ölçümü ve bankacılık sektöründe tercih edilen skordanın bu alanda kullanılması, çalışmanın öne çıkan özelliklerindedir.

## 2. MATERYAL VE METOT (MATERIAL AND METHOD)

### 2.1. Veriseti (Dataset)

Çalışmanın anakütlesi Türkiye'de yaşayan 18 yaş üstü bireyler olarak belirlenmiş ve toplamda 394 kullanıcı anket için katılım sağlamıştır. Kullanıcılara toplamda 20'si demografik, 32'si alışveriş deneyimi ile ilgili olan 52 soru yöneltilmiştir. Anket, Google Forms üzerinden Aralık 2021-Ocak 2022 tarihleri arasında çevrimiçi olarak tamamlanmıştır [1]. Kullanıcılara toplam 53 soru sorulmuştur. İlk soru çevrimiçi market alışveriş deneyimi olup olmadığı ile ilgilidir. Bu soruya verilen cevap evet ise geriye kalan 52 sorunun cevabı alınmıştır. Anket sorularından bir kısmı aşağıdaki gibidir:

- Cinsiyetiniz nedir?
- Medeni durumunuz nedir?

- Kaç çocuğunuz var?
- Yaşınız?
- Öğrenim durumunuz?
- Aylık geliriniz nedir?
- Çalışma durumunuz nedir?
- İkamet ettiğiniz şehir hangisidir?
- Hangi sektörde çalışıyorsunuz.

Anket sorularına verilen her yanıtın matematiksel bir değeri olduğundan anket sonucunda bir skor elde edilmektedir. Anket çalışmasında kullanılan ölçeklerin güvenilirlik ve geçerlilik analizleri yapılmış olup, analize uygun olup olmadığını ortaya koyan değerlerden Kaiser-Mayer-Olkin (KMO) değeri 0.840 ve Bartlett testi sonucu anlamlılık değeri  $P=0.000$  ve Cronbach's Alpha ( $\alpha$ ) değeri 0.852 olarak hesaplanmıştır.

Modelleme esnasında eğitim ve test setlerinin belirlenmesi için K çapraz sorgulama yöntemi kullanılarak  $K=5$  ve  $K=10$  için çalışma yapılmıştır.  $K=10$  için veri seti 10 eşit parçaya bölünmüştür ve algoritmadan 10 defa ölçüm alınmıştır. Her ölçümde 1 parça test için kalan 9 parça ise eğitim için kullanılmıştır. Bu yöntem ile birlikte K değeri 10 olarak belirlenerek, %90 eğitim, %10 test seti ile doğruluk ölçütlerinde en iyi değerler elde edilmiştir.

Ayrıca uygulanan modelleme için parametre seçimi yapılırken, çevrimiçi market üzerinde kişisel bakım ürünlerini satın alan veya almayan müşterilerin tüm değişkenler ile ilişki aranmaktadır. Bu durum için Gini Endeksi ve Kanıtın Ağırlığı açıklayıcı yöntemleri kullanılmıştır.

Gini Endeksi, dağılımın tekdüze durumunu ortaya koyan bir ölçüttür. Gini endeksinin matematiksel olarak formülü denklem 1'deki gibidir. Denklemde m sınıf sayısını, N tercih durumu için örneklerin sayısını,  $S_i$  ilgili durumun i sınıfındaki örneklerin sayısını ifade etmektedir.

$$GINI_{Tercih} = 1 - \sum_{i=1}^m \left( \frac{S_i}{N_{Tercih}} \right)^2, \quad GINI_{Tercihsizlik} = 1 - \sum_{i=1}^m \left( \frac{S_i}{N_{Tercihsizlik}} \right)^2, \quad (1)$$

$$GINI = \frac{1}{n} (|N_{Tercih}| GINI_{Tercih} + |N_{Tercihsizlik}| GINI_{Tercihsizlik})$$

Bir niteliğe veya grup seviyesine ait bağlantılı riskin ölçülmesinde kullanılan Kanıtın Ağırlığı, bu çalışmada "tercih eden" veya "tercih etmeyen" olarak belirlenmiş bağımlı değişkenin değeri ile doğrudan bağlantılıdır. Kanıtın Ağırlığı, tüm grup aşamalarında tercih eden referansların tercih etmeyen referanslara olan oranına odaklıdır. Bir değişkene ait Kanıtın Ağırlığı değerinin hesaplanması denklem 2'de belirtilmiştir. Denklemde, "ln" doğal logaritmayı, "Tercih Dağılımı" belirli bir gruptaki tercihlerin yüzdesini, "Tercihsizlik Dağılımı" ise belirli bir gruptaki tercihsizlik yüzdesini vermektedir.

$$Kanıtın\ Ağırlığı = \ln \left( \frac{Tercih\ Dağılımı}{Tercihsizlik\ dağılımı} \right) \quad (2)$$

Skorkart her bir bağımlı değişkenin bağımsız değişkeni ne ölçüde açıkladığını ifade etmektedir. Her bir değişkenin sahip olduğu değer için bir skor ataması yapılır. Yapılan skor atamasından sonra tüm skorlar toplanarak bir skorkarne elde edilir. Skorkarnede elde edilen toplam puanın yine model tarafından belirlenen toplam puan gruplamasına göre konumu incelenir. Sürece ait akış Şekil 1'de verilmiştir.



Şekil 1. Lojistik regresyon ve skoreleme süreci.

Figure 1. Logistic regression and scoring process.

## 2.2. Lojistik Regresyon ve Skoreleme (Logistic Regression and Scoring)

Lojistik Regresyon, sisteme problem ile ilgili giriş değerlerine karşılık olması gereken sınıf bilgisinin verilmesi ile öğrenme gerçekleştirilir. Bu sürecin sonucunda elde edilen model genelleme yeteneği ile daha önce karşılaşmadığı ve sınıf bilgisi olmayan herhangi bir giriş değeri için anlamlı öngörüler yapabilmektedir. Modelleme yapılırken, olması gereken en yakın sonuca ulaşabilmek amacıyla en uygun fonksiyonu bulmayı hedeflemektedir. Hatanın sisteme öğrenme olarak geri dönüşü sebebiyle, denetimsiz öğrenmeye nazaran süreç çok daha hızlıdır [16].

Lojistik regresyon az değişken sayısı üzerinden bağımlı değişken ile bağımsız değişken arasındaki ilişkinin oluşturulması mantığına sahip olan yöntemdir. Lojistik regresyonu, Lineer regresyondan ayıran en önemli özellik değişkenin normal dağılım, sabit varyans ve lineer olma durumu gibi kriterlere ihtiyacı olmadan modellemenin sağlanabilmesidir [17]. Lojistik regresyon sapmalarına ait en küçük kareleri minimize etmek yerine, bir durumun muhtemel gerçekleşme durumunu maksimize eder. Lojistik Regresyon yöntemi, odds ve odds değerlerinin matematiksel olarak logaritmasını uygulamaktadır. Odds, lojistik regresyon yöntemi için bir durumun meydana gelme olasılığının meydana gelmeme olasılığına oranı olarak kullanılmaktadır. Lojistik regresyon açısından önemli bir kavram olan logit kavramı, odds oranının doğal logaritması alınarak bulunur [18]. Bir durumun gerçekleşme  $p(x)$  ve gerçekleşmeme durumunu  $(1-p(x))$  ifade eden odds denklem 3 ile bulunmaktadır.

$$\text{Odds} = \frac{p(x)}{1-p(x)} \quad (3)$$

Modelleme sonrası hazırlanan skor değerinin güvenilirliği Receiver Operating Characteristic - Alıcı İşletim Karakteristiği eğrisi (ROC) ve Gini Katsayısı gibi yöntemler yardımı ile değerlendirilmiştir. ROC eğrisi ürünü tercih eden ve tercih etmeyen kullanıcıların birbirlerine karşı hareketlerine odaklanmaktadır. Kişisel bakım alanında alışveriş yapmayı tercih edenlerin kümülatif oranına göre tercih etmeyenlerin yüzdesini tahmin etmektedir. Eğri üzerindeki noktaların her biri, eşige ait skoru ifade etmektedir. Dikey ekseninde tercih etmeyenlerin oranı, yatay ekseninde ise tercih edenlerin oranı gösterilmektedir.

Gini katsayısının sifıra eşit olması kişisel bakım kategorisinden alışveriş yapmayı tercih edenlerin ve tercih etmeyenlerin ayrımının rastgele olarak yapıldığını göstermektedir. Değerin bir olması durumu ise tercih eden ve tercih etmeyen ayrıştırmasının tam olarak yapıldığını ifade etmektedir. Bu sayede, tercih eden ve tercih etmeyen kullanıcılar arasında farklılaşma başarısı ve belirlenen eşik puanının uygunluğu değerlendirilmektedir. Elde edilen değer 0 ise tercih eden ile tercih etmeyen kullanıcılar arasındaki ayrıştırmanın başarısız olduğu anlamına gelirken, 100 değeri ayrıştırmanın etkili olduğunu ifade etmektedir [19].

Gauss Dağılımı literatürde normal dağılım ve çan eğrisi olarak da adlandırılmaktadır. Gauss Dağılımını etkileyen iki parametre ortalama ve standart sapma değerleridir. Normal dağılım gösteren değişkenlerin daha yüksek doğrulukta tahmin edilmesine olanak sağlamaktadır. Gauss dağılımında ortalama, mod ve medyan gibi değerlerin birbirine eşitliği ya da yakınlığı söz konusu ise normal bir dağılımdan bahsedilmektedir [20].

Günlük yaşamda gözlenen olayların çoğunun uyumlu olduğu Gauss dağılımı sürekli olasılık dağılımları içerisinde bulunmaktadır. Bu şekilde olan bir dağılımda aşağıdaki özellikler sıralanabilir;

- Aritmetik ortalama, mod ve medyan birbirine eşittir.
- Modun medyana eşit olduğunu gösteren eğrinin tepe noktası aritmetik ortalamayı ifade etmektedir.
- Aritmetik ortalamanın sağında ve solunda bulunan eğriler simetriktir. Her bir alanın değeri 0.5'tir.
- Verilerin çoğunluğu ortalama değerin etrafında kümelenir [21].

### 2.3. Karar Ağaçları (Decision Trees)

En iyi sonucu tespit etmeye çalışırken birçok durum üzerinden ilerleyen karar ağaçlarında her bir durum karar ağacının dallarını oluşturur. Karar verme süreci ağacın en ucu olarak sayılan yaprak düğümüne kadar devam eder. Ağacın kökünden yaprak düğümüne kadar olan yol hedefin sınıflandırıldığı "kural" olarak adlandırılmaktadır. Karar ağaçlarında temel olarak kullanılan yapı "eğer-ise" şeklinde devam etmektedir. Yaygın olarak;

- Yeni bir verinin hangi sınıfın üyesi olabileceğinin tahmininde,
- Tıp alanında çeşitli vakaların Yüksek-Orta-Düşük olacak şekilde risk gruplarının ayrıştırılmasında,
- Eğer-sonra yapısı ile ileride gerçekleşebilecek olayların tahmin edilebilmesi mekanizma kurallarının oluşturulmasında,
- Alt gruplara ait olan bazı ilişkilerin belirlenmesinde,
- Parametrik modeller için bir veri seti içerisinde kullanılmak üzere faydalı olacakların belirlenmesinde kullanılmaktadır [22].

### 2.4. Rastgele Orman (Random Forest)

Rastgele Orman yöntemi, ağaç-tabanlı sınıflandırma metodudur. Orijinal veri seti üzerinden yeni bir eğitim seti oluşturan Rastgele Orman, bütün değişkenler arasında optimal bölünme sayesinde tüm düğümleri bölmemektedir. Her bir düğüm, gelişigüzel olarak seçimi yapılan tahmin ediciler arasında en başarılısını bularak bölünmektedir. Ardından, isteğe bağlı eleman seçimi kullanılarak bir ağaç geliştirilir. Bu prosedür, Rastgele Orman'ı hassasiyet ve doğruluk bakımından performansı yüksek bir yöntem olmasını sağlamaktadır. Rastgele Orman, aynı zamanda son derece hızlı ve fazla takılmaya karşı güçlüdür. Bunun yanında modelleyen kişinin ihtiyaç duyduğu kadar çok ağacın oluşturulması bu yöntem ile mümkündür. Rastgele Orman algoritmasının başlatılması için büyütülecek ağaç sayısı ve düğümü bölmek için kullanılacak değişkenlerin sayısını belirten parametrelerinin tanımlanması gerekmektedir [23].

### 2.5. K-En Yakın Komşu (K Nearest Neighbor)

Sınıflandırma problemlerinin çözümünde kullanılan K-En Yakın Komşu algoritması, sınıflandırılmamış verinin sınıflandırılmış veriler ile belirlenen uzaklık ölçütü kullanılarak mesafelerinin hesaplanması mantığını taşımaktadır. Elde edilen uzaklık değeri sınıflandırılmış veriler ile sınıflandırılmamış veri arasındaki benzerliği ortaya koymaktadır. Bu değerler arasında en yakın k adeti üzerinden sınıf kararı verilmektedir [24].

Makine öğrenmesi algoritmaları içinde çokça bilinen ve tercih edilen K-En Yakın Komşu algoritması, verinin sahip olduğu bir özelliğin kendisine en yakın olan başka bir özellik ile arasındaki uzaklık-yakınlık ilişkisine bağlı olarak sınıflandırma yapan bir algoritmadır [25].

### 2.6. Gradyan Arttırılmış Ağaçlar (Gradient Augmented Trees)

Hem regresyon hem de sınıflandırma problemlerinde kullanabilen Gradyan Arttırılmış Ağaçlar algoritması (GAA), veriler üzerinden çıkarımda bulunmaya ihtiyaç duymadığı için görsel takip

algoritmalarının trafik sistemleri ve öneri mekanizmalarının optimize edilmesinde sık tercih edilen güçlü bir ağaç modelidir. Çeşitli niteliklerdeki veri setleri ile çalışabilmesi, tek bir karar ağacı karşılaştırmasında daha performanslı öngörü gücüne sahip olması, daha büyük veri kümelerini işleme esnekliği ve dengesiz veri setlerindeki optimizasyon başarısı gibi özellikleri GAA algoritmasının güçlü yönleri olarak söylenebilmektedir. Yöntemin asıl amacı, çoklu yinelemeler yoluyla çok sayıda zayıf olan sınıflandırıcılar oluşturmasıdır. Bu sınıflandırıcılar her yinelemede güçlendirilmektedir. Elde edilen değerleri daha iyi bir sonuç haline getirebilmek için yeni oluşturulacak olan kombinasyon modeli gradyan yönünde oluşmaktadır. Bu işlem kalıtım azaltma işlemi olarak isimlendirilmektedir [26].

### 3. DENEYSEL ÇALIŞMALAR VE BULGULAR (EXPERIMENTAL STUDIES AND FINDINGS)

Çalışmada, Python programlama dili üzerinden Numpy, Matplotlib, Sklearn kütüphaneleri kullanılmıştır. Ön işlem adımında, veri setinde bulunan eksik veriler temizlenip ayrıştırılarak veriler modellemeye uygun hale getirilmiştir. Veri seti içerisinde KATEGORİ6 isimli değişken (Kişisel Bakım) tahmini için "1" değeri "Tercih Eden", "0" değeri için "Tercih Etmeyen" olarak etiketlenmiştir. Ardından K Çapraz Sorgulama yöntemi ile K=10 için veri setinde bulunan veriler %90 eğitim seti, %10 test seti olarak ayrıştırılmıştır. Veri seti uygulama için hazırlandıktan sonra çalışmada Lojistik Regresyon, Karar Ağacı, K-En Yakın Komşu, GAA ve Rastgele Orman yöntemleri ile modelleme yapılmıştır. Çalışmada skorkart uygulaması sadece Lojistik Regresyon modeli için modellenmiştir. Regresyon işleminin mantığı, problemin hangi durumların etkisinde olup olmadığının analizidir. Lojistik regresyon yöntemi, bir bağımlı değişkenin hem bağımsız değişken ile hem de bağımlı değişkenin odds değerinin logaritması ile doğrusal ilişkisi bulunması tezi ile meydana gelmektedir. Bağımsız değişkendeki değişimlerin, bağımlı değişkenin odds değerinin logaritmik sonucu üzerinde ne kadar farklılık göstereceğini lojistik regresyon yöntemi neticesinde elde edilen katsayılar ifade edeceğinden ötürü analiz zorlaşmaktadır. Bu durumdan ötürü elde edilen katsayılar için skor uygulaması ile dönüşüm işlemi yapılarak anlam çıkarabilme konusunda yaşanan zorluk hafifletilebilmektedir. Skor uygulaması ile skorkart lojistik regresyon yöntemi ile birlikte kullanıldığında modellemenin güvenilirliği ve uygulanabilirliği konusunda ciddi bir yol gösterici olmaktadır [19].

İlk olarak bağımsız değişkenler ile hedef değişkeni açıklayan ve değişkenlerin birbirleri arasındaki anlamlılık gücünü tespit etmek amacıyla Lojistik regresyon yöntemi uygulanmıştır. Modelleme neticesinde anlamlı değişkenler Çizelge 1'de verilmiştir.

Çizelge 1'de gösterilen  $Pr > Chisq$  ifadesi bir değişkenin diğer tüm değişkenler ile hedef değişkeni hangi oranda açıkladığını ifade etmektedir.  $Pr > Chisq$  sifıra yakınlığı değişkenin anlam değerinin fazlalığını göstermektedir. Çalışmada belirlenen alt sınır %95 olarak belirlenmiş olup, %95 altında anlamlı olan değişkenler regresyon sonuçlarına göre elenmiştir. Anlamlı bulunan değişkenlerin birbirleri arasındaki ilişkinin yönünü ve gücünü tespit etmek amacıyla korelasyon uygulanmış; ortaya çıkan korelasyon matrisi Çizelge 2'de gösterilmiştir. Çizelge 1, Çizelge 2 ve Çizelge 3 için kullanılan "AD2" alışveriş değerini, "AF6" algılanan faydayı, "AR2" algılanan riski, "INT\_GUN\_SURE" günlük internet kullanım süresini, "K\_KAPI\_ODEME" çevrimiçi alışverişte ödeme yöntemi seçimini, "YAS" yaşı ifade etmektedir.

**Çizelge 1.** Lojistik regresyon modeli sonucunda anlamlı bulunan değişkenler.*Table 1. Variables found to be significant as a result of the logistic regression model.*

Değişken	Chi-Square	Pr > ChiSq
AD2	116.756	0.0006
YAS	97.595	0.0018
K_KAPI_ODEME	74.703	0.0063
AR2	67.030	0.0096
INT_GUN_SURE	61.282	0.0133
AF6	52.196	0.0223

**Çizelge 2.** Korelasyon matrisi sonuçları*Table 2. Correlation matrix results.*

Parameter	AD2	AF6	AR2	INT_GUN_SURE	K_KAPI_ODEME	YAS
AD2	1	-0,18	-0,033	-0,043	0,029	0,069
AF6	-0,18	1	-0,03	0,008	0,099	0,053
AR2	-0,033	-0,03	1	0,065	0,08	0,026
INT_GUN_SURE	-0,043	0,008	0,065	1	0,178	0,013
K_KAPI_ODEME	0,029	0,099	0,08	0,178	1	-0,025
YAS	0,069	0,053	0,026	0,013	-0,025	1

Değişkenler arasındaki korelasyon incelendiğinde %80'in üzerinde değere sahip olan değişken bulunmadığı tespit edilmiş ve lojistik regresyon yöntemi sonucunda elde edilen bağımsız değişkenlerin tümü algoritmaya dahil edilmiştir.

Daha sonraki adımda ise skorkart dağılımı incelenmiştir. Modelin atamış olduğu skorlar ile oluşan skorkart kullanıcı dağılımı Şekil 2'de verilmiştir. Buna göre çoğunluğun orta değerde dağılması, en düşük ve en yüksek değerlerin en az sayıda kullanıcı ile sınırlı kalması modelin doğru kurulduğuna ve gauss dağılımını net şekilde yansıttığını göstermektedir.

Anlamlı bulunan değişkenler için, gruplara ayırma işlemi uygulanmıştır. Bu sonuca göre, kişisel bakım alışverişini tercih eden ve etmeyen dağılımlarına bakılarak skor ataması yapılmıştır (Çizelge 3).

**Şekil 2.** Skorkart kullanıcı adet dağılımı.*Figure 2. Distribution of scorecard users.*

**Çizelge 3.** Bağımlı değişken skorkart sonuçları.*Table 3. Dependent variable scorecard results.*

Değişken	Değişken Değeri	Skorkart Sonucu	Tercih Sonucu
AD2	AD2 < 3	43	29.81
	3 ≤ AD2 < 4	49	36.76
	4 ≤ AD2	60	49.48
AF6	AF6 < 2	7	10
	2 ≤ AF6 < 3	42	30.38
	3 ≤ AF6 < 4	45	33.33
	4 ≤ AF6 < 5	51	38.42
	5 ≤ AF6	71	57.69
AR2	AR2 < 3	75	59.38
	3 ≤ AR2 < 4	53	39.47
	4 ≤ AR2 < 5	49	36.55
	5 ≤ AR2	43	31.5
INT_GUN_SURE	INT_GUN_SURE < 2	44	32.74
	2 ≤ INT_GUN_SURE < 3	45	33.75
	3 ≤ INT_GUN_SURE	74	56.06
K_KAPI_ODEME	K_KAPI_ODEME < 2	57	42.05
	2 ≤ K_KAPI_ODEME < 4	50	37.59
	4 ≤ K_KAPI_ODEME	28	24.68
YAS	YAS < 6	53	39.64
	6 ≤ YAS < 7	49	36.84
	7 ≤ YAS < 8	26	21.05
	8 ≤ YAS	9	13.04

Skor dağılımı için her bir değişkenin değer gruplarından aldığı puanlar toplanmaktadır. Bu durumun neticesinde, kullanıcının tercih etme ya da tercih etmeme eğilimine göre nihai skor oluşturulmaktadır. Skor elde edilmesi ile kullanıcının kişisel bakım kategorisinden alışveriş yapma ya da alışveriş yapmama öngörüsüne göre gruplama yapılmıştır. Gruplar kullanıcıların hangi oranda ihtimalle alışveriş yapmayı tercih edeceğine dair ifadeleri içermektedir:

- Çok yüksek (Skor >= 338)
- Yüksek (304 ≤ Skor < 338)
- Orta (270 ≤ Skor < 304)
- Düşük (242 ≤ Skor < 270)
- Çok düşük (Skor < 242)

Skor puanları ve modelleme neticesinde bulunan skorkartın hesaplanması için regresyona ait parametrelerin ölçeklenmesi işlemi bu adımda yapılmıştır. Bu algoritma ile uygulanan modelin tahminine ilişkin sonuçlar Çizelge 4'te verilmiştir. Kullanıcıların skorkart sonucunda elde ettikleri toplam skor arttıkça satın alma ihtimali de artmaktadır.

Kullanıcılara ait kişisel bakım kategorisinden alışveriş yapmayı tercih etme durumunun gerçekleşme oranları ile modelin tahmin ettiği gerçekleşme durumu arasındaki ilişki Şekil 3'te verilmiştir.

Çizelge 4. Model tahmin sonuçları.

Table 4. Model prediction results.

Skor Adı	Skor Aralığı	Sayaç	Tercih Etme	Tercih Etmeme	Model Tercih Oranı %	Gerçek %
Çok Yüksek	Skor>=338	21	16	5	78,548	76,19
Yüksek	304<=Skor<338	108	62	46	53,937	57,407
Orta	270<=Skor<304	200	61	139	31,814	30,5
Düşük	242<=Skor<270	52	6	46	13,465	11,538
Çok Düşük	Skor<242	13	1	12	4,802	7,6923

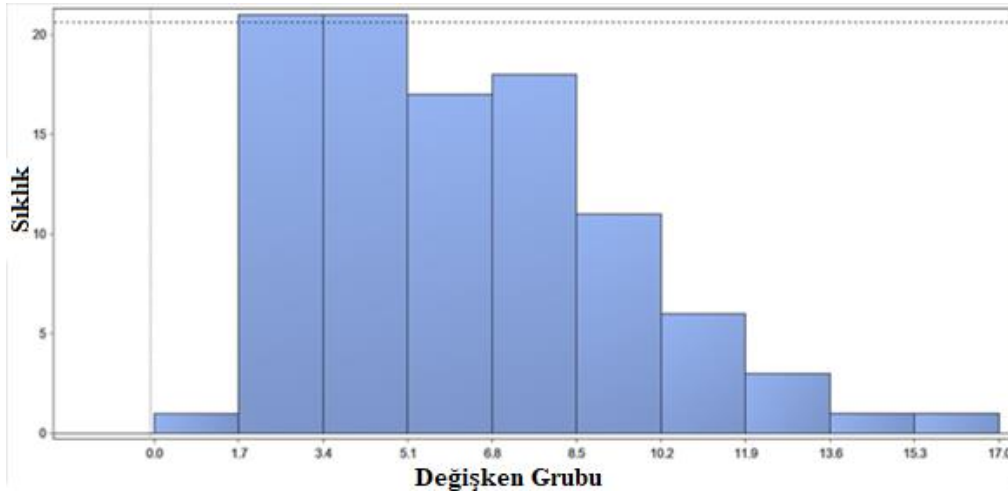


Şekil 3. Modelin tahmin ve gerçekleştirme durumu.

Figure 3. Model prediction and realization status.

Çalışmada daha sonraki adımda ise aynı problem Karar ağacı yöntemi ile modellenmiştir. Oluşturulan modelde ağacın 7 derinlik ve 56 yaprak sayısı bulunmaktadır. Değişkenlerin sıklık değerleri modeli açıklamak için yeterli düzeyde olduğu tespit edilmiştir. Modelde yer alan her bir değişken grubunun birden fazla benzersiz değerde cevap içerdiği Şekil 4'te gözlemlenmektedir.

Önemlilik değerleri yüksek olan değişkenler ve bölme kuralı sayı adetlerine ilişkin örnek Çizelge 5'te verilmiştir. Çizelge 6'da "KATEGORİ7" ev&yaşam kategorisini, "KATEGORİ8" ev&bakım&temizlik kategorisini, "KATEGORİ4" atıştırma kategorisini, "G4" alışverişteki gizlilik durumunu, "T3" sosyal tutumu, "SURE\_CEVIRIMICI\_ALISVERIS" çevrimiçi alışveriş kullanım geçmişini, "KATEGORİ5" süt&kahvaltı kategorisini ve "SEKTÖR" çalışılan sektör bilgisini ifade etmektedir.



Şekil 4. Karar ağacı sıklık grafiği.

Figure 4. Decision tree frequency graph.

Çizelge 5. Bölme kural sayı adetleri.

Table 5. Number of partition rules.

Değişken Adı	Bölme Kural Sayısı	Önem Değeri
KATEGORI7	17.0	1
KATEGORI8	12.0	0,8458
KATEGORI4	5.0	0,5665
G4	8.0	0,4577
YAS	8.0	0,4115
K_KAPI_ODEME	5.0	0,4112
T3	6.0	0,396
SURE_CEVIRIMICI_ALISVERIS	4.0	0,3771
KATEGORI5	2.0	0,3661
AR2	7.0	0,3603
SEKTOR	5.0	0,3584

Çalışmanın son adımında ise modelleme için K-En Yakın Komşu, GAA ve Rastgele Orman yöntemleri uygulanmıştır. Uygulanan makine öğrenmesi yöntemlerine ait parametreler Çizelge 6'da verilmektedir.

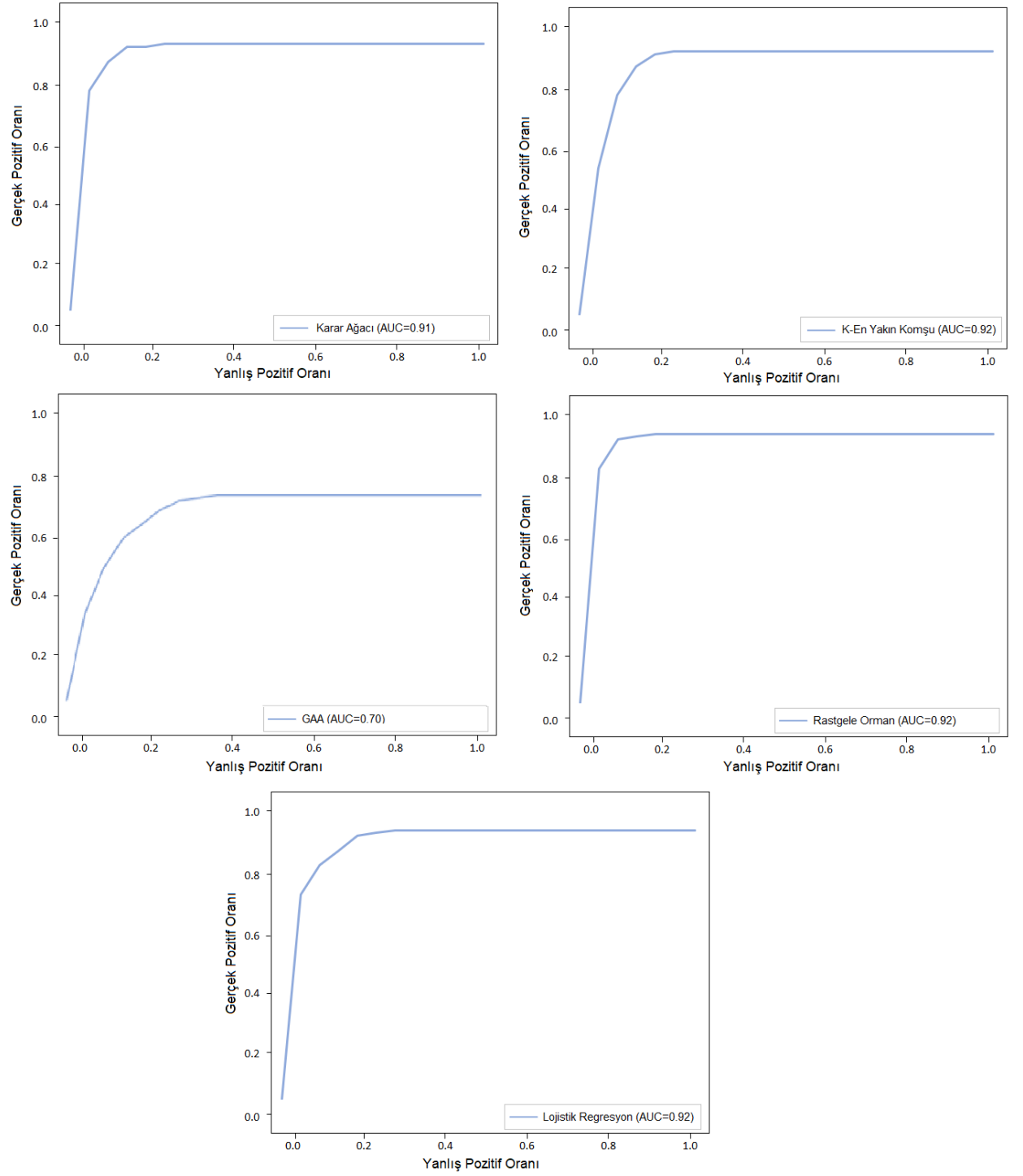
Çizelge 6. Uygulanan yöntemlerin parametre değerlerinin kullanımı.

Table 6. Use of the parameter values of applied methods.

Yöntem Adı	Parametrik Kullanım
Lojistik Regresyon	{'C': 2.7825594022071245, 'penalty': 'l2'}
Karar Ağacı	{'criterion': 'gini', 'max_depth': 40, 'max_features': 8, 'random_state': 50}
K-En Yakın Komşu	{'metric': 'euclidean', 'n_neighbors': 3, 'weights': 'distance'}
GAA	{'learning_rate': 0.03, 'max_depth': 8, 'n_estimators': 1000, 'subsample': 0.2}
Rastgele Orman	{'criterion': 'gini', 'max_depth': 8, 'max_features': 'auto', 'n_estimators': 200}

Çalışmada uygulanan tüm yöntemler ile ilgili elde edilen doğruluk ölçütleri, performans karşılaştırılması ortaya konmuştur. Uygulanan yöntemlerin doğruluk, AUC, Hassasiyet, F<sub>1</sub>, Geri Çağırma değerlerinin karşılaştırılması Çizelge 7'de gösterilmiştir.

Çalışmada uygulanan tüm yöntemlere ait ROC eğrisi grafikleri Şekil 5'te gösterilmiştir.



Şekil 5. Uygulanan yöntemleri ROC ve AUC değerleri.

Figure 5. ROC and AUC values for applied methods.

Çizelge 7. Uygulanan yöntemlerin performans karşılaştırılması.

Table 7. Performance comparison of the applied methods.

Yöntem Adı	Doğruluk	ROC-AUC	Hassasiyet	F <sub>1</sub>	Geri Çağırma
Lojistik Regresyon	0.831	0.90	0.829	0.84	0.832
Karar Ağacı	0.912	0.91	0.907	0.90	0.916
K-En Yakın Komşu	0.921	0.92	0.918	0.92	0.919
GAA	0.704	0.70	0.704	0.70	0.70
Rastgele Orman	0.928	0.92	0.921	0.92	0.924

#### 4. SONUÇLAR ve TARTIŞMALAR (RESULTS and DISCUSSIONS)

Literatürde, ilgili alanda benzer veri setleri ile genellikle tüketici tercihlerinin açıklanmasına yönelik çalışmalar yapılmıştır. Bu çalışmada, bir kullanıcının bir kategoriden alışveriş yapma olasılığını öngörülmesi ve bu tercihi etkileyen demografik özellikler üzerine odaklanılmıştır. Bu açıdan yaklaşıma sahip fazla sayıda çalışmalara rastlanmadığından, çalışmanın alanında özgün bir araştırma olduğu ifade edilebilmektedir. Ayrıca çalışmadaki diğer özgün katkı ise genellikle e-tedarik sistemlerinin performans ölçümü, bankacılık sektöründeki kredi risk yönetimi, gibi konularda kullanılmış olan skorkart ve skorkarne terimlerinin bu alanda kullanılmasıdır.

Çalışmada seçilen problemi modellemek için sık kullanılan makine öğrenmesi algoritmalarından Lojistik Regresyon, Karar Ağacı, K-En Yakın Komşu, GAA ve Rastgele Orman yöntemleri uygulanmıştır. Her yöntem, her bir değişkenin bağımlı değişken ile olan anlamlılığını ölçmektedir. Uygulanan tüm yöntemler için ilk olarak 52 değişken dikkate alınmış olup; anlamlılık durumuna göre analiz yapılmıştır. Karar Ağacı, K-En Yakın Komşu, GAA ve Rastgele Orman algoritmalarındaki sınıflandırma sonucunda en anlamlı sonucu veren 11 değişken belirlenmiştir. Belirlenen bu 11 değişkenin tamamının kendi içerisinde anlamlı olmadığı belirlenmiştir. Ancak lojistik regresyon ve skorkart uygulaması ile 6 değişkenin tamamının kendi içerisinde de anlamlı olduğu sonucu ortaya çıkmıştır. Sonuçların karşılaştırılması sadece tek bir skorkart uygulaması için yapılmıştır.

Modellere ait sonuçlar incelendiğinde Rastgele Orman yöntemi ile uygulanan modelinin 0.928 doğruluk oranı ile en yüksek performansı gösterdiği ve 0.921 AUC değeri ile modelin yüksek bir sınıflandırma başarısına ulaştığı görülmektedir. En düşük performansın ise 0.704 doğruluk oranı ve 0.702 AUC değeri ile GAA algoritmasına ait olduğu gözlenmiştir.

Ayrıca çalışmada Makine öğrenmesi algoritmalarından Lojistik regresyon ile gauss dağılımı uygulandığında 3 ana demografik özelliğin etken olduğu analiz edilmiştir. Bunun yanında çalışmada oluşturulan skorkart ile de elde edilen bu sonuçlar desteklenmektedir. Değişkenlerin, hedef değişken ile olan ilişkisi uygulanan yöntemler ile ortaya koyulmaya çalışılmıştır. Çalışmada lojistik regresyon yöntemi, skorkart ile modellendiğinde 6 değişkenin tamamının kendi arasında anlamlı ve ilişkili olduğu sonucu elde edilmiştir. Kullanıcıların demografik özelliklerinden olan yaş, günlük olarak internette geçirdikleri süre ve kapıda kredi kartı ile ödeme yapmayı tercih etme durumu kişisel bakım kategorisinden alışveriş yapmayı doğrudan etkileyen faktörler arasında yer aldığı elde edilen bulgular ile ortaya konmuştur.

Çalışmada elde edilen analiz bulgularına göre; çevrimiçi market alışverişinde kişisel bakım kategorisi için, 43 ile 47 yaş aralığından daha küçük yaşta olup, günlük internet kullanımı süresi 7-10 saat arasında olan ve ayrıca kapıda kredi kartı kullanım seçeneğini "Hiç kullanmam" veya "Nadiren kullanırım" şeklinde tercih eden kullanıcılar için kampanya uygulanması halinde hedef kitleye ulaşılmış olacaktır. Oraya konan bu ifadeler neticesinde, çalışmanın en büyük katkılarından biri kişisel bakım kategorisinden alışveriş yapabilecek kullanıcının sahip olması gereken özellikleri açıkça ortaya koyabilmektir.

Yapılan çalışmada perakende sektöründe faaliyet gösteren ve çevrimiçi market uygulaması ya da web hizmeti sunan tüm firmaların fayda sağlayabilmesi amaçlanmıştır. Buna göre elde edilen veriler ile

ilgili kategoriden yapılan satışların arttırılması ve bu kategori ile ilgili yapılacak olan kampanyaların başarıya ulaşması adına bu çalışmanın fayda sağlayacağı düşünülmektedir.

#### **Etik Standartlar Bildirimi (Declaration of Ethical Standards)**

Çalışma etik standartlara uygun olarak gerçekleştirilmiştir.

#### **Yazar Katkı Beyannamesi (Credit Authorship Contribution Statement)**

Tüm yazarlar usulüne uygun olarak makaleye katkıda bulunmuştur. Yazarlar yüksek lisans tez öğrencisi ve tez danışmanıdır. Burak Bahçivan: Veri elde etme, veri modeli oluşturma, deneylerin tasarlanması, araştırma, deneysel çalışmaların yürütülmesi, analiz Atınç Yılmaz: Veri modeli oluşturma, analiz, orijinal taslak yazma-düzenleme-revizyon, kontrol

#### **Çıkar Çatışması Beyannamesi (Declaration of Competing Interest)**

Yazarlar herhangi bir çıkar çatışması olmadığını beyan etmektedir.

#### **Destek / Teşekkür (Funding / Acknowledgements)**

Yazarlar, çalışmaya değerli zamanlarını ayırarak katkılarını sunan dergi editörleri ve hakemlere teşekkür etmektedir. Çalışma, Doç.Dr. Atınç Yılmaz'ın danışmanlığında yürütülen Burak Bahçivan'ın yüksek lisans tezinden türetilmiştir.

#### **Veri Kullanılabilirliği (Data Availability)**

Veriseti çevrimiçi market davranışları konusunda anket yolu ile Google Forms üzerinden Aralık 2021-Ocak 2022 tarihleri arasında elde edilmiştir; uygulanamaz.

#### **KAYNAKLAR (REFERENCES)**

- [1] B. Bahçivan, "Demografik Özelliklerin Online Market Kullanımına Etkisinin Makine Öğrenmesi Yöntemleri ile Tahmini", Yüksek Lisans Tezi", *Beykent Üniversitesi Lisansüstü Eğitim Enstitüsü*, İstanbul, 2022.
- [2] Y. Wang, J. Lin, B. Sheng, C. Sun, L. Si, and X. Liu, "Adaptive multi-task positive-unlabeled learning for joint prediction of multiple chronic diseases using online shopping behaviors", *Expert Systems with Applications*, Vol. 191, pp. 116232, 2022.
- [3] N. N. Moon, I. M. Talha, and I. Salehin, "An advanced intelligence system in customer online shopping behavior and satisfaction analysis", *Current Research in Behavioral Sciences*, Vol. 2, pp. 100051, 2021.
- [4] D. Koehn, S. Lessmann, and M. Schaal, "Predicting online shopping behaviour from clickstream data using deep learning", *Expert Systems with Applications*, Vol. 150, pp. 113342, 2020.
- [5] L. Wang, S. He, S. Su, Y. Li, L. Hu, and G. Li, "Urban neighborhood socioeconomic status (SES) inference: A machine learning approach based on semantic and sentimental analysis of online housing advertisements", *Habitat International*, Vol. 124, pp. 102572, 2022.
- [6] G. Volkmar, P. M. Fischer, and S. Reinecke, "Artificial Intelligence and machine learning: Exploring drivers, barriers, and future developments in marketing management", *Journal of Business Research*, Vol. 149, pp. 599-614, 2022.

- [7] J. Salminen, V. Yoganathan, J. Corporan, B. J. Jansen, and S. G. Jung, "Machine learning approach to auto-tagging online content for content marketing efficiency: A comparative analysis between methods and content type", *Journal of Business Research*, Vol. 101, pp. 203-217, 2019.
- [8] S. Can, "Lise öğrencilerinin üniversiteye giriş başarılarının eğitsel veri madenciliği ile tahmini", Yüksek Lisans Tezi, Beykent Üniversitesi Lisansüstü Eğitim Enstitüsü, 2021.
- [9] O. Kaynar, M. F. Tuna, Y. Görmez, and M. A. Deveci, "Makine öğrenmesi yöntemleriyle müşteri kaybı analizi", *Cumhuriyet Üniversitesi İktisadi ve İdari Bilimler Dergisi*, Vol. 18, No. 1, pp. 1-14, 2017.
- [10] P. Işık, and M. Öz, "Online alışveriş yapan süpermarket tüketicilerinin tüketim tercihlerinin teknoloji kabul modeliyle açıklanması", *OPUS Uluslararası Toplum Araştırmaları Dergisi*, Vol. 18, pp. 1538-1572, 2021.
- [11] A. T. Danışmaz, "Covid-19 salgınının tüketicilerin online alışveriş tercihine etkisi", *Social Sciences Research Journal*, Vol. 9, No. 2, pp. 83-90, 2020.
- [12] H. Nizam, and S. S. Akın, "Sosyal medyada makine öğrenmesi ile duygu analizinde dengeli ve dengesiz veri setlerinin performanslarının karşılaştırılması", XIX. Türkiye'de İnternet Konferansı, pp. 1-6, 2014.
- [13] R. Saydan, "Tüketicilerin online alışverişe yönelik risk ve fayda algılamaları", *Elektronik Sosyal Bilimler Dergisi*, Vol. 7, No. 23, pp. 386-402, 2008.
- [14] V. Hendri, C. Mawardi, and D. N. Santun, "Website based application of doctor selection classification derive from patient complaints using the C4.5 method and k-Nearest neighbor", *IOP Conference Series: Materials Science and Engineering*, Vol. 1007, pp. 012124, 2020.
- [15] M. Saygılı, "Faydacı ve hazcı alışveriş motivasyonlarının online satın alma niyeti üzerine etkisi", Yüksek Lisans Tezi, Sakarya Üniversitesi Sosyal Bilimler Enstitüsü, 2014.
- [16] E. S. Erdem, "Ses Sinyallerinde Duygu Tanıma ve Geri Erişim", Yüksek Lisans Tezi, Başkent Üniversitesi Fen Bilimleri Enstitüsü, Ankara, 2014.
- [17] S. Şenel, and B. Alatlı, "Lojistik Regresyon Analizinin Kullanıldığı Makaleler Üzerine Bir İnceleme", *Eğitimde ve Psikolojide Ölçme ve Değerlendirme Dergisi*, Vol. 5, No. 1, pp. 35-52, 2014.
- [18] Ö. Çokluk, "Lojistik Regresyon Analizi: Kavram ve Uygulama", *Kuram ve Uygulamada Eğitim Bilimleri*, Vol. 10, No. 3, pp. 1359-1407, 2010.
- [19] B. Kasapoğlu, "Kredi Riskinin Hesaplanmasında Skorlama Yaklaşımı", Yüksek Lisans Tezi, İstanbul Teknik Üniversitesi Sosyal Bilimler Enstitüsü, İstanbul, 2009.
- [20] M. Akıllı, N. Yılmaz, and K. G. Akdeniz, "Study of the q-Gaussian distribution with the scale index and calculating entropy by normalized inner scalogram", *Physics Letters A*, Vol. 338, No. 11, pp. 1099-1104, 2019.
- [21] D. G. Altman, and J. M. Bland, "Statistics notes: The normal distribution", *BMJ*, Vol. 310, No. 6975, pp. 298, 1995.
- [22] G. G. Emel, and Ç. Taşkın, "Veri madenciliğinde karar ağaçları ve bir satış analizi uygulaması", *Eskişehir Osmangazi Üniversitesi Sosyal Bilimler Dergisi*, Vol. 6, No. 2, pp. 221-239, 2005.
- [23] Ö. Akar, and O. Güngör, "Rastgele orman algoritması kullanılarak çok bantlı görüntülerin sınıflandırılması", *Jeodezi ve Jeoinformasyon Dergisi*, Vol. 106, pp. 139-146, 2012.
- [24] M. A. Pala, M. E. Çimen, Ö. F. Boyraz, M. Z. Yıldız, and A. F. Boz, "Meme kanserinin teşhis edilmesinde karar ağacı ve KNN algoritmalarının karşılaştırmalı başarımları analizi", *Academic Perspective Procedia*, Vol. 2, No. 3, pp. 544-552, 2019.

- [25] D. Kılınç, E. Borandağ, F. Yücalar, V. Tunalı, M. Şimşek, and A. Özçift, "KNN algoritması ve R dili ile metin madenciliği kullanılarak bilimsel makale tasnifi", *Marmara Fen Bilimleri Dergisi*, Vol. 28, No. 3, pp. 89-94, 2016.
- [26] L. Yang, X. Zhang, S. Liang, Y. Yao, K. Jia, and A. Jia, "Estimating surface downward shortwave radiation over china based on the gradient boosting decision tree method", *Remote Sensing*, Vol. 10, No. 2, pp. 185, 2018.

## EFFECT OF LOW-VELOCITY IMPACT DAMAGE ON THE ELECTROMAGNETIC INTERFERENCE SHIELDING EFFECTIVENESS OF CFRP COMPOSITES

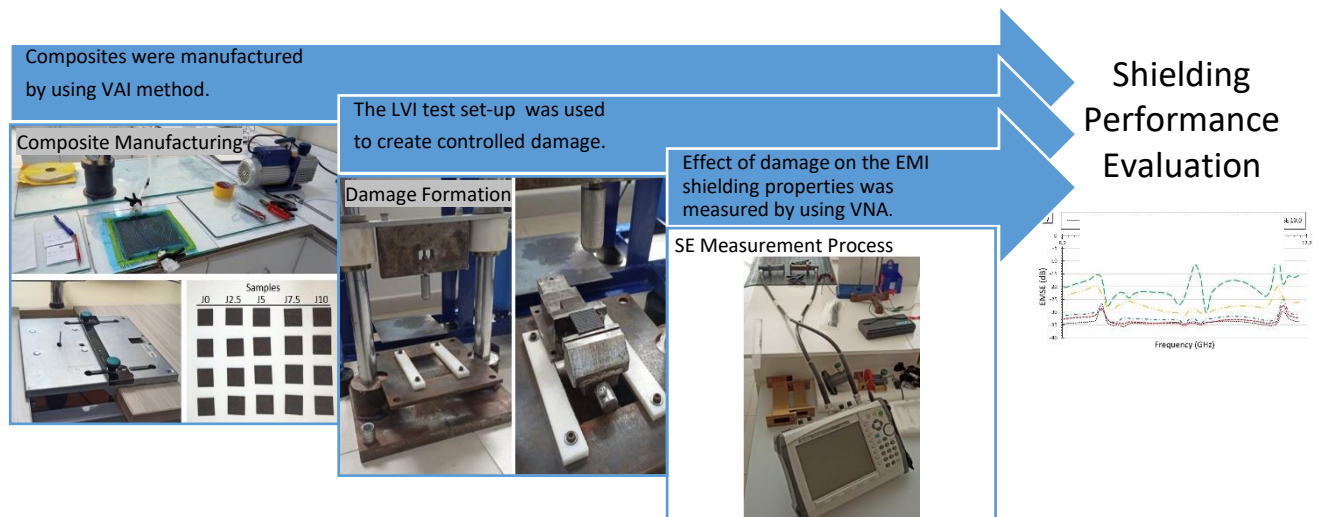
\*Ferhat YILDIRIM 

Çanakkale Onsekiz Mart University, Biga Vocational School, Machine and Metal Technologies Department,  
Çanakkale, TÜRKİYE  
[ferhatyildirim@comu.edu.tr](mailto:ferhatyildirim@comu.edu.tr)

### Highlights

- Carbon fiber composites are used as EMI shields due to their in plane electrical conductivity.
- However, damages during in use may harm the composite and knowing the EMI performance losses in a strategic product is an important issue.
- Accordingly, the applied 10 joule impact energy to the manufactured composite reduces the electrical conductivity by 74.3% and the EMSE by 40.5%.
- The effect of impact causes fragmentation of matrix and fibers and resulting disconnections of the conductive network of composite.
- 5 joule impact energy is assumed as a threshold value for the composite, and higher impact energies may cause to performance losses that can finish the service life of the 6 layered CFRP composite.
- The deterioration in the carbon-based conductive network, transforms the shielding characteristic from absorbance to reflectance.

### Graphical Abstract



Flowchart of the designed experimental study.



## EFFECT OF LOW-VELOCITY IMPACT DAMAGE ON THE ELECTROMAGNETIC INTERFERENCE SHIELDING EFFECTIVENESS OF CFRP COMPOSITES

Ferhat YILDIRIM 

*Çanakkale Onsekiz Mart University, Biga Vocational School, Machine and Metal Technologies Department,  
Çanakkale, TÜRKİYE  
[ferhatyildirim@comu.edu.tr](mailto:ferhatyildirim@comu.edu.tr)*

(Received: 25.05.2023; Accepted in Revised Form: 13.08.2023)

**ABSTRACT:** Carbon fiber reinforced polymer (CFRP) composites are widely used engineering materials in aerospace technologies. These electrically conductive carbon-based materials, due to the lightness advantages, are preferred as shields against electromagnetic radiation, especially in aircraft and satellites. However, the performance losses caused by damage because of flying object collision such as bird, hail, or projectile contain significant uncertainty. Herein, the CFRP composite material was structurally damaged by low velocity impact test set-up at various energy levels between 2.5 to 10 joules, and then its electromagnetic interference (EMI) shielding performance was investigated. In addition, the electrical properties of the material were also examined, and the occurred damage status was evaluated by microscopy studies. Intrinsically, the increase in impact energy increases the grade of damage on body of the material. This results in a drastic decrease in electrical conductivity and EMI performance. In experiments, where 5 joule energy is detected as a threshold level, it has been observed that irreparable damage occurs at energy levels above this value.

**Keywords:** CFRP composite, Damage, Electromagnetic interference shielding, Electrical conductivity, Low velocity impact

### 1. INTRODUCTION

The increase in the number of communication devices and electronic systems such as 5G network and GPS satellite signals in recent years has caused increasing electromagnetic (EM) radiations and consequently electromagnetic interference (EMI) [1]. It has been proven by scientific studies that this electromagnetic radiation has many negative effects such as, distortion of wireless phones, radio or TV signals for electronic devices and damaging the DNA and cell structure for living organisms [2, 3]. For this reason, protecting from electromagnetic waves or reducing their effects has become an important research issue [4]. Also, in areas such as military aviation, avoiding EM waves is already an important requirement for strategical aircrafts or satellite. Electromagnetic shielding is known as stopping or limiting electromagnetic radiation with conductive or magnetic barriers and it depends on charge, current and polarization capability of the outer and inner structure of materials [5-7]. Electrically conductive materials come to the forward in this respect, since the shielding is provided by mechanisms such as reflecting the radiation from the outer surface or absorbing it in the inner structure [8]. Metal materials offer good shielding performance due to their electrical conductivity. However, the fact that the main shielding mechanism is reflection, causes the continuation of the damage of the EM effect in different areas with secondary reflections. In addition, the corrosion tendency and high density of metals limiting their usage areas for some sectors such as aviation [9].

Nowadays carbon-based polymer composites are rapidly progressing to become an alternative to metals in terms of EM shielding, as in many other fields [10, 11]. They are preferred for necessary shielding activities, especially in areas such as aviation where low weight is very important. Moreover, easy processibility and the structural diversity of carbon (particle, fiber, foam, etc.) offers a wide range of usage options in different fields [12]. Long service life and low maintenance requirements are other important factors for the use of composite materials as shielding elements [13, 14]. However, deformations and

\*Corresponding Author: Ferhat YILDIRIM, [ferhatyildirim@comu.edu.tr](mailto:ferhatyildirim@comu.edu.tr)

possible damages due to usage conditions can occur. According to the report of European Aviation Safety Agency [15], the kinetic energy at the time of collision of an aircraft and a bird (bird masses above 0.78 kg) can reach up to 1500 joule. According to the same report, it was stated that this value is 2.7 to 6.6 times higher than the minimum requirements for fixed wing aircraft with certification requirements. It is emphasized here that speed and mass are the main factors determining the energy and constitute new areas on material performances that need to be examined. These impacts can result in mechanical electrical or EMI performance losses in composites as in every material. For example, a stealth capable aircraft or drone may be damaged while on duty, such as hail, projectile or bird strikes, and any deformations like scratching, cracking, or bending may occur on the structural shield material [16]. So, the electromagnetic wave will leak from the damaged area of the body and effect all system performance. This may cause it to lose the invisibility advantage that it gained by absorbing radar waves. It is vital that military vehicles and devices do not lose their EMI performance to maintaining their combat survivability [17]. This makes it necessary to constantly monitor the performance losses of materials due to damage against similar cases.

Some studies in the literature reveal that changes occur in electrical and shielding properties even under limited deformation conditions to which materials are exposed. For example, some researchers studying flexible film and foam materials have reported the electrical conductivity and EMI performance of the material decreasing when bending application. Yang et al. found that the average EMI performance decrease from 26.5 dB to 25.8 dB and resistivity slightly increase after continuous bending (1000 cycles) process on their study that investigate the flexible silicon rubber/CNT/Fe<sub>3</sub>O<sub>4</sub> nanocomposite characterization [18]. Similarly, Jiang et al. investigated the thermoplastic polyurethane/reduced graphene oxide composite materials. They found that the thin foam materials EMI values decreased from 21.5 dB to 16.5 dB at 1000 cycled and 2 mm curvature radius bending period [19]. Ravindren et al. have tested the ethylene-co-methyl acrylate (EMA), ethylene octene copolymer (EOC), and carbon nanotube (CNT) composites in terms of EMI properties. They found that the average EMI decrease from 33 dB to 32 dB after 500 cycled bending process [20]. Zhou et al. investigated the electrical conductivity of the graphene/carbon nanotube hybrid composite films after multiple bending movement. They pointed out the electrical conductivity slightly decrease after 1000 cycled bending at smaller than 1 mm curvature radius [21].

Wei et al. studied the effect of CNT coating on electrical conductivity properties of pre-cracked and rolled GFRP composites samples. The results showed that CNTs help maintain electrical conductivity while cracks develop, the conductivity decrease while the mechanical strain occurred by rolling [22]. Some studies have focused on self-healing mechanisms to compensate for the loss of performance caused by damage. Sim et al. studied on self-healing graphene oxide/silver nanowire films and textile. They found that the EMI SE was decreased from 72 dB to 56 dB, the resistivity was increased from 15 to 40 M $\Omega$  when the samples were cracking damaged. They also declared that the self-healed material regains the similar EMI performance again with 71 dB [13]. Ma et al. were able to develop a MXene melamine sponge mechanism that regain performance at ratio of 99.99% after breaking damage by repairing itself with the application of PU substrate [23]. Wang et al. researched the CNT reinforced dynamic crosslinked polyurethane (PUDA) polymer composite as a self-heal material. They declared when the sample cracked the EMI value decrease from 30.7 dB to 16.8 dB. Also, their self-healing mechanism repaired itself approximately at ratio level of 97% after multiple cracking-healing cycles [24]. On another study of Wang et al. they found that the EMI value decrease from 35.5 dB to 17.1 dB after cracked by blade and EMI value decrease from 33.8 dB to 32.3 dB after 5000 times bending at another CNT reinforcement level [16].

There are different studies too, showing that the need for EMI shielding is not just aviation oriented. The same performance can be expected from buildings that will protect ground personnel from bursts of electromagnetic radiation. Yoo et al. investigated the CNT added cement that proposed for construction of military building designed against to protect electromagnetic radiation. They pointed out CNT reinforcement offers beneficial EMI performance in the construction but emphasized that the EMI performance decrease when the microcracks occurred on the cement [25]. Kim et al reported similar results on CNT reinforced concrete. They said that the EMI performance decreases approximately levels of 40-

50% compared to the non-cracked samples when different sized cracks that detected with image processing and appear on samples [26].

The main subject of all these studies presented in the literature is depending on the operational conditions, many cracks or damage may occur in the composites and the material may not give expected performance. For this reason, the relationship between damage in the structure and EMI shielding effectiveness should be evaluated. Most of the literature focuses on the electrical and EMI performance loss and healing properties of flexible, film, and foam materials. Unlike the literature, the study focuses on the damage-loss relationship of the most basic composite material currently in use on aviation sector such as aircraft bodies, landing gear covers, satellite housing elements, electronic device boxes etc. However, post-damage EMI performances of CFRP composites, which are widely used in areas such as military aviation, have not been extensively investigated. In this study, changes in electrical conductivity and electromagnetic shielding performance of CFRP composites that damaged by various level of impact energies were investigated experimentally. Thus, an analysis on damage resulted shielding performance losses that may occur during service life, especially aircraft or drones, has been tried to be presented.

## 2. MATERIAL AND METHODS

### 2.1. Materials

Used carbon fiber fabric as the reinforcement material in the study has 7  $\mu\text{m}$  diameter and 240  $\text{gr}/\text{m}^2$  density with twill woven. The epoxy matrix with two components as known commercial code MGS L285/H285 has aviation certificated and both materials was purchased from Dost Kimya, Türkiye.

### 2.2. Manufacturing of Samples

The vacuum infusion method was chosen for the composites manufacturing (Figure 1). Thus, it was aimed to produce samples with the balanced matrix distribution and stable thickness. The carbon fabrics prepared by cutting in size of 300×300 mm was arranged in 6-layers and after the peel ply and vacuum net were added, the layers were covered with vacuum nylon. After resin infused the composite was cured at room temperature for 8 hour and post cured at 70 °C in an oven for 2 hours. 20 samples were prepared by cutting the composite in 40×40 mm that manufactured according to the designed experimental setup.

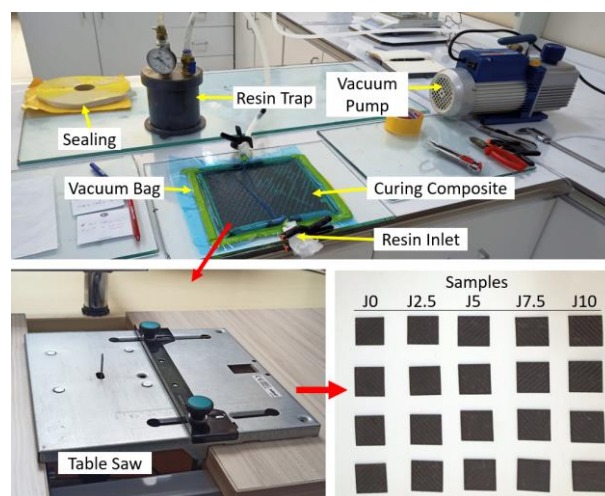


**Figure 1.** Composite manufacturing and sample preparation.

Although it is common application to positioned Teflon or nylon film between fabric layers for obtaining crack in the literature, these samples are used in Mode-I and Mode-II interlaminar shear tests [27]. In addition, since these cracks occur between the layers and in plane direction, they are incompatible

with the subject of this study and therefore they were not preferred. On the other side, scratching with a knife is another way to obtaining crack [24]. But this application preferred for sponge, film or foam materials and because of the regularity shape does not coincide with natural damage case. Thus, the low velocity impact test device given in Figure 2 was used to create damage on the samples.

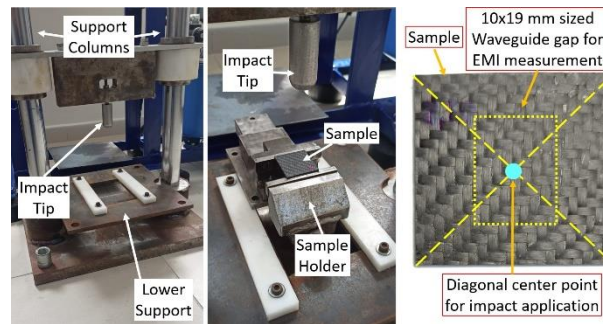


Figure 2. Impact application set-up.

Since the aim of this study is mapping the EMI shielding performance loss, 2.5, 5, 7.5, and 10 joule impact energy values were chosen as the main examination range. A possible hail, bird or any other particle strike scenario was tried to be obtained by applying four different energy level of impact to the 40×40 mm samples that positioned on the sample holder. The impact was applied to the diagonal center of the samples. For this aim steel impact tip that has 10 kg mass were dropped from a height of 25, 50, 75, and 100 mm, respectively. The used potential energy formula has been given in equation 1. Accordingly, 4 samples were used for impact application at each energy level, and 3 measurements were made for EMI and 7 measurements were made for electrical conductivity on each sample after damage occurred. Experimental design has been given in Table 1.

$$E=mgh \quad (1)$$

Here are the  $E$  is energy (joule),  $m$  is the mass (kg),  $g$  is gravity ( $m/s^2$  and it is assumed as 10), and  $h$  is the height (m).

Table 1. Experimental parameters and sample codes.

Sample Code	Applied Impact Energy (J)	Impact height (mm)	Impact speed (m/s)
J0	0	0	0
J2.5	2.5	25	0.707
J5	5.0	50	1
J7.5	7.5	75	1.224
J10	10.0	100	1.414

### 2.3. Experimental procedure

Electrical conductivity has a direct effect on EMI. In order to examine the EMI performance of the material, it is necessary to measure the electrical conductivity of the material. Only in this way damage and EMI can be linked each other established and discussed. Two probe method was used for measuring electrical conductivity of composite materials with using an ohmmeter according to ASTM D4496-13. The electrical resistance and resistivity were calculated using following equations from 2 to 4 [28].

$$R=V/I \quad (2)$$

$$\rho=(R \times A)/l \quad (3)$$

$$\sigma=1/\rho \quad (4)$$

Here are the  $\rho$  is resistivity,  $R$  is resistance (ohm), and  $V$  is electric potential difference (Voltage). Cross-sectional of measured area is  $A$  (cm<sup>2</sup>), contact length of probes  $l$  (cm), and electrical conductivity is  $\sigma$  (S/cm).

The vector network analyzer with two WR-90 waveguide set was used for electromagnetic shielding effectiveness (EMSE) measurements at X-band (8.2–12.4 GHz). Electromagnetic frequency, consisting of 8.2 and 12.4 GHz frequencies, is referred to as X-Band. It is widely used in many sectors, especially in aviation, defiance, marine and satellite systems, for radar observation, navigation, communication and meteorological forecasting [29]. These properties of the X-Band have enabled to selected as the target frequency range of the study especially focused aviation materials. On the other hand, the used waveguide technique is one of the non-standardized SE measurement techniques according to the IEEE 2715-2023 standard report document. it is a combination of ASTM D-4935 and IEEE-299 standards. It has a very popular and widespread usage areas thanks to its easy application, small sample size requirement and ability to measure high frequencies such as 8.2-12.4 GHz [9, 27, 29-34]. In this technique, the samples were positioned between two insulating sample holder that they have 10×19 mm sized gap by aligning the center of the impact and waveguide gap. Thus, it was ensured that the samples were not fragmented due to cracks and that the scattering  $S$  parameters were measured only with electromagnetic waves that spreading from the waveguide and crossing passed through the gap of sample holder [35, 36].

Total shielding effectiveness ( $SE_{Tot}$ ) was calculated using following equation 5.  $SE_{Tot}$  is equal to sum of shielding effectiveness of reflectance ( $SE_R$ ), shielding effectiveness of absorbance ( $SE_A$ ), and shielding effectiveness of multiple inner reflectance ( $SE_M$ ).  $SE_M$  is neglected, when the  $SE_{Tot}$  is greater than  $\pm 10$  dB [9].

$$SE_{Tot} (dB) = SE_R + SE_A + SE_M = 10 \log\left(\frac{P_i}{P_t}\right) \quad (5)$$

Here are, the power of the incident electromagnetic waves is  $P_i$  and power of transmitted electromagnetic waves is  $P_t$ . The required  $SE_A$ ,  $SE_R$ , and  $SE_T$  parameters were calculated by using the following equations from 6 to 8 according to the measured  $S$  parameters with network analyzer [36, 37].

$$SE_A (dB) = 10 \log\left(\frac{1-S_{11}^2}{S_{12}^2}\right) = 10 \log\left(\frac{1-S_{22}^2}{S_{21}^2}\right) = 10 \log\left(\frac{1-R}{T}\right) \quad (6)$$

$$SE_R (dB) = 10 \log\left(\frac{1}{1-S_{11}^2}\right) = 10 \log\left(\frac{1}{1-S_{22}^2}\right) = 10 \log\left(\frac{1}{1-R}\right) \quad (7)$$

$$SE_T (dB) = 10 \log\left(\frac{1}{S_{12}^2}\right) = 10 \log\left(\frac{1}{S_{21}^2}\right) = 10 \log\left(\frac{1}{T}\right) \quad (8)$$

Here are, the absorbance is  $A$ , the reflectance is  $R$  and the transmittance is  $T$ . To verification of the system, the sum of  $A$ ,  $R$  and  $T$  must be equal to 1 [36, 37].

The penetration ability of electromagnetic radiations into an electrically conductive material is limited to its surface thickness that related with charge current and polarization, also known as the skin effect. The shielding effectiveness of absorption is inversely proportional to the skin depth ( $\delta$ ), where the field reduces to 1/e of the incident value [38, 39]. The relation between  $SE_A$  and skin depth is calculated by using equation 9 [40].

$$\delta = -8.68 \left[ \frac{t}{SE_A} \right] \quad (9)$$

Finally, the SOIF BK5000 optical microscope (OM) was used to investigate the microstructure and crack propagation of composites due to the impact application.

### 3. RESULTS AND DISCUSSIONS

#### 3.1. Electrical properties

The electrical conductivity and resistivity tests results are given in Figure 3. The damaged materials offer various resistivity and conductivity values according to applied impact energy levels. The measurements show that the electrical resistance increases as the damage on the material increases. While the non-damaged J0 sample gave a resistivity value of 25.64  $\Omega\text{cm}$ , the resistivity of the most damaged J10 sample increased approximately 3.7 times and was calculated as 95.84  $\Omega\text{cm}$ . Similarly, the intrinsic conductivity values change inversely with the damage. While the intrinsic conductivity value for the undamaged J0 sample was 0.039 S/cm, it was calculated as 0.01 S/cm for the damaged J10 sample. The effect of the damage on the electrical conductivity values can be analyzed better in the drawn graph.

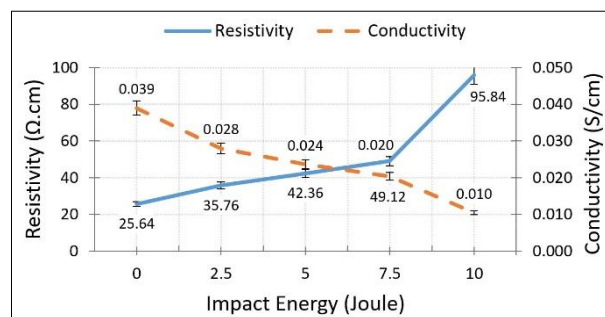


**Figure 3.** Electrical conductivity and resistivity results.

The literature reveal that changes occur in electrical properties under limited deformation conditions to which materials are exposed [18-21]. Wei et al. declared that the electrical conductivity decreases while the mechanical strain occurred and cracks develop on GFRP composites [22]. It is thought that the main reason of this change in conductivity and resistivity is the fragmentation of carbon fibers by impact. The integrity of the fragmented and separated carbon fibers is disrupted, and this reveals that the existing electrical network is weakens and broken. In other words, the reduced ability of electron transfer leads to an increase in the resistance of the material, resulting in a decrease in its conductivity [41, 42]. It is observed that the J10 sample, damaged with 10 joule impact energy, shows a large jump in resistivity results. This change in electrical properties also gives us information about the damage status of the material and suggests that the larger area of damage occurred in this sample. Because the increase in resistance for equivalent material and fixed probe range is explained by the reduction of the cross-sectional area according to the formulation [28]. Here, change in contact area of fibers can be calculated by operating the formula in reversely in accordance with resistivity-area relationship of the J0 sample and the resistance values of the J2.5, J5, J7.5, and J10 samples. Accordingly, observed decrease in contact area proves the existence of broken and fragmented fiber groups [25, 26]. It should be noted that although the formula defines a 2-dimensional area, it is possible the fracture can be occurred in 3-dimensional formation. Because the weaving of carbon fiber fabric is 0-90 twill knitted. Warp and weft weaving makes it possible to crack propagate in both the X and Y directions. However, when the effect of the impact force in the Z direction is added to material, the vectoral forces promote the fracture formation in all 3-dimensions. Accordingly, as the impact energy increases, the damage on the material is spreading, and the contact area of the fibers decreases due to fiber fragmentation. Finally, decrease on area of carbon fibers that contact with each other, it results in a decrease in electrical conductivity [25, 26]. The relationship between the impact energy and the contact area of fibers are given in Figure 4.

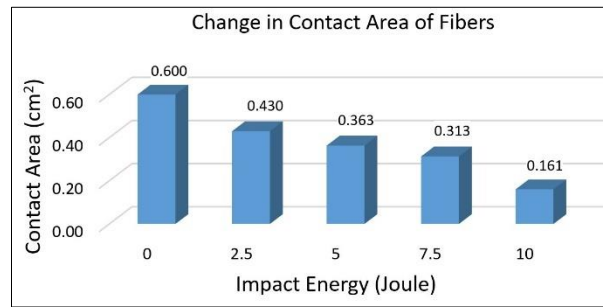


**Figure 4.** Relationship between the impact energy and the contact area of fibers according to the resistivity measurements.

### 3.2. Shielding Effectiveness (SE) results

The SE Tot results as a function of the frequency are presented in Figure 5a. Non-damaged J0 sample gives -33.928 dB SE Tot value. The calculated SE Tot values of other samples J2.5, J5, J7.5, and J10 are -33.175, -31.956, -26.745, and -20.184 dB, respectively. The drastic decrease on SE Tot can easily see when the impact energy increase. Decrease rates for J2.5, J5, J7.5, and J10 were calculated as 2.2, 5.8, 21.1, and 40.5% compared to the J0, respectively. Electrical conductivity plays an important role in attenuating EM waves on the material [9, 41, 43]. As EM waves move through the structure, they dispersed by electrical charge transportation and is absorbed by converting to heat [4, 44, 45]. Therefore, the width of the conductive mesh is important. Since the epoxy matrix is an insulator, it is completely permeable to EM waves. In other words, epoxy has no efficient shielding ability [29]. The occurred damage by the impact does not change this effect, too. So, it can be said that the epoxy matrix is not responsible for decrease of shielding ability. The damage, caused by the impact means the breaking and fragmentation of the carbon fibers as much as the matrix fragmentation. Thus, electrically conductive networks get weakens and the impedance mismatching between material surface and air is reduces [8, 20, 41, 46]. The SE Tot values decreased with the reduce of electrical conductivity due to the damage occur. Thus, non-damaged J0 sample gives the highest SE Tot due to all fibers stay together, contrary the J10 has the minimum SE Tot value.

Although the first noticeable result is the dramatic decrease in SE Tot values another interesting issue is the stability of the respond to EM waves is impaired and the frequency range at which it exhibits sensitivity is expanding. As can be seen from the reduction of the straight sectors of the curve the sensitivity range shown at the frequencies of 8.8 and 11.8 GHz has expanded to 8.5-9.0, 9.8-10.5, and 11.4-12.0 GHz ranges. This proves the serious SE Tot performance losses occurs in the material. Also, while the J0 sample easily reaches up the commercially required -30 dB SE Tot values [4, 47, 48], only the J2.5 and J5 samples have been able to maintain its effectiveness. The other J7.5 and J10 samples shows enormous performance decrease after impact damaged. Thus, it is obviously seen that shield could not fulfill her duty and the materials should be fix or replaced with a backup before any other usage.

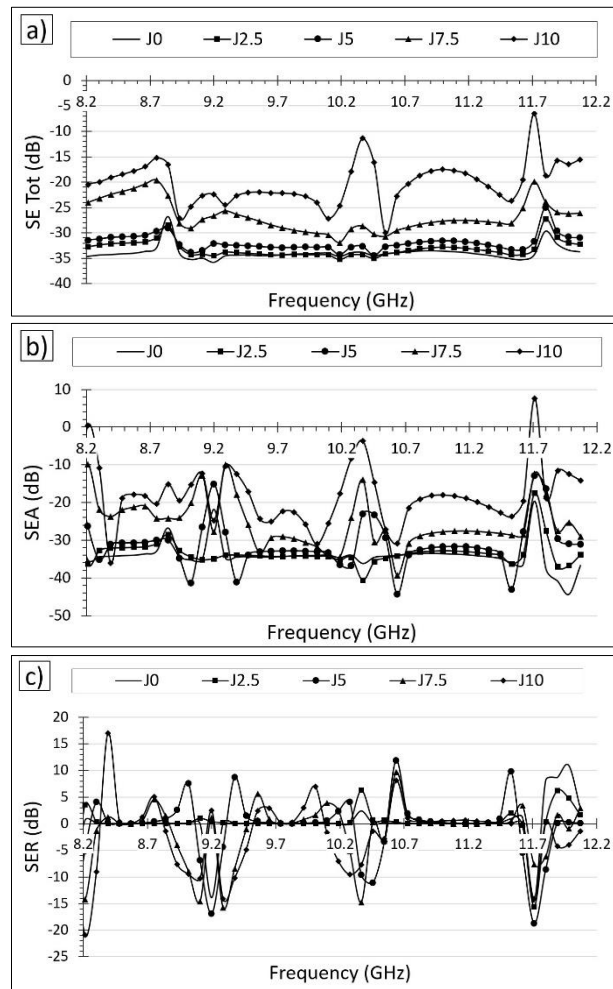


**Figure 5.** Shielding results of the damaged samples; a) SE Tot, b) SEA, and c) SER.

Figure 5b and 5c gives the SEA and SER results of the samples. The trend of SEA curves show similarity with the EMSE curves. While absorbance lines are clustered around -33 dB and shifted towards the zero as the impact energy increased, reflectance lines are located on the center zero region. Another information that can be obtained from the curves is that the absorption sensitivity of the material is impaired. According to the literature, materials that provide excellent shielding performance offers flatter curves [13, 23]. The fact that the curves of the damaged samples has more zigzag shape indicates that the reduces ability of response according to the changing frequency. Although the mean values seem numerically significant, the shielding change observed at close frequencies reveals that the characteristic of the material is deteriorated.

Figure 6 gives the comparison of SE Tot, SEA, and SER results. The SEA values of the samples J0, J2.5, J5, J7.5, and J10 are calculated as -33.868, -33.077, -30.857, -25.316, and -18.310 dB, respectively. The SER values was also calculated as -0.061, -0.098, -1.098, -1.429, and -1.873 dB for J0, J2.5, J5, J7.5, and J10 samples, respectively. The obtained results reveal that the main shielding mechanism of the composite material is absorbance. The absorption dominated shielding characteristic is, proving its potential for use in applications where low radar visibility and high electronic protection is required [49].

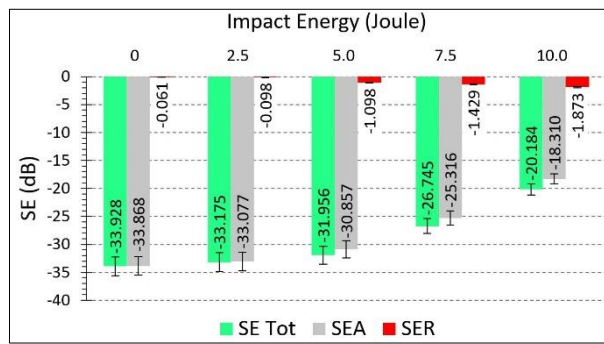


Figure 6. Comparison of SE Tot, SEA, and SER results.

However, the absorbance ability of the material decreases significantly with the damage caused by the impact. As in the SE Tot, decrease from -33 dB to -18 dB show an absorption performance loss at ratio of 45%. The results reveal that the conductive network which the electromagnetic wave propagates in the material is damaged. In fact, this situation shows parallelism with the decreasing in electrical conductivity. In addition, while the absorbance decreases, the EM reflectance values of the material significantly increase. The calculated increase rate is about 2970%. It is thought that the increased micro surface area due to the fractured fibers lead to more reflection of EM waves. It has been stated in the literature that surface-enlarging factors such as intra-structure pores increase the reflection [38]. The findings can be considered as a comment compatible with the literature. This marginal increase means that the shield lost its mission capability by turning EM waves into the reflection after a damage due to the impact while absorbing radar waves.

The skin depth, which is the effective thickness that EM waves is absorbed by dispersing in the material and related with frequency, material permeability, and conductivity [39, 50]. The calculated skin depth values for all materials are given in the Figure 7. The calculated skin depth of the non-damaged J0 sample is 0.512 mm versus 33.868 dB SEA value. This value is the required thickness for absorbing EM waves of CFRP composite material during shielding. Carbon fibers increase impedance mismatching and skin depth with lower magnetism and high electrical conductivity [38]. The other skin depths were calculated as 0.524, 0.532, 0.685, and 0.948 for J2.5, J5, J7.5, and J10 samples, respectively. As can be seen on combine graph at Figure 7, while the applied impact energy increases, the thickness required by the material for absorbance increases due to the conductive network damaged that emits EM waves. Even though the absorbance value offered by the material decreased from -33 dB to -18 dB, the skin depth value increased almost 2 times from 0.512 mm to 0.948 mm. These values show the size of the damage on the J10 sample and how effects the material shielding characteristics. In another aspect, the calculated skin depth differences quite little between the J0, J2.5, and J5 samples, which reveal that the damage is formed at a small area (occurred on material surface) for J2.5 and J5 samples. Therefore, it can be said that there was no internal structure damage has occurred for these materials at the impact energies mentioned. In addition, this result is confirmed in the "microscopy studies" section by images that obtaining from optical microscope.

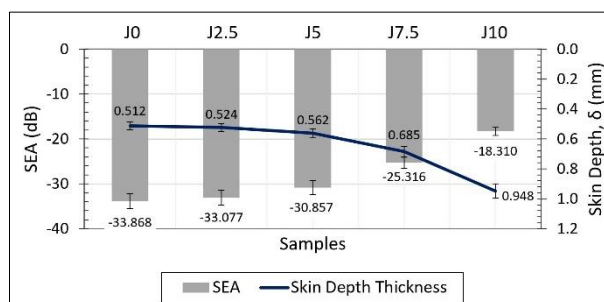
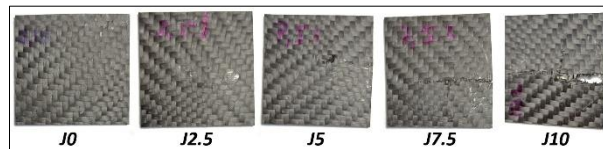


Figure 7. Skin depth absorbance relation versus impact energy.

### 3.3. Optic microscopy studies

Optical imaging studies are important in terms of investigating the causes of the change observed in electrical and shielding properties. The impact zone images given in Figure 8 prove the fiber fragmentation hypothesis. With the increasing impact energy, the damage area grows and deepens. Although the absolute area cannot be calculated exactly, it was detected that the damage size increased exponentially while the impact energy increased linearly. In addition, while the damage was observed only on the surface for J2.5 and J5 samples, it was developed in penetration and form of complete disintegration for J7.5 and J10 samples. In other words, while the damage is 2D (X-Y plane) for J2.5 and J5, it is occurred on 3D (X-Y plane and Z direction) for J7.5 and J10. Considering that the reparability and reusability, it is thought that renovation is possible for J2.5 and J5 samples, since the damage occurs on the surface. However, since the damage deeply penetrated into structure and resulted with dividing in two parts, it is thought that it is not possible to repair it efficiently for J7.5 and J10 samples.



**Figure 8.** Makro images of samples after impact application.

The damage size, which is relatively low for J2.5 sample, increases rapidly for the J5, J7.5 and J10 samples with the increase of impact energy. While a very deep crack was formed in Z direction for J7.5, the full separation limit was reached for J10 sample. The observed great damage illuminates the reason for the conductivity and therefore SE losses of the materials in line with the literature [22, 25, 26]. Magnified images of the damage areas are presented in Figure 9. It can be seen in Figure 9a, that the damage in J2.5 in the form of matrix fracture and is superficial. It was observed that some of the fibers in the top layer of composite were broken for a very limited area and the damage did not progress into the structure. As given in Figure 9b, it was determined that the matrix cracked more intensely in the J5 sample, and the top carbon fiber bundle completely separated from each other at woven intersection region in the plane direction. Some cracks have been measured average width of 100  $\mu\text{m}$ . As can be seen in Figure 9c, there is a significant damage on the J7.5 sample. The average crack widths are around 300  $\mu\text{m}$  and they penetrate deeply into the composite. Unlike the J5 samples, the damage occurred suddenly and in the form of complete breakage without waiting for the cracks reach up to the warp-weft intersection regions. As given in Figure 9d, J10 samples were completely fragmented. The material was not only separated in the plane direction but also delaminated due to the impact. Multiple damage occurred at various direction and delamination between the layers have increased the loss of conductivity. And thus, shielding performance against to EM waves decreased to levels that render the product useless.

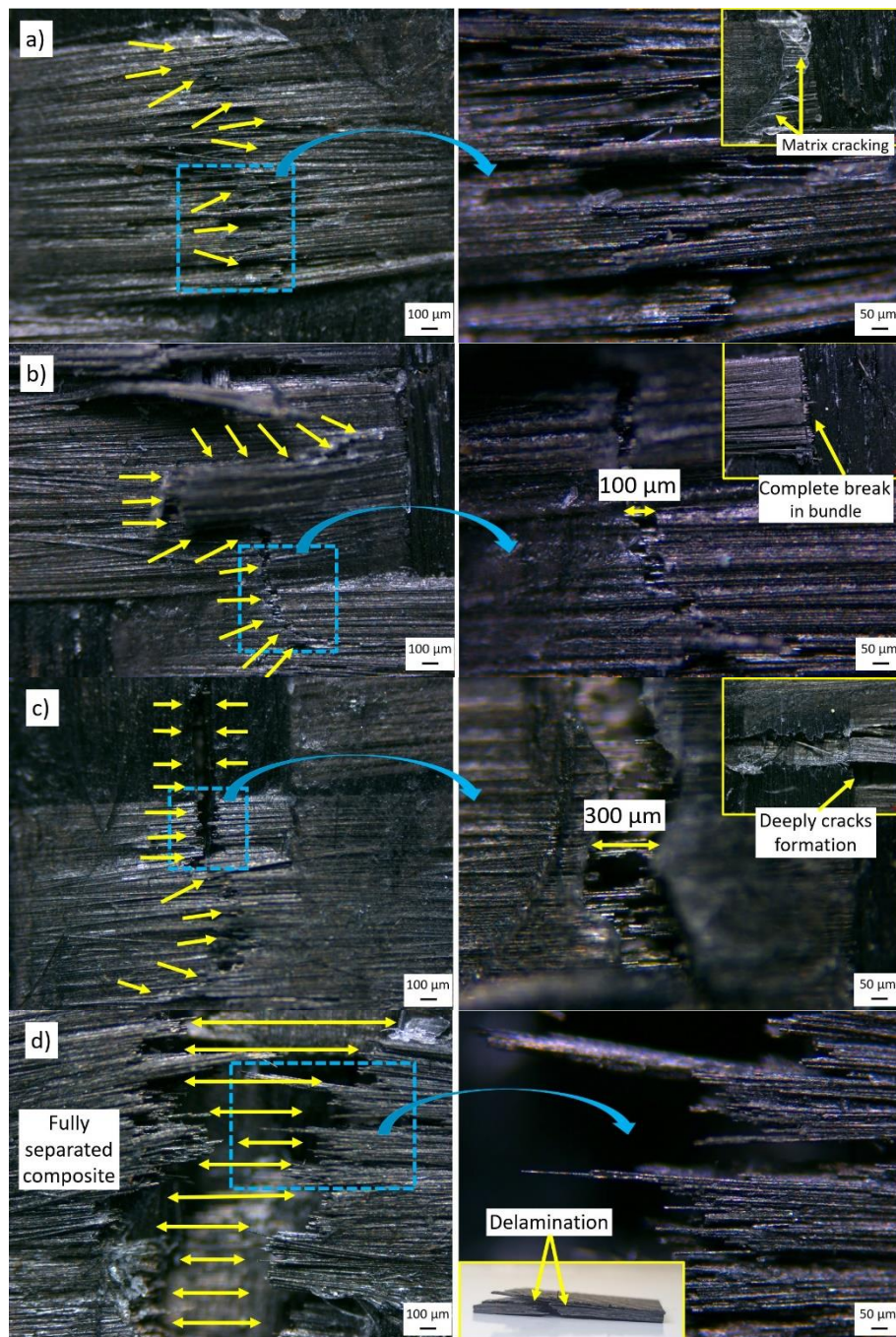


**Figure 9.** OM images of the samples, a) J2.5, b) J5, c) J7.5, and d) J10.

In terms of the reparability of the material, it is considered that repair is possible in the J2.5 and J5 samples, since the damage occurred on the surface. In addition, even though these two samples suffer 2.2% and 5.8% performance loss in EM shielding, they are still above the 30 dB commercially required shielding limit. However, since the damage in J7.5 and J10 samples is affecting the internal structure of the material, it is thought that it is not possible to repair it. Thus, it can be concluded that the impact energy of 5 joule is the threshold value for a composite material designed as in the study. It is considered that the material exposed to values above 5 joules, it can no longer in use due to the damage.

#### 4. CONCLUSIONS

This study addresses the effect of the damages after low velocity impact at various energy levels (2.5, 5, 7.5, and 10 joules) on the electrical conductivity and the EMSE performance of carbon fiber reinforced polymer composite. According to the results, the electrical resistance increases as the damage on the material increases. While the non-damaged J0 sample gave a resistivity value of 25.64  $\Omega\text{cm}$ , the resistivity of the most damaged J10 sample increased approximately 3.7 times and was calculated as 95.84  $\Omega\text{cm}$ . One of the other findings of the study is that the 6-layer CFRP composite can easily reach up the 30 dB SE Tot level that require for commercial products. While non-damaged J0 sample gives -33.928 dB SE Tot value, the other samples J2.5, J5, J7.5, and J10 are -33.175, -31.956, -26.745, and -20.184 dB, respectively. The applied impact energy has a direct effect on the damage that occurred on the material. The damage that grows with increasing impact energy, weakens the electrically conductive network on the material. Since SE is associated with electrical conductivity, decreasing conductivity reduces the shielding performance of the material. Decrease rates for J2.5, J5, J7.5, and J10 were calculated as 2.2, 5.8, 21.1, and 40.5% compared to the J0, respectively. This proves the hypothesis, that impact damages can reduce the SE performance of CFRP composites. The SEA values of the samples J0, J2.5, J5, J7.5, and J10 are calculated as -33.868, -33.077, -30.857, -25.316, and -18.310 dB, respectively. The results prove that main shielding mechanism of the produced composite is absorbance. However, the absorbance ability of the material decreases significantly with the damage caused by the impact. As in the SE Tot, decrease from -33 dB to -18 dB show an absorption performance loss at ratio of 45%. 5J impact energy is a threshold value for the material, and greater impact energies may cause to shielding performance losses that can finish the service life of the material. In addition, the deterioration in the carbon-based conductive network with the impact damage, transforms the shielding characteristic of the material from absorbance to reflectance. Finally, microscopy studies have shown that it is difficult to repair the damaged material due to the completely broken, for gaining shielding capability again. Accordingly, it can be recommended that the materials should be designed considering the effects of the harsh conditions they may encounter during their duties and that they should be constantly checked.

#### Declaration of Ethical Standards

The author declares that all ethical guidelines including authorship, citation, data reporting, and publishing original research are followed.

#### Declaration of Competing Interest

The author declares that there is no conflict of interest.

#### Funding / Acknowledgements

This study did not receive funding from any provider.

#### Data Availability

The data that support the findings of this study are available from the corresponding author upon reasonable request.

#### REFERENCES

- [1] M. Han, C. E. Shuck, R. Rakhmanov, D. Parchment, B. Anasori, C. Min Koo, G. Friedman, and Y. Gogotsi, "Beyond Ti3C2Tx: MXenes for Electromagnetic Interference Shielding", *ACS Nano*, vol. 14, no. 4, pp. 5008–5016, 2020.

- [2] D. Carpenter, "Human disease resulting from exposure to electromagnetic fields", *Reviews on Environmental Health*, vol. 28, no. 4, pp. 159-172, 2013.
- [3] D. A. Yilmaz, İ. H. Çağiran, G. Dege, and M. S. Yildirim, "Effects of Electromagnetic Pollution on Health", *MAUNSağBil.Derg.* vol. 2, no. 2, pp. 67-79.
- [4] D. Munalli, G. Dimitrakis, D. Chronopoulos, S. Greedy, and A. Long, "Electromagnetic shielding effectiveness of carbon fibre reinforced Composites", *Composites Part B*. vol. 173, pp. 106906, 2019.
- [5] D. D. Soyaslan, "Design and Manufacturing of Fabric Reinforced Electromagnetic Shielding Composite Materials", *Textile and Apparel*, vol. 30, no. 2, June, pp. 92-98, 2020.
- [6] X. Jia, Y. Li, B. Shen, and W. Zheng, "Evaluation, fabrication and dynamic performance regulation of green EMI-shielding materials with low reflectivity: A review". *Composites Part B* vol. 233, pp. 109652, 2022.
- [7] H. Abbasi, M. Antunes, and J. I. Velasco, "Recent advances in carbon-based polymer nanocomposites for electromagnetic interference shielding", *Progress in Materials Science*, vol. 103, pp. 319-373.
- [8] Y. Chen, L. Pang, Y. Li, H. Luo, G. Duan, C. Mei, W. Xu, W. Zhou, K. Liu, and S. Jiang, "Ultra-thin and highly flexible cellulose nanofiber/silver nanowire conductive paper for effective electromagnetic interference shielding", *Composites Part A*, vol. 135. pp. 105960, 2021.
- [9] F. Yildirim, E. Kabakçı, H. S. Şaş, and V. Eskizeybek, "Multi-walled carbon nanotube grafted 3D spacer multi-scale composites for electromagnetic interference shielding", *Polymer Composite*, vol. 43, pp. 5690, 2020.
- [10] M. S. Cao, W. L. Song, Z. L. Hou, B. Wen, and J. Yuan, "The effects of temperature and frequency on the dielectric properties, electromagnetic interference shielding and microwave-absorption of short carbon fiber/silica composites", *Carbon*, vol. 48, no. 3, pp. 788-796, 2010.
- [11] J. M. Thomassin, C. Jérôme, T. Pardoën, C. Bailly, I. Huynen, and C. Detrembleur, "Polymer/carbonbased composites as electromagnetic interference (EMI) shielding materials", *Materials Science and Engineering: R*, vol. 74, no. 7, pp. 211-232, 2013.
- [12] R. Kumar, S. Sahoo, E. Joanni, R. K. Singh, W. K. Tan, K. K. Kar, and A. Matsuda, "Recent progress on carbon-based composite materials for microwave electromagnetic interference shielding", *Carbon*, vol. 177, pp. 304-331, 2021.
- [13] H. J. Sim, D. W. Lee, H. Kim, Y. Jang, G. M. Spinks, S. Gambhir, D. L. Officer, G. G. Wallace, and S. J. Kim, "Self-healing graphene oxide-based composite for electromagnetic interference shielding", *Carbon*, vol. 155, pp. 499-505, 2019.
- [14] H. Zhang, X. Zheng, R. Jiang, Z. Liu, W. Li, and X. Zhou, "Research progress of functional composite electromagnetic shielding materials", *European Polymer Journal*, vol. 185, pp. 111825, 2023.
- [15] European Aviation Safety Agency, "Bird Strike Damage & Windshield Bird Strike Final Report", 5078609-rep-03 Version 1.1,
- [16] T. Wang, W. C. Yu, W. J. Sun, L. C. Jia, J. F. Gao, J. H. Tang, H. J. Su, D. X. Yan, and Z. M. Li, "Healable polyurethane/carbon nanotube composite with segregated Structure for efficient electromagnetic interference shielding", *Composites Science and Technology*, vol. 200, pp. 108446, 2020.
- [17] W. Cai, N. Shao, X. Shao, and Z. Pan, "Structural analysis of carbon clusters by using a global optimization algorithm with Brenner potential", *Journal of Molecular Structure: THEOCHEM*, vol. 678, no. 1-3, pp. 113-122, 2004.
- [18] J. Yang, X. Liao, J. Li, G. He, Y. Zhang, W. Tang, G. Wang, and G. Li, "Light-weight and flexible silicone rubber/MWCNTs/Fe<sub>3</sub>O<sub>4</sub> nanocomposite foams for efficient electromagnetic interference shielding and microwave absorption", *Composites Science and Technology*, vol. 181, pp. 107670, 2019.
- [19] Q. Jiang, X. Liao, J. Li, J. Chen, G. Wang, J. Yi, Q. Yang, and G. Li, "Flexible thermoplastic polyurethane/reduced graphene oxide composite foams for electromagnetic interference shielding with high absorption characteristic", *Composites Part A: Applied Science and Manufacturing*, vol. 123, pp. 310-319, 2019.

- [20] R. Ravindren, S. Mondal, K. Nath, and N. C. Das, "Investigation of electrical conductivity and electromagnetic interference shielding effectiveness of preferentially distributed conductive filler in highly flexible polymer blends nanocomposites", *Composites Part A: Applied Science and Manufacturing*, vol. 118, pp. 75-89, 2019.
- [21] E. Zhou, J. Xi, Y. Guo, Y. Liu, Z. Xu, L. Peng, W. Gao, J. Ying, Z. Chen, and C. Gao, "Synergistic effect of graphene and carbon nanotube for high-performance electromagnetic interference shielding films", *Carbon*, vol. 133, pp. 316-322, 2018.
- [22] L. Wei, N. Li, G. D. Wang, X. L. Liu, Y. X. Liu, and Y. C. Shen, "The effect of rolling process on the mechanical and electrical properties of CNTs-enhanced GFRP", *Materials Today Communications*, vol. 32, pp. 103998, 2022.
- [23] W. Ma, W. Cai, W. Chen, P. Liu, J. Wang, and Z. Liu, "A novel structural design of shielding capsule to prepare high-performance and self-healing MXene-based sponge for ultra-efficient electromagnetic interference shielding", *Chemical Engineering Journal*, vol. 426, pp. 130729, 2021.
- [24] T. Wang, W. C. Yu, C. G. Zhou, W. J. Sun, Y. P. Zhang, L. C. Jia, J. F. Gao, K. Dai, D. X. Yan, and Z. M. Li, "Self-healing and flexible carbon nanotube/polyurethane composite for efficient electromagnetic interference shielding", *Composites Part B: Engineering*, vol. 193, pp. 108015, 2020.
- [25] D. Y. Yoo, M. C. Kang, H. J. Choi, W. Shin, and S. Kim, "Electromagnetic interference shielding of multi-cracked high-performance fiber-reinforced cement composites – Effects of matrix strength and carbon fiber", *Construction and Building Materials*, vol. 261, pp. 119949, 2020.
- [26] S. Kim, Y. S. Jang, T. Oh, S. K. Lee, and D. Y. Yoo, "Effect of crack width on electromagnetic interference shielding effectiveness of high-performance cementitious composites containing steel and carbon fibers", *Journal of Materials Research and Technology*, vol. 20, pp. 359-372, 2022.
- [27] G. Mutlu, F. Yildirim, H. Ulus, and V. Eskizeybek, "Coating graphene nanoplatelets onto carbon fabric with controlled thickness for improved mechanical performance and EMI shielding effectiveness of carbon/epoxy composites", *Engineering Fracture Mechanics*, vol. 284, pp. 109271, 2023.
- [28] D. Mi, X. Li, Z. Zhao, Z. Jia, and W. Zhu, "Effect of dispersion and orientation of dispersed phase on mechanical and electrical conductivity", *Polymer Composites*, vol. 42, pp. 4277, 2021.
- [29] V. Zaroushani, A. Khavanin, S. B. Mortazavi, and A. J. Jafari, "Efficacy of Net Epoxy Resin for Electromagnetic Shielding in X-Band Frequency Range", *Health Scope*, vol. 5(3), pp. e30203, 2016.
- [30] A. Andrea, A. Suarez, J. Torres, P. A. Martinez, R. Herraiz, A. Alcarria, A. Benedito, R. Ruiz, P. Galvez, and A. Penades, "Shielding Effectiveness Measurement Method for Planar Nanomaterial Samples Based on CNT Materials up to 18 GHz", *Magnetochemistry*, vol. 9, pp. 114, 2023.
- [31] IEEE Standards Association, IEEE Std 2715-2023, "IEEE Guide for the Characterization of the Shielding Effectiveness of Planar Materials", *IEEE Electromagnetic Compatibility Society Approved 15 February 2023*.
- [32] IEEE Standards Association, IEEE Std 521-2019, "IEEE Standard Letter Designations for Radar-Frequency Bands", *IEEE Aerospace and Electronic Systems Society, Approved 7 November 2019*.
- [33] J. Baker-Jarvis, "Transmission/Reflection and Short-Circuit Line Permittivity Measurements", NIST Technical Note 1341, published by the National Institute of Standards and Technology (NIST), Boulder, CO, USA, 1990.
- [34] B. Clarke, A. Gregory, D. Cannel, M. Patrick, S. Wylie, I. Youngs, and H. Hill, "A Guide to Characterization of Dielectric Materials at RF and Microwave Frequencies", London: NPL, 2003. ISBN:0904457389.
- [35] C. Fan, B. Wu, R. Song, Y. Zhao, Y. Zhang, and D. He, "Electromagnetic shielding and multi-beam radiation with high conductivity multilayer graphene film", *Carbon*, vol. 155, pp. 506-513, 2019.
- [36] A. Kaushal and V. Singh, "Electromagnetic interference shielding response of multiwall carbon nanotube/polypropylene nanocomposites prepared via melt processing technique", *Polymer Composites*, vol. 42, pp. 1148-1154, 2021.

- [37] H. Oraby, I. Naeem, M. Darwish, M. H. Senna, and H. R. Tantawy, "Effective electromagnetic interference shielding using foamy polyurethane composites", *Polymer Composites*, vol. 42, pp. 3077, 2021.
- [38] V. Shukla, "Review of electromagnetic interference shielding materials fabricated by iron ingredients", *Nanoscale Adv*, vol. 1, pp. 1640-1671, 2019.
- [39] R. Kumar, S. R. Dhakate, T. Gupta, P. Saini, B. P. Singh, and R. M. Mathur, "Effective improvement of the properties of light weight carbon foam by decoration with multi-wall carbon nanotubes", *Journal of Materials Chem A*, vol. 1, pp. 5727-5735, 2013.
- [40] R. Pal, S. L. Goyal, I. Rawal, and A. K. Gupta, "Tailoring of EMI shielding properties of polyaniline with MWCNTs embedment in X-band (8.2–12.4 GHz)", *Journal of Physics and Chemistry Solids*, vol. 169, pp. 110867, 2022.
- [41] C. Liang, M. Hamidinejad, L. Ma, Z. Wang, and C. B. Park, "Lightweight and flexible graphene/SiC-nanowires/ poly(vinylidene fluoride) composites for electromagnetic interference shielding and thermal management", *Carbon*, vol. 156, no. 58-66, 2020.
- [42] Z. Zeng, M. Chen, H. Jin, W. Li, X. Xue, L. Zhou, Y. Pei, H. Zhang, Z. Zhang, "Thin and flexible multi-walled carbon nanotube waterborne polyurethane composites with high-performance electromagnetic interference shielding", *Carbon*, vol. 96, pp. 768, 2016.
- [43] K. Jagatheesan, A. Ramasamy, A. Das, and A. Basu, "Electromagnetic shielding behaviour of conductive filler composites and conductive fabrics – A review", *Indian Journal of Fibre & Textile Research*, vol. 39, pp. 329-342, 2014.
- [44] H. Lv, X. Liang, G. Ji, H. Zhang, and Y. Du, "Porous three-dimensional flower-like Co/ CoO and its excellent electromagnetic absorption properties", *ACS Applied Material Interfaces*, vol. 7, pp. 9776–9783, 2015.
- [45] C. Wang, Y. Ding, Y. Yuan, X. He, S. Wu, S. Hu, M. Zou, W. Zhao, L. Yang, A. Cao, and Y. Li, "Graphene aerogel composites derived from recycled cigarette filters for electromagnetic wave absorption", *Journal of Materials and Chemistry. C*, vol. 3, pp. 11893–11901, 2015.
- [46] B. P. Singh, Prasanta, V. Choudhary, P. Saini, S. Pande, V. Singh, and R. Mathur, "Enhanced microwave shielding and mechanical properties of high loading MWCNT–epoxy composites", *Journal of Nanoparticle Research*, vol. 15, pp. 1, 2013.
- [47] D. Bigg, "The effect of chemical exposure on the EMI shielding of conductive Plastics", *Polymer Composites*, vol. 8, no. 1, pp. 1–7, 1987.
- [48] T. Peng, S. Wang, Z. Xu, T. Tang, and Y. Zhao, "Multifunctional MXene/Aramid Nanofiber Composite Films for Efficient Electromagnetic Interference Shielding and Repeatable Early Fire Detection", *ACS Omega*, vol. 7, no. 33, pp. 29161-29170, 2022.
- [49] J. He, M. Han, K. Wen, C. Liu, W. Zhang, Y. Liu, X. Su, C. Zhang, and C. Liang, "Absorption-dominated electromagnetic interference shielding assembled composites based on modular design with infrared camouflage and response switching", *Composites Science and Technology*, vol. 231, pp. 109799, 2023.
- [50] X. Hong, T. Peng, C. Zhu, J. Wan, and Y. Li, "Electromagnetic shielding, resistance temperature-sensitive behavior, and decoupling of interfacial electricity for reduced graphene oxide paper", *Journal of Alloys and Compounds*, vol. 882, pp. 160756, 2021.

## IMPROVEMENT OF HIGH PLASTICITY CLAY BY USING FILTER SLUDGE

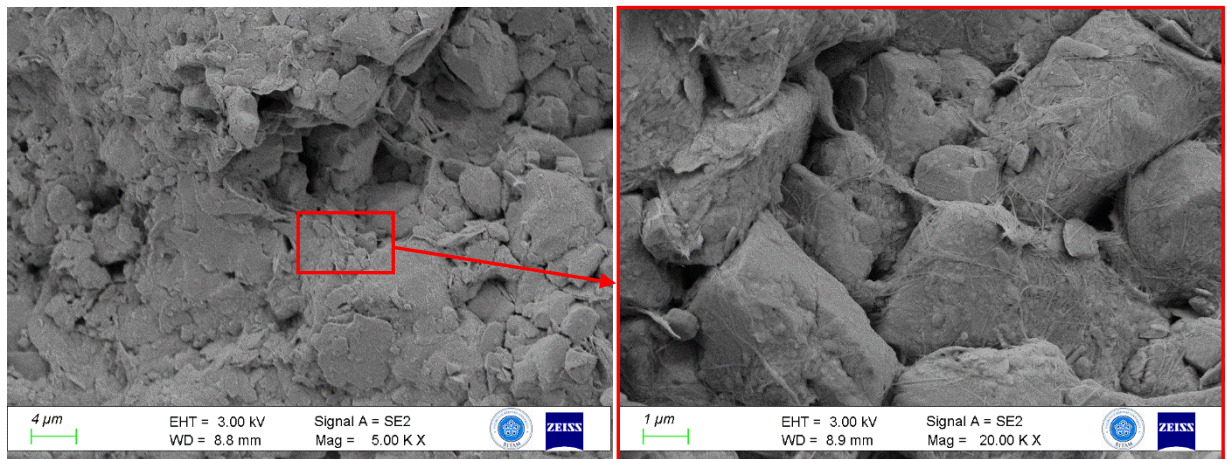
<sup>1</sup>İlyas ÖZKAN , <sup>2,\*</sup> Yavuz YENGİNAR 

Necmettin Erbakan University, Engineering Faculty, Civil Engineering Department, Konya, TÜRKİYE  
<sup>1</sup>iozkan@erbakan.edu.tr, <sup>2</sup>yyenginar@erbakan.edu.tr

### Highlights

- Feasible usage of the filter sludge, a waste material of the sugar industry, is investigated to stabilize high plasticity clay.
- The plastic limit and optimum water content increase as the FS content increases; liquid limit, plasticity index, and maximum dry density decrease.
- Improved soil strength increases as the curing time and FS amount increase, and the highest strength was obtained with 15% of FS.
- At the optimum additive ratio, the unconfined compressive strength increases by 33% and the swelling percentage decreases by 53%.
- With the use of filter sludge in soil improvement applications, the storage cost of the waste material and its harm to the environment will be reduced.

### Graphical Abstract



Microstructural change of the clay stabilized with filter sludge



## IMPROVEMENT OF HIGH PLASTICITY CLAY BY USING FILTER SLUDGE

İlyas ÖZKAN<sup>1</sup>,<sup>2,\*</sup> Yavuz YENGİNAR<sup>2</sup>

*Necmettin Erbakan University, Engineering Faculty, Civil Engineering Department, Konya, TÜRKİYE*

<sup>1</sup>[iozkan@erbakan.edu.tr](mailto:iozkan@erbakan.edu.tr), <sup>2</sup>[yyenginar@erbakan.edu.tr](mailto:yyenginar@erbakan.edu.tr)

**(Received: 07.06.2023; Accepted in Revised Form: 13.08.2023)**

**ABSTRACT:** Filter sludge (FS) is a waste material that occurs during sugar production in the sugar industry, and since it is not used anywhere, it creates a problem due to storage costs and environmental damage. In the present study, high plasticity clay was stabilized with a filter sludge which has never been used for soil stabilization in field cases. The changes in the geotechnical properties of a high plasticity clay (CH) with the additive of filter sludge (FS) were investigated. The amount of FS mixed into CH soil is 3-6-9-12-15% by dry weight of the soil. Changes in geotechnical properties such as consistency limits, compaction parameters, strength, swelling potential, CBR value of improved soils were determined. The plastic limit and optimum water content increase as the FS content added to the soil increases; liquid limit, plasticity index, and maximum dry density decrease. Improved soil strength increases as the curing time and FS amount increase, and the highest strength was obtained with 15% of FS. At the optimum additive ratio, the unconfined compressive strength increases by 33%. The swelling percentage of CH clay decreases from 42.5% to 20%. According to the wet CBR test results, the bearing capacity of the improved soil increased from %1.1 to %4.4. As a result of this study, it was seen that the FS waste material improved the geotechnical properties of the soil.

**Keywords:** *Clay, Filter Sludge, Soil Stabilization, Strength, Swelling Potential*

### 1. INTRODUCTION

In geotechnical engineering, soft clayey or silty soils and loose sandy or gravelly soils pose significant challenges. Engineering structures built on such these soils may encounter problems with bearing capacity, settlement, liquefaction, stability, and stiffness under static and dynamic loads. Before proceeding to the design and construction of engineering structures on problematic soils, these soils need improvement with surface or deep soil improvement methods depending on the superstructure and soil properties.

High plasticity clayey soils can lead to various issues such as bearing capacity, settlement, swelling, and shrinkage depending on the void ratio, water content, and consistency properties. Semi-saturated high-plasticity clays have a variety of volume changes according to their initial water content, which results in swelling or shrinking due to an increase or decrease in water content, respectively. Swelling soils can cause substantial damage to lightweight structures, roads, highways, airport runways, and pipelines. Lightweight structures built on swelling soils require special precautions during the construction process, as they are prone to damage but not life-threatening. As a result, swelling soils are a worldwide problem that poses several challenges for civil engineers [1].

The regions most affected by swelling soils are found in semi-arid climatic regions, encompassing six continents and forty countries [2]. In Turkey, swelling soils are prevalent in Central Anatolia and a part of Western Anatolia, Southeastern Anatolia, and Eastern Anatolia [3].

According to the Highways Technical Specification [4], high-plasticity clays with a plasticity index greater than 10%, must be stabilized with lime. High plasticity clays with a liquid limit value greater than 90% and a plasticity index greater than 65% cannot be used as filling material. Therefore, swelling soils need to be improved before using as construction materials [5].

Various methods are employed for the stabilization of high plasticity clays with high swelling potential and low bearing capacity. These methods include replacing soil, pre-wetting, chemical

**\*Corresponding Author:** Yavuz YENGİNAR, [yyenginar@erbakan.edu.tr](mailto:yyenginar@erbakan.edu.tr)

stabilization, geotextile usage, preloading, thermal methods, and compaction in the field [6], [7]. Chemical stabilization is commonly preferred in the improvement process of high-plasticity clays.

The materials used in the chemical stabilization method are cement [6]–[8], lime [9]–[11], fly ash [12]–[14], marble dust [15]–[17], silica fume [18]–[20], and blast furnace slag [21]–[23]. When clayey soils are stabilized with these additives, liquid limit, plasticity index, and optimum water content decrease, and plastic limit, maximum dry density, and strength increase.

Sugar production stages in the sugar industry are listed as follows: 1) washing, slicing, and boiling the sugar beet; 2) separating the raw sherbet from the beet pulp; 3) precipitating non-sugar substances by mixing raw sherbet with lime milk; 4) precipitation of raw sherbet by carbonation. In the final stage, muddy sherbet comes out with the precipitation of the raw sherbet, which is compressed in the press filters, and the sugar and sludge are separated from each other. The resulting sludge is “filter sludge”. The filtered sludge released during sugar production is stored around the factory or in waste storage centers. As a result, the storage costs of waste increase and environmental problems occur. Filter sludge was used to increase soil fertility [24], to produce biodiesel [25], and to use in animal breeding [26]. Studies on the use of filter sludge are very limited.

In this study, the potential use of filter sludge in the stabilization of high-plasticity clays was investigated to reduce the storage cost of the waste material and mitigate its environmental impact. The study aimed to determine the consistency limits, compaction behavior, strength, and swelling properties of the improved soil by incorporating filter sludge in different proportions into the high plasticity clayey soil.

## 2. MATERIAL AND METHODS

### 2.1. Materials

The soil used in the study was obtained from the plain of Konya. Before conducting the experiments, the soil was sieved using a No. 40 sieve to obtain a homogenous specimen. According to the Unified Soil Classification System (USCS) [29], the soil is classified as high plasticity clay (CH), as shown in Table 1.

**Table 1.** The geotechnical properties of soil

Properties	Value
Plastic limit (%)	24
Liquid limit (%)	99
Plasticity index (%)	75
Maximum dry density (g/cm <sup>3</sup> )	1.570
Optimum water content (%)	23.15

Filter sludge (FS) is a waste material that obtained from Konya Şeker Factory. The initial water content of FS was 30%. Filter sludge is not an effective material for soil stabilization due to its organic content. The presence of organic matter in waste materials added to soils can lead to decay over time, resulting in mold growth. Consequently, the strength of stabilized soils decreases over time. To address this issue, it is essential to purify the filter sludge from these organic materials before using it in soil stabilization. Before purification, FS was dried in the oven at 60°C for 24 hours to avoid mass loss since organic matter may burn at higher temperatures. After that, FS was sieved through No. 40 sieve before usage. In the purification stage, the filter sludge was incinerated at 440°C following the ASTM D2974 [27] standard. The amount of organic matter was determined as ~10. Figure 1 illustrates the natural and burned filter sludge used in this study.

Furthermore, the chemical composition of both CH (high plasticity clay) and FS materials was determined through X-ray Fluorescence (XRF) analysis, and the results are presented in Table 2.



**Figure 1.** Natural (left side) and burned (right side) filter sludge

**Table 2.** Chemical composition of materials

Material	Al <sub>2</sub> O <sub>3</sub>	SiO <sub>2</sub>	Fe <sub>2</sub> O <sub>3</sub>	CaO	MgO	K <sub>2</sub> O	TiO <sub>2</sub>	ZrO <sub>2</sub>	SO <sub>3</sub>
CH	10.9	36.7	4.82	19.9	1.73	2.58	0.64	0.34	0.05
FS (natural)	0.45	1.51	0.23	49.6	1.84	0.13	0.05	0.33	0.71
FS (burned)	0.66	2.10	0.39	51.4	1.75	0.19	0.09	0.35	0.72

## 2.2. Testing procedures

Some laboratory test and analyzes were performed to investigate the stabilization of high plasticity clay with filter sludge. At the scope of this study, experimental program consists of three parts that are index properties, engineering properties, and mineralogical properties, respectively.

### 2.2.1 Index properties

The influence of the filter sludge on the index properties of CH specimen was investigated by evaluating various parameters, including Atterberg limits, maximum dry densities, optimum water contents, and swelling potentials of the stabilized soil specimens.

While determining the geotechnical properties of the FS stabilized CH soil samples, the materials were mixed with a spatula in dry condition and then sieved twice through the No.40 sieve to increase the homogeneity of the mixture. The dry weight percentages of stabilized soil specimens with filter sludge are presented in Table 3. The maximum amount of FS is limited to 15% because lime stabilization usually includes between 7-9% lime [28]. Since 51.4% CaO is present in FS waste, ettringite formation may occur if more than 15% FS is added, which causes swelling in the improved soil structure. Moreover, since FS waste is burned at 440 °C, the amount of FS is limited to 15% in order not to increase energy consumption.

**Table 3.** The dry weight percentages of stabilized soil specimens with filter sludge

Stabilized Specimens	CH	Filter sludge
%3 FS	97	3
%6 FS	94	6
%9 FS	91	9
%12 FS	88	12
%15 FS	85	15

Atterberg limits (liquid limit, plastic limit, and plasticity index) are key parameters for high plasticity clay. It is important to note that the Atterberg limits may change due to the chemical interactions between filter sludge (FS), high plasticity clay (CH), and water when these materials are mixed. The consistency properties of stabilized soils were specified with respect to ASTM D4318 [29].

In the shallow stabilization process, the soil and additive (filter sludge) were compacted together to enhance the durability and strength of the stabilized soil. The outputs of standard proctor test that maximum dry density and optimum water content are essential parameters for stabilization process. The standard proctor test was performed according to ASTM D 698 [30].

### 2.2.2 Engineering properties

A parameter called as swelling potential should be determined before the design of the lightweight structures such as one-story buildings, pavements, etc. Since most of the damage that occurs on these structures results from the volume change of high plasticity clay soils. Swelling potentials of both CH and stabilized soils were found after free swell tests were performed with respect to ASTM D4546 [31].

The strength of soil depends on many factors such as field condition, ground water table, soil type, air content, and more. For this reason, some strength parameters of soils such as angle of internal friction, cohesion, value of CBR, and unconfined compressive strength have been developed for last decades. Two laboratory tests were done to determine the strength parameters of both CH and stabilized soils in this study are given below;

1. High plasticity clay is known for its cohesive nature, and as such, unconfined compression tests were conducted in this study to assess the unconfined compressive strength, which is a more suitable strength parameter for cohesive soils. The testing procedure followed in this part was ASTM D 2166 [33].
2. The usage of filter sludge in the subgrade of either pavement or highway was thought due to the storage problem of waste material. California Bearing Ratio (CBR) test generally performed for quality control of subgrade of some structures such as pavement and highway. ASTM D1883 [32] was pursued. CBR test can be done at two different types that are dry and wet. Wet CBR test was done on stabilized soil specimen since it was more suitable for cohesive soils.

The samples used in the UCS, standard proctor, CBR and swelling tests were obtained by compressing in suitable molds according to the optimum water content and maximum dry density of each mixture. The diameters of UCS, standard proctor, CBR and swelling test specimens are 50, 105.6, 152, and 50 mm, and their lengths are 100, 115.5, 127, and 20 mm. The stabilized soil specimens were subjected to curing for 7 days, 28 days, and 56 days to observe the effect of curing duration on the engineering properties of the stabilized high plasticity clay. This investigation aimed to understand how the inclusion of filter sludge influenced the strength and other engineering properties of the stabilized soil over time. Figure 2 shows the laboratory tests on stabilized specimens.

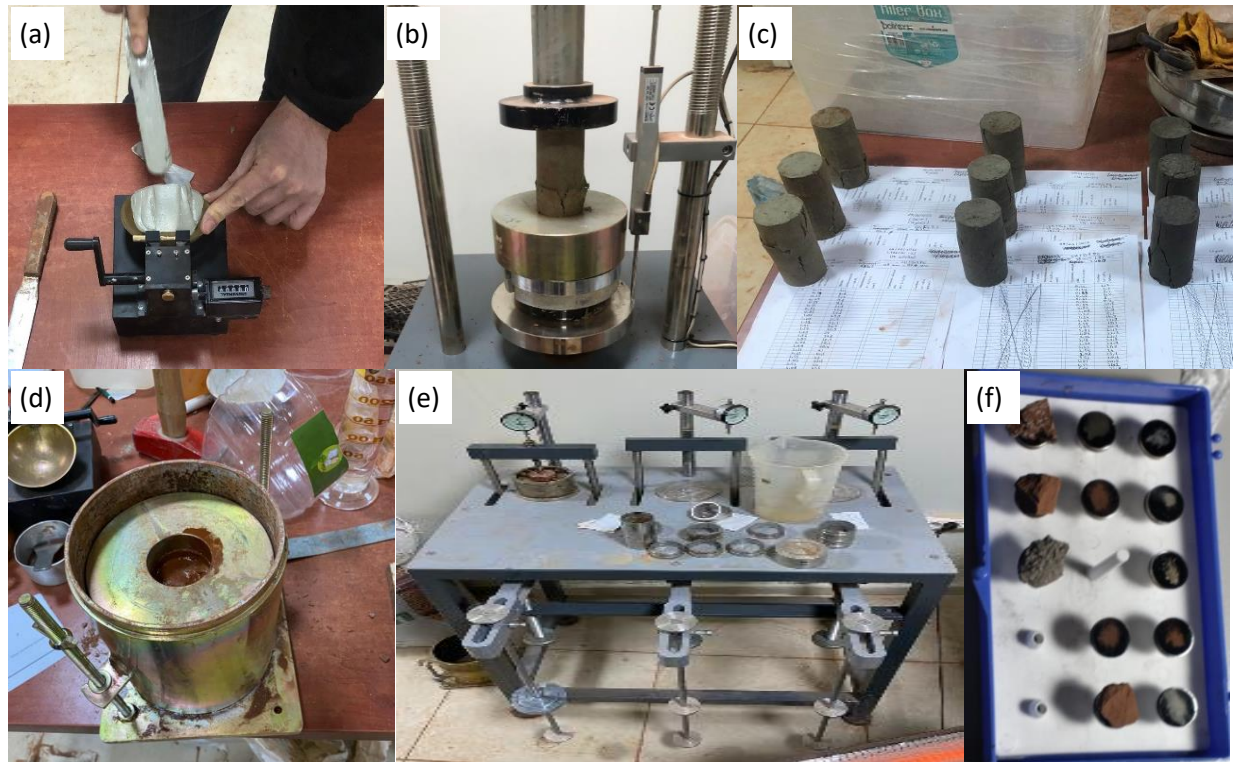


**Figure 2.** Laboratory tests on stabilized specimens: a) liquid limit test, b) UCS test, c) shear surface of stabilized specimens after UCS tests, d) CBR test specimen, e) swelling test, and f) SEM testing

### 2.2.3 Microstructural properties

The alteration of CH, FS and stabilized soil microstructure was observed by Scanning Electron Microscope (SEM) analyses. SEM images were taken by using a ZEISS EVO LS10 field emission machine at NEÜ BİTAM Laboratory. Firstly, samples used in the analysis were dried at 105°C to obtain dry specimen. Since water vapor into the specimen may damage the scanning electron microscope. CH and FS materials were pulverized before SEM imaging. For the SEM analysis of the stabilized soil samples, SEM images were taken from 1x1x1 cm cubic pieces extracted from the shear surfaces of unconfined compression (UCS) test samples. Then, these specimens were coated with gold and palladium for SEM Analysis.

SEM images were taken at different magnification factors to observe the change of microstructural characteristic for selected specimens.

## 3. RESULTS AND DISCUSSION

The parameters of stabilized soils were divided into two groups that are index properties and engineering properties. First group that is called as index properties that consist of Atterberg limits, maximum dry density and optimum water content. Then, engineering properties include the swelling potentials and strength parameters of stabilized soils.

### 3.1. Index Properties

Index properties play a crucial role in understanding the fundamental characteristics of both soils and the stabilization process in this study. Thus, the change of some parameters of stabilized soil specimens prepared in this study were determined. These specimen parameters determined in this study are plastic limit (PL), liquid limit (LL), maximum dry density (MDD), and optimum water content (OWC).

### 3.1.1 Atterberg limits of stabilized soil specimens

The values of plastic limit and liquid limit of stabilized specimens were measured and the plasticity index (PI) of them were calculated. Consistency limits of stabilized specimens are illustrated in Figure 3.

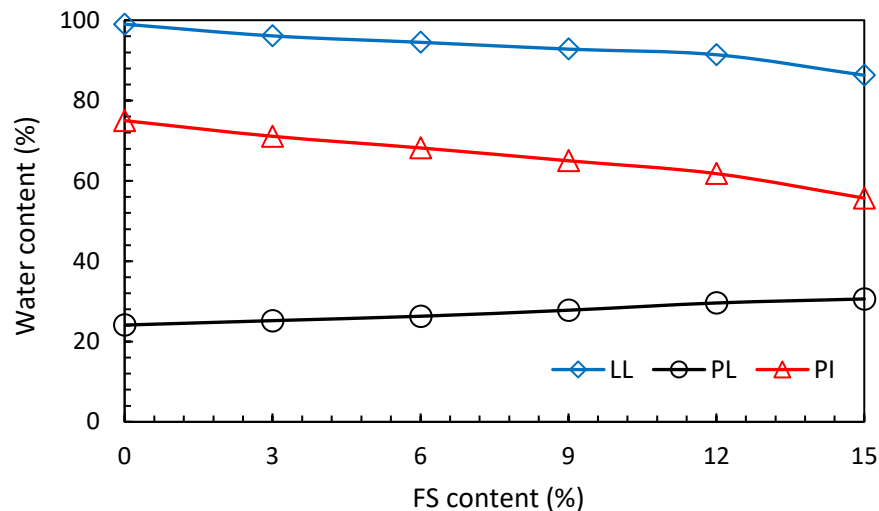


**Figure 3.** Plastic limit, liquid limit, and plasticity index of stabilized soil specimens

The addition of filter sludge (FS) to the high plasticity clay (CH) soil leads to a decrease in the liquid limits of the stabilized specimens. This is a notable observation because of the cation exchange mechanism, flocculation, and agglomeration that occur when the waste material is mixed with the CH specimens. Since Filter sludge, being a calcareous material with 51.4% CaO, plays a significant role in triggering both the flocculation and agglomeration processes. As a result of these processes, the workability of the soil specimens improves, and they reach a liquid-like consistency with less water. Consequently, the liquid limit of the stabilized soil specimens decreases as the ratio of filter sludge additive increases.

According to these results, the increase of the addition percentage of FS result in rise of the plastic limit of stabilized soil specimens. Since the water requirements of the stabilized soil specimens increase with the addition amount of FS into CH. The reason is that ss FS is a calcareous material, it has a higher water demand when mixed with the CH soil. Therefore, as the stabilized soil specimen reach a plastic consistency with more water, the plastic limit increases as the additive ratio increases.

The plasticity index is the difference between the liquid limit and the plastic limit and shows the plasticity of the soil. As the additive ratio increases, the plasticity properties of stabilized soil specimens decrease. This indicates that the relationship between the stabilized soil specimens and water weakens with the addition of FS.

The change in the plasticity index directly affects the engineering parameters of the stabilized soil specimens such as strength and swelling. The decrease in the plasticity index both generally causes an increase in strength parameters and result in the reduction of the swelling potential of clays. Therefore, the changes in the strength parameters of the stabilized soil specimens with FS were monitored by unconfined compressive strength and CBR tests. In addition to these experiments, free swelling test was performed to observe the changes in swelling potential.

### 3.1.2 Compaction characteristics of stabilized soil specimens

The alteration of both maximum dry density (MDD) and optimum water content (OWC) of stabilized soil specimens were observed by performing standard proctor test (Figure 4).

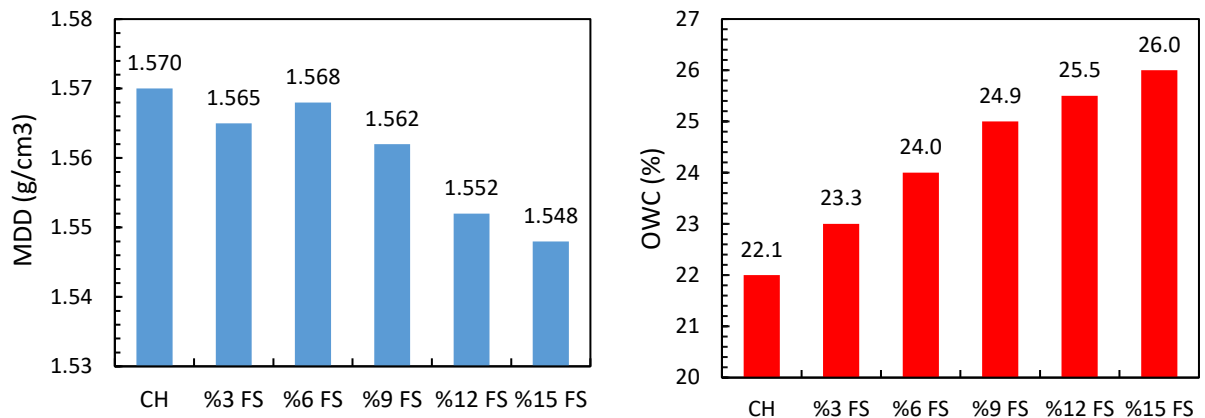


Figure 4. The values of a) MDD and b) OWC of stabilized soil specimens with FS

According to the results of standard proctor tests, the values of MDD of stabilized soil specimens decrease from 1.570 g/cm<sup>3</sup> to 1.548 g/cm<sup>3</sup> with the amount of FS increases. This is because the specific density of the FS material is lower than that of the CH specimen. As the amount of additive increases, the optimum water content values of the mixtures increase from 22.1% to 26%. The reason for this is that due to the small grain structure of FS, the water requirements of the stabilized soil specimens increase.

### 3.2. Engineering Properties

Engineering properties of stabilized soil specimens prepared in this study are divided into two subtitles that are swelling potential and strength parameters of stabilized soil specimens.

#### 3.2.1 Swelling potentials of stabilized soil specimens

Swelling potentials of stabilized soil specimens were determined under 1 kPa surcharge pressure. The results obtained from these tests are given in Figure 5. As the addition ratio of FS increases, the swelling potential of stabilized soil specimens gradually decrease. Additionally, the curing time also influences the swelling potentials, as they decrease with an increase in curing duration.

The lowest swelling potential (%20) was obtained by specimen with %15 FS waited in 56 days curing. It was determined that the swelling potential of this specimen was reduced by more than % 50.

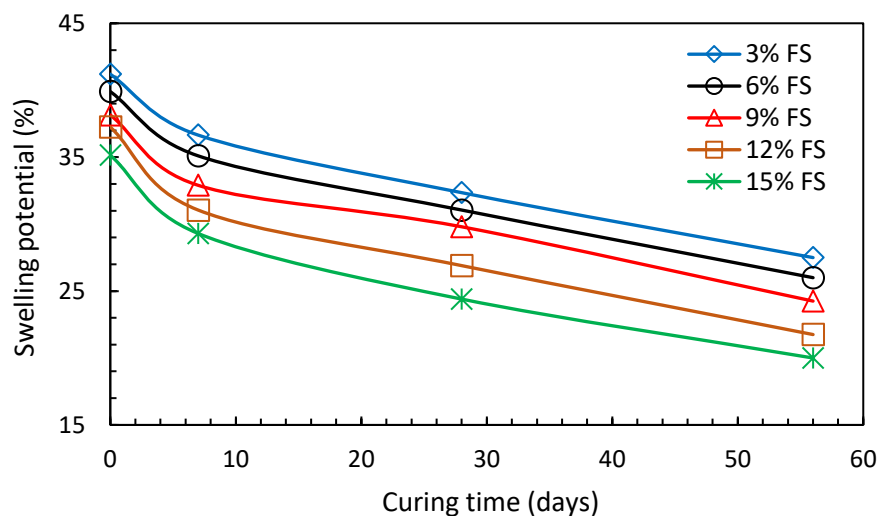


Figure 5. Swelling potentials of stabilized soil specimens with FS

3.2.2 Strength parameters of stabilized soil specimens

Firstly, the unconfined compressive strength tests were done to determine the alteration of strength parameter of stabilized soil specimens. This test was chosen as a reference test for the California Bearing Ratio (CBR) test due to its quicker and simpler nature. The unconfined compressive strength test provides valuable insights into the strength behavior of the stabilized soil. The results of unconfined compression test are presented in Figure 6.

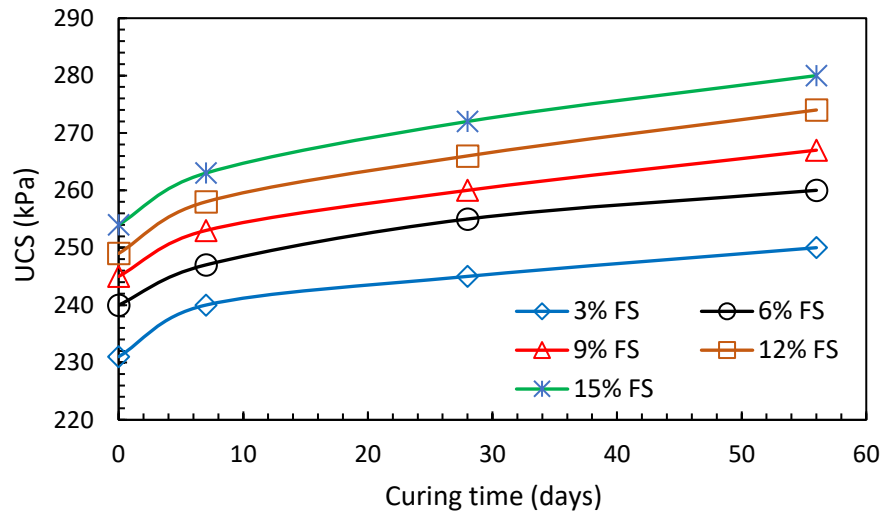


Figure 6. Unconfined compressive strengths of stabilized soil specimens with FS

The unconfined compressive strength (UCS) of CH was measured 210 kPa. This parameter of all stabilized soil specimens increased with both addition ratio of FS and curing period. For instance, this parameter of stabilized soil specimen included %15 FS was increased from 250 kPa to 280 kPa for 56 days curing period. This result can mean that there is an interaction between FC and CH. This condition will be investigated by SEM analysis.

According to both free swell tests and unconfined compression test, the best parameters of this study were obtained from stabilized soil specimen with %15 FS in 56 days curing period. For this reason, both CBR test and SEM analysis were only performed on this stabilized soil specimens.

High plasticity clay swells when it is submerged in water. Then, the strength of this soil decreases. For this reason, CH specimen was separately tested by following procedures of both dry and wet CBR tests to determine the difference of CBR values. The outputs obtained from these tests are given in Table 4.

Table 4. Dry and wet CBR tests results on CH

Test	CBR swell (%)	CBR (%)
Dry CBR	-	17.5
Wet CBR	%38.3	1.1

CH specimen swells when it is submerged in water. While the strength of CH specimen is sufficient at the dry condition, the strength of this specimen at wet condition is very poor and insufficient.

Graphs of both load-displacement and CBR swelling drawn at wet CBR tests conducted within the scope of the study are given in Figure 7.

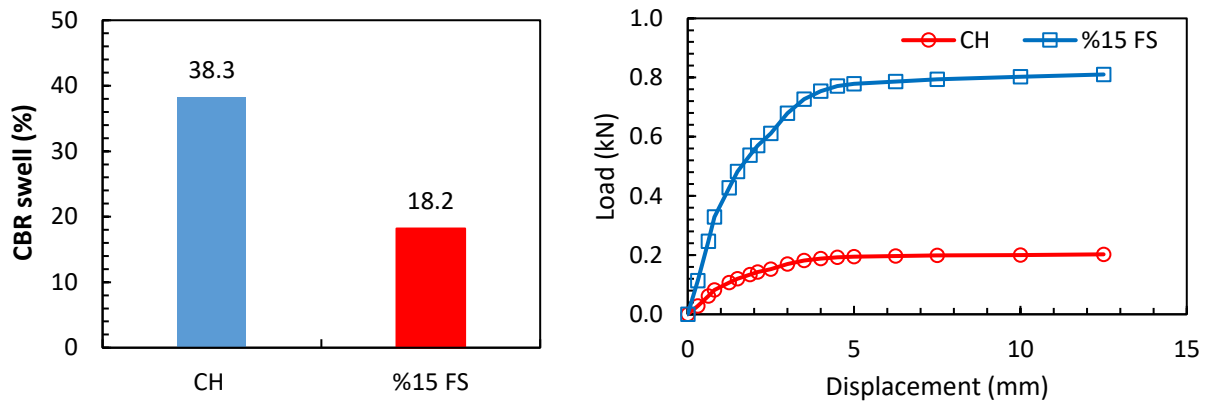


Figure 7. Wet CBR test results: a) swell ratio and b) load-displacement curves

As a result of the experiment, it was found that the CBR swelling value of the stabilized soil specimen with 15% filter sludge (FS) and 56 days of curing was 18.2%, while the CBR value was 4.375%. Comparatively, the CBR swelling value of the high plasticity clay (CH) specimen decreased by more than 50%, and the CBR value of CH increased by approximately four times after the addition of filter sludge.

The addition of filter sludge to CH specimen provided firstly the reduction of swelling potential and then the increase of the strength of this soil. This condition will be analyzed by SEM images.

### 3.3 Mineralogical properties of stabilized soil specimens

The microstructure of the CH clay was determined by SEM images of the unimproved soil. Kaolin type clay minerals are visible in the image magnified 10000 times (Figure 8a). The shapes of CH crystals are thin plate-like particles. When the image is approached 50000 times, the presence of montmorillonite type clay minerals has been detected in some regions (Figure 8b). The montmorillonite type clays in the soil impart high plasticity to the soil. The results obtained from the SEM images support the consistency limit results.

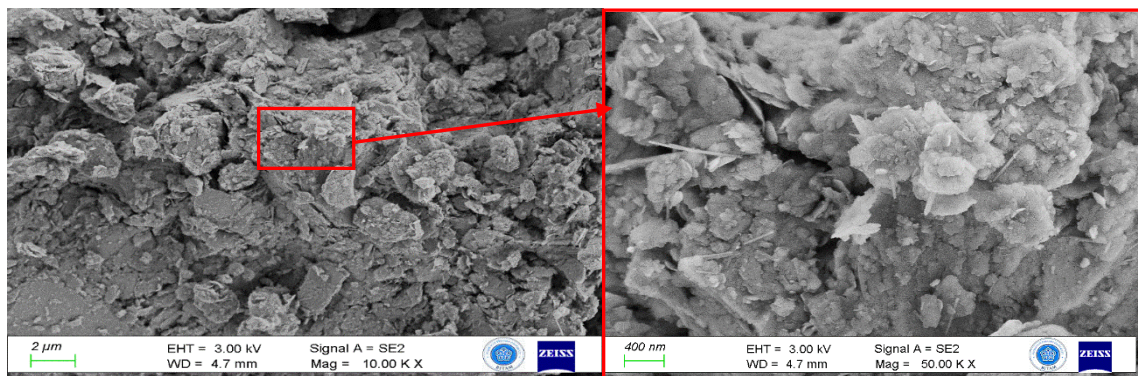
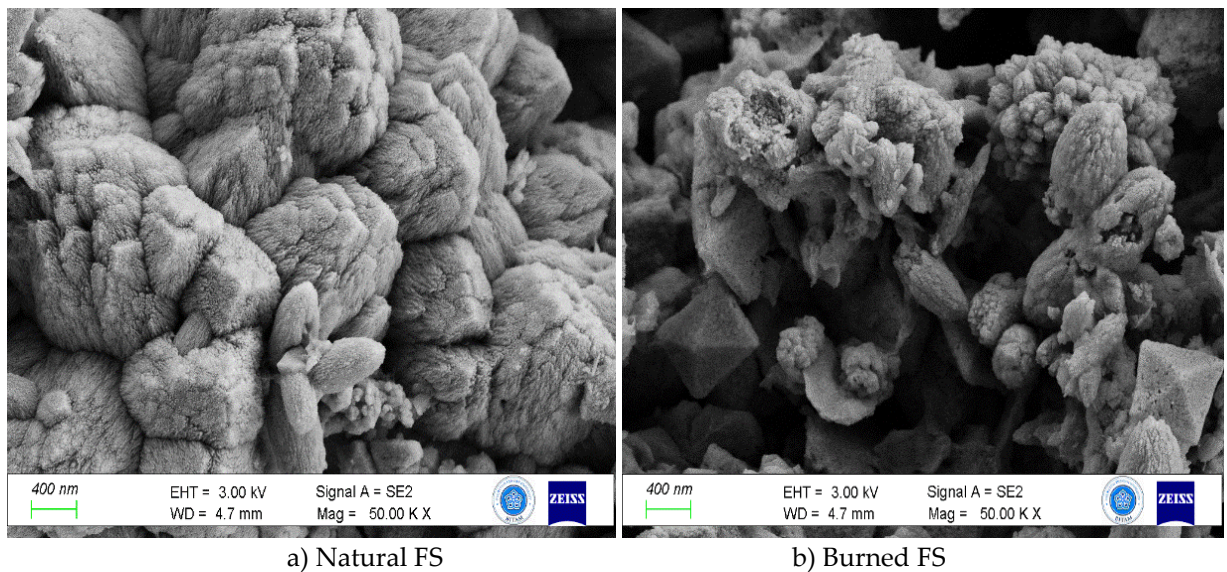


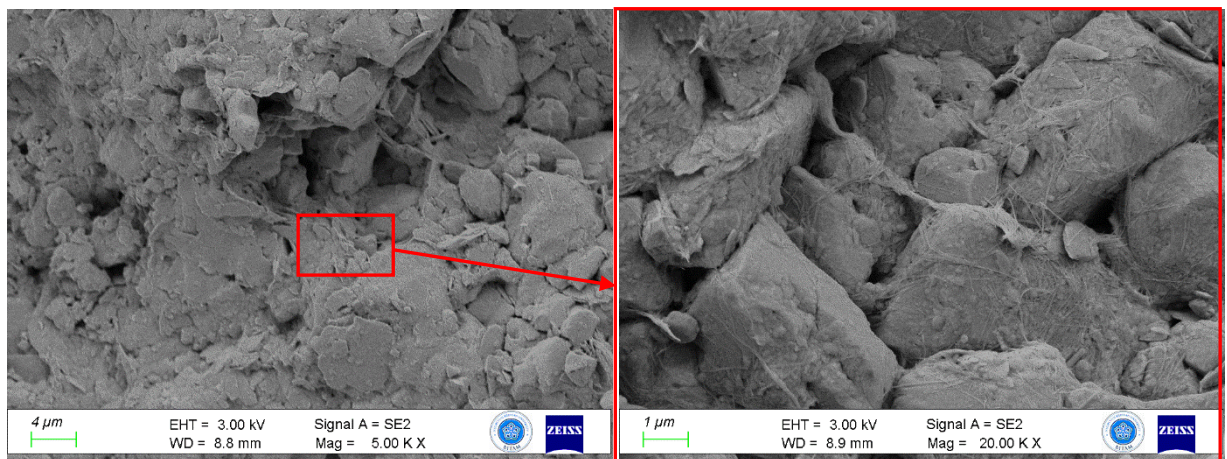
Figure 8. SEM image of CH: magnification factor is 10000 (left) and 50000 (right)

Figure 9 shows the SEM images of natural and burned filter sludge. Since the filter sludge contains organic matter, a fibrous and amorphous structure appears in the SEM image of natural filter sludge (Figure 9a). Figure 9b illustrates that the fibrous structure reduces by burning process of filter sludge. When organic materials are burned, it is seen that pyramidal structures appear in the FS microstructure, the amorphous structure changes somewhat and the spacing between minerals increases (shrinkage effect).



**Figure 9.** SEM image of filter sludge (magnification factor=50000)

Amongst the stabilized soil samples, the mixture has the best performance (maximum strength, minimum swelling and plasticity properties) is the CH sample amended with 15% FS and cured 56 days. The SEM image of the stabilized specimen is given in Figure 10. Clay minerals appear to be covered with FS in 5000 times magnified SEM images (Figure 10a). However, in SEM images taken at 20000 times magnification, it was observed that there was interaction between the CH-FS particles, the grains were bonded to each other and the grain size increased, as a result, there was agglomeration, and there were filamentous structures on the newly formed large grains (Figure 10b).



**Figure 10.** SEM image of the stabilized specimen with filter sludge for 56 days curing period

#### 4. CONCLUSIONS

In the present study, high plasticity clay soil was stabilized by using filter sludge, a waste product of sugar industry. Meanwhile, geotechnical properties of stabilized soil were investigated. The findings and evaluations obtained within the scope of this study are summarized in below.

1. Since the filter sludge material contains organic matter, it is not suitable for use in soil improvement in natural form. Because organic materials rot in the soil over time, and the specimen becomes moldy. This situation reduces the strength parameters of the soil. Therefore, before using the filter sludge, the organic substances in it were removed by burning at 450°C.

2. With the addition of filter sludge to the high plasticity clay specimens, the plasticity properties of these soils decreased.
3. Addition of FS to the high plasticity clay specimens; while decreasing the maximum dry density, it increased the optimum water content.
4. The unconfined compressive strength of the specimens improved with both the addition of filter sludge and increased curing time (0-56 days).
5. As a result of wet CBR test, belonging to high plasticity clay specimens; while the CBR swelling value was high, the CBR value was very low. Wet CBR test was carried out on the specimens with 15% filter sludge. As a result of this experiment; while the CBR swelling value decreased by 52.5%, the CBR value increased approximately 4 times.
6. The swelling potential values obtained from the free swell test indicated that the filter sludge additive ratio and curing time positively affected the improvement of the stabilized soil.
7. According to the SEM analysis, filamentous binders between the thin plate particles of CH specimen formed with FS stabilization process of high plasticity clay.

### Declaration of Ethical Standards

The authors declare that they comply with all ethical standards.

### Credit Authorship Contribution Statement

**Author 1:** Resources, Investigation, Experimentation, Writing – original draft **Author 2:** Resources, Investigation, Experimentation, Formal analysis, Validation, Methodology, Visualization, Writing – original draft

### Declaration of Competing Interest

The authors have no competing interests to declare that are relevant to the content of this article.

### Funding / Acknowledgements

This research is supported by the Necmettin Erbakan University Scientific Research Projects Coordinatorship (Grant No: 221219003)

### Data Availability

All data generated or analyzed during this study are included in this published article.

### REFERENCES

- [1] G. T. Hong, *Earth pressures and deformations in civil infrastructure in expansive soils*. Texas A&M University, 2008.
- [2] J. D. Nelson, K. C. G. Chao, D. D. Overton, and E. J. Nelson, *Foundation Engineering for Expansive Soils*. Hoboken, NJ, USA: John Wiley & Sons, Inc, 2015. doi: 10.1002/9781118996096.
- [3] E. Çokça, "Use of Class C Fly Ashes for the Stabilization of an Expansive Soil," *Journal of Geotechnical and Geoenvironmental Engineering*, vol. 127, no. 7, pp. 568–573, Jul. 2001, doi: 10.1061/(ASCE)1090-0241(2001)127:7(568).
- [4] HTS, "Highway technical specification," General Directorate of Highways, Ankara, Turkey., 2013.
- [5] Highways Agency, *Manual of Contract Documents for Highway Works: A User's Guide and Commentary: 1993/94 Amendments*. Thomas Telford Ltd, 2009. doi: 10.1680/m9394a.20887.
- [6] P. Ghadir, M. Zamanian, N. Mahbubi-Motlagh, M. Saberian, J. Li, and N. Ranjbar, "Shear strength and life cycle assessment of volcanic ash-based geopolymer and cement stabilized soil: A

- comparative study," *Transportation Geotechnics*, vol. 31, p. 100639, Nov. 2021, doi: 10.1016/j.trgeo.2021.100639.
- [7] M. Olgun, "Effects of polypropylene fiber inclusion on the strength and volume change characteristics of cement-fly ash stabilized clay soil," *Geosynth Int*, vol. 20, no. 4, pp. 263–275, Aug. 2013, doi: 10.1680/gein.13.00016.
- [8] M. Bekhiti, H. Trouzine, and M. Rabehi, "Influence of waste tire rubber fibers on swelling behavior, unconfined compressive strength and ductility of cement stabilized bentonite clay soil," *Constr Build Mater*, vol. 208, pp. 304–313, May 2019, doi: 10.1016/j.conbuildmat.2019.03.011.
- [9] S. GhavamShirazi and H. Bilsel, "Characterization of volume change and strength behavior of micro-silica and lime-stabilized Cyprus clay," *Acta Geotech*, vol. 16, no. 3, pp. 827–840, Mar. 2021, doi: 10.1007/s11440-020-01060-1.
- [10] X. Bian, L. Zeng, X. Li, X. Shi, S. Zhou, and F. Li, "Fabric changes induced by super-absorbent polymer on cement–lime stabilized excavated clayey soil," *Journal of Rock Mechanics and Geotechnical Engineering*, Apr. 2021, doi: 10.1016/j.jrmge.2021.03.006.
- [11] M. Koohmishi and M. Palassi, "Mechanical Properties of Clayey Soil Reinforced with PET Considering the Influence of Lime-Stabilization," *Transportation Geotechnics*, vol. 33, p. 100726, Mar. 2022, doi: 10.1016/j.trgeo.2022.100726.
- [12] S. R. Abdila *et al.*, "Potential of Soil Stabilization Using Ground Granulated Blast Furnace Slag (GGBFS) and Fly Ash via Geopolymerization Method: A Review," *Materials*, vol. 15, no. 1, p. 375, Jan. 2022, doi: 10.3390/ma15010375.
- [13] A. L. Murmu, A. Jain, and A. Patel, "Mechanical Properties of Alkali Activated Fly Ash Geopolymer Stabilized Expansive Clay," *KSCE Journal of Civil Engineering*, vol. 23, no. 9, pp. 3875–3888, Sep. 2019, doi: 10.1007/s12205-019-2251-z.
- [14] E. Coudert, M. Paris, D. Deneele, G. Russo, and A. Tarantino, "Use of alkali activated high-calcium fly ash binder for kaolin clay soil stabilisation: Physicochemical evolution," *Constr Build Mater*, vol. 201, pp. 539–552, Mar. 2019, doi: 10.1016/j.conbuildmat.2018.12.188.
- [15] H. A. M. Abdelkader, M. M. A. Hussein, and H. Ye, "Influence of Waste Marble Dust on the Improvement of Expansive Clay Soils," *Advances in Civil Engineering*, vol. 2021, pp. 1–13, Sep. 2021, doi: 10.1155/2021/3192122.
- [16] A. K. Jain, A. K. Jha, and Shivanshi, "Geotechnical behaviour and micro-analyses of expansive soil amended with marble dust," *Soils and Foundations*, vol. 60, no. 4, pp. 737–751, Aug. 2020, doi: 10.1016/j.sandf.2020.02.013.
- [17] O. Sivrikaya, F. Uysal, A. Yorulmaz, and K. Aydin, "The Efficiency of Waste Marble Powder in the Stabilization of Fine-Grained Soils in Terms of Volume Changes," *Arab J Sci Eng*, vol. 45, no. 10, pp. 8561–8576, Oct. 2020, doi: 10.1007/s13369-020-04768-0.
- [18] B. R. Phanikumar, J. R. m, and R. R. e, "Silica fume stabilization of an expansive clay subgrade and the effect of silica fume-stabilised soil cushion on its CBR," *Geomechanics and Geoengineering*, vol. 15, no. 1, pp. 64–77, Jan. 2020, doi: 10.1080/17486025.2019.1620348.
- [19] A. Saygili and M. Dayan, "Freeze-thaw behavior of lime stabilized clay reinforced with silica fume and synthetic fibers," *Cold Reg Sci Technol*, vol. 161, pp. 107–114, May 2019, doi: 10.1016/j.coldregions.2019.03.010.
- [20] S. Ghavami, H. Naseri, H. Jahanbakhsh, and F. Moghadas Nejad, "The impacts of nano-SiO<sub>2</sub> and silica fume on cement kiln dust treated soil as a sustainable cement-free stabilizer," *Constr Build Mater*, vol. 285, p. 122918, May 2021, doi: 10.1016/j.conbuildmat.2021.122918.
- [21] L. Lang, B. Chen, and B. Chen, "Strength evolutions of varying water content-dredged sludge stabilized with alkali-activated ground granulated blast-furnace slag," *Constr Build Mater*, vol. 275, p. 122111, Mar. 2021, doi: 10.1016/j.conbuildmat.2020.122111.
- [22] J. He, X. Shi, Z. Li, L. Zhang, X. Feng, and L. Zhou, "Strength properties of dredged soil at high water content treated with soda residue, carbide slag, and ground granulated blast furnace slag," *Constr Build Mater*, vol. 242, p. 118126, May 2020, doi: 10.1016/j.conbuildmat.2020.118126.

- [23] M. Parsaei, A. H. Vakili, M. Salimi, M. S. Farhadi, and A. Falamaki, "Effect of electric arc and ladle furnace slags on the strength and swelling behavior of cement-stabilized expansive clay," *Bulletin of Engineering Geology and the Environment*, vol. 80, no. 8, pp. 6303–6320, Aug. 2021, doi: 10.1007/s10064-021-02316-0.
- [24] G. Özyazici, O. Özdemir, S. Pinar Özer, and Z. Kalcioğlu, "The Effect of Sugar Industry Waste Slime Used as Liming Material on Yield, Quality and Soil Properties of Tea Plant (in Turkish)," *Turk Tarim Arast Derg*, vol. 1, pp. 43–54, 2014.
- [25] Ö. Bedir and T. H. Doğan, "Use of sugar industry waste catalyst for biodiesel production," *Fuel*, vol. 286, p. 119476, Feb. 2021, doi: 10.1016/j.fuel.2020.119476.
- [26] N. Özen and E. Arat, "Possibilities of Using Rotating Pit of Sugar Factory Waste as a Source of Calcium in Quail Diets (in Turkish)," *J. of Veterinary and Animal Sciences*, vol. 23, pp. 35–40, 1999.
- [27] ASTM D2974-20e1, *Standard Test Methods for Determining the Water (Moisture) Content, Ash Content, and Organic Material of Peat and Other Organic Soils*. ASTM International, West Conshohocken, PA, 2020.
- [28] B. G. Gidday and S. Mittal, "Improving the characteristics of dispersive subgrade soils using lime," *Heliyon*, vol. 6, no. 2, p. e03384, Feb. 2020, doi: 10.1016/j.heliyon.2020.e03384.
- [29] ASTM D4318, "Standard test methods for liquid limit, plastic limit, and plasticity index of soils," in *Book of Standards Volume: 04.08*, ASTM International, West Conshohocken, PA, 2017. doi: 10.1520/D4318-17.
- [30] ASTM D698-12, "Standard Test Methods for Laboratory Compaction Characteristics of Soil Using Standard Effort (12,400 ft-lbf/ft<sup>3</sup> (600 kN-m/m<sup>3</sup>)),", ASTM International, West Conshohocken, PA, 2021. doi: 10.1520/D0698-12E01.
- [31] ASTM D4546-21, "Standard Test Methods for One-Dimensional Swell or Collapse of Soils," ASTM International, West Conshohocken, PA., 2021. doi: 10.1520/D4546-14.
- [32] ASTM D1883-16, "Standard test method for California Bearing Ratio (CBR) of laboratory-compacted soils," in *Book of Standards Volume: 04.08*, ASTM International, West Conshohocken, PA: ASTM International, West Conshohocken, PA, 2016. doi: 10.1520/D1883-16.



## MINIMIZING ERRORS IN PCB MILLING PROCESSES THROUGH A 3-AXIS PCB ROUTER

<sup>1,\*</sup>Emrehan YAVSAN , <sup>2</sup>Burak SELVI , <sup>3</sup>Tarik UNLER , <sup>4</sup>Ilhan ILHAN 

<sup>1</sup> Tekirdağ Namık Kemal University, Electronics and Automation Department, Tekirdağ, TÜRKİYE

<sup>2,4</sup> Necmettin Erbakan University, Engineering Faculty, Mechatronics Department, Konya, TÜRKİYE

<sup>3</sup> Necmettin Erbakan University, Aeronautics and Astronautics Faculty, Avionics Department, Konya, TÜRKİYE

<sup>1</sup>[eyavsan@nku.edu.tr](mailto:eyavsan@nku.edu.tr), <sup>2</sup>[buraksselvi@gmail.com](mailto:buraksselvi@gmail.com), <sup>3</sup>[tunler@erbakan.edu.tr](mailto:tunler@erbakan.edu.tr), <sup>4</sup>[ilhan@erbakan.edu.tr](mailto:ilhan@erbakan.edu.tr)

### Highlights

- Homogeneous milling achieved with multi-point referencing
- Precise and stable PCB milling with Z-axis homogeneity
- Low dimensions and metal body to reduce vibrations
- Mechanical CNC method for prototyping without environmental harm



## MINIMIZING ERRORS IN PCB MILLING PROCESSES THROUGH A 3-AXIS PCB ROUTER

<sup>1,\*</sup>Emrehan YAVSAN , <sup>2</sup>Burak SELVI , <sup>3</sup>Tarik UNLER , <sup>4</sup>Ilhan ILHAN 

<sup>1</sup> Tekirdağ Namık Kemal University, Electronics and Automation Department, Tekirdağ, TÜRKİYE

<sup>2,4</sup> Necmettin Erbakan University, Engineering Faculty, Mechatronics Department, Konya, TÜRKİYE

<sup>3</sup> Necmettin Erbakan University, Aeronautics and Astronautics Faculty, Avionics Department, Konya, TÜRKİYE

<sup>1</sup>eyavsan@nku.edu.tr, <sup>2</sup>buraksselvi@gmail.com, <sup>3</sup>tunler@erbakan.edu.tr, <sup>4</sup>ilhan@erbakan.edu.tr

(Received: 04.04.2023; Accepted in Revised Form: 15.08.2023)

**ABSTRACT:** Printed circuit boards (PCBs) can be produced by chemical or mechanical methods. Continuous copper paths are difficult to print in the chemical method and breaks may occur in copper paths. In addition, this method is harmful to human health and the environment, as various chemicals are used. In the mechanical method, PCB is processed with computer-controlled numerical workbenches (CNC). Although prototyping can be done quickly and without harming the environment with these benches, the desired results may not be obtained. Reasons for unsuccessful machining in CNC machines; manufacturing and assembly errors in the production of benches, the use of low quality mechanical and electronic components, and the reference of a single point especially for the Z-axis of the part connected to the benches. In this paper, a precise and stable PCB Router is presented to make fast, cost-effective and successful PCB machining. In order to minimize the vibration and oscillations of the PCB Router caused by manufacturing and assembly errors, the dimensions of the router were kept low and metal material was preferred for the router body. Precision is ensured by quality motor drivers and stepper motors. The PCB Router is controlled by an original control board. This card is equipped with a multi-point referencing feature for the Z-axis. Thus, homogeneous machining in the Z-axis for the entire surface of the PCB can be realized by performing referencing operations on the PCB connected to the workbench as many points as the user enters. With the developed router, PCBs with rectangular and circular patterns were engraved at cutting depths of 0.030 mm and 0.050 mm with 0.20 mm and 0.30 mm diameter milling tools with a 30-degree tip angle, respectively. Moreover, a 16-terminal integrated circuit element was successfully engraved at a cutting depth of 0.040 mm with a 0.34 mm diameter V-tip with a 30-degree tip angle. Homogeneous milling was achieved utilizing the proposed multi-point referencing feature. Each milling operation was completed in approximately 30 min - 45 min.

**Keywords:** Printed circuit board, Computer-aided design, Computer-aided manufacturing, CNC, 3-Axis Milling

### 1. INTRODUCTION

There are various methods for the production of printed circuit boards (PCB) [1]. These methods can be grouped under two headings. The first method; It is based on etching the copper with various chemicals, and the second method is based on engraving the copper with Computer Aided Numerical Control (CNC) benches [2]. It is difficult to print continuous copper paths with the first method [3]. Besides, as the various chemicals are used, they have negative effects on human health and the environment. In the second method, production is made with PCB CNC Router devices without harming nature and humans [4], [5]. Rapid prototyping can be done with these benches, also called PCB Routers. PCB Router machines work on a 3-axis (XYZ) [6], [7]. In these benches, besides the drive motors that provide movement in 3 axes, there is 1 Spindle motor that enables the engraving of copper from the PCB plate and 1 cutting tip/milling tool connected to this motor. Each motor is driven by a motor driver and these drivers are controlled by a control card [8].

Madekar, K. J. et al. [9] produced a mini CNC machine with a developer board with an ATMEGA 328 controller. In this way, they tried to reduce the cost. However, the output of a processed PCB sheet was not included in their work. In addition, their workbenches are not suitable for PCB processing, as

\*Corresponding Author: Emrehan YAVSAN, [eyavsan@nku.edu.tr](mailto:eyavsan@nku.edu.tr)

they use wooden materials on the chassis or the body of their workbenches like Yildirim et al. [10]. Shilpa et al. [11] also introduced a 3-axis CNC PCB machine with low cost motivation. Although they presented a more rigid body than Madekar, K. J. et al., a processed PCB image was not included in their work. Mahesh Raut et al. [12] presented a prototype-level desktop PCB machining bench. The machine they offer has rudimentary mechanics and is therefore inadequate for machining PCBs. Apart from these studies, Vegard Størkersen [13] carried out a hybrid study by combining mechanical and chemical methods. In his work, he etches/corrodes the PCB with a chemical, not mechanically removing. In none of the studies presented within the scope of the literature review, dynamic zeroing in the Z axis or multi-reference process was not mentioned. However, this feature is very critical for machining PCBs by mechanical method. Otherwise, the cutting tip breaks in Figure 1 and, accordingly, the unsuccessful machining in Figure 5 are obtained.

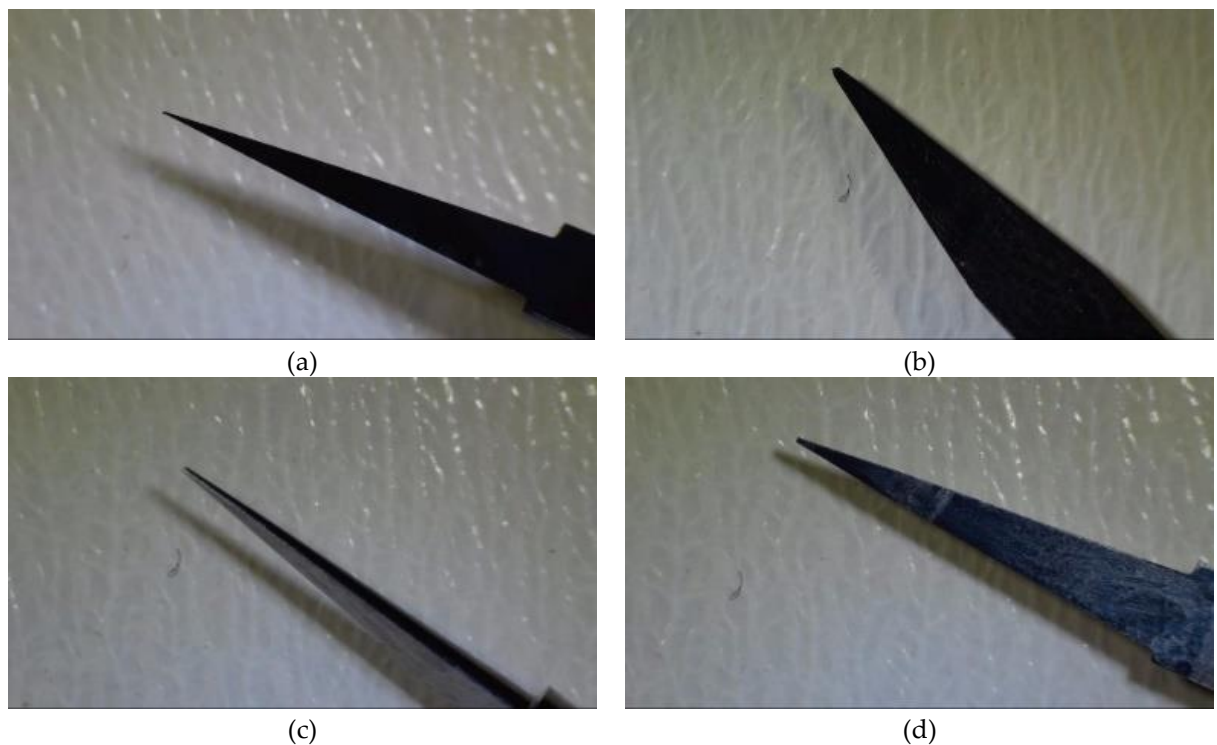


**Figure 1.** The cutting tips used for machining PCBs on a CNC machine without multi-point referencing. (a) V-tip before the milling, (b), (c) and (d) images of the broken V-tips after the milling under the microscope from various angles

Although solutions such as laser processing in Figure 2, using a vacuum table in Figure 3 and increasing the quality of the table surface to which the PCB will be attached in Figure 4 were tried to prevent tip breakage in Figure 1 and unsuccessful PCB processing, positive results could not be obtained.

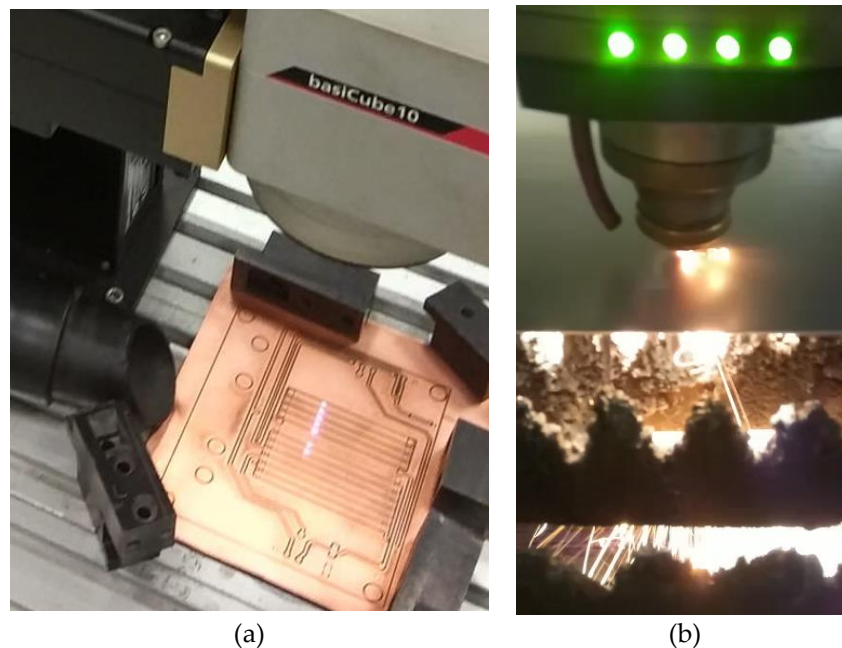


**Figure 2.** Commercial CNC machines used for laser processing of PCBs

The workbench in Figure 2a is a costly solution and has burnt on the PCB. It is difficult to configure the characteristics of the laser for different PCB machining. On the workbench in Figure 2b, there are serious reflections from the PCB surface. This not only hinders the processing of the PCB, but also damages the laser machine.



**Figure 3.** Vacuumed table production

In Figure 3, a vacuum table is machined to prevent swelling of the PCB when the PCB is attached to the table and to connect the PCB plate to the bench more easily. Although the vacuum table pulled the PCB homogeneously, problems were encountered due to the heterogeneous distribution in the Z axis. On top of that, the surface quality improvement solution in Figure 4 was tried, but this solution did not yield any results. Again, there are height differences in the Z axis. These differences pose a problem in removing the thin copper layer (1 oz) from the PCB surface.

Figure 5 shows PCB circuits designed in various geometries. Figure 1a and Figure 1b show the geometries that are tried to be printed by chemical means, and the Figure 5c, Figure 5d and the Figure 5e show the geometries processed on an industrial 3-axis CNC Router [16]. As can be seen from the image, there are breaks in the copper roads in these Figures.

Copper thicknesses on PCB plates can vary between 0.5 – 2 oz (0.035 mm – 0.070 mm) [14], [15]. The homogeneous etching of this copper at every point of the PCB plate is the key to successful engraving.

However, this cannot be achieved in most PCB Routers. In order to achieve homogeneous engraving or successful machining, engravings of the same depth must be made all over the PCB connected to the router table. Otherwise, the cutting tips break, the copper paths of the electronic circuit break or the PCB cannot be engraved to the desired thickness. In addition, most PCB Routers remain idle or at best are used for rough machining such as wood, plastic or metal, out of purpose.

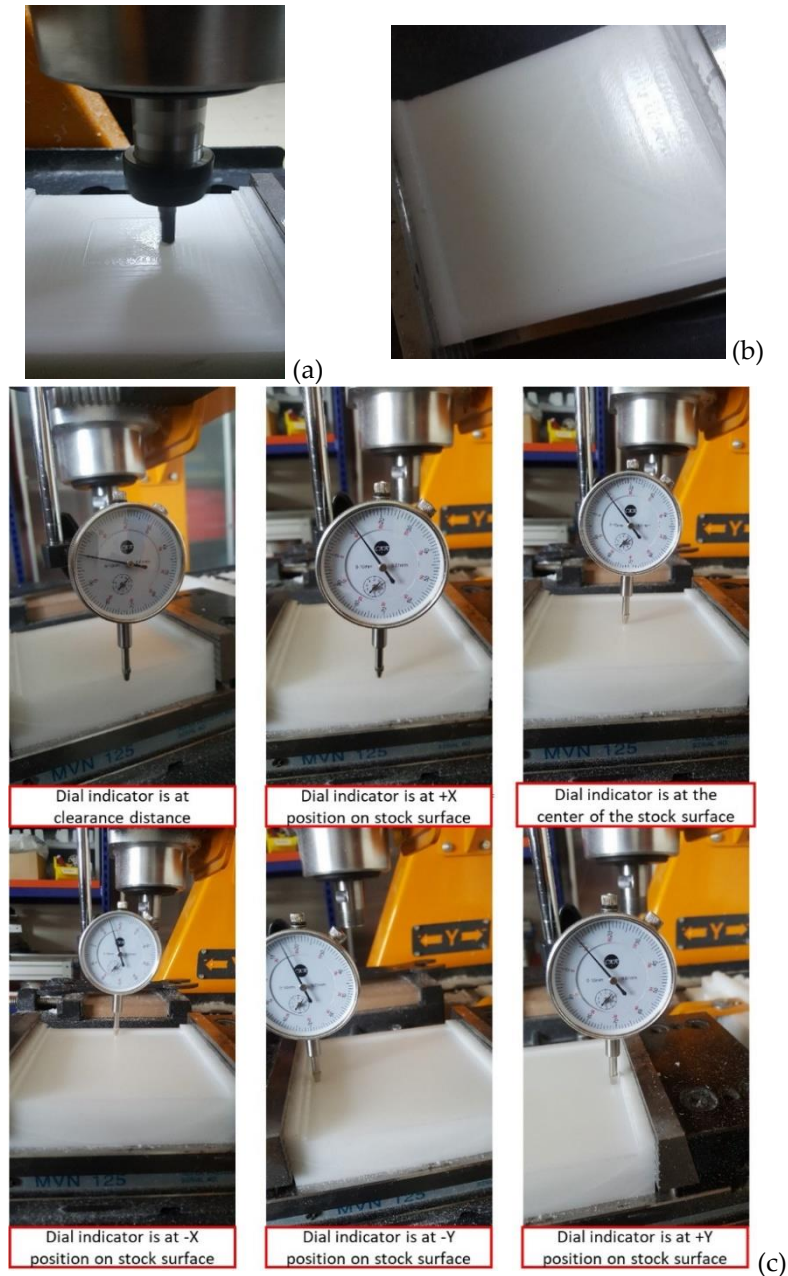


**Figure 4.** Increasing the surface quality and obtaining a homogeneous height on the surface by machining the surface to which the PCB will be attached with an end mill with low depth and low lateral shifts. (a) Table surface machined with a flat end mill, (b) Table surface obtained after machining, and (c) Checking the table surface after machining with a dial indicator

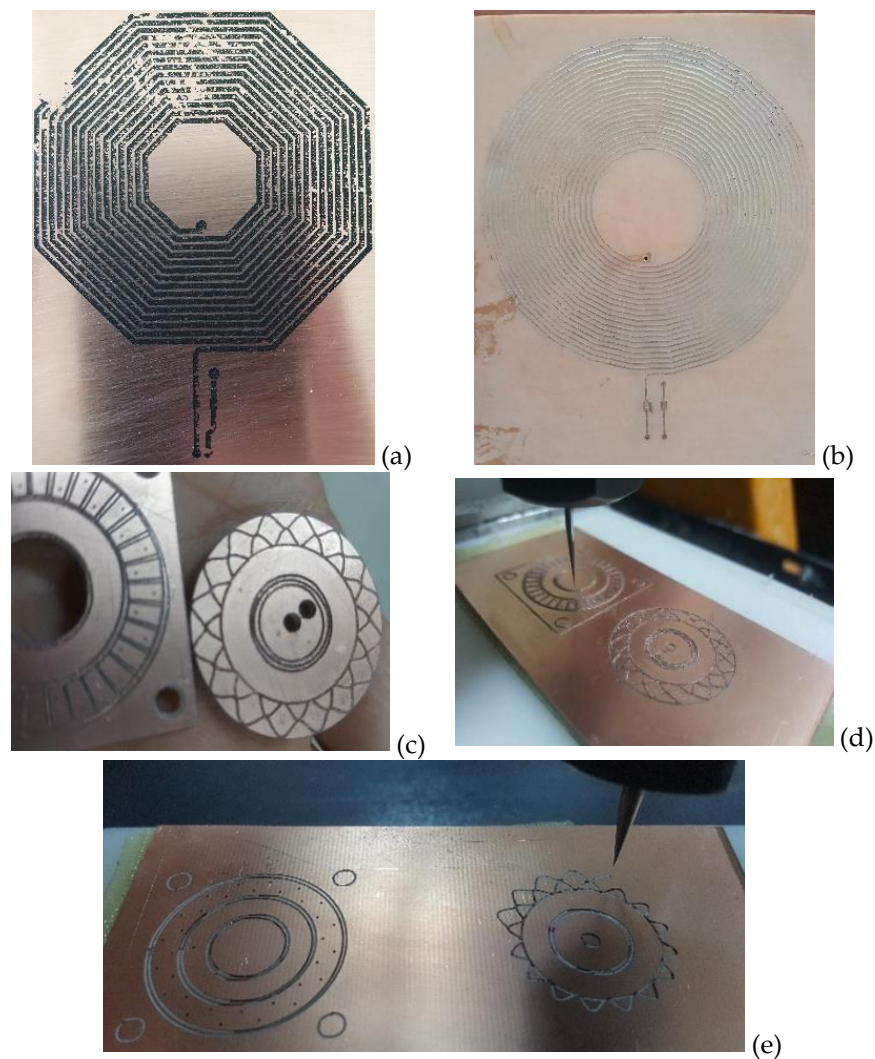


**Figure 5.** The geometries processed on the PCB surface by chemical and machining methods. (a) and (b) geometries printed by chemical methods, (c), (d) and (e) milling with a single point zeroing/referencing with a 3-axis commercial router

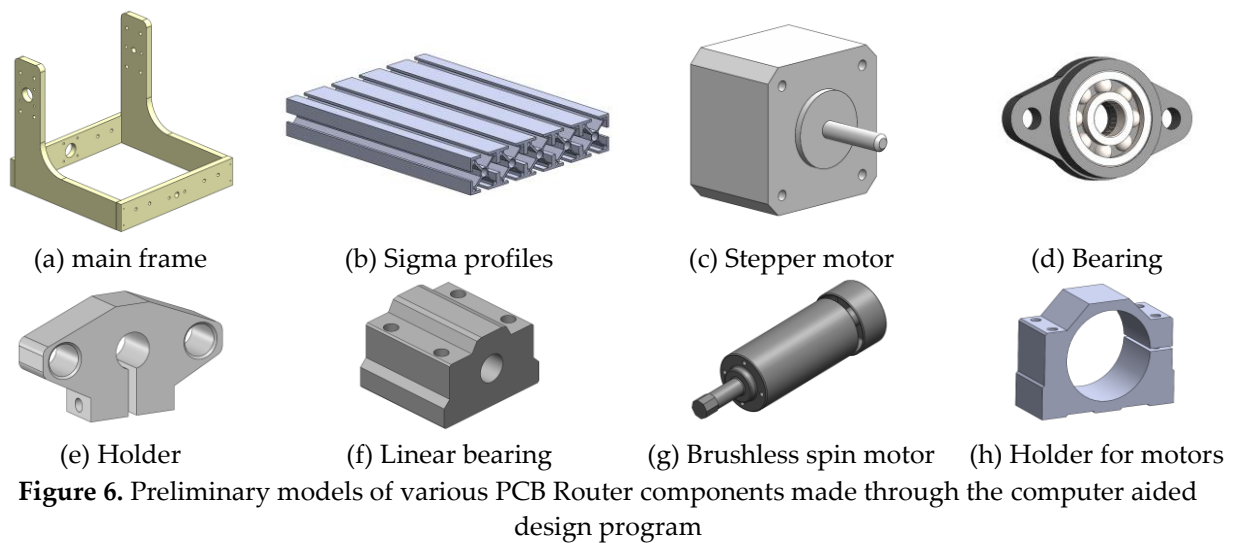
In this research, it is desired to carry out successful PCB processing in order to avoid the unsuccessful engravings in Figure 5. For this, it is aimed to prevent possible imbalances with a small router, to protect the accuracy and sensitivity in these movements with step motors for the axis movements of the router, and to perform successful processing by performing a multi-point zeroing process instead of a single point, unlike most existing PCB Routers.

One of the key points of the study is the multi-point zeroing solution. Because in most routers, the PCB connected to the bench is referencing from a single point. This situation leads to tip breakage due to the insertion of the cutting tip insert too deep at different points of the PCB, as in Figure 5c, Figure 5d and Figure 5e, or Failure processing of copper tracks due to inability to reach the desired depth. In this study, a solution to this problem was sought by zeroing at multiple points before starting the PCB engraving process.

## 2. MATERIAL AND METHODS

### 2.1. Design and Modeling

Computer aided design programs were used to model the PCB Router. In Figure 6, the preliminary model designs for the various components of the machine are given respectively.



Using the components in Figure 6, the PCB Router was assembled in Figure 7 on the computer aided design program.

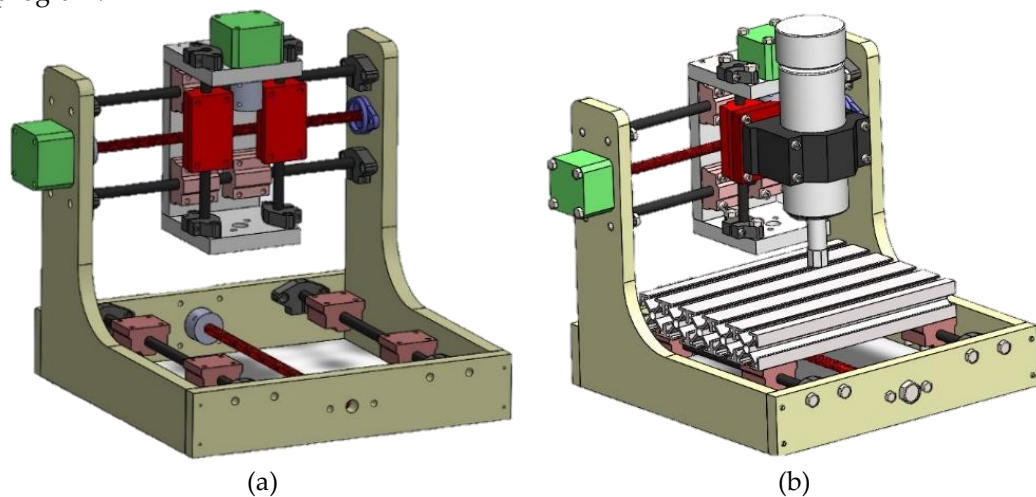


**Figure 7.** PCB Router preliminary design. (a) Preliminary design including body, shafts, holders, bearings and couplings, (b) Preliminary design to which spindle motor and sigma profile table are added.

The model and assembly drawings presented at this stage constitute the first stage of the study. After this first stage, the following parts were modeled and produced for the chassis of the router using the models in Figure 6 and Figure 7.

The assembly image of the parts was created by using the computer aided design program of the designed body models. At this stage, all the fasteners used in the assembly image were taken from the library of the relevant design program. The compatibility of the designed parts with each other was checked at the first stage, and the parts that did not fit into the assembly were modeled with alternative dimensions and replaced with other parts. The router body assembly, in which a virtual environment is created using the parts in Figure 8, is given in Figure 9.

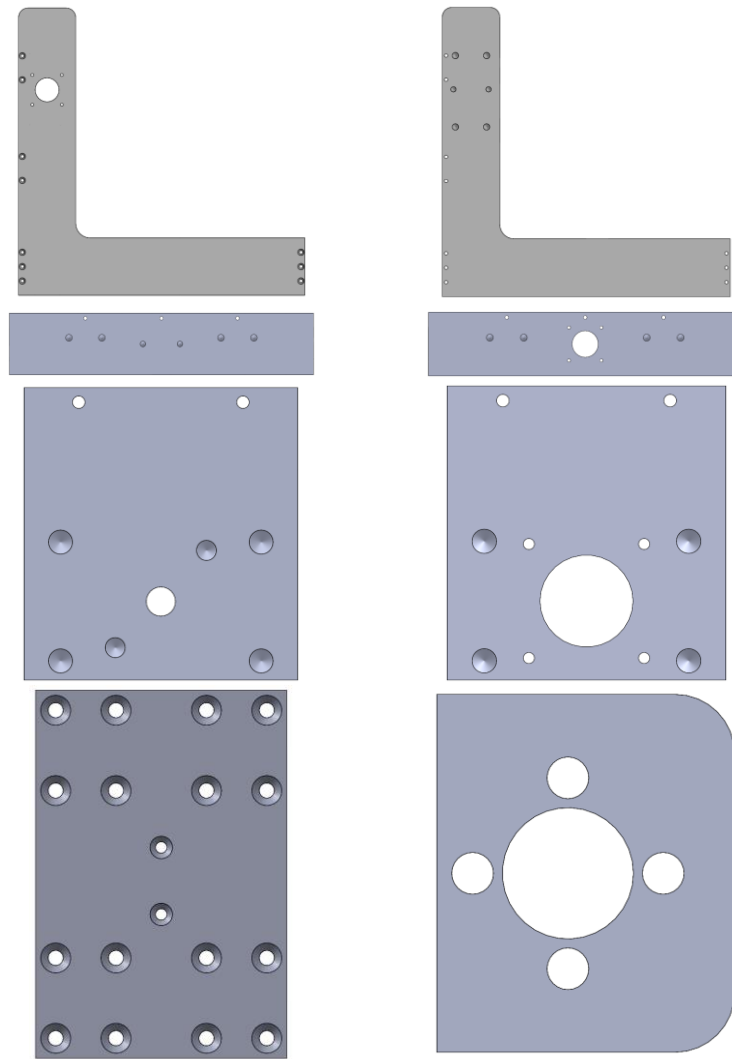


Figure 8. Parts designed for the router frame in the second step

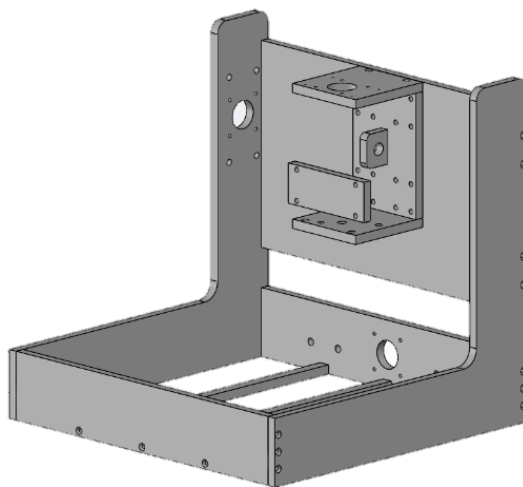
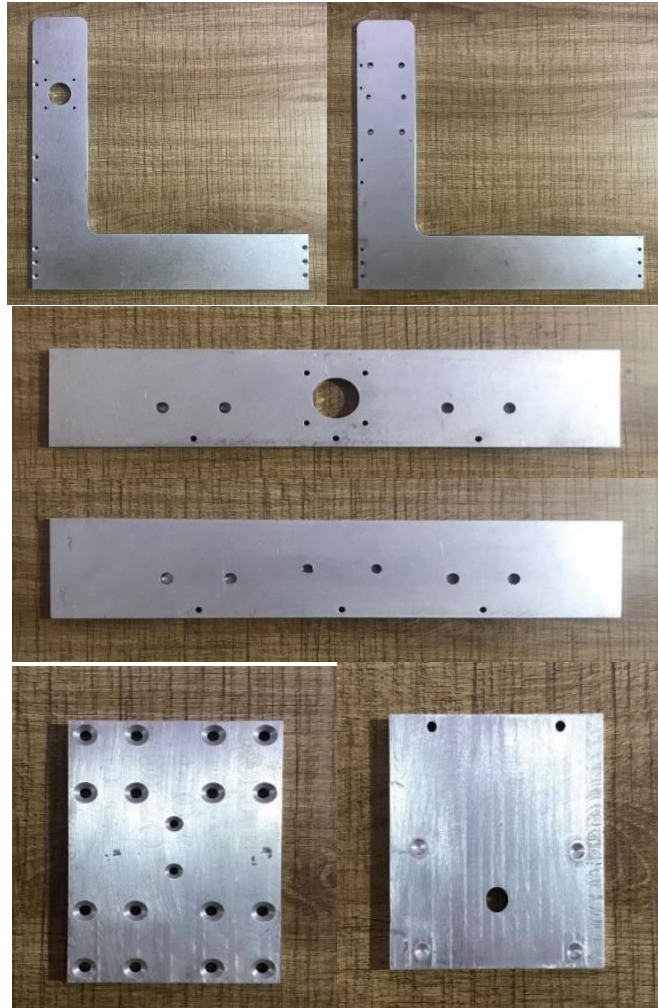


Figure 9. Mounted view of the designed frame parts

## 2.2. Production and Assembly

After the solid modeling of the body parts was completed, the production of these parts was started with various methods. Since there is too much burr on the edges and corners of the parts while aluminum plate is produced by laser cutting method, it has been decided to use machining methods instead of laser cutting method. After the parts were produced with the machining method, the assembly phase was started. The components of the machine body, whose production has been completed and whose mounting holes have been drilled, are given in Figure 10.



**Figure 10.** Parts produced for the router body

With the assembly of the mechanical parts of the PCB Router and the axis motors, the assembly steps in Figure 11 were followed, and the assembly of electronic components in the bench mechanics was started after the bench mechanics in Figure 12 were created.

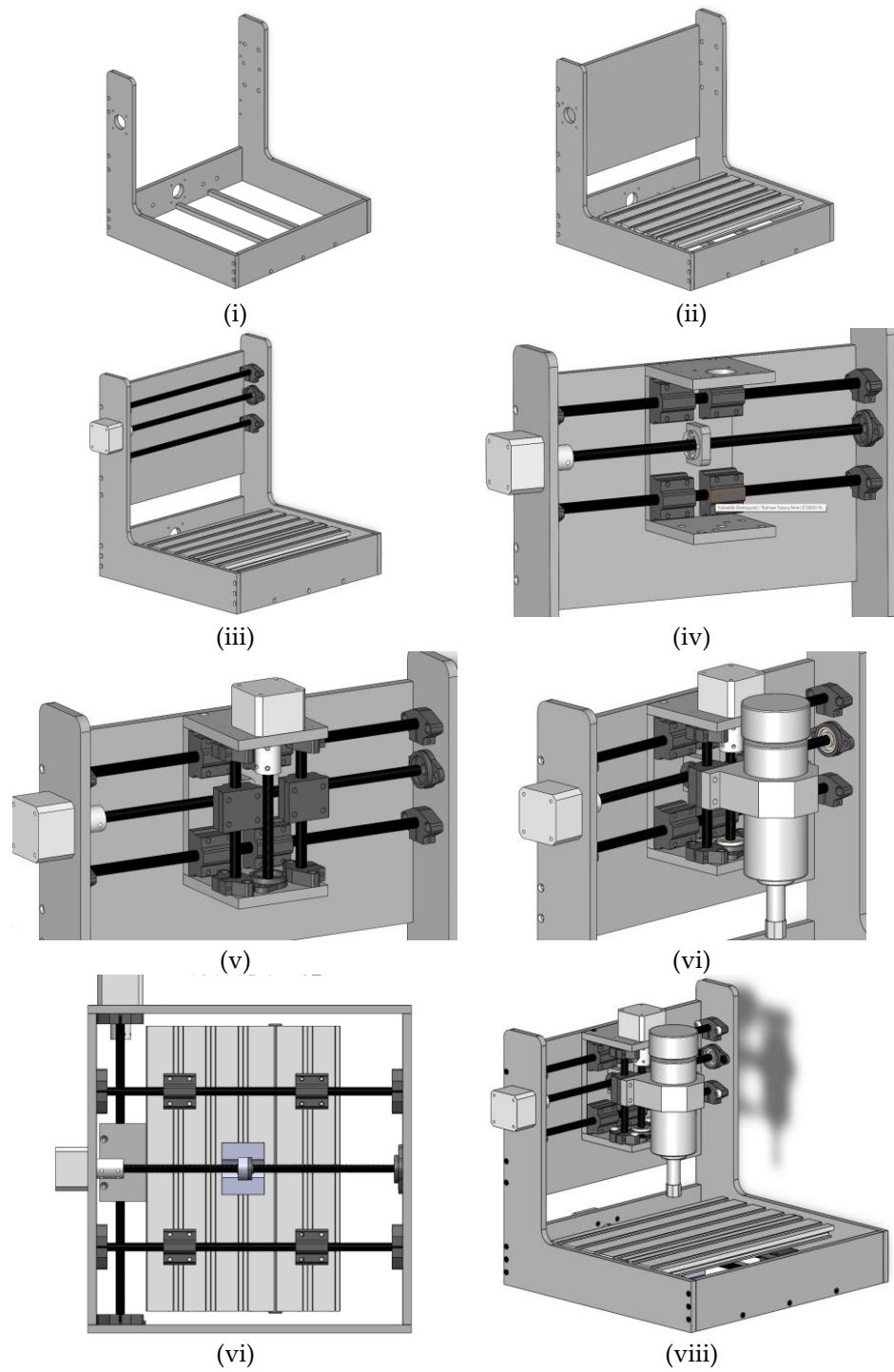


**Figure 11.** Machine mechanics via assembly steps

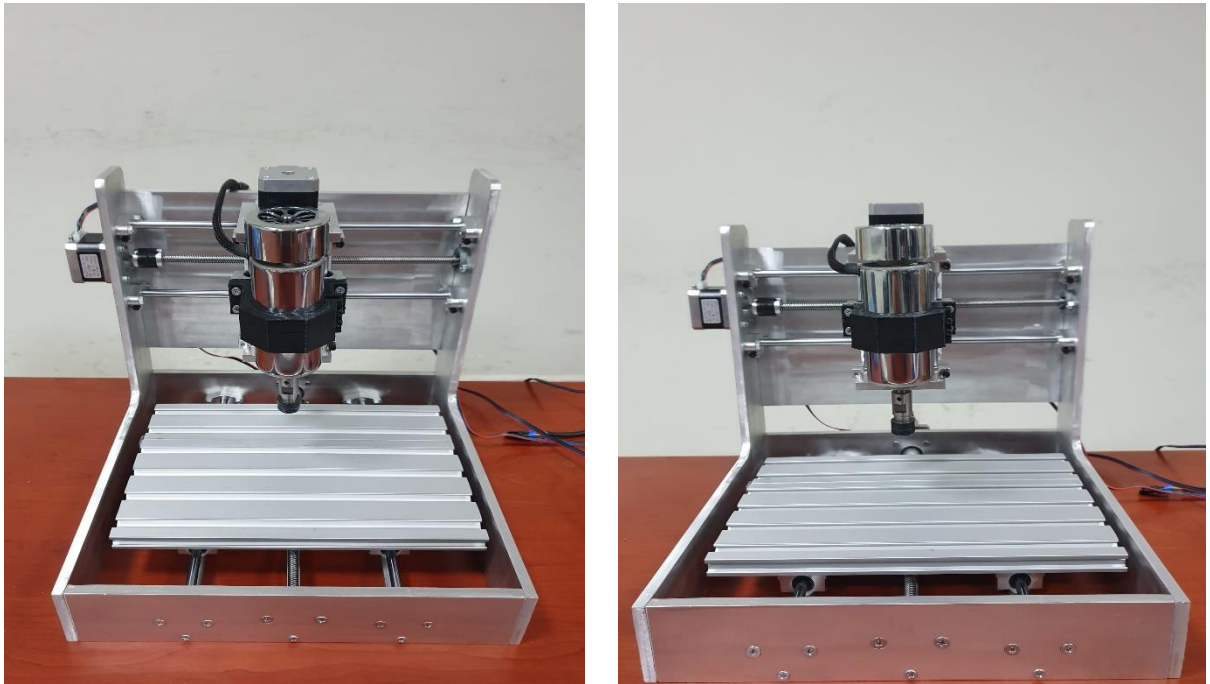


**Figure 12.** PCB Router after production and assembly stages

The processing area of the PCB machine is given in the technical drawings in Figure 13.

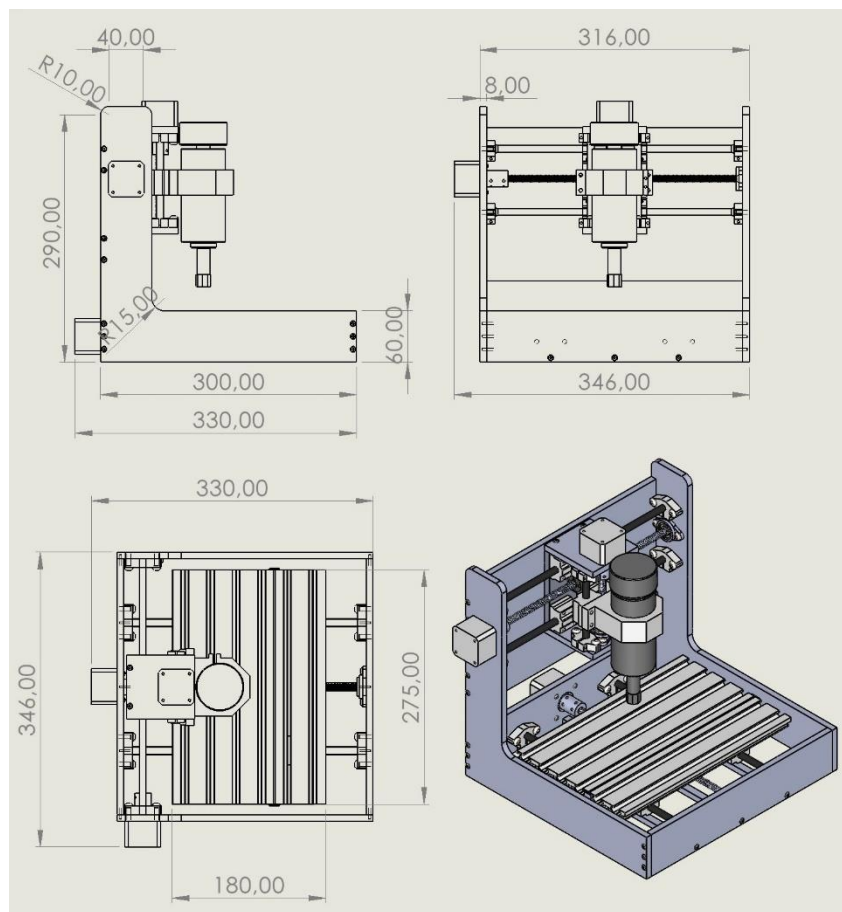


**Figure 13.** Technical drawings of the PCB machine and its processing area

### 2.3. Electronic components of the PCB router

Basic components of router electronics; control card and motor drivers. Power supplies are sub-components. Other essential components of machine electronics are motor drives. These drivers, which will work in harmony with the control card, can be practically connected to the control card with various expansion cards. For bench electronics; the application diagram of the control card, motor drivers, power supplies and motors is given in Figure 14.

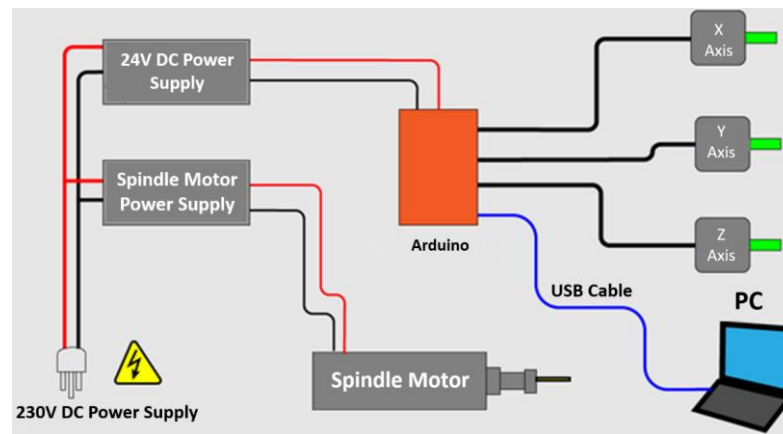


**Figure 14.** The basic components diagram of the PCB Router electronics

The original development board in Figure 15 was used as the control board [17]. Mach3 control cards are used in most of the 3-axis CNC machines in the market [18]. The reason for using an original control card in this project; is to bring the multiple reset feature to the PCB Router. Because the desired results could not be obtained in the multi-point reference applications we made on Mach3 and other non-original cards.

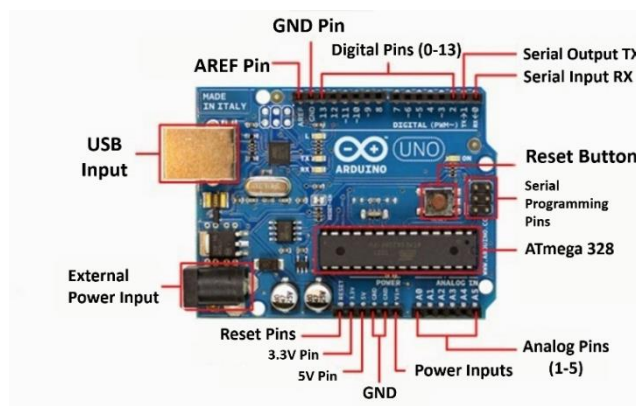


**Figure 15.** The original control card to be used in the control of axis movements [17]

Figure 16 shows the control unit with integrated axis motor drives. The drivers of the control unit, which are disassembled in Figure 16a, were updated with more sensitive ones and mounted on the control card with the same expansion card, and motor-driver connections were made.

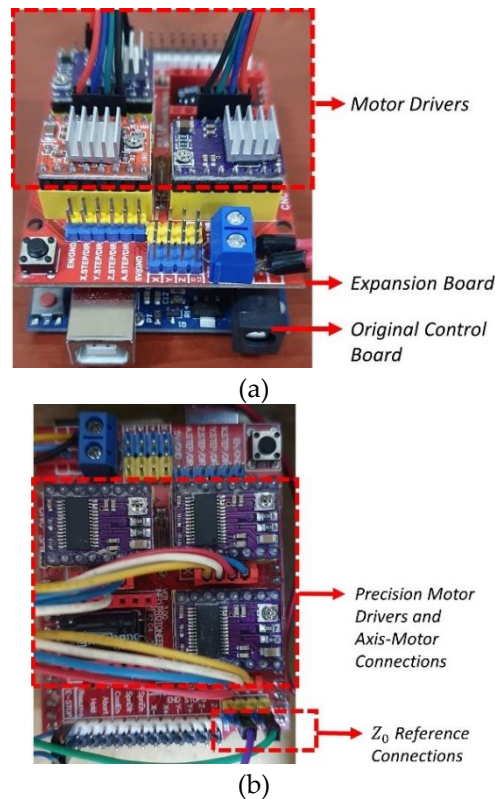


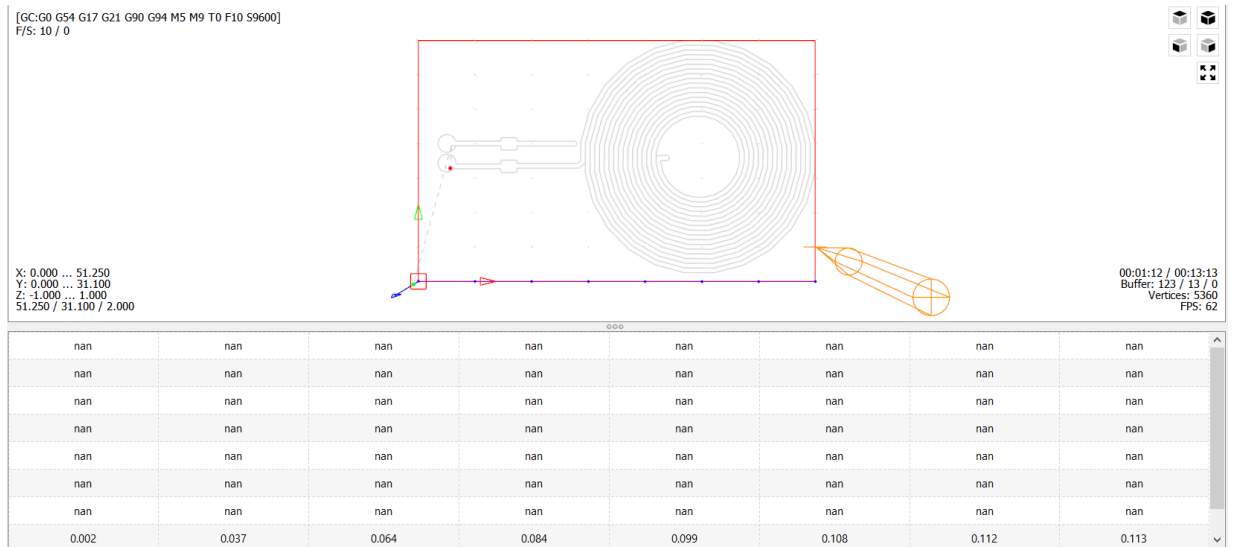
**Figure 16.** Electronic control unit

## 2.4. Multipoint Referencing

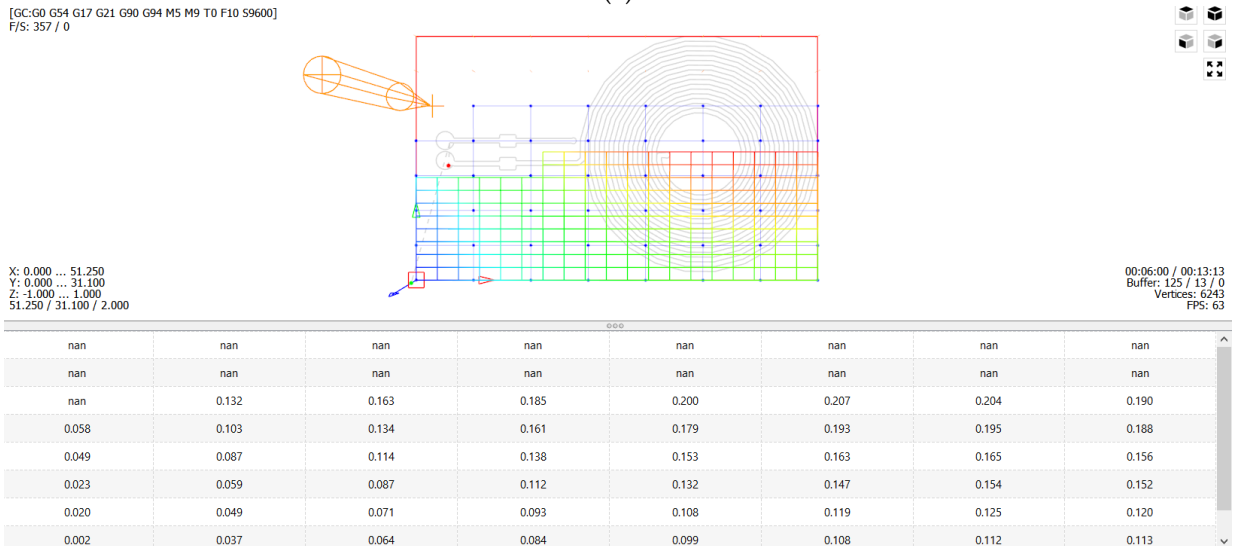
One of the most common problems in PCB milling in routers is that the entire surface of the copper plate on which the engraving will be made cannot be homogeneously. This problem may occur due to various reasons such as the material to be processed is not connected to the workbench in properly, swelling occurs in the connected part, or the material surface is uneven. In the present study, the multi-point referencing or zeroing feature has been added to the router workbench, which was developed to overcome this problem. With the multi-point referencing feature, before starting the engraving process, the distance between the engraving tip and the copper plate is measured, and reference values are taken from the points desired by the user. A height mapping is made on the basis of these references.

The reference value ( $Z_0$ ) for the Z axis may not be the same at every point of the plate. When multi-point referencing is performed, the router engraves each region of the PCB plate not at the same depth, but according to the reference values it receives from the relevant points determined by the user. Thus, since the depths of the copper paths on the PCB are equal, short circuits as a result of less engraving between the paths or disconnections as a result of excessive engraving are prevented. At the same time, cutting tips breakage is largely prevented.

In Figure 17, height mapping images related to the multi-point zeroing process performed within the scope of this study are given. In Figure 17a, the PCB surface to be engraved was determined and this PCB surface was divided into an 8x8 (row x column) matrix. Figure 17b shows the process of sequentially referencing from a total of 64 points of the 8x8 matrix. Figure 17c shows the height map of the PCB surface referenced from 64 points in total. Here, regions with a lower height compared to other points with a blue hue, and regions with a relatively higher height with a red hue are indicated. As can be seen from Figure 17c, height differences are noticeable in a certain PCB area. The points that make up these differences are the multiple reference ( $Z_0$ ) points on the surface of the same PCB during the processing of the PCB. While processing the PCB, milling is carried out by taking these points into consideration.



(a)



(b)

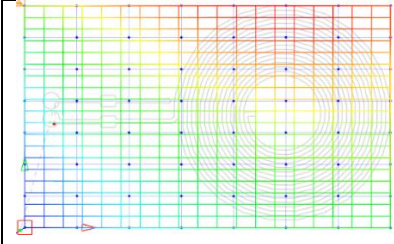


(c)

Figure 17. Multi-point referencing interface

Table 1 gives the height differences on the surface of the PCB connected to the router table with dimensions of approximately 51x31 mm. If multiple referencing is not performed, these heterogeneous height distributions cause tip fractures and breaks in the continuous copper paths as shown in Figure 5. However, with the method used in this study, the height differences given in Table 1 can be tolerated. Homogeneity can be improved by increasing the number of reference points, but this will increase the processing time. In addition, possible vibrations in the router and the milling tool quality have an impact on the PCB processing. These limitations will be addressed in future work. In the PCB image in Table 1, the height of the point in the red square is 0.002 mm

**Table 1.** Heterogeneous height distribution on the PCB surface

PCB Surface	Reference Point Heights (mm)							
	0.152	0.185	0.211	0.231	0.242	0.246	0.240	0.224
	0.106	0.148	0.179	0.205	0.223	0.231	0.231	0.220
	0.091	0.132	0.163	0.185	0.200	0.207	0.204	0.190
	0.058	0.103	0.134	0.161	0.179	0.193	0.195	0.188
	0.049	0.087	0.114	0.138	0.153	0.163	0.165	0.156
	0.023	0.059	0.087	0.112	0.132	0.147	0.154	0.152
	0.020	0.049	0.071	0.093	0.108	0.119	0.125	0.120
	0.002	0.037	0.064	0.084	0.099	0.108	0.112	0.113

### 3. RESULTS

#### 3.1. Testing and Analysis

For the multi-point referencing, the probes are connected to the PCB plate and the engraving tool/cutting tip as seen in Figure 18. When the cutting tip touches the PCB plate, the probes are short-circuited and the circuit used for referencing is completed. A signal is given from the relevant pin of the control card to the probe connected to the cutting tip. This signal is grounded through the other probe connected to the plate surface when the cutting tip touches the plate surface. This process is also called as short circuit test within the scope of the study. The short-circuit test is repeated at various points on the PCB surface as many as the number entered by the user, and the Z-axis of the Router is zeroing as a result of each test. Thanks to this zeroing process, the same depth of processing can be achieved for the entire surface of the PCB.



**Figure 18.** Connections to plate surface and insert for multi-point reference

After providing the PCB Router with multi-point referencing capability, various geometries and electronic integrated circuit in Figure 19 were successfully processed. Images of the processing process are given in Figure 20.

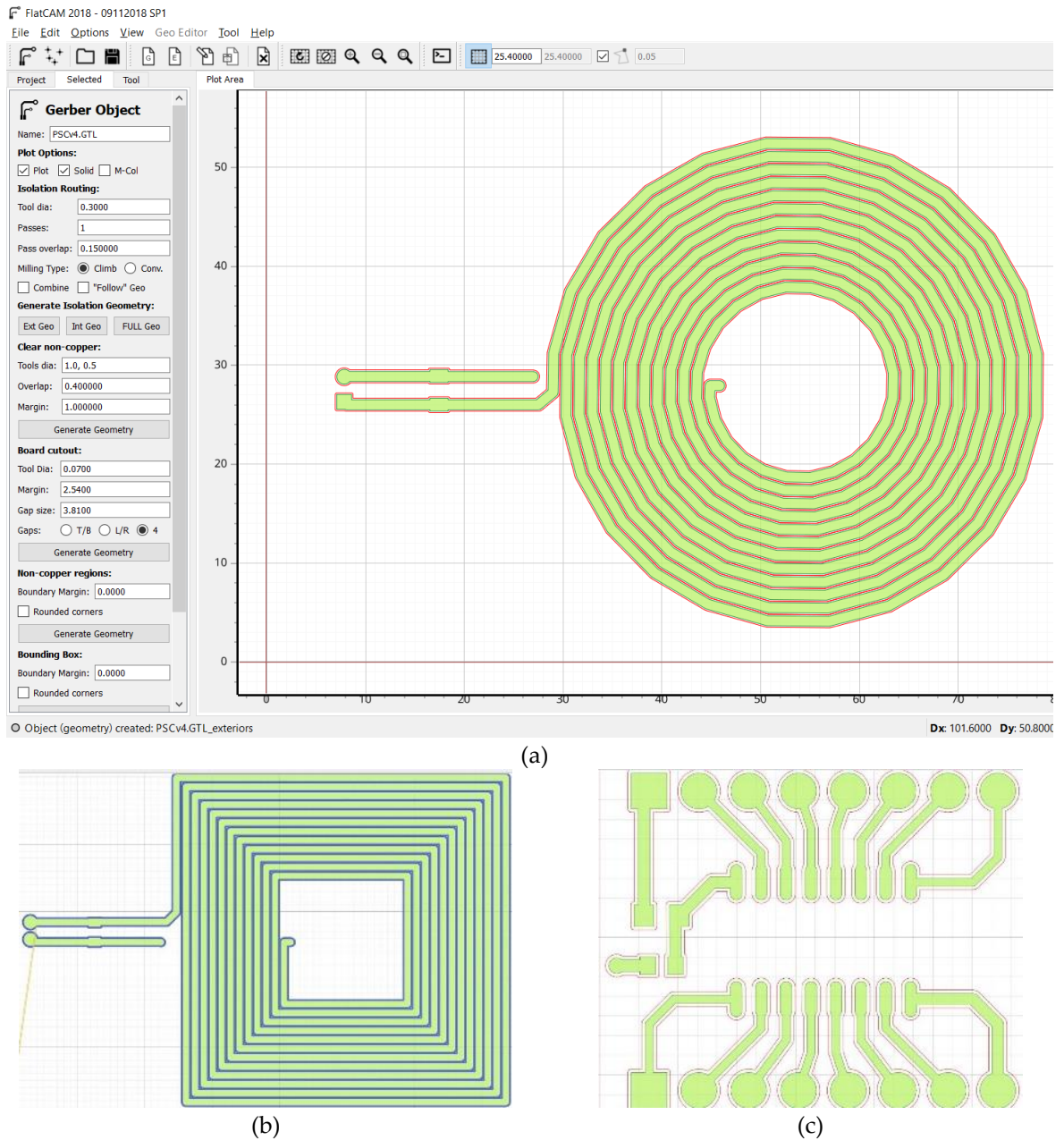


**Figure 19.** Circuits to be extracted G-Code with the electronic circuit production program. (a) circular, (b) square geometries and (c) electronic integrated circuit to be used as SMD-DIP converter.

In Figure 20, the circuits with the g-codes are engraved on the PCB and processed mechanically. As a result of the process, both circuits were checked for breaks and short circuits in the copper paths. No disconnection or short circuit was found during the controls. Especially the successful processing of different geometries forms the basis of his future studies. In this way, the PCB Router has been successfully tested.

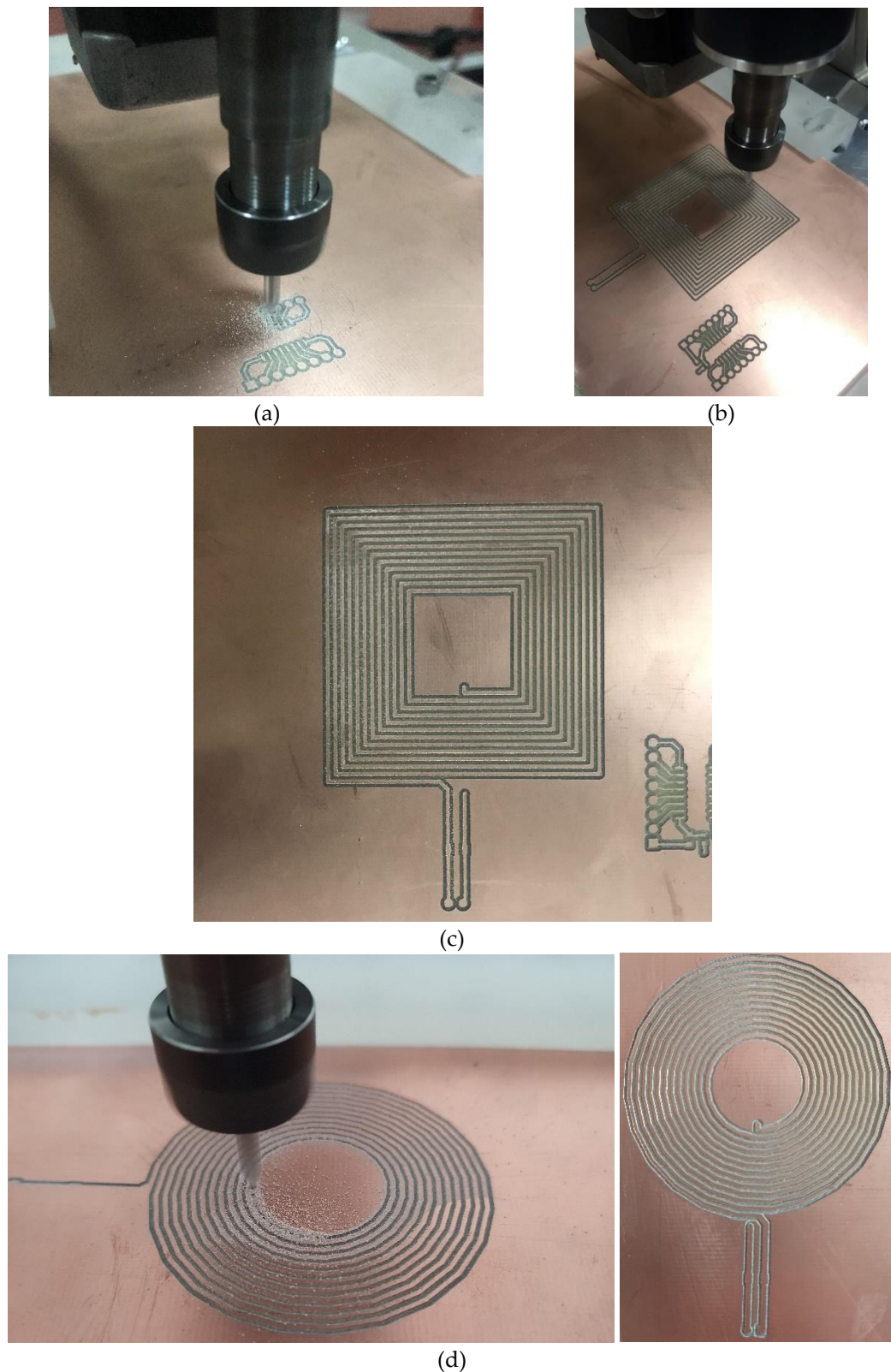


**Figure 19.** PCB engraving process and the outputs obtained at the end of the engraving. (a) Package converter, (b) and (c) planar square and (d) circle geometries.

To numerically verify the homogeneous distribution on the PCB surface, the thickness of the copper tracks was measured with a digital caliper on the PCB in Figure 19c. Similar measurements were taken from various regions of the PCB. The measurements are shown in Figure 20.

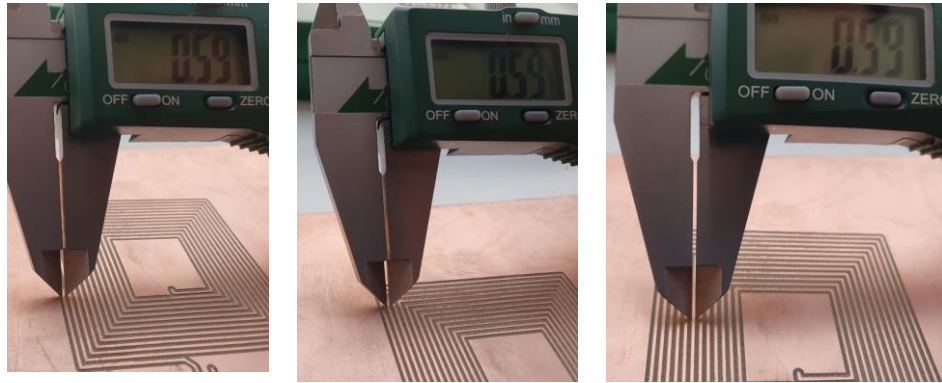


**Figure 20.** Testing for homogeneous distribution

For the test phase, first of all, the relevant electronic circuits were designed from the electronic circuit design programs and the gerber outputs were taken. After these gerber outputs were transferred to the CAM programs used to generate the g-code, the necessary production parameters/limitations were entered into the related program and the g-codes were obtained.

As can be seen from the output images in Figure 19, successful PCB milling processes were carried out. There is no breakage or any short circuit on the copper paths for the PCBs in Figure 19. These PCBs were processed with the parameters in Table 2. The values of the processing parameters in Table 2 were determined by the experience gained from the experimental applications and the information obtained from the expert opinions.

**Table 2.** Key parameters of various PCB milling with the developed router machine

No	PCB	Tools (V shape)	Passes / Pass overlap	Feed / Plunge / Rapid Movement Speed (mm/min)	Depth Cut	Height Map Matrix Dimensions [rows x columns]
1	SMD-DIP Chip	Dia: 0.34 mm, Tip angle: 30°	1 / 0.15 mm	%80 / %40 / %80	-0.040 mm	2 x 2
2	Quadratic PCB	Dia: 0.20 mm, Tip angle: 30°	1 / 0.15 mm	%80 / %40 / %80	-0.030 mm	8 x 8
3	Circular PCB	Dia: 0.30 mm, Tip angle: 30°	1 / 0.15 mm	%80 / %40 / %80	-0.050 mm	8 x 8

The key machining parameters of the PCB engravings and the values selected for these parameters are given in Table 2. It was observed that less burrs remained in PCB-1 and PCB-3 compared to PCB-2. This may be due to manual referencing at the beginning or the depth cut. PCB-3 production took 33.20 minutes. PCB-2 was completed in approximately 47 minutes. Since the surface area of the PCB-1 is smaller than the others, the time record was not kept. In the future, PCB processing with different and various cutting tips is considered. Because the cutting tip is one of the most important factors affecting the engraving quality. Another important factor is the zeroing on the Z-axis. Also in the future, manual zeroing for the starting point is also planned to be automatically provided before the height map is generated.

In this study, a PCB router was developed with a cost effective solution. The developed PCB machine was cost analyzed by comparing it with various routers in the market. Table 3 is presented for cost analysis.

**Table 3.** The cost analysis list

PCB Machines	Type	Cost (€)
WEGSTR PCB [19], [20]	Commercial	3874.89
VOLTERA V-ONE [21]	Commercial	4797.29
CUBE 3D XR PRO [22]	Commercial	4299.00
PCB ROUTER DESKTOP [23]	Commercial	1556.64
R-CNC [24]	Hobbyist/personal use	601.36
PCB-CNC [25]	Hobbyist/personal use	513.10
Our PCB Machine	Laboratory	471.92

#### 4. CONCLUSIONS

In this study, a 3-axis precision router has been developed for successful PCB processing. Electronic circuits in various geometries are processed with this machine. The PCB workbench works by taking reference from multiple points. Thus, engravings can be made at homogeneous depths in the Z axis across the entire PCB surface. Thanks to the multiple referencing, tip breakage and copper path breaks are largely prevented. Although breakage can still be observed at 10-degree V-ends, the breakage rate is much lower at wider angle V-ends, and in this study, successful PCB machining was performed with 80% feed and 40% plunge speed ratios between 0.035 mm - 0.07 mm depths without breakage. In addition to the feed rates, to determine the cutting tip and the engraving depth are the key factors in PCB machining.

#### Declaration of Ethical Standards

Not applicable.

#### Credit Authorship Contribution Statement

E.Y.: Conceptualization, Investigation, Methodology, Software, Writing – review, Original draft & editing, Funding acquisition, Supervision, Validation, Design and Manufacturing. B.S.: Conceptualization, Investigation, Methodology, Software, Writing - review, Software, Original draft & editing, Design and Manufacturing. T.U.: Conceptualization, Investigation, Methodology, Software, Writing – review, Design and Manufacturing. I.I.: Conceptualization, Investigation, Methodology, Software, Writing – review.

#### Declaration of Competing Interest

The authors declare that they have no known competing financial interests or personal relationships that could have appeared to influence the work reported in this paper.

#### Funding / Acknowledgements

This study was supported by Scientific Research Projects Unit with project number 221219011.

#### Data Availability

Not applicable.

#### REFERENCES

- [1] H. Shamkhalichenar, C. J. Bueche, and J. W. Choi, "Printed Circuit Board (PCB) Technology for

- Electrochemical Sensors and Sensing Platforms," *Biosensors*, vol. 10, no. 11, 2020, doi: 10.3390/bios10110159.
- [2] Y. Dong, C. Bao, and W. S. Kim, "Sustainable Additive Manufacturing of Printed Circuit Boards," *Joule*, vol. 2, no. 4, pp. 579–582, 2018, doi: 10.1016/j.joule.2018.03.015.
- [3] Y. Huang, J.-S. Zhang, X.-Y. Chen, W.-Y. Ho, and W. Li, "Comparison of Cutting Performance of Router with CrAlSiN and DLC Hard Coatings," *Int. J. Mater. Mech. Manuf.*, vol. 7, no. 3, pp. 124–127, 2019, doi: 10.18178/ijmmm.2019.7.3.444.
- [4] U. Shinde, R. Somalwar, N. A. Kale, A. J. Nandeshwar, and A. V. Mendhe, "Short Paper on Cnc Based Pcb Milling Machine Considering Human Safety," *J. Res. Eng. Appl. Sci.*, vol. 5, no. 3, pp. 104–107, 2020, doi: 10.46565/jreas.2020.v05i03.005.
- [5] H. Kaygisiz and K. Çetinkaya, "CNC Milling Training Set Design and Application," *SDU Int. J. Technol. Sci.*, vol. 2, no. 3, pp. 53–71, 2010.
- [6] M. Demir, M. Kuncan, and H. Ertunç, "3 Eksenli Mini Cnc Freze Tezgâhı Tasarımı Ve İmalatı," in *Otomatik Kontrol Ulusal Toplantısı, TOK2013*, 2013, pp. 26–28.
- [7] N. Camuscu and E. Aslan, "Comparison of the Performances of Coated Sintered Carbide and Coated Cermet Cutting Tools in End Milling of X210CR12 Cold Work Tool Steel with Different Hardnesses," 2005.
- [8] F. Gümüş, "Bilgisayarla Bütünleşik İmalat Sistemi Tasarımı," pp. 53–69, 2017.
- [9] K. J. Madekar, K. R. Nanaware, P. R. Phadtare, and V. S. Mane, "Automatic mini CNC machine for PCB drawing and drilling," *Int. Res. J. Eng. Technol.*, pp. 3–7, 2016, [Online]. Available: [www.irjet.net](http://www.irjet.net)
- [10] F. Yıldırım, O. Doğan, L. Elen and B. Çiçek, "Transfer of Project Development Training to Vocational High School Students To Three Axis Mini Cnc Router Design: An Applied Study", *Uluslararası Eğitim Bilim ve Teknoloji Dergisi*, vol. 3 no.3, Dec., pp. 125-134, 2017.
- [11] V. J. Shilpa, "Design and Implementation of Three-Axis Cost Efficient CNC PCB Milling Machine," *2018 Int. Conf. Recent Trends Electr. Control Commun.*, pp. 106–109, 2018.
- [12] M. Raut, G. Shete, S. Vipul, and S. Ashok, "Automatic mini cnc machine for pcb drawing using arduino," *Ijciras*, vol. 2, no. August, pp. 51–58, 2019.
- [13] V. Størkersen, "Configuring electrochemical 3D printer for PCB production," UiT, 2022.
- [14] PCB Universe, "Technical Tips for PCB's," 2022. <https://www.pcbuniverse.com/pcb-tech-tips.php?a=4>
- [15] JLCPCB, "PCB Manufacturing & Assembly Capabilities," 2023. <https://jlcpcb.com/capabilities/Capabilities>
- [16] E. Yavsan, "Development of Innovative and High-Performance Capacitive Rotary Encoder," Necmettin Erbakan University, 2020.
- [17] Arduino, "Arduino UNO Overview," 2022. <https://docs.arduino.cc/hardware/uno-rev3>
- [18] Mach Support, "Mach3 Mill Install Config," 2022. [https://www.machsupport.com/Mach3Mill\\_Install\\_Config.pdf](https://www.machsupport.com/Mach3Mill_Install_Config.pdf)
- [19] ProSMT "3 Eksenli CNC Freze Makinesi WEGSTR PCB Devre Kazıma Makinesi", [prosmt.com](http://prosmt.com), Available:<https://www.prosmt.com/urunler/wegstr-3-eksenli-cnc-freze-makinesi>, [Accessed :Feb. 12, 2023].
- [20] Wegstr, "CNC Wegstr ", [wegstr.com](http://wegstr.com). [Online]. Available: [https://wegstr.com/CNC-Wegstr-\(English\)](https://wegstr.com/CNC-Wegstr-(English)), [Accessed: Jul 7, 2023].
- [21] Voltera, "V-One", [www.voltera.io](http://www.voltera.io). Available: <https://www.voltera.io/v-one>. [Online]. [Accessed Jul 7, 2023].
- [22] Derinmotion, "CUBE 3D RF Pro PCB Prototipleme Makinesi", [derinmotion.com](http://derinmotion.com). [Online]. Available: <https://derinmotion.com/urunler/cube-3d-rf-pro>, [Accessed: Jul 7, 2023].
- [23] Meonotomasyon, "Pcb Ahşap Masaüstü Cnc Router", [meonotomasyon.com](http://meonotomasyon.com). [Online]. Available: <https://www.meonotomasyon.com/urun/pcb-ahsap-masaustu-cnc-router>, [Accessed Jul 7, 2023].
- [24] MakerFR, "R-CNC", [makerfr.com](http://makerfr.com), Available:<https://www.makerfr.com/en/cnc/r-cnc/>, [Accessed Jul

- 7,2023].
- [25] Github, " DIY Printed small PCB CNC for fast Prototyping ", *github.com*. [Online]. Available: <https://github.com/Shortcircuitboards/PCB-CNC>, [Accessed Jul. 7, 2023].



## A COMPARATIVE STUDY OF RELEASE KINETICS BEHAVIOR MODELS AND SHELF LIFE ASSESSMENT OF BACITRACIN ZINC-LOADED PLA COMPOSITES

<sup>1,\*</sup> Ali Can ÖZARSLAN , <sup>2</sup>Fatih CİFTÇİ 

<sup>1</sup> Yildiz Technical University, Chemical and Metallurgical Engineering Faculty, Bioengineering Department, Istanbul, TÜRKİYE

<sup>2</sup> Fatih Sultan Mehmet Vakıf University, Biomedical Engineering Department, Istanbul, TÜRKİYE

<sup>1</sup> [alicanozarслан@gmail.com](mailto:alicanozarслан@gmail.com), <sup>2</sup> [fciftci@fsm.edu.tr](mailto:fciftci@fsm.edu.tr)

### *Highlights*

- Investigation of release kinetic behavior of Bacitracin Zinc in PLA using mathematical models.
- Comparison of PLA composite biomaterials having different Bacitracin Zinc content ratio.
- Assessing shelf life and suitability of PLA/Bacitracin Zinc composites for biomedical usage.



## A COMPARATIVE STUDY OF RELEASE KINETICS BEHAVIOR MODELS AND SHELF LIFE ASSESSMENT OF BACITRACIN ZINC-LOADED PLA COMPOSITES

<sup>1,\*</sup> Ali Can ÖZARSLAN , <sup>2</sup>Fatih CİFTÇİ 

<sup>1</sup> Yildiz Technical University, Chemical and Metallurgical Engineering Faculty, Bioengineering Department, Istanbul, TÜRKİYE

<sup>2</sup> Fatih Sultan Mehmet Vakıf University, Biomedical Engineering Department, Istanbul, TÜRKİYE

<sup>1</sup> [alicanozarслан@gmail.com](mailto:alicanozarслан@gmail.com), <sup>2</sup> [fciftci@fsm.edu.tr](mailto:fciftci@fsm.edu.tr)

(Received: 17.07.2023; Accepted in Revised Form: 13.09.2023)

**ABSTRACT:** Mathematical modeling aims to simplify the complex process of drug release and to gain knowledge about the release mechanisms specific to a given material system. Consequently, a mathematical model focuses primarily on one or two important factors. Drug release aims to maximize the bioactivity of both naturally derived and synthetically derived macromolecules, thus increasing their clinical applicability and improving the overall quality of life. This study focused on fabricating PLA composites with different weight percentages of Bacitracin Zinc (0.5, 1.0, and 2.0) and evaluating their potential as a drug delivery system. To understand the release mechanism of Bacitracin Zinc from the PLA composites, we developed a Franz diffusion kinetic model and a mathematical model for cumulative release kinetics. The Franz diffusion model was utilized to analyze the release behavior of the PLA/Bacitracin Zinc composite structure. The results indicated a sustained release rate, following a Zero Order release kinetics pattern. Furthermore, the shelf life of the composite structure was determined to be 125 days. Python programming was employed to model the release behavior and estimate the shelf life of Bacitracin Zinc (0.5, 1.0, and 2.0) incorporated into the PLA matrix to compare different weight percentages' behavior and shelf life.

**Keywords:** Bacitracin Zinc, Composite, PLA, Drug release kinetic, Franz diffusion kinetic model

### 1. INTRODUCTION

The solute transport from drug-loaded polymeric matrices occurs via the diffusion of the active substance, which entails the swelling and erosion of the matrix structure of the polymeric material, whether it is biodegradable [1]. Non-biodegradable and biodegradable polymers are widely used in drug delivery systems because they can be used as a drug carrier [2], [3]. The solute transport system in non-biodegradable polymeric matrices is primarily governed by diffusion. Reservoir-type non-biodegradable polymers encompass systems that employ an inert coating material to serve as a membrane controlling the release rate. In such polymers, the release kinetics remain relatively constant and are unaffected by the concentration gradient, instead primarily governed by the thickness and permeability of the polymeric membrane. In contrast to matrix-type non-biodegradable polymers, the release mechanism in reservoir-type systems is predominantly driven by Fickian diffusion, wherein the release rate correlates with the concentration gradient, diffusion distance, and degree of swelling [4], [5]. On the other hand, biodegradable polymers exhibit a predisposition towards undergoing degradation via hydrolysis or enzymatic reactions. These polymers commonly incorporate chemically unstable bonds, including ester, amide, and anhydride bonds, which are prone to undergoing cleavage during degradation processes [6], [7]. Surface and bulk degradation are two distinct modes of degradation commonly observed in polymers. Surface-degrading polymers exhibit degradation primarily on the outer surface of the material, whereas bulk-degrading polymers experience degradation uniformly throughout the bulk. Water plays a critical role in hydrolysis, making water ingress into the polymer device crucial for investigating both release and dissociation kinetics [8], [9]. The degradation of semicrystalline polymers unfolds in two distinct stages. In the initial stage, water permeates the amorphous regions, initiating random hydrolytic cleavage of

\*Corresponding Author: Ali Can ÖZARSLAN, [alicanozarслан@gmail.com](mailto:alicanozarслан@gmail.com)

susceptible bonds, such as ester bonds. The subsequent stage commences as a substantial portion of the amorphous regions becomes disrupted. As degradation progresses, the polymer chains undergo breakage, leading to measurable changes in the average molecular weight of the polymer. Consequently, assessing temporal alterations in the average molecular weight is a quantitative measure for tracking the degradation process [10].

Bacitracin Zinc is a widely utilized antibiotic medication in topical ointments and creams. It exhibits efficacy against specific bacterial strains and is primarily employed for preventing and treating skin infections. The mechanism of action of Bacitracin Zinc involves interference with bacterial cell wall synthesis, leading to the inhibition of bacterial growth and facilitating the process of wound healing [11]. Multiple factors, particularly topical formulations, influence the release kinetics of Bacitracin Zinc. The diffusion-controlled release is a common mechanism whereby the release rate depends on the formulation's concentration gradient and diffusion properties. Matrix-controlled release is another approach employed in certain formulations wherein Bacitracin Zinc is incorporated within a matrix or polymer system [12]. Release occurs through either diffusion or erosion of the matrix, impacting the release kinetics. For solid dosage forms, the dissolution-controlled release may be predominant, where the dissolution rate and solubility of Bacitracin Zinc determine the release profile. Some formulations may exhibit a combination of release mechanisms, such as an initial burst release followed by sustained release. It is crucial to acknowledge that specific release kinetics can vary based on formulation design, manufacturing processes, and the presence of excipients [13]–[15].

PLA (polylactic acid), a biodegradable polyester, is a prominent polymer utilized to develop particulate drug delivery systems [16]. It belongs to a class of polymers distinguished by the presence of ester bonds. The synthesis of PLA involves the ring-opening copolymerization of two monomers [17]. Exploiting its hydrophobic nature, various emulsification processes are employed to fabricate PLA nano/microparticles with core-shell architectures, enabling the encapsulation of hydrophobic drugs within their hydrophilic cores [18]. It is worth noting that hydrophobic drugs tend to disperse preferentially in hydrophobic environments [19]. The release behavior of PLA particle delivery systems typically exhibits an initial burst phase followed by a nearly zero-order release phase [20]. Biodegradable polyesters, such as PLA and PLGA (poly(lactic-co-glycolic acid)), have been extensively utilized to develop controlled delivery systems, including implants and microparticles, for intramuscular or subcutaneous administration [21]. The primary goals of this research endeavor encompass examining the mathematical behavior model concerning the release kinetics of Bacitracin Zinc when incorporated into PLA polymer for drug release applications. Additionally, the study uses mathematical models to compare the PLA composite biomaterial loaded with different weight percentages of Bacitracin Zinc (0.5, 1.0, 2.0) while assessing and comparing the shelf life of PLA/Bacitracin Zinc composites. Consequently, the study intends to deliberate on the applicability and suitability of these composites for biomedical purposes.

## 2. MATERIAL AND METHODS

### 2.1. Production of Bacitracin Zinc-Loaded Pla Composites

Poly (lactic acid) (PLA 4060D, pellet form) was procured from Nature Works LLC. The solvents used chloroform (CHL, with a molecular weight of 119.38 g/mol), were obtained from Merck without requiring additional purification. Bacitracin (catalog no. B0125, Poole, UK) was purchased from Merck. Item № 21212; CAS № 1405-89-6; Purity  $\geq 70\%$  (Bacitracin A, B1, B3 mixture; Molecular formula;  $C_{66}H_{101}N_{17}O_{16}S \cdot Zn$ ; Formula weight: 1486). To prepare the PLA solution, PLA was dissolved at a weight ratio of 12% using 100 mL of CHL. The prepared PLA solution added various weight percentages of Bacitracin Zinc (0.5, 1.0, and 2.0 wt. %). The mixture was stirred using a magnetic stirrer for 2 hours at room temperature. The resulting working groups were designated as PLA/Bacitracin Zinc (0.5), PLA/Bacitracin Zinc (1.0), and PLA/Bacitracin Zinc (2.0). Subsequently, 25 mL of each working group was poured into 9 cm glass Petri dishes and dried in an oven at 40°C for 24 hours. The dried composites were then stored in a desiccator for further analysis.

## 2.2. Characterization of Bacitracin Zinc-Loaded Pla Composites

The structural characteristics of the Bacitracin Zinc-loaded PLA composites were performed using Fourier Transform Infrared Spectroscopy (FT-IR; Thermo Scientific. Ltd., US) to identify the covalent bonds in the structure of composites. The spectra were obtained in transmission mode, with scans ranging from 4000 to 400  $\text{cm}^{-1}$  wavenumber, and a resolution of 2  $\text{cm}^{-1}$ . A total of 15 readings were collected. Scanning Electron Microscopy (SEM; TESCAN. Ltd., Czech Republic (VEGA 3 LMH)) analysis was employed for examining the surface morphology features of the Bacitracin Zinc-loaded PLA composites. To enhance conductivity, a thin layer of gold was deposited on the samples using a sputter coater device (Emitech K550X, UK) at around 1 kV. Imaging was conducted at an accelerating voltage of 15 kV, with images captured at varying magnification levels.

## 2.3. Mathematical Modeling of In Vitro Franz Diffusion Release for Bacitracin Zinc-Loaded Pla Composites

To begin the study, linear calibration curves were constructed for five concentrations of Bacitracin Zinc (0.5, 1.0, and 2.0 wt. %). The release characteristics of Bacitracin Zinc from the composites were then investigated at various intervals. The first step involved weighing and placing 10, 20, and 30 mg of Bacitracin Zinc-loaded PLA composites into separate Eppendorf tubes containing 1 ml of phosphate-buffered saline (PBS) with a pH of 7.4. The release of Bacitracin Zinc from the 12% PLA composites was conducted using a thermal shaker (BIOSAN TS-100C) and 1 ml of fresh PBS. At different time intervals, 1 ml of PBS was withdrawn from the Eppendorf tubes and transferred to a quartz bath with a capacity of 1 ml. The initial procedure involved obtaining calibration graphs to identify the primary peak corresponding to fucoïdan in all the composites. For this purpose, a Shimadzu UV-1280 UV-VIS spectrophotometer machine was utilized. The process commenced by allowing the PBS solution to remain in the Eppendorf tubes and the samples to shake inside the thermal shaker for 15 minutes. After 15 minutes, the solutions were removed from the Eppendorf tubes and individually analyzed using the spectrophotometer. After analysis, fresh PBS was added again, and the samples were left in the thermal shaker for up to 150 hours.

Determining the drug's dissolution profile can be accomplished by employing diverse mathematical models, where choosing an appropriate mathematical function is crucial in defining the profile. These models, including the zero-order, first-order, and Higuchi models, elucidate the underlying mechanism governing the drug's release process. Specifically, the zero-order equation:

$$Q_t = Q_0 + K_0t \quad (1)$$

Where the amount of drug ( $Q_t$ ) dissolved over a given period ( $t$ ) with the inclusion of the initial amount of drug ( $Q_0$ ) in the solution, which is usually equal to zero, and the zero-order release constant ( $K_0$ ) in units of concentration per time. Similarly, the first-order equation:

$$\log C = \log C_0 - K_1/2.303t \quad (2)$$

Where measures the rate of change of the initial concentration of the drug ( $C_0$ ) over time ( $t$ ) and the first-order constant ( $K_1$ ). Higuchi's equation:

$$Q_t = K_H * t^{1/2} \quad (3)$$

Where the amount of drug ( $Q_t$ ) is released over a given period ( $t$ ) using the release rate constant ( $K_H$ ) for the Higuchi model, the data is fitted according to the Korsmeyer–Peppas model to ascertain the precise mechanism behind the drug release process. This model:

$$M_t/M_\infty = K * t^n \quad (4)$$

Where describes the general solute release behavior from a controlled release polymer system and uses the fraction of drug ( $M_t/M_\infty$ ) released over time ( $t$ ), the release rate constant ( $K$ ), and the release exponent ( $n$ ) to characterize different releases for cylindrical-shaped matrices.

#### 2.4. Bacitracin Zinc Stability

The most commonly employed *in vitro* technique for assessing dermal absorption involves the topical application of the active ingredient in a suitable formulation onto the surface of a skin sample [22]. Dissolution tests, predominantly utilizing the Franz Diffusion device, are widely utilized for evaluating composite formulations [23], [24]. In this study, composite samples containing the active substance benzalkonium chloride (Bacitracin) were carefully placed on the membranes within Franz diffusion cells. The composite samples were centrally positioned within the Franz device, ensuring consistent exposure. The lower compartment of the cells was filled with a 2.5 mL volume of media, while the upper compartment accommodated a 1.5 mL sample for examination. The experiment was meticulously conducted under controlled conditions, maintaining a constant ambient temperature of 37°C with continuous agitation. At pre-determined intervals, specifically at the 15<sup>th</sup> and 30<sup>th</sup> minutes, and subsequently at the 1<sup>st</sup>, 2<sup>nd</sup>, 4<sup>th</sup>, 6<sup>th</sup>, 8<sup>th</sup>, and 24<sup>th</sup> hours, 2.5 mL aliquots of the sample were withdrawn from the lower compartment and promptly replaced with fresh medium equilibrated to 37°C. This process was repeated throughout the experimental period to ensure continuous monitoring. The concentration of the active substance in the collected samples was subsequently quantified using high-performance liquid chromatography (HPLC). The cumulative percentage of the active substance passing through the cells was plotted against time to evaluate the cumulative dermal absorption profile. The cumulative percentage of the active substance passing through the cells at the end of the 24 hours was calculated by analyzing the resulting curve. Statistical analysis of the cumulative mass losses for the composite samples was conducted using a Python program.

### 3. RESULTS AND DISCUSSION

Figure 1A. shows the FT-IR spectra of PLA, Bacitracin Zinc, and PLA/Bacitracin Zinc (2.0) samples. The shared identifiable peaks within the FT-IR spectrum of both PLA and PLA/Bacitracin Zinc composites were found to be in the regions of 1900–1650  $\text{cm}^{-1}$  (corresponding to the stretching vibration of C=O) and 1300–1000  $\text{cm}^{-1}$  (indicating the stretching vibration of C–O and the framework vibration of C–C). Notably, two distinct peaks emerged within the range of 3540–3180  $\text{cm}^{-1}$  due to the presence of NH<sub>2</sub> and NH groups in the PLA structure [25], [26]. In the FT-IR spectrum, the specific absorption peaks (1746  $\text{cm}^{-1}$ , 1092  $\text{cm}^{-1}$ ) characterizing PLA remained unchanged without any noticeable deviation. The key chemical constituents of Bacitracin Zinc encompass C=O, C=N, NH<sub>2</sub>, NH, –OH, and C–S groups. An overlapping of peaks from certain functional groups within PLA, and Bacitracin Zinc was evident due to their shared chemical moieties. The intensity of the characteristic absorption peaks (3244  $\text{cm}^{-1}$ , 1651  $\text{cm}^{-1}$ , and 1539  $\text{cm}^{-1}$ ) associated with Bacitracin Zinc [27] experienced a significant reduction. This decline pointed out a physical interaction between Bacitracin Zinc and the carrier materials, implying that the incorporation of Bacitracin Zinc into PLA did not result in alterations to their underlying chemical structures. Figure 1B. and Figure 1C. demonstrate the SEM images of PLA and PLA/Bacitracin Zinc(2.0) samples, respectively. Upon analysis of SEM in Figure 1B., it becomes evident that the PLA polymer demonstrated a film structure devoid of any observable deformations. This observation shows the PLA polymer's capability to undergo successful film formation. In contrast, Figure 1C, depicting the surface imagery of the film specimen incorporating Bacitracin Zinc within the PLA polymer, revealed an absence of adverse effects on PLA film formation attributed to Bacitracin Zinc. Notably, no deformations were induced by Bacitracin Zinc. Consequently, a deduction can be drawn that the composite materials comprising Bacitracin Zinc-loaded PLA can indeed be effectively produced without compromising the film formation process. Moreover, the obtained results exhibit concurrence with prior research conducted on polymeric

composites loaded with biomolecules [28]–[30].

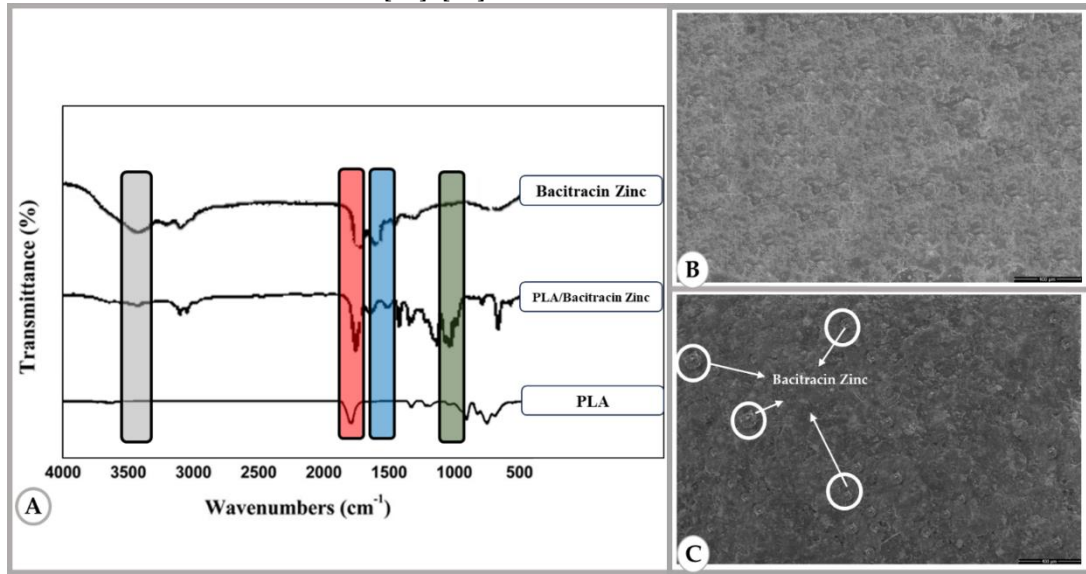


**Figure 1.** A. FT-IR spectra of Bacitracin Zinc, PLA and Bacitracin Zinc (2.0)-loaded PLA, B. SEM images of PLA and C. of Bacitracin Zinc (2.0)-loaded PLA composite

**Table 1.** Franz diffusion cumulative release kinetics model ( $R^2$  value after 24 hours)

Bacitracin Zinc-loaded PLA composite materials			
Model	PLA/Bacitracin Zinc(0.5)	PLA/Bacitracin Zinc(1.0)	PLA/Bacitracin Zinc(2.0)
Korsmeyer-Peppas	0.9023	0.8854	0.9020
Zero-order	0.9965	0.9897	0.9952
Firs-order	0.9423	0.9406	0.9343
Hixson	0.9817	0.9817	0.9817
Higuchi	0.9682	0.9556	0.9670

Understanding release kinetics systems and the intricate interplay between the active ingredient and the biomaterial system is crucial for designing effective delivery systems tailored to specific applications. Furthermore, developing doped polymeric matrices necessitates the utilization of robust mathematical models to uncover the underlying solute transport mechanisms. This study group aims to offer a fresh perspective on the structure-function relationship of biodegradable PLA polymers, specifically focusing on drug release kinetics and employing mathematical modeling techniques. The cumulative release kinetics model for PLA polymer containing 0.5% bacitracin zinc exhibited a zero-order pattern, with a correlation coefficient ( $R^2$ ) of 0.9968 (Figure 2.A). Similarly, the cumulative release behavior of 1% Bacitracin zinc loaded into PLA polymer adhered to a zero-order kinetics model, displaying a correlation coefficient ( $R^2$ ) of 0.9897 (Figure 2.B). The release kinetics model for PLA composite loaded with 2% Bacitracin zinc demonstrated a zero-order trend as well, with a correlation coefficient ( $R^2$ ) of 0.9952 (Figure 2.C). The study employed Fick's law as the basis for modeling the drug release kinetics of Bacitracin zinc. The cumulative logarithmic linear release model of Bacitracin zinc is illustrated in Figure 1.D, representing its relationship with logarithmic time. The release kinetics analysis for Bacitracin zinc-loaded PLA composites consistently yielded zero-order kinetics across all three ratios (0.5, 1.0, and 2.0), as evident in Figures 2A, 2B, and 2C. Comparative analysis of Korsmeyer-Peppas, zero-order, first-order, Hixson, and Higuchi models, each possessing correlation coefficients of 0.90 and above, was performed (Table 1.). This evaluation revealed that the zero-order model exhibited the best fit, with the optimal ratio being "0.5". In a prior investigation, drug delivery kinetics were explored on Poly(lactic acid-co-lysine) (PLL)/poly(L-lactic acid) (PLLA)/Bacitracin (BAC) nanofibers, resulting in a correlation coefficient ( $R^2$ ) of 0.98. The

relatively high PLLA ratio hindered complete diffusion of BAC from the nanofibers due to BAC encapsulation. Consequently, the researchers concluded that this circumstance contributed to the cumulative release of BAC [25]. According to Gokhale [31], the diffusion biodegradability of the drug system, swelling of the polymeric matrix, and material degradation are the key factors influencing solute transport from drug-containing polymeric matrices. By utilizing various mathematical models, the optimized composites for achieving the desired drug release profile were determined as PLA/Bacitracin Zinc(0.5), PLA/Bacitracin Zinc(1.0), and PLA/Bacitracin Zinc(2.0). Several mathematical models were examined to describe the emission pattern, including Zero Order, First Order, Higuchi, Hixon, and Korsmeyer-Peppas release kinetic models. The Fickian linear curve profile was observed, indicating a Zero Order release kinetic diffusion profile. Statistical analysis in Python was conducted to determine the cumulative amount of the active ingredient at the end of 30 days. In line with Fu et al. [32], the PLA polymer material used in this study is biodegradable, and the implementation of the Franz diffusion mathematical model was deemed appropriate for the release of active drug materials within this structure. Similarly, Bao et al. [33] performed in vitro release kinetic modeling using the Franz diffusion method for an ointment formulation, considering the high viscosity of the ointment and extended contact times. During their Franz diffusion study, Salamanca et al. [27] obtained a working profile following Zero Order diffusion, with an  $R^2$  value of 0.929, in a linear Fickian equation applied in a cellulose membrane environment (pH 7.4). Gokhale [31] determined the release kinetics working model as Korsmeyer-Peppas, yielding an  $R^2$  value of 0.996 based on the Fickian law. Baert et al. [34] employed the Franz diffusion model to create release kinetics in both skin and artificial skin media, yielding an  $R^2$  value of 0.926 after 24 hours of measurement, and identified the release profile according to Korsmeyer.

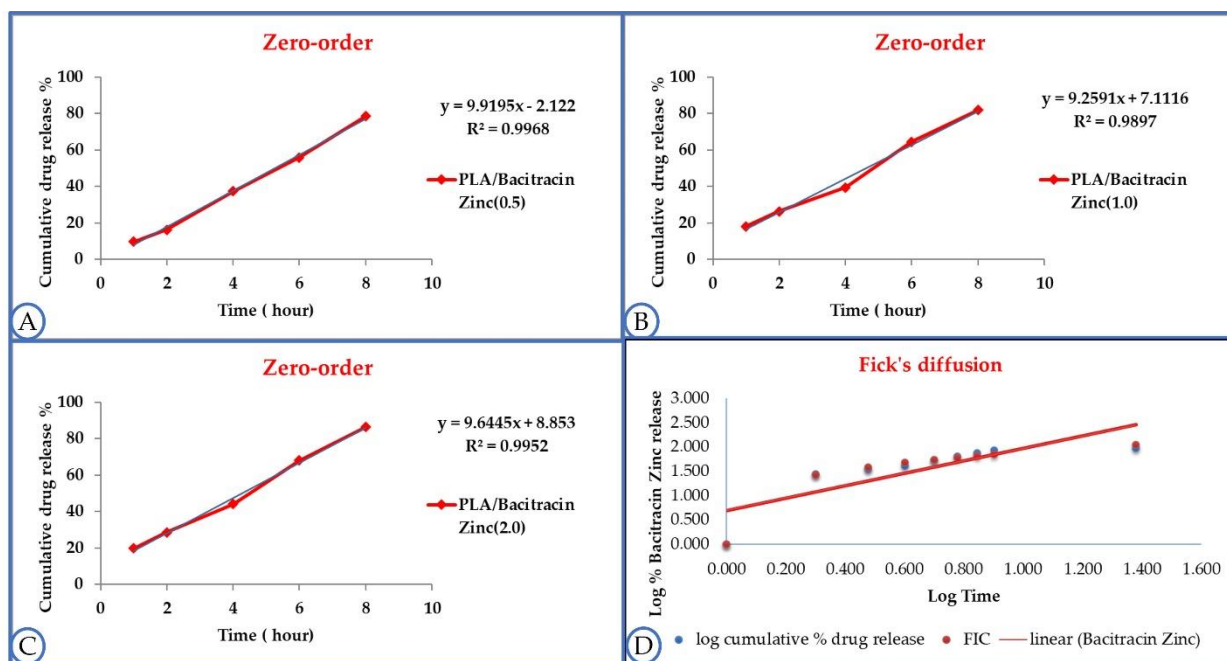


**Figure 2.** Franz Diffusion mathematical models A. Zero Order modeling of PLA/Bacitracin Zinc(0.5), B. Zero Order modeling of PLA/Bacitracin Zinc(1.0), C. Zero Order modeling of PLA/Bacitracin Zinc(2.0), D. Fick's diffusion of Bacitracin Zinc

The stability specification study revealed significant findings regarding the PLA/Bacitracin Zinc composites. For the PLA/Bacitracin Zinc(0.5) composite, the shelf life was 31.6 days (Figure 3A.), falling within a time range where we can have at least 50-95% confidence in the response. Similarly, the PLA/Bacitracin Zinc(1.0) composite exhibited a shelf life of 35.4 days (Figure 3B.), within a time range where we can have at least 50-95% confidence in the response. In the case of the PLA/Bacitracin Zinc(2.0) composite, the shelf life was 125.2 days (Figure 3C.), within a time range where we can be at least 50-95%

certain of the response. Overall, the release kinetics and shelf-life statistics analysis of the PLA study group indicate that the best working sample within the specified range (90-110%) is the PLA/Bacitracin Zinc(2.0) composite, with a shelf life of 125 days. Enhanced and extended shelf life holds significant prominence for polymers and composites destined for diverse applications across multiple domains, including biophysics, medicine, biomedical, and various other realms within biotechnology [35]–[37]. Based on these results, even if all samples have an acceptable shelf life, PLA/Bacitracin Zinc(2.0) may be the preferred better choice for different biomedical applications. In addition, the results obtained are in agreement with the studies on the shelf life of bacitracin biomolecule [38], [39].

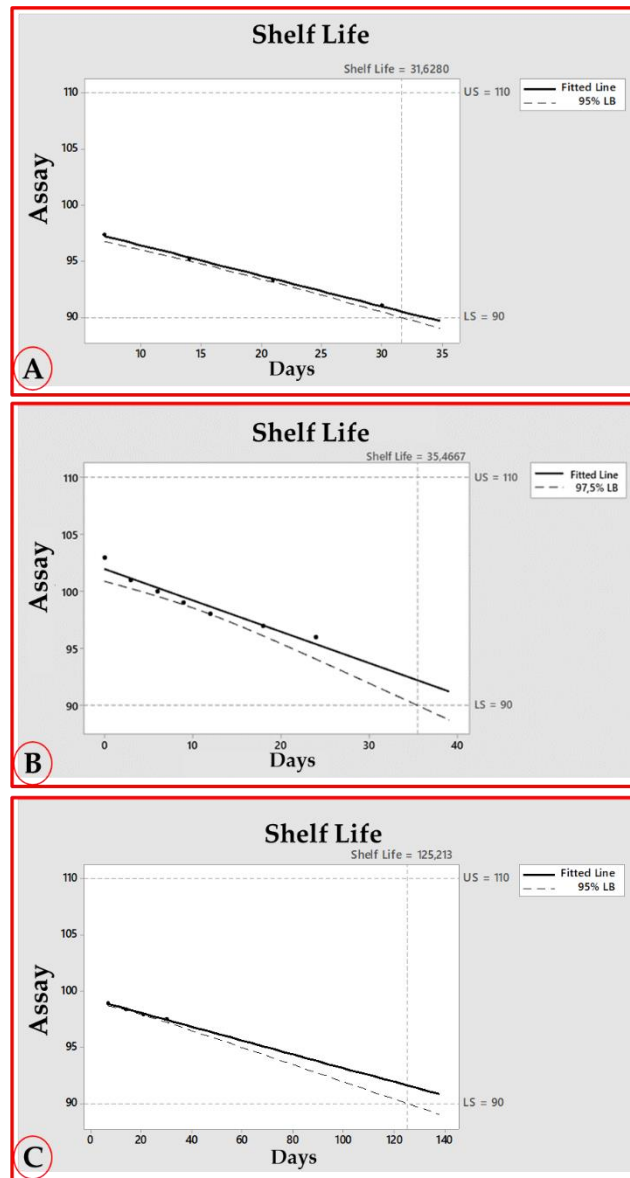


**Figure 3.** A shelf life of A. PLA/Bacitracin Zinc(0.5), B. PLA/Bacitracin Zinc(1.0), C. PLA/Bacitracin Zinc(2.0)

#### 4. CONCLUSIONS

In this study, Bacitracin Zinc biomolecule with different amounts was loaded into PLA polymer and Bacitracin Zinc-loaded PLA composite materials were successfully prepared with simple casting method. As a result of the loading of Bacitracin Zinc into PLA polymer, PLA/Bacitracin Zinc(2.0) showed the best

shelf life and PLA/Bacitracin Zinc(0.5) showed the best behavior kinetics. Zero-order model of the release behavior obtained by the Franz diffusion study was observed as the most appropriate behavior. In the zero-order mathematical model,  $R^2$  values of PLA/Bacitracin Zinc(2.0) and PLA/Bacitracin Zinc(0.5) were obtained as 0.9952 and 0.9968, respectively. The shelf life of PLA/Bacitracin Zinc(2.0) with Phyton analysis was found as 125 days, and the usability of PLA/Bacitracin Zinc(2.0) composite biomaterial in biomedical applications may be more effective in terms of the shelf life behavior. Nevertheless, the PLA/Bacitracin Zinc(0.5) composite, which displayed favorable and suitable release kinetics, also demonstrated an adequate shelf life. This suggests that these materials could be considered a favorable option for potential utilization in biomedical applications.

#### Declaration of Ethical Standards

The authors followed all ethical guidelines, including authorship, citation, data reporting, and publishing original research.

#### Declaration of Competing Interest

The authors declare that they have no known competing financial interests or personal relationships that could have appeared to influence the work reported in this paper.

#### Funding / Acknowledgements

Not applicable.

#### Data Availability

Not applicable.

#### 5. REFERENCES

- [1] D. Y. Arifin, L. Y. Lee, and C. H. Wang, "Mathematical modeling and simulation of drug release from microspheres: Implications to drug delivery systems," *Advanced Drug Delivery Reviews*, vol. 58, no. 12-13, pp. 1274-1325, 2006, doi: 10.1016/j.addr.2006.09.007.
- [2] O. Pillai and R. Panchagnula, "Polymers in drug delivery," *Current Opinion in Chemical Biology*, vol. 5, no. 4, pp. 447-451, 2001, doi: 10.1016/S1367-5931(00)00227-1.
- [3] M. Chasin and R. Langer, Eds., *Biodegradable polymers as drug delivery systems*. New York: Marcel Dekker, 1990.
- [4] J. Siepmann and F. Siepmann, "Mathematical modeling of drug delivery," *International Journal of Pharmaceutics*, vol. 364, no. 2, pp. 328-343, 2008, doi: 10.1016/j.ijpharm.2008.09.004.
- [5] S. B. Lin, K. S. Hwang, S. Y. Tsay, and S. L. Cooper, "Segmental orientation studies of polyether polyurethane block copolymers with different hard segment lengths and distributions," *Colloid Polym. Sci.*, vol. 263, pp. 128-140, 1985, doi: 10.1007/BF01412787.
- [6] L. K. Fung and W. M. Saltzman, "Polymeric implants for cancer chemotherapy," *Advanced Drug Delivery Reviews*, vol. 26, no. 2-3, pp. 209-230, 1997, doi: 10.1016/S0169-409X(97)00036-7.
- [7] J. Heller, R. W. Baker, R. M. Gale, and J. O. Rodin, "Controlled drug release by polymer dissolution. I. Partial esters of maleic anhydride copolymers—properties and theory," *J. Appl. Polym. Sci.*, vol. 22, no. 7, pp. 1991-2009, 1978.
- [8] J. Heller, "Controlled release of biologically active compounds from bioerodible polymers," *Biomaterials*, vol. 1, no. 1, pp. 51-57, 1980, doi: 10.1016/0142-9612(80)90060-5.
- [9] K. R. Kamath and K. Park, "Biodegradable hydrogels in drug delivery," *Adv. Drug Deliv. Rev.*, vol. 11, no. 1-2, pp. 59-84, 1993, doi: 10.1016/0169-409X(93)90027-2.
- [10] U. Edlund and A. C. Albertsson, "Degradable polymer microspheres for controlled drug

- delivery," in *Degradable Aliphatic Polyesters, Advances in Polymer Science*, Springer, Berlin, Heidelberg, vol. 157, pp. 67-112, 2002, doi: 10.1007/3-540-45734-8\_3.
- [11] J. Yao, S. Zhang, W. Li, Z. Du, and Y. Li, "In vitro drug controlled-release behavior of an electrospun modified poly (lactic acid)/bacitracin drug delivery system," *RSC Adv.*, vol. 6, no. 1, pp. 515-521, 2016.
- [12] M. A. Repka, S. Prodduturi, M. Munjal, and P. Mididoddi, "Matrix-and reservoir-based transmucosal delivery systems: tailoring delivery solutions," *Am. J. Drug Deliv.*, vol. 2, pp. 173-192, 2004.
- [13] D. Cai, B. Zhang, J. Zhu, H. Xu, P. Liu, Z. Wang, J. Li, Z. Yang, X. Ma, and S. Chen, "Enhanced bacitracin production by systematically engineering S-adenosylmethionine supply modules in *Bacillus licheniformis*," *Front. Bioeng. Biotechnol.*, vol. 8, pp. 305, 2020.
- [14] M. Goldraich and J. Kost, "Glucose-sensitive polymeric matrices for controlled drug delivery," *Clin. Mater.*, vol. 13, no. 1-4, pp. 135-142, 1993.
- [15] I. Lavon and J. Kost, "Mass transport enhancement by ultrasound in non-degradable polymeric controlled release systems," *J. Control. release*, vol. 54, no. 1, pp. 1-7, 1998.
- [16] L. Singh, V. Kumar, and B. D. Ratner, "Generation of porous microcellular 85/15 poly (DL-lactide-co-glycolide) foams for biomedical applications," *Biomaterials*, vol. 25, no. 13, pp. 2611-2617, 2004, doi: 10.1016/j.biomaterials.2003.09.040.
- [17] C. E. Astete and C. M. Sabliov, "Synthesis and characterization of PLGA nanoparticles," *Journal of Biomaterials Science, Polymer Edition*, vol. 17, no. 3, pp. 247-289, 2006, doi: 10.1163/156856206775997322.
- [18] Y. Kakizawa, R. Nishio, T. Hirano, Y. Koshi, M. Nukiwa, M. Koiwa, J. Michizoe, and N. Ida, "Controlled release of protein drugs from newly developed amphiphilic polymer-based microparticles composed of nanoparticles," *J. Control. Release*, vol. 142, no. 1, pp. 8-13, 2010, doi: 10.1016/j.jconrel.2009.09.024.
- [19] D. K. Sahana, G. Mittal, V. Bhardwaj, and M. N. V. R. Kumar, "PLGA nanoparticles for oral delivery of hydrophobic drugs: Influence of organic solvent on nanoparticle formation and release behavior in vitro and in vivo using estradiol as a model drug," *J. Pharm. Sci.*, vol. 97, no. 4, pp. 1530-1542, 2008, doi: 10.1002/jps.21158.
- [20] Y. P. Li, Y. Y. Pei, X. Y. Zhang, Z. H. Gu, Z. H. Zhou, W. F. Yuan, J. J. Zhou, J. H. Zhu, and X. J. Gao, "PEGylated PLGA nanoparticles as protein carriers: Synthesis, preparation and biodistribution in rats," *J. Control. Release*, vol. 71, no. 2, pp. 203-211, 2001, doi: 10.1016/S0168-3659(01)00218-8.
- [21] L. Brannon-Peppas, "Recent advances on the use of biodegradable microparticles and nanoparticles in controlled drug delivery," *International Journal of Pharmaceutics*, vol. 116, no. 1, pp. 1-9, 1995, doi: 10.1016/0378-5173(94)00324-X.
- [22] T. J. Franz, "Percutaneous absorption. On the relevance of in vitro data," *J. Invest. Dermatol.*, vol. 64, no. 3, pp. 190-195, 1975, doi: 10.1111/1523-1747.ep12533356.
- [23] L. Bartosova and J. Bajgar, "Transdermal Drug Delivery In Vitro Using Diffusion Cells," *Curr. Med. Chem.*, vol. 19, no. 27, pp. 4671-4677, 2012, doi: 10.2174/092986712803306358.
- [24] B. Godin and E. Touitou, "Transdermal skin delivery: Predictions for humans from in vivo, ex vivo and animal models," *Advanced Drug Delivery Reviews*, vol. 59, no. 11, pp. 1152-1161, 2007, doi: 10.1016/j.addr.2007.07.004.
- [25] J. Yao, S. Zhang, W. Li, Z. Du, and Y. Li, "In vitro drug controlled-release behavior of an electrospun modified poly(lactic acid)/bacitracin drug delivery system," *RSC Adv.*, vol. 6, no. 1, pp. 515-521, 2015, doi: 10.1039/c5ra22467e.
- [26] F. Ciftci, N. Duygulu, Y. Yilmazer, Z. Karavelioğlu, R. Çakır Koç, O. Gündüz, and C. B. Ustündag, "Antibacterial and cellular behavior of PLA-based bacitracin and zataria multiflora nanofibers produced by electrospinning method," *Int. J. Polym. Mater. Polym. Biomater.*, vol. 72, no. 4, pp. 319-334, 2023, doi: 10.1080/00914037.2021.2008391.
- [27] S. Afzal, K. Barkat, M. U. Ashraf, I. Khalid, Y. Mehmood, N. H. Shah, S. F. Badshah, S. Naem, S.

- A. Khan, and M. Kazi, "Formulation and Characterization of Polymeric Cross-Linked Hydrogel Patches for Topical Delivery of Antibiotic for Healing Wound Infections," *Polymers (Basel)*, vol. 15, no. 7, pp. 1652, 2023.
- [28] F. Ciftci, "Release kinetics modelling and in vivo-vitro, shelf-life study of resveratrol added composite transdermal scaffolds," *Int. J. Biol. Macromol.*, vol. 235, pp. 123769, 2023, doi: 10.1016/j.ijbiomac.2023.123769.
- [29] Y. Srisuwan and Y. Baimark, "Preparation of biodegradable silk fibroin/alginate blend films for controlled release of antimicrobial drugs," *Adv. Mater. Sci. Eng.*, vol. 2013, Article ID 412458, 2013, <https://doi.org/10.1155/2013/412458>.
- [30] M. Makaremi, H. Yousefi, G. Cavallaro, G. Lazzara, C. B. S. Goh, S. M. Lee, A. Solouk, and P. Pasbakhsh, "Safely dissolvable and healable active packaging films based on alginate and pectin," *Polymers (Basel)*, vol. 11, no. 10, pp. 1594, 2019.
- [31] A. Gokhale, "Achieving zero-order release kinetics using multi-step diffusion-based drug delivery," *Pharm. Technol. Eur.*, vol. 38, no. 5, 2014.
- [32] Y. Fu, G. Fodorean, P. Navard, and E. Peuvrel-Disdier, "Study of the partial wetting morphology in polylactide/poly[(butylene adipate)-co-terephthalate]/polyamide ternary blends: case of composite droplets," *Polym. Int.*, vol. 67, no. 10, pp. 1378–1385, 2018, doi: 10.1002/pi.5651.
- [33] Q. Bao, J. Shen, R. Jog, C. Zhang, B. Newman, Y. Wang, S. Choi, and D. J. Burgess, "In vitro release testing method development for ophthalmic ointments," *Int. J. Pharm.*, vol. 526, no. 1-2, pp. 145–156, 2017, doi: 10.1016/j.ijpharm.2017.04.075.
- [34] B. Baert, J. Boonen, C. Burvenich, N. Roche, F. Stillaert, P. Blondeel, J. van Bocxlaer, and B. de Spiegeleer, "A new discriminative criterion for the development of franz diffusion tests for transdermal pharmaceuticals," *J. Pharm. Pharm. Sci.*, vol. 13, no. 2, pp. 218–230, 2010, doi: 10.18433/j3ws33.
- [35] J. F. PJ, K. J. Arun, A. A. Navas, and I. Joseph, "Biomedical applications of polymers—An overview," *Macromolecules*, vol. 28, no. 4, pp. 939–944, 2018.
- [36] F. Cavalieri, A. El Hamassi, E. Chiessi, and G. Paradossi, "Stable polymeric microballoons as multifunctional device for biomedical uses: synthesis and characterization," *Langmuir*, vol. 21, no. 19, pp. 8758–8764, 2005.
- [37] J. C. Middleton and A. J. Tipton, "Synthetic biodegradable polymers as orthopedic devices," *Biomaterials*, vol. 21, no. 23, pp. 2335–2346, 2000.
- [38] R. Waterman, J. Lewis, and K. C. Waterman, "Accelerated stability modeling for peptides: a case study with bacitracin," *AAPS PharmSciTech*, vol. 18, no. 5, pp. 1692–1698, 2017.
- [39] M. Asghari, A. AlizadehDoghikalaey, R. Safari, and A. Arshadi, "The effect of the Z bacitracin on the shelf-life of the silver carp during refrigeration," *Iran. J. food Nutr.*, vol. 3, pp. 31–38, 2011.



## DETERMINING THE OPTIMUM PARKING ANGLES FOR VARIOUS RECTANGULAR-SHAPED PARKING AREAS: A PARTICLE SWARM OPTIMIZATION-BASED MODEL

<sup>1</sup>Ziya ÇAKICI , <sup>2,\*</sup>Abdullah Tahir ŞENSOY 

<sup>1</sup>*İzmir Democracy University, Engineering Faculty, Civil Engineering Department, İzmir, TÜRKİYE*

<sup>2</sup>*Samsun University, Engineering Faculty, Biomedical Engineering Department, Samsun, TÜRKİYE*

<sup>1</sup>[ziya.cakici@idu.edu.tr](mailto:ziya.cakici@idu.edu.tr), <sup>2</sup>[tahir.sensoy@samsun.edu.tr](mailto:tahir.sensoy@samsun.edu.tr)

### *Highlights*

- The developed Particle Swarm Optimization-based model can increase the capacity of parking lots by up to 50% compared to fixed-parking angles.
- The optimum parking angle directly depends on the dimensions of the rectangular-shaped parking lot, which contradicts existing literature.
- The developed model can be applied to all rectangular-shaped parking lots, making it a useful tool for achieving better urban planning and reducing financial costs.



## DETERMINING THE OPTIMUM PARKING ANGLES FOR VARIOUS RECTANGULAR-SHAPED PARKING AREAS: A PARTICLE SWARM OPTIMIZATION-BASED MODEL

<sup>1</sup>Ziya ÇAKICI , <sup>2,\*</sup>Abdullah Tahir ŞENSOY 

<sup>1</sup>İzmir Democracy University, Engineering Faculty, Civil Engineering Department, İzmir, TÜRKİYE

<sup>2</sup>Samsun University, Engineering Faculty, Biomedical Engineering Department, Samsun, TÜRKİYE

<sup>1</sup>[ziya.cakici@idu.edu.tr](mailto:ziya.cakici@idu.edu.tr), <sup>2</sup>[tahir.sensoy@samsun.edu.tr](mailto:tahir.sensoy@samsun.edu.tr)

(Received: 09.05.2023; Accepted in Revised Form: 21.09.2023)

**ABSTRACT:** Reducing financial costs as much as possible through the effective and efficient use of parking areas is an important issue for sustainable urban planning. This can be achieved by optimizing the placement of angles of parking-lots. In this study, to determine the optimum parking angles for rectangular-shaped parking areas, a Particle Swarm Optimization-based model that aims to maximize the capacity of parking areas is developed. In the scope of the study, firstly, 324 parking area scenarios which have different dimensions from each other are created for testing the effectiveness of the model developed. Each scenario is separately analyzed by considering the optimization-based model and fixed-parking angles (0°, 30°, 45°, 60° and 90°) used in parking area planning. In the last step, parking area capacities obtained by applying different parking angles for each scenario and the total parking capacities for all scenarios are compared in detail. Results show that the capacities of parking areas can be increased up to approximately 50% with the model created. Besides, in contrast to existing literature, the findings of this study have proven that the optimum parking angle directly depends on the topology of the land. The model developed can be applied to all rectangular-shaped parking areas to achieve better urban planning.

**Keywords:** Parking Angle, Parking-Lot, Particle Swarm Optimization, Sustainable Urban Planning

### 1. INTRODUCTION

#### 1.1. Background

People can access many things which are useful for themselves by moving from one place to another. These movements generally include different purposes such as work, education, health, travel, entertainment, shopping, etc. The factors of safety, comfort and speed have great importance in these short or long-term travels which are realized to reach the destination. While high-quality travels (safe, comfortable, and fast) make daily life much easier, low-quality travels (unsafe, uncomfortable, and slow) adversely affect road users economically and psychologically [1, 2]. The quality of urban and interurban travel is directly related to the qualifications of the transportation facilities, the integration of transportation systems with each other and/or with the environment, and the structural (physical) properties of existing transportation infrastructures. Hence, it can be said that travel quality can be significantly improved with optimally planned and appropriately designed transportation facilities, transportation systems which are integrated with each other and/or with the environment and the most properly designed transportation infrastructures.

In recent years, the population densities especially in large and medium-sized cities in developed and developing countries show an increasing trend. Therefore, these cities have been rapidly growing and continuously developing. This also triggers an increment in urban travel demands [3]. Since the distances between the origin and destination points of travel are usually long, many road users prefer motorized vehicles (private cars, public transportation vehicles) to reduce their travel times. Therefore, especially in medium and large-sized cities, the number of motorized vehicles has been rapidly increasing day by day.

\*Corresponding Author: Abdullah Tahir ŞENSOY, [tahir.sensoy@samsun.edu.tr](mailto:tahir.sensoy@samsun.edu.tr)

Today, the number of motorized vehicles in the world is about 1.2 billion and by the year 2035, it is expected that this number will exceed 2 billion. This also shows that the increment in the number of vehicles will continue as considerably in the course of time [4, 5]. In general, it can be thought that the increment in the number of motorized vehicles may provide big advantages such as ease of travel and simplifying daily life. But this is not an exactly correct perspective. An increment in the number of motorized vehicles brings along several problems such as traffic congestion, fatal and/or injured traffic accidents, environmental pollution and parking area insufficiencies. Indeed, it is not possible to totally overcome the aforementioned problems. However, these problems can be minimized by taking various precautions and/or by applying some structural strategies. In this context, one of the most applied strategies on highways is also the most appropriate design of transportation infrastructures. Highway transportation infrastructures consist of several components such as roads, bicycle roads, sidewalks, crosswalks, bus stops, and parking lots. While some of these components (roads, bicycle roads, and parking lots) serve the nonmotorized and/or motorized vehicles, the rest (sidewalks, crosswalks, and bus stops) serves the pedestrians. Positive impacts of appropriate designs on urban traffic are proved in many previous studies in the literature many times [6-10].

The vast majority of motorized vehicles (except for motorized vehicles which are used for transporting goods and passengers in urban and interurban) are static over most of the daily timeframe (over 90% of the day) [3]. Therefore, when the increasing number of motorized vehicles is also considered, it can be said that parking area requirements, especially in city centers, show an increasing trend. Especially in medium and large-sized cities, in case of the number of parking space are low and the capacities of the parking area are insufficient, the number of untidy parking along the roadsides also increases. This can adversely affect the continuity and regularity of traffic flows and can cause traffic congestion in certain areas. Possible problems that may occur can be minimized by increasing the number of parking lots, by appropriately designing of parking areas and by effectively using of parking areas. In brief, it can be said that urban traffic circulation can be improved by appropriately designed and optimally planned parking areas. In addition to this, in the case of the charged parking, it should be noted that parking operators may obtain more financial gains by appropriately designed and optimally planned parking areas. When all of these are considered together, it can be concluded that the parking lots have great importance in terms of urbanization, the future of cities and the economy. Hence, especially for the last 30-35 years, many scientific studies on designing, planning, and operating of parking areas have been conducted [11-18].

This study consists of four main parts. In the first part of the study, general information, background and literature review related to parking planning are given. In the second part, parking planning strategies, modeling method as well as PSO-based optimization model which is developed for optimal parking planning are explained in detail. In the third part, the scenarios created for testing the model are described. Besides, analysis results for rectangular-shaped and different-sized parking areas are comprehensively presented and the results are discussed with reference to the literature. In the last part of the study, the general findings of the study are evaluated and a possible future perspective is given.

## 1.2. Literature Review

In the scope of this study, since only the “planning” factor is taken into account, the studies related to “planning of parking lots” are investigated in detail. Some of these studies can be summarized as follows: Bingle et al. suggested a new method to determine optimal size and placement of parking spaces and approach corridors in a car parking lot which is sized 100'×200' in England [19]. As a result, they pointed out that the wasted area can be minimized by using 90° parking angle instead of diagonal parking angles. Chen et al. studied on the determination of optimum parking angle in the large parking lots. At the end of some field studies and mathematical analysis, they stated that the capacities of parking lots can be maximized by using 70° parking angle. Besides, in the scope of the study, the planning with 70° parking angle was compared with the planning with 90° parking angle. They concluded that the planning with 70° parking angle is more appropriate than the planning with 90° parking angle in terms of parking maneuvers and traffic safety [20]. Iranpour and Tung developed a new method to maximize the capacities

of parking lots. It was stated that the parking maneuvers can be made safer and the capacities of parking lot can be increased by applying different parking angles at different regions in a parking area [21]. Brown-West proposed an optimization model for planning and designing of parking lots at campus environments. The effective use of campus lands was aimed with the proposed model. In the scope of the study, various helpful (critical) suggestions were presented to campus planner and university administrators for the planning of the parking lots [22]. Munzir et al., in their study, used linear integer programming method for optimizing the parking lots. The optimization model was created using survey and observation data [23]. As a result, it was indicated that a new user requirement based model for parking space optimization was developed. Robert and Drago focused on the applicability of information technologies which are used for the optimization of parking spaces. Obtained results showed that effective use of capacity in parking areas can be achieved with applied different technologies [24]. Abdullah et al. developed a new mathematical model to maximize the capacity of the parking area which is limited to a certain land. In the scope of the study, three different parking plannings were taken into consideration and then they were compared with each other. As a result, it was pointed out that the capacities of parking areas can be increased by using the model developed [25]. Guo and Guo suggested a new method which considers automatic planning and manual adjustments together for the planning of parking lots in the parking areas. Then, the effectiveness of the suggested method was proved in a sample study [26]. Wang and Yuan, in their study, presented several planning suggestions related to parking lots and parking garages to decision-makers and planners [27]. Abdelfatah and Taha studied on the determination of the optimum angles of parking lots. They used a linear integer programming method for determining the optimum parking angles. In the analyses carried out for three different parking areas, the effects of different parking angles on the capacities of parking areas were determined [28]. Zhao et al. developed a new parking planning method for smart parking systems. In the scope of the study, the parking planning problem was transformed into a kind of linear assignment problem. As a result, it was seen that effective and successful results can be obtained by using the developed model in the planning of the parking lots [29]. Oladejo and Awuley used a linear programming method for the optimization of the parking spaces. At the end of the study, it was pointed out that the user satisfaction level can decrease due to the limited maneuvering area when the parking capacity in a certain area increases [30]. Ramli et al. developed a new approach which maximizes the number of parking lots in a parking area considering different parking angles. In the research, it was determined that parking revenues can be increased over 15% with this new approach [31]. Yang and Huang focused on existing problems related to urban parking planning. Besides, they discussed measures (precautions) which should be applied in order to prevent possible problems. In the scope of the study, the importance of parking lots planning was emphasized [32]. Ramli et al. studied on a new mathematical model for the optimization of triangular-shaped parking lots. They aimed the maximization of the parking capacities by using linear integer programming. Consequently, it was specified that the developed model is an effective and applicable model under certain conditions [33]. Shayrini et al. developed a new model for planning of parking lots in triangular-shaped parking areas. In the research, a linear integer programming method was used to determine the maximum number of parking lots in a certain area. In the scope of the study, obtained results for isosceles and equilateral triangular-shaped parking areas were evaluated and interpreted, separately [34]. Putri et al. studied on the optimization of parking spaces in parallelogram-shaped and right triangle-shaped parking areas. They developed different mathematical models for both type of parking areas. As a result, it was seen that developed models are utilizable and applicable for parking planning [35]. Dianawati and Kristianto focused on the planning of parking lots in a recreational area. In the study, linear integer programming method was used for determining the optimum parking angle and the number of parking lots. As a result, it was specified that parking revenues can be increased and the comfort of recreational area can be improved by using the model suggested [36]. Hasbiyati et al. aimed to optimize parking lots in parallelogram-shaped parking areas considering rectangle and right triangle concept, separately. Obtained results showed that the parking angle of  $90^\circ$  is the most appropriate parking angle for parallelogram shaped parking areas [37]. Yildirim et al. used the cutting-stock formulation for the

planning of a rectangular-shaped university campus parking area. In the study, they aimed to maximize the capacities of stated parking area. At the end of the study, it was seen that the parking capacity can be increased about 15% by using the proposed approach [38].

When the previous studies are investigated carefully, it can be seen that the parking spaces in the parking lots were planned considering constant parking angles (0°, 30°, 45°, 60° and 90°) generally. Similar methods were used in the optimization process in most of these studies. In this study, as a differ from the literature, parking lots in parking areas were optimized considering all angle values between 0° and 90°. In addition, meta-heuristic Particle Swarm Optimization (PSO) algorithm which provides fairly good results in solving of the many engineering problems was preferred as solution method instead of conventional methods.

## 2. MATERIAL AND METHODS

### 2.1. Planning of Parking Lots

In urban planning, one of the most important land-use patterns is also parking lot. Since the activities and mobilities are intense at the regions such as stadiums, airports, terminals, shopping malls, residential areas, and business centers, higher capacity parking areas are needed at these regions (Table 1) [39]. This situation causes an increment in land use in the specified regions and brings about additional land costs. Well-planned parking lots are seen as an important step to minimize stated negations.

**Table 1.** Average parking spaces requirements for some regions

The Type of Confined Area	For each 100 m <sup>2</sup> of Confined Area	
	Average	Limit Values
<b>Bank</b>	5.4	1.8 – 10.8
<b>Terminal</b>	4.8	1.7 – 7.9
<b>Hospital</b>	3.8	1.1 – 8.6
<b>Government Agency</b>	3.6	1.2 – 6.0
<b>Shopping Mall</b>	2.8	1.4 – 5.1
<b>Restaurant</b>	2.1	0.9 – 3.3
<b>Commercial Building</b>	1.5	0.4 – 2.9
<b>Hotel</b>	0.6	0.4 – 1.0

Parking are classified as roadside parking and off-street parking in generally. In the roadside parking lots, users can park their vehicles on the roadsides or parking bays for limited duration or indefinitely. In these type of parking lots, a part of the road is occupied in most of the time. Therefore, traffic congestion can be seen at these areas. Roadside parking lots can be planned considering different parking angles (0°, 30°, 45°, 60° and 90°) [40, 41]. Dimensions of parking spaces for each parking angle are shown in Figure 1 in detail [39].

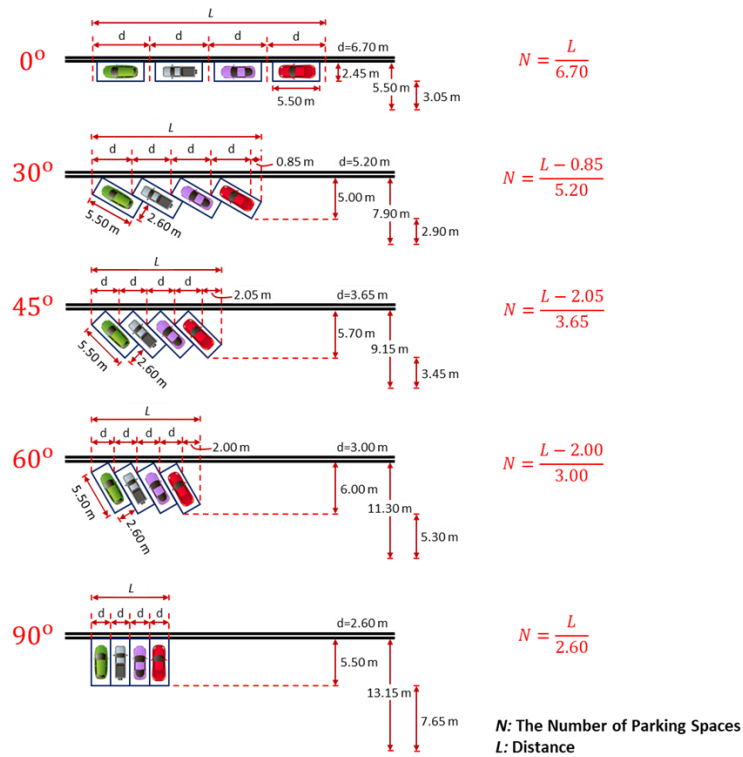
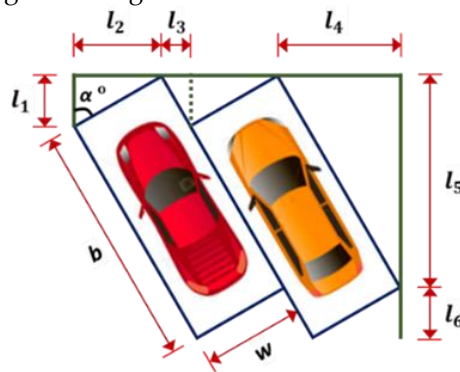


Figure 1. Dimensions of roadside parking spaces for each parking angle [39]

As can be seen from the Figure 1, when the parking angle increases, both the parking capacity and the width of corridor increase. According to this, it is thought that ensuring the balance of parking capacity and land use is quite important issue in parking planning. The calculations of lengths of occupied area in the angled parking planning are given in Figure 2.



$b$  = Length of the parking space

$w$  = Width of the parking space

$\alpha^\circ$  = Parking angle

$$l_1 = w * \cos(\alpha^\circ) ; l_2 = w * \sin(\alpha^\circ)$$

$$l_3 = x_1 * \cot(\alpha^\circ) ; l_4 = b * \cos(\alpha^\circ)$$

$$l_5 = b * \sin(\alpha^\circ) ; l_6 = w * \cos(\alpha^\circ)$$

Figure 2. The calculations of lengths of occupied area in the angled parking planning

Off-street parking spaces (parking lots and parking garages) are the specific areas where users can park their vehicles for a long duration. In these type of parking areas, there is no continuous interaction with urban traffic flows. Therefore, it can be said that off-street parking lots are safer than roadside parking lots. In off-street parking lots, planning strategies like roadside parking lots are applied. In the planning stage, the same values of parking space dimensions and the corridor widths can be used [39, 42, 43].

Two-row parking plans for commonly used different parking angles are depicted in Figure 3. As can be seen from Figure 3, the corridor widths for 0°, 30°, 45°, 60° and 90° are calculated as 3.05, 2.90, 3.45, 5.30 and 7.65, respectively. Besides, when the angle of parking lots increases, the width of parking area decreases and length of parking area increases.

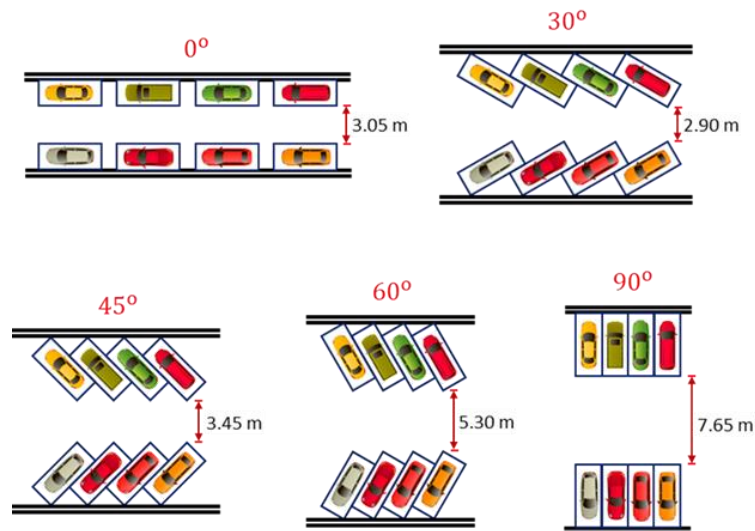


Figure 3. Two-row parking plans for different parking angle

In a parking area, corridor widths directly depend on parking angle as shown in Figure 3. The findings demonstrate that there is not a significant change in corridor widths with the increment of parking angle from 0° to 30°. However, as shown in Figure 4, the for higher parking angle values than 30° the corridor widths remarkably increases.

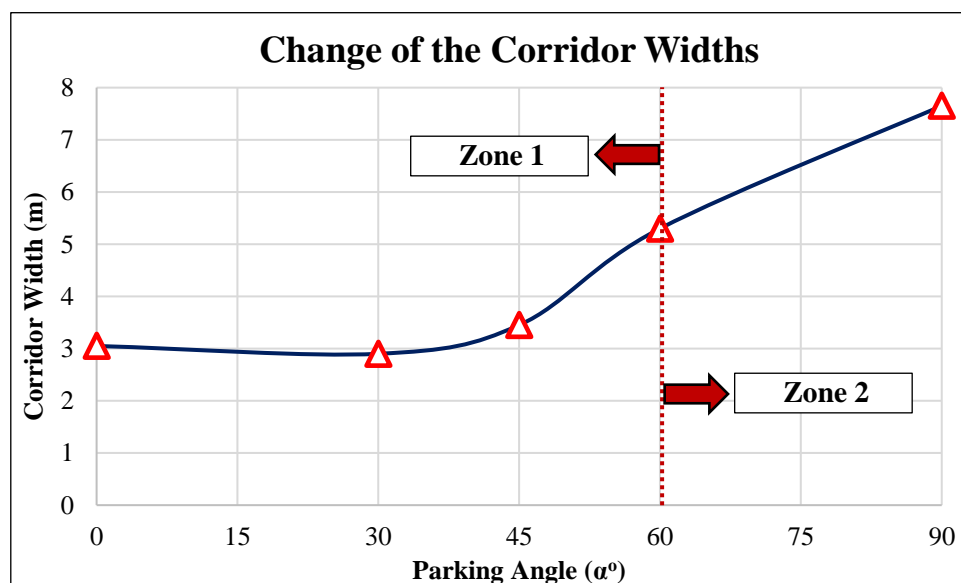


Figure 4. The change of corridor widths depending on the parking angles

As it has been mentioned before, the optimization of parking angles is aimed in the scope of this study. Thus, by using the most appropriate corridor widths for the most used angle values (0°, 30°, 45°, 60° and

90°) in the literature [11, 40, 41], a generalized model for representing all angle values between 0° and 90° and have to be formulated. When the Figure 4 is examined carefully, in case of parking angle is between 0° and 60° it is seen that corridor widths increase in a polynomial way (Zone 1). Since, there is not any data in the literature representing the relationship between the parking angle and the corridor width for any angle value in the range of 60° and 90°, it is assumed that the corridor widths increase as linearly (Zone 2). This assumption is also verified for interpolated values with trigonometric calculations. Therefore, these two zones (Zone 1 and Zone 2) are handled separately in the modelling stage of the corridor widths. For both zones, obtained results from the modelling which made by applying the curve fitting approach are presented in Figure 5 in details.

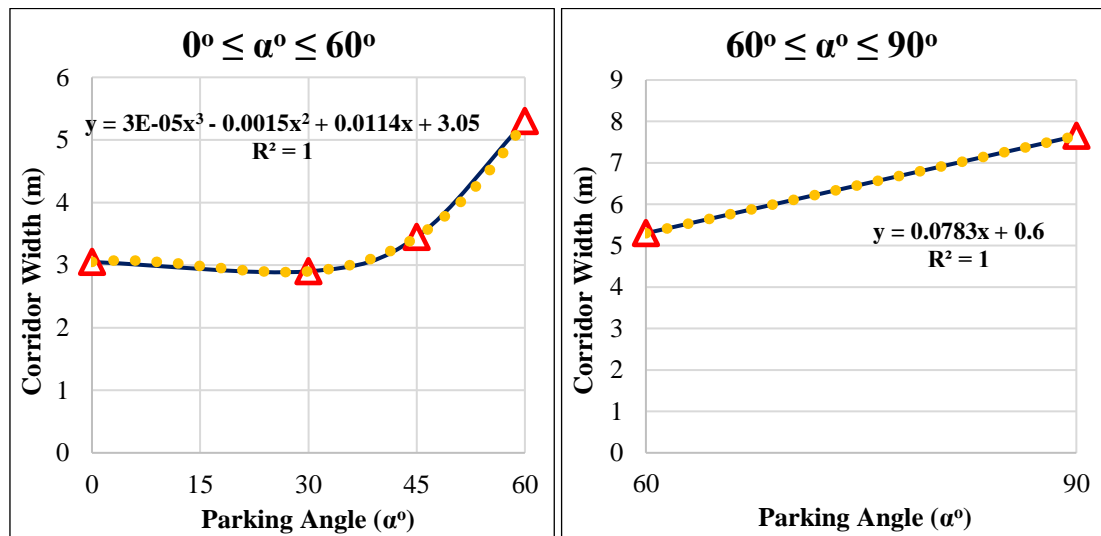


Figure 5. Corridor width modelling depending on the parking angles for both zones

In Figure 5, when the obtained determination coefficient values ( $R^2$ ) for both zones are investigated carefully, it is seen that these values equal to 1. This shows that the variance of dependent variable (corridor width) can be explained by independent variable (parking angle) at high levels. According to this, it can be said that the reliability levels of obtained relations (corridor width-parking angle) are quite high.

In case of parking angle ( $\alpha$ ) is between 0° and 60°, corridor width can be calculated by Equation 1:  
 $CW = 0.00003272 \times (\alpha)^3 - 0.0015278 \times (\alpha)^2 + 0.011389 \times (\alpha) + 3.05$  ..... (1)

In case of parking angle ( $\alpha$ ) is between 60° and 90°, corridor width can be calculated by Equation 2:  
 $CW = 0.0783 \times (\alpha) + 0.60$  ..... (2)

where;  
 $CW$  = Corridor widths in meters,  
 $\alpha$  = Parking angle in degrees.

**2.2. Modeling**

In this part of the study, the maximum number of vehicle ( $F$ ) in a rectangular-shaped parking areas is parametrically defined as a function of the dimensions of the parking lot as follows (Equation 3):

$F = N_1 \times N_2$  ..... (3)

where  $N_1$  and  $N_2$  are the number of vehicles that fit to  $L_1$  (width of the parking area) and  $L_2$  (length of the parking area), respectively.

Here,  $N_1$  and  $N_2$  are determined according to the following equations (Equation 4-20):

**\* for  $N_1$ ;**

➤ **If  $\alpha = 0^\circ$ ;**

$$N_1 = \text{fix}\left(\frac{L_1}{6.7}\right) \dots\dots\dots (4)$$

➤ **Elseif  $0^\circ < \alpha \leq 90^\circ$**

$$N_1 = \text{fix}\left(\left(L_1 - 5.5 \times \cos(\alpha) + \frac{2.6 \times \cos^2(\alpha)}{\sin(\alpha)}\right) / \left(2.6 \times \sin(\alpha) + \frac{2.6 \times \cos^2(\alpha)}{\sin(\alpha)}\right)\right) \dots\dots\dots (5)$$

**\* for  $N_2$ ;**

➤ **If  $\alpha = 0^\circ$ ;**

$$s = \text{fix}\left(\frac{L_2}{7.95}\right) \dots\dots\dots (6)$$

$$n = s \times 7.95 \dots\dots\dots (7)$$

$$t = L_2 - n \dots\dots\dots (8)$$

here  $s$  and  $n$  are the net number of two-row parking and total length used for two-row parking, respectively. Besides,  $t$  is residual length in case of two-row parking.

**If  $t \geq 5.5$**

$$N_2 = 2 \times s + 1 \dots\dots\dots (9)$$

**else**

$$N_2 = 2 \times s \dots\dots\dots (10)$$

➤ **If  $60^\circ > \alpha > 0^\circ$**

$$s = \text{fix}\left(\frac{L_2}{5.5 \times \sin(\alpha)} + 2.6 \times \cos(\alpha) + CW\right) \dots\dots\dots (11)$$

$$n = s \times (CW + (2 \times (5.5 \times \sin(\alpha) + 2.6 \times \cos(\alpha)))) \dots\dots\dots (12)$$

$$t = L_2 - n \dots\dots\dots (13)$$

**If  $t \geq (5.5 \times \sin(\alpha) + 2.6 \times \cos(\alpha) + CW)$ ;**

$$N_2 = 2 \times s + 1 \dots\dots\dots (14)$$

**else**

$$N_2 = 2 \times s \dots\dots\dots (15)$$

➤ **If  $90^\circ \geq \alpha \geq 60^\circ$**

$$s = \text{fix}\left(\frac{L_2}{5.5 \times \sin(\alpha)} + 2.6 \times \cos(\alpha) + CW\right) \dots\dots\dots (16)$$

$$n = s \times (CW + (2 \times (5.5 \times \sin(\alpha) + 2.6 \times \cos(\alpha)))) \dots\dots\dots (17)$$

$$t = L_2 - n \dots\dots\dots (18)$$

**If  $t \geq (5.5 \times \sin(\alpha) + 2.6 \times \cos(\alpha) + CW)$ ;**

$$N_2 = 2 \times s + 1 \dots\dots\dots (19)$$

**else**

$$N_2 = 2 \times s \dots\dots\dots (20)$$

### 2.3. Optimization

Particle Swarm Optimization (PSO) is a nature-inspired stochastic method which is based on mimicking the social learning behavior of birds and fishes [44, 45]. This algorithm has been of interest to scientists searching for optimum parameters for various engineering areas including biomechanics [46], food engineering [47], traffic and transportation engineering [48], etc. In this algorithm, each particle, representing a member of the swarm population, is considered as a feasible solution for the optimization problem. In PSO technique, each particle is characterized by different parameters representing the position ( $x_i$ ) and velocity ( $v_i$ ) of the  $i$ 'th particle in D-dimensional vectors and are expressed as:

$$x_i = (x_{i1}, x_{i2}, \dots, x_{iD}) \dots\dots\dots (21)$$

$$v_i = (v_{i1}, v_{i2}, \dots, v_{iD}) \dots\dots\dots (22)$$

In each iteration, the position and velocity values of the particles are updated according to the following equations:

$$x_i(t + 1) = x_i(t) + v_i(t + 1) \dots\dots\dots (23)$$

$$v_i(t + 1) = wv_i(t) + R_1c_1(P_i - x_i(t)) + R_2c_2(P_g - x_i(t)) \dots\dots\dots (24)$$

where  $w$  represents the inertia coefficient,  $R_1$  and  $R_2$  stand for two distinct, randomly selected values between 0 and 1,  $c_1$  and  $c_2$  represent the individual and social acceleration parameters respectively;  $P_i$  denotes the particle's best individual position encountered so far, and  $P_g$  signifies the best position among all individuals in the swarm. In this study, PSO is simply implemented to parking lot planning problem as follows:

$$\begin{aligned} \max F_{cap} &= f(x_1) \\ \text{s. t.} \\ 90 &\geq x_1 \geq 0 \end{aligned}$$

where  $F_{cap}$  and  $x_1$  denote maximum parking area capacity and parking angle, respectively. To decrease the computational expense and to increase the efficiency of the codes, the master program is linked to 2 slave subroutines. Master program basically includes 4 main steps which are problem definition, defining PSO parameters, calling 1st slave subroutine and storing the results, respectively. In the problem definition section, the optimization problem is defined and connected to the 1st slave subroutine in order to iteratively get the fitness value of each particle. In the 2nd main step, PSO parameters are defined. Individual and social acceleration coefficients ( $c_1$  and  $c_2$ ) are set as 2.00 for both parameters. The inertia coefficient ( $w$ ), the most dominant parameter on convergence characteristics of the algorithm, is defined as linearly decreased in each iteration from the value of 1.00 with a damping coefficient of 0.99. The maximum number of iterations and population size are selected as 100 and 10, respectively. The 3rd section involves calling 2nd slave subroutine. This subroutine initiates the swarm population members by generating a random position and velocity for each particle. After assignment of the initial values of the swarm members, the main iterative loop is run in order to reach the possible global best value. The fitness values evaluated for each particle are stored and compared with its previous ones in order to iteratively update the personal best ( $P_{best}$ ). The global best value is obtained by comparing the  $P_{best}$  with the global best ( $G_{best}$ ) in each iteration. Once the stopping criteria is satisfied, the process terminates and the optimum value is obtained. The last step of the main program is storing the best results obtained and plotting the convergence curve of the process. The outline of the optimization process conducted in this study is given in Figure 6.

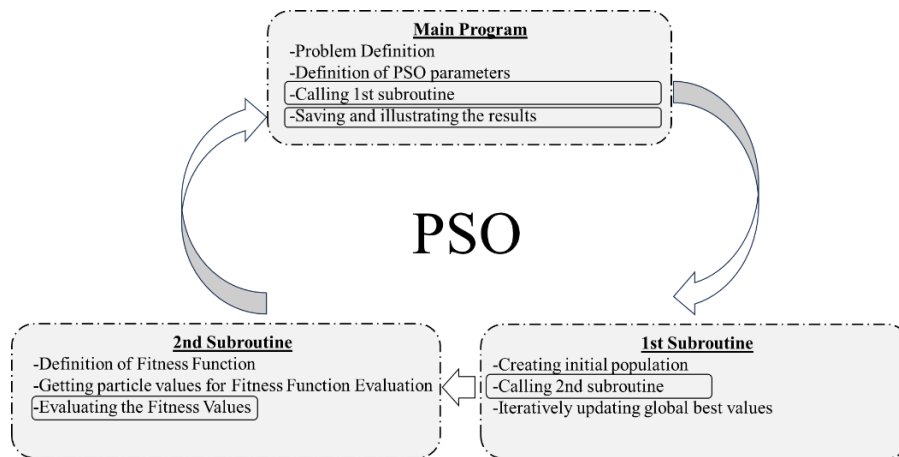


**Figure 6.** The flowchart of the MATLAB optimization process

Using the aforementioned method, the best parking angles in terms of maximum vehicle capacity are separately determined for various rectangular-shaped parking lot cases and are presented in the following section in detail.

### 3. RESULTS AND DISCUSSION

In this part of the study, it is aimed to test the performance of the developed optimization model for different rectangular-shaped parking areas. For this reason, firstly, four different land types are considered for parking scenarios. The minimum parking area is determined by multiplying the minimum width by the minimum length, while the maximum parking area is determined by multiplying the maximum width by the maximum length. Both edges are increased from by 10 meter until the maximum value and 81 sample cases ( $9 \times 9 = 81$ ) are created for each land type. Information related to each land type is given in Table 2.

**Table 2.** Topology of the Land Types

Land Type I (width x length) (m x m)	Land Type II (width x length) (m x m)	Land Type III (width x length) (m x m)	Land Type IV (width x length) (m x m)
15 x 15	20 x 15	15 x 20	20 x 20
15 x 25	20 x 25	15 x 30	20 x 30
...	...	...	...
15 x 95	20 x 95	15 x 100	20 x 100
25 x 15	30 x 15	25 x 20	30 x 20
25 x 25	30 x 25	25 x 30	30 x 30
...	...	...	...
25 x 95	30 x 95	25 x 100	30 x 100
...			
95 x 15	100 x 15	95 x 20	100 x 20
95 x 25	100 x 25	95 x 30	100 x 30
...	...	...	...
95 x 95	100 x 95	95 x 100	100 x 100

Since each land type has 81 sample cases, 324 different parking scenarios were created. The upper and lower limits of the parking lots are defined as 225 m<sup>2</sup> (15 m\*15 m) and 10000 m<sup>2</sup> (100 m\*100 m), respectively. Dimensions of the parking lots for randomly selected scenarios are presented in detail in Table 3.

Table 3. Parking dimensions for different land types

No	Land Type I		Land Area (m <sup>2</sup> )	No	Land Type III		Land Area (m <sup>2</sup> )
	Width (m)	Length (m)			Width (m)	Length (m)	
1	15	15	225	170	85	20	1700
6	65	15	975	176	55	30	1650
14	55	25	1375	184	45	40	1800
26	85	35	2975	192	35	50	1750
33	65	45	2925	207	95	60	5700
41	55	55	3025	216	95	70	6650
58	45	75	3375	225	95	80	7600
64	15	85	1275	231	65	90	5850
75	35	95	3325	238	45	100	4500
81	95	95	9025	243	95	100	9500
No	Land Type II		Land Area (m <sup>2</sup> )	No	Land Type IV		Land Area (m <sup>2</sup> )
	Width (m)	Length (m)			Width (m)	Length (m)	
86	60	15	900	250	80	20	1600
98	90	25	2250	261	100	30	3000
105	70	35	2450	268	80	40	3200
119	30	55	1650	276	70	50	3500
124	80	55	4400	287	90	60	5400
131	60	65	3900	294	70	70	4900
140	60	75	4500	300	40	80	3200
149	60	85	5100	311	60	90	5400
157	50	95	4750	322	80	100	8000
162	100	95	9500	324	100	100	10000

In the second stage, parking capacities have been determined for each scenario in case of different parking angles (0°, 30°, 45°, 60° and 90°) are applied. Thereafter, using the PSO-based optimization algorithm, optimum parking angles and the corresponding vehicle capacities have been determined for each scenario. Subsequently, the results have been comparatively evaluated and some of the comparisons have been shown in Table 4. The maximum parking capacity obtained for each scenario has been marked in green color.

As seen in Table 4, the proposed method based on PSO has provided promising results in terms of parking lot planning. When all the obtained results were carefully examined, it was determined that parking capacities could be increased up to 25% with the optimization-based approach conducted in this study. The scenarios with the highest capacity increment rates for four different land types considered within the scope of the study are detailedly presented in Table 5.

**Table 4.** Parking capacity results for some sample scenarios

No	Land Type	Width (m)	Length (m)	Land Area (m <sup>2</sup> )	Optimum Parking Angle Determined(°)	Parking Capacity (veh)					This study
						0°	30°	45°	60°	90°	
7	I	75	15	1125	45.62	33	28	38	24	28	<b>40</b>
21	I	35	35	1225	60.33	40	30	36	<b>44</b>	39	<b>44</b>
35	I	85	45	3825	57.83	120	96	132	108	128	<b>135</b>
42	I	65	55	3575	72.09	117	96	119	126	125	<b>138</b>
54	I	95	65	6175	52.22	<b>224</b>	180	200	217	216	<b>224</b>
66	I	35	85	2975	69.90	105	72	99	99	104	<b>108</b>
71	I	85	85	7225	69.73	252	192	242	243	256	<b>270</b>
80	I	85	95	8075	86.87	276	224	264	270	<b>320</b>	<b>320</b>
91	II	20	25	500	47.94	12	9	12	12	14	<b>15</b>
97	II	80	25	2000	47.55	<b>66</b>	45	63	52	60	<b>66</b>
114	II	70	45	3150	57.67	100	78	108	88	104	<b>110</b>
116	II	90	45	4050	45.42	130	102	<b>144</b>	116	136	<b>144</b>
126	II	100	55	5500	72.12	182	152	182	192	190	<b>216</b>
132	II	70	65	4550	53.59	160	130	144	154	156	<b>168</b>
150	II	90	85	7650	70.21	273	204	264	261	272	<b>288</b>
160	II	80	95	7600	83.34	253	210	252	260	<b>300</b>	<b>300</b>
175	III	45	30	1350	65.45	42	32	44	42	34	<b>45</b>
178	III	75	30	2250	45.65	77	56	76	72	56	<b>80</b>
192	III	35	50	1750	70.79	<b>60</b>	42	54	55	52	<b>60</b>
194	III	55	50	2750	77.64	96	70	84	85	84	<b>100</b>
198	III	95	50	4750	77.36	168	126	150	155	144	<b>175</b>
211	III	45	70	3150	88.50	102	80	99	112	<b>119</b>	<b>119</b>
233	III	85	90	7650	65.84	264	208	264	270	288	<b>290</b>
241	III	75	100	7500	79.72	264	210	247	264	<b>280</b>	<b>280</b>
254	IV	30	30	900	67.48	28	20	28	27	22	<b>30</b>
260	IV	90	30	2700	45.37	91	68	<b>96</b>	87	68	<b>96</b>
268	IV	80	40	3200	80.62	110	90	105	104	<b>120</b>	<b>120</b>
272	IV	30	50	1500	79.58	48	35	42	45	44	<b>55</b>
279	IV	100	50	5000	55.86	168	133	156	160	152	<b>186</b>
295	IV	80	70	5600	80.94	187	150	189	208	<b>210</b>	<b>210</b>
308	IV	30	90	2700	66.88	88	65	84	90	99	<b>100</b>
314	IV	90	90	8100	66.46	286	221	288	290	306	<b>310</b>

**Table 5.** The scenarios with the highest capacity increment rates for four different land types

No	Land Type	Width (m)	Length (m)	Optimum Parking Angle Determined (°)	Parking Capacity (veh)					Improvement Rates (%)	
					0°	30°	45°	60°	90°		This study
43	I	75	55	72.54	143	112	133	<b>144</b>	140	<b>162</b>	<b>12.50</b>
123	II	70	55	71.96	130	104	126	<b>132</b>	130	<b>150</b>	<b>13.64</b>
191	III	25	50	79.84	<b>36</b>	28	<b>36</b>	35	<b>36</b>	<b>45</b>	<b>25.00</b>
273	IV	40	50	55.43	<b>60</b>	49	<b>60</b>	<b>60</b>	<b>60</b>	<b>72</b>	<b>20.00</b>

In the next stage of the study, the total parking capacities for all land types have been separately determined in case of applying different parking angles for the created parking scenarios. Thereafter, the obtained total parking capacity values were compared with each other by considering the parking angles. The hierarchical structure created for comparisons is shown in Figure 7.

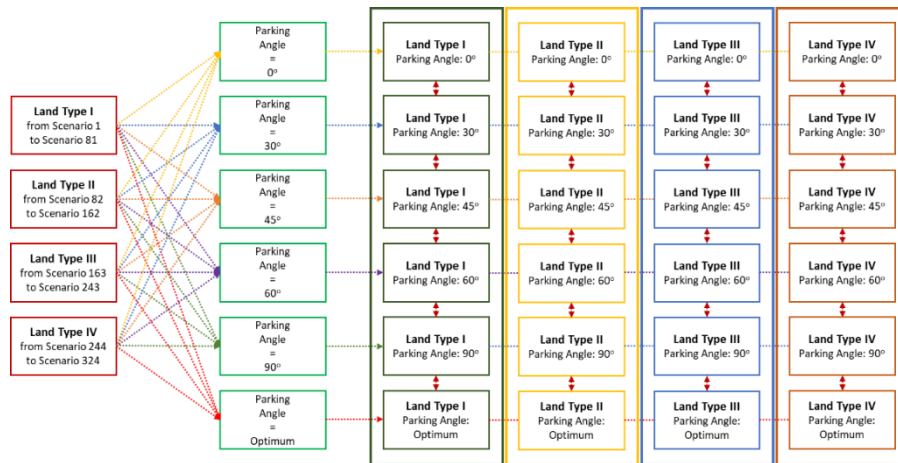


Figure 7. Hierarchical structure created for the comparison of total parking capacities

As can be seen from Figure 7, total capacity comparisons have been made for each land type. For four different land types, the total parking capacities obtained from the analyzes conducted considering different parking angles have graphically presented in Figure 8.

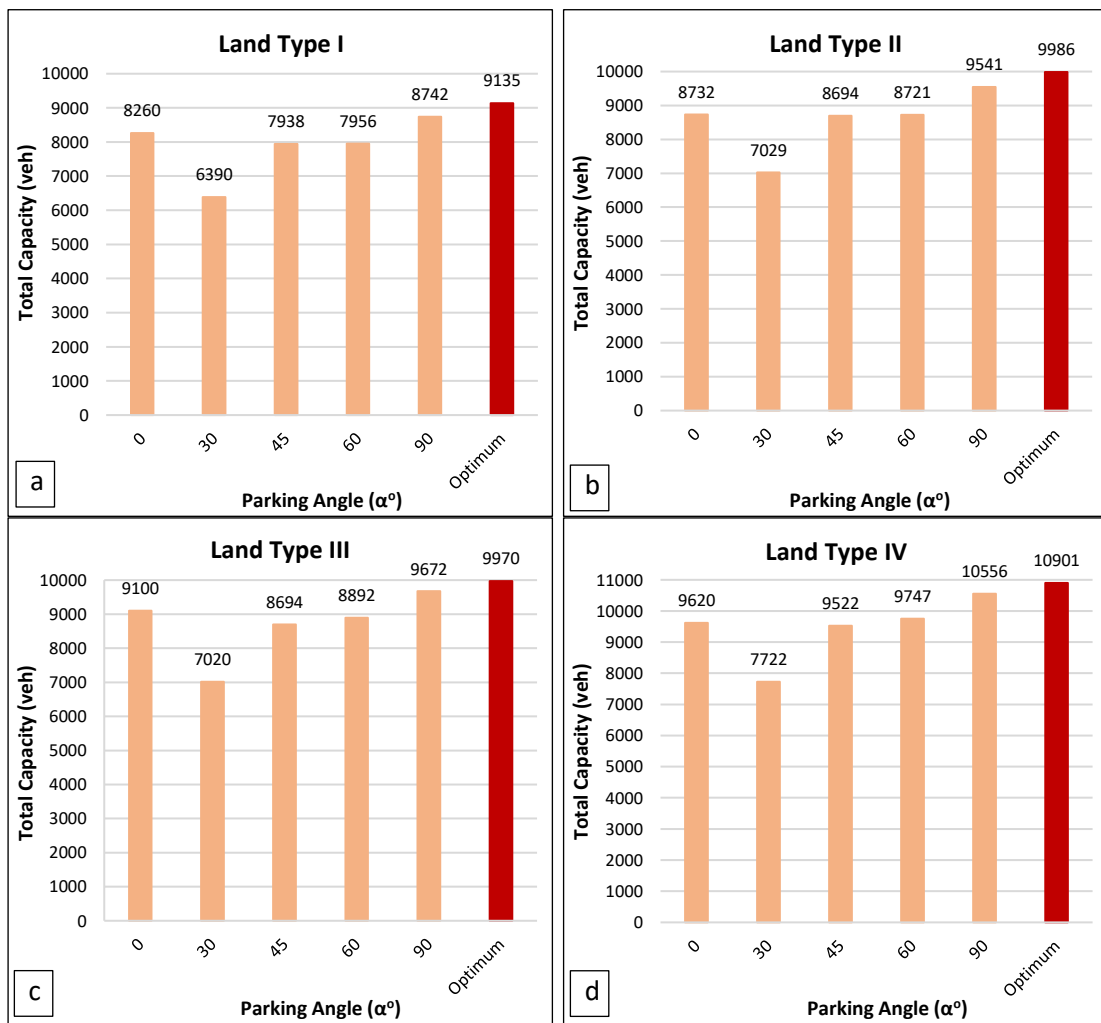


Figure 8. Total parking capacity reached in case of different parking angles are applied for four different land types: (a)Land Type I, (b)Land Type II, (c)Land Type III and (d)Land Type IV

From Figure 8, it can be seen that the highest total parking capacity values for all land types are obtained using the optimization-based approach developed within the scope of this study. Total capacities are determined as 9135, 9986, 9970 and 10901 vehicles for land types I to IV, respectively. Additionally, it has been concluded that the lowest total capacity values are also obtained when the parking angle is 30°. If the parking angle is equal to 90°, the results are closer to the total vehicle capacities obtained by applying the optimum parking angle for parking lot planning.

It has been found that if the parking angles are designed as 0°, 45° and 60°, similar capacity values are obtained. However, it has been determined that these values are lower than the total capacity values obtained when the parking angle is designed as 90°. When Figure 8 is carefully examined, it can be said that the total parking area capacities can be increased by applying the optimum parking angle approach. In the case of optimum parking angle application, the capacity increment rates obtained for each land type compared to fixed parking angle applications are shown in detail in Figure 9.

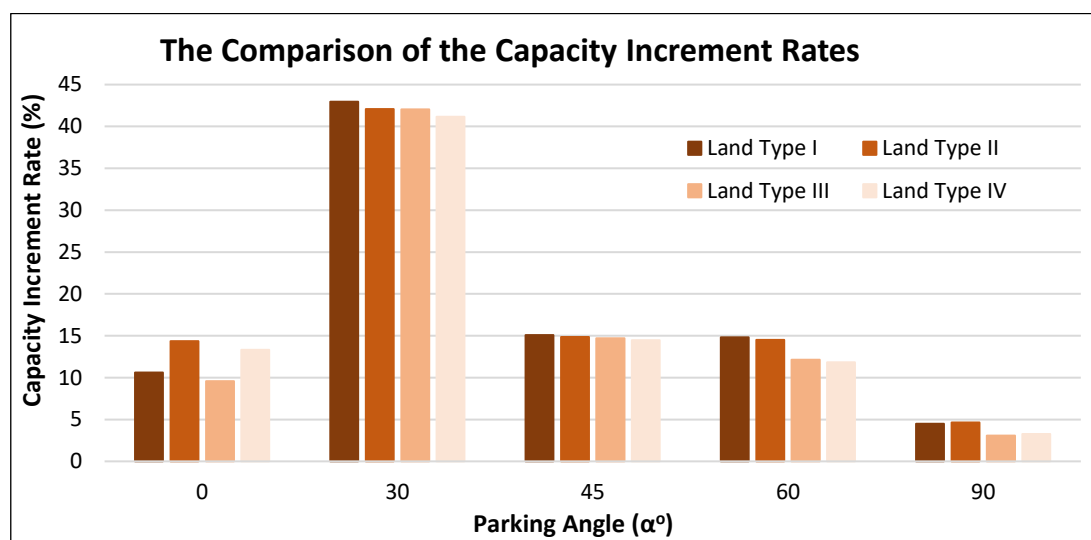
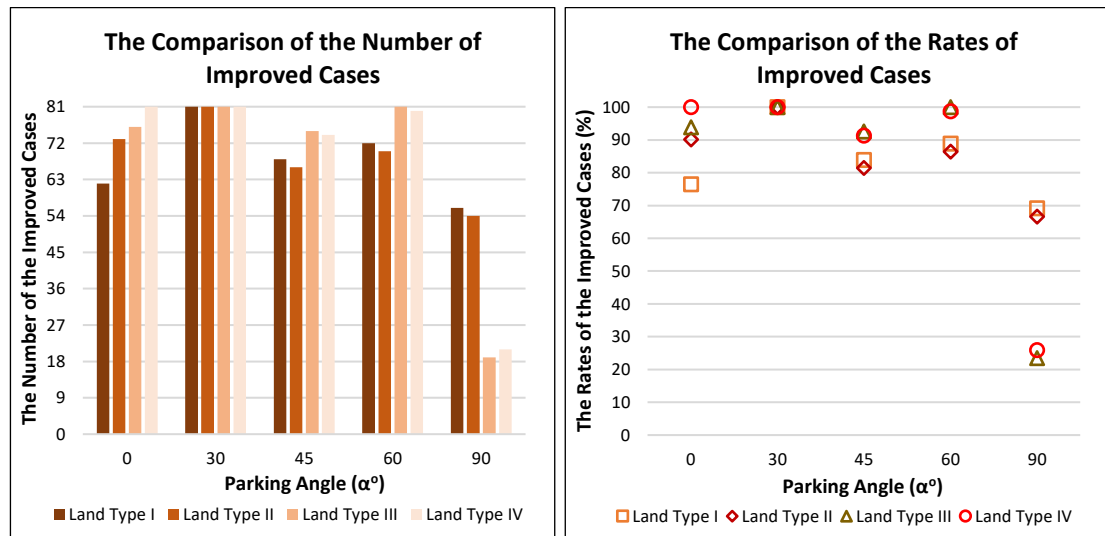


Figure 9. Capacity increment rates compared to fixed parking angle applications in the case of optimum parking angle application

As can be seen from Figure 9, the lowest and highest capacity increments are obtained when the parking angle is applied as 90° and 30°, respectively. If the parking angle is equal to 90°, the capacity increment rates are between 3% and 5%, whereas if the parking angle is equal to 30°, the increase rates range from about 41% to 43%. If the parking angles are equal to 0°, 45° or 60°, the increments in total parking capacities are approximately in the range of 10% to 15%. In addition, when Figure 9 is examined carefully, it can be seen that there is no significant difference in capacity increment rates for the same parking angle values in four different land types.

In this part of the study, for four different land types, the number and percentages of the scenarios whose capacities that can be increased by applying the optimum parking angle instead of fixed parking angles have been determined. At this stage, the obtained results have been evaluated by considering the parking angles and the land types separately. For each land type, instead of fixed parking angles, the scenario numbers and percentages, whose capacities can be increased if the optimum parking angle is applied, are graphically shown in Figure 10.



**Figure 10.** The number and percentages of the improved scenarios if optimum parking angle is applied instead of fixed parking angles

From Figure 10, it can be seen that in all land types, parking capacities can be increased for all scenarios if the optimum parking angle is applied instead of 30° parking angle (worst parking angle for created cases). In the case of 30° parking position, since the vehicles are parked close to horizontal, the horizontal occupancy of the parcel increases. In addition, the vertical occupancy also increases due to higher values of corridor widths. In such cases, it is expected that the parking capacity decreases. In the literature, there are several studies considering the parking angles of 0°, 30°, 45°, 60° and 90°. However, none of these studies suggest 30° parking position due to decrease in total capacity [28, 31, 36]. The results of the current study also verify this information (Figure 8-10). If the optimum parking angle is applied instead of a 90° parking angle, it can be said that the parking capacity can be increased in approximately 70% of the scenarios for Land Type I-II and approximately 25% of the scenarios for Land Type III-IV. Additionally, in all land types, it is seen that the scenario rate, whose capacity can be increased even if the optimum parking angle is applied instead of parking angles of 0° - 45° or 60°, varies between 75% and 100%.

In previous studies, parking lots are generally located considering the fixed parking angles [11, 40, 41]. However, the results of the current study demonstrate that optimizing the parking angles depending on the topology of the parking area has a crucial importance in terms of increasing the parking capacities. Moreover, one can find contradictory results in the literature in terms of determining the optimum parking angle. While some researchers claim that the best parking angle is 90° [19, 37], others argue that it is 70° [20]. However, the findings of this study have proven that the optimum parking angle, which provides maximum parking capacity, directly depends on the dimensions of the parking area (width and length). Therefore, a specific approach should be applied for each parking area and a universal optimum angle can not be offered as done in the aforementioned studies. By using the optimization-based approach, it has been determined that the capacities of the rectangular-shaped car parking areas can be increased up to 25%.

#### 4. CONCLUSIONS

In this study, it is aimed to optimally plan the rectangular-shaped car parking lots. In this context, a new model based on parking angle optimization has been developed in MATLAB using the Particle Swarm Optimization (PSO) algorithm. The effectiveness of the developed model has been tested on 324 scenarios which have different sizes of car parking areas considering the parking capacity criteria. According to the results of all scenarios considered within the scope of the study, total capacity increment rates obtained using the optimum parking angle approach are as follows:

- Approximately 41% to 43%, compared to 30° fixed parking angle;
- Between 10% and 15%, in comparison with the fixed parking angles of 0°, 45° or 60°;
- Between 3% and 5%, compared to the fixed parking angle of 90°.

As stated earlier, in this study, the maximum parking area is limited to 10000 m<sup>2</sup>.

If the maximum parking area is limited to 5000 m<sup>2</sup> using the same parking area examples; total capacity increment rates are as follows:

- Approximately 43% to 47%, compared to 30° fixed parking angle;
- Between 11% and 17%, in comparison with the fixed parking angles of 0°, 45° or 60°;
- Between 5.5% and 6.5%, compared to the fixed parking angle of 90°.

According to these results, it can be concluded that if the maximum parking area is decreased, total capacity increment rates are increased. In all land types considered within the scope of the study, it was concluded that the scenario rate, whose capacity can be increased if the optimum parking angle is applied instead of fixed parking angles, varies between approximately 25% and 100%.

In summary, it can be stated that, with the developed optimization-based approach, the parking lots can be optimally planned in order to efficiently use the parking areas as much as possible. It is thought that the developed approach may also provide an opportunity to reduce the high budgets allocated for parking areas. As mentioned earlier, this study covers only the planning of rectangular-shaped parking lots. In future studies, it is aimed to consider different land topologies (trapezoidal, triangular, etc.) and to develop new planning models for these land types.

#### **Declaration of Ethical Standards**

Authors declare to comply with all ethical guidelines, including authorship, citation, data reporting, and original research publication.

#### **Credit Authorship Contribution Statement**

Z. CAKICI: Methodology, Conceptualization, Resources, Investigation, Writing - review & editing, Supervision.

A. T. ŞENSOY: Methodology, Conceptualization, Resources, Investigation, Writing - review & editing, Supervision.

#### **Declaration of Competing Interest**

The authors declare that they have no known competing financial interests or personal relationships that could have appeared to influence the work reported in this paper.

#### **Funding / Acknowledgements**

No funding received.

#### **Data Availability**

The dataset generated during the current study are available from the corresponding author on reasonable request.

## REFERENCES

- [1] F. Dion, H. Rakha, and Y. S. Kang, "Comparison of delay estimates at under-saturated and over-saturated pre-timed signalized intersections," (in English), *Transport Res B-Meth*, vol. 38, no. 2, pp. 99-122, Feb 2004, doi: 10.1016/S0191-2615(03)00003-1.
- [2] W. Xu and L. Yang, "Evaluating the urban land use plan with transit accessibility," *Sustainable Cities and Society*, vol. 45, pp. 474-485, 2019/02/01/ 2019, doi: <https://doi.org/10.1016/j.scs.2018.11.042>.
- [3] Z. Cakici and Y. S. Murat, "A Differential Evolution Algorithm-Based Traffic Control Model for Signalized Intersections," (in English), *Adv Civ Eng*, vol. 2019, Dec 21 2019, doi: Artn 7360939 10.1155/2019/7360939.
- [4] H. Ceylan, O. Baskan, and C. Ozan, "Modeling and Forecasting Car Ownership Based on Socio-Economic and Demographic Indicators in Turkey," (in English), *Tema*, pp. 47-66, 2018, doi: 10.6092/1970-9870/5452.
- [5] A. Zerouala, F. Harrou, Y. Sun, and N. Messai, "Monitoring road traffic congestion using a macroscopic traffic model and a statistical monitoring scheme," (in English), *Sustainable Cities and Society*, vol. 35, pp. 494-510, Nov 2017, doi: 10.1016/j.scs.2017.08.018.
- [6] W. K. Alhajyaseen and H. Nakamura, "Design criteria for crosswalk width and position at signalized intersections," *Journal of Civil Engineering and Architecture*, vol. 6, no. 6, pp. 844-857, 2012.
- [7] M. M. Aydin, "The Investigation of Geometric Indiscipline at Urban Intersections by Optimizing," PhD, Akdeniz University, Institute of Natural and Applied Sciences, 2017.
- [8] A. A. Ceder, M. Butcher, and L. Wang, "Optimization of bus stop placement for routes on uneven topography," *Transportation Research Part B: Methodological*, vol. 74, pp. 40-61, 2015.
- [9] R. Mauro and F. Branco, "Comparative Analysis of Compact Multilane Roundabouts and Turbo-Roundabouts," (in English), *J Transp Eng-Asce*, vol. 136, no. 4, pp. 316-322, Apr 2010, doi: 10.1061/(Asce)Te.1943-5436.0000106.
- [10] M. Mesbah, R. Thompson, and S. Moridpour, "Bilevel optimization approach to design of network of bike lanes," *Transportation research record*, vol. 2284, no. 1, pp. 21-28, 2012.
- [11] S. HALDENBİLEN, Y. Ş. MURAT, N. BAYKAN, and N. MERİÇ, "Parking problems in cities: Sample of Denizli," 1999.
- [12] M. I. Idris, Y. Leng, E. Tamil, N. Noor, and Z. Razak, "Car park system: A review of smart parking system and its technology," *Information technology journal*, vol. 8, no. 2, pp. 101-113, 2009.
- [13] J. Parmar, P. Das, and S. M. Dave, "Study on demand and characteristics of parking system in urban areas: A review," *Journal of Traffic and Transportation Engineering (English Edition)*, vol. 7, no. 1, pp. 111-124, 2020.
- [14] P. Šeba, "Parking in the City," *Acta Physica Polonica A*, vol. 112, no. 4, pp. 681-690, 2007.
- [15] M. Stubbs, "Car parking and residential development: sustainability, design and planning policy, and public perceptions of parking provision," *Journal of Urban Design*, vol. 7, no. 2, pp. 213-237, 2002.
- [16] W. Young, R. G. Thompson, and M. A. P. Taylor, "A review of urban car parking models," *Transport Reviews*, vol. 11, no. 1, pp. 63-84, 1991/01/01 1991, doi: 10.1080/01441649108716773.
- [17] M. Yun, Y. Lao, Y. Ma, and X. Yang, "Optimization model on scale of public parking lot considering parking behavior," in *Logistics: The emerging frontiers of transportation and development in China*, 2009, pp. 2692-2699.
- [18] X. Zhao, K. Zhao, and F. Hai, "An algorithm of parking planning for smart parking system," in *Proceeding of the 11th World Congress on Intelligent Control and Automation*, 2014: IEEE, pp. 4965-4969.
- [19] R. Bingle, D. Meindertsma, W. Oostendorp, and G. Klaasen, "Designing the optimal placement of spaces in a parking lot," *Mathematical Modelling*, vol. 9, no. 10, pp. 765-776, 1987.

- [20] C. S. Chen and P. Schonfeld, "Optimum stall angle for large parking lots," *Journal of transportation engineering*, vol. 114, no. 5, pp. 574-583, 1988.
- [21] R. Iranpour and D. Tung, "Methodology for optimal design of a parking lot," *Journal of transportation engineering*, vol. 115, no. 2, pp. 139-160, 1989.
- [22] O. G. Brown-West, "Optimization model for parking in the campus environment," *Transportation research record*, vol. 1564, no. 1, pp. 46-53, 1996.
- [23] S. Munzir, M. Ikhsan, and Z. Amin, "Linear programming for parking slot optimization: A case study at Jl. T. Panglima Polem Banda Aceh," in *Proceedings of the 6th IMT-GT Conference on Mathematics, Statistics and its Applications*, 2010, pp. 462-472.
- [24] M. Robert and P. Drago, "APPLICABILITY OF INFORMATION TECHNOLOGIES IN PARKING AREA CAPACITY OPTIMIZATION," *Interdisciplinary Management Research*, vol. 6, 2010.
- [25] K. Abdullah, N. H. Kamis, N. F. N. Azahar, S. F. Shariff, and Z. C. Musa, "Optimization of the parking spaces: A case study of dataran mawar, UiTM Shah Alam," in *2012 IEEE Colloquium on Humanities, Science and Engineering (CHUSER)*, 2012: IEEE, pp. 684-687.
- [26] C. Guo and P. Guo, "Research on parking space optimal design method in parking lots," *Advanced Science Letters*, vol. 11, no. 1, pp. 698-701, 2012.
- [27] R. Wang and Q. Yuan, "Parking practices and policies under rapid motorization: The case of China," *Transport Policy*, vol. 30, pp. 109-116, 2013.
- [28] A. S. Abdelfatah and M. A. Taha, "Parking capacity optimization using linear programming," *Journal of traffic and logistics engineering*, vol. 2, no. 3, 2014.
- [29] C. Zhao, S. Li, W. Wang, X. Li, and Y. Du, "Advanced parking space management strategy design: An agent-based simulation optimization approach," *Transportation Research Record*, vol. 2672, no. 8, pp. 901-910, 2018.
- [30] N. Oladejo and B. D. Awuley, "Application of Linear Programming in optimization of parking slot: A case study of Tamale-Bolgatanga lorry station in Ghana," *International Journal of Emerging Technology and Advanced Engineering*, vol. 6, no. 11, pp. 147-154, 2016.
- [31] M. Ramli, D. P. Sary, and V. Halfiani, "Optimization model of parking charge and income using Lagrange multiplier method," in *AIP Conference Proceedings*, 2016, vol. 1775, no. 1: AIP Publishing LLC, p. 030034.
- [32] S. Yang and L. Huang, "Research on planning and management of urban parking lot—taking Hangzhou as an example," *Current Urban Studies*, vol. 5, no. 4, pp. 379-386, 2017.
- [33] M. Ramli, T. Sundari, and V. Halfiani, "Mathematical optimization model of parking capacity for parking area in triangular shape," in *2018 International Conference on Electrical Engineering and Informatics (ICELTICs)*, 2018: IEEE, pp. 164-167.
- [34] I. Syahrini, T. Sundari, T. Iskandar, V. Halfiani, S. Munzir, and M. Ramli, "Mathematical model of parking space unit for triangular parking area," in *IOP Conference Series: Materials Science and Engineering*, 2018, vol. 300, no. 1: IOP Publishing, p. 012012.
- [35] W. Putri, I. Hasbiyati, and M. D. H. Gamal, "Optimization of Parking Lot in the Forms of Parallelogram and Right Triangle for Cars and Motorbikes," *vol*, vol. 4, pp. 64-71, 2019.
- [36] F. Dianawati and J. Kristianto, "Rest Area Parking Design Using Integer Linear Programming," in *Proceedings of the 2019 5th International Conference on Industrial and Business Engineering*, 2019, pp. 218-222.
- [37] I. Hasbiyati, W. Putri, and A. Adnan, "Parking lot optimization in parallelogram using the concept area of rectangular and right triangle," *Pure and Applied Mathematics Journal*, vol. 8, no. 4, pp. 77-82, 2019.
- [38] G. YILDIRIM, B. YILDIRIM, and B. SATIR, "Design of a Rectangular Parking Lot Using a Cutting-Stock Formulation," *Cankaya University Journal of Science and Engineering*, vol. 16, no. 1, pp. 1-16, 2019.
- [39] A. Tunc, *Traffic Engineering and Its Applications 1st edition*. Ankara: Asil Yay. Dag. Ltd. Şti., 2003.

- [40] C. Cicek, "Investigation of Applicability of New Technologies Used in the Parking Lots in Turkey," MSc, Institute of Natural and Applied Sciences, Eskisehir Osmangazi University, 2015.
- [41] M. Ozen, "Parking Planning and Management in Small Cities," MSc Yildiz Technical University, İstanbul, 2014.
- [42] J. D. Edwards, *Transportation planning handbook*. Prentice Hall, 1992.
- [43] M. Özdirim, *Trafik mühendisliği*. T.C. Bayındırlık ve İskan Bakanlığı Karayolları Genel Müdürlüğü, 1994.
- [44] R. Eberhart and J. Kennedy, "Particle swarm optimization," in *Proceedings of the IEEE international conference on neural networks*, 1995, vol. 4: Citeseer, pp. 1942-1948.
- [45] M. H. Amini, M. P. Moghaddam, and O. Karabasoglu, "Simultaneous allocation of electric vehicles' parking lots and distributed renewable resources in smart power distribution networks," *Sustainable cities and society*, vol. 28, pp. 332-342, 2017.
- [46] A. T. Şensoy, I. Kaymaz, and Ü. Ertaş, "Development of particle swarm and topology optimization-based modeling for mandibular distractor plates," *Swarm and Evolutionary Computation*, vol. 53, p. 100645, 2020.
- [47] A. T. Şensoy, H. İspirli, and E. Dertli, "Determining the optimum model parameters for oligosaccharide production efficiency using response surface integrated particle swarm optimization method: an experimental validation study," *Preparative biochemistry & biotechnology*, vol. 50, no. 8, pp. 820-826, 2020.
- [48] H. Zhao, G. Han, and X. Niu, "The signal control optimization of road intersections with slow traffic based on improved PSO," *Mobile Networks and Applications*, vol. 25, pp. 623-631, 2020.

## ANALYSIS OF SPATIAL AND TEMPORAL VARIABILITY OF AEROSOL OPTICAL DEPTH OVER KARABUK USING MODIS

<sup>1,\*</sup> Duygu ARIKAN , <sup>2</sup> Ferruh YILDIZ 

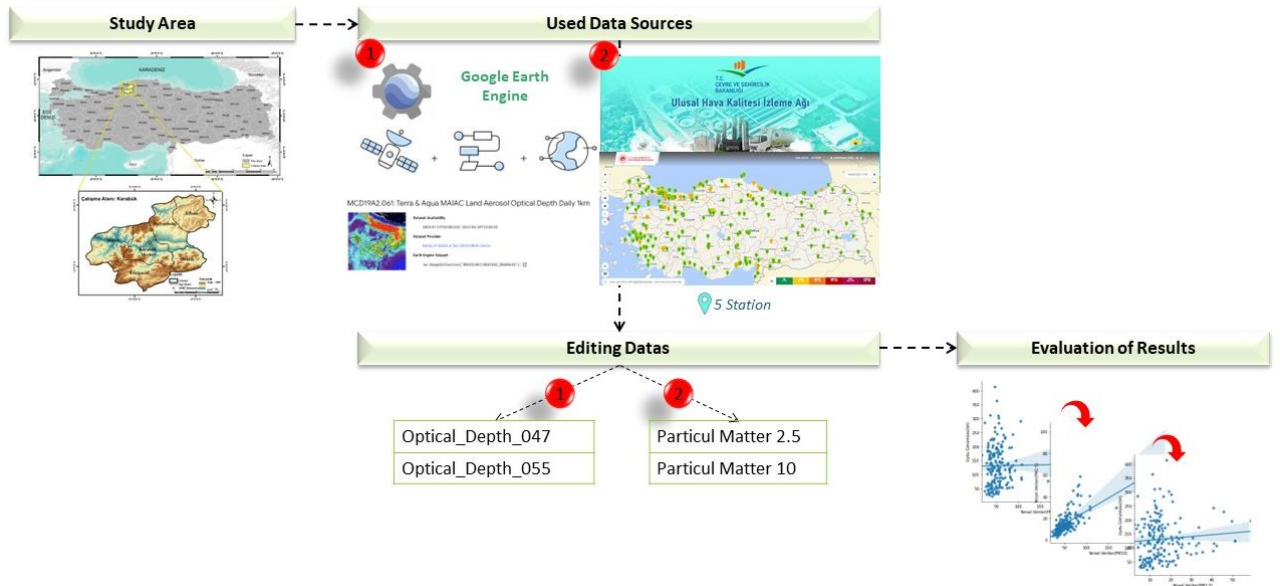
Konya Technical University, Engineering and Natural Science Faculty, Geomatics Engineering, Konya,  
TÜRKİYE

<sup>1</sup> [darikan@ktun.edu.tr](mailto:darikan@ktun.edu.tr), <sup>2</sup> [fyildiz@ktun.edu.tr](mailto:fyildiz@ktun.edu.tr)

### Highlights

- Investigation of aerosol optical depth from ground-based stations and satellite images, analysis and evaluation of results
- Positional examination of blue and green land surface bands from MODIS satellite
- Temporal analysis of PM2.5 and P10 data from National Air Quality Monitoring Stations

### Graphical Abstract (Optional)



Flowchart



## ANALYSIS OF SPATIAL AND TEMPORAL VARIABILITY OF AEROSOL OPTICAL DEPTH OVER KARABUK USING MODIS

<sup>1,\*</sup> Duygu ARIKAN , <sup>2</sup> Ferruh YILDIZ 

*Konya Technical University, Engineering and Natural Science Faculty, Geomatics Engineering, Konya, TÜRKİYE*

<sup>1</sup> [darikan@ktun.edu.tr](mailto:darikan@ktun.edu.tr), <sup>2</sup> [fyildiz@ktun.edu.tr](mailto:fyildiz@ktun.edu.tr)

(Received: 27.07.2023; Accepted in Revised Form: 24.09.2023)

**ABSTRACT:** The concept of aerosol refers to the combination of microscopic solid or liquid particles present in the atmosphere along with a mixture of gases. These particles are suspended in the air at different sizes and are evaluated based on their ability to scatter or absorb light, which is quantified through a measurement known as aerosol optical depth. These particles' quantities are determined using specialized devices, commonly referred to as "aerosol optical depth meters" or "optical thickness meters." Additionally, through remote sensing technology, aerosol optical depth can also be measured via satellites.

In this study, aerosol optical depth has been examined temporally and spatially in the Karabük province for 2022. For this aim, data from National Air Quality Monitoring Stations (NAQMS) situated nationwide was employed, along with MODIS satellite images. Data from five stations in Karabük province, namely Kardemir1, Kardemir2, Tören Alanı, 75.yıl, and Safranbolu, were used for temporal analysis, while satellite imagery was used for spatial analysis. The relationship between aerosol optical depths derived from MODIS satellite data using green and blue band information and station data was investigated. As a result, a 99% positive correlation was found between the two bands obtained from the MODIS satellite, and a significant correlation was observed between ground-based particulate matter 2.5 (PM<sub>2.5</sub>) and particulate matter 10 (PM<sub>10</sub>) data. Data from the Tören Alanı station, which had a higher amount of data (357 days) compared to other stations, was used to determine this correlation. It was found that there was an 86.35% positive correlation among particulate matters. A moderate correlation was also identified between ground-based data and aerosol optical depth obtained from satellite imagery.

**Keywords:** *Aerosol optical depth, Air quality, Google earth engine, MODIS sensor, Particulate matter*

### 1. INTRODUCTION

Within the Earth's atmosphere, diverse gases exist in various ratios. Moreover, aerosols, formed by the suspension of solid and liquid particles in a gaseous phase, are also present. [1]. Aerosols with particle sizes ranging from 2.5 to 10 µm are commonly used as a parameter to assess air quality. High aerosol optical depth indicates increased particulate matter pollution in the air. These particles can originate from various natural or human activities and become mixed into the atmosphere [2]. For instance, natural sources include volcanic eruptions [3], forest fires [4, 5, 6], soil or desert dust [7, 8]. At the same time, human-induced factors comprise industrial activities [9], emissions from vehicles [10], and the combustion of fuels used for heating in homes [11].

Various reasons lead to forming these tiny particles, which can linger in the atmosphere for long periods and be transported in different directions by the wind [12, 13]. With sizes ranging from a few nanometers to a few micrometers, these structures can cause short-term effects such as nasal and eye irritation in the human body, and they can also penetrate deep into the lungs [14]. As a result, they can reduce visibility. These tiny particles also impact on lung function, leading to respiratory problems such as respiratory tract diseases [15]. Additionally, changes in aerosols in the air can influence the heating and cooling processes, altering the thermal state of the atmosphere. This has contributed to the recent changes we have been experiencing in the climate [16]. Aerosols directly and indirectly, affect regional and global

\*Corresponding Author: Duygu ARIKAN, [darikan@ktun.edu.tr](mailto:darikan@ktun.edu.tr)

climate change [17-19]. Therefore, monitoring air quality and taking necessary measures are essential.

Turkey's Ministry of Environment, Urbanization, and Climate Change have established national air quality monitoring stations in urban centers, industrial areas, and regions with heavy transportation lines to achieve this goal. As of 2022, there are a total of 365 stations throughout Turkey [20]. The air quality index is calculated using data obtained from these stations, which includes measurements of particulate matter (PM<sub>10</sub>, PM<sub>2.5</sub>), carbon monoxide (CO), sulfur dioxide (SO<sub>2</sub>), nitrogen dioxide (NO<sub>2</sub>), and ozone (O<sub>3</sub>). Additionally, free access to this data is provided through a website [21]. However, there are some limitations in ground-based observation data due to deficiencies and the limited number of stations in certain locations. Insufficient station points make determining air quality over a large area challenging. While the number of stations can be increased, it is not a definitive or cost-effective solution.

In addition to ground-based stations, remote sensing technology allows the detection and monitoring of aerosols in the atmosphere through Aerosol Optical Depth (AOD) measurements using various satellites [22]. Satellites such as The Moderate Resolution Imaging Spectroradiometer (MODIS) Terra and Aqua, Ozon Monitoring Instrument (OMI Aura), Visible Infrared Imaging Radiometer Suite (VIIRS Suomi NPP), and Sentinel-5P (TROPOMI) are used for this purpose. The Sentinel-5 TROPOMI satellite is preferred for the detection and monitoring of various gases in the atmosphere using satellite imagery. The preferred satellite for the detection and monitoring of various gases in the atmosphere, as well as for examining NO<sub>2</sub> and CO emissions in a metropolitan city [23], establishing the relationship between CO and NO<sub>2</sub> pollutants in the Western Black Sea region using the UV\_AER index [24], investigating the health impact of CO emissions in the Iran region [25], evaluating NO<sub>2</sub> and CO pollutants in terms of geography and population [26], determining the temporal and spatial distribution of CH<sub>4</sub>, NO<sub>2</sub>, O<sub>3</sub>, and CO emissions and identifying factors contributing to their increase in pollution [27] in various studies, is the Sentinel-5 satellite. For aerosol optical depth data, the Terra and Aqua satellites of the MODIS satellite system, which provide daily data, are preferred [28]. This satellite is preferred due to its proven effectiveness in providing global and regional results [29, 30].

This study obtained aerosol optical depth (AOD) data for 2022 in Karabük, one of Turkey's significant iron and steel industry cities. The aerosol optical values in Karabük were analyzed both spatially and temporally. For this purpose, data from five stations located within the region (Kardemir1, Kardemir2, Tören Alanı, 75.yıl, and Safranbolu) were used, which were established to monitor air quality within the country. Additionally, MODIS satellite images were used to examine aerosol values in other parts of the region. The Terra and Aqua systems were chosen due to their ability to provide data twice a day and their common usage in the literature. The acquisition and processing of satellite images were done using the Google Earth Engine (GEE) platform. Both types of data were analyzed, and their results were compared. The aim of this study is to analyze and interpret air quality not only on a point basis but also spatially. In this context, the sources responsible for the increase in pollution levels can be identified, or it can contribute to the more effective management of air quality.

## 2. MATERIAL AND METHODS

### 2.1. Study Area

The study area is located in northern Turkey's Western Black Sea region. It focuses explicitly on the province of Karabük, situated at an elevation of 270 meters above sea level (Figure 1). Based on the data from the address-based population registration system as of December 31, 2021, the population of Karabük is 249,287. The province's largest settlement and central district is Karabük, and the other districts include Eflani, Eskipazar, Ovacık, Safranbolu, and Yenice [31]. The historical, natural beauty and cultural architecture make the province rich, with its historic houses in the Safranbolu district listed as a UNESCO World Heritage site. Moreover, economically speaking, Karabük is one of Turkey's significant provinces in terms of industry. It houses several factories and industrial facilities, primarily focused on steel, mining, and iron-steel sectors. Establishing the first facilities in 1937 transformed the province into an industrial city. The data and workflow diagram used in the study are given in Figure 2.

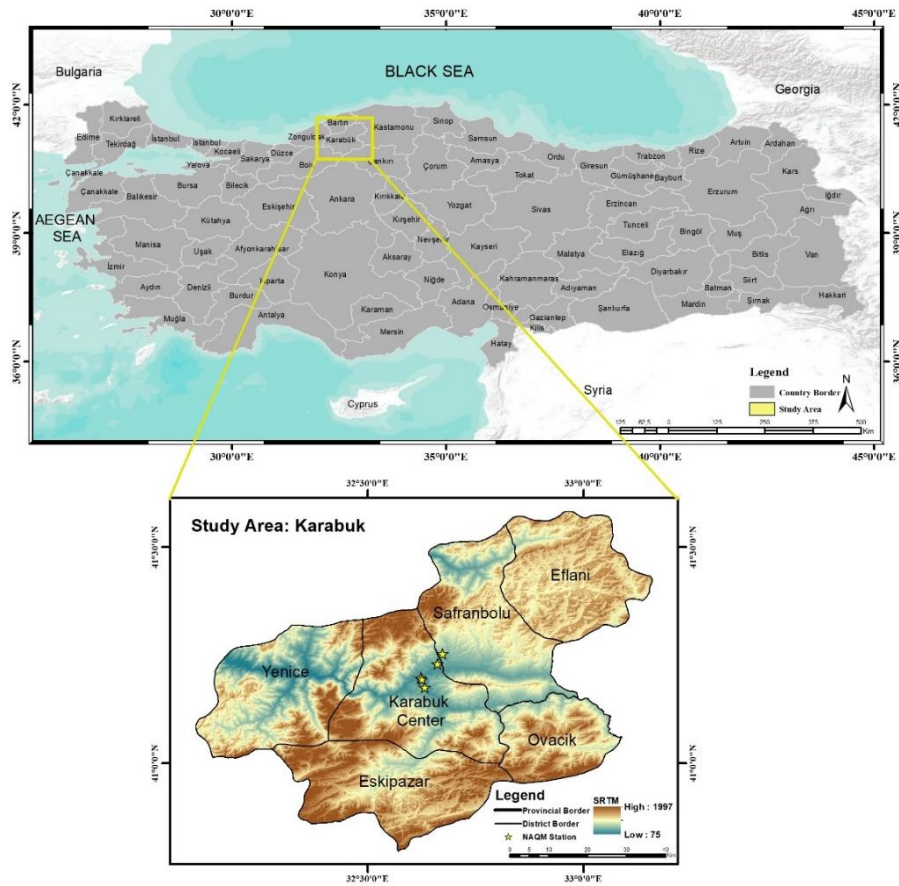


Figure 1. Using SRTM-DEM, visual representations of the study area, Karabuk, and the ground stations are presented

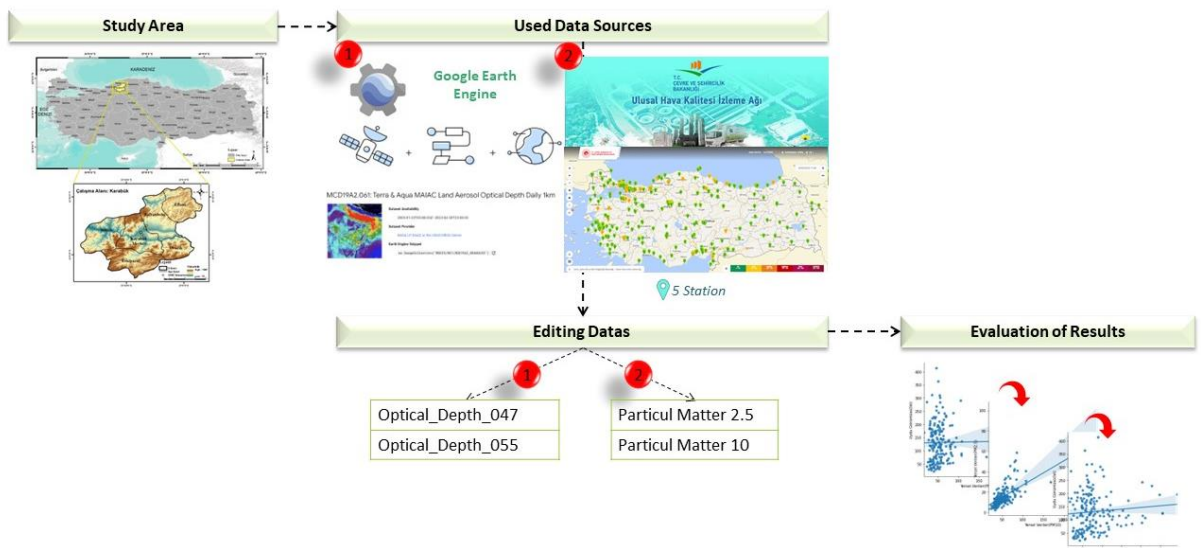


Figure 2. Work-flow diagram.

2.2. Used Data

Aerosol optical depth (AOD) is a parameter used to gauge the extent to which aerosols in the atmosphere scatter or absorb light of a particular wavelength along a given path. As it is a unitless

quantity, it is denoted by the symbol " $\tau$ " in the literature [32, 33]. Typically, AOD values range between 0 and infinity. These values are associated with the particulate matter present in vertical columns of the atmosphere. Therefore, to interpret the atmospheric pollution, it is expressed that this value varies between 0 and 1. AOD values approaching zero (0) indicate a low amount of aerosols, representing a clean atmosphere in terms of particles. On the other hand, AOD values approaching one (1) show a high amount of aerosols, meaning a layer of heavily polluted atmosphere.

AOD can be determined using specially established ground-based stations. For this purpose, 365 stations have been installed within the boundaries of our country. Initially, in 2005, only sulfur dioxide ( $\text{SO}_2$ ) and PM10 particulate matter data were collected, but later on, data for ozone ( $\text{O}_3$ ), carbon monoxide (CO), nitrogen dioxide ( $\text{NO}_2$ ), and 2.5  $\mu\text{m}$  particulate matter were also collected. The amount of pollutants is measured and recorded on an hourly and daily basis, and the data is shared. Through these stations, the levels of air pollution in different regions of Turkey can be monitored and tracked. National and international regulations have set specific limits for the quantity of pollutants in the air. Our legislation aims to achieve the air quality standards specified by the European Union. desired not to exceed the pollutant criteria set for 2019 and 2024 [34]. When these limits are exceeded, or the established threshold levels are reached, necessary measures and precautions are taken to reduce pollution [35].

AOD can be measured using ground-based data and satellite data in recent times [2]. In this study, the MODIS satellite was used, specifically the MCD19A2 V.6 data product. It has a resolution of 1 km and can collect data daily. At two different wavelengths, namely 470 nm (blue band) and 550 nm (green band), MCD19A2 supplies AOD data for the benefit of users. [19].

Among the available options, AOD at 550 nm (green band) from the V.6 product file was selected for the study because it displayed better consistency. [19, 36]. The product file contains information about water vapor (column) from the land surface, aerosol optical depth and type, AOD uncertainty, and smoke cloud height, as well as AOD outside of the glint area (glint angle  $\geq 40^\circ$ ) and sensitive mode fraction data from the water surface [35]. Table 1 contains the specifics of the AOD product employed in the present study. Data for the months and the entire year of 2022 were obtained through coding on the GEE platform. This platform is free and open to everyone. Through the web-based application, analysis and visualization tasks can be completed quickly [6]. GEE libraries can be used to create programs in JavaScript and Python [37]. The data were downloaded for each station and the entire study area, and then exported. By examining the relationship between the stations, data processing, map preparation, and evaluation of the results were carried out using GIS software.

**Table 1.** Description of the AOD product utilized in the current research

Datasets	Period of time	Chosen band	Spatial resolution	Temporal resolution	Citation
MCD19A2 (Aerosol Optical Depth) V6	01.01.2022- 31.12.2022	550 nm (green band)	1 km	Daily	[18]

### 3. RESULTS AND DISCUSSION

In the conducted study, AOD was determined using both ground-based stations and satellite images. The study's main objective was to obtain clear information about AOD for the region where fixed stations were installed while making interpretations for certain distance areas. However, AOD obtained from satellite images allows for spatially distributed results.

In the study's first stage, data was gathered from all stations in the national monitoring of air quality network located within the study area. (Table 2). Data for both particle sizes, 2.5  $\mu\text{m}$  and 10  $\mu\text{m}$ , were downloaded. It should be noted that data for particle size 2.5  $\mu\text{m}$  is not available for Kardemir 1 and Kardemir 2 stations, and data for particle size 10  $\mu\text{m}$  is not available for the 75.yıl station. The air pollution

legislation sets different limits for PM10 to protect human health on an hourly, winter season (October to March), and annual basis. As of January 1, 2019, the daily national limit for particulate matter is  $70 \mu\text{g}/\text{m}^3$ , while the international limit is  $50 \mu\text{g}/\text{m}^3$ . The annual national limit is  $48 \mu\text{g}/\text{m}^3$ , and the international limit is  $40 \mu\text{g}/\text{m}^3$  [19]. According to the obtained data, except for Kardemir 1 and Kardemir 2 stations, all other stations have not exceeded these legal limits. It should be noted that there is no specific standard for PM2.5 in the air quality index of our country.

Figure 3 presents the particulate matter data collected from the national air quality monitoring station for PM2.5, while Figure 4 illustrates the data for PM10. It can be observed that during the winter season, both PM2.5 and PM10 values are higher. This increase in values is attributed to an increase in the use of fuel for heating purposes and the activities of the iron and steel industry present in the region.

The data presented in Figure 3 reveals that the Safranbolu station experiences higher particulate matter levels in the times of July, August, and September. This can be attributed to Safranbolu being a popular tourist destination during the summer season, leading to an increase in the population and transportation activities in the region.

The higher levels of particulate matter during specific periods in both Safranbolu and the winter season indicate the influence of local activities and seasonal factors on air quality in the region. Monitoring and understanding these variations in particulate matter levels are crucial for implementing appropriate measures to mitigate air pollution and improve air quality in the area.

**Table 2.** Information from Air Quality Stations

Stations	Parameters	Unit	Minimum Value	Maximum Value	Average Value	Standard Deviation	Number of Data	Accessible Data Percentage
75. Yıl	PM 2.5	$\mu\text{g}/\text{m}^3$	4,16	83,4	19,69	14,06	328	89,86
Kardemir 1	PM 2.5	$\mu\text{g}/\text{m}^3$	-	-	-	-	0	0
Kardemir 2	PM 2.5	$\mu\text{g}/\text{m}^3$	-	-	-	-	0	0
Safranbolu	PM 2.5	$\mu\text{g}/\text{m}^3$	1,45	53,7	16,15	9,46	314	86,03
Tören Alanı	PM 2.5	$\mu\text{g}/\text{m}^3$	0,93	84,54	14,75	12,12	363	99,45
75. Yıl	PM10	$\mu\text{g}/\text{m}^3$	-	-	-	-	0	0
Kardemir 1	PM10	$\mu\text{g}/\text{m}^3$	12,18	311,11	67,39	38,93	271	74,25
Kardemir 2	PM10	$\mu\text{g}/\text{m}^3$	10,52	694,12	50,75	47,9	275	75,34
Safranbolu	PM10	$\mu\text{g}/\text{m}^3$	2	161,02	43,5	19,68	349	95,62
Tören Alanı	PM10	$\mu\text{g}/\text{m}^3$	8,67	136,63	47,31	22,58	357	97,81

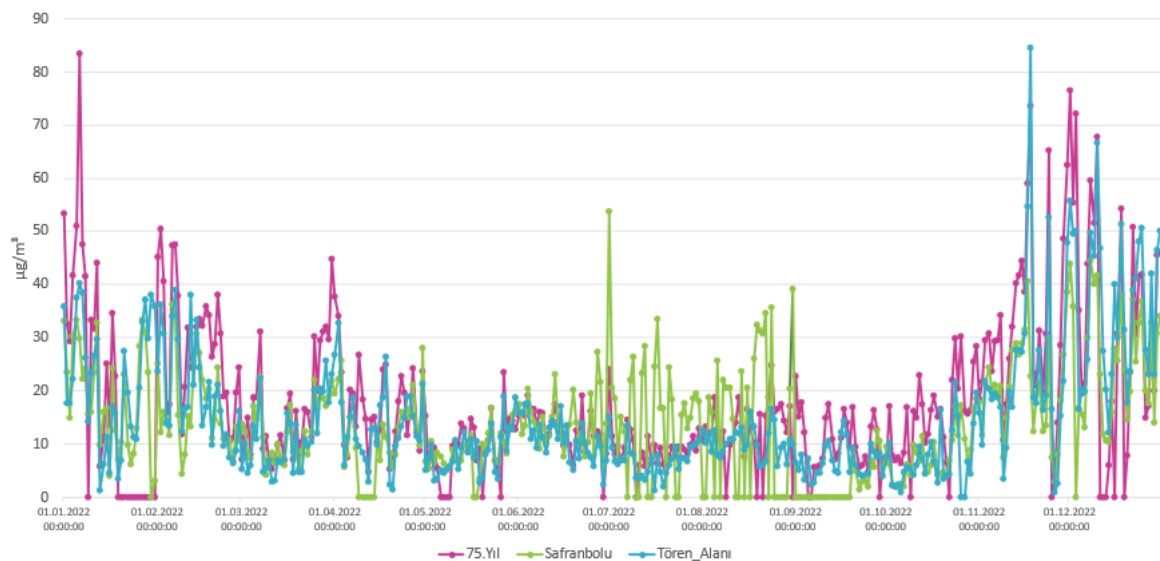


**Figure 3.** NAQMS Karabuk province PM2.5 values

The analysis of the PM10 graph also shows that particulate levels are higher during the winter season compared to the summer season (Figure 4). Among the four stations (Tören Alanı, Safranbolu, Kardemir 1, and Kardemir 2) that provide PM10 data, Kardemir 1 and Kardemir 2 stations have higher levels of particulate matter. These two stations are located close to iron and steel factories in the center of Karabük. Consequently, the higher values recorded in these two stations can be attributed to the active operations of these factories compared to the others.

Starting from October, both Kardemir 1 and Kardemir 2 stations have not recorded any data. Until October 2022, data sharing was possible for both stations. However, due to the change in servers, data access for this time period is currently unavailable. Initially, data sharing was done through the FTP system, but it has been transitioned to the VPN system. Since then, data for both stations is no longer publicly accessible but can be obtained upon official request. It is essential to consider the absence of data for the Kardemir 1 and Kardemir 2 stations when analyzing and interpreting the overall air quality trends in the region. The lack of data for these two stations during the specified period might influence the overall assessment of air quality for that time frame. Efforts should be made to address these data gaps and ensure a continuous and comprehensive monitoring system for air quality in the region.

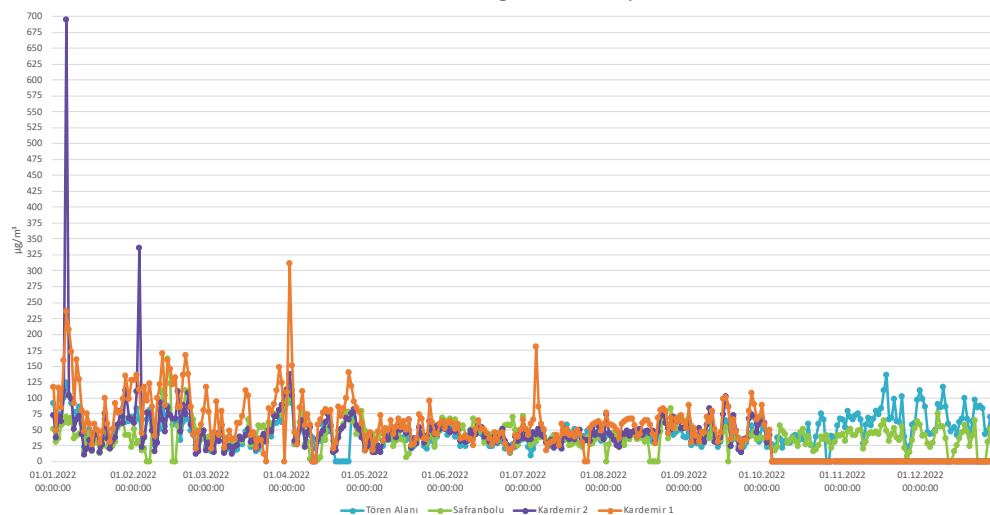


**Figure 4.** NAQMS Karabuk province PM10 values.

The majority of the monitoring stations established in our country are located in urban centers, resulting in limited coverage in rural areas. Additionally, some stations have missing data, and the point-based data collection method has its limitations. Due to these factors, satellite imagery has been utilized to complement and supplement the station data.

In the GEE platform, the locations of the stations were defined, and AOD data for the visible wavelength blue band and green band from the MODIS satellite were downloaded for each station. For each station, AOD over land graphs in the  $0.47 \mu\text{m}$  band are shown in Figure 5, and AOD graphs in the  $0.55 \mu\text{m}$  band are shown in Figure 6. Both bands provide four values for each day, resulting in some days having continuous data, while others have data gaps throughout the day. Furthermore, in some months such as January, February, and December, some data points are missing during the winter season, mainly due to climatic factors like snowfall. Snow particles can obscure particulate matter and lead to lower reflectance [22]. Generally, based on the data obtained from station points, higher AOD values are observed during the summer months.

To analyze the correlation between AOD values obtained from station points and satellite imagery, the Tören Alanı station was chosen due to its abundant data. As a result, a significant correlation was established between the two data sets. Therefore, monthly AOD maps for the entire study area were created using satellite imagery.

The utilization of satellite data in addition to station data allows for a broader spatial coverage and

helps overcome the limitations associated with station locations and data gaps. The use of satellite derived AOD maps provides significant understanding of the air quality trends and changes across the study area. This comprehensive approach enhances the understanding of aerosol distribution and its impact on the region's air quality.

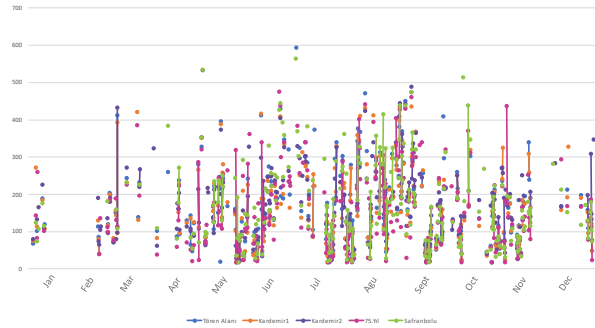


**Figure 5.** Blue band ( $0.47 \mu\text{m}$ ) AOD over land

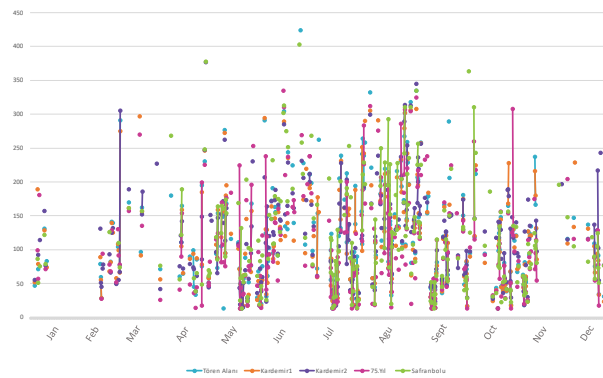


**Figure 6.** Green band ( $0.55 \mu\text{m}$ ) AOD over land

The average AOD for the year 2022 and each month was calculated and analyzed using Google Earth Engine. The downloaded images were then mapped to create visual representations of the AOD values. Figure 7 shows the map of the average AOD for the year 2022, while Figure 8 presents the maps for each month of 2022. In the maps for February and March, some areas appear white, indicating that they do not have any AOD values. This is because during the winter season, snowfall can cover dust particles on the ground, resulting in a bright background in the satellite image. This variation in the reflective surface leads to the absence of AOD values in these regions [22]. Obtaining AOD values from satellite imagery during the winter season poses the biggest disadvantage due to this snow-cover issue. However, when calculating AOD for the entire region spatially rather than for individual stations, using satellite imagery becomes advantageous.

Overall, looking at all the monthly maps, it is evident that AOD values are higher in the city center. This is mainly attributed to the presence of iron and steel factories and private sector rolling mills in the city center. Additionally, higher population density in the urban areas and higher traffic circulation due to more motor vehicles contribute to this trend. As of 2022, there were 69,711 motor vehicles registered in Karabük, which means approximately one-third of the population (243,614) owns a vehicle [31]. The high number of vehicles generates exhaust pollution and releases multiple pollutants into the atmosphere. AOD levels are particularly high in areas with transportation networks. The months of July and August also show higher AOD levels compared to other periods. This trend is observed in the Safranbolu station as well, as previously mentioned. For other districts, especially Eskipazar and Yenice, AOD values are higher. Eskipazar attracts tourists due to the presence of an ancient city, while Yenice shows higher AOD levels until October.

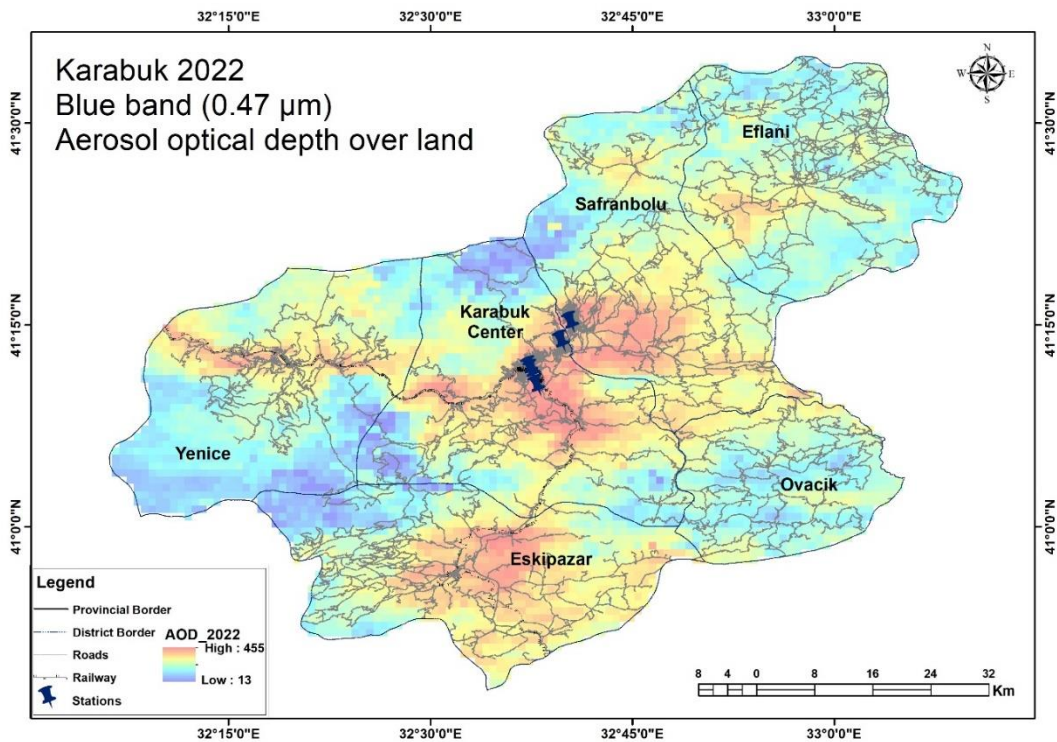


Figure 7. Blue band (0.47 μm) mean AOD over land map for 2022

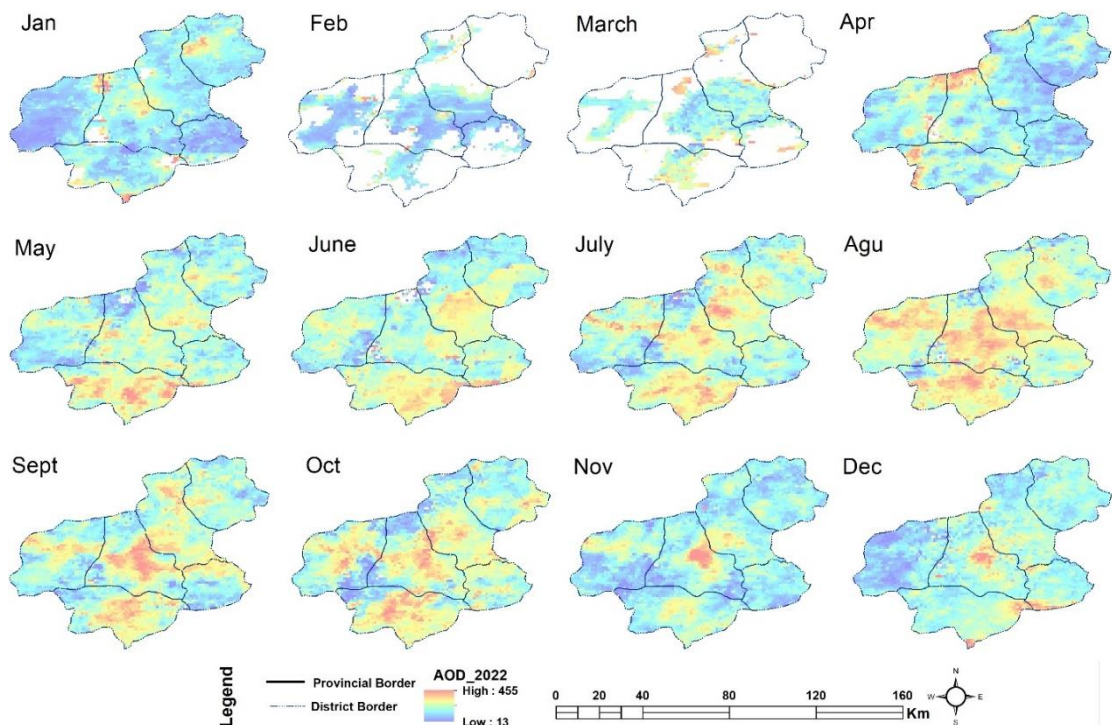
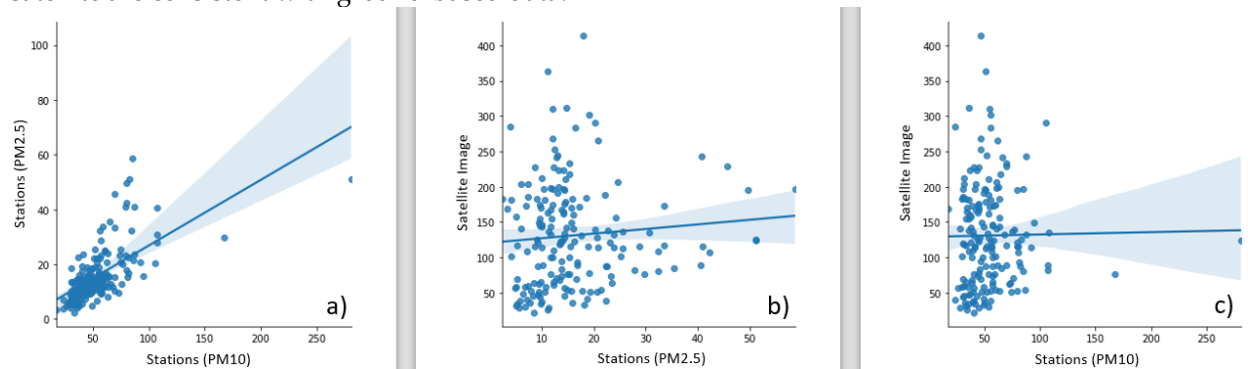


Figure 8. 2022 monthly AOD map

Figure 9 shows the graphs explaining the relationship between the two data by taking the average of the data from the satellite image and the terrestrial stations. In 'Figure 9a, the relationship between PM10 and PM2.5 is shown, while 'Figures 9b and 9c' depict the relationship between satellite imagery and ground-based data. There is a positive correlation of 85.24% among particulate matter obtained from ground stations. There is a 38.69% correlation between satellite imagery and PM2.5, and a correlation of

31.1811% between satellite imagery and PM10. Kaufman et al. (1997), Safarianzengir et al. (2020), and Makineci (2022) emphasized in their studies that the data obtained from Sentinel-5 and EOS Moderate Resolution Imaging Spectroradiometer are significant and positively correlated with the ground-based station data. In this study, it has been understood that, unlike other satellite systems, data from the MODIS satellite are consistent with ground-based data.



**Figure 1.** a) Relationship between PM10 and PM2.5, b) Relationship between satellite image and PM2.5, c) Relationship between satellite image and P10

#### 4. CONCLUSIONS

In this study, the spatial-temporal variation of AOD derived from MODIS was monitored and investigated. The GEE platform was used in the implementation phase for satellite image acquisition, processing, and data analysis. A correlation was established between the AOD data derived from the ground based PM2.5 and PM10 measurements obtained from the Turkey National Air Quality Monitoring Stations and the satellite images. It was shown that there is a moderate link between the two, which is a substantial and positive association.

The presence and active operation of iron-steel factories and the high number of vehicles in the region cause to the increase in AOD levels. There is a direct proportionality between AOD and the amount of air pollution. When AOD levels are high, the pollution in the surrounding area also increases.

The AOD analysis investigated the monthly and annual changes within the year 2022. The results showed significant variations in AOD values among the four seasons (spring, summer, autumn, winter). During the summer season, anthropogenic activities led to higher AOD values compared to the winter season, with August showing the highest values.

According to the literature, it has been determined that humans may survive without food for five weeks, drink water for five days, and air for five minutes. However, humans need to receive a minimum of 15  $\mu\text{g}/\text{m}^3$  of clean air daily. Pollutant gases are released into the atmosphere throughout the region, posing a significant impact on the quality of human life. Therefore, monitoring air pollution in the region and implementing measures to reduce pollutant levels are essential for safeguarding public health.

Thanks to this study, the AOD in Karabük, a region with a significant presence of the iron and steel industry, has been examined not only temporally but also spatially. This enhances the region's capacity to understand and monitor air quality. It proves to be a valuable tool for identifying sources of air pollution and developing air quality management strategies. Furthermore, it has been demonstrated that satellite imagery can be utilized when there is a lack of data at ground stations. Thus, satellite data can make a valuable contribution to filling data gaps in the air quality monitoring system.

In conclusion, this study represents significant research highlighting the potential of remote sensing and satellite data for monitoring air quality and filling data gaps. It also provides valuable insights for experts working in atmospheric sciences.

### Declaration of Ethical Standards

Authors declare to comply with all ethical guidelines, including authorship, citation, data reporting, and original research publication.

### Declaration of Competing Interest

The authors declare that they have no known competing financial interests or personal relationships that could have appeared to influence the work reported in this paper.

### Funding / Acknowledgements

This study was orally presented at the 12th National Photogrammetry and Remote Sensing Association Symposium (TUFUAB'XII).

### 5. REFERENCES

- [1] J. Xin, Q. Zhang, L. Wang, C. Gong, Y. Wang, Z. Liu and W. Gao, "The empirical relationship between the PM<sub>2.5</sub> concentration and aerosol optical depth over the background of North China from 2009 to 2011", *Atmospheric Research*, 138: p. 179-188, 2014.
- [2] X. Wei, N. B. Chang, K. Bai and W. Gao, "Satellite remote sensing of aerosol optical depth: advances, challenges, and perspectives", *Critical Reviews in Environmental Science and Technology*, 50(16): p. 1640-1725, 2020.
- [3] D. A. Ridley, S. Solomon, J. E. Barnes, V. D. Burlakov, T. Deshler, S. I. Dolgii and J. P. Vernier, "Total volcanic stratospheric aerosol optical depths and implications for global climate change", *Geophysical Research Letters*, 41(22): p. 7763-7769, 2014.
- [4] C. Paton-Walsh, N. B. Jones, S. R. Wilson, V. Haverd, A. Meier, D. W. Griffith and C. P. Rinsland, "Measurements of trace gas emissions from Australian forest fires and correlations with coincident measurements of aerosol optical depth", *Journal of Geophysical Research: Atmospheres*, 110(D24), 2005.
- [5] R. Mathur, "Estimating the impact of the 2004 Alaskan forest fires on episodic particulate matter pollution over the eastern United States through assimilation of satellite-derived aerosol optical depths in a regional air quality model", *Journal of Geophysical Research: Atmospheres*, 113(D17), 2008.
- [6] D. Arıkan, F. Yildiz, "Investigation of Antalya forest fire's impact on air quality by satellite images using Google earth engine", *Remote Sensing Applications: Society and Environment*, 29, 100922, 2023.
- [7] C. Toledano, M. Wiegner, M. Garhammer, M. Seefeldner, J. Gasteiger, D. Müller and P. Koepke, "Spectral aerosol optical depth characterization of desert dust during SAMUM 2006", *Tellus B: Chemical and Physical Meteorology*, 61(1): p. 216-228, 2009.
- [8] D. Tanré, P. Y. Deschamps, C. Devaux and M. Herman, "Estimation of Saharan aerosol optical thickness from blurring effects in Thematic Mapper data", *Journal of Geophysical Research: Atmospheres*, 93(D12): p. 15955-15964, 1988.
- [9] L. Saidi, M. Valari and J. Ouarzazi, "Air quality modeling in the city of Marrakech, Morocco using a local anthropogenic emission inventory", *Atmospheric Environment*, 293: p. 119445, 2023.
- [10] S. Öztürk, D. Gerçek, İ. T. Güven, E. Gaga, Ö. Ö. Üzmez and M. Civan, "Kocaeli İzmir İlçesi'nde Partikül Madde (PM<sub>2.5</sub>) Konsatrasyon Seviyeleri Mekansal ve Mevsimsel Değerlendirilmesi", *Mühendislik Bilimleri ve Tasarım Dergisi*, 9(3): p. 809-821, 2021.
- [11] N. Dekhoda, J. Sim, S. Joo, S. Shin and Y. Noh, "Retrieval of Black Carbon Absorption Aerosol Optical Depth from AERONET Observations over the World during 2000–2018", *Remote Sensing*, 14(6): p. 1510, 2022.
- [12] M. Coşkun, H. Şahiner and O. Canbulat, "Covid-19 Sürecinde Coğrafi Özellikler ve Atmosfer

- Kararlılığına Göre Karabük İl Merkezi ve Zonguldak'ın Ereğli İlçesinde Aerosol Optik Derinlik Analizi", *International Journal of Geography and Geography Education*, (45): p. 380-403, 2022.
- [13] J.H. Seinfeld and S.N. Pandis, "Atmospheric chemistry and physics: from air pollution to climate change", *John Wiley & Sons*, 2016.
- [14] T. Koçak and F. Ebrahimi, "Uydulardan elde edilebilen aerosol optik derinlik verilerini kullanarak zemin seviyesi ince partikül konsantrasyonlarını tahmin etmek için doğrusal olmayan bir model geliştirilmesi", *Ulusal Çevre Bilimleri Araştırma Dergisi*, 3(3): p. 119-127, 2020.
- [15] M. Dehghani, L. Keshtgar, M. R. Javaheri, Z. Derakhshan, G. Oliveri Conti, P. Zuccarello and M. Ferrante, "The effects of air pollutants on the mortality rate of lung cancer and leukemia", *Molecular medicine reports*, 15(5): p. 3390-3397, 2017.
- [16] J. Huang, P. Minnis, Y. Yi, Q. Tang, X. Wang, Y. Hu and D. Winker, "Summer dust aerosols detected from CALIPSO over the Tibetan Plateau", *Geophysical Research Letters*, 34(18), 2007.
- [17] S. Menon, J. Hansen, L. Nazarenko and Y. Luo, "Climate effects of black carbon aerosols in China and India", *Science*, 297(5590): p. 2250-2253, 2002.
- [18] W. Huang, J. Cao, Y. Tao, L. Dai, S. E. Lu, B. Hou and T. Zhu, "Seasonal variation of chemical species associated with short-term mortality effects of PM<sub>2.5</sub> in Xi'an, a central city in China", *American journal of epidemiology*, 175(6): p. 556-566, 2012.
- [19] A.K. Ranjan, A. Patra and A. Gorai, "Effect of lockdown due to SARS COVID-19 on aerosol optical depth (AOD) over urban and mining regions in India", *Science of the Total Environment*, 745: p. 141024, 2020.
- [20] National Air Quality Monitoring Network, Available: <https://sim.csb.gov.tr/intro/uhkia> [Accessed: Jan 11, 2023]
- [21] National Air Quality Monitoring Station and Data, Available: <https://www.havaizleme.gov.tr/> [Accessed: Dec 24, 2022]
- [22] J. Li, X. Ge, Q. He and A. Abbas, "Aerosol optical depth (AOD): spatial and temporal variations and association with meteorological covariates in Taklimakan desert, China", *PeerJ*, 9: p. e10542, 2021.
- [23] H. B. Makineci "İstanbul İli Merkez İlçelerindeki NO<sub>2</sub> ve CO Emisyonlarının Uzaktan Algılama ve Yersel İstasyon Verileri Kullanılarak İncelenmesi", *Türkiye Uzaktan Algılama Dergisi*, 4(2), 62-74, 2022.
- [24] D. Arıkan, F. Yıldız, "Spatial and Temporal Analysis of Pollutant Gases in Western Black Sea of Türkiye", *The International Archives of the Photogrammetry, Remote Sensing and Spatial Information Sciences*, 48, 463-470, 2023.
- [25] V. Safarianzengir, B. Sobhani, M.H. Yazdani, M. Kianian, "Monitoring, analysis and spatial and temporal zoning of air pollution (carbon monoxide) using Sentinel-5 satellite data for health management in Iran, located in the Middle East. Air Quality ", *Atmosphere & Health*, 13, 709-719, 2020.
- [26] G.Kaplan, Z. Y. Avdan, "Space-borne air pollution observation from sentinel-5p tropomi: Relationship between pollutants, geographical and demographic data", *International Journal of Engineering and Geosciences*, 5(3), 130-137, 2020.
- [27] H. B. Makineci, D. Arıkan, D. Alkan, L. Karasaka, "Spatio-temporal Analysis of Sentinel-5P Data of Konya City Between 2019", *Harita Dergisi*, 170, 23-40, 2023.
- [28] Y. J. Kaufman, D. Tanré, L. A. Remer, E. F. Vermote, A. Chu and B. N. Holben, "Operational remote sensing of tropospheric aerosol over land from EOS moderate resolution imaging spectroradiometer", *Journal of Geophysical Research: Atmospheres*, 102(D14): p. 17051-17067, 1997.
- [29] Y. Wang, J. Wang, R. C. Levy, Y. R. Shi, S. Mattoo and J. S. Reid, "First retrieval of AOD at fine resolution over shallow and turbid coastal waters from MODIS", *Geophysical research letters*, 48(17): p. e2021GL094344, 2021.
- [30] P. Wang, Q. Tang, Y. Zhu, Y. He, Q. Yu, T. Liang and K. Zheng, "Spatial-Temporal Variation of AOD Based on MAIAC AOD in East Asia from 2011 to 2020", *Atmosphere*, 13(12): p. 1983, 2022.

- [31] Turkish Statistical Institute (TUIK), Available: <https://www.tuik.gov.tr/> [Accessed: Jan 11, 2023]
- [32] S. M. Sakerin, L. P. Golobokova, D. M. Kabanov, D. A. Kalashnikova, V. S. Kozlov, I. A. Kruglinsky and D. G. Chernov, "Measurements of physicochemical characteristics of atmospheric aerosol at research station Ice Base Cape Baranov in 2018", *Atmospheric and Oceanic Optics*, 32: p. 511-520, 2019.
- [33] D. Kabanov, S. Sakerin and Y.S. Turchinovich, "Interannual and seasonal variations in the atmospheric aerosol optical depth in the region of Tomsk (1995–2018)", *Atmospheric and Oceanic Optics*, 32: p. 663-670, 2019.
- [34] Ö. Zeydan and Y. Wang, "Using MODIS derived aerosol optical depth to estimate ground-level PM<sub>2.5</sub> concentrations over Turkey", *Atmospheric Pollution Research*, 10(5): p. 1565-1576, 2019.
- [35] Google Earth Engine (GEE), Available: <https://earthengine.google.com/> [Accessed: Dec 20, 2022]
- [36] A. Lyapustin and Y. Wang, "MODIS Multi-Angle Implementation of Atmospheric Correction (MAIAC)", *Data User's Guide*, 2018.
- [37] P. Karakus, "Investigation of Meteorological Effects on Çivril Lake, Turkey, with Sentinel-2 Data on Google Earth Engine Platform ", *Sustainability*, 15(18), 13398, 2023.

## A TWO STAGE MODEL FOR DAY-AHEAD ELECTRICITY PRICE FORECASTING: INTEGRATING EMPIRICAL MODE DECOMPOSITION AND CATBOOST ALGORITHM

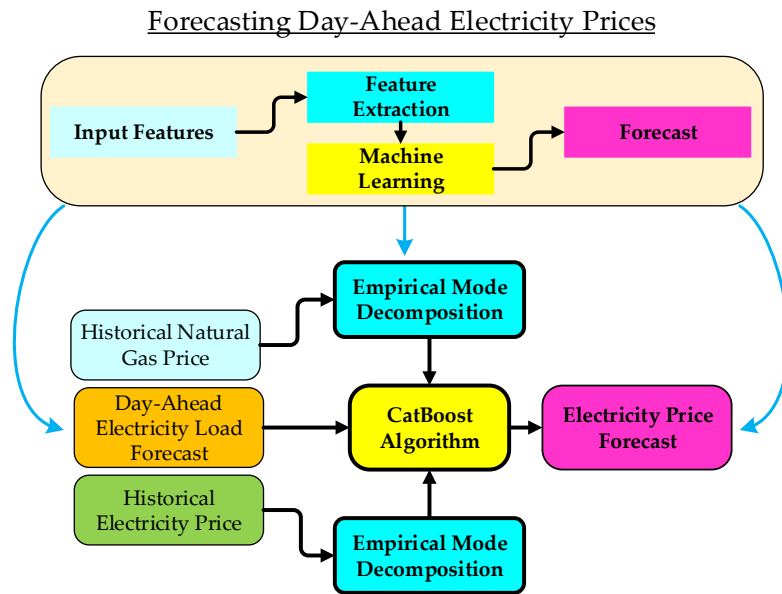
Ceyhun YILDIZ 

Kahramanmaraş İstiklal University, Elbistan Vocational School, Electricity and Energy Department,  
Kahramanmaraş, TÜRKİYE  
[ceyhun.yildiz@istiklal.edu.tr](mailto:ceyhun.yildiz@istiklal.edu.tr)

### Highlights

- A two-stage model for day-ahead electricity price forecasting was introduced
- The proposed model combines empirical mode decomposition and CatBoost algorithm
- Empirical mode decomposition was employed for feature extraction
- CatBoost algorithm was utilized for electricity price forecasting
- Comparisons with benchmark models confirmed the effectiveness of the proposed model

### Graphical Abstract



Proposed electricity price forecasting model



## A TWO STAGE MODEL FOR DAY-AHEAD ELECTRICITY PRICE FORECASTING: INTEGRATING EMPIRICAL MODE DECOMPOSITION AND CATBOOST ALGORITHM

Ceyhun YILDIZ

*Kahramanmaraş İstiklal University, Elbistan Vocational School, Electricity and Energy Department,  
Kahramanmaraş, TÜRKİYE  
ceyhun.yildiz@istiklal.edu.tr*

(Received: 01.05.2023; Accepted in Revised Form: 03.10.2023)

**ABSTRACT:** Electricity price forecasting is crucial for the secure and cost-effective operation of electrical power systems. However, the uncertain and volatile nature of electricity prices makes the electricity price forecasting process more challenging. In this study, a two-stage forecasting model was proposed in order to accurately predict day-ahead electricity prices. Historical natural gas prices, electricity load forecasts, and historical electricity price values were used as the forecasting model inputs. The historical electricity and natural gas price data were decomposed in the first stage to extract more deep features. The empirical mode decomposition (EMD) algorithm was employed for the efficient decomposition process. In the second stage, the categorical boosting (CatBoost) algorithm was proposed to forecast day-ahead electricity prices accurately. To validate the effectiveness of the proposed forecasting model, a case study was conducted using the dataset from the Turkish electricity market. The proposed model results were compared with benchmark machine learning algorithms. The results of this study indicated that the proposed model outperformed the benchmark models with the lowest root mean squared error (RMSE), mean absolute error (MAE), mean absolute percentage error (MAPE), and correlation coefficient (R) values of 8.3282%, 5.2210%, 6.9675%, and 86.2256%, respectively.

**Keywords:** *CatBoost regression, Electricity price forecasting, Empirical mode decomposition*

### 1. INTRODUCTION

Forecasting electricity prices is essential for the secure and economic operation of interconnected electrical grid systems. Power generation companies use price forecasts to plan their generation, aiming to maximize their profit, while consumers use forecasts to avoid high electricity prices and minimize their costs. However, with the liberalization of the energy industry, electricity price data presents increasingly complex dynamics and uncertainties. The liberalized electricity market operations are highly intricate due to stochastic factors such as meteorological conditions, the balance of generation and demand, grid system constraints, fuel prices, and energy policies. As a result of the complex relationships between these factors, predicting electricity prices with a high level of accuracy is challenging.

Over the past twenty years, numerous approaches and models have been proposed for electricity price forecasting. Comprehensive literature reviews on the study of electricity price forecasting were introduced by [1] and [2]. The approaches in the literature for predicting electricity prices can be divided into three main sub-sections: (1) statistical models, (2) artificial intelligence models, and (3) hybrid models.

Statistical models typically use historical data, as well as other input features, to perform the forecasting process. Although statistical models were frequently employed for predicting electricity prices, they faced some restrictions and difficulties. Unlike the linear relationships between variables that statistical models are intended to model, typical electricity price forecasting models capture the non-linear dynamics of electricity markets. The significance of taking nonlinearities into consideration when forecasting electricity prices was pointed out in the review article [2], which also discussed different approaches to this issue.

Artificial intelligence-based electricity price forecasting models employ machine learning (ML) and specifically deep learning (DL) approaches. In [3], different ML algorithms were investigated for day-

\*Corresponding Author: Ceyhun YILDIZ, [ceyhun.yildiz@istiklal.edu.tr](mailto:ceyhun.yildiz@istiklal.edu.tr)

ahead electricity price forecasting, and electricity market datasets from European countries were used to evaluate forecasting algorithms. An online self-adaptive forecasting method based on random forest (RF) was proposed in [4] to forecast electricity prices, which considers the concept drift phenomenon of the power market. The case studies were conducted on the data from Gansu province, China, to illustrate its effectiveness. An interesting approach based on an online sequential extreme learning machine (OS-ELM) was proposed in [5] for forecasting day-ahead and real-time market electricity prices. Performance tests were conducted using the dataset from the Australian Energy Market Operator (AEMO). In [6], deterministic and stochastic components of the electricity price signal were investigated, and several parametric and nonparametric approaches were employed for deterministic and stochastic component forecasting. The experimental studies were carried out using the dataset from the Italian electricity market (IPEX). An interesting DL model was proposed in [7] to forecast electricity prices. The proposed model was the new deep convolutional neural network (CNN) architecture based on GoogLeNet. The effectiveness of this model was tested on the dataset from the New York Independent System Operator (NYISO). Another model for NYISO data was introduced in [8]. The authors proposed a CNN-based autoencoder to forecast electricity prices. In [9], four DL-based electricity price forecasting models were proposed, and the results were compared with 27 state-of-the-art predictors. Simple neural network (NN) and DL-based models for electricity price forecasting were introduced in [10], and the experimental studies were conducted using the dataset from the Electric Reliability Council of Texas (ERCOT). However, the main drawbacks of these deep networks are their computational expense and black-box nature.

The third literature section comprises hybrid model approaches, several data preprocessing techniques, artificial intelligence algorithms, and statistical models that were combined to forecast electricity prices. [11] proposed a hybrid model based on data decomposition and the extreme learning machine (ELM) algorithm. The differential evolution (DE) algorithm was used to optimize ELM parameters. Electricity price datasets from Spanish and Australian electricity markets were used in the experimental study. [12] introduced a hybrid model for electricity price forecasting. The empirical wavelet transform (EWT) and an attention mechanism were proposed to decompose and select input features, respectively. The long-short-term-memory (LSTM) architecture was used to obtain final forecasts. Furthermore, the crisscross optimization algorithm (CSO) was used to determine fully connected layer parameters. Wind power generation, solar power generation, predicted electricity load, and historical electricity price data from the Danish energy market were used as model inputs. Another hybrid method based on the wavelet transform (WT) and an LSTM was proposed in [13] for forecasting electricity prices. The data from the Pennsylvania, New Jersey, and Maryland (PJM) and Spain electricity markets were used to evaluate the proposed method. A hybrid method based on model input decomposition and forecasting was proposed in [14]. EMD and DL-based methods were employed for decomposition and forecasting, respectively. The performance evaluations were realized on the datasets from the PJM and New South Wales electricity markets. [15] introduced an interesting hybrid model for day-ahead electricity price forecasting. The authors proposed an adaptive copula-based method and a new signal decomposition algorithm for feature selection and extraction. The effectiveness of the proposed model was validated using the dataset from the PJM electricity market. [16] proposed a two-stage ensemble learning-based approach for electricity price forecasting. The first stage comprises extreme gradient-boosted trees (XGBoost) and random forest (RF) to learn distinct features of the electricity price signal. The second stage includes Bayesian linear regression to obtain the final forecast values. The proposed model was tested on the Austrian electricity market dataset. [17] proposed another hybrid model based on CNN and LSTM. CNN was employed for extracting new features from model inputs. The extracted features were used as LSTM model inputs to obtain electricity price forecasts. The dataset from the Iranian electricity market was used to train and test the proposed forecasting model. Another approach was proposed in [18]. The authors proposed data augmentation methods and regression models (multilayer neural network (MLNN), CNN, and autoregressive model with exogenous inputs (ARX)) to forecast day ahead electricity prices. Electricity price datasets from Belgian and Dutch day-ahead electricity markets were employed in

the study. [19] proposed an electricity price forecasting model that combines WT, stacked autoencoder (SAE), and LSTM for the U.S. energy market. [20] introduced a hybrid model based on decomposition and forecasting. WT and LSTM were employed for decomposition and forecasting processes. The data set from the Australian Energy Market Operator (AEMO) was used for the experimental study. Another hybrid model was developed in [21] to forecast electricity prices in two main stages. An autoregressive time varying (ARXTV) model with exogenous variables was employed in the first stage to forecast electricity price values. In the second stage, support vector machine (SVM) and kernel regression models were used to detect and estimate price spikes. Another two-stage model based on feature selection and regression was proposed in [22]. The multi-objective binary-valued backtracking search algorithm (MOBBSA) and an optimized adaptive neuro-fuzzy inference system (ANFIS) were employed for feature selection and regression. The dataset from the Ontario power market was used to develop and test the proposed model. [23] proposed a hybrid model for electricity price forecasting that combines the artificial neural network (ANN) and the artificial cooperative search algorithm (ACS). Dataset from the Ontario electricity market was used in the study. [24] proposed another ensemble learning based model for electricity price forecasting in IPEX. The proposed model forecasts deterministic and stochastic components of the electricity price signal with semi-parametric techniques and ML algorithms, respectively. Another method that combines linear regression automatic relevance determination (ARD) and ensemble bagging extra tree regression (ETR) models was proposed in [25]. The experimental test studies of the study were conducted on a dataset from the Nord Pool electricity market. The LSTM and signal decomposition based model was proposed in [26]. The electricity price signal was decomposed and the tuned LSTM architectures were used to forecast high and low-frequency components. The sequence model-based optimization (SMBO) was employed for hyper parameter tuning. The datasets from the electricity markets of PJM were used in this study. [27] introduced another hybrid model based on DL architectures. The proposed model combines deep belief network (DBN), CNN, and LSTM for feature extraction and regression processes. The PJM market data was used in this study.

The papers reviewed above indicated that research in the field of electricity price forecasting has largely focused on the hybrid approach. Despite the impressive progress made in the literature on hybrid machine learning models, there are still a number of gaps that need to be filled. Many of the proposed hybrid electricity price forecasting models have a black-box nature, making it difficult to interpret how they make predictions. This is a significant issue, as it's important to have explainable models. Additionally, some hybrid models are computationally expensive, which limits their scalability to large datasets. Therefore, more research is needed to develop hybrid models that are both accurate, explainable, and computationally efficient.

This study proposes a hybrid model to accurately forecast day-ahead electricity prices. The model architecture comprises two main stages. In the first stage, data preprocessing, feature selection, and feature extraction processes were performed to determine appropriate input features. The second stage employed a computationally efficient and explainable regression method to obtain reliable and accurate forecasts. Additionally, several performance tests were conducted to confirm the effectiveness of the proposed forecasting model architecture.

This study makes the following contributions:

- 1-Introducing a hybrid method based on feature selection, feature extraction, and regression.
- 2-Employing the mutual information (MI)-based feature selection method to determine the important features of the investigated dataset. Then, using an effective signal decomposition algorithm called EMD to extract meaningful deep features.
- 3- Proposing the computationally efficient and powerful algorithm CatBoost for regression.
- 4- Conducting performance comparison tests with benchmark regression algorithms on the dataset from the Turkish electricity market.

The rest of the paper is organized as follows: The upcoming section describes the theoretical foundation of the methods used in this study and the structure of the proposed electricity forecasting model. Afterward, the section titled Data Description presents information on the datasets utilized in the

study. Then, the EMD Based Feature Extraction section describes the feature extraction procedure utilized in the study. The section called Experimental Study gives the details of the experiments conducted. The Results section presents a summary of the results. Finally, the last section concludes the study.

## 2. THEORETICAL BACKGROUND

In this study, a two-stage hybrid forecasting model was developed for day-ahead electricity price forecasting. The proposed model performs feature selection, feature extraction, and regression processes to forecast electricity prices using several effective methods. The first stage of the model employs MI-based feature selection and EMD-based feature extraction methods. In the second stage, the computationally efficient and explainable CatBoost algorithm was used for regression. The following subsections provide an overview of the theoretical basis of the methods employed in the study.

### 2.1. Mutual Information

Mutual information (MI) was first introduced as a measure of uncertainty in [28], to quantify the amount of information that can be transmitted between two systems. Since then, it has become widely used as a statistical measure of the dependence between two random variables in various fields. MI measures the information shared between variables, with a high MI indicating a strong relationship and a low MI indicating a weak relationship. The following equation defines the MI between two discrete random variables.

$$MI(X; Y) = \sum_{x \in \mathcal{X}} \sum_{y \in \mathcal{Y}} P(x, y) \log \frac{P(x, y)}{P(x)P(y)} \quad (1)$$

where  $X$  and  $Y$  are random variables with the joint distribution  $P(x, y)$ .  $P(x)$  and  $P(y)$  are the marginal distributions.

In this study, MI was used as a criterion for feature selection. The dataset investigated includes multiple features that may have a relationship with electricity prices. To determine the importance of each feature, MI values were calculated for each feature. Based on the calculated MI values, the two most important features, load forecast, and natural gas price were determined as exogenous inputs for the proposed electricity price forecasting model.

### 2.2. Empirical Mode Decomposition

The EMD algorithm was introduced in [29] for decomposing nonlinear and non-stationary signals. This algorithm has been widely used in various fields for extracting and analyzing the deep components of complex signals. The EMD algorithm performs a data-driven method that does not require any predefined mathematical model for the signal and can adaptively decompose the signal. This algorithm decomposes any complex signal into its simpler intrinsic mode functions (IMFs) and a residue. An IMF is an intrinsic oscillatory component of the original signal, and the residue represents the trend. An IMF was defined in [29] as a function with the following two properties: 1) the total number of local minimums and local maximums, and the number of zero crossings differ by at most one, and 2) the upper and lower envelopes derived from the local extrema have a mean value of zero. The following equation defines the relationships between the original signal and the extracted signals (IMFs and residue).

$$x(t) = \sum_{i=1}^N IMF_i(t) + r(t) \quad (2)$$

where  $x(t)$  is the original signal,  $N$  is the number of *IMFs*, and  $r$  is the residue.

In this study, historical electricity price signal, natural gas price signal and electricity load forecasts were used as input features for the forecasting model. The electricity price signal fluctuations depend on various factors such as weather conditions, electrical grid limitations, and complex market operations. Due to its high nonlinearity, volatility, and nonstationarity, decomposing this signal can enhance the performance of the forecasting model. Hence, in this study, the EMD algorithm was proposed to extract deep features from the price signal, resulting in six IMFs and a residue signal. Another uncertain input of the model was natural gas prices. EMD was also employed to decompose the natural gas price dataset into IMFs and a residue signal.

### 2.3. CatBoost

The powerful and versatile gradient boosting-based ML algorithm called CatBoost was introduced by [30] and has become famous for its ability to handle categorical features in datasets. Apart from handling categorical inputs, CatBoost offers several benefits compared to other machine learning algorithms. Firstly, the input features are automatically scaled, which can enhance the model's performance. Secondly, CatBoost uses randomized permutations to mitigate the impact of individual variables on the model and prevent overfitting. Lastly, the algorithm can automatically detect and handle missing values in the dataset. With its precision and speed, CatBoost is a powerful and flexible ML algorithm that outperforms alternative algorithms.

The general overview of the Catboost algorithm can be summarized with the following steps:

Step 1- Data Permutation: Algorithm starts with a training dataset ' $D$ ' containing ' $n$ ' instances. To create diversity, it randomly shuffles the  $D$ ,  $d$  times, generating  $d$  different training sets  $D_r$  (where  $r$  ranges from 1 to  $d$ ).

Step 2- Matrix Initialization: Algorithm sets up a matrix  $M$  where each element  $M(r, i)$  represents the initial prediction value for an instance  $i$  in training set  $D_r$ . Algorithm initializes these values to zero.

Step 3- CatBoost Training on a Random Set: Algorithm randomly chooses one of the permutation sets,  $D_r$ , for the following steps.

- Categorical Feature Encoding: Algorithm enhances categorical features using Ordered Target Statistics (TS) Encoding.

- Tree Construction: Algorithm builds a new Ordered Boosting tree ( $T$ ). This tree approximates the gradient or residual of each instance in  $D_r$  utilizing the  $M(r, )$  matrix during gradient calculations.

- Gradient Boosting Update: Algorithm uses the newly created tree  $T$  to predict outcomes for all permutation datasets. Then updates  $M$  based on these predictions using a gradient boosting strategy.

Step 4- Ensemble Prediction: Algorithm repeats the entire Step 3 process  $N$  times to build  $N$  trees. Finally, algorithm makes predictions for any instance by averaging the predictions from all  $N$  trees. This ensemble approach is similar to traditional Gradient Boosting.

In this study, CatBoost was proposed as the regression algorithm for the developed day-ahead electricity price forecasting model. To demonstrate its efficiency on electricity price forecasting, the results of CatBoost were compared with several benchmark algorithms such as linear regression (LR), ridge regression (Ridge), gradient boosting (GB), and SVM.

### 2.3. Proposed Forecasting Model

This subsection outlines the general architecture of the proposed forecasting model, which consists of three main input features, as illustrated in Figure 1. The general model structure comprises two main stages. In the first stage, the EMD algorithm was used to extract new features from the historical electricity price data and the natural gas data, while the electricity load forecast data was transferred to the second stage. To capture temporal dependencies in sequential data, lagged electricity price and natural gas price inputs were incorporated in the second stage. Finally, the CatBoost algorithm was employed to generate electricity price forecasts.

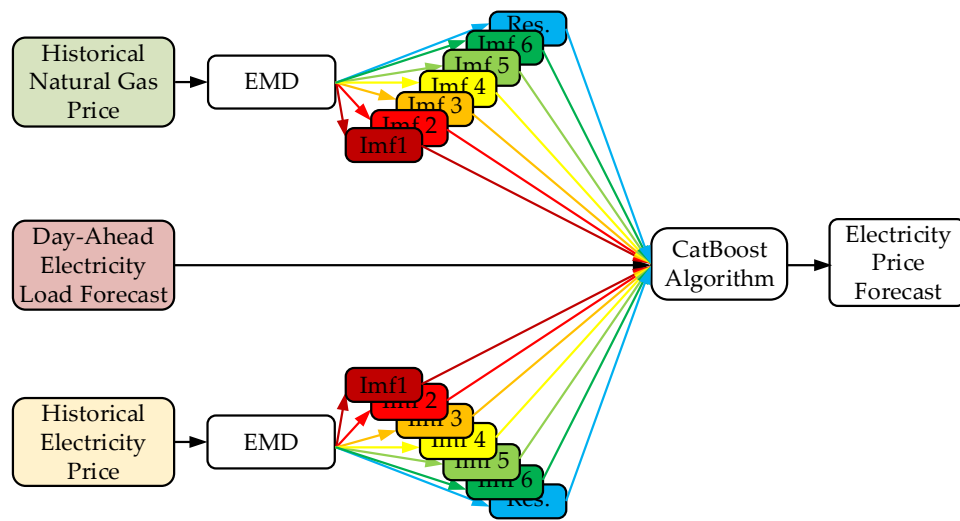


Figure 1. The proposed forecasting model framework

### 3. DATA DESCRIPTION

In this study, the dataset from the Turkish electricity market was used for developing and testing the proposed forecasting model. The dataset covers hourly samples for a one-year period from October 1, 2019 to December 31, 2019. The total of eight variables—wind, solar, hydro-dam, hydro-river, geothermal generation, day-ahead electricity load forecast, natural gas price, and electricity price values—constituted the dataset. The dataset is publicly available on the online data-sharing platform [31] of the Turkish electricity market. The MI-based feature selection method was used to select important features from the dataset. Figure 2 shows the MI values of the features. Two features with the highest MI values (load forecast and natural gas price) were selected.

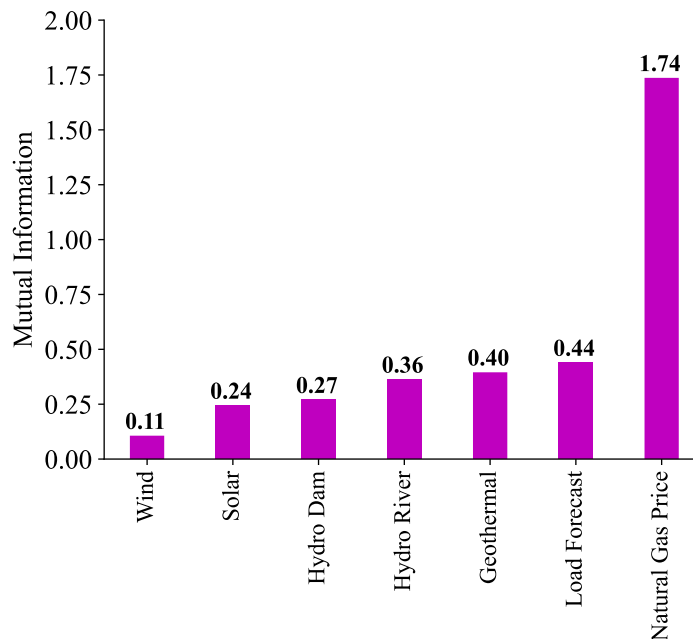


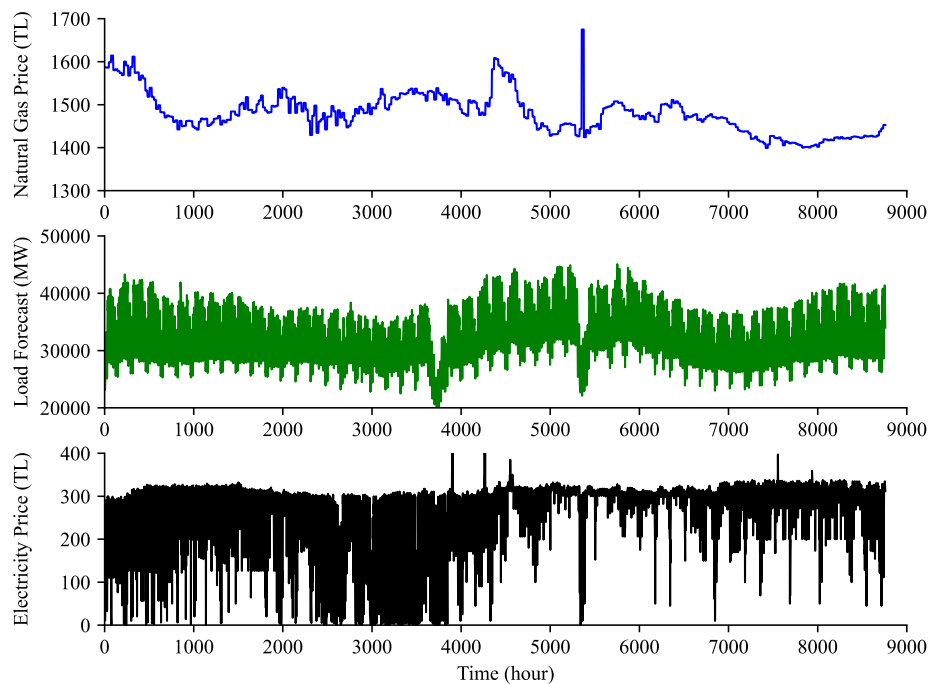
Figure 2. Mutual information between features and electricity price

Figure 3 displays the entire dataset, which consists of the target variable (electricity price (TL)) and the selected model input features (electricity load forecast (MW) and natural gas price (TL)). To provide an in-depth understanding of the dataset, some crucial statistical measures are presented in Table 1.

**Table 1.** The statistical properties of the dataset

Property	Natural Gas Price	Electricity Load Forecast	Electricity Price
Count	8760	8760	8760
Mean	1479.86	33161.91	260.32
Std.	47.03	4706.18	83.99
Min.	1399.18	18000.00	0.00
25%	1448.30	29300.00	229.99
50%	1474.86	33300.00	300.78
75%	1504.51	36700.00	313.98
Max.	1675.01	45100.00	500.00

The statistics table summarizes the statistical properties of the natural gas price, electricity load forecast, and electricity price datasets. The 8760 samples that made up the dataset included one entire year of hourly data collection. The Count row shows that there were no missing values in any of the three variables. The Mean row shows the average value of each variable. For example, the mean natural gas price was 1479.86 TL, the mean electricity load forecast was 33161.91 MW, and the mean electricity price was 260.32 TL. The Std. row shows the standard deviation of each variable, which is a measure of the spread of the data around the mean. For example, the standard deviation of the natural gas price was 47.03 TL, the standard deviation of the electricity load forecast was 4706.18 MW, and the standard deviation of the electricity price was 83.99 TL. The Min. and Max. rows show the minimum and maximum values of each variable, respectively. For example, the minimum natural gas price was 1399.18 TL, the minimum electricity load forecast was 18000 MW, and the minimum electricity price was 0 TL. The maximum natural gas price was 1675.01 TL, the maximum electricity load forecast was 45100 MW, and the maximum electricity price was 500 TL. The 25%, 50%, and 75% rows show the values that divide the data into quarters, also known as the first quartile, median, and third quartile, respectively. For example, the first quartile of natural gas prices was 1448.30 TL, the median was 1474.86 TL, and the third quartile was 1504.51 TL.



**Figure 3.** The whole dataset of electricity price, load forecast, and natural gas price

#### 4. EMD BASED FEATURE EXTRACTION

In this study, electricity price data and natural gas price data were decomposed in order to extract more deep features and improve forecasting accuracy. The electricity price data has volatile, nonlinear, and non-stationary characteristics. Several factors, such as complex electricity market operations, weather conditions, and fluctuating renewable generation, have an impact on electricity prices. In addition, natural gas price data has an uncertain nature, as can be seen in Figure 3. Therefore, deep features extracted from these datasets can represent important components of the data. The effective signal decomposition technique called EMD was employed in this study for decomposition. The extracted six IMFs and residue signals are presented in Figure 4. To identify the properties of these signals, some important statistical measures are given in Table 2.

**Table 2.** The statistical properties of the decomposed signals

Signal	Property	Imf1	Imf2	Imf3	Imf4	Imf5	Imf6	Residue
Electricity Price	Count	8760	8760	8760	8760	8760	8760	8760
	Mean	-0.51	0.67	0.60	0.40	0.43	0.88	257.74
	Std.	26.96	31.08	33.14	33.01	21.15	23.76	52.68
	Min.	-118.41	-147.25	-174.82	-143.19	-75.09	-107.14	93.32
	Max.	115.86	143.20	167.99	143.39	90.93	101.21	335.57
Natural Gas Price	Count	8760	8760	8760	8760	8760	8760	8760
	Mean	0.02	-0.16	-0.11	0.31	-1.17	-3.35	1484.32
	Std.	8.10	12.15	8.19	12.17	13.95	27.72	37.91
	Min.	-110.75	-151.95	-77.92	-80.84	-50.84	-67.45	1408.08
	Max.	107.07	164.72	68.69	68.85	48.70	74.15	1526.15

Table 2 summarizes the statistical properties of the decomposed signals of the electricity price and natural gas price variables using the EMD algorithm. The dataset consists of six intrinsic mode functions (IMFs) and one residue signal for each variable. The statistical properties for each signal are shown, including the number of data points, the average value, standard deviation, minimum, and maximum values. For the electricity price variable, the mean values of IMF1 to IMF6 range from -0.51 to 0.88, and the mean of the residue signal is 257.74. The standard deviation values of these signals range from 21.15 to 33.14, with the residue signal having the highest std. of 52.68. The minimum and maximum values of the IMFs and the residue signal range from -174.82 to 115.86 and 93.32 to 335.57, respectively. For the natural gas price variable, the mean values of IMF1 to IMF6 range from -3.35 to 0.31, and the mean of the residue signal is 1484.32. The standard deviation values of these signals range from 8.10 to 27.72, with the residue signal having the highest std. of 37.91. The minimum and maximum values of the IMFs and the residue signal range from -151.95 to 164.72 and 1408.08 to 1526.15, respectively. Overall, Table 2 provides a summary of the statistical properties of the decomposed signals, which can be useful for understanding the characteristics and behavior of the electricity and natural gas price variables.

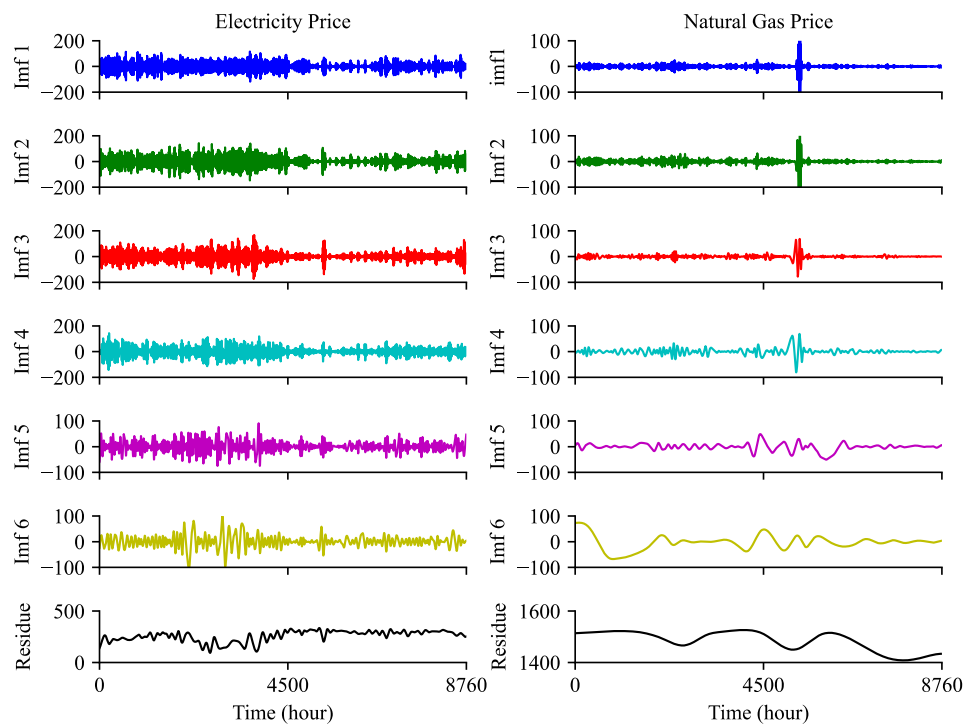


**Figure 4.** EMD results for electricity price and natural gas price datasets

### 5. EXPERIMENTAL STUDY

In this study, a two-stage hybrid model was proposed for day-ahead electricity power forecasting. The model was developed and tested on a dataset from the Turkish electricity market. This dataset included four types of features: renewable power generation, day-ahead electricity load forecasts, electricity prices, and natural gas prices. To reduce the number of features, the MI-based feature selection method was used. The two exogenous features, electricity load forecasts, and natural gas prices were selected from these features. Historical electricity prices, historical natural gas prices, and day-ahead electricity load forecasts were used as model input features. The EMD algorithm was employed to extract more deep features from the electricity price signal and the natural gas price signal. The lagged deep electricity price components, the lagged natural gas price components, and electricity load forecasts were used as the regression model inputs. Table 3 presents the model inputs.

**Table 3.** Inputs for regression

Input	Description	Number of features
Electricity price	Imf <sub>1-6</sub>	24, 48, 168 hours prior to the target hour
	Residue	24, 48, 168 hours prior to the target hour
Natural gas price	Imf <sub>1-6</sub>	24, 48 hours prior to the target hour
	Residue	24, 48 hours prior to the target hour
Electricity load forecasts	Forecast for target hour	1

The min-max normalization technique was used to scale the model inputs and output values to a range between 0 and 1. 90% of the dataset was allocated for developing (training and validating) the proposed model, whilst the remaining 10% was used for testing. The computationally efficient and effective CatBoost algorithm was used for regression. The Python programming language and Jupyter notebook environment were used to develop forecasting models. The open-source tools NumPy, Pandas, and Scikit-Learn were utilized to implement data preprocessing and ML algorithms. The experimental studies were conducted using the Google Colab platform. The benchmark models based on LR, Ridge, GB, and SVM were compared with the proposed model. The default hyper parameters provided by the

Scikit-Learn library were used in the study. Three error-based metrics, RMSE, MAE, and MAPE, and the correlation coefficient R were used to evaluate performances. The following equations were used to calculate performance metrics.

$$\text{RMSE}(\%) = 100 \times \sqrt{\frac{1}{N} \sum_{h=1}^N (P_a^h - P_f^h)^2} \quad (3)$$

$$\text{MAE}(\%) = 100 \times \frac{1}{N} \sum_{h=1}^N |P_a^h - P_f^h| \quad (4)$$

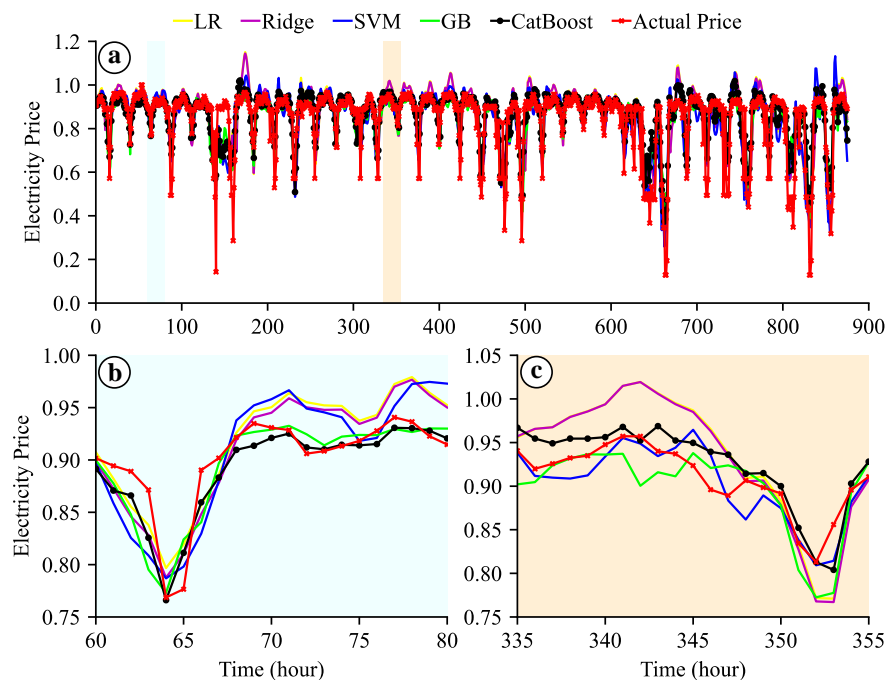
$$\text{MAPE}(\%) = 100 \times \frac{1}{N} \sum_{h=1}^N \left| \frac{P_a^h - P_f^h}{P_a^h} \right| \quad (5)$$

$$\text{R}(\%) = 100 \times \frac{\sum_{h=1}^N (P_f^h - \bar{P}_f)(P_a^h - \bar{P}_a)}{\sqrt{\sum_{h=1}^N (P_f^h - \bar{P}_f)^2 \sum_{h=1}^N (P_a^h - \bar{P}_a)^2}} \quad (6)$$

where  $N$  is the number of samples,  $a$  and  $f$  are the actual and forecasted values, respectively, and  $h$  denotes the hour.  $\bar{P}_a$  and  $\bar{P}_f$  are the averages of the actual and forecasted price values.

## 6. RESULTS

In this study, the results of the proposed and benchmark models were evaluated on a real dataset from the Turkish electricity market. The test results for both benchmark and proposed models are illustrated at the Figure 5.a, showing that all the forecasting models converged to the actual price values. To better demonstrate the forecasting performances, small intervals from the test data were selected and presented at the Figure 5.b and c. These two graphics demonstrated that the proposed CatBoost algorithm provided improved accuracy.



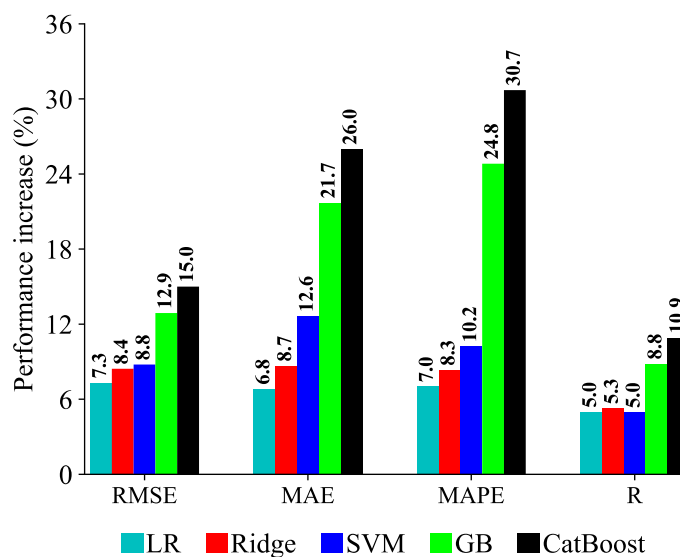
**Figure 5.** a. Overall results, b. Results for specific time interval, c. Results for specific time interval

Table 4 presents the forecasting results of benchmark and proposed models. Four performance metrics were calculated to evaluate the performance of the models. RMSE% is a well known error based metric. A lower RMSE% value indicates better accuracy in the model's predictions. In Table 4, the method with the lowest RMSE is CatBoost (8.3282%), indicating that it had the most accurate predictions among the methods tested. MAE represents the mean absolute difference between the actual values and the forecasted values. A lower MAE value indicates better accuracy in the model's predictions. In Table 4, the method with the lowest MAE is also CatBoost (5.2210%), indicating that it had the most accurate predictions among the methods tested. MAPE represents the mean absolute percentage difference error. A lower MAPE value indicates better accuracy in the model's predictions. In Table 4, the method with the lowest MAPE is once again CatBoost (6.9675%), indicating that it had the most accurate predictions among the methods tested. R% represents the coefficient of determination for actual and forecasted values. A higher R% value indicates that the model is better at predicting the actual values. In Table 4, the method with the highest R% value is CatBoost (86.2256%), indicating that it had the best predictive performance among the methods tested. Overall, the table illustrates that CatBoost outperformed the other methods in terms of accuracy and predictive power, as evidenced by its consistently lower RMSE, MAE, and MAPE values and higher R value.

**Table 4.** Forecasting results

Methods	Metrics			
	RMSE%	MAE%	MAPE%	R%
LR	9.0803	6.5729	8.7026	81.6213
Ridge	8.9713	6.4423	8.5794	81.8418
SVM	8.9384	6.1627	8.4436	81.5965
GB	8.5352	5.5233	7.4667	84.6193
CatBoost	8.3282	5.2210	6.9675	86.2256

To demonstrate the impact of EMD on forecasting performance, a further analysis was carried out on the results. The improvement in performance was calculated by comparing the benchmark and proposed models with the LR model without EMD. The results of this improvement in performance are presented in a bar graphic given in Figure 6.



**Figure 6.** Performance incensements compared to the LR without EMD

The bar graphic shows the performance increases in four metrics (RMSE, MAE, MAPE, and R) for five different methods (LR, Ridge, GB, SVM, and CatBoost) compared to the LR model without EMD decomposition. The performance increases are expressed as a percentage increase in each metric.

According to bar graphic given, it can be interpreted that the LR and Ridge had the smallest performance increase among all methods, with less than 10% increase in all metrics. The SVM and GB models showed moderate performance improvements, with 8.8-12.9% increase in RMSE, 12.6-21.7% increase in MAE, 10.2-24.8% increase in MAPE, and 5.0-8.8% increase in R. The proposed CatBoost method showed the largest improvement in all metrics, with a 15.8% increase in RMSE, 26.0% increase in MAE, 30.7% increase in MAPE, and 10.9% increase in R. This suggests that the CatBoost method outperformed the other methods and had the best performance improvement over the LR model, based on the given metrics.

## 7. CONCLUSION

In this study a two stage hybrid model was proposed for day ahead electricity price forecasting. MI and EMD were used in the first stage for feature selection and feature extraction, respectively. Day ahead electricity load forecasts, time lagged natural gas prices and time lagged electricity price signal components were used as second stage (regression model) inputs. The CatBoost algorithm was proposed for the second stage. LR, Ridge, GB, and SVM were used as benchmark regression algorithms. The implementation of the forecasting models were realized on the Turkish electricity market data. The experimental studies showed proposed forecasting model based on Catboost algorithm outperformed the benchmark models. The proposed model achieved minimum RMSE, MAE, and MAPE as 8.3282%, 5.2210%, and 6.9675% and maximum R value as 86.2256%. In addition the performance increase analysis confirmed the using EMD based decomposition improves the forecasting accuracy. The results of this study indicated that the proposed two-stage hybrid model has promising potential in forecasting day-ahead electricity prices in the Turkish electricity market. The future work that considers incorporating additional data sources, such as weather data or social media data, to further enhance the forecasting model will be interesting.

### Declaration of Ethical Standards

The author of this article declare that the materials and methods used in this study do not require ethical committee permission and/or legal-special permission.

### Credit Authorship Contribution Statement

Ceyhun Yıldız, conceptualized, conducted, and wrote the entire study.

### Declaration of Competing Interest

The author declares that he has no known competing financial interests or personal relationships that could have appeared to influence the work reported in this paper.

### Funding / Acknowledgements

This study was not funded by any institution.

### Data Availability

The author confirms that the datasets analyzed during the current study are available in public repositories (see reference [31]).

## 7. REFERENCES

- [1] J. Lago, G. Marcjasz, B. De Schutter, and R. Weron, "Forecasting day-ahead electricity prices: A review of state-of-the-art algorithms, best practices and an open-access benchmark," *Appl. Energy*, vol. 293, no. December 2020, p. 116983, 2021, doi: 10.1016/j.apenergy.2021.116983.
- [2] R. Weron, "Electricity price forecasting: A review of the state-of-the-art with a look into the future," *Int. J. Forecast.*, vol. 30, no. 4, pp. 1030–1081, 2014, doi: 10.1016/j.ijforecast.2014.08.008.
- [3] L. Tschora, E. Pierre, M. Plantevit, and C. Robardet, "Electricity price forecasting on the day-ahead market using machine learning," *Appl. Energy*, vol. 313, no. March, p. 118752, 2022, doi: 10.1016/j.apenergy.2022.118752.
- [4] P. Wang *et al.*, "An Online Electricity Market Price Forecasting Method Via Random Forest," *IEEE Trans. Ind. Appl.*, vol. 58, no. 6, pp. 7013–7021, 2022.
- [5] C. Xiao, D. Sutanto, K. M. Muttaqi, M. Zhang, K. Meng, and Z. Y. Dong, "Online sequential extreme learning machine algorithm for better predispach electricity price forecasting grids," *IEEE Trans. Ind. Appl.*, vol. 57, no. 2, pp. 1860–1871, 2021.
- [6] I. Shah, H. Bibi, S. Ali, L. Wang, and Z. Yue, "Forecasting one-day-ahead electricity prices for italian electricity market using parametric and nonparametric approaches," *IEEE Access*, vol. 8, pp. 123104–123113, 2020.
- [7] H. Yang and K. R. Schell, "GHTnet: Tri-Branch deep learning network for real-time electricity price forecasting," *Energy*, vol. 238, p. 122052, 2022, doi: 10.1016/j.energy.2021.122052.
- [8] H. Yang and K. R. Schell, "International Journal of Electrical Power and Energy Systems QCAE: A quadruple branch CNN autoencoder for real-time electricity price forecasting," *Int. J. Electr. Power Energy Syst.*, vol. 141, no. April, p. 108092, 2022, doi: 10.1016/j.ijepes.2022.108092.
- [9] J. Lago, F. De Ridder, and B. De Schutter, "Forecasting spot electricity prices: Deep learning approaches and empirical comparison of traditional algorithms," *Appl. Energy*, vol. 221, no. April, pp. 386–405, 2018, doi: 10.1016/j.apenergy.2018.02.069.
- [10] S. Luo and Y. Weng, "A two-stage supervised learning approach for electricity price forecasting by leveraging different data sources," *Appl. Energy*, vol. 242, no. February, pp. 1497–1512, 2019, doi: 10.1016/j.apenergy.2019.03.129.
- [11] T. Zhang, Z. Tang, J. Wu, X. Du, and K. Chen, "Short term electricity price forecasting using a new hybrid model based on two-layer decomposition technique and ensemble learning," *Electr. Power Syst. Res.*, vol. 205, no. July 2021, p. 107762, 2022, doi: 10.1016/j.epsr.2021.107762.
- [12] A. Meng *et al.*, "Electricity price forecasting with high penetration of renewable energy using attention-based LSTM network trained by crisscross optimization," *Energy*, vol. 254, p. 124212, 2022, doi: 10.1016/j.energy.2022.124212.
- [13] G. Memarzadeh and F. Keynia, "Short-term electricity load and price forecasting by a new optimal LSTM-NN based prediction algorithm," *Electr. Power Syst. Res.*, vol. 192, no. November 2020, p. 106995, 2021, doi: 10.1016/j.epsr.2020.106995.
- [14] Z. Shao, Q. Zheng, C. Liu, S. Gao, G. Wang, and Y. Chu, "A feature extraction- and ranking-based framework for electricity spot price forecasting using a hybrid deep neural network," *Electr. Power Syst. Res.*, vol. 200, no. September 2020, p. 107453, 2021, doi: 10.1016/j.epsr.2021.107453.
- [15] X. Xiong and G. Qing, "A hybrid day-ahead electricity price forecasting framework based on time series," *Energy*, vol. 264, no. November 2022, p. 126099, 2023, doi: 10.1016/j.energy.2022.126099.
- [16] K. Bhatia, R. Mittal, J. Varanasi, and M. M. Tripathi, "An ensemble approach for electricity price forecasting in markets with renewable energy resources," *Util. Policy*, vol. 70, no. July 2020, p. 101185, 2021, doi: 10.1016/j.jup.2021.101185.
- [17] M. Heidarpناه, F. Hooshyaripor, and M. Fazeli, "Daily electricity price forecasting using artificial intelligence models in the Iranian electricity market," *Energy*, vol. 263, no. PE, p. 126011, 2023, doi: 10.1016/j.energy.2022.126011.
- [18] S. Demir, K. Mincev, K. Kok, and N. G. Paterakis, "Data augmentation for time series regression: Applying transformations, autoencoders and adversarial networks to electricity price forecasting

- ☆," *Appl. Energy*, vol. 304, no. September, p. 117695, 2021, doi: 10.1016/j.apenergy.2021.117695.
- [19] W. Qiao and Z. Yang, "Forecast the electricity price of U . S . using a wavelet transform-based hybrid model," *Energy*, vol. 193, p. 116704, 2020, doi: 10.1016/j.energy.2019.116704.
- [20] K. Iwabuchi, K. Kato, D. Watari, I. Taniguchi, and F. Catthoor, "Energy and AI Flexible electricity price forecasting by switching mother wavelets based on wavelet transform and Long Short-Term Memory," *Energy AI*, vol. 10, no. May, p. 100192, 2022, doi: 10.1016/j.egyai.2022.100192.
- [21] D. H. Vu, K. M. Muttaqi, A. P. Agalgaonkar, and A. Bouzerdoum, "Short-term forecasting of electricity spot prices containing random spikes using a time-varying autoregressive model combined with kernel regression," *IEEE Trans. Ind. Informatics*, vol. 15, no. 9, pp. 5378–5388, 2019.
- [22] A. Pourdaryaei, H. Mokhlis, H. A. Illias, S. H. A. Kaboli, and S. Ahmad, "Short-Term Electricity Price Forecasting via Hybrid Backtracking Search Algorithm and ANFIS Approach," *IEEE Access*, vol. 7, pp. 77674–77691, 2019, doi: 10.1109/ACCESS.2019.2922420.
- [23] A. Pourdaryaei, H. Mokhlis, H. A. Illias, S. H. R. A. Kaboli, S. Ahmad, and S. P. Ang, "Hybrid ANN and artificial cooperative search algorithm to forecast short-term electricity price in de-regulated electricity market," *Ieee Access*, vol. 7, pp. 125369–125386, 2019.
- [24] N. Bibi, I. Shah, A. Alsubie, S. Ali, and S. A. Lone, "Electricity Spot Prices Forecasting Based on Ensemble Learning," *IEEE Access*, vol. 9, pp. 150984–150992, 2021, doi: 10.1109/ACCESS.2021.3126545.
- [25] A. L. I. N. Alkawaz and A. Abdellatif, "Day-Ahead Electricity Price Forecasting Based on Hybrid Regression Model," *IEEE Access*, vol. 10, no. October, pp. 108021–108033, 2022, doi: 10.1109/ACCESS.2022.3213081.
- [26] S. Zhou, L. Zhou, M. Mao, H.-M. Tai, and Y. Wan, "An optimized heterogeneous structure LSTM network for electricity price forecasting," *IEEE Access*, vol. 7, pp. 108161–108173, 2019.
- [27] R. Zhang, G. Li, and Z. Ma, "A deep learning based hybrid framework for day-ahead electricity price forecasting," *IEEE Access*, vol. 8, pp. 143423–143436, 2020.
- [28] C. E. Shannon, "A mathematical theory of communication," *Bell Syst. Tech. J.*, vol. 27, no. 3, pp. 379–423, 1948.
- [29] N. E. Huang *et al.*, "The empirical mode decomposition and the Hilbert spectrum for nonlinear and non-stationary time series analysis," *Proc. R. Soc. London. Ser. A Math. Phys. Eng. Sci.*, vol. 454, no. 1971, pp. 903–995, 1998.
- [30] L. Prokhorenkova, G. Gusev, A. Vorobev, A. V. Dorogush, and A. Gulin, "CatBoost: unbiased boosting with categorical features," *Adv. Neural Inf. Process. Syst.*, vol. 31, 2018.
- [31] "Energy Exchange Istanbul," 2023. <https://www.epias.com.tr>.

## OLIVE LEAF EXTRACT INCORPORATED CHITOSAN FILMS FOR ACTIVE FOOD PACKAGING

<sup>1,\*</sup> Aslıhan KAZAN , <sup>2</sup> Fatma DEMİRÇİ 

<sup>1</sup>Bursa Technical University, Engineering and Natural Sciences Faculty, Bioengineering Department, Bursa, TÜRKİYE

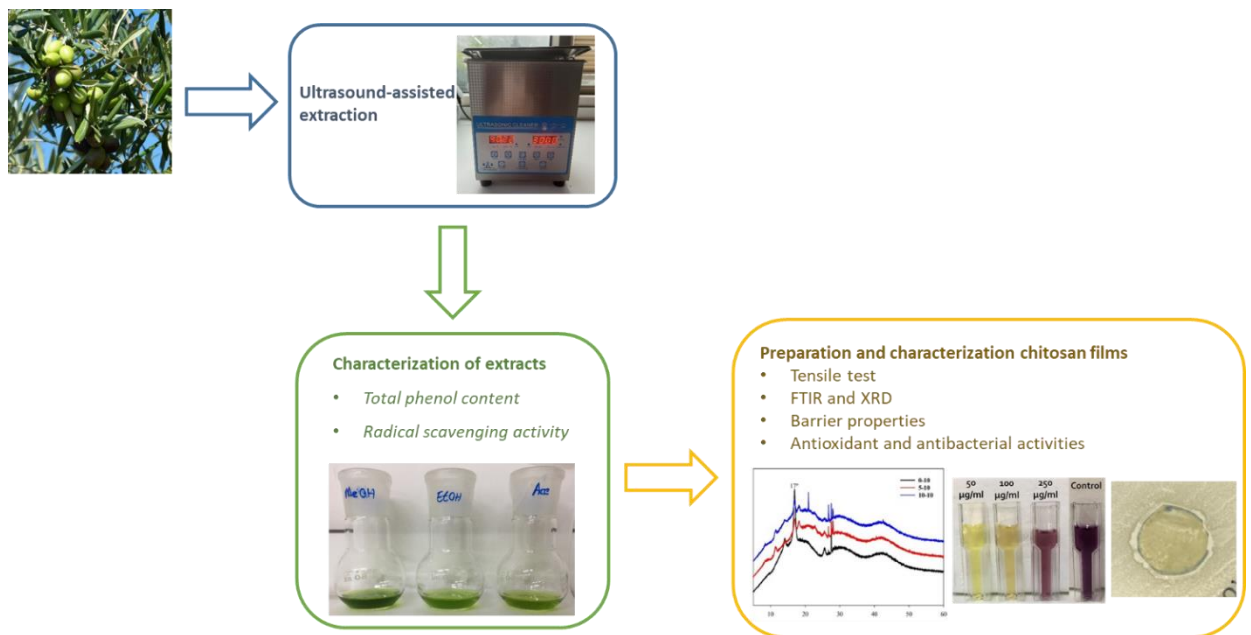
<sup>2</sup>Bursa Technical University, Engineering and Natural Sciences Faculty, Polymer Materials Engineering Department, Bursa, TÜRKİYE

<sup>1</sup>[aslihan.kazan@btu.edu.tr](mailto:aslihan.kazan@btu.edu.tr), <sup>2</sup>[fatma.demirci@btu.edu.tr](mailto:fatma.demirci@btu.edu.tr)

### Highlights

- Olive leaf extract (OLE) added chitosan films were produced.
- Barrier properties were improved by OLE addition.
- Tensile strength and elongation of OLE-added chitosan films were 32 MPa and 9.3%, respectively.
- Prepared films possessed antioxidant and antibacterial activities.
- OLE containing chitosan films were proved to be an alternative active packaging.

### Graphical Abstract



Flowchart for the preparation and characterization of olive leaf extract incorporated chitosan films



## OLIVE LEAF EXTRACT INCORPORATED CHITOSAN FILMS FOR ACTIVE FOOD PACKAGING

<sup>1,\*</sup> Aslıhan KAZAN , <sup>2</sup> Fatma DEMİRÇİ 

<sup>1</sup>Bursa Technical University, Engineering and Natural Sciences Faculty, Bioengineering Department, Bursa, TÜRKİYE

<sup>2</sup>Bursa Technical University, Engineering and Natural Sciences Faculty, Polymer Materials Engineering Department, Bursa, TÜRKİYE

<sup>1</sup>[aslihan.kazan@btu.edu.tr](mailto:aslihan.kazan@btu.edu.tr), <sup>2</sup>[fatma.demirci@btu.edu.tr](mailto:fatma.demirci@btu.edu.tr)

(Received: 06.06.2023; Accepted in Revised Form: 05.10.2023)

**ABSTRACT:** Packaging materials serve as a barrier to protect the food from the environment and new approaches with improved properties, such as active packaging, is gaining more attention nowadays. In this study, chitosan films containing olive leaf extract (OLE) as an additive were prepared and characterized in terms of mechanical, structural and biological properties. The addition of OLE improved not only the tensile strength (32 MPa) and elongation (9.3%) of chitosan films but also their barrier properties such as water vapor transmission rate of 657.52 g/m<sup>2</sup>day and moisture retention capability of 90.41%. Furthermore, chitosan films gained antibacterial properties with the addition of OLE and possessed a dose and time-dependent antioxidant activity compared to their extract-free equivalents. As a consequence, the present study suggests that chitosan films incorporated with OLE are a promising alternative as an active food packaging with enhanced mechanical, barrier, antioxidant and antibacterial properties.

**Keywords:** Active packaging, Antioxidant activity, Chitosan film, Mechanical properties, Olive leaf extract

### 1. INTRODUCTION

Packaging is defined as a barrier that separates the product from the environment, protects it from any damage that may occur during transportation and storage, and maintain its quality until consumption [1, 2]. The main goal of traditional packaging is to conserve quality as long as possible while reducing the interaction between the product and the packaging material. However, changes in consumer interests led to the search for packaging materials with enhanced properties and new packaging approaches have emerged, one of them being active packaging. Unlike traditional packaging, direct interaction between the product and the packaging material is consciously utilized in active packaging to contribute to the extension of the shelf life rather than merely serving as a barrier. The starting point for the design of an active packing is usually improvement of the most significant features for the product quality such as scavenging of oxygen, carbon dioxide or free radicals, removal of odors and flavors, reduction of spoilage, and prevention of color change [1, 3, 4].

Antioxidant additives such as butylated hydroxyanisole (BHA) or butylated hydroxytoluene (BHT) have been used for the packing of oxygen-sensitive foods. However, the utilization of synthetic antioxidants is questioned since they have potential risks for human health and strict control is required for their utilization. As they are nontoxic, natural antioxidants have been used to overcome these concerns during the preparation of active packaging as natural-based and eco-friendly alternatives [5, 6]. Most common natural additives are essential oils, fruit, and plant extracts especially rich in phenolic compounds and they have been used in the forms of crude extracts as well as isolated components. Among them, phenolic compounds are very popular since they not only improve the antioxidant and antimicrobial properties of the packaging material but also contribute to its physical and mechanical features by acting as crosslinking agents [7].

Olive (*Olea europaea*) is an evergreen tree belonging to the Oleaceae family that is native to the Mediterranean coast and cultivated for its fruit and oil [8, 9]. Large quantities of by-products such as olive

\*Corresponding Author: Aslıhan KAZAN, [aslihan.kazan@btu.edu.tr](mailto:aslihan.kazan@btu.edu.tr)

pomace, olive mill waste water, stones, seeds and leaves are released during olive oil production [10]. Olive leaf and its extract have been used in folk medicine for centuries due to their health promoting benefits. The leaves of the olive tree have been shown to possess a higher radical scavenging activity compared to the different parts of the plant [11].

Chitosan is a deacetylated derivative of chitin, the second most abundant polysaccharide after cellulose, and is used for various applications as being nontoxic, biocompatible, and biodegradable. In addition, its film forming ability, good mechanical features and barrier effect to gases such as CO<sub>2</sub> and O<sub>2</sub> make chitosan an excellent material for food packaging [12–14].

The aim of this study was to prepare and characterize chitosan films with OLE as an alternative active food packaging. For this purpose, chitosan films with and without OLE were prepared and compared in terms of mechanical, structural, antioxidant, and antibacterial properties.

## 2. MATERIAL AND METHODS

### 2.1. Chemicals and Plant Material

Folin-Ciocalteu agent and acetone are from Merck (Germany). Chitosan (85% deacetylated) was purchased from Alfa Aesar (Germany). Sodium carbonate was from AFG Bioscience (USA). Ethanol and methanol were obtained from Honeywell (Germany). Gallic acid was from Isolab (Germany) and 2,2-diphenyl-1-picrylhydrazyl hydrate (DPPH) from TCI (Japan). Olive leaves were purchased from a local market as dried and ground form.

### 2.2. Preparation and Characterization of Plant Extracts

#### 2.2.1. Ultrasonic-assisted extraction of olive leaf

0.5 g of ground leaves were mixed with 10 ml of extraction solvent (methanol, ethanol or acetone) and immersed in an ultrasonic bath with a constant temperature of 40°C. Continuous ultrasound was applied for 40 minutes. At the end of the extraction duration, leaves were removed by filtration and filtrate was centrifugated at 4000 rpm for 5 minutes. After centrifugation, the supernatant was evaporated under vacuum condition at 40°C. All extracts were stored at -20°C until experiments.

#### 2.2.2. Total phenol content of OLE

Extracts were characterized by Folin-Ciocalteu method in terms of total phenol content (TPC). 750 µl of Folin-Ciocalteu agent which was diluted in water for 10 folds, was added to 60 µl aliquot of extract. The mixture was vortexed and left to stand at room temperature for 5 minutes. Then, 600 µl saturated Na<sub>2</sub>CO<sub>3</sub> solution was added, vortexed, and kept in the dark at room temperature for 2 hours. The absorbance of the mixture was determined at 760 nm by a spectrophotometer [15]. Gallic acid was used as a reference standard and the total phenol content of the extracts was stated as mg gallic acid equivalent (GAE)/g extract. The analyses were carried out in duplicate.

#### 2.2.3. Radical scavenging activities and EC<sub>50</sub> values of OLE

The extracts were dissolved in 4 ml of methanol at three different concentrations as 50, 100, and 250 µg/ml. Then, 0.5 ml of DPPH solution (1 mM in methanol) was added and vortexed for 10 s. The mixture was kept at room temperature for 30 minutes. Absorbance measurement was conducted by a spectrophotometer at 517 nm and radical scavenging activity (RSA) was calculated by the following formula:

$$RSA\% = \frac{A_{DPPH} - A_{Extract}}{A_{DPPH}} \times 100 \quad (1)$$

where  $A_{DPPH}$  is the absorbance of DPPH solution without extract [16]. After determination of RSA% for different extract concentrations,  $EC_{50}$  values corresponding to 50% radical scavenging activity were calculated for each sample.

### 2.3. Preparation and Characterization of Chitosan Films

#### 2.3.1. Preparation of chitosan films

The film casting method was used to prepare the chitosan films. The chemical contents of the films are given in Table 1. For film production, chitosan was dissolved in acetic acid and distilled water mixture by mixing at 50°C for 48 hours. Then, a certain amount of glycerol was added to the solution and mixed for 1 hour at room temperature. While various amounts of methanol specified in Table 1 were included in the solution in pure chitosan samples, in doped samples OLE in methanol at 10% v/v concentrations were added to the solution and mixing was continued for one more hour at room temperature. The obtained solutions were poured into 9 cm diameter Petri dishes, left to dry for 48 hours at 40°C, and kept for 24 hours at room temperature before being removed from Petri dishes. The produced films were stored in a desiccator until tests were performed. The prepared films were named according to the amount of extract and methanol in their contents.

**Table 1.** Chemical compositions of the prepared films

Sample	Chemical Contents					
	Chitosan (g)	Acetic acid (ml)	MeOH (ml)	Distilled water (ml)	Glycerol (g)	Olive Leaf Extract (mg)
0-5	0.50	0.25	1.25	23.50	0.15	0
0-10	0.50	0.25	2.50	22.25	0.15	0
0-15	0.50	0.25	3.75	21.00	0.15	0
5-10	0.50	0.25	2.50	22.25	0.15	25
10-10	0.50	0.25	2.50	22.25	0.15	50

#### 2.3.2. Thickness and light barrier properties of prepared films

The thickness measurement of chitosan films was carried out at three random positions for each sample by using Leica-M125 stereomicroscope (Leica, Germany) under 100x magnification. The transmittance spectrum of each film between 200-800 nm was recorded by Shimadzu-UV3600 spectrophotometer (Shimadzu, Japan) and film transparency was calculated described by Terzioğlu et al. [17].

#### 2.3.3. Fourier transform infrared spectroscopy and X-ray diffraction analysis of prepared films

The prepared films were characterized with Fourier-transform infrared (FTIR-Thermo Nicolet, iS50 with an attenuated total reflectance (ATR) accessory) and X-ray diffraction (XRD-Bruker, D8 Advance) analyses. The FTIR spectra of the samples were recorded in the wavenumber range of 400 to 4,000  $cm^{-1}$  with 16 scans at 4  $cm^{-1}$  resolutions. XRD analysis of chitosan films was performed at experimental conditions of 3-70° scanning range and 0.5  $step^{-1}$  step size.

#### 2.3.4. Mechanical properties of prepared films

The mechanical performances of the prepared films were determined with a tensile test using a Shimadzu AGS X-Static Mechanical Tester following the modified ASTM Standard Test Method D 882-

12. (6.5 × 1 cm) samples were prepared and tested with an initial grip separation of 5 cm and 5 mm/s crosshead speed. Five replicates were tested for each film sample.

### 2.3.5. Water vapor transmission rate of prepared films

The water vapor transmission rate (WVTR) of the prepared films was determined according to the method used in a previous study [17] with slight modifications. 10 mL of distilled water was filled in a 1.13 cm diameter bottle and the bottle mouth was covered with prepared films with the help of parafilm. The film covered bottle samples were kept in a 40°C vacuum oven and weighted after 24 h, 48 h, 72 h, and 96 h. WVTR (g/m<sup>2</sup>day) of the films were performed for 3 replicates of each film sample and calculated by using the following formula

$$WVTR = \frac{W_i - W_t}{A \times t} \times 10^6 \quad (2)$$

where,  $W_i$  is the weight of the bottle before being placed in the oven,  $W_t$  is the weight of the bottle after being removed from the oven at a certain time ( $t$ ) (day), and  $A$  is the bottle mount area (mm<sup>2</sup>), respectively.

### 2.3.6. Moisture retention capability of prepared films

The moisture retention capability of the prepared films was determined according to a previous study [17]. 1 × 1 cm<sup>2</sup> square shape three samples of both films were placed into an 60°C oven for 6 h. The moisture retention capability of the films was calculated by using the following formula;

$$\text{Moisture Retention Capability} = \frac{W}{W_0} \times 100 \quad (3)$$

where,  $W_0$  is the weight of the films being placed in the oven and  $W$  is the weight of films after being removed from the oven, respectively.

### 2.3.7. Radical scavenging activities of prepared films

Chitosan films with and without OLE were cut into small pieces, and 20 mg of film samples were transferred to test tubes containing 4 ml of methanol. Then, 0.5 ml of 1 mM methanolic DPPH solution was added to each tube and absorbance was measured at 517 nm at time intervals. The RSA% of samples was calculated by using Eq. 1.

### 2.3.8. Antibacterial properties of prepared films

Inhibition zones of the chitosan films presence and absence of OLE were determined by disc diffusion method against *Staphylococcus aureus* (ATCC 25923). Bacterial suspension adjusted to the 0.5 McFarland Standard were dispersed homogeneously on nutrient agar and chitosan films with a diameter of 10 mm discs were placed onto the medium. After incubation at 37°C for 24 h, petri dishes were examined for zone formation and zone diameters were measured. Clear inhibition zones around the disks indicated antibacterial activity [18].

### 2.3.9. Statistical analysis

The paired Student's  $t$ -test was used and the normality of the data was analyzed by Kolmogorov-Smirnov test. In all tests, significant differences were considered when  $p < 0.05$ .

### 3. RESULTS AND DISCUSSION

#### 3.1. Characterization of Plant Extracts

Extraction of plant material was carried out with three different solvents and TPC of extracts was determined by Folin-Ciocalteu method. As shown in Table 2, the highest total phenolic content was obtained by methanol extraction and calculated as 106 mg GAE/g. Brahmi et al. [19], tested different solvents for the extraction of phenolic compounds from olive leaves and reported that the extraction solvent considerably affected the phenolic content of the obtained extracts and the highest amount of TPC was extracted by methanol. Kontogianni and Gerothanassis [20] extracted olive leaves with methanol by a one-week maceration process and the extracts were fractionated by solvents with different polarities. Total phenol content and EC<sub>50</sub> value of the chloroform fraction were determined as 106 mg/g and 69.1 µg/ml, respectively. These results are in agreement with the results obtained in our study.

EC<sub>50</sub> value, which is defined as the efficient concentration to reduce the initial amount of DPPH radical was calculated for extracts obtained by methanol, acetone and ethanol. The lowest EC<sub>50</sub> was obtained for methanolic extract while there was no significant difference between the RSA and EC<sub>50</sub> values of extracts obtained by acetone and ethanol. These results also indicated that there is a strong relationship between the TPC and RSA as previously reported [21, 22].

**Table 2.** Total phenol content, radical scavenging activity and EC<sub>50</sub> value of OLE obtained by different solvents

Extraction solvent	TPC (mg GAE/g)	RSA (%)	EC <sub>50</sub> (µg/ml)
Methanol	106.29±0.63	73.74±0.88	64.62±0.97
Ethanol	87.73±3.93	56.52±0.74	98.68±5.54
Acetone	90.84±2.04	57.19±0.74	94.49±1.30

#### 3.2. Characterization of Chitosan Films

##### 3.2.1. Thickness and light barrier properties of prepared films

The thickness of chitosan films with and without OLE was determined to vary between 0.05 mm and 0.065 mm. As seen in Figure 1, prepared films with and without OLE showed a homogenous structure and were clear enough to be utilized as see-through packaging. The incorporation of OLE in film structure resulted in a slight color change probably due to the chlorophyll content of OLE. Chitosan films containing 25 mg and 50 mg of OLE showed similar transparency as 25.49 mm<sup>-1</sup> and 26.35 mm<sup>-1</sup>, respectively.



**Figure 1.** Visual appearance of chitosan films absence and presence of OLE: 0-10 (a), 5-10 (b) and 10-10 (c).

##### 3.2.2. FTIR and XRD analysis of prepared films

Figure 2 demonstrated the FTIR spectra of the produced films according to the changes depending on the methanol ratio (Figure 2a) and OLE addition (Figure 2b) in 10% methanol-added films. In Figure 2a,

the asymmetric stretching of  $\text{NH}_2$  and OH caused a broad and strong band in the range of  $3200\text{ cm}^{-1}$  and  $3450\text{ cm}^{-1}$ . Amide I, Amide II, and Amide III related bands were shown at  $1638\text{ cm}^{-1}$ ,  $1561\text{ cm}^{-1}$ , and  $1327\text{ cm}^{-1}$ , respectively. C-O-C bridge asymmetric stretching and skeletal vibrations involving the C-O stretching were characteristic of saccharide structure and seen at  $1158\text{ cm}^{-1}$  and  $1030\text{ cm}^{-1}$ , respectively [23–25].

There were a number of characteristic bands in the FTIR spectrum of the OLE. The  $3310\text{ cm}^{-1}$  and  $1690\text{ cm}^{-1}$  bands corresponded to the oleuropein and other active compounds being presented in the OLE. The  $1607\text{ cm}^{-1}$  band represented the fingerprint region of functional groups such as C-O and O-H in the OLE structure. The  $1515\text{ cm}^{-1}$  and  $1386\text{ cm}^{-1}$  bands belonged to the Amide II and scissoring vibrations of the methylene in the proteins, respectively [26]. However, the FTIR spectra of the OLE added films were very similar to the 0-10 chitosan film and no evidence was found to show the interaction of chitosan and the OLE in the FTIR spectra of the films, as seen in Figure 2b. Similar results were obtained in the literature for OLE added chitosan microspheres [25].

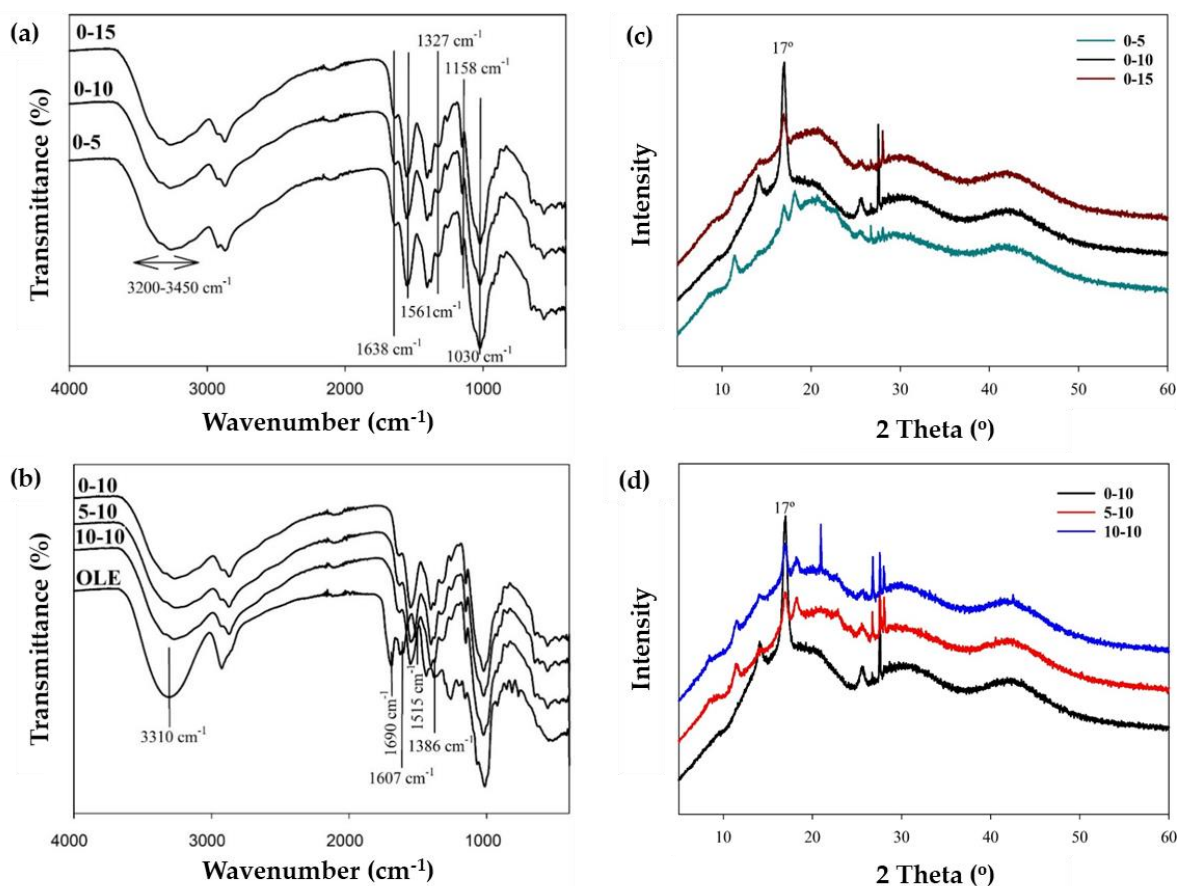


**Figure 2.** FTIR spectra (a), (b) and XRD pattern (c), (d) of chitosan films for different methanol and extract concentrations, respectively

XRD analysis was applied to the prepared films to demonstrate the effects of methanol addition and the interaction of the polyphenolic groups of OLE with chitosan. The XRD patterns of the 0-5, 0-10, and 0-15 were given in Figure 2c. As seen in Figure 2c and known in the literature, the solvent evaporation rate has an effect on the crystallization behavior of polymers, and the addition of methanol changed the crystallization behavior of chitosan [27]. Increasing the methanol ratio in the film solution up to 10% increased the crystallization rate due to the rapid evaporation of the solvent. However, increasing the solvent ratio further increased the solvent removal time, and the crystallization rate started to decrease again. Since 0-10 film showed the highest crystallization behavior, the OLE additive was included in the recipe at 10% methanol. The XRD patterns of the OLE added films (0-10, 5-10, and 10-10) were given in

Figure 2d. As seen in the figure, the addition of the OLE decreased the main peak intensity at 17°. However, with the addition of OLE, new crystallizations have been seen in the film structure. The effect of the change in the crystallization of the chitosan films was also seen in the mechanical test results.

### 3.2.3. Mechanical properties of prepared films

A tensile test was applied to determine the impact of methanol concentration and OLE addition on the mechanical properties of prepared films. Chitosan films prepared with 5% methanol concentration had the lowest tensile strength of 25 MPa and an increase in methanol concentration resulted in improved tensile strength. However, the difference between the tensile strengths of the chitosan films prepared with 10% and 15% methanol concentrations was insignificant (Figure 3a). To reduce the organic solvent consumption, 10% of the methanol concentration was chosen for subsequent experiments, which was also the concentration resulting in the highest crystallinity. Although the addition of OLE resulted in a slight decrease in the tensile strength from 32.8 MPa to 29.9 MPa compared to chitosan films without extract, this alteration was not statistically significant (Figure 3b).

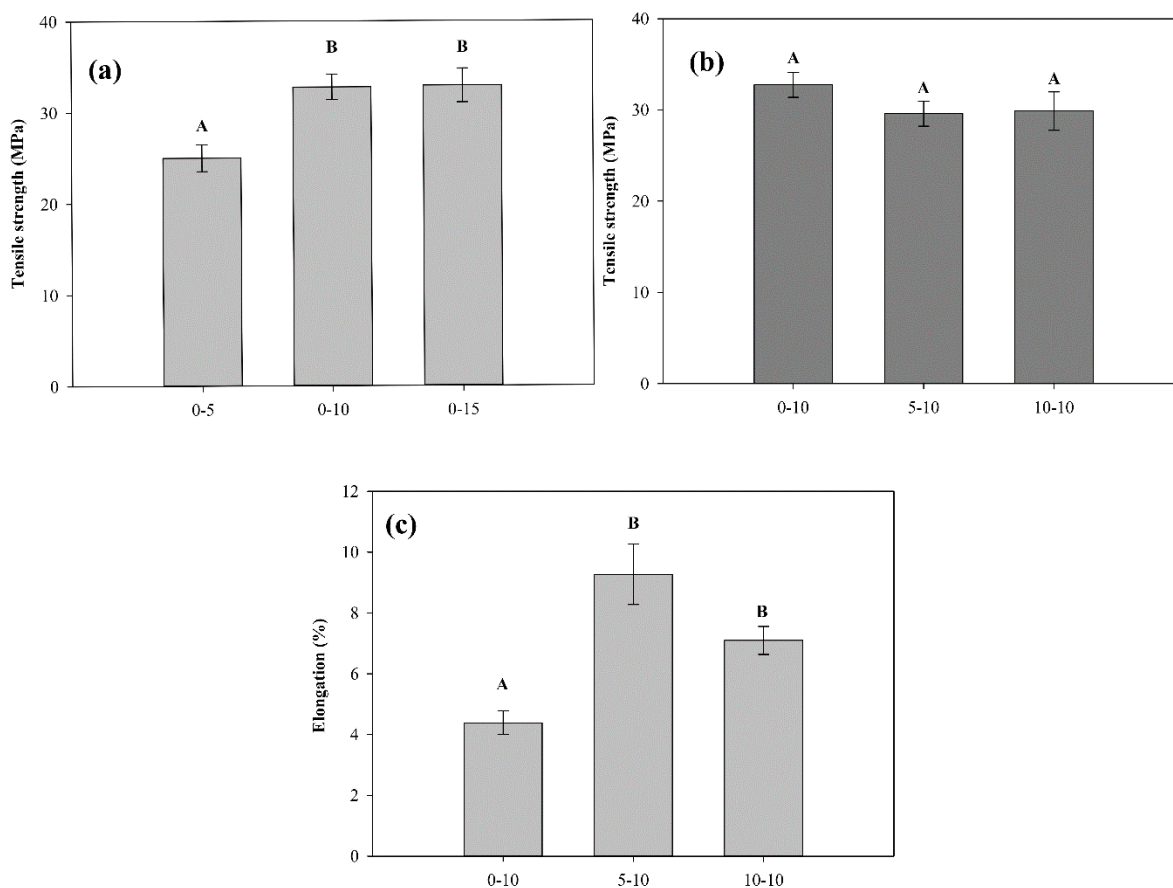


**Figure 3.** Mechanical properties of chitosan films: tensile strength at different methanol (a) and extract (b) concentration and percent elongation for different extract amount (c)

Chitosan films are known to be brittle and rigid in nature and commonly need plasticizers to improve their mechanical properties. However, the majority of commercial plasticizers are synthetic and may cause the migration of chemicals from packaging to food which may lead to consumer health risks and a change in the quality of food [28, 29]. In this study, prepared films were characterized in terms of percent elongation, which is a measure of stretching ability. The results showed that varying the methanol concentration from 5 to 15% did not lead to a significant difference in percent elongation while the addition

of OLE enhanced the flexibility and thus processability of prepared films. The additives are typically stated to affect the percent elongation and tensile strength of chitosan films inversely [12, 30]. Musella et al. [31], used OLE as an additive to produce chitosan films, however, the extract has not been uniformly distributed through the film structure resulting in the formation of visible insoluble particles. It has been reported that this non-homogeneity caused inconsistencies between the repetitions and affected the results of mechanical tests for chitosan films. On the other hand, the results of our study revealed that OLE can be used successfully to improve both the strength and flexibility of chitosan films (Figure 3c). Such a positive influence of OLE on tensile strength and percent elongation can be attributed to the good distribution of OLE in the chitosan film matrix with the help of methanol addition which was also revealed by the results of FTIR analysis.

### 3.2.4. Water vapor transmission rate and moisture retention capability of prepared films

It is known in the literature that the barrier and mechanical properties of the packaging films were affected by the water absorption and diffusion properties of the film. Therefore, WVTR and moisture retention capability are crucial properties for food packaging applications [23, 32, 33]. As seen in Figure 4, while the water vapor transition rate of the 10-10 sample was the lowest at 657.52 g/m<sup>2</sup>day, the moisture retention capability was the highest at 90.41%. These results demonstrated that the addition of OLE to the film structure has increased the potential of chitosan films to be utilized in food packaging applications.

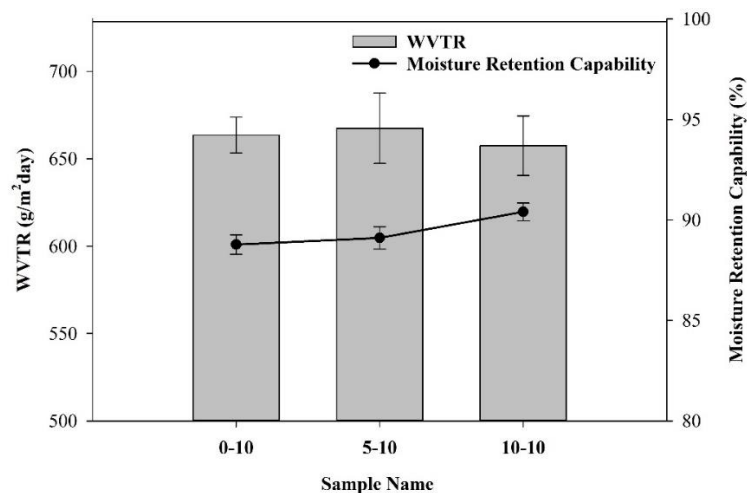


**Figure 4.** Water vapor transmission rate and moisture retention capability of chitosan films

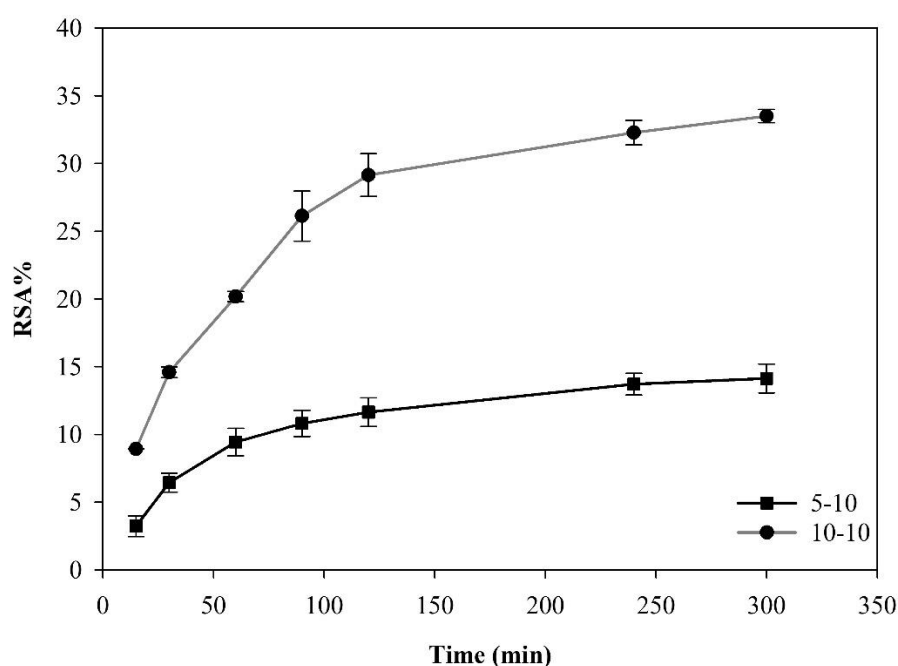
### 3.2.5. Radical scavenging activities of prepared films

Radical scavenging activity of prepared films was also elicited and results are presented in Table 3. Chitosan films without OLE have not possessed radical scavenging activity and the presence of the extract resulted in a significant increase of radical scavenging ability of the films. In addition, prepared films showed dose-dependent radical scavenging activity, which increased from 14% to over 35% by doubling the OLE content of chitosan films.

**Table 3.** Radical scavenging activity of prepared films at 300 min

Film	RSA%
0-5	NA
0-10	NA
0-15	NA
5-10	14.62
10-10	36.64

As seen in Figure 5, the RSA of OLE added chitosan films showed a time-dependent behavior. These results revealed the migration of active ingredients from prepared films and also the necessity of adding active components to improve the antioxidant properties of chitosan films.

**Figure 5.** Radical scavenging activity of prepared films at different time intervals

### 3.2.6. Antibacterial properties of prepared films

Antibacterial activity is a desirable feature of active food packaging that inhibits spoilage and contributes to shelf life extension [34]. In this study, disk diffusion method was applied to chitosan films with and without extract. The results showed that chitosan films without extract have not possessed antibacterial activity. Although chitosan is known to have antimicrobial properties, the limited diffusion in agar medium could be the reason for the absence of an inhibition zone [35]. Chitosan films containing 25 mg and 50 mg OLE showed inhibition zones with diameters of 11.9 mm and 11.4 mm, respectively (Figure 6). These findings clearly revealed the effect and potential of OLE containing chitosan films to extend the shelf life of food.

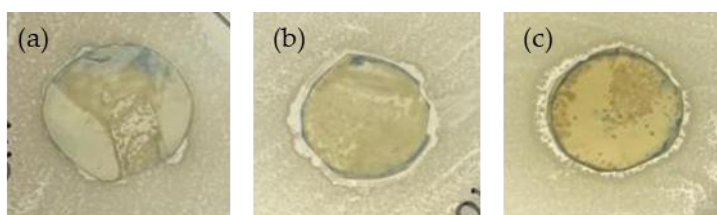


**Figure 6.** Inhibitory effect of chitosan films on the growth of *Staphylococcus aureus* absence (a) and presence (b), (c) of extract

#### 4. CONCLUSIONS

In this study, chitosan films were prepared for active food packaging and characterized in terms of mechanical, structural and biological properties. OLE was used as an active ingredient and the most suitable solvent for the ultrasonic-assisted extraction was determined as methanol yielding 106.3 mg GAE/g extract total phenol content and 64.6  $\mu\text{g/ml}$   $\text{EC}_{50}$  value for radical scavenging activity. By addition of OLE, chitosan films gained antioxidant and antibacterial activities compared to their extract-free equivalents. Furthermore, OLE added films possessed a time-dependent radical scavenging activity indicating the migration of active components from the film which is an important feature to be used as active packaging. XRD analysis indicated that the crystallization behavior of chitosan films was also affected by the addition of methanol and OLE to the film formulation while their barrier properties were also improved. The effect of methanol content and extract amount on the mechanical and structural properties of chitosan films was also examined. OLE was successfully distributed in chitosan films as elicited by FTIR spectra and the presence of methanol and OLE greatly influenced the mechanical properties resulting in more resistant and stretchable films compared to the control group. This study suggests that chitosan films incorporated with OLE are a promising alternative as active food packaging with enhanced mechanical, antioxidant and antibacterial features.

#### Declaration of Ethical Standards

The authors declare that all ethical guidelines including authorship, citation, data reporting, and publishing original research are followed.

#### Declaration of Competing Interest

The authors declare that there is no conflict of interest.

#### Funding / Acknowledgements

The authors declare that they have not received any funding or research grants during the review, research or assembly of the article.

#### Data Availability

The data that support the findings of this study are available from the corresponding author upon reasonable request.

#### REFERENCES

- [1] J. Wyrwa, and A. Barska, "Innovations in the food packaging market: active packaging," *Eur. Food Res. Technol.*, vol. 243, no. 10, pp. 1681–1692, 2017.

- [2] J. Jeevahan and M. Chandrasekaran, "Nanoedible films for food packaging: a review," *J. Mater. Sci.*, vol. 54, no. 19, pp. 12290–12318, 2019.
- [3] M. Ozdemir and J. D. Floros, "Active Food Packaging Technologies," *Crit. Rev. Food Sci. Nutr.*, vol. 44, no. 3, pp. 185–193, May 2004.
- [4] M. L. Rooney, "Introduction to active food packaging technologies," *Innov. Food Packag.*, pp. 63–79, Jan. 2005.
- [5] J. Gómez-Estaca, C. López-de-Dicastillo, P. Hernández-Muñoz, R. Catalá, and R. Gavara, "Advances in antioxidant active food packaging," *Trends Food Sci. Technol.*, vol. 35, no. 1, pp. 42–51, Jan. 2014.
- [6] H. Wang, J. Qian and F. Ding, "Emerging Chitosan-Based Films for Food Packaging Applications," *J. Agric. Food Chem.*, vol. 66, no. 2, pp. 395–413, Jan. 2018.
- [7] W. Zhang, Y. Zhang, J. Cao, and W. Jiang, "Improving the performance of edible food packaging films by using nanocellulose as an additive," *Int. J. Biol. Macromol.*, vol. 166, pp. 288–296, Jan. 2021.
- [8] Y. Orihara and Y. Ebizuk, "Production of Triterpene Acids by Cell-suspension Cultures of *Olea europaea*," *Olives Olive Oil Heal. Dis. Prev.*, pp. 341–347, Jan. 2010.
- [9] N. B. Ray, N. T. Lam, R. Luc, N. P. Bonvino, and T. C. Karagiannis, "Cellular and Molecular Effects of Bioactive Phenolic Compounds in Olives and Olive Oil," *Olive Olive Oil Bioact. Const.*, pp. 53–91, Jan. 2015.
- [10] M. A. Nunes, F. B. Pimentel, A. S. G. Costa, R. C. Alves, and M. B. P. P. Oliveira, "Olive by-products for functional and food applications: Challenging opportunities to face environmental constraints," *Innov. Food Sci. Emerg. Technol.*, vol. 35, pp. 139–148, Jun. 2016.
- [11] F. Rodrigues, F. B. Pimentel, and M. B. P. P. Oliveira, "Olive by-products: Challenge application in cosmetic industry," *Ind. Crops Prod.*, vol. 70, pp. 116–124, Aug. 2015.
- [12] Z. H. Zhang, Z. Han, X. A. Zeng, X. Y. Xiong, and Y. J. Liu, "Enhancing mechanical properties of chitosan films via modification with vanillin," *Int. J. Biol. Macromol.*, vol. 81, pp. 638–643, Nov. 2015.
- [13] J. F. Rubilar, R. M. S. Cruz, H. D. Silva, A. A. Vicente, I. Khmelinskii, and M. C. Vieira, "Physico-mechanical properties of chitosan films with carvacrol and grape seed extract," *J. Food Eng.*, vol. 115, no. 4, pp. 466–474, Apr. 2013.
- [14] A. Aryaei, A. H. Jayatissa, and A. C. Jayasuriya, "Nano and micro mechanical properties of uncross-linked and cross-linked chitosan films," *J. Mech. Behav. Biomed. Mater.*, vol. 5, no. 1, pp. 82–89, Jan. 2012.
- [15] H. Koyu, A. Kazan, S. Demir, M. Z. Haznedaroglu, and O. Yesil-Celiktas, "Optimization of microwave assisted extraction of *Morus nigra* L. fruits maximizing tyrosinase inhibitory activity with isolation of bioactive constituents," *Food Chem.*, vol. 248, pp. 183–191.
- [16] A. Kazan, H. Koyu, I. C. Turu, and O. Yesil-Celiktas, "Supercritical fluid extraction of *Prunus persica* leaves and utilization possibilities as a source of phenolic compounds," *J. Supercrit. Fluids*, vol. 92, pp. 55–59.
- [17] P. Mustafa *et al.*, "PVA/starch/propolis/anthocyanins rosemary extract composite films as active and intelligent food packaging materials," *J. Food Saf.*, vol. 40, no. 1, p. e12725, Feb. 2020.
- [18] Y. E. Agustin and K. S. Padmawijaya, "Effect of glycerol and zinc oxide addition on antibacterial activity of biodegradable bioplastics from chitosan-kepok banana peel starch," *IOP Conf. Ser. Mater. Sci. Eng.*, vol. 223, no. 1, p. 12046, 2017.
- [19] F. Brahmi, B. Mechri, S. Dabbou, M. Dhibi, and M. Hammami, "The efficacy of phenolics compounds with different polarities as antioxidants from olive leaves depending on seasonal variations," *Ind. Crops Prod.*, vol. 38, no. 1, pp. 146–152, Jul. 2012.
- [20] V. G. Kontogianni and I. P. Gerathanassis, "Phenolic compounds and antioxidant activity of olive leaf extracts," *Nat. Prod. Res.*, vol. 26, no. 2, pp. 186–189, Jan. 2012.
- [21] K. Kiritsakis, M. G. Kontominas, C. Kontogiorgis, D. Hadjipavlou-Litina, A. Moustakas, and A. Kiritsakis, "Composition and Antioxidant Activity of Olive Leaf Extracts from Greek Olive Cultivars," *J. Am. Oil Chem. Soc.*, vol. 87, no. 4, pp. 369–376, 2010.

- [22] D. Borjan, M. Leitgeb, Ž. Knez, and M. K. Hrnčič, "Microbiological and Antioxidant Activity of Phenolic Compounds in Olive Leaf Extract," *Molecules*, vol. 25, no. 24, 2020.
- [23] Z. Kalaycıoğlu, E. Torlak, G. Akın-Evingür, İ. Özen, and F. B. Erim, "Antimicrobial and physical properties of chitosan films incorporated with turmeric extract," *Int. J. Biol. Macromol.*, vol. 101, pp. 882–888, Aug. 2017.
- [24] N. Banik, A. Hussain, A. Ramteke, H. K. Sharma, and T. K. Maji, "Preparation and evaluation of the effect of particle size on the properties of chitosan-montmorillonite nanoparticles loaded with isoniazid," *RSC Adv.*, vol. 2, no. 28, pp. 10519–10528, 2012.
- [25] N. Acosta *et al.*, "Physical Stability Studies of Semi-Solid Formulations from Natural Compounds Loaded with Chitosan Microspheres," *Marine Drugs*, vol. 13, no. 9, pp. 5901–5919, 2015.
- [26] G. A. Nasir, A. K. Mohammed, and H. F. Samir, "Biosynthesis and Characterization of Silver Nanoparticles Using Olive Leaves Extract and Sorbitol," *Iraqi J. Biotechnol.*, vol. 15, no. 1, pp. 22–32, 2016.
- [27] H. Huang, Q. Yuan, and X. Yang, "Morphology study of gold–chitosan nanocomposites," *J. Colloid Interface Sci.*, vol. 282, no. 1, pp. 26–31, Feb. 2005.
- [28] W. Thakhiew, S. Devahastin, and S. Soponronnarit, "Effects of drying methods and plasticizer concentration on some physical and mechanical properties of edible chitosan films," *J. Food Eng.*, vol. 99, no. 2, pp. 216–224, Jul. 2010.
- [29] M. G. A. Vieira, M. A. Da Silva, L. O. Dos Santos, and M. M. Beppu, "Natural-based plasticizers and biopolymer films: A review," *Eur. Polym. J.*, vol. 47, no. 3, pp. 254–263, Mar. 2011.
- [30] S. Prateepchanachai, W. Thakhiew, S. Devahastin, and S. Soponronnarit, "Mechanical properties improvement of chitosan films via the use of plasticizer, charge modifying agent and film solution homogenization," *Carbohydr. Polym.*, vol. 174, pp. 253–261, Oct. 2017.
- [31] E. Musella *et al.*, "Preparation and Characterization of Bioactive Chitosan-Based Films Incorporated with Olive Leaves Extract for Food Packaging Applications," *Coatings*, vol. 11, no. 11, 2021.
- [32] P. Mustafa *et al.*, "Improving functional properties of PVA/starch-based films as active and intelligent food packaging by incorporating propolis and anthocyanin," *Polym. Polym. Compos.*, vol. 29, no. 9, pp. 1472–1484, Nov. 2020.
- [33] L. Cui *et al.*, "Preparation and characterization of chitosan membranes," *RSC Adv.*, vol. 8, no. 50, pp. 28433–28439, 2018.
- [34] L. Bastarrachea, S. Dhawan, and S. S. Sablani, "Engineering Properties of Polymeric-Based Antimicrobial Films for Food Packaging: A Review," *Food Eng. Rev.*, vol. 3, no. 2, pp. 79–93, 2011.
- [35] H. Haghighi *et al.*, "Development of antimicrobial films based on chitosan-polyvinyl alcohol blend enriched with ethyl lauroyl arginate (LAE) for food packaging applications," *Food Hydrocoll.*, vol. 100, p. 105419, Mar. 2020.



## THE IMPACT OF EUROPEAN UNION LEGISLATION ON CADASTRAL SURVEYORS: A COMPARATIVE ANALYSIS AND RESULTS IN THE EUROPEA AND TÜRKİYE

\* Orhan ERCAN 

*Ankara University, Applied Sciences Faculty, Real Estate Development and Management Department, Ankara,  
TÜRKİYE*  
[orhanercan@ankara.edu.tr](mailto:orhanercan@ankara.edu.tr)

### *Highlights*

- In member countries, there are differences in conducting cadastral surveyor activities.
- Türkiye, exhibits differences compared to the European country averages in certain aspects.
- It is an important necessity to enact an EU law that each country can use to ensure uniformity in implementation.



## THE IMPACT OF EUROPEAN UNION LEGISLATION ON CADASTRAL SURVEYORS: A COMPARATIVE ANALYSIS AND RESULTS IN THE EUROPEA AND TÜRKİYE

\* Orhan ERCAN 

Ankara University, Applied Sciences Faculty, Real Estate Development and Management Department, Ankara,  
TÜRKİYE  
[orhanercan@ankara.edu.tr](mailto:orhanercan@ankara.edu.tr)

(Received: 26.09.2023; Accepted in Revised Form: 11.10.2023)

**ABSTRACT:** The task of keeping the cadastre up to date, which is as crucial as its establishment, is carried out by cadastral surveyors. The Lisbon Treaty has been a crucial development that has had profound effects on various professions in the countries that are members of the European Union. This shift is bolstered by measures and legislations that encourage open markets, simplify information sharing, and promote the compatibility of data, exemplified by initiatives like INSPIRE, the Bologna Process, and Small Act Business. This article undertakes an examination of the implications of European Union legislation on the field of cadastral surveying, encompassing a comprehensive analysis of various facets, including the levels of education required, the procedures for licensing and authorization, the duration of validity, affiliations, operational modalities, activities, quality control mechanisms, responsibilities, professional insurance, and the continuous professional development requirements for licensed cadastral surveyors engaged in post-cadastre services across Europe and Türkiye. The article includes a comparative analysis of cadastral surveying practices in European countries and Türkiye, and provides recommendations for completing legislative efforts aimed at achieving greater uniformity in European practices and addressing identified deficiencies within Turkish practices.

**Keywords:** EU legislation, Turkish legislation, Cadastral surveyors, Post cadastre activities, INSPIRE

### 1. INTRODUCTION

The surveying profession is a combination of legal, economic, environmental, societal and technological aspects. There are two important branches of our profession as land management and geospatial technologies and they are complementary to each other.

The concept of cadastre, which lies at the core of modern land administration, serves as the primary tool for parcel management, essentially encompassing the land registry. The potential of cadastres to enhance land management and contribute to effective governance is particularly pronounced in contemporary land administration, as highlighted by sources such as [1]-[2]-[3], and the International Federation of Surveyors (FIG) in 1995. There is a digital divide in terms of cadastre establishment and management depending on the development level of the countries and the constructive ownership approach. Effective Land Management Framework – FELA [4] and Integrated Geospatial Information – IGIF [5] documents prepared, which can be accepted as framework documents on land management by the United Nations (UN) within the scope of 2030 Agenda, with the motto "no one left behind", in order to close the digital divide between countries in terms of cadastre and geospatial data production. These documents can be a guide both for countries that have not been cadastre until now, as well as for countries that have had cadastre but need renewal.

In general, a cadastre comprises the geometric description of a parcel, alongside other descriptive information about the parcel, including ownership, value, development, and more [6]. A succinct definition of cadastre can be found in Article 1 of the Turkish Cadastre Law, which defines it as follows: Cadastre is the process of establishing the land register, as stipulated by Turkish Civil Law, based on the

country's coordinate system and using cadastral or topographic cadastral maps. Its purpose is to define the legal status of land properties, delineate property boundaries on maps, and lay the infrastructure for a spatial information system.

The land registry is a direct outcome of the initial cadastre, providing a comprehensive view of both the geometric and legal aspects of properties. In countries where legal cadastre is maintained, these records are managed under the responsibility of the state, in accordance with the principles of registration and clarity, in order to show the property details and related rights in a transparent manner.

The recent priorities in Europe, whether they are members or not, indicate an almost historical necessity for cooperation, collaboration, and enhanced alignment among countries. However, every surveyor is aware that the foundation of their profession, which comprises legal and technical aspects such as private property rights, spatial planning, etc., is the prerogative of each state.

It is known that both a cadastre and a land registry are in operation in European Union (EU) Member Countries. The majority of the cadastral systems are either centred around fiscal or legal aspects, while some are transitioning from fiscal to legal orientations. National Mapping and Cadastral Agencies (NMCA) hold a significant role in relation to the activities of cadastral and property surveyors, frequently acting as license providers, supervisors, and coordinators [7]-[8]-[9].

The cadastre functions as a dynamic system, emphasizing the ongoing significance not only of its initial establishment but also of keeping it up to date [6]. The responsibility for conducting post-cadastral survey transactions and ensuring the system's up to date is carried out by Licensed Cadastral Surveyors (Property Surveyors) who are authorized to act on behalf of the public in Türkiye, as in most countries in EU.

In Türkiye, some of the demand-driven (post-cadastre) technical tasks related to cadastre were initiated to be carried out by the Licensed Survey and Cadastre Engineers' Bureaus (LIHKAB), established by the law enacted in 2005 [10]. During the process, disputes arose between Free Survey and Cadastre Engineers (SHKM) and LIHKABs, especially regarding authority, responsibility, and market share, leading to a re-evaluation of the law. In 2021, a new LIHKAB law came into effect. Although the new LIHKAB law appears to have resolved disputes between LIHKABs and SHKMs, it has brought along other problems [11]- [12].

While the impact of EU regulations on the surveying field may appear complex, many professional surveyors across EU have discovered that practical limitations imposed by national borders are less significant. Several studies have been conducted to understand the provisions of EU laws concerning surveyors in cross-border operations, as well as the issues related to the ability of surveyors to work in the EU free market and how to address them. The Council of European Geodetic Surveyors (CLGE) conducted the Impact of EU Legislation on Cadastral Surveying in 2010 [8], European Requirements for licensed cadastral surveyors Activities studies and 2018 [8] with the aim of establishing consistency in the implementation of cadastral surveyors' activities within the EU by defining their scope, national conditions, and requirements. The study from 2018 [9] underwent subsequent revisions and expansions, culminating in the publication of all three studies mentioned.

In this article, the legal framework of cadastral surveying, activities of cadastral surveyors, the impact of EU legislation on cadastral surveying, and the national terms and conditions, as well as common characteristics of licensed cadastral surveyors within the EU, are discussed. A comparative analysis has been conducted on education level, licenses/authorizations, validity period, affiliation, modes of practice (civil servant, individual, company, etc.), activities, quality control, liability, professional insurance, sanctions, and continuous professional development for licensed cadastral surveyors in the EU and Türkiye. Recommendations guiding the practices have been presented based on the research findings. Information regarding the activities of licensed cadastral surveyors in the EU, as required for the study, has been sourced from CLGE publications within the scope of the study.

## 2. CADASTRAL SURVEYING WITHIN THE FRAMEWORK OF THE EUROPEAN UNION LEGISLATION

The EU is a system that was established with the 1957 Treaty of Rome and has progressively evolved. This system, the phenomenon of the EU, is a system of values. At the core of the EU values system, there is the concept of democracy, human rights, the rule of law, and a free-market economy that operates with institutions and rules. Built upon these foundations, the EU has gradually become a centre of attraction for the continent and, more broadly, for the world.

With the approval of the Lisbon Treaty in December 2009, the path towards a more transparent and democratic Europe was opened. Various initiatives, such as INSPIRE, e-governance, Global Monitoring for Environment and Security (GMES), and Public Sector Information, grounded in the European legal framework, were initiated to achieve these intentions. In these initiatives, there are principles that point to the freedom of movement of workers, the freedom to establish a business, and the freedom to provide services in Member States [7]- [8].

### 2.1. Legal Framework of Cadastral Surveying in the EU

Articles 39, 45, 43, and 49 of the EU Treaty establish the legal framework for the cadastral surveying profession in the EU. In addition to this, the Bologna Process [13]-[14]-[7], the Lisbon Strategy [7]-[15] for Growth and Jobs 2008-2010 and 2009-2014, INSPIRE [16], and the Small Business Act also have impacts on the profession.

In Figure-1, the cadastre, property, and land management system mentioned are professionally operated by Publicly Appointed or Regulated Property Surveyors, all of whom operate within a liberal profession [17]. This profession plays a significant role in countries where the legal transfer of cadastre and land registration duties to the private sector has occurred.

Property surveyors can be defined in the cadastral process as follows:

- Civil Servants are government officials who conduct cadastral activities on behalf of the state.
- Publicly Appointed Property Surveyors act as the state's representatives during the cadastral process, essentially working "on the state's behalf" in this context.
- Regulated Property Surveyors operate within the cadastral process under varying degrees of public legal regulations that may be more or less restrictive.

As shown in Figure 1, as announced in 2008 and 2018, Article 39 of the EU Treaty deals with employment in the public sector, excluding activities under state monopoly, and the freedom of movement (activities carried out by civil servants). Article 43 regulates the freedom to establish businesses through professional agreements involving mutual recognition (activities conducted by private sector professionals acting on behalf of government authorities). Article 45 concerns the freedom to establish businesses, excluding activities connected with official authority (activities carried out by publicly appointed professionals). Article 49 pertains to the freedom to provide services (activities are not regulated, employment is regulated by the free market) [7].

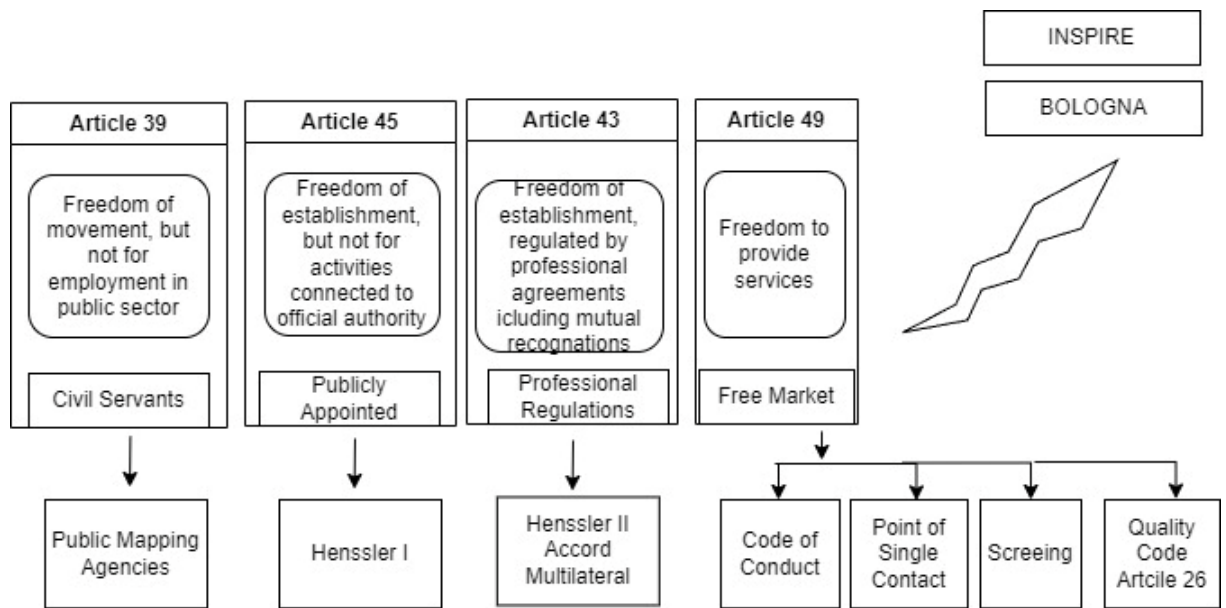


**Figure 1.** Context and impact of the Treaty establishing the European Community

Article 39 of the EU Treaty [16] grants freedom of movement to workers, excluding those in public services. This provision does not apply to employees in public services. The article also allows individuals to travel and work in another Member State and be treated as a national of that country.

Job-seeking surveyors (excluding public services) can freely move to other Member States and search for employment [18]. It is important to note that public service work is an exception for cadastral surveyors because in many countries, cadastral surveying activities are controlled by the government.

Article 45 of the EU Treaty makes an exception for activities related to "the exercise of official authority" apart from the right to establish a business. Article 45 refers to "activities" rather than "professions." Cadastral surveying carried out within the capacity of "Publicly Appointed Surveyors" on behalf of the State, based on national law, for the performance of specific activities, is interpreted as "exercise of official authority."

Article 43 of the EU Treaty provides the opportunity for surveyors to establish a business in another Member State under conditions similar to or the same as those granted to nationals of that State. These conditions include compliance with the professional rules, conditions, and qualifications in the host country. Directive 2005/36/EC on the "recognition of professional qualifications" provides guidelines for the interpretation of regulations in this regard [19].

Article 43 prohibits restrictions on the freedom to establish a business for nationals of one Member State within the territory of another Member State. This prohibition also applies to restrictions on the establishment of commercial agencies, branches, or subsidiaries set up within the territory of another Member State by nationals of any Member State.

The freedom to establish a business includes the right to start and operate as an independent worker and to establish and manage an enterprise, subject to the conditions established by the legislation of the host country, without prejudice to the provisions of the EU Treaty relating to capital.

Special qualifications, such as association memberships or supervision, allow a surveyor operating under the regulations/restrictions of a Member State to be part of a "Regulated Profession" under Article 43. Limitations within national laws may be acceptable, but they should not discriminate against other EU nationals; they should be appropriate, necessary, reasonable, and not overly restrictive. This aspect of the business is important for surveyors, particularly those covered by Article 45 - the exercise of official authority.

Any national of one Member State legally established in another Member State may provide services temporarily and occasionally with their professional qualifications without the obligation to meet the

qualifications of that State. However, service providers must also prove two years of professional experience if the profession is not regulated by that Member State.

The host Member State may request the service provider to submit a declaration, including details of insurance coverage and other documents such as a nationality certificate, a legal establishment certificate, and professional qualification documents, annually before providing any service within its borders.

Article 49 of the EU Treaty is important for surveyors because it offers the opportunity for activity in a free and unregulated market. Any service provided by Member States or private companies is subject to this directive. This article ensures the free movement of services between Member States and prohibits any restrictions on the provision of cross-border services (although certain qualifications may be required, as outlined in Article 43 and Directive 2005/36/EC) [19]. Services can be provided by both legal entities and individuals. Directive 2006/123/EC on Services is the relevant regulation in this regard.

## **2.2. Other Influences and Developments**

The Bologna Process, aimed at creating the European higher education area [13]-[14]-[7], the Lisbon Strategy that shapes the structure and overall perspective of the EU economy [7]-[20], and the INSPIRE Directive that focuses on the collection and sharing of environmental spatial data among public institutions [21]-[7], along with the Small Business Act (SBA) recognizing the central role of SMEs in the EU economy, are among the developments directly affecting the cadastral surveyor's profession, among others. At the core of these efforts lie principles related to freedom of movement of workers, the liberty to establish enterprises, and the freedom of providing services across the Member States.

### **2.2.1. Bologna Process**

The Bologna Process is a reform process aimed at establishing the European Higher Education Area (EHEA). The goal of the Bologna Process is to create a European higher education area by 2010. It aims to ensure that academic institutions in this area have comparable and compatible academic degree and quality standards across all of Europe. Based on the declaration signed in Bologna, Italy in 1999, three priorities were established: the introduction of bachelor's, master's, and doctoral degrees; quality assurance and recognition of qualifications; and finally, the study cycle. This commitment also entails professional quality assurance and recognition of engineers conducting surveying activities. Türkiye has been a part of the Bologna Process since 2001 [13].

### **2.2.2. Lisbon strategy 2008-2010**

The Bologna process initiated a series of reforms in Member States. This process aligns with the program of the Lisbon Strategy for Growth and Employment and establishes cooperation between Member States and the European Community. According to the Lisbon strategy, a stronger economy will promote sustainable development and social inclusion, along with social and environmental policies that encourage job creation. The Lisbon Strategy aimed to address the low productivity and economic growth stagnation in the EU, and it included the formulation of various policy initiatives to be implemented by all EU member states.

Between 2000 and 2010, the Lisbon program focused on advancing collaboration and promoting growth and employment. By adopting the Small Business Act to facilitate the potential growth of small enterprises and improve innovation conditions, the European Community supports the free movement of knowledge across all of Europe [30]-[7].

This open-market approach is related to the field of surveying. Open real estate markets are crucial for the development of a single market in Europe. Effective and efficient cadastre and land registry processes will significantly contribute to the objectives of the Lisbon Agenda.

### 2.2.3. INSPIRE Directive

The directive 2007/2/EC of the European Parliament and the Council dated March 14, 2007, established the Spatial Data Infrastructure (INSPIRE) in the European Community. The INSPIRE directive outlines a general framework for the Spatial Data Infrastructure, which is intended to serve the environmental policy objectives of the European Community. This directive has a focus beyond national borders. INSPIRE is based on and operates through the spatial data infrastructures established and maintained by the 27 Member States of the EU, addressing 34 spatial data themes necessary for environmental applications [21].

The INSPIRE Directive has requested that Member States commit to ensuring the compatibility and usability of their spatial data infrastructures within the Community and in a cross-border context by adopting additional legislation or common Implementing Rules (IRs) for certain specific areas, as follows:

1. Metadata
2. Interoperability of spatial data sets and services
3. Network services, e.g., data discovery and service viewing
4. Data specification and data and service sharing
5. Monitoring and reporting of services

The impact of the INSPIRE directive on cadastral surveying will be significant, as Member States are only required to expose the data they already possess, without any obligation to collect new data.

### 2.2.4. The Small Business Act

The Small Business Act (SBA) demonstrates the Commission's political will to acknowledging the pivotal role of Small and Medium-sized Enterprises (SMEs) within the EU economy by establishing a policy framework. Its primary objective is to enhance the overall approach to entrepreneurship and promote the principle of prioritizing small businesses in policy-making, spanning from regulations to public services. Its aim is to provide support to SMEs in addressing challenges that impede their growth. Across Europe, the SBA is applicable to all independent companies with fewer than 250 employees, encompassing 99% of all European businesses.

In some countries, the SBA can significantly influence various surveying activities and licensed surveyors/companies.

## 2.3. Impact of EU Legislation on Cadastral Surveying

Effective cadastre highlights land ownership, land value, land use, and land development matters for all individuals, aiming to enhance trust and confidence in real estate property, promote security, safety, peace, and peace-building, stimulate real estate markets and the construction sector, facilitate economic development through fair income systems, play an essential role in the development of states and economies by establishing preparedness, resilience (in the face of increasing climate sensitivities), sustainable consumption, and strong institutions [4]. The establishment, maintenance, and adaptation of cadastral systems at the country level must align with local conditions, changing global contexts, and evolving political, technological, economic, environmental, and societal landscapes. It is precisely at this point that the activities and applications of licensed cadastral surveyors will lead the way in this change and transformation.

The CLGE is a non-governmental organization that represents and supports the interests of the geodetic surveying profession in the private and public sectors in Europe [22]-[23]-[17]-[13]-[24]-[2]. The CLGE representing the majority of the geodetic surveying profession in Europe.

### 2.3.1. Cadastral Surveyors Activities in EU Countries

Cadastral surveying activities are typically regulated by the State and are only allowed to be conducted by licensed (authorized) individuals. Professional standards and qualifications for Publicly

Appointed and Regulated Surveyors vary across European countries. The main activities performed by EU Cadastre surveyors are defined under eight main headings [7]-[8]-[9], these are:

- i. Cadastral (technical) field measurements
- ii. Marking parcel corners
- iii. Providing advice/consultation to landowners
- iv. Certification, approval of cadastral plans obtained from relevant authorities
- v. Land valuation
- vi. Recording of updated cadastral data into cadastral databases
- vii. Defining land use restrictions
- viii. Preparation (correction) of land planning documents

**2.3.2. The national terms-conditions and common characteristics of cadastral surveyors within the EU**

There is a Cadastre and Land Registry in all EU member states. Just under 62% of countries have a single authority, while approximately 33% of them maintain separate authorities for overseeing both Cadastre and Land Registry. In some countries, cadastral work is ongoing, and a portion of the country has not yet been cadastrated. National Cadastre (and Mapping) and Land Registry Institutions play a significant role as providers, supervisors, and coordinators in cadastre and cadastral surveying activities.

Certain countries, including Norway, Spain, and Sweden, do not have a system for licensing cadastral surveyors. In these nations, the responsibilities of cadastral surveying are fulfilled either by employees of a NMCA (e.g., Sweden), municipal bodies (e.g., Norway), or through individual contracts with public authorities (e.g., Spain). The operational status of licensed cadastral surveyors is depicted in the Figure-2.

The guarantee of land ownership is a fundamental element for a stable and prosperous society as well as a modern economy. Europe's Cadastre and Land Registry organizations have long provided such secure, reliable, and authoritative information. In member countries, cadastral property measurements are carried out by public servants, publicly appointed surveyors, licensed cadastral surveyors, and unlicensed professional surveyors registered with the relevant professional association. Figure-2 indicates that 22% of cadastral surveying are conducted by public servants, 17% by publicly appointed surveyors, and 13% by surveyors registered with the chamber but without a license. Additionally, Figure-2 shows that 42% of cadastral measurements are carried out by licensed cadastral surveyors. These results demonstrate the absence of a standardized approach in European practices.

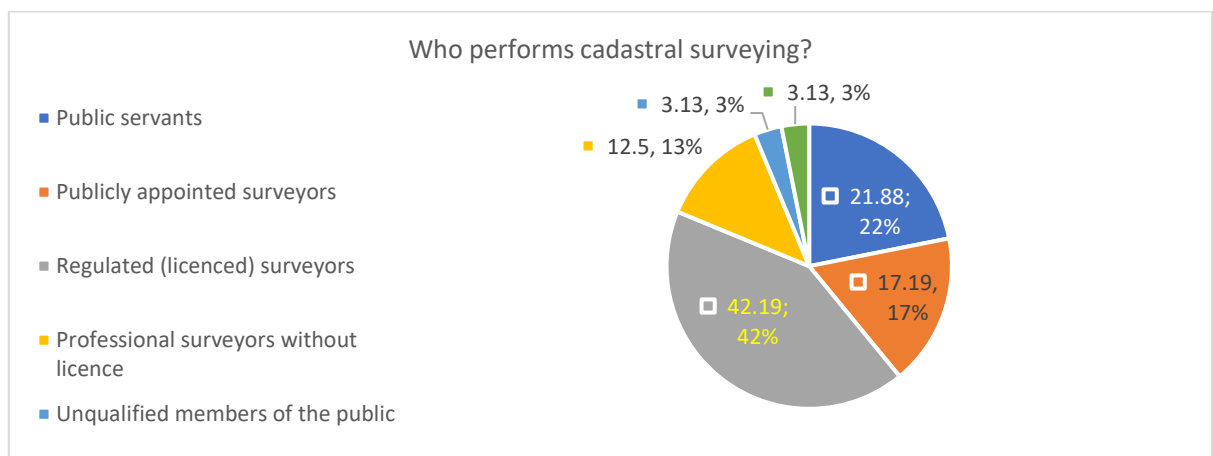


**Figure 2.** Who performs property surveying?

The number of surveyors in a country depends on the size of the market and the volume of work it generates. For example, in Balkan countries, as a result of the granting of property rights, there has been an increase in cadastral projects, and spatial planning, construction work, and real estate markets have

started to develop. As a result, the number of surveyors in these countries is higher than the number of cadastral surveyors in Western European countries, as can be seen in Figure 3. Countries such as Poland, Romania, Bulgaria, Greece, Latvia, and Serbia have a relatively higher number of licensed cadastral surveyors.

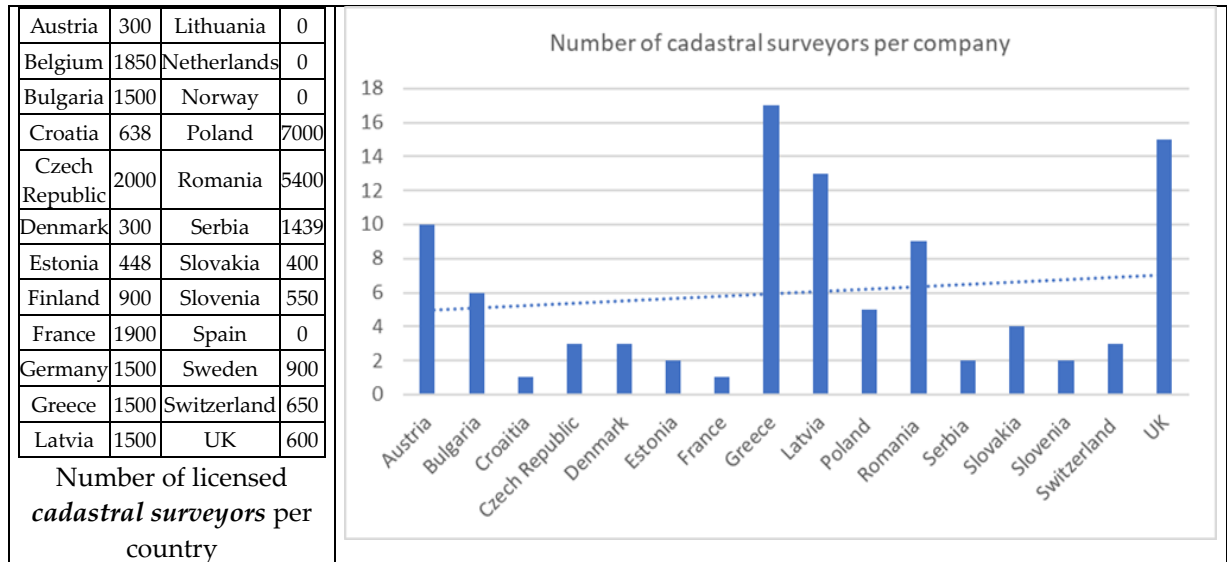


Figure 3. Number of licensed cadastral surveyors and licensed companies

Due to market conditions, the workforce intensity per licensed firm varies; small firms employ 1-2 licensed cadastral surveyors, while medium-sized firms (SME) employ 10-20 licensed cadastral surveyors (Figure 3). The level of development of cadastral systems in member countries varies depending on the development of their economies and real estate markets. This situation affects the number of cadastral surveying companies in each country (Figure 4). In some countries, cadastral surveying is a public task, and licensed companies do not exist in those countries (for example, Sweden and Finland). In other countries, individuals are licensed, and the licensing status of companies is not considered separately (for example, Germany).

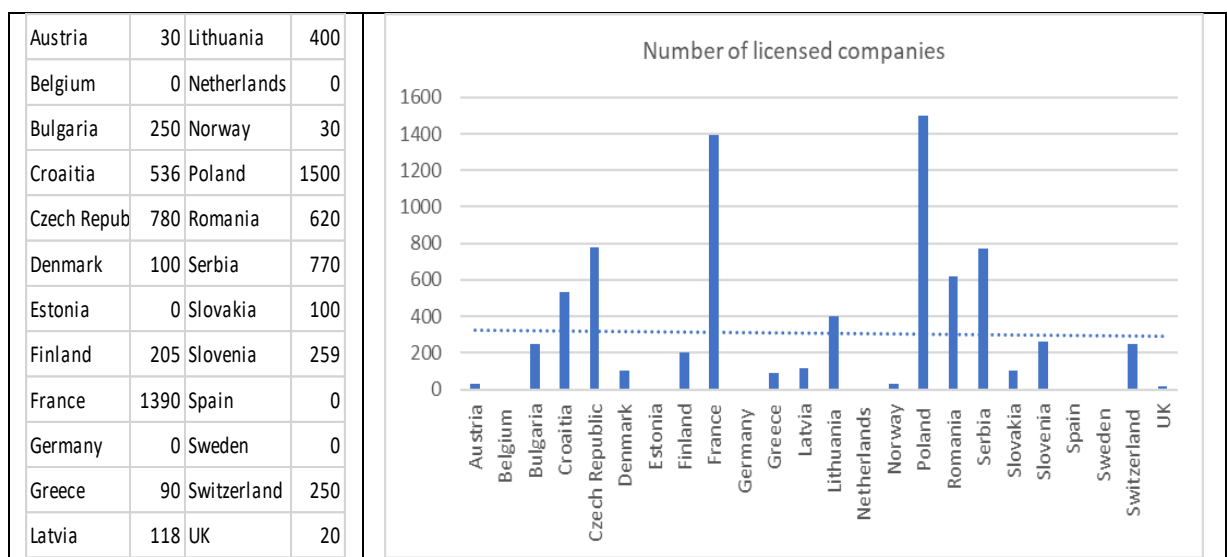


Figure 4. Number of licensed companies

In licensing (authorization) requirements (Figure 5), it can be observed that there are different conditions across Europe. Generally, the minimum requirements for Surveying Engineers applying for a

license typically include education in geodesy (or related fields) and a specified period of professional experience. Common requirements for a license in Europe: university education and professional practice.

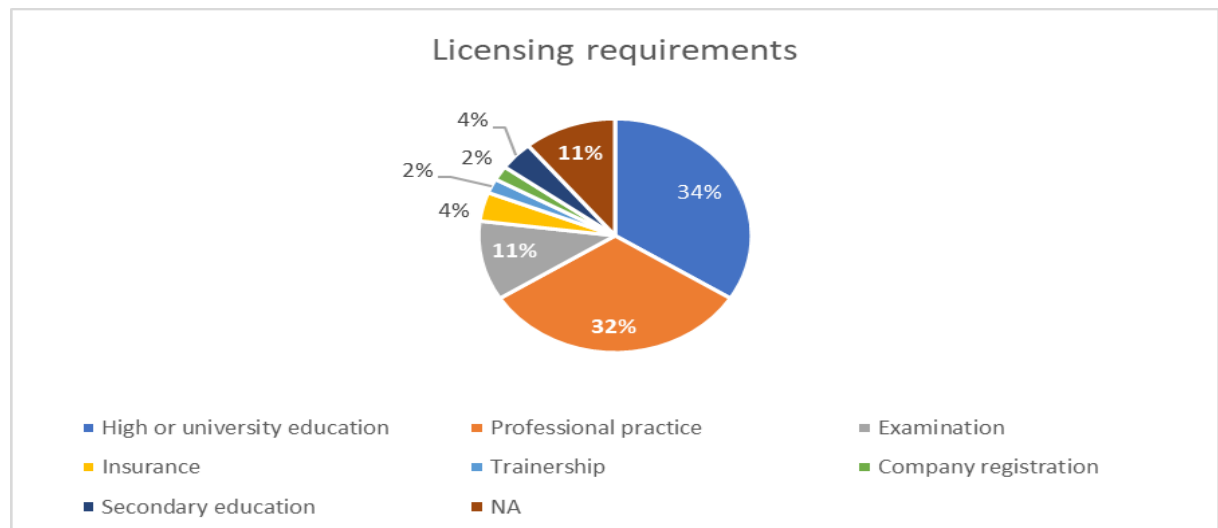


Figure 5. Licensing (authorisation) requirements

Usually, NMCA's or Chambers of Surveying Engineers provide licenses. In cases where Surveying Engineers are employed by NMCA's, a separate licensing is not required. However, in some member countries, licensing is provided in collaboration between the Ministry and the Chamber of Surveying Engineers (Figure 6).

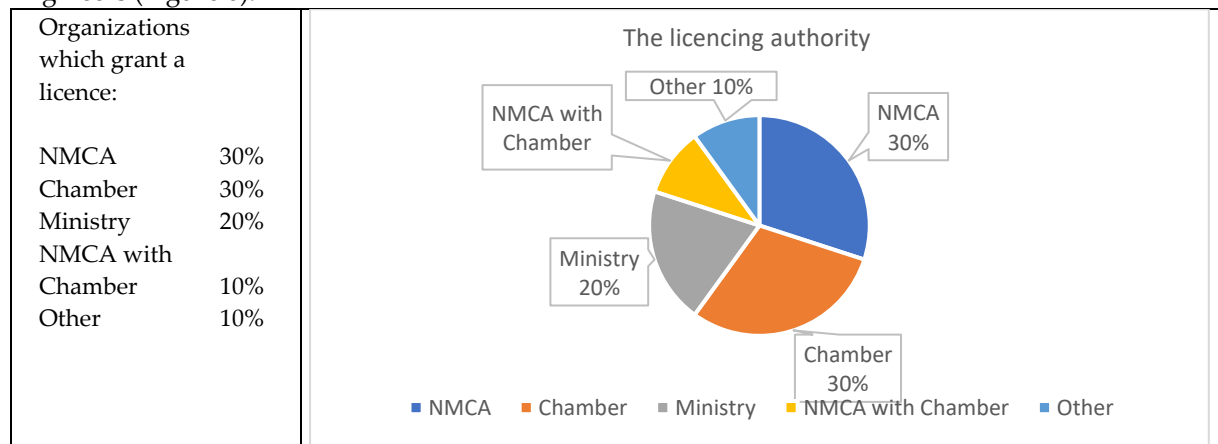


Figure 6. Licensing authorities

NMCAs, authorized to oversee the management of national cadastres and land registries, maintain a continuous interest in the work carried out by surveyors engaged in cadastral activities. These activities serve as the foundation for the cadastral database in numerous countries. In addition to data collection, the majority of respondents also noted that NMCAs are involved in various other responsibilities. These include coordinating the activities of licensed cadastral surveyors (Figure 7), quality control (Figure 8), supervising surveying activities (Figure 13), conducting training programs (Figure 15-16), and managing sanctions (Figure 14). In member countries, it can be observed that quality control is carried out to a significant extent by NMCA (49%), followed by Ministries (15%), Chambers (15%), and local authorities (12%) (Figure 8).

Continuous quality control is implemented for the activities of licensed cadastral surveyors, except for those serving as public servants in public organizations. In countries following a blended approach, both private licensed cadastral surveyors and government employees must adhere to identical regulations and be registered with or affiliated to the same register or chamber.

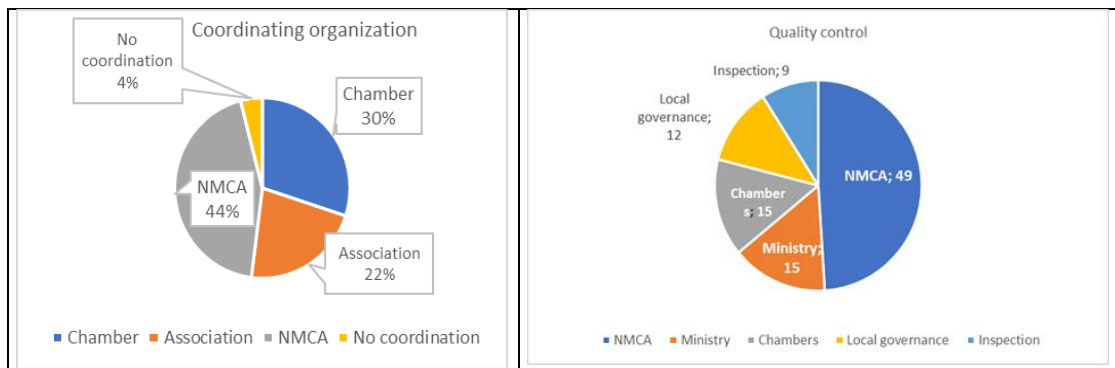


Figure 7. Coordinating organization

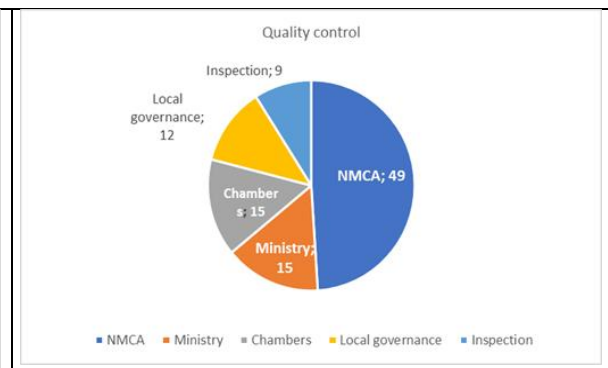


Figure 8. Quality control

The majority of licensed cadastral surveyors' bear liability for both their property surveys and the production of cadastral data. In Figure-9, liability is depicted in the data produced by cadastral surveyors. In all countries that responded to this question, it is observed that the responsibility is 5 years or more in duration, with approximately 78% indicating a duration of 10 years or more. The trend towards a mandatory insurance is growing. It has been observed that the responsibility for quality and accuracy lies with the cadastral surveyor in 75% of the member countries (Figure 9 and 10).

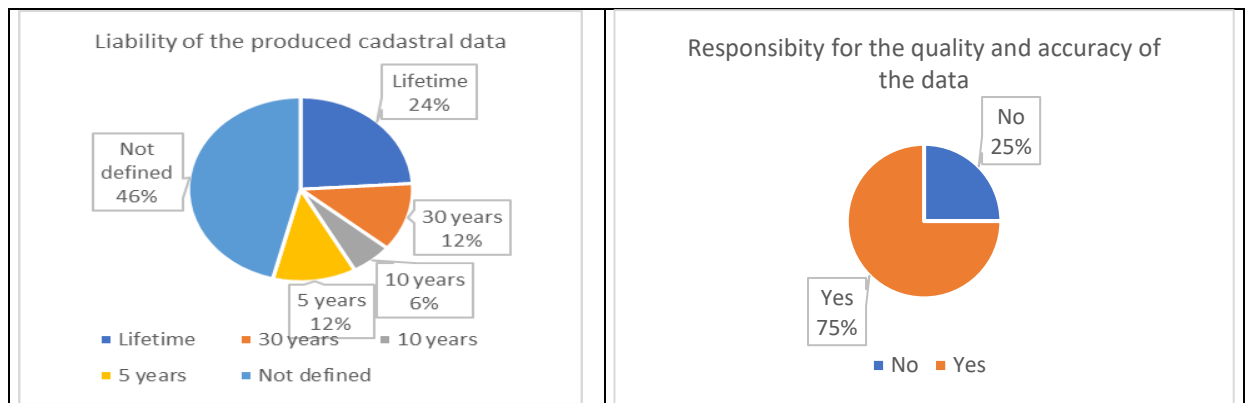


Figure 9. Liability of the produced cadastral data

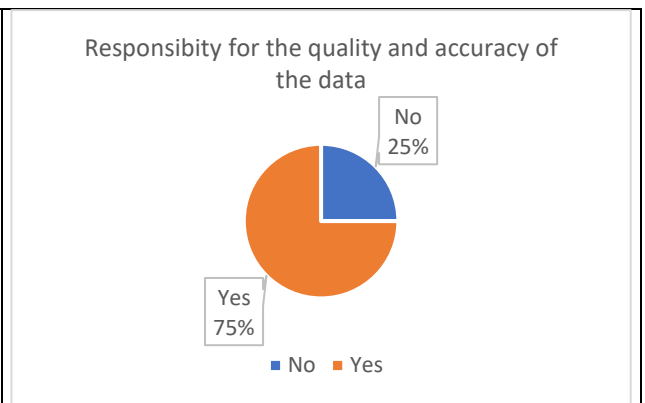


Figure 10. Responsibility of quality and accuracy

Compulsory insurance applies only to private licensed cadastral surveyors. State guarantees apply to the activities of Publicly Appointed Surveyors according to national public procurement conditions. Therefore, additional insurance is not necessary. Compulsory insurance terms and coverage may vary. For instance, errors in cadastral documents can be handled in different ways, such as addressing damage caused by licensed cadastral surveyors to a third party's property (e.g., fence, sidewalk, etc.). Figure-11 demonstrates that a significant amount of compulsory insurance is required for the license.

Throughout Europe, there is no common practice regarding the compulsory duration of practical experience that a cadastral surveyors must undergo before obtaining a license (Figure 12). The compulsory professional practice period varies between one and five years, typically around two or three years. In countries where licensed cadastral surveyors work as employees of the NMCAs, the compulsory professional practice period has not been defined.

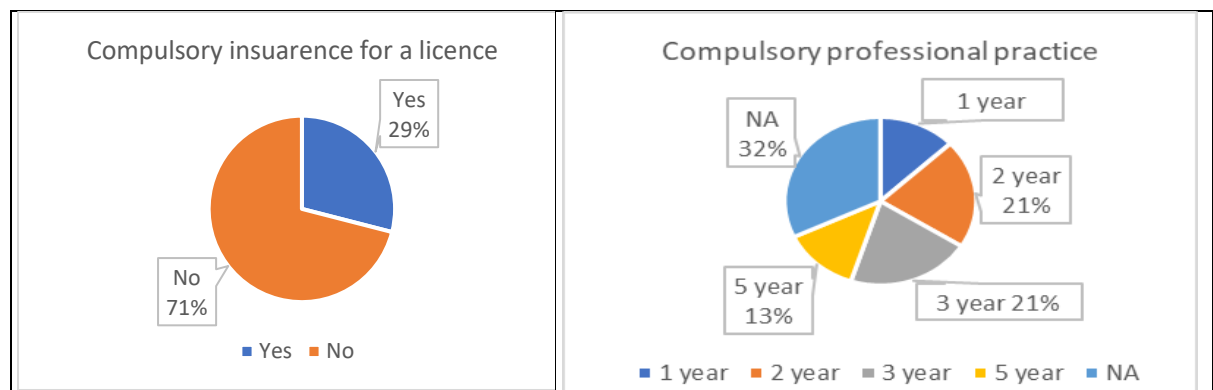


Figure 11. Compulsory insurance for licence

Figure 12. Compulsory professional practice

The supervision of licensed cadastral surveyors' activities is generally carried out by NMCAs (49%). Additionally, the Ministry, Chamber, and municipalities are also among the regulatory bodies (Figure 13). In the majority of the countries, sanctions continue to be enforced by the State Agency or chamber. The types of sanctions mainly include suspension (27%), termination (25%), fine (23%), and notice (27%). Extra training is also among the applied sanctions. The rate of resorting to court within the scope of sanctions is around 5% (Figure 14).



Figure 13. Supervision of licensed cadastral surveyors' activities

Figure 14. Sanctions

The common requirements for licensing of cadastral surveying activities are a high or university education in geodesy and related disciplines followed by a period of professional practice. In many countries, there is a state examination at the end of the traineeship. It appears that the mandatory Continuous Professional Development (CPD) experiences an increasing trend since it is required in more and more countries (Figure 15). Universities and high schools mainly provide training and education to licensed cadastral surveyors, but chambers and associations play an important role organising training courses and raising qualification (Figure 16).

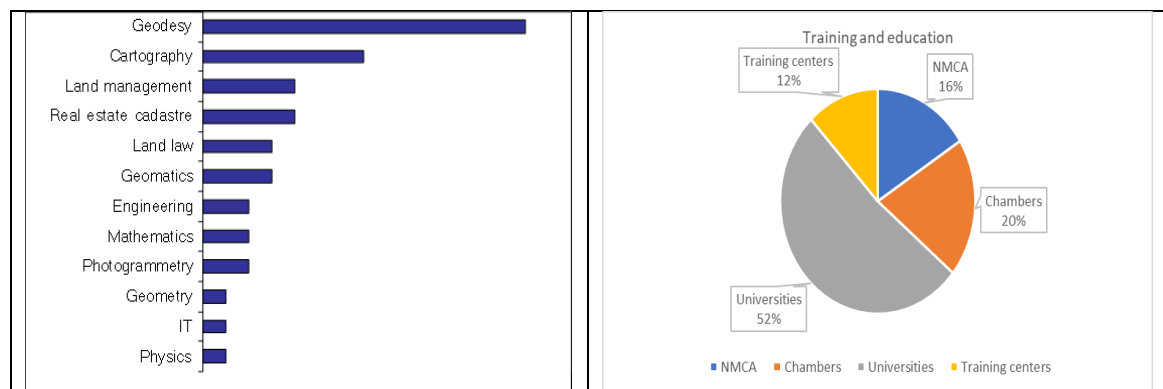


Figure 15. Disciplines for education

Figure 16. Training and education

### 3. LICENSED SURVEY AND CADASTRE ENGINEERING BUREAUS (LIHKAB) AND CADASTRAL SURVEYORS IN TÜRKİYE

#### 3.1. The legal framework and practices of the cadastre system in Türkiye

The highest legal norm governing ownership rights in Turkish law is the Constitution of the Republic of Türkiye. As outlined in the Constitution, individual possesses ownership and inheritance rights which may only be limited by laws in the interest of the public. The exercise of ownership rights must align with the public interest (Turkish Constitution, Article 35). Within the Turkish legal framework, the official land register is subject to state supervision and responsibility, and it records the legal status of real properties. The sole authority for land registration and land registry transactions related to real property in Türkiye is the (TKGM).

Cadastral parcels are demarcated by official boundaries and are assigned unique parcel numbers to establish precise land boundaries. In the cadastre system implemented in Türkiye, known as the judicial (legal) cadastre, there are typically two components. The first component is a written record containing information about the owner of each parcel and other details, such as rights, responsibilities, and restrictions related to the parcel. On the other hand, the second component encompasses a detailed demarcation of the parcel in the form of cadastral maps (plans) and field survey documents cross-referenced with the first part. The legal cadastre assumes that the boundaries of the parcels registered in the land book during the establishment of the cadastre were ensured by cadastral maps, which are an integral part of the legal cadastre [25]. In Türkiye, the initial cadastre has been completed. As of the year 2023, there are approximately a total of 58.8 million cadastre parcels, and the cadastre of more than 15 million rural parcels has been renewed with the participation of the private sector. Land registration transactions have been conducted through the Land Registry and Cadastre Information System (TAKBIS) since 2005.

#### 3.2. Licensed Survey and Cadastre Engineers and Bureaus (LIHKABs)

LIHKAB's are bureaus that operate on behalf of the public. Surveyors who meet the necessary requirements are authorized to work on behalf of the public with the license certificate they receive. The work they perform is considered a public service, and their activities are viewed as serving the public interest.

According to Law No. 5368, certain cadastral technical procedures that were previously monopolized and guaranteed by the state have been delegated to licensed bureaus established by law. These bureaus are granted both construction and control authority and responsibility. Therefore, the TKGM, being the primary entity responsible for public service, exercises superior monitoring and supervisory authority over these licensed bureaus, maintaining its responsibility. In this context, it follows the principle that these services are provided by cadastral directorates in locations where licensed bureaus have not been established.

##### 3.2.1. LIHKABs legislation

LIHKABs were established by Law No. 5368 in 2005 [10], and the operational guidelines and principles for these bureaus were specified by the Regulation, which came into effect in 2008. However, this Regulation was later repealed, and a new regulation was issued in 2013.

According to the Law No. 6083 dated 2010 regarding the Organization and Duties of the TKGM; the provision allowing the activities of LIHKAB to be supervised by the TKGM under the provisions of Law No. 5368, including granting licenses to LIHKAB and determining and monitoring the operational procedures and principles of these bureaus, was provided.

The above provision was reiterated while listing the duties of TKGM in the Presidential Decree No. 4 on the Organization of Ministries, Related and Associated Institutions and Organizations and Other Institutions and Organizations, published in 2018.

With the amendment to Law No. 7317 dated 2021 [11], Law No. 5368 regarding LIHKAB has been updated to its most current version. Consequently, with this change in law, the previous LIHKAB Regulation dated 2013 was repealed, and a new Regulation was published for LIHKAB [12]. Additionally, with the implementation of Directive No. 2022/2, TKGM repealed its directive regarding licensed bureaus, numbered 2010/13.

### 3.2.2. Duties of LIHKABs

The licensed bureau is responsible and authorized to perform and oversee cadastral technical services, including cadastral operations that are not subject to registration, cadastral surveys, land demarcation, and plan preparation. This includes responsibilities for changes in property use subject to registration, establishment or abandonment of easements, consolidations, and abandonment of rights.

The licensed bureau is also obligated to carry out other tasks and operations determined by the Authority, which are of a nature similar to cadastral technical services. The duties of Cadastre Directorates are outlined in Figure-17. Demand-dependent works shown in two separate boxes in Figure-17 are the responsibility of LIHKABs [26].

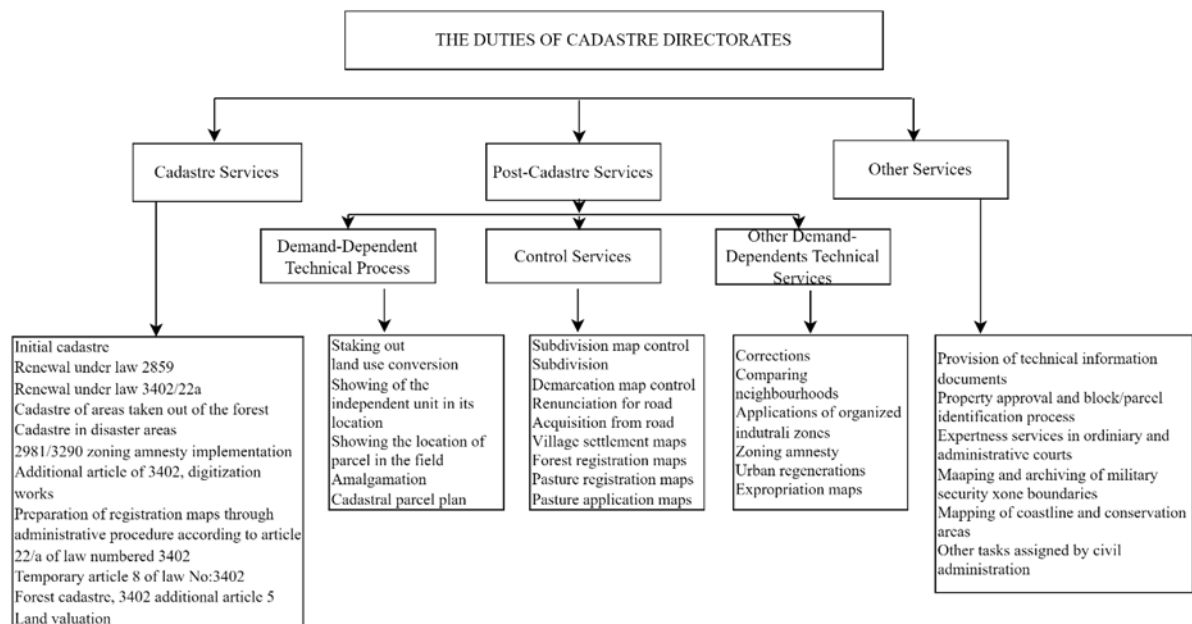


**Figure 17.** The duties of cadastre directorates and the responsibilities of LIHKABs.

Licensed cadastre surveyors may also engage in independent surveying and cadastre engineering and consulting activities during the period they conduct their activities under this Law.

### 3.2.3. Authorities, and Responsibilities of LIHKABs

#### 3.2.3.1 The conditions for obtaining a license and being able to open a licensed bureau

According to the LIHKAB Regulation, the requirements for obtaining a license and being able to open a licensed bureau are as follows:

- Being a citizen of the Republic of Türkiye,
- Not being deprived of public rights,
- Having the capacity to exercise civil rights,

- Not being sentenced to imprisonment, even if the specified periods have passed, according to the Turkish Penal Code,
  - Not having received a dismissal penalty from civil service,
- In addition to these general requirements, the specific requirements for being able to obtain a license are as follows:
- Being registered with the Chamber of Survey and Cadastre Engineers (HKMO),
  - Having worked as a survey and cadastre engineer in the public or private sector for a minimum of ten years,
  - Not having received a temporary suspension or dismissal penalty from the profession according to the provisions of the Turkish Union of Chambers of Engineers and Architects (TMMOB) Law at the time of application
  - Depositing the required collateral in the bank and having it blocked in the name of the TKGM.

### **3.2.3.2 Establishment**

An engineer who qualifies to receive a license shall submit the minimum required personnel and equipment list, along with a copy of the license, to the HKMO before commencing duties at the bureau address. The registration of the licensed bureau with HKMO is mandatory before commencing work at the bureau address.

### **3.2.3.3 Commencement of Work**

A licensed engineer must commence work within one month from the date of receiving the license, except in cases of force majeure. The licensed engineer shall notify the local authorities, cadastral directorate, and HKMO representatives in writing about starting work and the bureau address. The licensed bureaus cannot commence work unless a proper notification is made, and the relevant cadastral directorate approves compliance with the specified procedures by the Authority.

### **3.2.3.4 Cancellation of the License**

In addition to the permanent cancellation of the license, the license may also be cancelled upon the request of the license holder, upon reaching the age of 65, upon losing the conditions specified in the law to open a bureau, or upon later discovery that the conditions are not met. The license of those to whom the license is granted but do not open a bureau will be revoked by withdrawing and cancelling the license.

### **3.2.3.5 Training and Education of Licensed Engineers**

Licensed cadastral surveyors who qualify to establish a licensed bureau and commence operations shall undergo mandatory and paid practical training lasting at least two days on cadastral technical services and real property and cadastral legislation by the Authority. Additionally, participation in in-service training programs organized by TKGM is required.

Individuals who have completed their engineering education from any faculty or department related to Surveying Engineering, Geodesy and Photogrammetry Engineering, or Geomatic Engineering within Türkiye are eligible for membership in the HKMO. As outlined in Article 135 of the Constitution of the Republic of Türkiye, individuals working in public institutions and public economic enterprises have the choice of whether or not to become members of the chamber. However, for surveyors not covered by these exceptions, membership in the chamber is a mandatory requirement to practice their profession in this field. In this context, licensed bureaus and licensed cadastral surveyors are required to become members of the HKMO. Licensed bureaus, furthermore, have their own association, and membership in this association is not mandatory.

### 3.2.3.6 Personnel

To ensure the uninterrupted operation and provision of services, licensed bureaus are obliged to employ at least one engineer in addition to the license holder and at least two individuals with titles of technician or technologist related to the profession and field.

As of September 2023, there are 20,484 registered engineers with HKMO. Roughly one-third of the engineers registered with HKMO work in the public sector, while two-thirds work in the private sector. In the country, there are 1,476 private companies, 2,365 offices, and 689 LIHKABs, and their proportional distributions can be seen in Figure 18. Before the legislative change in 2021, the number of active LIHKABs was 225, employing 257 licensed cadastral surveyors and 756 technicians. After the change, the number of licensed cadastral surveyors is 1,468.

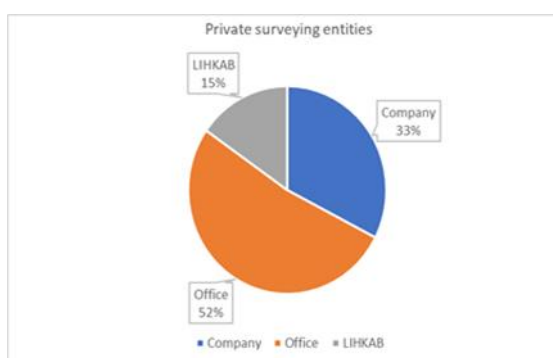


Figure 18. The distribution of companies, bureaus, and LIHKABs

### 3.2.3.7 Inspection

Licensed bureau activities are audited at least once a year by the TKGM Regional Directorate and twice a year by the cadastral directorate. Inspections are carried out by personnel authorized by the Authority for inspection purposes. Based on the evaluation of the inspection results and appeals by the Authority, penalties for deficiencies and shortcomings, depending on their nature and recurrence, may include warnings, reprimands, temporary or permanent license cancellations, and fines.

### 3.2.3.8 Return of the License Certificate

In the event of the cancellation of the license certificate, the licensed engineer or, in the event of the licensed engineer's death, their heirs must return the license certificate to the relevant cadastral directorate within three months. The received license certificate is promptly sent to the Directorate of Cadastre at the TKGM.

### 3.2.3.9 Legal and Criminal Liability

Individuals authorized to perform cadastral technical services under the Law in licensed bureaus are considered public officials for the purposes of the Turkish Penal Code. If any damage arises from the actions of the bureaus, those at fault will be held liable under Article 1007 of the Turkish Civil Code.

Licensed cadastral surveyors and their employees are prohibited from disclosing to third parties or using for purposes other than the provided service any information they acquire through their work, even after leaving the profession. They are also held responsible for any resulting damages, in accordance with Article 1020 of the Turkish Civil Code.

As in 2023, licensed cadastral surveyors are liable for their property surveys and cadastral data and document production.

### 3.2.3.10 Service Obligations and Code of Conduct

A licensed bureau is obligated to conduct cadastral technical services within its jurisdiction from the date it commences its activities. A licensed engineer demonstrates the required reputation and trust in both internal and external conduct related to the profession. They may not unjustly gain benefits from anyone in relation to their duties. Information and documents acquired by licensed cadastral surveyors and bureau employees due to their duties cannot be used in violation of the Personal Data Protection Law and relevant legislation.

### 3.2.3.11 Service Fees for Licensed Bureaus

The fee schedules for cadastral technical services provided by licensed bureaus, except for the initial determination, are determined and announced by the Authority, in consultation with HKMO, within the first week of January each year.

## 4. TRENDS

On an international level, significant efforts have been undertaken concerning cadastral systems and applications, such as Cadastre 2014, Vision Statement on Cadastre and Land Registration in Europe, 1998 [27], Impact of EU Legislation on Cadastral Surveying [6], European Requirements for Property Surveyors – ERfPS', 2018 [8], UN Framework for Effective Land Administration – FELA, [4], and 'Integrated Geospatial Information Framework – IGIF [5], as well as Fit for Purpose Land Administration [28]-[29], and more. One of the most pivotal publications that guide the future and applications of cadastre is Cadastre 2014. It has developed the vision of cadastre being highly specialized to a large extent, requiring cadastre to demonstrate the entire legal status of the land, eliminating the distinction between maps and records, and promoting collaboration between the public and private sectors [7]- [27].

Eurographics emphasizes the importance of securing property rights through state guarantee in property ownership and the continuation of public trust. It underscores the significance of cadastral systems in establishing an effective real property market and emphasizes the vital role of real property markets and related financial markets in contributing to economic development. It also underscores that cadastral parcel constitute the core data set of the INSPIRE Directive. In light of advancements in e-government and e-commerce, it calls for the integration of all legal and technical information related to cadastral parcels. Furthermore, it advocates the development of public-public and public-private partnerships, aligning with EU policies within the framework of social, economic, and environmental development [30].

The outcomes of these two studies shed light on the trends of surveyors worldwide, specifically within the EU. In summary:

1. The distinction between map and records will disappear. Technical and legal information of cadastral parcels should be shareable in an integrated manner.
2. Cadastre is of vital importance for effectively functioning real estate markets and related financial markets
3. Cadastral parcels constitute the core spatial data set of the INSPIRE Directive.
4. Cadastre is among the most crucial components supporting EU's economic, social, and environmental policies.
5. Cadastre will largely become privatized, and public-private partnerships practices will be developed
6. Aligned with this vision, cadastre will serve as the fundamental data provider for other public institutions (public-public).

Almost all of the mentioned trends are applicable within cadastral practices in Türkiye. Currently, within the completion project of initial cadastre works and immediately thereafter, in forest cadastre and rural cadastral renewal works, the technical aspects of the cadastre have been tendered to the private sector, ensuring significant participation from private entities in cadastral works. In recent years, three-dimensional cadastral projects have also been carried out with the participation of the private sector. Post-cadastral services have been provided by licensed cadastral surveyors through LIHKABs since 2005. Türkiye's cadastre has been the main data provider for approximately 1,000 institutions and organizations in recent years.

## 5. DISCUSSION and RESULTS

EU is a prominent political and economic union comprised of 27 member countries, collectively representing 30% of the nominal gross domestic product of world nations. The Union is in the process of enlargement, currently engaged in membership negotiations with 9 candidate countries and 1 potential country. The CLGE stands as a leading European Surveying Association, boasting 38 member countries (comprising 27 EU member states and 11 other European nations), and a membership base of approximately 100,000 surveyors. CLGE has undertaken significant initiatives related to cadastral surveyors, addressing critical aspects such as the preservation of real property, the role and future of cadastral surveyors within the profession, education, standards, codes, and the visibility of the profession. Notable efforts by CLGE encompass works such as the Code of Professional Qualifications, Sustainable Fit for Purpose, Portrait of EU Surveyors, and European Requirements for Property Surveyors.

In evaluating the conducted studies, it has been determined that, in certain countries, land registry and cadastre activities are executed under the responsibility of two separate institutions, resulting in the existence of two distinct databases. In many CLGE member countries, cadastral activities are conducted by cadastral surveyors. While many CLGE member countries engage cadastral surveyors in conducting cadastral activities, Table-1 illustrates variances among them concerning critical aspects such as professional qualifications, legal status, licenses/authorizations, liability, professional practice, insurance, quality control, affiliation, job and discipline requirements, and ethical codes.

As a consequence of this confusion, it has been understood that the profession of cadastral surveying, which does not reflect the basic competencies, qualifications, profile and expertise of licensed cadastral surveyors, and due to these differences, produces both cadastral maps and property records, integrates them and is the owner and updater of the basic data set of the European spatial data infrastructure, is not where it should be.

The European standard should be defined in accordance with EU Directive 2005/36, encompassing all aspects, from the establishment of licensed bureaus to their operations, including quality control and insurance. This aims to ensure consistent application across the activities of EU licensed cadastral surveyors. In this context, CLGE is actively engaged in formulating the European Geodetic Surveyors Act (EGSAct), aiming to create a comprehensive policy that delineates the position, function, and responsibilities of licensed cadastral surveyors in the future advancement of Europe. The goal is to promote awareness and understanding of the significance of geodesy and geoinformatics in cadastral survey activities and their role in the progress of both Europe and the world [23].

In Table-1, licensed bureaus in Türkiye, as detailed, exhibit similarities with EU practices in specific aspects. In Türkiye, some post-cadastre activities, previously managed by units within cadastral directorates, were shifted to LIHKABs under the law enacted in 2005. By 2021, this law underwent amendments, eliminating the mandatory licensing exam and granting licensing rights without examination to engineers who have completed 10 years since their diploma date. Prior to 2021, the number of LIHKABs was 225; however, after the legislative change, it significantly increased to 689.

Yet, another critical aspect pertains to professional practice. Survey engineering education in Türkiye generally focuses on geodesy, photogrammetry/remote sensing, and GIS, with minimal emphasis on land management and cadastre courses. Each faculty offers the option of pursuing a master's degree in cadastre for those interested in specialization. It is evident that enabling licensed cadastral surveyors to obtain a

license without prior practical experience in LIHKABs or cadastral directorates for a few years will pose certain challenges in property-related practices. Moreover, the limited duration of in-service programs provided to LIHKABs and the absence of ethical rules for practitioners in such a critical field as property are among other challenges.

2/3 of survey engineers working in the private sector in Türkiye categorically work in companies, free survey and cadastre engineering offices (SHKM) and LIHKABs. This situation has been posing longstanding problems between SHKMs and LIHKABs regarding their areas of duty, authority, and their potential to conduct business.

With the new law, LIHKABs were also given the authority to provide SHKM services. Conversely, since business owners working as SHKM may have the right to obtain a license after completing 10 years from the diploma date, similar to other engineers, they were also given the authority to establish LIHKABs. The advantage that this practice provides to LIHKABs is that they are given the authority to work in other areas of the sector in addition to the duties assigned to them by law.

**Table-1.** Comparative qualifications in the professional field, alongside business and disciplinary prerequisites.

EU (CLGE countries)	Türkiye
Is the Land Registry and Cadastre a single authority?	
Just under 62% of countries have a single authority.	Yes, single authority.
Is the cadastre completed for all countries?	
In some countries a portion of the countries has not been cadastrated yet.	Cadastre has been completed nationwide.
Who performs property surveying?	
approximately 77% of property surveying are performed by either public or private licensed cadastral surveyors, 28% of them are conducted by public, 48% by private cadastral surveyors, and 24% by both types.	Performed by LIHKABs, if there is no LIHKAB in that district, personnel appointed by the cadastre directorate.
Is there a property surveyor for all countries?	
Certain countries do not have a system for licensing cadastral surveyors.	Yes
Licensing requirements?	
Common requirements for a license in Europe: university education and professional practice.	University education and professional experience.
Licensing authority?	
Usually, NMCA's or Chambers of Surveying Engineers provide licenses.	TKGM
Is there a professional skills exam to obtain a license?	
Approval of professional skills, generally based on an examination, by state/federal board or commission, professional state recognized commission, second state examinations commission etc.	No. As professional experience, only the 10 years following the diploma are considered significant. Whether there is professional experience in the cadastre directorate or LIHKABs is not being requested.
Validity period	
The period of validity of licenses or authorisations has no limitation in time.	Up to the age of 65, 65 years is the mandatory retirement age of public staff in Türkiye.
Average number of licensed bureaus?	
In some countries, there are no licensed bureaus. In others, it varies in the range of 20 to 1,500.	692
Average number of employees in licensed bureaus?	
Due to market conditions, the workforce intensity per licensed firm varies; small firms employ 1-2 licensed cadastral surveyors, while medium-sized firms employ 10-20 licensed cadastral surveyors.	The minimum personnel required in each bureau is 4, including 2 engineers, one of them being a cadastral surveyor and 2 technicians.

	The number of personnel increases according to the workload of the bureau.
Who performs quality control?	
Quality control is carried out to a significant extent by NMCA (49%), followed by Ministries (15%), Chambers (15%), and local authorities (12%).	TKGM
Affiliation?	
Registration with the chamber is mandatory.	Yes, HKMO
Liability of produced cadastral data and/or documents?	
The majority of licensed cadastral surveyors' bear liability for both their property surveys and the production of cadastral data.	Licensed cadastral surveyors are liable for their property surveys and cadastral data/document production.
Responsibility for the quality and accuracy of the data?	
The responsibility for quality and accuracy lies with the cadastral surveyor in 75% of the member countries.	Fully responsible
Compulsory insurance for a licence?	
The compulsory insurance rate is 29% and applies only to private Licensed cadastral Surveyors.	There is no such requirement.
Compulsory professional practice?	
A minimum of 2-3 years of experience working in a licensed property surveyor's office or within cadastral administration, focused on performing cadastral tasks while pursuing additional education.	There is no requirement for licensed practice in an office and/or land administration as in the EU. Being a surveying engineer for 10 years is sufficient.
Supervision of licenced bureaus activities?	
Typically, NMCAs oversee around 49% of licensed cadastral surveyors' activities. Moreover, regulatory bodies such as the Ministry, Chamber, and municipalities also play a role in supervision.	TKGM
Sanctions?	
In the majority of the country, sanctions continue to be enforced by the State Agency or chamber. The types of sanctions mainly include suspension (27%), termination (25%), fine (23%), and notice (27%). Extra training is also among the applied sanctions. The rate of resorting to court within the scope of sanctions is around 5%.	There are sanctions at different levels.
Education?	
5 Years on University level consisting of a bachelor (3/4 years) and master (1/2 years) in surveying and cadastre science.	4 years on university level of a bachelor education in surveying and cadastre science.
Training?	
Universities and high schools mainly provide training and education to licensed cadastral surveyors, but chambers and associations play an important role organising training courses and raising qualification. The mandatory Continuous Professional Development (CPD) experiences an increasing trend since it is required in more and more countries.	TKGM organizes in-service training at long intervals. There is no Mandatory Continuous Professional Development (CPD) requirement.
Ethical code?	
In many countries, even if it exists in some, there are no written ethical rules.	There is no written ethical code.

## 6. CONCLUSIONS

The cadastre and land registry play a fundamental role in advancing sustainable development by meticulously collecting, verifying, and ensuring accessibility to pivotal data concerning land and its

inherent characteristics. The continuous maintenance and updating of the cadastre are equally imperative to its initial establishment, as they provide a secure underpinning for interactions between people and the land. NMCAs, serving as the regulatory, executive, and coordinative bodies for cadastral and, by extension, land registry undertakings, have historically furnished reliable and authoritative land information throughout Europe's evolutionary trajectory. In numerous Member States, activities related to cadastre and cadastral renewal hinge on the involvement of licensed private surveyors in addition to public surveyors.

One notable revelation stemming from this study is the conspicuous absence of an EU regulation overseeing the activities of cadastral surveyors across European nations despite the longstanding and efficacious endeavours undertaken by the CLGE. It is increasingly acknowledged as imperative and obligatory to establish legal frameworks that sustain property security and state guarantees, uphold public confidence in property rights and the property system, propel land markets within an efficient and dynamic framework, bolster economic growth, ease the cultivation of robust and sustainable institutional frameworks and societies, promote the evolution of professional policies within member countries, and ensure meaningful and enduring implementations of licensed cadastral surveyors' activities within the EU framework, in conformity with the INSPIRE Directives.

The intended legal framework should take the comprehensive shape of a policy and implementation document, providing guidance to Member States regarding the development, vitalization, strengthening, modernization, and standardization of both cadastre and land administration systems, as well as professional practices. Moreover, it should accommodate the unique characteristics of member countries' local conditions and remain adaptable to the dynamic interplay of global political, technological, economic, environmental, and social dynamics. Such adaptability positions it potentially as a foundational model for future guidance to other nations.

Another significant finding is that cadastral activities and licensed cadastral surveyors' activities in Türkiye are dynamic. The activities that initiated with the LIHKAB law enacted in 2005 were reorganized with the amended law in 2021. This regulation, on one hand, addresses the issues related to the sharing of activities between LIHKABs and SHKMs, while on the other hand, it brings up other problems. The most prominent of these challenges is the provision to grant licenses to engineers who have completed 10 years from the date of their diploma and are under 65 years of age, and if they request, a license will be granted without the need for a registered judicial and moral evaluation. The major issue among these problems is the provision stating that engineers who have completed 10 years from the date of their diploma but have not reached the age of 65 can be granted a license if they request, provided that they have no registered criminal or moral convictions.

In the context of the quality of documents and data of licensed cadastral surveyors and thus LIHKABs, the following recommendations have been developed:

- i. Grant licenses to cadastral surveyors who successfully achieve a certain outcome in the exams.
- ii. Ensure that surveyors intending to take the exam possess a minimum of 2 years of practical experience in LIHKABs or cadastral directorates before the exam date; disallow those who fail to meet this requirement from taking the exam.
- iii. Conduct the exam process through TKGM in coordination with the HKMO.
- iv. Prepare a detailed user guide that serves as a guide for licensed cadastral surveyors.
- v. Eliminate the requirement for licensed cadastral surveyors to open an office.
- vi. Provide licensed cadastral surveyors with a distinct priority status, both in the public and private sectors, similar to the "expert cadre in the public sector."
- vii. Determine LIHKAB working areas according to regional workload by TKGM.
- viii. Establish effective training and Continuous Professional Development (CPD) programs, determining their content and timing, and efficiently implement both theoretical and practical training.

Due to the increasing priority of land management and cadastre issues on a global scale, licensed cadastral surveyors and free surveyors need to possess knowledge and experience not only in the

technological aspects but also in legal, economic, social, and environmental dimensions of the profession. This will enhance the diversity of the profession and create new job opportunities for them. Another result emerging from this study is that the fields of activity of free surveyors and licensed cadastral surveyors are limited. Under the 'measure, cost, and value' approach, if surveyors actively engage in activities such as land and building valuation, quantity surveying, land acquisition, and technical supervision/advisory for property-related projects of other public institutions, the activities will diversify, and the volume of work will increase.

### **Declaration of Ethical Standards**

As the author of this study, I declare that all ethical standards have been complied with.

### **Credit Authorship Contribution Statement**

In this study, the author contribution rate was determined as 100%.

### **Declaration of Competing Interest**

As the author of this study, I declare that there are no declarations of conflict.

### **Funding / Acknowledgements**

As the author of this study, I declare that no funding or research grant was used in the preparation of this article."

### **Data Availability**

This study does not contain usable data.

### **REFERENCES**

- [1] I. Williamson, S. Enemark, J. Wallace, A. Rajabifard, *"Land Administration for Sustainable Development"*, Esri Press, 380 New York Street, Redlands, California 92373-8100, 2010.
- [2] S. Enemark, 2005, *"Understanding the Land Management Paradigm"*, FIG Commission 7 Symposium on Innovative Technologies for Land Administration, Madison, Wisconsin, USA, 19-25 June 2005.
- [3] Enemark, S, *The Evolving Role of Cadastral Systems in Support of Good Land Governance, The Digital Cadastral Map*", FIG Commission 7 Open Symposium Karlovy Vary, Czech Republic, 9 September 2010.
- [4] UN-GGIM, *"Framework for Effective Land Administration"*, UN Secretariat for the United Nations Committee of Experts on Global Geospatial Information Management Global Geospatial Information Management Section Statistics Division Department of Economic and Social Affairs United Nations, 2020.
- [5] UN-IGIF, *"United Nations Integrated Geospatial Information Framework"*, Second Edition, 2023
- [6] FIG 1995, International Federation of Surveyors (FIG) Publication No. 11, *"The FIG Statement on the Cadastre"*, ISSN:1018-6530 ISBN 0 644 4533 Canberra, Australia, 1998.
- [7] CLGE 2010, *"Impact of EU Legislation on Cadastral Surveying"*, Knowledge Exchange Network "Cadastre and Land Registry" Working Group "Impact of EU Legislation on Cadastral Surveying", Tech. Report, 2010
- [8] CLGE 2018, *"European requirements for cadastral surveyor activities"*, The European Cadastral Surveyor, Tech. Report, 2018

- [9] CLGE 2018R, "European Requirements for Property (Cadastral) Surveyor Activity", The European Cadastral Surveyor, Tech. Report, Revision of 2018.
- [10] LIHKAB 2005, "Law on Licensed Survey and Cadastre Engineers and Bureaus", Law Number: 5368, Ankara, Official Gazette: Date: 29/6/2005, Number: 25860, 2005.
- [11] LIHKAB 2021, "Law on amending the Law on Licensed Survey and Cadastre Engineers and Bureaus", Law Number: 7317, Ankara, Official Gazette: Date: 27/4/2021, Number: 32467, 2021.
- [12] LIHKAB 2021R, "Regulation on Licensed Survey and Cadastre Engineers and Bureaus", 25 September 2021, Ankara, Official Gazette Number: 31609, 2021.
- [13] Bologna Process 2018, "Bologna Process", <https://eua.eu/issues/10:bologna-process.html> bologna [Accessed August 2023]
- [14] Bologna Process 2010, "Bologna Process", <https://eua.eu/issues/10:bologna-process.html> bologna [Accessed August 2023].
- [15] Lisbon Strategy, *Briefing note for the meeting of the EMPL Committee 5 October 2009 regarding the exchange of view on the Lisbon Strategy and the EU cooperation in the field of social inclusion*, Directorate-General for Internal Policies Committee on Employment and Social Affairs the Secretariat, European Parliament, 2009-2014.
- [16] EU 2002, "Consolidated Version of The Treaty Establishing the European Community (97/C 340 /03 )", C 340/ 173, Official Journal of the European Communities, 1997.
- [17] CLGE 2021, "European Requirements for Property Surveyors", Presented at Athens (GR)- CLGE Seminar @ HARSE Congress, Athens, Greece, 2021.
- [18] A. Littler, "Member States versus the European Union", ISBN: 978-90-04-18658-3, Martinus NIJHOFF Publishers, Leiden, Boston, 2011.
- [19] EU 2005, "Directive 2005/36/EC of the European Parliament and of the Council of 7 September 2005 on the recognition of professional qualifications" (Text with EEA relevance)" (OJ L 255, 30.9.2005, p. 22), 2005.
- [20] FIG/WB, "Fit-For-Purpose Land Administration", joint FIG/World Bank publication No. 60., 2014.
- [21] EU, "Directive 2007/2/EC of the European Parliament and of the Council of 14 March 2007 establishing an Infrastructure for Spatial Information in the European Community" (INSPIRE), 25.4.2007 EN Official Journal of the European Union, 2007.
- [22] M. Grilc, V. Krupa, J. Y. Pirlot, "Towards the European Geodetic Surveyors 'Act, An introduction on Regulations for Property Surveyor in Europe", Romanian Surveying Week, Oradea, Romania, 2023.
- [23] V. Krupa, J. Y. Pirlot, F. Lebourdais, "Protecting Our World, The European Geodetic Surveyors Act, an introduction to a new ID for Geodetic Surveyors in Europe and in the World", FIG Working Week on Conquering New Frontiers Orlando, Florida, USA, 2023.
- [24] CLGE, 2022, "Working for the Profession" PCC - Paris (FR), 2022.
- [25] O. Ercan, "Evolution of the cadastre renewal understanding in Türkiye: A fit-for purpose renewal model proposal", Land Use Policy, Volume 131, August 2023, DOI: <https://doi.org/10.1016/j.landusepol.2023.106755>, 2023
- [26] N. I. Sarı, "Disiplin Hukuku Bakımından Sorumlulukları, Mali Yönden Sorumlulukları, Ceza Hukuku Yönüyle Sorumluluklar", TKGM Antalya Hizmetiçi Eğitim, 31 Mayıs 2023 (Responsibilities in Terms of Disciplinary Law, Financial Responsibilities, Responsibilities in Terms of Criminal Law, TKGM Antalya In-Service Training, 31 May 2023-).
- [27] J. Kaufman and D. Steudler, "Cadastre 2014 - a Vision on Future Cadastral Systems", Working Group 7.1 (Modern Cadastral Systems), Commission 7, FIG and owner of Kaufmann Consulting, Concepts and Project Management for Geomatics, Im Hauffeld, CH-8455 Rüdlingen, Switzerland, 1998.
- [28] UN/ECE, "Land Administration Guidelines", ECE/HBP/96. United Nations: New York, Geneva, 1996.

- [29] UN WPLA, "*Land Administration in Public Private Partnerships Workshop Customers - Co-operation – Service*", Vienna, 12 - 13 September 2002, United Nations Economic Commission for Europe, Working Party on Land Administration Working Party on Land Administration, 2002.
- [30] Larakker, P., 2008, EuroGeographics' Vision on Cadastre and Land Registration in Europe 2012, Integrating Generations FIG Working Week 2008 Stockholm, Sweden, 2008.



## THE EFFECT OF THE AEGEAN SEA EARTHQUAKE, OCCURRED ON OCTOBER 30, 2020, ON TUSAGA STATIONS

<sup>1,\*</sup> Tunahan GUNDOĞAN , <sup>2</sup>Sercan BÜLBÜL , <sup>3</sup>Cevat İNAL 

<sup>1</sup> General Directorate of Mapping (GDM), Ankara, TÜRKİYE

<sup>2,3</sup>Konya Technical University, Engineering and Natural Sciences Faculty, Geomatics Engineering Department,  
Konya, TÜRKİYE

<sup>1</sup> [tunahan.gundogan@harita.gov.tr](mailto:tunahan.gundogan@harita.gov.tr), <sup>2</sup> [sbulbul@ktun.edu.tr](mailto:sbulbul@ktun.edu.tr), <sup>3</sup> [cinal@ktun.edu.tr](mailto:cinal@ktun.edu.tr)

### *Highlights*

- The effects of The Aegean Sea Earthquake on GNSS measurements
- The effects of GNSS measurements time on point positioning
- The success of GNSS in detecting deformation



## THE EFFECT OF THE AEGEAN SEA EARTHQUAKE, OCCURRED ON OCTOBER 30, 2020, ON TUSAGA STATIONS

<sup>1,\*</sup>Tunahan GUNDOĞAN , <sup>2</sup>Sercan BÜLBÜL , <sup>3</sup>Cevat İNAL 

<sup>1</sup> General Directorate of Mapping (GDM), Ankara, TÜRKİYE

<sup>2,3</sup> Konya Technical University, Engineering and Natural Sciences Faculty, Geomatics Engineering Department, Konya, TÜRKİYE

<sup>1</sup> [tunahan.gundogan@harita.gov.tr](mailto:tunahan.gundogan@harita.gov.tr), <sup>2</sup> [sbulbul@ktun.edu.tr](mailto:sbulbul@ktun.edu.tr), <sup>3</sup> [cinal@ktun.edu.tr](mailto:cinal@ktun.edu.tr)

(Received: 29.09.2023; Accepted in Revised Form: 16.10.2023)

**ABSTRACT:** GNSS is used to determine the point positions on the earth with high accuracy. The accuracy that can be achieved with GNSS depends on the satellite system, processing software, logging interval, observation time, etc. varies depending on the effects.

In the study, the impact of the Aegean Sea Earthquake that occurred on November 30, 2020, on TUSAGA was investigated. For this purpose, 7 TUSAGA stations located in the earthquake-affected area were selected. The 24-hour RINEX data for these stations were obtained both 15 days before and after the earthquake. The 24-hour RINEX data of 7 TUSAGA were processed using the GAMIT/GLOBK, based on 14 IGS stations. Furthermore, the evaluations were repeated by dividing the 24-hour RINEX data into 2, 4, and 12-hour intervals. In the evaluation, the GPS+GLONASS+Galileo (MIX) satellite configuration was utilized. The daily solutions obtained to reveal the effect of the earthquake are divided into two parts as before/after the earthquake. For each of TUSAGA stations, pre- and post-earthquake coordinates and RMSE were calculated. With statistical tests, whether the changes in the points are significant or not, the amount and direction of the changes were determined with 95% statistical confidence. As a result, it was concluded that the changes before/after the earthquake were mostly in the MNTS, which is the closest to the earthquake base, the changes in the points generally decrease as you move away from the earthquake center, and the evaluation before/after the earthquake can be made more healthy as the observation time increases. In addition, 30-day coordinates were examined through time series, and only the graph of the change in MNTS was given since it was the closest station to the epicenter of the earthquake.

**Keywords:** *The Aegean Sea Earthquake, Galileo, GLONASS, GPS*

### 1. INTRODUCTION

According to national and international seismology centers, on October 30, 2020, at 14:51 local time in Turkey, an earthquake with its epicenter in the Aegean Sea, 8 kilometers north of Samos Island and at a depth of 10-12 kilometers occurred. The earthquake's magnitude was reported as Mw: 6.6 according to the Disaster and Emergency Management Authority (AFAD) data and Mw: 6.9 according to the Kandilli Observatory and Earthquake Research Institute (KRDAE). The earthquake was felt in various regions, primarily in İzmir, as well as in Muğla, Aydın, Denizli, Manisa, Uşak, Afyonkarahisar, Kütahya, Balıkesir, Bursa, Çanakkale, Istanbul, and Sakarya provinces, along with all of Western Anatolia and the North Aegean Islands [1].

The region where the October 30, 2020 Aegean Sea earthquake occurred represents a geographical area that includes the southern part of the Greek mainland to the west, the Aegean Sea in the middle, and Western Anatolia to the east. The Aegean Region, extending over approximately 800 kilometers along a North-South direction, experiences deformation under the North-South extension tectonics due to the subduction of the African plate beneath the Eurasian plate [2].

The Aegean Sea Earthquake took place in the central part of the Aegean Region, which is significantly deformed due to the effects of the North-South extension tectonics. This area is characterized by the subduction of the African plate beneath the Eurasian plate, resulting in substantial crustal deformation. It

\*Corresponding Author: Tunahan GÜNDOĞAN, [tunahangundogan7@gmail.com](mailto:tunahangundogan7@gmail.com)

is also a seismogenic zone where intense seismic activity occurred both before and after the year 1900 [1].

Contemporary regional positional changes after earthquakes can be estimated by utilizing continuously monitored GNSS (Global Navigation Satellite System) stations [3]. Numerous studies have been conducted in this regard. In Thailand, following the 2004 earthquake near Banda-Aceh with a magnitude of  $M_w$ : 9.3 and the 2005 earthquake near Nias Island in Sumatra with a magnitude of  $M_w$ : 8.7, the effects of these earthquakes on the Thai Geodetic GPS Network were investigated using the PPP (Precise Point Positioning) method with GIPSY-OASIS-II software. As of the end of 2006, horizontal movements of up to 55 cm in the south and 6 cm in the north of Thailand were determined [4]. Vertical movements in Houston, a subsidence area for many years, have been attempted to be determined using the CORS network. OPUS, a web-based GNSS evaluation software, and the scientific GNSS evaluation software GIPSY/OASIS were used to evaluate the measurements. Subsidence up to 0.5 cm per year can be detected using the OPUS software with long-term GNSS data of 5 years or more [5]. A method has been developed for real-time and high-precision tracking of earthquakes using a single-frequency GPS receiver. The analysis of the Wenchuan earthquake with a magnitude of  $M_w$ : 8.0, the Tohoku-Oki earthquake with a magnitude of  $M_w$ : 9.0, and the Lushan earthquake with a magnitude of  $M_w$ : 6.6 has been performed. The results show that accurate and reliable results can be obtained using the developed method [6]. When analyzing landslides in Alaska through time series of GPS observations spanning 4 years, horizontal movements of 5.5 cm/year in the east-west direction and vertical movements of 2.6 cm/year have been detected in the north [7]. By using measurements from 43 GNSS stations scattered throughout the Southern Patagonian Icefield region, horizontal velocities with an accuracy of approximately 1 mm/year and vertical velocities of about 6 mm/year have been determined, and these velocities were used to determine the shape and magnitude of horizontal and vertical crustal deformation [8]. GPS observations with 30-second recording intervals conducted on July 15-18, 2013, and December 7-10, 2013, were used to investigate the post-seismic movement of the strike-slip fault in Northern Sumatra following the Aceh earthquake with a magnitude of 6.1 that occurred on July 2, 2013. The measurements were evaluated using the Bernese v5.2 software. As a result of the post-seismic deformation analysis of the Aceh earthquake, it was observed that the earthquakes that occurred before, in 2004 and 2012, were still affecting Northern Sumatra, with effects of approximately 12 mm and 10 mm, respectively [9]. Deformations resulting from the earthquake with a magnitude of  $M_w$ : 7.9 that occurred on April 25, 2015, in Gorkha have been determined based on measurements made before and after the earthquake using 6 GNSS stations. In the evaluation of the measurements, the Bernese v5.2 software was used, and post-seismic displacement was obtained from daily time series data that had been corrected for interseismic deformation and seasonal changes [10]. It is also known that earthquakes with a seismic moment magnitude of less than  $M_w$  6.0 do not create surface displacements measurable with the global positioning system (GPS) [11]. Studies have shown that increasing the observation duration and using multiple satellite systems together improve positional accuracy [12]. Earthquake monitoring studies with GNSS have been one of the topics of interest in recent years [13]–[18].

In this context, GNSS receivers at TUSAGA points in the earthquake region were able to record data from GPS, GLONASS, and Galileo satellite systems, so all three satellite systems were used in the study. Daily RINEX data from 7 TUSAGA stations (AKHI, BOZU, CINC, ESME, MNTS, SHUT, and TVAS) were divided into 2, 4, and 12-hour segments, and the solutions were evaluated using the GAMIT/GLOBK data evaluation software with GPS+GLONASS+Galileo (MIX) satellite combination.

## 2. EXPERIMENTAL DETAILS

On October 30, 2020, a very powerful earthquake occurred in the Aegean Sea, between the north of Samos Island and the Doğanbey-İzmir offshore area (37.9020 North, 26.7942 East) at 14:51 local time, according to AFAD (Disaster and Emergency Management Authority). The earthquake was reported to have a magnitude of  $M_w$ =6.6 by AFAD and  $M_w$ =6.9 by KRDAE. The depth of the earthquake's focus was approximately 12 kilometers, indicating it was a shallow-focus earthquake. The earthquake was felt in a wide area, including İzmir province and its districts, as well as the Aegean and Marmara regions.

The Turkey Earthquake Hazard Map was updated on January 1, 2019, and came into effect. In this map, instead of earthquake zones, the largest ground acceleration values (PGA: Peak Ground Acceleration) were shown, and the maximum acceleration value for İzmir province was determined to be between 0.3-0.5g (PGA  $475_{year}$ ). These values indicate a high earthquake hazard in the region (Figure 1).

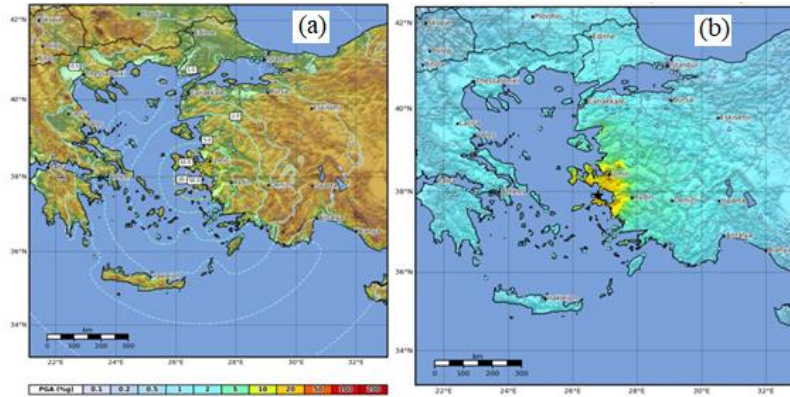


**Figure 1.** Aegean Sea Earthquake (a) PGA and (b) Intensity Map (<https://earthquake.usgs.gov/earthquakes/eventpage/us7000c7y0/shakemap/intensity>)

The province of İzmir is located at the western end of the Gediz Graben system, which is under the influence of the Western Anatolian Extensional Regime. As can be seen in the Turkey Active Fault Map prepared by the MTA (General Directorate of Mineral Research and Exploration) in 2011, east-west trending normal faults are situated at the western end of the Gediz Graben, whereas especially northeast-southwest and northwest-southeast trending faults concentrate around the İzmir region. Apart from the Gediz Graben, active faults in the region that could contribute to earthquake activity include the Tuzla, Seferihisar, Gülbahçe, Mordağan, Gümüldür, İzmir, Menemen, Güzelhisar, Yeni Foça, and Kiraz faults ([http://www.koeri.boun.edu.tr/sismo/2/wp-content/uploads/2020/10/20201030\\_izmir\\_V1.pdf](http://www.koeri.boun.edu.tr/sismo/2/wp-content/uploads/2020/10/20201030_izmir_V1.pdf)).

To determine the changes in the region affected by the Aegean Sea earthquake on October 30, 2020, GNSS data from 7 TUSAGA points were used (Figure 2).

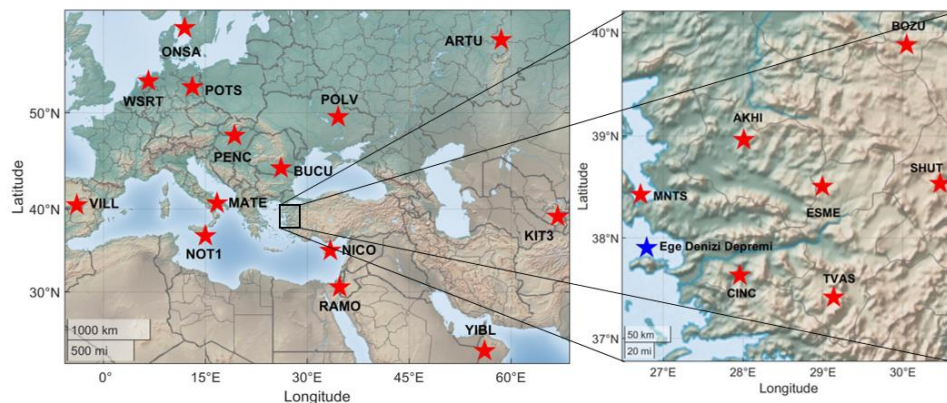


**Figure 2.** Used IGS (left) and TUSAGA Stations (right)

To investigate the changes in the TUSAGA stations in the earthquake region, RINEX data for 2, 4, and 12-hour intervals were collected using GNSS from the Akhisar (AKHI), Bozüyük (BOZU), Çine (CINC), Eşme (ESME), Menteş (MNTS), Şuhut (SHUT), and Tavas (TVAS) TUSAGA stations. The GAMIT/GLOBK software was used for the MIX solution. In the analysis of the selected TUSAGA stations, the IGS stations ARTU, BUCU, KIT3, MATE, NICO, NOT1, ONSA, PENC, POLV, POTS, RAMO, VILL, WSRT, and YIBL were used as references (Figure 2).

To investigate changes in the TUSAGA stations, RINEX data for 2, 4, and 12-hour intervals were

obtained between October 15, 2020 (day 289 of 2020) and November 13, 2020 (day 318 of 2020), with the earthquake time as the reference. The obtained RINEX data were processed daily using the GAMIT/GLOBK scientific data evaluation software for all satellite combinations (MIX). The evaluation strategy included:

- IGS precise orbits (sp3),
- usno\_bull\_b orbit parameters,
- 14 IGS stations,
- Reference Frame: ITRF 2014,
- Ocean Loading Effect: FES2004,
- Zenith Delay: PWL (piecewise linear),
- Dry/Wet Troposphere: VMF1 (Vienna Mapping Function 1),
- Precursory Tropospheric Model: Global Pressure Temperature Model (GPT 50).

A total of 90 evaluations were performed, each evaluation varying between approximately 20 minutes and 60 minutes depending on the measurement duration (Gündoğan, 2023).

To investigate the earthquake's impact on point positioning, the average coordinate values before and after the earthquake were calculated for two different time periods: pre-earthquake and post-earthquake. The average errors of these values were also computed. Errors were calculated using the following parameters:

$$vx_{\ddot{o}/s_i} = x_{\ddot{o}/s_i} - x_{ort_{\ddot{o}/s}} \quad vy_{\ddot{o}/s_i} = y_{\ddot{o}/s_i} - y_{ort_{\ddot{o}/s}} \quad vh_{\ddot{o}/s_i} = h_{\ddot{o}/s_i} - h_{ort_{\ddot{o}/s}} \quad (1)$$

The calculations were obtained using the equation for errors. In the equation, the subscript  $\ddot{o}/s$  "pre/post" represents pre-earthquake and post-earthquake, "i" represents the order of measurement, and "ort $_{\ddot{o}/s}$ " represents the pre-earthquake and post-earthquake averages. After obtaining the errors, the root mean square errors ( $m_x, m_y, m_h$ ) were calculated using;

$$m_{x_{\ddot{o}/s}} = \pm \sqrt{\frac{vx_{\ddot{o}/s_i}^2 + vx_{\ddot{o}/s_i}^2}{(n-1)}} \quad m_{y_{\ddot{o}/s}} = \pm \sqrt{\frac{vy_{\ddot{o}/s_i}^2 + vy_{\ddot{o}/s_i}^2}{(n-1)}} \quad m_{h_{\ddot{o}/s}} = \pm \sqrt{\frac{vh_{\ddot{o}/s_i}^2 + vh_{\ddot{o}/s_i}^2}{(n-1)}} \quad (2)$$

In the calculations, since data for 15 days before and after the earthquake were evaluated, "n" was taken as 15 in the equation. The differences between the average coordinate values calculated before and after the earthquake were calculated using;

$$dx = x_{ort_{\ddot{o}}} - x_{ort_s} \quad dy = y_{ort_{\ddot{o}}} - y_{ort_s} \quad dh = h_{ort_{\ddot{o}}} - h_{ort_s} \quad (3)$$

The equation for the average error of the difference components was used in calculating the average error:

$$m_{d_x} = \pm \sqrt{m_{x_{\ddot{o}}}^2 + m_{x_s}^2} \quad m_{d_y} = \pm \sqrt{m_{y_{\ddot{o}}}^2 + m_{y_s}^2} \quad m_{d_h} = \pm \sqrt{m_{h_{\ddot{o}}}^2 + m_{h_s}^2} \quad (4)$$

For each component, the test value was calculated using;

$$t_x = \frac{|dx|}{m_{d_x}} \quad t_y = \frac{|dy|}{m_{d_y}} \quad t_h = \frac{|dh|}{m_{d_h}} \quad (5)$$

The calculated test values were compared with the table value ( $t_{table} = t_{f_1+f_2, 1-\alpha} = t_{28, 0.95} = 1.701$ ) obtained from the t-distribution table. If the test value for even one component of a point was greater than the table value, it was determined that the point had displaced significantly. In determining the table value,  $f_1$  represents the degrees of freedom before the earthquake,  $f_2$  represents the degrees of freedom after the earthquake, and  $\alpha$  represents the significance level (0.05).

### 3. RESULTS AND DISCUSSION

The comparison results of the t-distribution are provided in Tables 1-3.

**Table 1.** Statistical Information for 2-Hour Measurements

Stations ID	Coordinate differences (mm)	rmse of coordinates differences (mm)	Test Value	Comparison	Result	
AKHI	dy	13.4*	±2.1	6.500	$t_y > t_{table}$	Unstable
	dx	1.2	±1.2	1.000	$t_x < t_{table}$	
	dh	23.7*	±3.1	7.780	$t_h > t_{table}$	
BOZU	dy	6.2	±2.6	2.410	$t_y > t_{table}$	Unstable
	dx	12.0	±1.0	12.720	$t_x > t_{table}$	
	dh	8.7	±3.3	2.620	$t_h > t_{table}$	
CINC	dy	5.4	±2.6	2.090	$t_y > t_{table}$	Unstable
	dx	11.8	±1.1	10.890	$t_x > t_{table}$	
	dh	14.2	±4.1	3.470	$t_h > t_{table}$	
ESME	dy	9.1	±2.3	3.940	$t_y > t_{table}$	Unstable
	dx	3.8	±1.0	3.760	$t_x > t_{table}$	
	dh	6.1	±3.9	1.570	$t_h < t_{table}$	
MNTS	dy	0.1	±2.5	0.040	$t_y < t_{table}$	Unstable
	dx	39.1*	±0.9	45.550	$t_x > t_{table}$	
	dh	22.0	±3.6	6.100	$t_h > t_{table}$	
SHUT	dy	4.7	±2.6	1.840	$t_y > t_{table}$	Unstable
	dx	6.8	±1.0	6.990	$t_x > t_{table}$	
	dh	3.8	±4.0	0.970	$t_h < t_{table}$	
TVAS	dy	6.7	±2.8	2.370	$t_y > t_{table}$	Unstable
	dx	10.7	±1.0	10.410	$t_x > t_{table}$	
	dh	6.6	±4.3	1.520	$t_h < t_{table}$	

As a result of the evaluation of the 2-hour measurements, it is observed that the maximum coordinate differences are at the AKHI station with 13.39 mm in the y-axis direction, at the MNTS station with 39.05 mm in the x-axis direction, at the AKHI station with 23.70 mm in the h-direction (vertical).

**Table 2.** Statistical Information for 4-Hour Measurements

Stations ID	Coordinate differences (mm)	rmse of coordinates differences (mm)	Test Value	Comparison	Result	
AKHI	dy	0.9	±0.3	3.080	$t_y > t_{table}$	Unstable
	dx	2.0	±0.7	3.050	$t_x > t_{table}$	
	dh	0.1	±1.6	0.050	$t_h < t_{table}$	
BOZU	dy	0.8	±0.2	4.500	$t_y > t_{table}$	Unstable
	dx	0.1	±0.3	0.440	$t_x < t_{table}$	
	dh	0.6	±1.0	0.630	$t_h < t_{table}$	
CINC	dy	0.4	±0.2	1.530	$t_y < t_{table}$	Unstable
	dx	0.9	±0.2	3.540	$t_x > t_{table}$	
	dh	2.3	±1.3	1.720	$t_h > t_{table}$	
ESME	dy	2.0	±0.3	8.070	$t_y > t_{table}$	Unstable
	dx	1.0	±0.4	2.460	$t_x > t_{table}$	
	dh	12.7*	±1.8	7.180	$t_h > t_{table}$	
MNTS	dy	6.8*	±0.3	26.400	$t_y > t_{table}$	Unstable
	dx	47.7*	±0.3	186.930	$t_x > t_{table}$	
	dh	7.9	±1.0	8.240	$t_h > t_{table}$	
SHUT	dy	0.3	±0.2	1.050	$t_y < t_{table}$	Unstable
	dx	1.2	±0.2	6.400	$t_x > t_{table}$	
	dh	6.2	±0.8	8.190	$t_h > t_{table}$	
TVAS	dy	0.9	±0.4	2.220	$t_y > t_{table}$	Unstable
	dx	1.4	±0.3	4.760	$t_x > t_{table}$	
	dh	0.7	±1.0	0.680	$t_h < t_{table}$	

As a result of the evaluation of the 4-hour measurements, it is observed that the maximum coordinate differences are at the MNTS station with 6.84 mm in the y-axis direction, at the MNTS station with 47.71 mm in the x-axis direction, at the ESME station with 12.70 mm in the h-direction (vertical).

**Table 3.** Statistical Information for 12-Hour Measurements

Stations ID	Coordinate differences (mm)	rmse of coordinates differences (mm)	Test Value	Comparison	Result	
AKHI	dy	3.3	$\pm 0.2$	20.080	$t_y > t_{table}$	Unstable
	dx	5.0	$\pm 0.2$	20.380	$t_x > t_{table}$	
	dh	<b>3.4*</b>	$\pm 0.6$	6.000	$t_h > t_{table}$	
BOZU	dy	0.6	$\pm 0.1$	4.440	$t_y > t_{table}$	Unstable
	dx	0.2	$\pm 0.2$	1.370	$t_x < t_{table}$	
	dh	0.9	$\pm 0.4$	2.060	$t_h > t_{table}$	
CINC	dy	0.8	$\pm 0.1$	5.320	$t_y > t_{table}$	Unstable
	dx	0.8	$\pm 0.1$	7.600	$t_x > t_{table}$	
	dh	2.5	$\pm 0.4$	5.840	$t_h > t_{table}$	
ESME	dy	1.5	$\pm 0.2$	8.610	$t_y > t_{table}$	Unstable
	dx	0.8	$\pm 0.1$	5.700	$t_x > t_{table}$	
	dh	0.3	$\pm 0.5$	0.660	$t_h < t_{table}$	
MNTS	dy	<b>7.0*</b>	$\pm 0.2$	43.660	$t_y > t_{table}$	Unstable
	dx	<b>48.0*</b>	$\pm 0.1$	376.420	$t_x > t_{table}$	
	dh	3.0	$\pm 0.4$	7.120	$t_h > t_{table}$	
SHUT	dy	1.5	$\pm 0.2$	7.790	$t_y > t_{table}$	Unstable
	dx	0.4	$\pm 0.2$	2.380	$t_x > t_{table}$	
	dh	2.7	$\pm 0.6$	4.760	$t_h > t_{table}$	
TVAS	dy	0.5	$\pm 0.2$	2.100	$t_y > t_{table}$	Unstable
	dx	1.0	$\pm 0.1$	7.160	$t_x > t_{table}$	
	dh	2.5	$\pm 0.7$	3.750	$t_h > t_{table}$	

As a result of the evaluation of the 12-hour measurements, it is observed that the maximum coordinate differences are at the MNTS station with 6.96 mm in the y-axis direction, at the MNTS station with 48.01 mm in the x-axis direction and at the AKHI station with 3.40 mm in the h-direction (vertical).

The daily coordinate data from the stations were evaluated with time series analysis. As a result of these evaluations, a total of 21 graphs were plotted using GMT (The Generic Mapping Tools) for all stations. Since the station with the most significant change is MNTS, a graph from this station is provided as an example (Figure 3-5). In the graphs, the points in the middle of the vertical lines represent the station's location, and the length of the line represents the confidence interval.

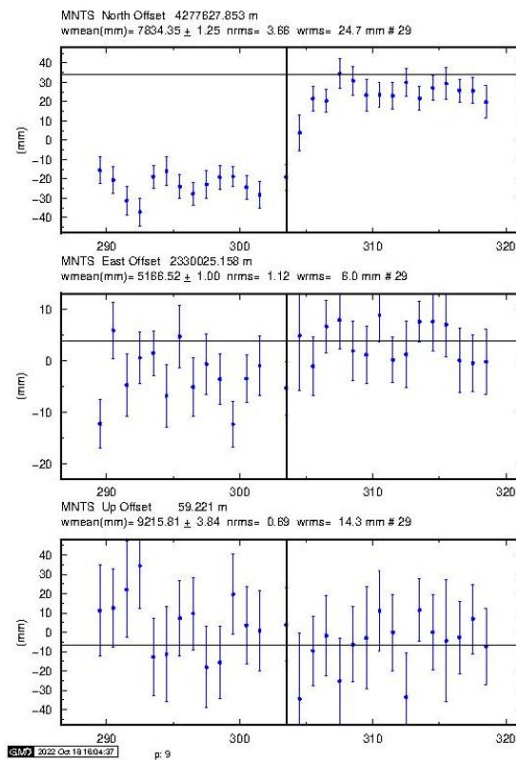


Figure 3. Time Series Analysis of Data from the MNTS Station with 2-Hour MIX Measurements

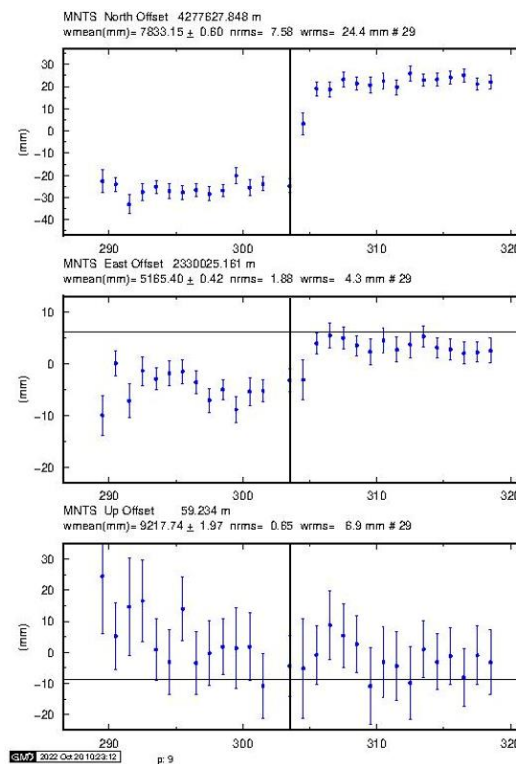
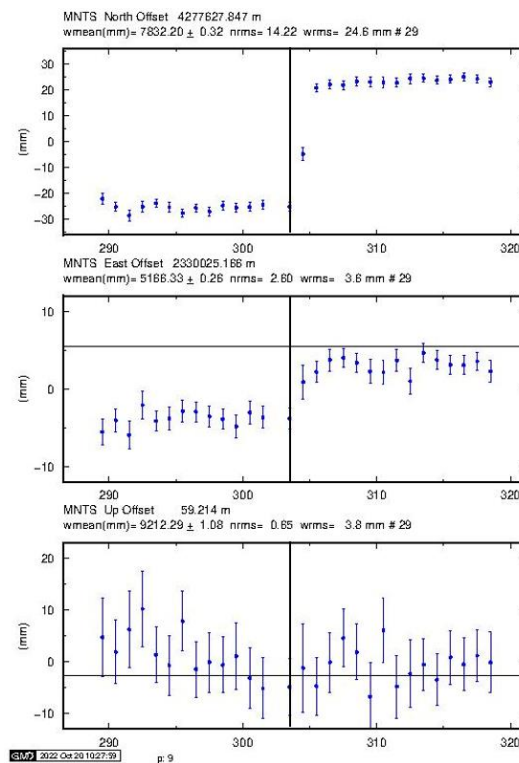


Figure 4. Time Series Analysis of Data from the MNTS Station with 4-Hour MIX Measurements



**Figure 5.** Time Series Analysis of Data from the MNTS Station with 12-Hour MIX Measurements

When examining Figures 3-5, it can be observed that as the measurement duration increases, the reliability of the measurements improves, and the changes at the points are better represented with 12-hour measurements.

#### 4. CONCLUSIONS

In this study, the impact of the Aegean Sea Earthquake on TUSAGA stations was investigated. For this purpose, 7 stations located in the earthquake zone were used. The distances of these points to the earthquake center vary between ~60 and ~400 km. The stations considered for evaluation are AKHI, BOZU, CINC, ESME, MNTS, SHUT, and TVAS. The GNSS data for the GPS+GLONASS+Galileo combination at these stations were divided into groups of 2, 4, and 12 hours, considering 15 days before the earthquake, the earthquake day, and 15 days after the earthquake, with the earthquake hour as the reference point. The data were evaluated using 14 IGS stations in the GAMIT/GLOBK software. The coordinates before and after the earthquake in the selected stations were determined, and whether the differences between them are significant was investigated through statistical tests, with the results shown in Tables 1-3.

When examining Tables 1-3, it can be observed that as the measurement duration increases, the accuracy of coordinate differences improves. The best results were obtained with 12-hour measurements, and the largest displacement occurred at the MNTS station, which is the closest to the earthquake center. Following MNTS, the stations with the largest displacements are AKHI, ESME, SHUT, TVAS, CINC, and BOZU. The largest displacements at MNTS were 6.96 mm in the y-axis direction and 48.01 mm in the x-axis direction. The largest vertical displacement occurred at the AKHI station, with 3.40 mm. As the measurement duration increases, the impact of the earthquake on point positions becomes more evident. This is confirmed by the analysis of the data from the MNTS station in Figure 5.

#### Declaration of Ethical Standards

As the authors of this study, we declare that all ethical standards have been complied with.

### Credit Authorship Contribution Statement

Author contribution rates in this study as follows: Tunahan Gündoğan 40%, Sercan BÜLBÜL 30%, Cevat İnal 30%.

### Declaration of Competing Interest

The authors declare no conflict of interest.

### Acknowledgements

This study was produced based on the Master's Thesis titled "The Effect of the Galileo Satellite System on Point Positioning" prepared by Tunahan GÜNDOĞAN under the supervision of Prof. Dr. Cevat İNAL in the Department of Geomatics Engineering at Konya Technical University, Graduate School of Natural and Applied Sciences.

### Data Availability

All data used for this study are available from the corresponding author upon reasonable request.

## 5. REFERENCES

- [1] A. Kürçer, H. Elmacı, F. Savaş, Ö. Kayadibi, "30 Ekim 2020 Ege Denizi Depremi (Mw 6,9) üzerine bir değerlendirme," *MTA Doğal Kaynaklar ve Ekonomi Bülteni*, vol. 30, pp. 57–75, 2020.
- [2] Y. Yılmaz, "Ege Bölgesinin Aktif Tektoniği," in *Batı Anadolu'nun Depremselliği Sempozyumu*, 2000, pp. 3–14.
- [3] S. Yaprak, O. Yildirim, and C. Inal, "Determination of 2011 Van/Turkey earthquake (M = 7.2) effects from measurements of CORS-TR network," *Geomatics, Natural Hazards and Risk*, vol. 5, no. 2, pp. 132–144, 2014, doi: 10.1080/19475705.2013.789453.
- [4] C. Satirapod, W. J. F. Simons, and C. Promthong, "Monitoring Deformation of Thai Geodetic Network due to the 2004 Sumatra-Andaman and 2005 Nias Earthquakes by GPS," *Journal of Surveying Engineering*, vol. 134, no. 3, pp. 83–88, 2008, doi: 10.1061/(ASCE)0733-9453(2008)134:3(83).
- [5] G. Wang and T. Soler, "Using OPUS for Measuring Vertical Displacements in Houston, Texas," *Journal of Surveying Engineering*, vol. 139, no. 3, pp. 126–134, 2013, doi: 10.1061/(ASCE)SU.1943-5428.0000103.
- [6] M. Li, W. Li, R. Fang, C. Shi, and Q. Zhao, "Real-time high-precision earthquake monitoring using single-frequency GPS receivers," *GPS Solutions*, vol. 19, no. 1, pp. 27–35, 2015, doi: 10.1007/s10291-013-0362-4.
- [7] G. Wang, Y. Bao, Y. Cuddus, X. Jia, J. Serna, and Q. Jing, "A methodology to derive precise landslide displacement time series from continuous GPS observations in tectonically active and cold regions: a case study in Alaska," *Natural Hazards*, vol. 77, no. 3, pp. 1939–1961, 2015, doi: 10.1007/s11069-015-1684-z.
- [8] A. Richter *et al.*, "Crustal deformation across the Southern Patagonian Icefield observed by GNSS," *Earth Planet Sci Lett*, vol. 452, pp. 206–215, 2016, doi: <https://doi.org/10.1016/j.epsl.2016.07.042>.
- [9] E. Gunawan, S. Widiyantoro, Zulfakriza, I. Meilano, and C. Pratama, "Postseismic deformation following the 2 July 2013 Mw 6.1 Aceh, Indonesia, earthquake estimated using GPS data," *J Asian Earth Sci*, vol. 177, pp. 146–151, 2019, doi: <https://doi.org/10.1016/j.jseaes.2019.03.020>.
- [10] F. Jouanne *et al.*, "Postseismic deformation following the April 25, 2015 Gorkha earthquake (Nepal): Afterslip versus viscous relaxation," *J Asian Earth Sci*, vol. 176, pp. 105–119, 2019, doi: <https://doi.org/10.1016/j.jseaes.2019.02.009>.

- [11] D. Baysal, B. Aktuğ, and A. Koçyiğit, "GPS Nokta Koordinatlarındaki Zamana Bağlı Değişimlerin Analizi ve Yorumu: İzmir Bölgesinde Uygulama," *Harita Dergisi*, vol. 144, pp. 29–39, Jul. 2010.
- [12] T. Gündoğan, "Galileo Uydu sisteminin Nokta Konumlamaya Etkisi," Graduate Education Institute, Konya, 2023.
- [13] R. M. Parameswaran, R. Grapenthin, M. E. West, and A. Fozkos, "Interchangeable Use of GNSS and Seismic Data for Rapid Earthquake Characterization: 2021 Chignik, Alaska, Earthquake," *Seismological Research Letters*, vol. 94, no. 3, pp. 1367–1378, Mar. 2023, doi: 10.1785/0220220357.
- [14] S. Baselga and J. Najder, "Automated detection of discontinuities in EUREF permanent GNSS network stations due to earthquake events," *Survey Review*, vol. 54, no. 386, pp. 420–428, 2022, doi: 10.1080/00396265.2021.1964230.
- [15] S. A. Younes, "Study of crustal deformation in Egypt based on GNSS measurements," *Survey Review*, vol. 55, no. 391, pp. 338–349, Jul. 2023, doi: 10.1080/00396265.2022.2099690.
- [16] H.-U. Kim and T.-S. Bae, "Monitoring of Possible Activities of Yangsan Fault Zone Using GNSS," *Applied Sciences*, vol. 13, no. 3, 2023, doi: 10.3390/app13031862.
- [17] S. Joshi, S. Kannaujiya, and U. Joshi, "Analysis of GNSS Data for Earthquake Precursor Studies Using IONOLAB-TEC in the Himalayan Region," *Quaternary*, vol. 6, no. 2, 2023, doi: 10.3390/quat6020027.
- [18] M. J. Fuchs, M. Rexer, and F. Schaidler, "Detection and analysis of seismic induced GNSS station motion in a North American network following the 2017 Chiapas earthquake," *J Geodyn*, vol. 149, p. 101881, 2022, doi: <https://doi.org/10.1016/j.jog.2021.101881>.



## SPACE COOLING WITH GROUNDWATER PUMPED BY A SOLAR DRIVEN PUMP

<sup>1,\*</sup> Hakan DUMRUL , <sup>2</sup> Selcuk SELİMLİ , <sup>3</sup> Sezayi YILMAZ , <sup>4</sup> Baris KORKMAZ 

<sup>1</sup> *Sirnak University, Engineering Faculty, Energy Systems Engineering Department, Sirnak, TÜRKİYE*  
<sup>2,3,4</sup> *Karabuk University, Technology Faculty, Energy Systems Engineering Department, Karabuk, TÜRKİYE*  
<sup>1</sup> [hakandumrul@sirnak.edu.tr](mailto:hakandumrul@sirnak.edu.tr), <sup>2</sup> [selcukselimli@karabuk.edu.tr](mailto:selcukselimli@karabuk.edu.tr),  
<sup>3</sup> [syilmaz@karabuk.edu.tr](mailto:syilmaz@karabuk.edu.tr), <sup>4</sup> [korkmazbaris59@gmail.com](mailto:korkmazbaris59@gmail.com)

### Highlights

- The cooling of a space with a solar PV pumping system integrated well water supplied fan coil was studied.
- CPEP showed that the possibility of a space with well water is possible.
- The cooling performance of solar water pump fan coil couple is dependent on the flow rate of well water.



## SPACE COOLING WITH GROUNDWATER PUMPED BY A SOLAR DRIVEN PUMP

<sup>1,\*</sup> Hakan DUMRUL , <sup>2</sup> Selcuk SELİMLİ , <sup>3</sup> Sezayi YILMAZ , <sup>4</sup> Baris KORKMAZ 

<sup>1</sup>Sirnak University, Engineering Faculty, Energy Systems Engineering Department, Sirnak, TÜRKİYE  
<sup>2,3,4</sup>Karabuk University, Technology Faculty, Energy Systems Engineering Department, Karabuk, TÜRKİYE  
<sup>1</sup>[hakandumrul@sirnak.edu.tr](mailto:hakandumrul@sirnak.edu.tr), <sup>2</sup>[selcukselimli@karabuk.edu.tr](mailto:selcukselimli@karabuk.edu.tr),  
<sup>3</sup>[syilmaz@karabuk.edu.tr](mailto:syilmaz@karabuk.edu.tr), <sup>4</sup>[korkmazbaris59@gmail.com](mailto:korkmazbaris59@gmail.com)

(Received: 11.07.2023; Accepted in Revised Form: 31.10.2023)

**ABSTRACT:** In this study, it was experimentally investigated that the groundwater of a well is brought to the surface using solar energy, which is one of the renewable energy sources, and the cooling of a place with this water with low energy density. The study evaluated cooling performance on two different days (Exp. 1 and Exp. 2) and at two different cooling water flow rates. The efficiency of the PV system was found to be  $8.33 \pm 0.44\%$  in Exp. 1 and  $8.3 \pm 0.44\%$  in Exp. 2. The cooling loads of the cooled buildings differ in Exp. 1 and Exp. 2 due to ambient conditions. The cooling load in Exp. 1 was determined to be  $572 \pm 22.8$  W and in Exp. 2 about  $828 \pm 33.1$  W. The heat loads extracted from the building by the groundwater used as a cooling fluid are  $410 \pm 16.4$  W and  $786 \pm 31.4$  W for Exp. 1 and Exp. 2. The cooling performance evaluation criteria (CPEP) value was found to be 0.72 for Exp. 1 and 0.95 for Exp. 2. Although there was a significant difference between the cooling loads for Exp. 1 and Exp. 2, the cooling load coverage increased with the increase in cooling water flow rate according to the CPEP values. Although in both experiments the cooling load was not fully met and the temperature inside the structure rose slightly during the experiment, it was kept cool.

**Keywords:** Solar water pumping, Space cooling, Cooling performance, Efficiency

### 1. INTRODUCTION

The rapid depletion of energy resources in the face of increasing consumption, the difficulty of accessing them, and rising costs are drawing attention to renewable energy resources in all aspects of life. 70% of the world's energy is consumed as thermal energy, and in parallel, the cost of energy is continuously increasing [1]. Pumps are widely used to meet water needs for industrial processes, irrigation and drinking water. They are mainly powered by electricity from fossil sources [2]. The idea of integrating PV solar systems with water pumps has been taken up by many researchers worldwide [3]. In India, 0.1 million solar photovoltaic water pumps were in operation for irrigation and drinking water supply between 2014 and 2015, and the government's goal is to reach 1 million by the end of 2021 [4]. Kumar et al. investigated the use of a buck converter in a PV system to pump water. Results proved a suitable combination for solar PV-based water pumping [5]. Speidel attempted to design and build a water pumping system based on solar energy. Solar based pumping system is evaluated as economical and practical feasible [6]. Chinthamalla et al. presented a single-stage solution for a PV-fed three-phase induction motor-driven water pumping system. They concluded that the proposed system provides better performance of the PV source and the induction motor [7]. Bataineh studied the performance of a solar thermal system for driving irrigation pumps. They claim that the optimal efficiency of the pump in May is 14%, in July it is 18% [8]. Foster and Cota discussed that photovoltaic water pumping systems are expected to grow tremendously due to decreasing costs and high reliability and will allow a greater number of farmers and ranchers to take advantage of this low-cost technology [9]. Saini et al. suggested solar energy as the most efficient and economical method for driving a centrifugal pump [10]. Yousuf et al. intend to develop a three-phase induction motor control for a solar-powered water pump. The experimental results met the requirements, as we were able to operate a water pump with a three-phase asynchronous motor with optimal cost efficiency [11]. Renu et al. studied the energy performance of

\*Corresponding Author: Hakan DUMRUL, [hakandumrul@sirnak.edu.tr](mailto:hakandumrul@sirnak.edu.tr)

solar-powered water pumps. They argued that the AC power pumps have an energy efficiency of more than 28% [12]. Ramazan studied the technical feasibility of a photovoltaic water pumping system. He claims that pumping 50 m<sup>3</sup> of water requires about 5.6 kWp of PV capacity [13]. Hammad studied PV modules with integrated water pumping system equipped with technical capacity. He said that the efficiency of PV systems and pumps on a monthly average is about 4% and 20%, respectively [14]. Daud and Mahmoud studied the energetic performance of a solar-powered water pump operating at a desert well. They concluded that the overall efficiency of the solar water pump is above 3% [15]. Meah et al. discussed the advantages of small-scale remote water pumping: no fuel, low maintenance costs, and a zero-emission process [16]. Meah et al. have investigated the possibilities of solar water pumping systems from a technical and economic point of view. They argued that solar water pumping systems can be economically viable compared to diesel generator water pumps [17]. Chandel et al. have studied the economic and technological benefits of solar water pumping systems. The payback period of the investment in a solar water pump system is estimated at 4-6 years [18]. Hassanien et al. have studied solar energy technologies and their control. They have found that solar energy can be used in an environmentally friendly and cost-effective way to irrigate agricultural fields around the world [19]. Sontake and Kalamkar attempted the review the types of solar water pumping systems and their development period in years. They argued that solar water pumping systems can be a good alternative to meet drinking and irrigation water needs [20]. Arghand et al. experimentally studied direct groundwater cooling of a room with fan coil application. They concluded that the change in groundwater temperature of about 2.2 °C provides more than 3 °C cooling opportunities for space [21]. Zhao et al. proposed to determine the thermal performance of a fan coil unit for cooling an indoor space with cold chilled water. They argued that the heating of the inlet water by 5 °C causes the cooling of the fresh air supply by 4 °C [22]. Solar energy, which is mainly used for heating, is also used for cooling, given the increase in energy costs in recent years [23].

In this study, the cooling of a building by the circulation of groundwater obtained by a pump driven by the electrical energy generated by the PV system through the fan coil was experimentally investigated. Storage of heated water after air conditioning for use and as irrigation water was also evaluated.

Governing equations:

The total efficiency ( $\eta_{pv}$ ) of the PV module can be calculated with Eq. (1) [24].

$$\eta_{pv} = \frac{E_p}{G \cdot A_{PV}} = \frac{VI}{G A_{PV}} \quad (1)$$

( $A$ ) is the PV area exposed to solar radiation, ( $V$ ) is the voltage, and ( $I$ ) is the current output of the PV array. ( $E_p$ ) is the electrical power output of the PV array. The efficiency of the motor-pump pair of the control unit is denoted as ( $\eta_{mp-cu}$ ) and can be determined by Eq. (2).

$$\eta_{mp-cu} = \frac{P_h}{E_p} = \frac{\rho_w \cdot g \cdot \dot{v} \cdot H}{VI} \quad (2)$$

In Eq. (2), ( $P_h$ ) is the hydraulic power, ( $\rho_w$ ) is the density of liquid water, ( $g$ ) is the gravitational acceleration, ( $\dot{v}$ ) is the volumetric flow rate, ( $H$ ) is the hydraulic head [18], [25]. Pumped groundwater flows through the fan coil unit and is directed into the cooled space. The heat transfer rate between the water and air sides is approximately the same and can be equated as in Eq. (3) [26].

$$\dot{Q}_w \cong \dot{Q}_a \quad (3)$$

In Eq. (4), ( $\dot{Q}_w$ ) and ( $\dot{Q}_a$ ) denote the rate of heat transfer from the air and to the water.

$$\dot{Q}_w = \dot{m}_w c_w (T_{wo} - T_{wi}) \quad (4)$$

( $\dot{m}_w$ ) is the mass flow rate of water, ( $c_w$ ) is the specific heat of water, ( $T_{wi}$ ) and ( $T_{wo}$ ) are the inlet and outlet temperatures of water.

$$\dot{Q}_a = \dot{m}_a c_{pa} (T_{ai} - T_{ao}) \quad (5)$$

( $\dot{m}_a$ ) is the mass flow rate of air, ( $c_{pa}$ ) is the specific heat of air, ( $T_{ai}$ ) and ( $T_{ao}$ ) are the inlet and outlet temperatures of air. The average heat exchange between the water and air can be equated with Eq. (6).

$$\dot{Q}_{avg} = \frac{\dot{Q}_w + \dot{Q}_a}{2} \quad (6)$$

The total heat transfer coefficient ( $U$ ) of the process can be calculated with Eq.(7) [27].

$$U = \frac{\dot{Q}_{avg}}{A_{fc} F \Delta T_{LMTD}} \quad (7)$$

( $A_{fc}$ ) is the heat transfer area, ( $F$ ) is the temperature correction factor, ( $\Delta T_{LMTD}$ ) is the log mean temperature difference and equated is as in Eq. (8) [28].

Where;

$$\Delta T_{LMTD} = \frac{\Delta T_1 - \Delta T_2}{\ln \frac{\Delta T_1}{\Delta T_2}} \quad (8)$$

Cooling load estimation

When calculating the cooling load of the house ( $\dot{Q}_{CL}$ ), internal ( $\dot{Q}_i$ ) and external ( $\dot{Q}_e$ ) heat loads were determined separately. The internal loads are calculated by considering the lighting ( $\dot{Q}_l$ ) and electrical ( $\dot{Q}_a$ ) appliances. External loads are solar ( $\dot{Q}_s$ ), conduction ( $\dot{Q}_c$ ) heat transfer from walls, doors, glasses, and infiltration from doors and glasses. The cooling load was determined by Eq. (9).

$$\dot{Q}_{CL} = \dot{Q}_i + \dot{Q}_e \quad (9)$$

The heat load caused by lighting can be determined by Eq. (10) [29].

$$\dot{Q}_l = P_l k_u k_s CLF \quad (10)$$

Where  $P_l$  is the lightning wattage,  $k_u$  and  $k_s$  are the usage and ballast factors,  $CLF$  is the cooling load factor. The heat load from electrical appliances can be calculated using Eq. (11) [30].

$$\dot{Q}_a = 0.293 P_a k_a CLF \quad (11)$$

In Eq. (11),  $P_a$  and  $k_a$  are the manufacturer input rating and the load factor, respectively. 0.293 is the unit conversion factor from Btu/h to W. The solar heat load from glasses can be calculated by Eq. (12) [31].

$$\dot{Q}_s = 0.293 A SC SCL \quad (12)$$

Where  $A$  is solar imposed glass area,  $SC$  is the shading coefficient,  $SCL$  is the solar cooling load factor. The conduction heat load on the surfaces of the test structure can be determined using the general relationship in Eq. (13) [32].

$$\dot{Q}_c = 0.293 U A_w CLTD \quad (13)$$

In Eq. (13),  $U$  is the coefficient of transmission,  $A_w$  is the wall cross sectional area,  $CLTD$  is the cooling load temperature difference. Infiltration heat load can be defined by Eq. (14) [33]–[35].

$$\dot{Q}_{inf} = ACF\rho_a Vc_{pa}\Delta T \quad (14)$$

In Eq. (14),  $ACF$  is the air change factor,  $\rho_a$  and  $c_{pa}$  are leakage air density and specific heat,  $V$  is the space volume,  $\Delta T$  is the inner and outer temperature difference. Cooling performance evaluation criteria ( $CPEP$ ) is defined as in Eq. (15).

$$CPEP = \frac{\dot{Q}_{avg}}{\dot{Q}_{CL}} \quad (15)$$

The error rate of the study can be evaluated with Eq. (16).

$$w_R = \left[ \left( \frac{\partial R}{\partial x_1} w_1 \right)^2 + \left( \frac{\partial R}{\partial x_2} w_2 \right)^2 + \dots + \left( \frac{\partial R}{\partial x_n} w_n \right)^2 \right]^{\frac{1}{2}} \quad (16)$$

In Eq. (16),  $w_R$  denotes the uncertainty of the calculated result, and the  $w_n$  values are the uncertainty of each measured independent parameter [36].

## 2. EXPERIMENTATION SETUP DESCRIPTION

The experiments were conducted in a one-story building with two rooms and four windows on the campus of Karabuk University on two different sunny days, July 26, and August 2, 2019. The experiments conducted on these dates are defined as Exp. 1 and Exp. 2, respectively. The solar radiation values and ambient temperature for Exp.1 and Exp.2 are shown in Figure 1.

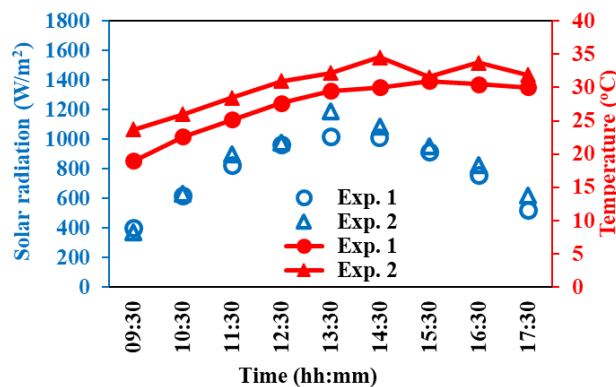


Figure 1. Solar radiation values for two different flow rate experiences

As seen in Figure 1, solar radiation tended to increase until 14:30 and ambient temperature until 13:30 in both experiments. In Exp. 1, the solar radiation and ambient temperature values at 9:30 were  $399 \pm 20$  W/m<sup>2</sup> and  $19 \pm 0.08$  °C, respectively, and by 13:30 they reached  $1018 \pm 41$  W/m<sup>2</sup> and  $29.5 \pm 0.12$  °C. By 17:30, solar radiation had decreased to  $525 \pm 26.5$  W/m<sup>2</sup>, while ambient temperature increased slightly, reaching up to  $30 \pm 0.12$  °C. In Exp. 2, the solar radiation was  $373 \pm 18.6$  W/m<sup>2</sup> and the temperature at 09:30 was  $23.7 \pm 0.1$  °C. By 13:30, solar radiation and temperature increased to  $1191 \pm 56$  W/m<sup>2</sup> and  $32.2 \pm 0.13$  °C. At 17:30, solar radiation and ambient temperature reached  $618 \pm 31$  W/m<sup>2</sup> and  $31.9 \pm 0.13$  °C, respectively. The average values of solar radiation and ambient temperature were  $782 \pm 39$  W/m<sup>2</sup> and  $27 \pm 0.1$  °C for Exp.

1 and  $839 \pm 42 \text{ W/m}^2$  and  $30 \pm 0.12 \text{ }^\circ\text{C}$  for Exp. 2. The daily relative humidity and wind speed values for Exp. 1 and Exp. 2 are 68%, 66%, and  $0.08 \pm 0.003 \text{ m/s}$  and  $0.12 \pm 0.005 \text{ m/s}$ , respectively. The construction plan of the building, the experimental measuring points and the arrangement of the devices are shown in Figure 2 (a, b).

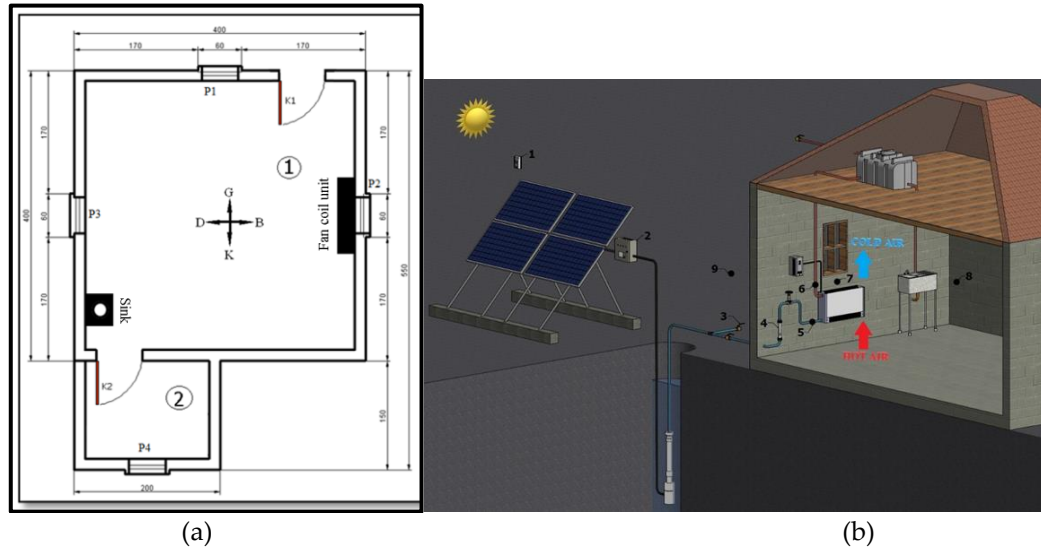


Figure 2 (a, b). Cooling experiment structure

DC voltage obtained from four PV panels, each with a power of 200 W, integrated into the experimental setup, is fed to the Lorentz brand PS1200 model solar pump control unit. The power of the PV modules arranged in the control unit of the model PS1200 was fed into the submersible pump, and the water extracted from the 10 m deep water well was directed to the existing fan coil unit of the building where the experiments were carried out. In the experiments, it was aimed to cool the building by absorbing the ambient heat into the cool groundwater passing over the fan coil, and both the experimental setup and the flow arrangement were prepared in this way. In Exp. 1 and Exp. 2, water circulation was carried out in the fan coil unit with a flow rate of  $0.3 \pm 0.008 \text{ m}^3/\text{h}$  and  $0.7 \pm 0.018 \text{ m}^3/\text{h}$ , respectively. The flow pattern of the experimental setup is shown in Figure 3.

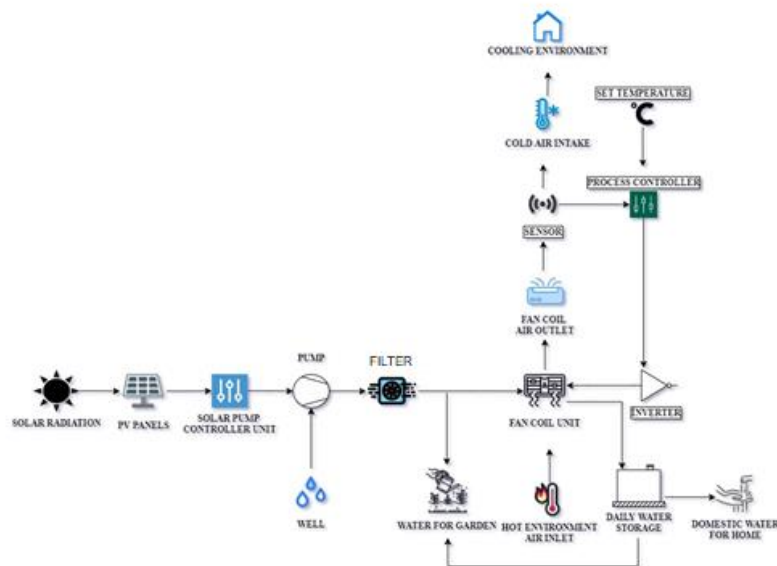


Figure 3. Flow configuration of experimentation setup

The technical data of the PV panels driving the pumps are listed in Table 1.

**Table 1.** PV panel specifications

Peak Power	200 W
Peak Power Voltage	27,5 V
Peak Power Current	7,28 A
Modul Efficiency	%13,6
PV STC: AM = 1.5, I = 1000 W/m <sup>2</sup> , T <sub>p</sub> = 25 °C	

The measurement equipment for the experimental setup, the specifications and uncertainties, and the descriptions of the measurement points are listed in Table 2.

**Table 2.** Measurement points and instruments specification

Measurement Point	Measured value	Name of the device	Device properties	Uncertainty
1	Solar radiation	TESS 133 Solar meter 88598 4 channel K	Irradiance range: 0-2000 W/m <sup>2</sup> ,	5%
5,6,7	Temperature	thermometer SD card data logger	-200 to 1370 °C, ± (0.3% rdg + 1 °C)	0.42%
9	Temperature	CEM DT-3891G 4 channel data logger	-200°C to 1372°C, (0.15% rdg+1°C)	0.37%
8	Temperature	Process control equipment	Brand: ORDEL Model: PC440; 4 W, 100–240 VAC, auto-tuning, PID control.	0.2%
2	DC Voltage and current	Digital wattmeter	Working voltage: 6.5-100V DC Voltage test range: 6.5-100V DC, Rated power: 20A / 2000W	V~1.06% A~5%
2	AC Current	Clamp meter	Model: Tt-Technic Model: DT-266C 1000A AC 20 - 1000A	3.01%
2	AC Voltage	Multimeter	Brand: UNI-T Model: UT33C; AC Voltage: 200V/500V	4.53%
3, 4	Volumetric flow rate	Flow meter	Model: LZS-15 Type: Long tube Pressure: ≤1Mpa Temperature: 0~60 °C.	4%
7	Air Flow Velocity	Testo 435, anemometer, Vane probe, Ø 16 mm, with telescopic handle max. 720 mm	Measurement range 0.6-40 m/s, operation temperature 0-60 °C	0.5%

In this study, part of the water coming from the pump was directed to the fan coil, while the remaining part was stored for domestic use.

### 3. RESULTS AND DISCUSSIONS

In this study, the cooling of the space by circulating groundwater brought to the surface by a solar-powered submersible pump fed by PV modules from a fan coil unit positioned in a structure was experimentally examined. The cooling load of the building and the cooling performance of the process were evaluated. The calculated solar energy values based on solar radiation for Exp. 1 and Exp. 2 are shown in Figure 4.

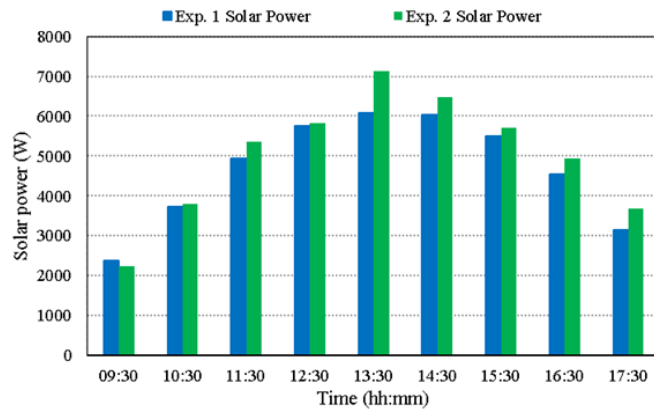


Figure 4. Solar power

The solar energy applied to the PV modules was determined as  $2384 \pm 178$  W and  $2229 \pm 167$  W for Exp. 1 and Exp. 2, respectively, at 9:30, as seen in Figure 4. The maximum solar power values were found to be  $6083 \pm 456$  W for Exp. 1 and  $7117 \pm 533$  W for Exp. 2, respectively. The average solar energy values for Exp. 1 and Exp. 2 are  $4675 \pm 350$  and  $5014.33 \pm 376$  W, respectively. The air flow rate of fan coil unit controlled as a function of indoor temperature are shown in Figure 5.

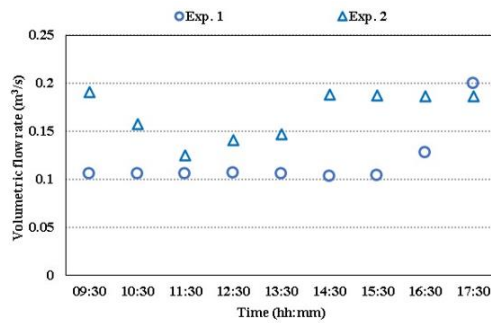


Figure 5. Fan coil fan air flow rate

Figure 5 shows the average values of the time-dependent fan coil air flows for Exp. 1 and Exp. 2 as  $0.12 \pm 0.003$  m<sup>3</sup>/s and  $0.17 \pm 0.004$  m<sup>3</sup>/s, respectively. The PV panel and pump hydraulic power values are shown in Figure 6 for Exp. 1 and Exp. 2. Also shown are the PV efficiency and the pump controller pair efficiency.

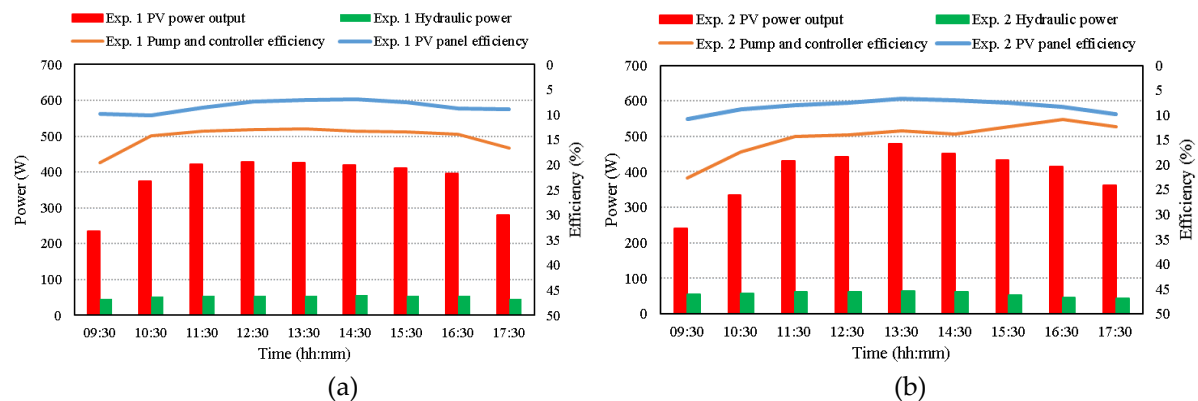
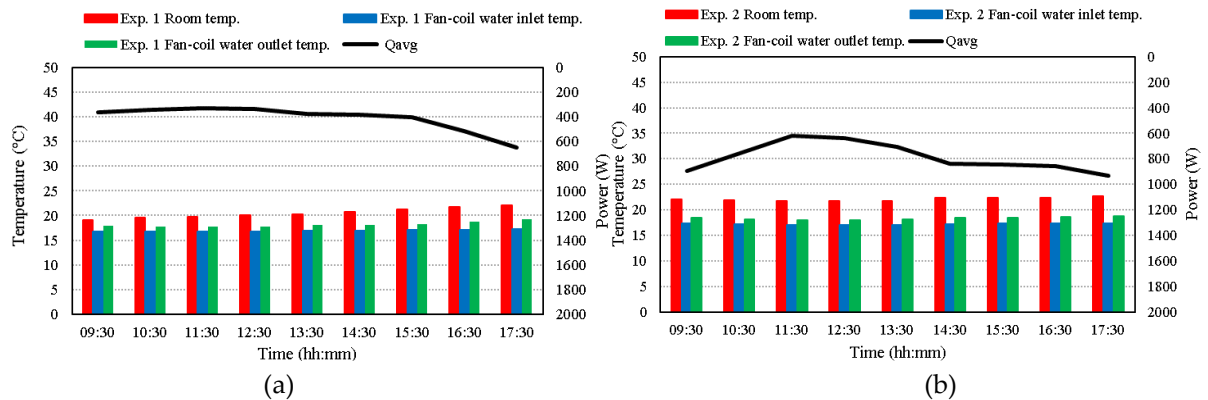


Figure 6. PV electrical power, pump hydraulic power, PV efficiency, and pump controller pair efficiency, (a) for Exp. 1, and (b) for Exp. 2

As can be seen in Figure 6, the average electrical output power of the PV system is  $376 \pm 20.3$  W, and the hydraulic output power of the pump is  $53 \pm 2.8$  W on average for Exp.1. In Exp. 2, the average PV output power is  $398 \pm 21.5$  W, and the hydraulic power is  $56 \pm 3$  W. The efficiency of the PV system and the pump control pair were determined to be approximately  $8.33 \pm 0.44\%$  and  $14.46 \pm 0.78\%$ , respectively, for Exp. 1. For Exp. 2, these values are  $8.3 \pm 0.44\%$  and  $14.55 \pm 0.78\%$ , respectively. The decrease in PV efficiency observed in Exp. 2 can be explained by the increasing temperature of the PV cells with increasing irradiance. Khatip reported in his comparative study of solar pump systems that the energy efficiency of a solar submersible pump is in the 10-20% range [37]. The building internal temperature, the fan coil water inlet and outlet temperatures, and the heat load values transferred from the air to the water are shown in Figure 7(a, b).



**Figure 7.** Cooling space temperature, fan coil water inlet, outlet temperatures, and heat loaded from space air to water (a) for Exp. 1, (b) for Exp. 2

Looking at the bar graphs in Figure 7, we see that the indoor temperature of the building is about  $20 \pm 0.08$  °C and  $22 \pm 0.09$  °C in Exp. 1 and Exp. 2, respectively. Since the experimental studies were conducted on two different days, the cooling load of the building increased due to the increased radiation and was higher in Exp. 2. This could explain the temperature difference of  $2 \pm 0.008$  °C between the average building interior temperatures in the two experiments. The average water inlet and outlet temperatures of the fan coil unit are  $16.9 \pm 0.06$  °C and  $18.2 \pm 0.07$  °C for Exp.1. For Exp. 2, the water inlet temperature of the fan coil unit was measured as  $17.2 \pm 0.07$  °C and the outlet temperature as  $18.3 \pm 0.07$  °C. It was found that the water passing through the fan coil is cooler than the ambient air passing through the fan coil, so it extracts some heat from the ambient air and cools the ambient air as it leaves the fan coil. In Figure 2, the average temperature change of the water flowing through the fan coil was found to be about  $2.3 \pm 0.009$  °C for Exp. 1 and  $1.1 \pm 0.004$  °C for Exp. 2. Compared to Exp. 1, the decrease in temperature difference in Exp. 2 can be explained by the increase in the amount of fluid passing through the fan coil per unit time. A significant increase in the heat load transferred to the water was observed with the increase in flow rate. The heat load transferred to the water was determined to be  $410 \pm 16.4$  W for Exp. 1 and  $786 \pm 31.4$  W for Exp. 2. The building heat load, the heat load dissipated by water from inside the building, and the CPEP are calculated and shown in Figure 8.

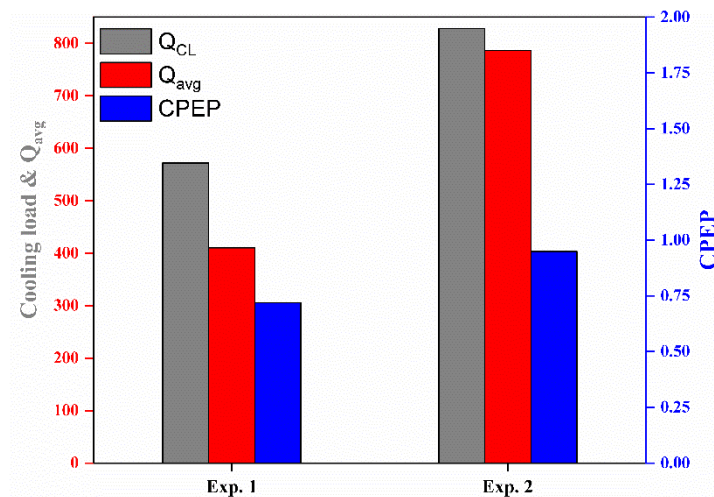


**Figure 8.** Cooling load, cooling heat rate, and CPEP

According to Figure 8, the heat load values, which are the sum of the internal and external heat loads of the building, were calculated to be  $572 \pm 22.8$  W and  $828 \pm 33.1$  W for Exp. 1 and Exp. 2, respectively. For Exp. 1 and Exp. 2, it was shown that  $410 \pm 16.4$  W and  $786 \pm 31.4$  W of heat can be removed from the building interior by dissipation in the groundwater in the fan coil. CPEP values were determined to be 0.72 for Exp. 1 and 0.95 for Exp. 2. It was found that the cooling capacity obtained in Exp. 2 increased with increasing cooling water flow rate. This study investigated the success of using a solar-powered pump to raise groundwater to the surface and cool a building. Although the cooling load of the building could not be fully absorbed by the groundwater in the fan coil unit and the internal temperature of the building increased slightly during the tests, coolness was achieved inside the building.

#### 4. CONCLUSIONS

The subject of this study is the cooling of an example building with groundwater extracted from the well by a submersible pump powered by a PV module. The work is characterised by its environmentally friendly and energy-saving potential. The study was conducted experimentally with two different groundwater flow rates on two different days. A flow rate of  $0.3 \pm 0.008$  m<sup>3</sup>/h was used in Exp. 1 and a flow rate of  $0.7 \pm 0.018$  m<sup>3</sup>/h in Exp. 2. PV panel efficiency was determined to be  $8.33 \pm 0.44\%$  for Exp. 1 and  $8.3 \pm 0.44\%$  for Exp. 2. In Exp. 1, the building is under the influence of a heat load of  $572 \pm 22.8$  W, while in Exp. 2 this load is  $828 \pm 33.1$  W. A heat load of  $410 \pm 16.4$  W in Exp. 1 and  $786 \pm 31.4$  W in Exp. 2 was transferred from the interior environment of the building to the groundwater circulating in the fan coil in the cooled building. CPEP values were compared to evaluate the relationship between cooling demand and heat load removed from the area by groundwater. While the CPEP value in Exp. 1 was 0.72, a value of 0.95 was determined in Exp. 2. At this point, it was noted that it is possible to cool a room using cool groundwater brought into the ground by a submersible pump powered by solar energy. Furthermore, it was observed in Exp. 2 that despite the increased cooling load, the affordability of the cooling load could be increased by increasing the cooling water flow rate. On both days of the experiment, part of the cooling load of the building was met and it could be kept cool.

#### Declaration of Ethical Standards

Authors declare to comply with all ethical guidelines, including authorship, citation, data reporting, and original research publication.

### Credit Authorship Contribution Statement

**Hakan DUMRUL:** Conceptualization, Investigation, Methodology, Writing-original draft. **Selcuk SELİMLİ:** Conceptualization, Methodology, Writing – review & editing. **Sezayi YİLMAZ:** Conceptualization, Funding acquisition, Supervision, Writing – review & editing. **Baris KORKMAZ:** Conceptualization, Investigation, Methodology, Writing-original draft.

### Declaration of Competing Interest

The authors declare that they have no known competing financial interests or personal relationships that could have appeared to influence the work reported in this paper.

### Funding / Acknowledgements

The authors declare that they have not received any funding or research grants during the review, research, or assembly of the article.

### Data Availability

Research data has not been made available in a repository.

### REFERENCES

- [1] E. Özbaş, "Experimental study of thermal performance and pressure differences of different working fluids in two-phase closed thermosyphons using solar energy," *Journal of Polytechnic*, vol. 22, no. 1, pp. 121–128, 2018.
- [2] P. Sahw and P. Gaur, "Photovoltaic Powered Centrifugal Water Pump," *International Journal of Electronic and Electrical Engineering*, vol. 7, no. 3, pp. 247–254, 2014.
- [3] M. S. Y. Ebaid, H. Qandil, and M. Hammad, "A unified approach for designing a photovoltaic solar system for the underground water pumping well-34 at Disi aquifer," *Energy Conversion and Management*, vol. 75, pp. 780–795, 2013.
- [4] P. K. S. Rathore, S. S. Das, and D. S. Chauhan, "Perspectives of solar photovoltaic water pumping for irrigation in India," *Energy Strategy Reviews*, vol. 22, pp. 385–395, 2018.
- [5] R. Kumar and B. Singh, "Buck-boost converter fed BLDC motor drive for solar PV array based water pumping," *2014 IEEE International Conference on Power Electronics, Drives and Energy Systems (PEDES)*, 2014, pp. 1-6.
- [6] K. Speidel, "Simple water pump, powered by solar energy," *International Symposium–Workshop on Solar Energy June 1978*, 1980, pp. 1748–1761.
- [7] C. Ramulu, P. Sanjeevikumar, R. Karampuri, S. Jain, A. H. Ertas, and V. Fedak, "A solar PV water pumping solution using a three-level cascaded inverter connected induction motor drive," *Engineering Science and Technology, an International Journal*, vol. 19, no. 4, pp. 1731–1741, 2016.
- [8] K. M. Bataineh, "Optimization analysis of solar thermal water pump," *Renewable and Sustainable Energy Reviews*, vol. 55, pp. 603–613, 2016.
- [9] R. Foster and A. Cota, "Solar water pumping advances and comparative economics," *Energy Procedia*, vol. 57, pp. 1431–1436, 2014.
- [10] A. Saini, Anish; Kohli, Shivam; Pillai, "Solar powered stirling engine driven water pump," *International Journal of Research in Engineering and Technology*, vol. 02, no. 11, pp. 615–620, 2013.
- [11] N. B. Yousuf, K. M. Salim, R. Haider, M. R. Alam, and F. B. Zia, "Development of a three phase induction motor controller for solar powered water pump," in *Proceedings of 2nd International Conference on the Developments in Renewable Energy Technology, ICDRET 2012*, 2012, pp. 312–316.
- [12] Renu, B. Bora, B. Prasad, O. S. Sastry, A. Kumar, and M. Bangar, "Optimum sizing and

- performance modeling of solar photovoltaic (SPV) water pumps for different climatic conditions," *Solar Energy*, vol. 155, pp. 1326–1338, 2017.
- [13] R. Senol, "An analysis of solar energy and irrigation systems in Turkey," *Energy Policy*, vol. 47, pp. 478–486, 2012.
- [14] M. A. Hammad, "Characteristics of solar water pumping in Jordan," *Energy*, vol. 24, no. 2, pp. 85–92, 1999.
- [15] A. K. Daud and M. M. Mahmoud, "Solar powered induction motor-driven water pump operating on a desert well, simulation and field tests," *Renewable Energy*, vol. 30, no. 5, pp. 701–714, 2005.
- [16] K. Meah, S. Fletcher, and S. Ula, "Solar photovoltaic water pumping for remote locations," *Renewable and Sustainable Energy Reviews*, vol. 12, no. 2, pp. 472–487, 2008.
- [17] K. Meah, S. Ula, and S. Barrett, "Solar photovoltaic water pumping-opportunities and challenges," *Renewable and Sustainable Energy Reviews*, vol. 12, no. 4, pp. 1162–1175, 2008.
- [18] S. S. Chandel, M. Nagaraju Naik, and R. Chandel, "Review of solar photovoltaic water pumping system technology for irrigation and community drinking water supplies," *Renewable and Sustainable Energy Reviews*, vol. 49, pp. 1084–1099, 2015.
- [19] R. H. E. Hassanien, M. Li, and W. Dong Lin, "Advanced applications of solar energy in agricultural greenhouses," *Renewable and Sustainable Energy Reviews*, vol. 54, pp. 989–1001, 2016.
- [20] V. C. Sontake and V. R. Kalamkar, "Solar photovoltaic water pumping system - A comprehensive review," *Renewable and Sustainable Energy Reviews*, vol. 59, pp. 1038–1067, 2016.
- [21] T. Arghand, A. Trüschel, J.-O. Dalenbäck, and S. Javed, "Dynamic thermal performance and controllability of fan coil systems," *Cold Climate HVAC Conference*, 2018, pp. 351–361.
- [22] K. Zhao, X. H. Liu, and Y. Jiang, "Application of radiant floor cooling in a large open space building with high-intensity solar radiation," *Energy and Buildings*, vol. 66, pp. 246–257, 2013.
- [23] M. Daşkın and İ. G. Aksoy, "Simulation of a solar assisted absorption cooling system for air-conditioning purposes," *Batman University Journal of Life Sciences*, vol. 4, no. 1, pp. 52–65, 2014.
- [24] R. A. Khan, L. A. Khan, and S. Z. Hussain, "Design and Simulation of 0.75hp Soft Start AC Water Pump Powered by PV Solar System," *Universal Journal of Mechanical Engineering*, vol. 3, no. 4, pp. 113–121, 2015.
- [25] D. B. Singh, A. Mahajan, D. Devli, K. Bharti, S. Kandari, and G. Mittal, "A mini review on solar energy based pumping system for irrigation," *Materials Today: Proceedings*, vol. 43, pp. 417–425, 2020.
- [26] M. Altwieb, K. J. Kubiak, A. M. Aliyu, and R. Mishra, "A new three-dimensional CFD model for efficiency optimisation of fluid-to-air multi-fin heat exchanger," *Thermal Science and Engineering Progress*, vol. 19, p. 100658, 2020.
- [27] Y. Kim and Y. Kim, "Heat transfer characteristics of flat plate finned-tube heat exchangers with large fin pitch," *International Journal of Refrigeration*, vol. 28, no. 6, pp. 851–858, 2005.
- [28] Y. Vermahmoudi, S. M. Peyghambarzadeh, S. H. Hashemabadi, and M. Naraki, "Experimental investigation on heat transfer performance of Fe<sub>2</sub>O<sub>3</sub>/water nanofluid in an air-finned heat exchanger," *European Journal of Mechanics, B/Fluids*, vol. 44, pp. 32–41, 2014.
- [29] Y. M. Degu, "Cooling Load Estimation and Air Conditioning Unit Selection for Hibir Boat," *The International Journal Of Engineering And Science*, vol. 3, no. 5, pp. 63–72, 2014.
- [30] K. G. Acharya, G. P. Yewale, M. V. Tendolkar, and S. H. Kulkarni, "Estimation and Analysis of Cooling Load for Indian Subcontinent by CLD/SCL/CLF method at part load conditions," *Journal of Physics: Conference Series*, vol. 1240, no. 1, 2019.
- [31] M. Ashiq, M. Naveed Gull, R. Kalvin, and M. A. Khan, "Cooling Load Estimation of Auditorium by CLTD Method and its Comparison with HAP and TRACE Software," *Pakistan Journal of Engineering and Technology*, vol. 04, no. 01, pp. 18–25, 2021.
- [32] S. Zaphar and T. Sheworke, "Computer Program for Cooling Load Estimation and Comparative Analysis with Hourly Analysis Program (HAP) Software," *International Journal of Latest Technology in Engineering, Management & Applied Science*, vol. 7, no. 6, pp. 53–61, 2018.

- [33] Y. Ji, L. Duanmu, and S. Hu, "Prediction model of air infiltration in single-zone buildings with high airtightness," *Energy and Built Environment*, vol. 4, no. 6, pp. 653–668, 2023.
- [34] G. T. Tamura, "Measurement of air leakage characteristics of house enclosures," *ASHRAE transactions*, vol. 81, no. 1, pp. 202–208, 1975.
- [35] I. American Society of Heating Refrigerating and Air Conditioning Engineers, "Cooling and heating load calculation manual," HUD- PDR-533, Washington, 1980.
- [36] M. E. H. Attia, A. E. Kabeel, M. Abdelgaied, F. A. Essa, and Z. M. Omara, "Enhancement of hemispherical solar still productivity using iron, zinc and copper trays," *Solar Energy*, vol. 216, pp. 295–302, 2021.
- [37] T. Khatib, "Design of photovoltaic water pumping systems at minimum cost for Palestine: A review," *Journal of Applied Sciences*, vol. 10, no. 22, pp. 2773–2784, 2010.

## GENDER IDENTIFICATION FROM LEFT HAND-WRIST X-RAY IMAGES WITH A HYBRID DEEP LEARNING METHOD

<sup>1,\*</sup> Cüneyt ÖZDEMİR , <sup>2</sup> Mehmet Ali GEDİK , <sup>3</sup> Hüdaverdi KÜÇÜKER , <sup>4</sup> Yılmaz KAYA 

<sup>1</sup> Siirt University, Engineering Faculty, Computer Engineering Department, Siirt, TÜRKİYE

<sup>2,3</sup> Kütahya Health Sciences University, Eoliya Çelebi Training and Research Hospital, Radiology Department, Kütahya, TÜRKİYE

<sup>4</sup> Batman University, Engineering Faculty, Computer Engineering Department, Batman, TÜRKİYE

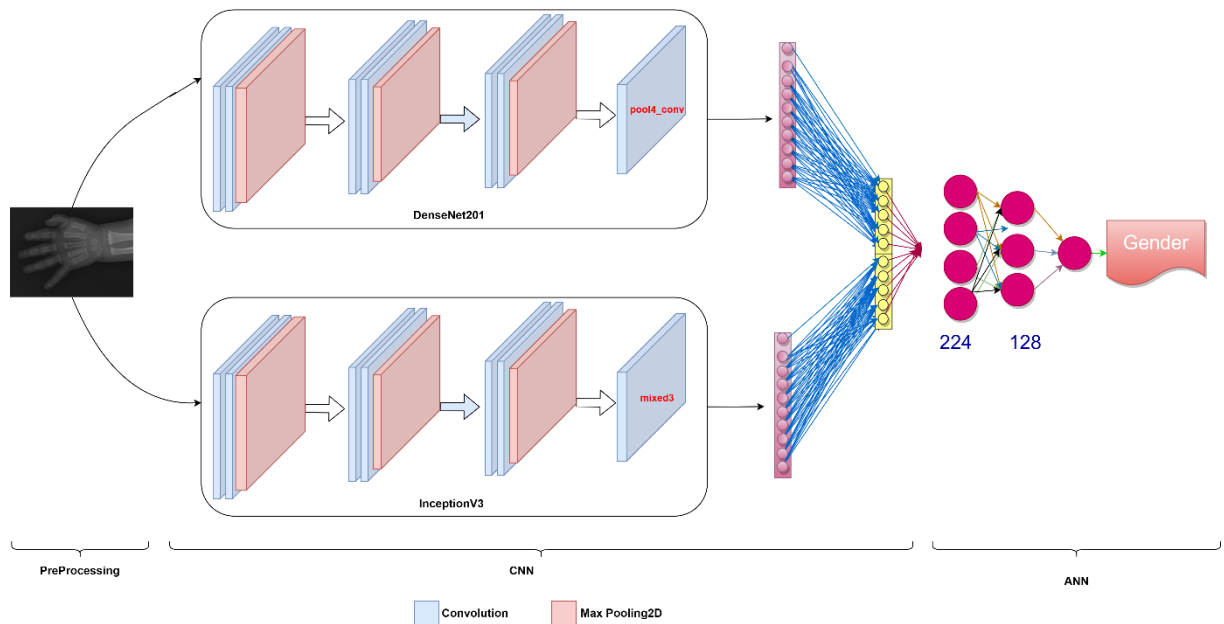
<sup>1</sup>cozdemir@siirt.edu.tr, <sup>2</sup>mehmetaligedik@gmail.com, <sup>3</sup>hudaverdi.kucuker@ksbu.edu.tr,

<sup>4</sup>yilmaz.kaya@batman.edu.tr

### Highlights

- The success of transfer learning models on wrist images was compared.
- A Hybrid model was created from transfer learning models. While designing hybrid models, which layers should be preferred from transfer learning models was determined.
- Model's focus points while making gender discrimination were determined by observing heat maps, regions where gender discrimination is made on the wrist were identified.
- The effects of the model on age groups and the reasons for these effects were investigated.
- A high success rate of 96.3% was observed with proposed method for gender identification.

### Graphical Abstract



Proposed gendering network architecture



## GENDER IDENTIFICATION FROM LEFT HAND-WRIST X-RAY IMAGES WITH A HYBRID DEEP LEARNING METHOD

<sup>1,\*</sup> Cüneyt ÖZDEMİR , <sup>2</sup> Mehmet Ali GEDİK , <sup>3</sup> Hüdaverdi KÜÇÜKER , <sup>4</sup> Yılmaz KAYA

<sup>1</sup> Siirt University, Engineering Faculty, Computer Engineering Department, Siirt, TÜRKİYE

<sup>2,3</sup> Kütahya Health Sciences University, Eoliya Çelebi Training and Research Hospital, Radiology Department, Kütahya, TÜRKİYE

<sup>4</sup> Batman University, Engineering Faculty, Computer Engineering Department, Batman, TÜRKİYE

<sup>1</sup> [cozdemir@siirt.edu.tr](mailto:cozdemir@siirt.edu.tr), <sup>2</sup> [mehmetaligedik@gmail.com](mailto:mehmetaligedik@gmail.com),

<sup>3</sup> [hudaverdi.kucuker@ksbu.edu.tr](mailto:hudaverdi.kucuker@ksbu.edu.tr), <sup>4</sup> [yilmaz.kaya@batman.edu.tr](mailto:yilmaz.kaya@batman.edu.tr)

(Received: 08.05.2023; Accepted in Revised Form: 03.11.2023)

**ABSTRACT:** In forensic investigations, characteristics such as gender, age, ethnic origin, and height are important in determining biological identity. In this study, we developed a deep learning-based decision support system for gender recognition from wrist radiographs using 13,935 images collected from individuals aged between 2 and 79 years. Differences in all regions of the images, such as carpal bones, radius, ulna bones, epiphysis, cortex, and medulla, were utilized. A hybrid model was proposed for gender determination from X-ray images, in which deep metrics were combined in appropriate layers of transfer learning methods. Although gender determination from X-ray images obtained from different countries has been reported in the literature, no such study has been conducted in Turkey. It was found that gender discrimination yielded different results for males and females. Gender identification was found to be more successful in females aged between 10 and 40 years than in males. However, for age ranges of 2-10 and 40-79 years, gender discrimination was found to be more successful in males. Finally, heat maps of the regions focused on by the proposed model were obtained from the images, and it was found that the areas of focus for gender discrimination were different between males and females.

**Keywords:** Hand-Wrist X-ray images, Gender identification, Hybrid model, InceptionV3, DenseNet201

### 1. INTRODUCTION

In legal terms, gender identification is a primary component in forensic medicine practices related to the human body. Although there are bones such as skull bones and pelvis bones that facilitate gender determination, it is a medico-legal need to be able to determine gender from other bones in cases of increasing terror, murders, explosions, fires, and murder-accidental cases where the human body is dismembered and the above-mentioned bones are not found. In addition, gender determination is a necessity in murder-dismemberment and burning incidents against LGBT individuals.

Determining gender can also help us to understand the social and cultural origins of skeletal and human remains at archaeological sites [1].

Gender identification is also important for biological profiling, as is age and height, as well as for the evaluation of biological profile [2]. Human remains discovered in many forensic events may be fragmented or incomplete. In such a case, gender identification is important to obtain maximum information from the existing components of the skeleton [3]. Forensic anthropologist expertise is required when the forensic specialist cannot visually identify an individual's biological characteristics.

Accurate gender identification is often a crucial step in a forensic case as it can potentially narrow down the number of possible victims. However, determining gender can be challenging when dealing with incomplete or fragmentary remains, and morphological methods may not always be effective [4].

Since one of the most important biological markers for human identity in forensic cases is gender identification, researchers have tried to establish various osteometric standards by using different bones of the human skeleton. The skull is considered the most traditional and reliable part of the skeleton for

\*Corresponding Author: Cüneyt ÖZDEMİR, [cozdemir@siirt.edu.tr](mailto:cozdemir@siirt.edu.tr)

gender identification. In cases of skull fragmentation, the evaluation of bones is quite difficult. Therefore, with the increase in the use of long bones for reliable gender identification, there has been a growing need for the use of alternative gender identification methods. It is stated that in forensic cases, the bones in the skeletal structure that are longer tend to be well-maintained and can be measured easily, making them dependable materials for determining an individual's gender. [5-9].

Gender identification is an integral part of constructing the biological profile. The inability to predict gender will further increase the difficulty in establishing estimates of race, weight, height, and age in a forensic setting. Prediction of biological traits is highly dependent on accurate gender determination.

Wrist radiographs are widely used in Turkey for the preparation of age determination reports requested by the courts in forensic cases. The "Sky Atlas", which was adapted from the atlas of Greulich Pyle (G-P), published by Şemsi Gök and his friends in 1969 and published in 1985, is used most frequently in forensic medicine practices in age determination. In addition, Greulich Pyle (G-P) atlas prepared according to the standards of western societies and Tanner Whitehouse (TW) method are also used [10].

There has been no previous study on gender determination from radius and ulna in Turkish society. Many of the studies in the literature have been done with traditional metric methods using ulna and radius images through the developed formulas.

In the literature research, it was observed that many different parts of the human were used for gender determination, but there were very few studies made from wrist radiographs. It has been observed that there are very few studies in which gender determination from wrist radiographs is made with artificial intelligence. For gender determination, the importance and success of wrist radiographs were measured. In this study, a deep learning-based decision support system using wrist bones was developed for gender determination. Deep learning is a branch of machine learning that utilizes artificial neural networks and algorithms modeled after the human brain's functioning to gain knowledge and insights from data. Similar to people's experience, it does a better job with a little tweaking each time to improve the result.

In this study, a decision support system has been developed by using deep learning methods in gender identification to overcome the problems that occur due to manual techniques. With the developed decision support system, it will be easier to get better results in a short time for gender determination, and quantitative and accurate evaluations will be provided. Furthermore, the regions where deep learning models focus on gender discrimination were determined using heat maps. In addition, the success of deep learning models in different age groups according to gender was compared, and the reasons for different success results according to gender were emphasized. In this study, 13935 left hand-wrist images were used to test the proposed hybrid model.

Some of the main contributions of this study are:

- The success of transfer learning models on wrist images was compared.
- A Hybrid model was created from transfer learning models. While designing hybrid models, which layers should be preferred from transfer learning models was determined.
- Model's focus points while making gender discrimination were determined by observing heat maps, regions where gender discrimination is made on the wrist were identified.
- The effects of the model on age groups and the reasons for these effects were investigated.
- A high success rate of 96.3% was observed with proposed method for gender identification.

## 2. LITERATURE STUDIES

There is limited research on gender identification from hand-wrist radiographs in the literature review. It has been observed that there are very few studies in the literature in which gender estimation is made using deep learning method from hand-wrist x-rays. In the literature research, it was observed that many different parts of the human were used for gender identification.

Many researchers have tried to determine gender by using different human body parts. Some of those include fingerprint [11, 13], iris ([14, 16] , palm print [17], chest X-ray [18], face[19, 21], hand

geometry [22], dental [23], skull [24], hair volume, face shape [25], ear [26], speech [27, 28], Coronavirus [48] and walking [29, 30]. These parts have been studied and these studies have obtained competitive results.

It has been observed that the number of studies that make gender identification from hand-wrist radiographs is relatively low. Only the research done by Yune et. al. [31] determines gender from bone, especially with artificial intelligence applications. Yune et al. [31] conducted their research on 10,607 images, 5459 females and 5148 males. They trained to fine-tune the VGG16 model, one of the transfer deep learning models, and then 95.9% accuracy was achieved in the tests performed on 1531 images.

Barnes et al. [32] used carpal bones on hand radiographs to determine gender in forensic cases in Thailand. Fifteen (15) measurements were made on seven carpals from 100 skeletons (50 males, 50 females) who died. As a result, they achieved a success rate of 91.8% in their study with statistical methods.

Studies have been conducted to determine gender using different human body parts. One of them is a study conducted by Vila-Bianco et al. [33], which determines gender from dental panoramic images. According to this research, three fully automated approaches based on deep learning architectures were compared in a database of 3400 dental panoramic images. The results provided 90% to 96% accuracy in patients older than 20 years.

Bewes et al. [34]; developed a deep learning system that makes gender identification from skeletal remains. The model trained with 900 skull images showed an accuracy of 95% with the GoogleNet model in determining gender.

Korot et al.[35] used deep learning models for gender identification from retinal fundus images. A model was trained on 84,743 retinal fundus photographs from the UK Biobank dataset. 86.5% success was reported in their studies.

Gornale et al.[36] stated that gender estimation is a process that helps to increase the security and efficiency of biometric systems, in their study. Gender identification using biometric features is mainly used to reduce search area lists, indexes and generate statistical reports. They achieved 99.9% success in their study with AlexNet, one of the deep learning models, with a dataset containing 15052 images. In addition, more successful results were obtained by modifying the transfer deep learning models.

In this study, the success of wrist X-rays, which is a different part of the body, was measured for gender prediction. It is the first to be conducted using deep learning models of gender identification with wrist x-rays collected on the Turkish population.

The data set KACRD (Kütahya Adult-Child Radiology Dataset) created by us was used to gender identification from hand-wrist X-ray images (approved by Kütahya University of Health Sciences, Ethical Committee Decision No: 221/07 dated 15.04.2021). The images in the data set were obtained from 4 different hospitals, collected from individuals aged 1-85 years. Dataset contains 13935 left hand-wrist x-rays, 7744 images from females, and 6192 images from males. Images were selected from the hospital archive among the left hand-wrist radiographs taken in patients admitted to the emergency department between 2013 and 2021. Images were obtained from different devices such as CR and digital radiography (DR). Due to the shooting in different centers and devices, some of the images' brightness and contrast settings differed from each other. Images are then converted to JPEG format and normalized. These images were excluded from the data set due to the very few images belonging to those younger than 2 years old and older than 79 years old. Studies were carried out on images aged 2-79 years. The distribution of images by gender in the data set is given in Table 1. An example of male and female x-ray images in the dataset is given in Figure 1.

**Table 1.** Distribution of datasets by gender

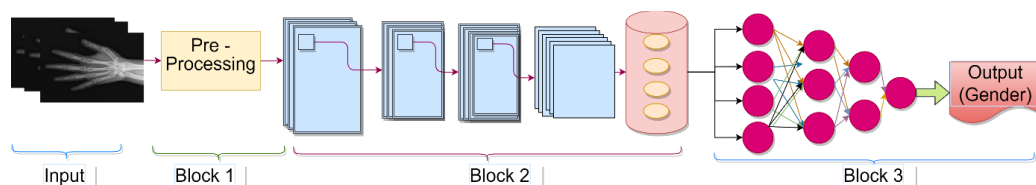
Gender	#images
Male	6191 (44.43%)
Female	7744 (55.57%)
<b>Total Image</b>	13935

**Figure 1.** sample images from KACRD dataset

## 4. Method

### 4.1. Gender Detection Block Diagram

The deep learning architecture for determining gender from hand-wrist radiographs is outlined in this section. The approach proposed involves using 4 blocks, as depicted in Figure 2. The actions performed within each block are summarized.

**Figure 2.** The general architecture of proposed deep learning method for gender identification

**Block 1:** It is the preprocessing stage. Necessary preprocesses are applied to all images in the dataset to remove brightness and contrast differences. Since the images were taken in different hospitals and from different angles, it was determined that many images' brightness and contrast settings were different from each other. The contrast limited adaptive histogram equalization method is used to solve this problem. After adjusting the contrast and brightness of the images in the preprocessing stage, the scaling process was performed. Deep learning methods involve complex mathematical operations, and reducing the size of the images can improve the speed of these operations [37]. The images were resized according to the target width and height, keeping the image aspect ratio the same without breaking them.

**Block 2:** After the preprocessing stage, the images are passed through the CNN block where various types of information and characteristics are extracted. At this block, InceptionV3 and DenseNet20 transfer deep learning methods were used.

**Block 3:** At this stage, classification is performed using the features from the previous block. A cause-effect relationship is determined between the features coming from the CNN block and the gender of the person.

## 4.2. Convolutional neural networks

In classical machine learning approaches, the extracted features were given to the classification algorithms after the features were extracted from the images with specific techniques. CNN is an artificial neural network that automates the feature extraction process. CNNs work with raw images as input, which are then processed through a multi-layer feedforward neural network composed of various types of layers such as convolution, activation, pooling, feature extraction with batch normalization, and a fully connected output layer. CNNs are designed to detect all types of information and features in images.

A key feature of deep learning is that overfitting can occur during training if the dataset is limited. Transfer learning methods are used to overcome this problem.

## 4.3. Transfer learning

CNN is better trained with large data sets. In certain fields, there may be a lack of data to train neural networks, leading to unsuccessful training and inadequate classification results. In such cases, using the transfer learning approach can be beneficial [38]. The performance of the neural network is affected by the success of the model and the number of operations in the network model. Therefore, using previously trained models and weights can improve the performance of the neural network, making the training process faster and more accurate. There are various transfer learning models available that can be used for different image classification or regression tasks. Transfer learning models are pre-trained models that can be used for different image classification or regression problems.

Morid et al.[39] conducted a large-scale study of medical images. A large-scale review of transfer learning in medical image analysis was conducted on 102 studies. According to this article, the most successful popular transfer learning models used for various anatomical regions are shown in Table 2.

**Table 2.** Popular transfer learning models used for different anatomical regions [39]

Anatomical Region	Model
Ultrasound, endoscopy, and skeletal system	Inception
For eye, skin, dental X-rays	VGGNet
For brain MRIs and breast X-rays	AlexNet
For chest X-rays	DenseNet

As can be seen from Table 2, Inception is shown as the successful transfer learning model on super skeletal systems. In this study, InceptionV3 and DenseNet20 models, which were frequently used in studies on medical problems, were used.

### 4.3.1. InceptionV3

The InceptionV3 consists of 42 layers. The main idea of the model is to learn multi-scale representations and replace small kernels with large kernels to reduce computational complexity and the total number of parameters [40]. This model was built using the GoogLeNet network architecture. The layout of the InceptionV3 network is illustrated in Figure 3.

The numbers "x3, x4, x2" in Figure 3 represent the number of times the process is repeated.

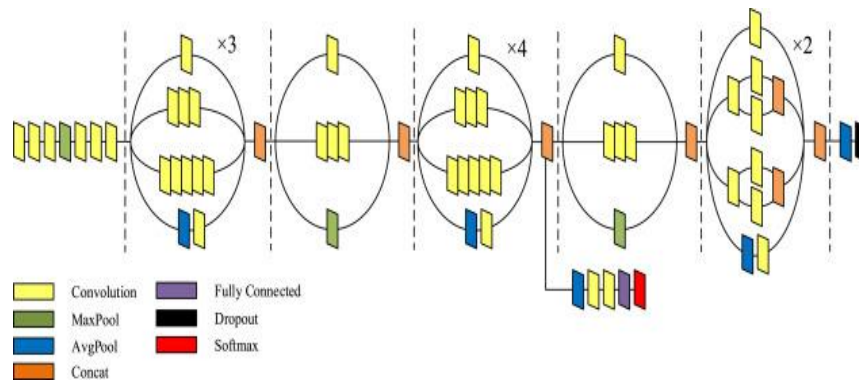


Figure 3. InceptionV3 network architecture [38]

### 4.3.2. DenseNet

DenseNet feed-forward connects each layer to every other layer, giving the properties of all previous layers as input to each layer. With this property, DenseNet enables the reuse of image features. The DenseNet network architecture is shown in Figure 4 [41]. It consists of 305 layers and 4 dense blocks. Each block has 128 and 32 convolutional blocks from 1x1 and 3x3 filters. Transition layers between two adjacent blocks with convolution and Max pooling (1 × 1 Convolution, 2 × 2 Max pooling) reduce the size of the feature maps. This is done to reduce bottleneck input feature maps and make convolution process more efficient.

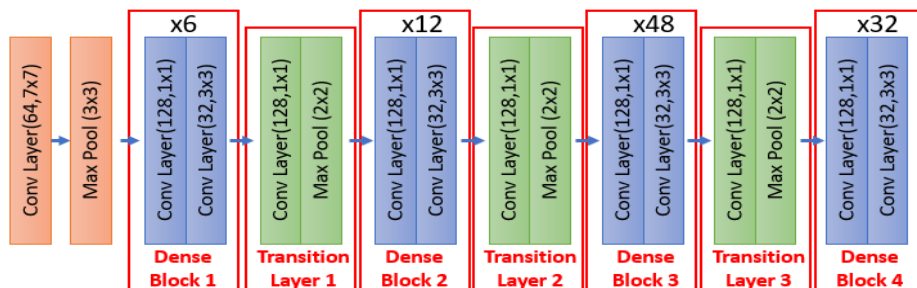


Figure 4. DenseNet201 layer architecture [41]

### 4.4. Proposed network architecture for gender identification

Table 4 shows the most successful results were obtained with the InceptionV3 and DenseNet201 models as a result of the experimental studies. For this reason, the layers that produce the best features in these 2 models were determined and a hybrid model consisting of these layers was designed. The designed hybrid model is shown in Figure 5. By looking at the activations in each layer of the InceptionV3 and DenseNet201 deep transfer models, the activations in the layers are visualized. These operations were performed for all layers. The visualized activations in each layer were then visually examined, and deep metrics were taken from the layer before the layer where the images started to deteriorate. Gender recognition was performed by combining deep metrics from InceptionV3 and DenseNet201 and giving them to the Fully Connected layer.

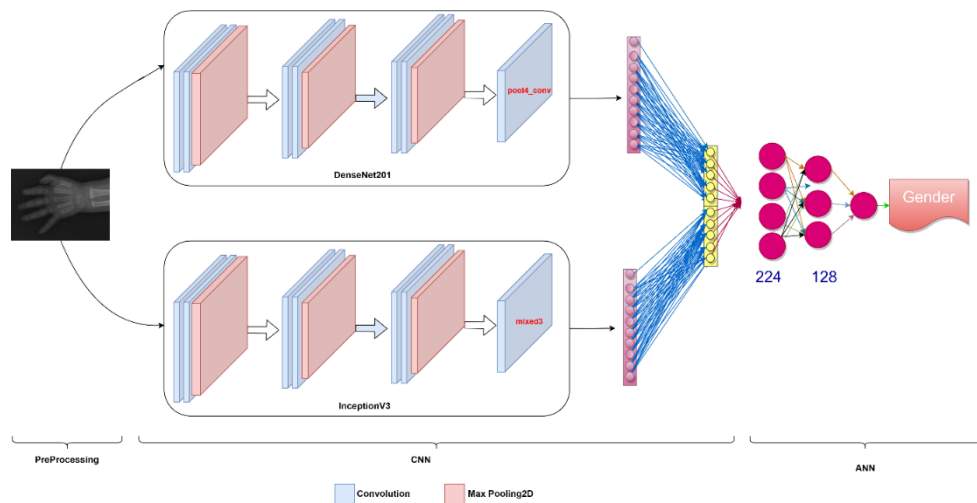


Figure 5. Proposed gendering network architecture

#### 4.4. Performance Metrics

The proposed approach is evaluated using criteria such as accuracy, precision, sensitivity, and F-measure. The Recall value is the general name given to the metric value that shows how many of the transactions we need to predict positively. The accuracy is calculated by the ratio of the correctly predicted gender to the total data set. Precision is the general name of the metric value that allows us to test how many of the values we predicted as positive are positive. The F-measure is the harmonic mean of recall and precision. F-measures reveal realistic results that include all error costs in unevenly distributed datasets or datasets with unknown distribution. Equations of metrics are given in Table 3.

Table 3. Mathematical formulas of the performance parameters.

Parameter	Formula
Accuracy	$(TP + TN)/(TP + TN + FP + FN)*100$
Recall	$TP/(TP + FN)$
Precision	$TP/(TP + FP)$
F-Measure	$\{2 \times (Recall \times Precision)\}/(Recall + Precision)$

In these equations, T, F, P, and N stand for True, False, Positive, and Negative, respectively. For instance, TP represents the number of correctly classified positive samples, and FN represents the number of incorrectly classified negative samples.

## 5. EXPERIMENTAL RESULTS

It has been determined that the sizes of the images obtained for this study are different. Inspired by the previous work of Ozdemir et al. [10], the image dimensions were set to 500\*500 to prevent the loss of valuable information in the image. A special data generator method (imagedatagenerator) has been applied to keep and process images at this scale in RAM without any problems. In this method, 16 images with 500\*500 dimensions were taken and processed in each step. Since ram error is received when more images are taken, all models are also taken as batch\_size 16. Using this unique data generator method, the number of images up to batch size is given to the system in each epoch instead of all images. Thus, the encountered RAM problem has been eliminated.

To increase the models' performance, an automatic cropping process has been applied to the images. The state of an image after resizes and crop operation is given in figure 6.

Data augmentation was applied to the images as they were taken from various angles. The

normalization method of the transfer learning model used, rotation between -15 and +15, and 5% horizontal and vertical shift operations were applied to the training dataset during data augmentation. Only normalization method was applied to the images kept for validation and testing datasets. Learning rate 0.0001 epoch 100, batch size 12 and softmax as activation function were used.

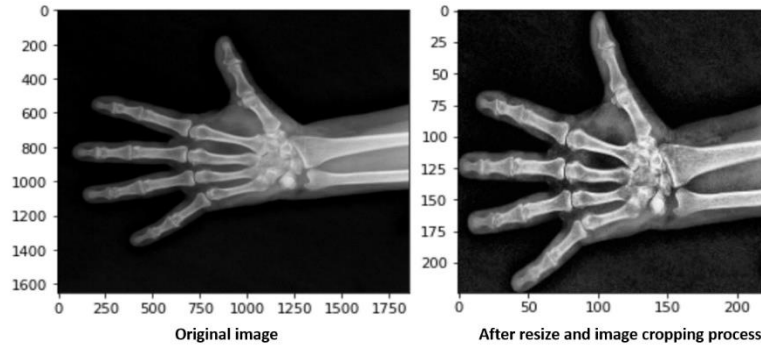


Figure 6. Resize and cropping of image

Different metrics were used to evaluate the performance of the models. Of the total 13935 images in the dataset, 10069 (70%) were used for training, 1776 (15%) for validation and 2090 (15%) for testing. The performance values obtained for the test dataset of the 4 models are presented in Table 4.

Table 4. Results according to transfer learning models

Method	Accuracy	Recall	Precision	F1-Measure
InceptionV3	94.71%	94.71%	94.72%	94.71%
ResNet152	92.93%	92.92%	92.93%	94.91%
DenseNet201	94.23%	94.23%	94.35%	94.24%

Table 4 shows successful results were obtained with DenseNet201 and InceptionV3 models. Hence, to improve the model success, a hybrid model consisting of these two models was created. For this purpose, 2 ways are preferred. First, experimental studies were carried out by taking the layers of the models by trial and error. One of these experimental studies; A new hybrid model was created by taking the “mixed1” layer from the InceptionV3 model and the “Pool2\_pool” layer from the DenseNet201 model. This model is called “Mixed1Pool2” model. As a result of this and similar experimental studies, it has been determined that this method gives good results, as seen in Table 5. As an alternative, a method that decides by looking at the effect of the layers of the trained model on the images was used and named as cross-layer display method. In this method, the layers were decided by applying the interlayer imaging method on both models and a new hybrid model was created. In the cross-layer display method; It was decided to select the layers by visualizing which features were learned by each layer in which the model processed the input image and which features passed to the deeper layers. Cross-layer display method shows which layer of the models learning took place and from which layer learning did not occur. Figure 7 shows visualized effects of InceptionV3 model layers on an image a with this method.

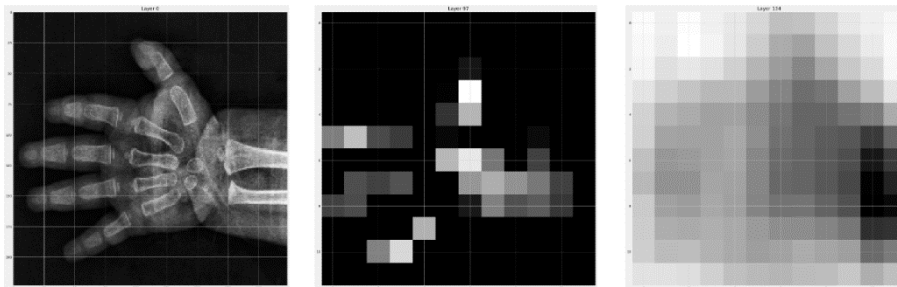


Figure 7. The effect of layers on the image

The InceptionV3 model consists of 317 layers. In Figure 7, a normal image is given on the left. The second image shows the original image at Layer 97 of the InceptionV3 model. The last image shows the image in Layer 134 of the InceptionV3 model. As can be seen in Figure 7, in a model consisting of 317 layers, visuals can be understood up to the 97th layer. Therefore, the effect of the layers after this point on the model performance is very limited. The model learning takes place up to the “Mixed3” layer in the InceptionV3 model, and learning takes place up to the “pool4\_conv” layer in the DenseNet201 model. Therefore, a new hybrid model named “Mixed3Pool4” was created by taking the relevant layers from each models. Table 5 shows the performance of hybrid model.

**Table 5.** Results according to transfer learning models

Method	Accuracy	Recall	Precision	F1-Measure
Mixed1Pool2	95.19%	95.19%	95.26%	95.2%
Mixed3Pool4	<b>96.29%</b>	<b>96.29%</b>	<b>96.29%</b>	<b>96.28%</b>

The hybrid models give more successful results than traditional transfer learning models which is shown in Table 5. Among all the experimental studies, the highest scoring classification results were obtained with the Mixed3Pool4 model with an accuracy rate of 96.29%. Figure 8 shows the accuracy and error values of the Mixed3Pool4 model during training.

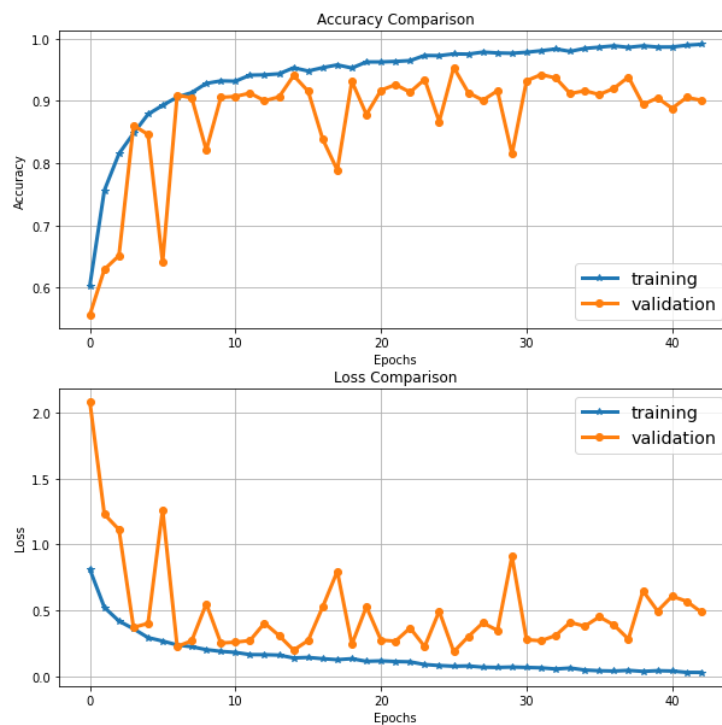


**Figure 8.** Training-validation accuracy and loss of Mixed3Pool4

For the Mixed3Pool4 model, the actual gender and predicted gender information of the images of a few randomly selected samples are given in Figure 9.

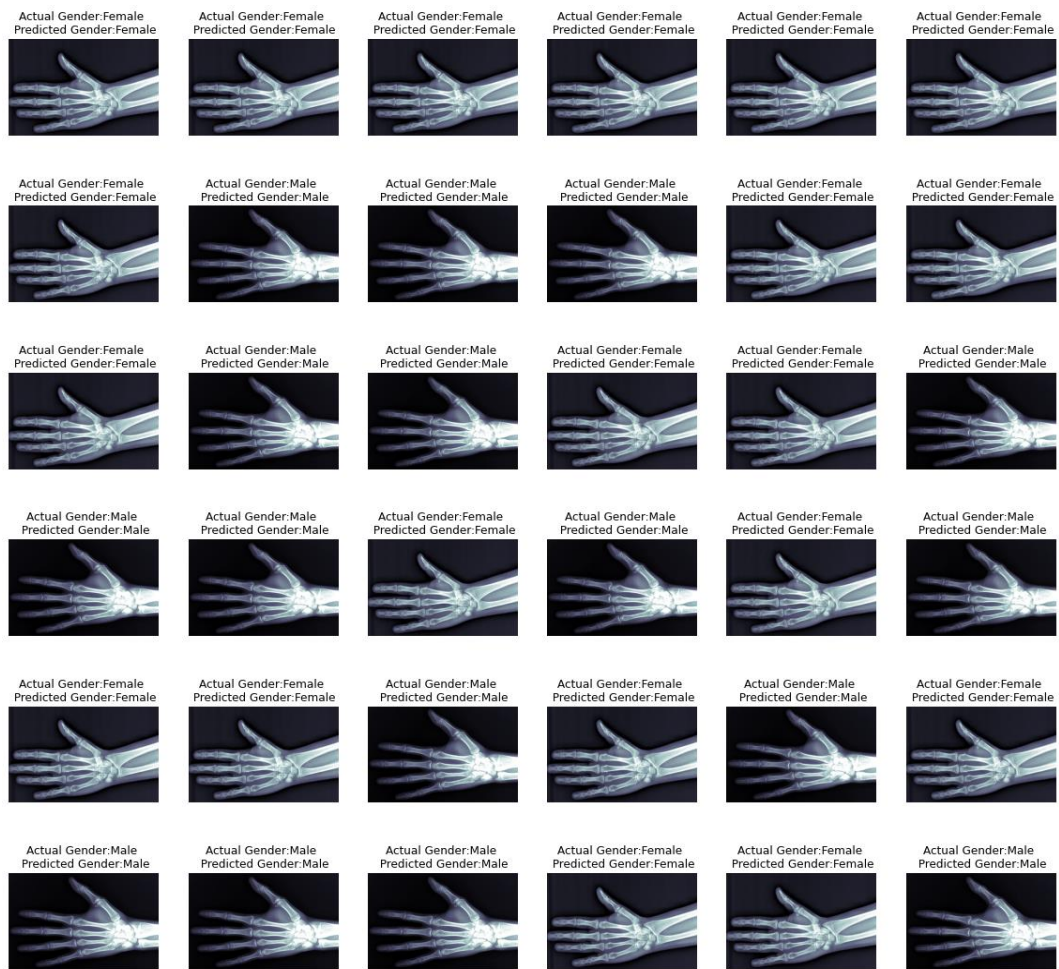


**Figure 9.** A sample of actual and predicted gender results obtained with the Mixed3Pool4 method

The Grad-CAM (Gradient weighted Class Activation Mapping) method is used to show the critical regions that the model focuses on while estimating the image of the trained model. Figure 10 shows the heat map of the regions where the trained Mixed3Pool4 model focuses on images of males, Figure 11 on females.

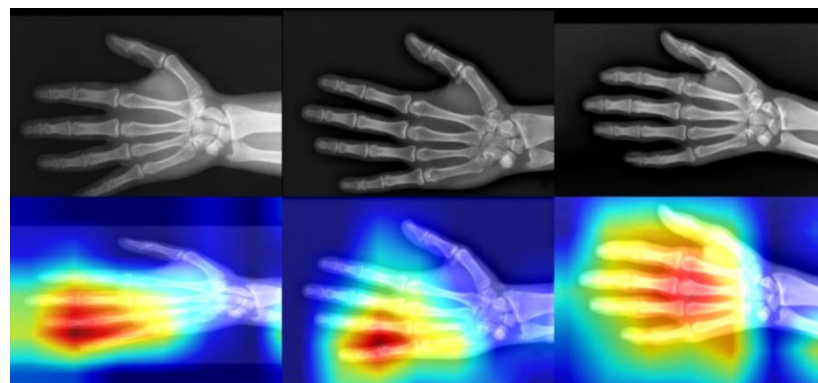


**Figure 10.** Heatmap (GradCam) on Male images of the trained Mixed3Pool4 model

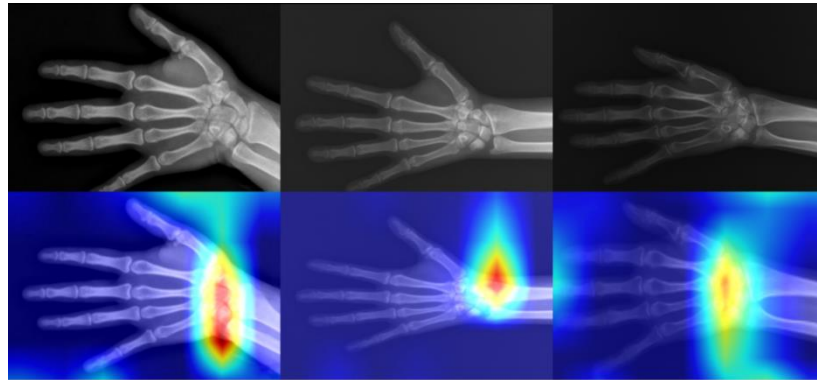


**Figure 11.** Heatmap (GradCam) of the trained Mixed3Pool4 model on the Female images

When we look at the heat maps, the Mixed3Pool4 model, in which we obtained the best results, focused mainly on the phalanx, carpal, and metacarpal bones in male and mainly on the distal radius and ulna in female. However, our model did not focus on the same points by gender in all images. Sometimes it focused on the carpal area for male, sometimes on the points between the fingers for female.

Images were divided into genders and decades of 10 to measure the success of the Mixed3Pool4 model. Then, with the Mixed3Pool4 model, the prediction success of the model was measured on the images divided into age groups according to gender. The success of the Mixed3Pool4 model on age groups according to gender in all images is shown in Table 6.

**Table 6.** Accuracies of the Mixed3Pool4 model by age groups and gender

Age Ranges	Male Success Rate	Female Success Rate	#Tested Image
	(#Images)	(#Images)	
2-10	0,978 (851)	0,969 (866)	1717
11-20	0,982 (1657)	0,990 (2512)	4169
21-30	0,986 (639)	0,990 (1372)	2011
31-40	0,992 (1196)	0,994 (802)	1998
41-50	0,996 (757)	0,988(755)	1512
51-60	0,988 (761)	0,977 (564)	1325
61-70	%100 (450)	0,975 (325)	775
71-79	0,996 (274)	0,910 (154)	428

As shown in Table 6, the images are concentrated in the 10-30 age range. The images in other age groups are close to each other in terms of gender. Mixed3Pool4 model was more successful for male in the 2-10 age range. It has been determined that the model is more successful for females in the 10-40 age range and for male over 40 years.

In the literature, many studies have been carried out for gender estimation. In the studies, the success of the models was generally evaluated based on accuracy. Some of the studies carried out are given in Table 6. When the results of the proposed approach of this study and the studies in Table 6 are compared, it is seen that successful results are obtained with the proposed approach.

**Table 7.** Studies in the literature in which gender identification was made from hand-wrist images

Authors	Method	DataSet	Accuracy (%)
Karadayi et. al. [42]	Manuel	255 males and 155 females.	86.6%
Jee et. al. [43]	t-test Discriminant analysis	+ 167 Male ve 154 Female	Male=88.6% Female= 89.6%
Prabhat et. al. [44]	t-test Discriminant analysis	+ 15 males and 15 females	Male 80.0 % Female 86.7%
Yune et. al. [31]	CNN	5459 Female and 5148 Male	95.9%
DeSilva et. al. [45]	Manuel	150 adult males and 150 adult females	85.3%
Barnes et. al. [32]	Statistical	50 Male, 50 Female	91.8%
<b>Proposed Method</b>	<b>CNN</b>	<b>Male 6191, Female 7744</b>	<b>96.3%</b>

Many different methods were used for gender estimation using wrist length, and there were very few studies on gender estimation from wrist radiographs. As can be seen from Table 7, our study is the research with the highest number of images and achieved the highest success when looking at the studies in the literature.

## 6. CONCLUSION

The intrinsic diversity in hand-wrist morphologies among individuals, stemming from the multifaceted influence of environmental factors on human development, is an established phenomenon. Through the lens of this investigation, a pioneering decision support system has been meticulously devised to proffer rapid gender delineation, lending its potential to both legal contexts and the augmentation of model expert analyses. Gender identification, bearing substantial pertinence within the domain of forensic sciences, has garnered extensive attention through diverse scholarly inquiries endeavoring to discern gender via anatomical measurements.

This study, distinguished by its novel approach, embarks upon the avenue of gender estimation hinged on X-ray depictions of hand-wrist bone structures. Drawing from an expansive dataset culled from four distinct medical institutions, encompassing a demographic spanning ages 1 to 85 years, the repository amalgamates a total of 13,935 X-ray images. Ingeniously employing deep learning models, the exploratory phase unfolded through experimental forays into the potent DenseNet201 and InceptionV3 models. The culmination of this endeavor surfaced in the formulation of a pioneering hybrid model, a harmonious amalgamation of these aforementioned architectures.

Central to the model's design was the methodical determination of layers through visualization of transfer learning algorithmic strata. Employing this strategy, layers extending up to the threshold of learning saturation were strategically embraced. The culmination of these efforts yielded a compelling success rate of 96.3% for the proposed hybrid model. This pivotal study stands as the inaugural investigation within our nation's confines, engendering gender estimation through deep learning constructs, predicated upon an exclusive repository of hand-wrist radiographs.

Additionally, this study ventures into the intriguing landscape of age-dependent gender distinctions, ascertaining nuanced variances within different age cohorts. The findings underscore the superiority of gender identification accuracy for boys within the 2-10 age bracket, with a converse trend in the 10-40 range, favoring females. Remarkably, this pattern inverts once more within the 40-79 age range, favoring males. The discernment that females manifest heightened accuracy prior to the age of 40, contrasted by males emerging triumphant after 40, conceivably aligns with the specter of osteoporosis. As a prevalent ailment, osteoporosis [46] marks a poignant disparity in bone density and microarchitecture, thus presenting significant public health challenges. Delving further, the differential

impact of osteoporosis on genders emerges, wherein the protective role of premenopausal estrogen grants females comparative resilience, in contrast to the heightened susceptibility post-menopause [47].

this inquiry yields a resounding success in gender identification through X-ray imagery, underpinned by the innovative hybrid fusion of DenseNet and InceptionV3 deep learning paradigms. The emergent ramifications of this study crystallize in a cascade of opportunities for future exploration. The rich tapestry of insights unveiled within these findings augurs the cultivation of novel paradigms in forensic gender identification, potentially fostering interdisciplinary collaborations and spurring innovation within medical imaging and artificial intelligence realms alike.

### Declaration of Competing Interest

The authors declare no conflict of interest

### Funding

The author(s) received no financial support for this article's research, authorship, and/or publication.

### Declaration of Ethical Standards

All procedures performed in studies involving human participants were in accordance with the ethical standards of the institutional and/or national research committee and with the 1964 Helsinki declaration and its later amendments or comparable ethical standards.

### REFERENCES

- [1] M. Y. İşcan ve M. Steyn, "The Human Skeleton in Forensic Medicine," 3rd ed.
- [2] A. P. Agelarakis, "Studies in Crime: An Introduction to Forensic Archaeology. By John R. Hunter, Charlotte A. Roberts, and Anthony L. Martin. Making Faces: Using Forensic and Archaeological Evidence. By John Prag and Richard Neave," *Am J Archaeol*, vol. 102, 1998. [Online]. Available: <https://doi.org/10.2307/506107>
- [3] M. Didi AL, R. R. Azman, ve M. Nazri, "Sex determination from carpal bone volumes: A Multi Detector Computed Tomography (MDCT) study in a Malaysian population," *Leg Med*, vol. 20, 2016. [Online]. Available: <https://doi.org/10.1016/j.legalmed.2016.04.002>
- [4] ILO Barrier ve EN L'Abbé, "Sex determination from the radius and ulna in a modern South African sample," *Forensic Sci Int*, vol. 179, 2008. [Online]. Available: <https://doi.org/10.1016/j.forsciint.2008.04.012>
- [5] T. K. Black, "A new method for assessing the sex of fragmentary skeletal remains: Femoral shaft circumference," *Am J Phys Anthropol*, vol. 48, 1978. [Online]. Available: <https://doi.org/10.1002/ajpa.1330480217>
- [6] L. R. Frutos, "Metric determination of sex from the humerus in a Guatemalan forensic sample," *Forensic Sci Int*, vol. 147, 2005. [Online]. Available: <https://doi.org/10.1016/j.forsciint.2004.09.077>
- [7] M. Y. İşcan, "Forensic anthropology of sex and body size," *Forensic Sci Int*, vol. 147, 2005. [Online]. Available: <https://doi.org/10.1016/j.forsciint.2004.09.069>
- [8] K. Sakaue, "Sexual determination of long bones in recent Japanese," *Anthropol Sci*, vol. 112, 2004. [Online]. Available: <https://doi.org/10.1537/ase.00067>
- [9] M. Šlaus, Ž. Bedić, D. Strinović, ve V. Petrovečki, "Sex determination by discriminant function analysis of the tibia for contemporary Croats," *Forensic Sci Int*, vol. 226, 2013. [Online]. Available: <https://doi.org/10.1016/j.forsciint.2013.01.025>
- [10] C. Ozdemir, M. A. Gedik, ve Y. Kaya, "Age Estimation from Left-Hand Radiographs with Deep Learning Methods," *Trait du Signal*, vol. 38, 2021. [Online]. Available: <https://doi.org/10.18280/ts.380601>

- [11] S. Gornale, A. Patil, ve C. V, "Fingerprint based Gender Identification using Discrete Wavelet Transform and Gabor Filters," *Int J Comput Appl*, vol. 152, 2016. [Online]. Available: <https://doi.org/10.5120/ijca2016911794>
- [12] X. Li, X. Zhao, Y. Fu, ve Y. Liu, "Bimodal gender recognition from face and fingerprint," in: *Proceedings of the IEEE Computer Society Conference on Computer Vision and Pattern Recognition*
- [13] R. K, A. Patil, ve S. Gornale, "Fusion of Features and Synthesis Classifiers for Gender Classification using Fingerprints," *Int J Comput Sci Eng*, vol. 7, 2019. [Online]. Available: <https://doi.org/10.26438/ijcse/v7i5.526533>
- [14] S. Aryanmehr, M. Karimi, ve F. Z. Boroujeni, "CVBL IRIS Gender Classification Database Image Processing and Biometric Research, Computer Vision and Biometric Laboratory (CVBL)," In: *2018 3rd IEEE International Conference on Image, Vision and Computing, ICIVC 2018*.
- [15] M. Singh, S. Nagpal, M. Vatsa, ve diğerleri, "Gender and ethnicity classification of Iris images using deep class-encoder," In: *IEEE International Joint Conference on Biometrics, IJCB 2017, 2018*.
- [16] V. Thomas, N. V. Chawla, K. W. Bowyer, ve P. J. Flynn, "Learning to predict gender from iris images," In: *IEEE Conference on Biometrics: Theory, Applications and Systems, BTAS'07, 2007*.
- [17] S. S. Gornale, A. Patil, M. Hangarge, ve R. Pardesi, "Automatic human gender identification using palmprint," In: *Smart Computational Strategies: Theoretical and Practical Aspects, 2019*.
- [18] E. Tartaglione, C. A. Barbano, C. Berzovini, ve diğerleri, "Unveiling COVID-19 from chest x-ray with deep learning: A hurdles race with small data," *Int J Environ Res Public Health*, vol. 17, 2020. [Online]. Available: <https://doi.org/10.3390/ijerph17186933>
- [19] Y. Kaya ve Ö. F. Ertuğrul, "Gender classification from facial images using gray relational analysis with novel local binary pattern descriptors," *Signal, Image Video Process*, vol. 11, 2017. [Online]. Available: <https://doi.org/10.1007/s11760-016-1021-3>
- [20] L. Bui, D. Tran, X. Huang, ve G. Chetty, "Classification of gender and face based on gradient faces," In: *3rd European Workshop on Visual Information Processing, EUVIP 2011 - Final Program, 2011*.
- [21] A. Hasnat, S. Halder, D. Bhattacharjee, ve M. Nasipuri, "A proposed system for gender classification using the lower part of the face image," In: *Proceedings - IEEE International Conference on Information Processing, ICIP 2015, 2016*.
- [22] M. Wu ve Y. Yuan, "Gender classification based on geometry features of palm image," *Sci World J*, vol. 2014. [Online]. Available: <https://doi.org/10.1155/2014/734564>
- [23] M. V. Rajee ve C. Mythili, "Gender classification on digital dental x-ray images using deep convolutional neural network," *Biomed Signal Process Control*, vol. 69, 2021. [Online]. Available: <https://doi.org/10.1016/j.bspc.2021.102939>
- [24] S. Babacan, S. Isiklar, I. M. Kafa, ve G. Gokalp, "Redesign of missing mandible by determining age group and gender from morphometric features of the skull for facial reconstruction (approximation)," *Archaeol Anthropol Sci*, vol. 13, 2021. [Online]. Available: <https://doi.org/10.1007/s12520-021-01315-2>
- [25] T. Danisman, I. M. Bilasco, ve J. Martinet, "Boosting gender recognition performance with a fuzzy inference system," *Expert Syst Appl*, vol. 42, 2015. [Online]. Available: <https://doi.org/10.1016/j.eswa.2014.11.023>
- [26] P. Gnanasivam ve S. Muttan, "Gender classification using ear biometrics," In: *Lecture Notes in Electrical Engineering, 2013*.
- [27] R. Djemili, H. Bourouba, ve M. C. A. Korba, "A speech signal-based gender identification system using four classifiers," In: *Proceedings of 2012 International Conference on Multimedia Computing and Systems, ICMCS 2012, 2012*.
- [28] L. Zimman, "Transgender voices: Insights on identity, embodiment, and the gender of the voice," *Lang Linguist Compass*, vol. 12, 2018. [Online]. Available:

- <https://doi.org/10.1111/lnc3.12284>
- [29] A. B. A. Graf ve F. A. Wichmann, "Gender classification of human faces," In: *Lecture Notes in Computer Science (including subseries Lecture Notes in Artificial Intelligence and Lecture Notes in Bioinformatics)*, 2002.
- [30] X. Li, S. J. Maybank, S. Yan, ve diğerleri, "Gait components and their application to gender recognition," *IEEE Trans. Syst. Man Cybern. Part C Appl. Rev.*, vol. 38, 2008.
- [31] S. Yune, H. Lee, M. Kim, ve diğerleri, "Beyond Human Perception: Sexual Dimorphism in Hand and Wrist Radiographs Is Discernible by a Deep Learning Model," *J Digit Imaging*, vol. 32, 2019. [Online]. Available: <https://doi.org/10.1007/s10278-018-0148-x>
- [32] A. E. Barnes, D. T. Case, S. E. Burnett, ve P. Mahakkanukrauh, "Sex estimation from the carpal bones in a Thai population," *Aust J Forensic Sci*, vol. 52, 2020. [Online]. Available: <https://doi.org/10.1080/00450618.2019.1620856>
- [33] N. Vila-Bianco, R. R. Vilas, M. J. Carreira, ve I. Tomás, "Towards deep learning reliable gender estimation from dental panoramic radiographs," In: *CEUR Workshop Proceedings*, 2020.
- [34] J. Bewes, A. Low, A. Morphet, ve diğerleri, "Artificial intelligence for sex determination of skeletal remains: Application of a deep learning artificial neural network to human skulls," *J Forensic Leg Med*, vol. 62, 2019. [Online]. Available: <https://doi.org/10.1016/j.jflm.2019.01.004>
- [35] E. Korot, N. Pontikos, X. Liu, ve diğerleri, "Predicting sex from retinal fundus photographs using automated deep learning," *Sci Rep*, vol. 11, 2021. [Online]. Available: <https://doi.org/10.1038/s41598-021-89743-x>
- [36] S. Gornale S, A. Patil, ve R. K, "Multimodal Biometrics Data Analysis for Gender Estimation Using Deep Learning," *Int J Data Sci Anal*, vol. 6, 2020. [Online]. Available: <https://doi.org/10.11648/j.ijdsa.20200602.11>
- [37] Ş. Kılıç ve Y. Doğan, "Deep learning-based gender identification using ear images," *Traitement du Signal*, vol. 40, 2023. [Online]. Available: <https://doi.org/10.18280/ts.400431>
- [38] Y. Doğan, "Derin Öğrenme Yöntemleriyle Çapraz Veri Seti Değerlendirmesi Altında COVID-19 Tespiti," *Gazi University Journal of Science Part C: Design and Technology*, vol. 11, no. 3, 2023.
- [39] M. A. Morid, A. Borjali, ve G. Del Fiol, "A scoping review of transfer learning research on medical image analysis using ImageNet," *Comput. Biol. Med.*, vol. 128, 2021.
- [40] C. Szegedy, W. Liu, Y. Jia, ve diğerleri, "Going deeper with convolutions," In: *2015 IEEE Conference on Computer Vision and Pattern Recognition (CVPR)*, 2015.
- [41] G. Huang, Z. Liu, L. Van Der Maaten, ve K. Q. Weinberger, "Densely connected convolutional networks," In: *Proceedings - 30th IEEE Conference on Computer Vision and Pattern Recognition, CVPR 2017*, 2017.
- [42] B. Karadayi, A. Kaya, H. Koc, ve diğerleri, "Sex determination for using hand and wrist measurements in the Turkish population," *Turkish J Forensic Med*, vol. 28, 2014. [Online]. Available: <https://doi.org/10.5505/adlitip.2014.98700>
- [43] S. C. Jee, S. Bahn, ve M. H. Yun, "Determination of sex from various hand dimensions of Koreans," *Forensic Sci Int*, vol. 257, 2015. [Online]. Available: <https://doi.org/10.1016/j.forsciint.2015.10.014>
- [44] M. Prabhat, S. Rai, M. Kaur, ve diğerleri, "Computed tomography-based forensic gender determination by measuring the size and volume of the maxillary sinuses," *J Forensic Dent Sci*, vol. 8, 2016. [Online]. Available: <https://doi.org/10.4103/0975-1475.176950>
- [45] R. DeSilva, A. Flavel, ve D. Franklin, "Estimation of sex from the metric assessment of digital hand radiographs in a Western Australian population," *Forensic Sci Int*, vol. 244, 2014. [Online]. Available: <https://doi.org/10.1016/j.forsciint.2014.08.019>
- [46] T. Sozen, L. Ozisik, ve N. Calik Basaran, "An overview and management of osteoporosis," *Eur J Rheumatol*, vol. 4, 2017. [Online]. Available: <https://doi.org/10.5152/eurjrheum.2016.048>
- [47] F. Cosman, S. J. de Beur, M. S. LeBoff, ve diğerleri, "Clinician's Guide to Prevention and Treatment of Osteoporosis," *Osteoporos Int*, vol. 25, 2014. [Online]. Available:

- <https://doi.org/10.1007/s00198-014-2794-2>
- [48] Ş. Öztürk, U. Özkaya, ve M. Barstuğan, "Classification of Coronavirus (COVID-19) from X-ray and CT images using shrunken features," *Int J Imaging Syst Technol*, vol. 31, no. 1, 2021. [Online]. Available: <https://doi.org/10.1002/ima.22432>



## THEORETICAL ANALYSIS OF SOLAR THERMOELECTRIC GENERATORS INTEGRATED WITH RADIATIVE COOLER

\*Aminu YUSUF 

*Istanbul University-Cerrahpaşa, Engineering Sciences Department, Istanbul, TÜRKİYE*  
[aminu.yusuf@iuc.edu.tr](mailto:aminu.yusuf@iuc.edu.tr)

### *Highlights*

- Solar thermoelectric generator is passively cooled by a radiative cooler.
- Ambient temperature has a positive influence on the cooling power.
- Wind speed has a negative influence on the cooling power.
- An increase in the relative humidity reduces the generator's output power.



## THEORETICAL ANALYSIS OF SOLAR THERMOELECTRIC GENERATORS INTEGRATED WITH RADIATIVE COOLER

\*Aminu YUSUF 

*Istanbul University-Cerrahpaşa, Engineering Sciences Department, Istanbul, TÜRKİYE*  
[aminu.yusuf@iuc.edu.tr](mailto:aminu.yusuf@iuc.edu.tr)

(Received: 07.08.2023; Accepted in Revised Form: 21.11.2023)

**ABSTRACT:** A comprehensive analysis of solar thermoelectric generators integrated with radiative cooling technology (STEG-RC) is presented in this study. Basically, the STEG-RC operates outdoors; therefore, the effects of various weather parameters on the output performance of the STEG-RC are determined. The results reveal that the most efficient way of enhancing the output performance of the STEG-RC is by concentrating solar energy. The radiative cooling power increases linearly with the ambient temperature achieving the maximum cooling power of 135 W/m<sup>2</sup> and 232 W/m<sup>2</sup> at solar concentration ratios of  $C = 1$  and  $C = 5$ , respectively. The maximum output power of 1.5 mW and 459.6 mW at the optimum wind speeds of 3 m/s and 2 m/s are obtained for  $C = 1$  and  $C = 5$ , respectively. There were no significant changes in the power output and radiative cooling power when relative humidity was varied. The cooling power is linearly proportional to solar irradiance for both concentrated and unconcentrated cases.

**Keywords:** *Cooling power, Passive cooling, Radiative cooling, Renewable energy, Thermoelectric generator*

### 1. INTRODUCTION

The high cost of fossil fuels and the increase in the greenhouse effect are some of the reasons that necessitate the search for other alternative energy sources [1]. Solar energy is the most abundant free energy on earth, and if harnessed efficiently, the greenhouse effect can be alleviated. A thermoelectric generator (TEG) is one of the energy harvesters that converts thermal energy directly into electrical energy [2]–[5]. A selective absorber exposed under the sun can absorb solar radiation energy and convert it into thermal energy for TEG, leading to a solar TEG (STEG). A TEG does not only operate in the daytime but also at nighttime; it has no moving parts, no noise, or vibration [6]. In the last decade, research interest in solar TEGs (STEGs) has increased significantly; this is to ensure optimum utilization of the solar spectrum. For example, Bekele and Ancha [7] proposed a solar concentrator integrated with Stirling and TEG to power a water pump for irrigation purposes. The TEG achieved a maximum output power of 5.2 W and an energy conversion efficiency of 2.78%. Although the system is capable of powering a water pump, the authors suggested that the system needs further optimization. Liu et al. [8] developed a solar selective absorber (CuCrMnCoAlN-based) to enhance the performance of a STEG. The as-synthesized solar selective absorber has an absorptivity of 95.2% and emissivity of 10.9%. Integrating the solar absorber with a commercial STEG results in an output power of 1.99 mW. Sun et al. [9] developed a transient model of STEG using a three-dimensional numerical model. For a solar concentration ratio of 150, the annual energy production of the developed model was 49.79 kW/h, and the cost-recovery cycle was found to be 1.61 years. Alobaid et al. [10] compared the thermo-mechanical performance of frustrum-shaped, trapezoidal-shaped, and rectangular-shaped thermoelectric legs using a three-dimensional finite element model. The study also reveals that the output performance prediction using a neural network is 702 times faster than the performance prediction using the numerical analysis method.

STEGs like photovoltaics operate only during the day; however, nighttime operation can be achieved by coupling phase change material (PCM) on the hot side of the STEG. The PCM absorbs and stores a large amount of solar energy until phase transformation is completed [11], [12]. Thus, the PCM provides

\*Corresponding Author: Aminu YUSUF, [aminu.yusuf@iuc.edu.tr](mailto:aminu.yusuf@iuc.edu.tr)

stable and uniform thermal energy to the STEG during and after the sunshine hours. Since most of the commercial PCMs have poor heat transfer due to low thermal conductivity, the thermal performance can be increased by mixing metal particles with the PCM [13]. PCM can also serve as a heat sink when integrated on the cold side of the STEG [14]. In this manner, the PCM absorbs and stores the heat from the cold side of the STEG.

Using a different approach, radiative cooling (RC) can be employed to achieve 24-hour power generation of the STEG [15]. Radiative cooling passively cools the cold side temperature of the STEG in the daytime, nighttime, and a combination of the two [16]. The RC reflects the solar energy in the daytime and emits radiation at nighttime through a sky window (wavelength between 8 – 13  $\mu\text{m}$ ) [17]. An ideal RC for 24-hour operation should have high solar energy reflectivity in the daytime and high emissivity at nighttime. However, an ideal radiative cooling material has not been found yet. In the past, radiative cooling technology has been used in the cooling of photovoltaics, buildings, power plant condensers, and dew water harvesting [18]. The radiative cooling technology is capable of lowering the temperature of a surface to 14  $^{\circ}\text{C}$  and 12  $^{\circ}\text{C}$  below the ambient temperature in laboratory and outdoor tests, respectively [19]. This indicates that RC can significantly enhance the output performance of a STEG. To validate that, Liu et al. [20] developed a model of TEG integrated with a heat sink – RC (TEG-HS-RC) and another model consisting of only TEG-HS. The analysis revealed that the TEG-HS-RC model is superior to the TEG-RH model by about 32%.

Although STEG has been extensively studied, the integration of radiative cooling with the STEG has only been recently considered; hence, many research gaps need to be addressed. Most importantly, the STEG-RC operates outdoors; therefore, its operation can be influenced by weather parameters. In line with that, this study is carried out to determine the influence of ambient temperature, wind speed, relative humidity, and solar irradiance on the output performance of the STEG-RC. Additionally, the influence of concentrating solar energy on the operation of the STEG-RC is investigated.

## 2. MATERIAL AND METHODS

The model presented in Figure 1 consists of a solar concentrator (reflective mirror), an STEG coated with a selective absorber on the hot side, and a radiative cooler on the cold side. Solar energy is concentrated on the hot side of the STEG where the energy is absorbed by the selective absorber. On the hot side, both radiation and convection losses occur, and eventually, the STEG converts part of the absorbed energy into electrical power while the rest is transferred to the cold side via conduction. The balanced energy transfer process is mathematically given as:

$$A_{TE}CG\tau_g\alpha_{sa} = A_{TE}\varepsilon\sigma_s(T_h^4 - T_{sky}^4) + A_{TE}h_{conv}(T_h - T_a) + \frac{N[S(T_h - T_c)]^2}{4R} + \frac{T_c - T_{rc}}{R_{c-rc}} \quad (1)$$

where the term on the left-hand side is the energy input, the first and second terms on the right-hand side are the radiation and convection losses, and the third and fourth terms are the maximum output power and energy transferred by conduction.  $C$  and  $G$  are the concentration ratio and solar irradiance,  $\tau_g$  and  $\alpha_{sa}$  are the transmissivity of glass and absorptivity of the selective absorber,  $\varepsilon$  and  $\sigma_s$  are the emissivity of the hot side and Stefan Boltzmann constant,  $N$  is the number of thermocouples,  $T_{sky}$  is the temperature of the sky,  $T_h$  and  $T_c$  are the temperatures of hot and cold sides,  $T_{rc}$  and  $R_{c-rc}$  are the temperature of the radiative cooler and the thermal resistance between the cold side and the radiative cooler,  $S$ ,  $A_{TE}$ ,  $R$  are the Seebeck coefficient, surface area, and internal resistance of the STEG, respectively. A windshield cover is not integrated into this model; therefore, the convective heat transfer coefficient can be given as [21]:

$$h_{conv} = 8.3 + 2.5v \quad (2)$$

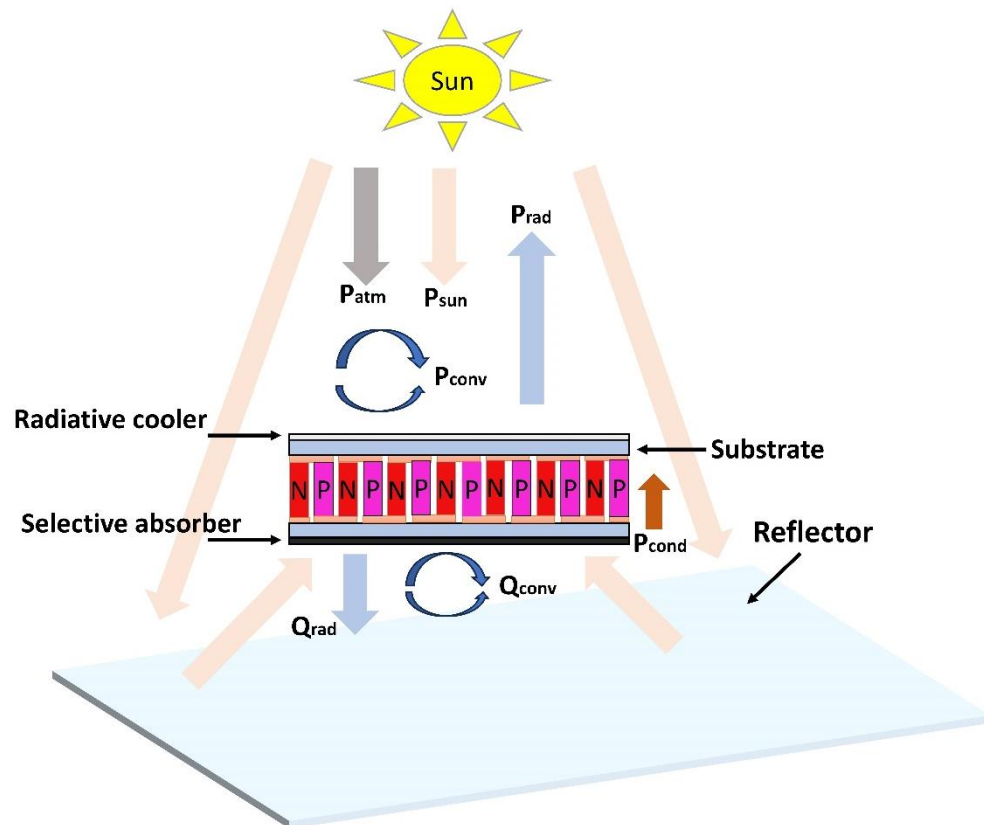


**Figure 1.** Solar-concentrated thermoelectric generator

The density of the energy transferred by conduction from the hot side to the cold is the same as the density of the energy transferred from the cold side to the radiative cooler and is given as:

$$P_{cond} = \frac{T_h - T_c}{A_{TE} R_{KTE}} = \frac{T_c - T_{rc}}{A_{TE} R_{c-rc}} \quad (3)$$

At a steady state, the sum of the energy radiated by the radiative cooler and the convection loss should be equal to the sum of the energy absorbed by the radiative cooler, atmospheric energy absorption by the radiative cooler, and the energy absorbed through the conduction:

$$P_{rad} + P_{conv} = P_{sun} + P_{atm} + P_{cond} \quad (4)$$

The energy radiated by the radiative cooler also known as the cooling power is [22]:

$$P_{rad}(T_{rc}) = \int_0^{2\pi} d\varphi \int_0^{\frac{\pi}{2}} \sin\theta \cos\theta d\theta \int_0^{\infty} I_{bb}(\lambda, T_{rc}) \varepsilon_{rc}(\lambda, \theta, \varphi) d\lambda \quad (5)$$

where  $\varphi$  is the solid angle,  $\theta$  is the zenith angle,  $\lambda$  is the wavelength,  $\varepsilon_{rc}(\theta, \lambda)$  is the emissivity of radiative cooler, the spectral radiance of a blackbody  $I_{bb}(\lambda, T_{rc})$  at temperature  $T_{rc}$  is defined as [23]:

$$I_{bb}(\lambda, T_{rc}) = \frac{2hc^2}{\lambda^5 \left( e^{\frac{hc}{\lambda k T_{rc}}} - 1 \right)} \quad (6)$$

where Planck's constant  $h = 6.626 \times 10^{-34}$  J s, Boltzmann constant  $k = 1,381 \times 10^{-23}$  J/K, speed of light  $c = 2,998 \times 10^8$  m/s.

The convection density is thus given as:

$$P_{conv} = h_{conv}(T_{rc} - T_a) \quad (7)$$

The sun energy absorbed by the radiative cooler can be calculated from:

$$P_{sun} = \int_0^{\infty} I_{solar}(\lambda) \varepsilon_{rc}(\lambda) \cos\theta d\lambda \quad (8)$$

where  $I_{solar}(\lambda)$  is the solar spectral irradiation intensity.

The atmospheric power absorbed by the radiative cooler is given as:

$$P_{atm}(T_a) = \int_0^{\infty} \int_0^{2\pi} \int_0^{\frac{\pi}{2}} \alpha_{rc}(\lambda, \theta, \varphi) I_{\lambda,b}(T_a, \lambda) \varepsilon_{atm}(\lambda, \theta) \sin\theta \cos\theta d\lambda d\varphi d\theta \quad (9)$$

where  $T_a$  is the ambient temperature,  $I_{\lambda,b}(T_a, \lambda)$  is the spectral irradiance of a blackbody at the ambient temperature,  $\alpha_{rc}(\lambda, \theta, \varphi)$  is the absorptivity of the radiative cooler,  $\varepsilon_{atm}(\lambda, \theta)$  is the atmospheric emissivity given as [24]:

$$\varepsilon_{atm} = 0.727 + 0.006T_{dew} \quad (10)$$

where  $T_{dew}$  (°C) is the dew point temperature, which is calculated from:

$$T_{dew} = \frac{243.12 \left[ \ln\left(\frac{RH}{100}\right) + \frac{17.62T_a}{243.12 + T_a} \right]}{17.62 - \left[ \ln\left(\frac{RH}{100}\right) + \frac{17.62T_a}{243.12 + T_a} \right]} \quad (11)$$

where the unit of  $T_a$  in Eq. 11 is °C. The relationship between the temperature of the sky and the emissivity of the sky is:

$$T_{sky} = \varepsilon_{atm}^4 T_a \quad (12)$$

The thermal resistance between the cold side and the radiative cooler is:

$$R_c = \frac{L_c}{K_c A_c} \quad (13)$$

where  $L_c$  is the thickness of the cold side,  $K_c$  and  $A_c$  are the thermal conductivity and surface area of the cold side.

The internal resistance of a unicouple STEG, which is used to calculate the output power is:

$$R = \frac{L_p}{\sigma_p A_p} + \frac{L_n}{\sigma_n A_n} \quad (14)$$

where  $L$  is the length of the TE leg,  $A$  is the cross-sectional area of the TE legs,  $\sigma$  is the electrical conductivity,  $k$  is the thermal conductivity, subscripts  $p$  and  $n$  represent the type of TE materials.

The thermal resistance of the STEG is one of the factors that affects the temperature gradient of the STEG. The temperature gradient increases with an increase in the thermal resistance. As given in equation 15, the longer the leg length, the higher the thermal resistance.

$$R_{KTE} = \frac{L}{N(A_n k_n + A_p k_p)} \quad (15)$$

Herein, the adopted radiative cooler (TiO<sub>2</sub> + SiO<sub>2</sub>) has a reflectivity in the solar spectrum of 90.7% and an emittance of 90.11% in the sky window [25]. Likewise, Al<sub>2</sub>O<sub>3</sub>-filled nanocavity photonic crystal is the adopted selective absorber with an average solar absorptivity of 0.8 in the solar spectrum [26]. The

transport properties of the TE materials are given in Table 1 and the parameters of STEG are given in Table 2.

**Table 1. Thermoelectric properties of the chalcogenides [27]**

Property	Expression
$S_p$	$(1.023898 - 7.301 \times 10^{-3} T + 2.22834 \times 10^{-5} T^2 - 2.24407 \times 10^{-8} T^3) \times 10^{-3}$ V/K
$S_n$	$(-9.54589 \times 10^{-4} + 6.203 \times 10^{-6} T - 1.77163 \times 10^{-8} T^2 + 1.68178 \times 10^{-11} T^3)$ V/K
$\sigma_p$	$(1.60117 \times 10^{-5} - 0.01853 \times 10^{-5} T + 7.77051 \times 10^{-10} T^2 - 7.75456 \times 10^{-13} T^3)$ S/m
$\sigma_n$	$(2.11951 \times 10^{-5} - 1.715 \times 10^{-7} T + 6.09155 \times 10^{-10} T^2 - 6.04782 \times 10^{-14} T^3)$ S/m
$k_p$	$(8.726 - 0.05011 T + 1.03491 \times 10^{-4} T^2 - 5.82609 \times 10^{-8} T^3)$ W/(m K)
$k_n$	$(5.09531 - 0.02057 T + 2.81722 \times 10^{-5} T^2 + 3.76869 \times 10^{-9} T^3)$ W/(m K)

**Table 2. Parameters of the STEG**

Parameter	value
TE leg	$1 \times 1 \times 1.5$ mm <sup>3</sup>
Number of TE couples	127
Thickness of Al <sub>2</sub> O <sub>3</sub> substrate	0.5 mm <sup>3</sup>
Thickness of copper electrode	50 μm
Thickness of radiative cooler	10 μm
Thickness of selective absorber	10 μm
Thickness of glass cover	1 mm
Module size	$40 \times 40 \times 2.6$ mm <sup>3</sup>

The above equations are solved in MATLAB to determine the cooling performance of the radiative cooler and the output power of the STEG. Unlike stated otherwise, the ambient temperature of 23 °C, relative humidity of 30%, solar radiation of 1000 W/m<sup>2</sup>, and wind speed of 2 m/s are used.

### 3. RESULTS AND DISCUSSION

To determine the effect of solar concentration on both the performance of the radiative cooler and the STEG, the performance of concentrated ( $C = 5$ ) and unconcentrated ( $C = 1$ ) STEGs is investigated. The operation of both the radiative cooler and STEG strongly depends on weather parameters such as ambient temperature, relative humidity (RH), wind speed, and solar irradiance. The influence of these parameters, one at a time, is parametrically investigated.

#### 3.1. Influence of ambient temperature on the output performance of the STEG-RC

As shown in Figure 2, the ambient temperature is varied from 5 °C to 45 °C to cover four weather seasons of a typical city in the Mediterranean region (Antalya, Türkiye). Figure 2a presents the hot and cold side temperatures of the STEG and the temperature of the radiative cooler at  $C = 1$ . The temperatures monotonically increase with the increase in the ambient temperature. The temperature gradient of the STEG decreases with the increase in the ambient temperature, and at a particular point, the temperature gradient approaches zero. The temperatures of the cold side and the radiative cooling surface are almost identical because the thermal resistance between the two surfaces is very low. Figure 2b presents the output power of the unconcentrated STEG and the radiative cooling power. The output power decreases with the increase in the ambient temperature due to the decrease in the temperature gradient. At  $T_a = 5$  °C, the STEG generates an output power of 4 mW, while it reduces to zero at  $T_a = 45$  °C. On the contrary, the radiative cooling power increases with the increase in the ambient temperature; this is mainly due to the increase in spectral radiance. At  $T_a = 5$  °C, the RC cooling power is about zero, while it increases to 135 W/m<sup>2</sup> at  $T_a = 45$  °C. Figure 2c presents the variation of the temperatures of the hot and cold sides and the temperature of the RC surface at  $C = 5$ . The temperatures increase with the

increase in the ambient temperature. Unlike in Figure 2a, where the temperature gradient approaches zero with the increase in the ambient temperature, a substantive temperature gradient is maintained in Figure 2c because the hot side kept increasing due to the concentration of solar energy. Figure 2d shows the output power of the STEG and the cooling power of RC at  $C = 5$ . The output power reduces from 510 mW to 30 mW, while the cooling power increases from 160 W/m<sup>2</sup> to 230 W/m<sup>2</sup> as the ambient temperature increases from 5 °C to 45 °C. These results indicate that the ambient temperature has a negative impact on the output performance of STEGs while it has a positive influence on the cooling performance of the RC. It can also be seen that by concentrating the solar energy by a ratio of 5, the cooling power is enhanced by 70.4%, and the output power is enhanced by more than 500%, indicating that concentrating the solar energy is the best way of enhancing the output performance of the STEG-RC.

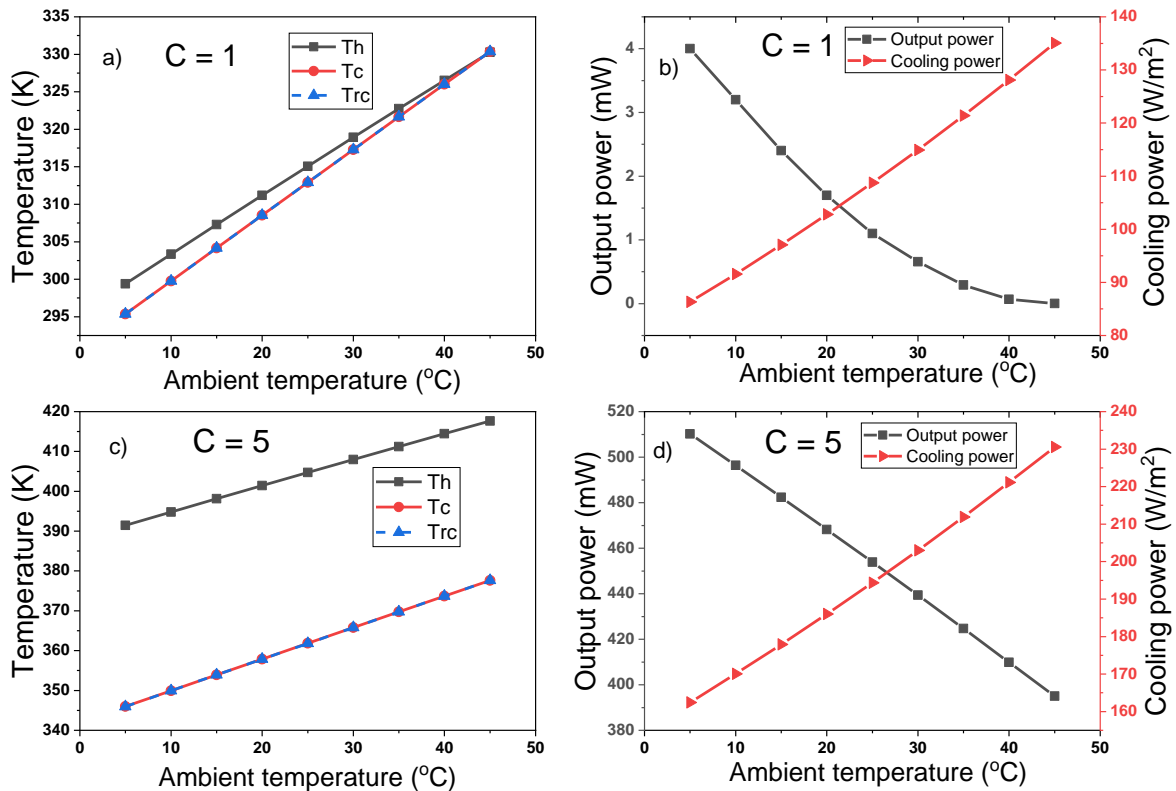


**Figure 2.** Effect of ambient temperature on a) temperatures of un-concentrated STEG, b) output power of un-concentrated STEG, c) temperatures of concentrated STEG, d) output power of concentrated STEG

### 3.2. Influence of relative humidity on the output performance of the STEG-RC

Figure 3 shows the effect of variations in relative humidity (RH) on the temperatures, output power, and cooling power for both concentrated and un-concentrated STEGs. As RH is varied from 10% to 90%, temperatures of both the STEG and RC slightly increase, as shown in Figure 3a. This result indicates that RH does not have much influence on the temperatures because its primary effect is on atmospheric emissivity through the dew point temperature. Figure 3b presents the output power of the STEG and the cooling power of the RC at  $C = 1$ . The output power reduces with the increase in RH from 10% to 60%, after which it remains almost stable at about 1.2 mW. The cooling power, on the other hand, shows only a slight increase over the range of RH variation. A maximum cooling power of 106.8 W/m<sup>2</sup> is achieved at RH = 90%. Figure 3c presents the variation of the temperatures of the STEG and RC at  $C = 5$ . Over the range of RH variation, the temperature of the hot side remains almost constant, while the temperatures

of the cold side and RC surface slightly increase. This means that the temperature gradient of the STEG decreases with the increase in RH, as can be understood from the output power in Figure 3d. The output power reduces by about 1.5%, while the cooling power increases by 0.84% as RH is increased from 10% to 90%. In summary, RH has an insignificant influence on the output performance of both the STEG and RC for the concentrated and unconcentrated cases.

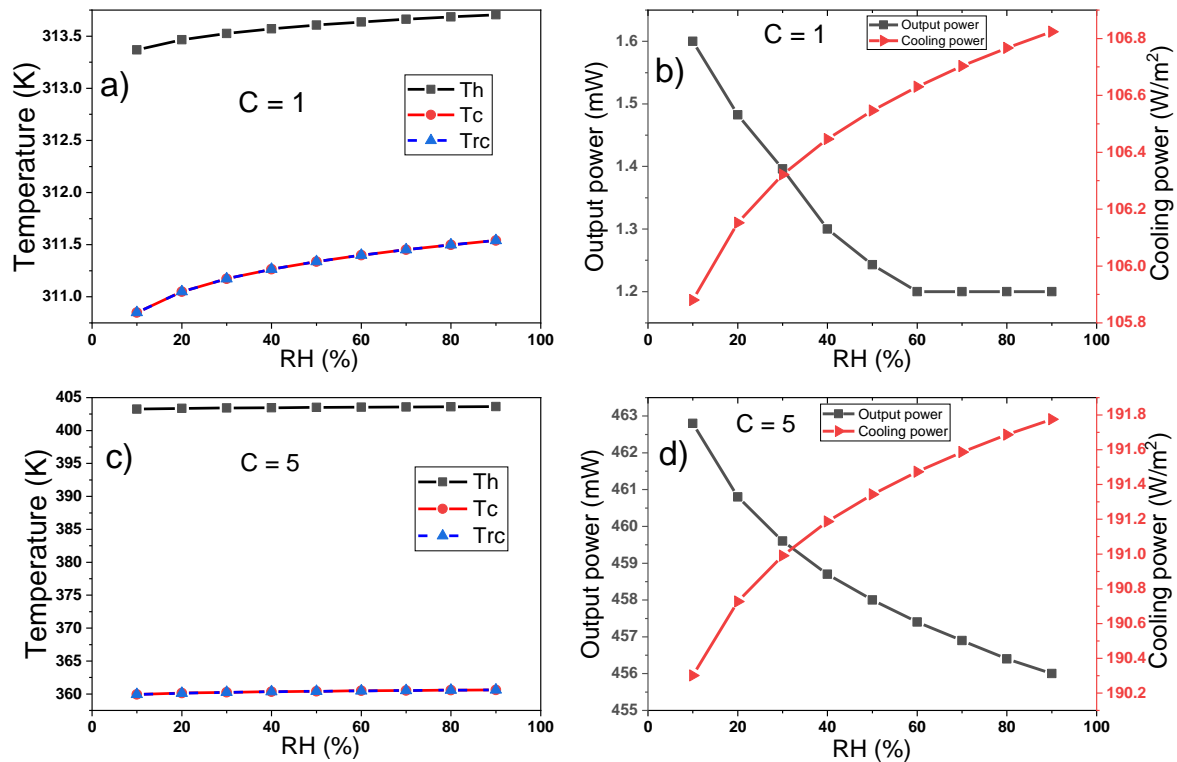


**Figure 3.** Effect of Relative humidity on a) temperatures of unconcentrated STEG, b) output power of unconcentrated STEG, c) temperatures of concentrated STEG, d) output power of concentrated STEG

### 3.3. Influence of wind speed on the output performance of the STEG-RC

The variation in temperatures of the unconcentrated STEG and RC surface with wind speed is shown in Figure 4a. Wind speed is associated with convection energy, and as wind speed increases, convection cooling also increases. Convection cooling affects both the hot and cold sides of the STEG, leading to a decrease in temperatures with an increase in wind speed. As wind speed is varied from 0 to 8 m/s, the temperature gradient increases from 1.9 to 2.5 K, resulting in the enhancement of output power as shown in Figure 4b. It can be observed that the output power starts decreasing once the optimum wind speed is exceeded. Determining the optimum wind speed is crucial to achieve the best output performance of a STEG. It should be noted that wind speed has a different impact on the cooling power of the RC. As per Equation 4, it is obvious to see that as wind speed increases, convection losses increase, which, in turn, decreases radiative cooling power. As wind speed increases from 0 to 8 m/s, the radiative cooling power decreases from 116  $W/m^2$  to 96  $W/m^2$ , indicating that wind speed has a negative influence on cooling power. This is why a wind shield is usually employed in radiative cooling applications. Figure 4c presents the temperatures of the STEG and RC surface at C = 5. Figure 4c and Figure 4a show a similar trend, indicating that wind speed has the same effect on both concentrated and unconcentrated solar energy. Initially, the output power in Figure 4d increases and then decreases with the increase in wind speed. As mentioned earlier, the output power has a maximum value at the optimum wind speed. Herein, a maximum output power of 459.6 mW is achieved at the optimum wind speed of 2 m/s. As seen

in Figure 4b, the radiative cooling power in Figure 4d also decreases with the increase in wind speed for the same reasons mentioned earlier. As wind speed increases from 0 to 8 m/s, the radiative cooling power decreases from 255.7 W/m<sup>2</sup> to 128 W/m<sup>2</sup>. In summary, wind speed has a negative effect on the radiative cooler; however, the optimum wind speed enhances the output power of a STEG.

Top of Form

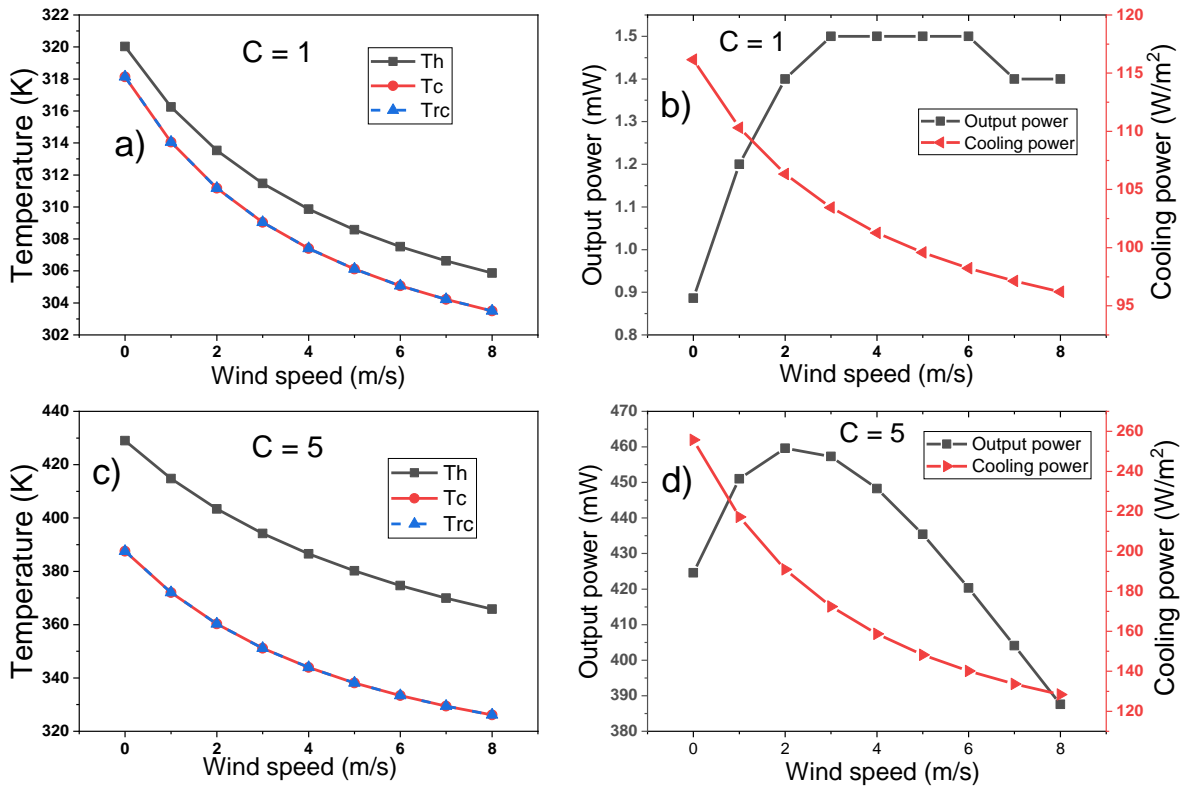


**Figure 4.** Effect of wind speed on a) temperatures of un-concentrated STEG, b) output power of un-concentrated STEG, c) temperatures of concentrated STEG, d) output power of concentrated STEG

### 3.4. Influence of solar irradiance on the output performance of the STEG-RC

Figure 5a presents the variation in temperatures of the STEG and RC surface with the variation in solar irradiance for the un-concentrated STEG. For a typical winter case (low solar irradiance), the surface temperature of the RC is higher than the temperature of the hot side. As solar irradiance increases from 100 W/m<sup>2</sup> to 700 W/m<sup>2</sup>, the temperature of the hot side increases and becomes equal to the surface temperature of the RC. A further increase in solar irradiance leads to a further increase in the hot side temperature above the surface temperature of the RC. Figure 5b presents the output power of the STEG and the radiative cooling power of the RC at C = 1. Typically, a negative output power is expected when the temperature of the cold side is higher than that of the hot side due to the reverse current flow. However, in this analysis, absolute values of the output power are considered. Having said that, the output power decreases from 7.1 mW to 0 mW as solar irradiance increases from 100 W/m<sup>2</sup> to 700 W/m<sup>2</sup>, after which the output power slightly increases. On the contrary, the radiative cooling power increases linearly with the increase in solar irradiance, in agreement with equation 5.

Figure 5c shows the temperatures of the STEG and the surface of RC with the variation of solar irradiance at C = 5. At a solar irradiance of 100 W/m<sup>2</sup>, the temperatures have the same values; however, as solar irradiance increases, the hot side temperature becomes increasingly higher than the other temperatures. This is because the hot side receives 5-fold more energy than the cold side/RC. Figure 5d

presents the output power and the radiative cooling power at  $C = 5$ . The output power exponentially increases from 0 to 375 mW as solar irradiance increases from 100  $\text{W}/\text{m}^2$  to 900  $\text{W}/\text{m}^2$ . Similarly, the radiative cooling power increases linearly with solar irradiance. A maximum radiative cooling power of 180  $\text{W}/\text{m}^2$  is achieved at a solar irradiance of 900  $\text{W}/\text{m}^2$ . In summary, the unconcentrated STEG should not be operated at low solar irradiance to avoid reverse current flow. On the other hand, solar irradiance has a positive influence on the output power of the concentrated STEG. In both concentrated and unconcentrated cases, the radiative cooling power linearly increases with solar irradiance.

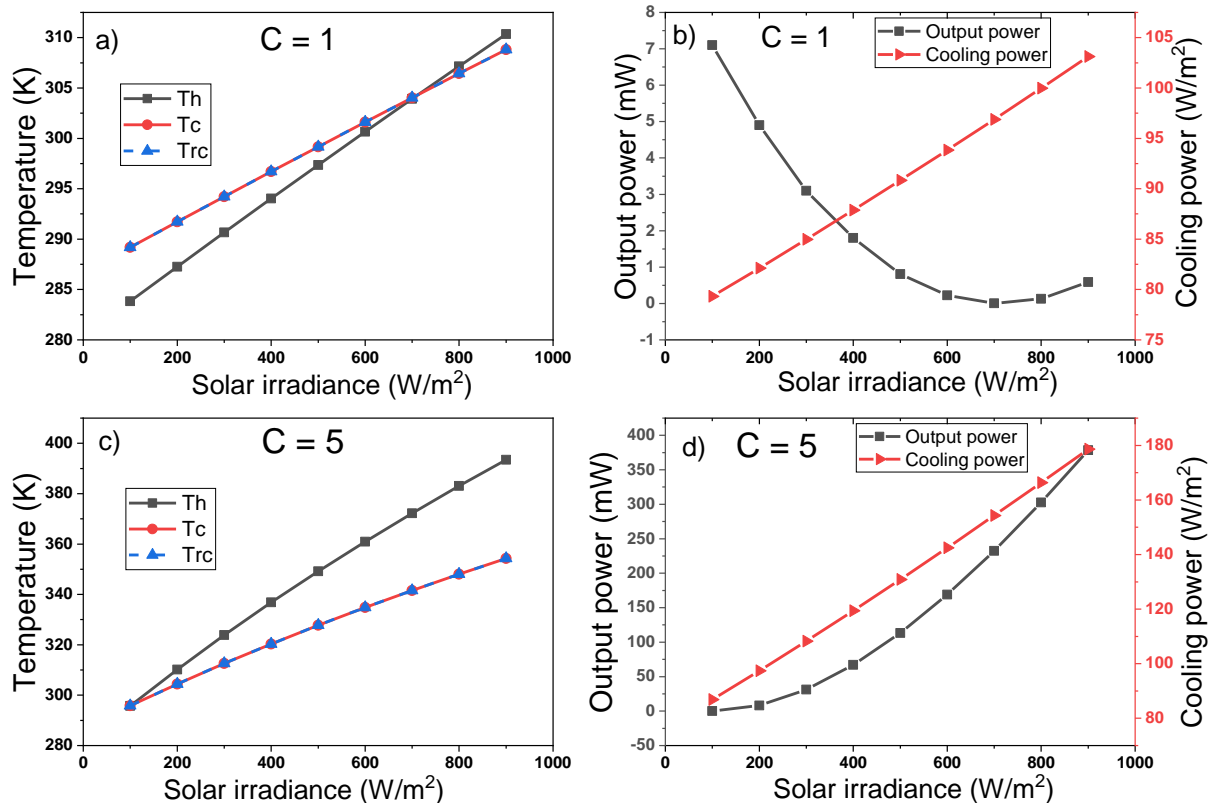


**Figure 5.** Effect of solar irradiance on a) temperatures of unconcentrated STEG, b) output power of unconcentrated STEG, c) temperatures of concentrated STEG, d) output power of concentrated STEG

The average cost of the unconcentrated and concentrated STEG-RC systems is about \$10 and \$50, respectively [28, 29]. A typical thermoelectric generator with chalcogenide TE materials operates in a temperature range of 300 – 500 K, which is the temperature range covered by this study. When operated properly, it can have a lifespan of 20 years or more [30], indicating its suitability for long-term energy harvesting applications. This also means a relatively competitive levelized cost of energy.

#### 4. CONCLUSIONS

This study presents a steady-state theoretical analysis of STEG-RC for both concentrated and unconcentrated cases. Since the STEG-RC is expected to operate outdoors, the effect of weather parameters on the system's output performance needs to be determined. Based on the results presented, the main findings can be summarized as follows:

- Concentrating solar energy is the most effective way to enhance the output performance of STEG-RC.
- Ambient temperature negatively affects the output of the STEGs. At  $C = 5$ , the output power reduces from 510 mW to 395 mW when the ambient temperature increases from 5  $^{\circ}\text{C}$  to 45  $^{\circ}\text{C}$ .

Similarly, the output power of the unconcentrated STEG reduces from 4 mW to 0 mW when the temperature changes from 5 °C to 45 °C.

- Relative humidity has an insignificant influence on both the output power and the radiative cooling power.
- An optimum wind speed is required to achieve the maximum output power of STEG-RC. The optimum wind speed is found to be 3 m/s and 2 m/s for  $C = 1$  and  $C = 5$ , respectively.
- Solar irradiance has a negative influence on the output power of the unconcentrated STEG; however, it has a positive influence on the output power of the concentrated STEG. The radiative cooling power also increases linearly with solar irradiance for both concentrated and unconcentrated cases.

Although the concentrated STEG-RC has higher output performance compared to the unconcentrated case, long-term exposure to the sun may lower the output performance due to the low cooling performance of the radiative cooler. This limitation can be clearly seen in transient analysis, which is considered one of the future research directions of this study. It should also be noted that in practice, a single or dual-axis solar tracker is needed for the concentrated STEG-RC system, which means additional energy consumption for the system. Having said that, these two limitations are minimal for the unconcentrated STEG-RC system. Therefore, by integrating a heat sink with the radiative cooler, the output performance of the unconcentrated STEG-RC can be further enhanced.

### Funding / Acknowledgement

This research is funded by the Scientific and Technological Research Council of Türkiye with Project number 123E144 and Scientific Research Unit of Istanbul University-Cerrahpaşa with Project number FBA-2023-37401.

### REFERENCES

- [1] M. A. Zoui, S. Bentouba, D. Velauthapillai, N. Zioui, and M. Bourouis, "Design and characterization of a novel finned tubular thermoelectric generator for waste heat recovery", *Energy*, Aug., vol. 253, p. 124083, 2022.
- [2] D. Astrain, J. J. Fernandez, M. Araiz, A. Francone, L. Catalan, A. J. -Martín, P. Alegría, and C. M. S.-Torres, "Enhanced behaviour of a passive thermoelectric generator with phase change heat exchangers and radiative cooling", *Applied Thermal Engineering*, May, vol. 225, p. 120162, 2023.
- [3] A. Yusuf and S. Ballikaya, "Electrical, thermomechanical and cost analyses of a low-cost thermoelectric generator", *Energy*, Feb., vol. 241, p. 122934, 2022.
- [4] S. Qing, H. Yuan, C. Chen, S. Tang, X. Wen, J. Zhong, and X. Gou, "Characteristics and single/multi-objective optimization of thermoelectric generator by comprehensively considering inner-connection-and-contact effects and side-surface heat loss", *Energy Conversion and Management*, Jan., vol. 251, p. 115003, 2022.
- [5] T. Koshi, K. Okawa, Y. Amagai, N. Sakamoto, K. Nomura, and M. Yoshida, "High-performance stretchable thermoelectric generator using serpentine interconnects encapsulated in an ultrasoft silicone sponge", *Flex. Print. Electron.*, vol. 7, no. 2, p. 025008, 2022.
- [6] A. Yusuf, Y. Demirci, T. Maras, S. E. Moon, J. Pil-Im, J. H. Kim, and S. Ballikaya, "Experimental and Theoretical Investigation of the Effect of Filler Material on the Performance of Flexible and Rigid Thermoelectric Generators", *ACS Appl. Mater. Interfaces*, vol. 13, no. 51, pp. 61275–61285, 2021.
- [7] E. A. Bekele and V. R. Ancha, "Transient performance prediction of solar dish concentrator integrated with stirling and TEG for small scale irrigation system: A case of Ethiopia", *Heliyon*, vol. 8, no. 9, p. e10629, 2022.
- [8] X. Liu, P. Zhao, C.-Y. He, W.-M. Wang, B.-H. Liu, Z.-W. Lu, Y.-F. Wang, H.-X. Guo, G. Liu, and X.-H. Gao, "Enabling Highly Enhanced Solar Thermoelectric Generator Efficiency by a

- CuCrMnCoAlN-Based Spectrally Selective Absorber", *ACS Appl. Mater. Interfaces*, Vol. 14, no. 44, pp. 50180-50189, 2022.
- [9] Z. Su, D. Luo, R. Wang, Y. Li, Y. Yan, Z. Cheng, and J. Chen, "Evaluation of energy recovery potential of solar thermoelectric generators using a three-dimensional transient numerical model", *Energy*, Oct., vol. 256, p. 124667, 2022.
- [10] M. Alobaid, C. Maduabuchi, A. Albaker, A. Almalaq, M. Alanazi, and T. Alsuwian, "Machine learning and numerical simulations for electrical, thermodynamic, and mechanical assessment of modified solar thermoelectric generators", *Applied Thermal Engineering*, Feb., vol. 220, p. 119706, 2023.
- [11] A. Yusuf and S. Ballikaya, "Performance analysis of concentrated photovoltaic systems using thermoelectric module with phase change material", *Journal of Energy Storage*, Mar., vol. 59, p. 106544, 2023.
- [12] K. Karthick, S. Suresh, M. M. M. D. Hussain, H. M. Ali, and C. S. S. Kumar, "Evaluation of solar thermal system configurations for thermoelectric generator applications: A critical review", *Solar Energy*, Aug., vol. 188, pp. 111-142, 2019.
- [13] H. Jo, Y. Joo, and D. Kim, "Thermal design of solar thermoelectric generator with phase change material for timely and efficient power generation", *Energy*, Jan., vol. 263, p. 125604, 2023.
- [14] J. Ko, S.-Y. Cheon, Y.-K. Kang, and J.-W. Jeong, "Design of a thermoelectric generator-assisted energy harvesting block considering melting temperature of phase change materials", *Renewable Energy*, Jun., vol. 193, pp. 89-112, 2022.
- [15] Z. Xia, Z. Zhang, Z. Meng, and Z. Yu, "A 24-hour thermoelectric generator simultaneous using solar heat energy and space cold energy", *Journal of Quantitative Spectroscopy and Radiative Transfer*, Aug., vol. 251, p. 107038, 2020.
- [16] H. Pan and D. Zhao, "An improved model for performance predicting and optimization of wearable thermoelectric generators with radiative cooling", *Energy Conversion and Management*, May, vol. 284, p. 116981, 2023.
- [17] J. Guo and X. Huai, "Maximizing Electric Power through Spectral-Splitting Photovoltaic-Thermoelectric Hybrid System Integrated with Radiative Cooling", *Advanced Science*, vol. 10, no. 10, p. 2206575, 2023.
- [18] D. Zhao, A. Aili, Y. Zhai, S. Xu, G. Tan, X. Yin, and R. Yang, "Radiative sky cooling: Fundamental principles, materials, and applications", *Applied Physics Reviews*, vol. 6, no. 2, p. 021306, 2019.
- [19] L. Zhou, H. Song, N. Zhang, J. Rada, M. Singer, H. Zhang, B. S. Ooi, Z. Yu, and Q. Gan, "Hybrid concentrated radiative cooling and solar heating in a single system", *Cell Reports Physical Science*, vol. 2, no. 2, p. 100338, 2021.
- [20] J. Liu, Y. Zhang, D. Zhang, S. Jiao, Z. Zhang, and Z. Zhou, "Model development and performance evaluation of thermoelectric generator with radiative cooling heat sink", *Energy Conversion and Management*, Jul., vol. 216, p. 112923, 2020.
- [21] D. Zhao, A. Aili, Y. Zhai, J. Lu, D. Kidd, G. Tan, X. Yin, and R. Yang, "Subambient Cooling of Water: Toward Real-World Applications of Daytime Radiative Cooling", *Joule*, vol. 3, no. 1, pp. 111-123, 2019.
- [22] Y. Ji and S. Lv, "Experimental and numerical investigation on a radiative cooling driving thermoelectric generator system", *Energy*, Apr., vol. 268, p. 126734, 2023.
- [23] C.-H. Wang, H. Chen, Z.-Y. Jiang, and X.-X. Zhang, "Design and experimental validation of an all-day passive thermoelectric system via radiative cooling and greenhouse effects", *Energy*, Jan., vol. 263, p. 125735, 2023.
- [24] P. Berdahl and R. Fromberg, "The thermal radiance of clear skies," *Solar Energy*, vol. 29, no. 4, pp. 299-314, 1982.

- [25] H. Bao, C. Yan, B. Wang, X. Fang, C. Y. Zhao, and X. Ruan, "Double-layer nanoparticle-based coatings for efficient terrestrial radiative cooling", *Solar Energy Materials and Solar Cells*, Aug., vol. 168, pp. 78–84, 2017.
- [26] D. Jiang, Z. Fan, M. Dong, Y. Shang, X. Liu, G. Chen, and S. Li, "Titanium nitride selective absorber enhanced solar thermoelectric generator (SA-STEG)", *Applied Thermal Engineering*, Aug., vol. 141, pp. 828–834, 2018.
- [27] C. Maduabuchi, C. Eneh, A. A. Alrobaian, and M. Alkhedher, "Deep neural networks for quick and precise geometry optimization of segmented thermoelectric generators", *Energy*, Jan., vol. 263, p. 125889, 2023.
- [28] Amazon, "SP1848-27145-Thermoelectric-Generator," 2023. [Online]. Available: <https://www.amazon.com/SP1848-27145-Thermoelectric-Generator-Temperature-Generation/dp/B07J54H41F>. [Accessed August 22, 2023].
- [29] Robotistan, "Solarx güneş takip sistemi - 2. nesil," 2023. [Online]. Available: <https://www.robotistan.com/solarx-gunes-takip-sistemi-elektronikli>. [Accessed September 20, 2023].
- [30] Ferrotec, "Reliability of thermoelectric cooling module," 2023. [Online]. Available: <https://thermal.ferrotec.com/technology/thermoelectric-reference-guide/thermalref10/> [Accessed September 20, 2023].